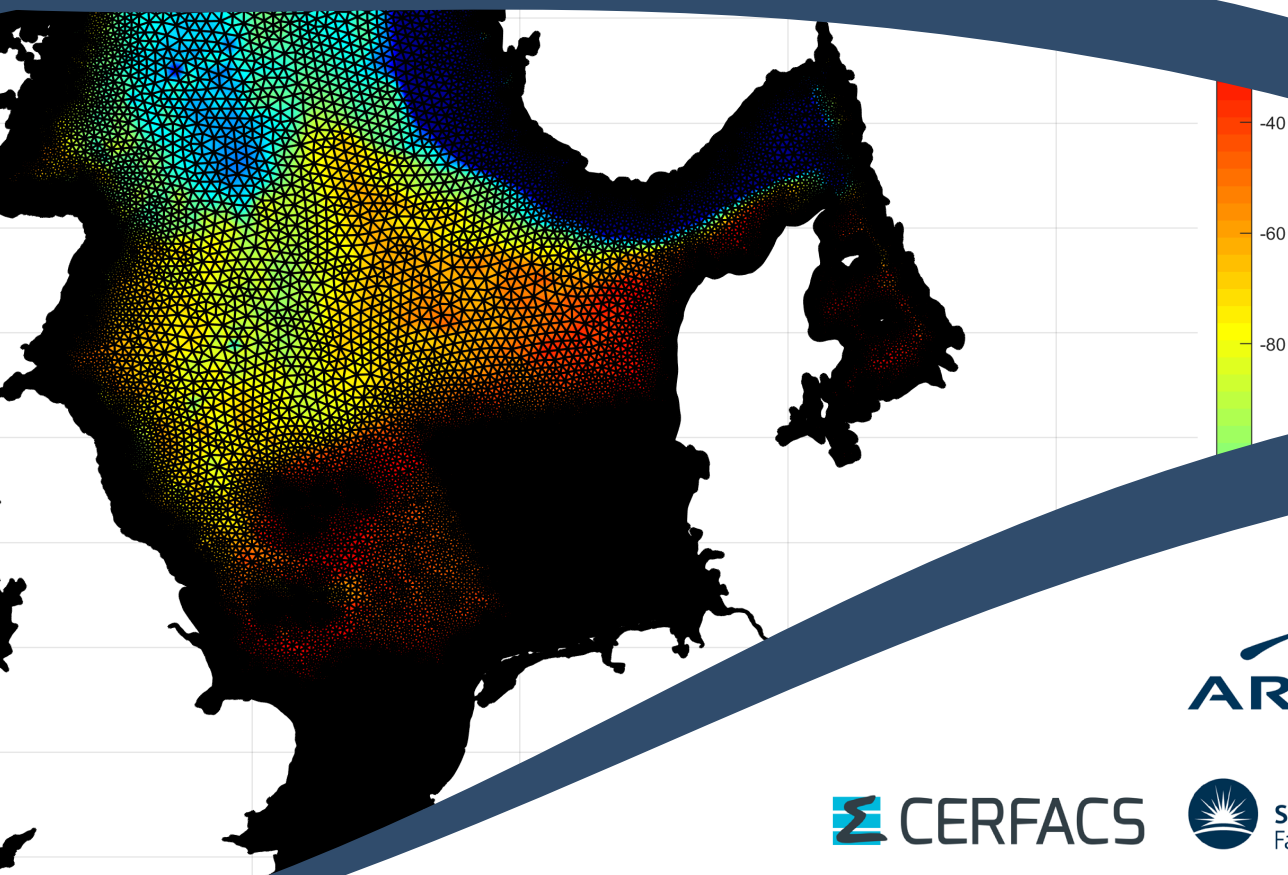




Online proceedings of the papers submitted to the  
**2020 TELEMAT-MASCARET**  
User Conference

October 2020

# TUC 2020



Online proceedings of the papers submitted to the  
**2020 TELEMAR-MASCARET**  
User Conference

**Organized by**

---

International Marine & Dredging Consultants (IMDC)  
Van Immerseelstraat 66  
2100 Antwerp  
Belgium  
Tel: +32 3 270 92 95  
tuc2020@imdc.be  
<https://tuc2020.org/>

**Edited by**

---

W.A. Breugem  
L Frederickx  
T Koutrouveli  
R Kulkarni  
K Chu  
B Decrop

**Design**

---

L Frederickx

**Published by**

---

©2020 International Marine & Dredging Consultants

ISBN 9789464207194

## TELEMAC-MASCARET Core Group



Artelia  
[www.arteliagroup.com](http://www.arteliagroup.com)



Bundesanstalt für Wasserbau  
Federal Waterways Engineering and Research Institute  
[www.baw.com](http://www.baw.com)



Centre d'études et d'expertise sur les risques,  
l'environnement, la mobilité et l'aménagement  
[www.cerema.fr](http://www.cerema.fr)



Centre Européen de Recherche et de Formation Avancée  
en Calcul Scientifique  
[www.cerfacs.fr](http://www.cerfacs.fr)



Électricité de France  
[www.edf.com](http://www.edf.com)



HR Wallingford  
[www.hrwallingford.com](http://www.hrwallingford.com)



Science and Technology Facilities Council  
[www.stfc.ac.uk](http://www.stfc.ac.uk)



## Introduction by the local organizers

October 2020

Dear TUC2020 delegates,

2020 has been a different year from all the previous ones. In the beginning of the year, it became clear that COVID-19 had developed into a global pandemic. By the end of spring, the pandemic seemed to be decreasing, which gave us hope that organising TELEMAC-MASCARET User Conference (TUC) could still be a reality. However, a second COVID-19 wave started developing in summer 2020. Therefore, it was not possible to organise the yearly TELEMAC-MASCARET User Conference, and we had to make the decision to postpone the conference by one year. Instead of the TUC, a webinar was organized on October 15<sup>th</sup> 2020 with over 190 participants from all over the world. Hopefully, the situation will normalize in the coming year, such that we will all be able to gather in Antwerp in October 2021 for the 27th TELEMAC- MASCARET User Conference.

At the moment when we took the decision to postpone the TUC, many papers had already been submitted. It was decided to publish the proceedings of the 2020 TUC, even though the conference was postponed, whereby all authors were given the option to submit their papers either for these proceedings or for the 2021 TUC. This has resulted in the submission of twenty-two papers for the present proceedings, covering various interesting topics related to almost all TELEMAC-MASCARET modules.

These proceedings would not be possible without the contribution of many people, which we would hereby like to thank. First of all, we are deeply indebted to the authors who contributed their papers. In addition, we would also like to extend our gratitude towards the reviewers from the TELEMAC consortium for their valuable comments on the papers.

The local organizing committee,

Alexander Breugem  
Lesley Frederickx  
Theofano Koutrouveli  
Kai Chu  
Rohit Kulkarni  
Boudewijn Decrop





## Introduction by the president of the TELEMAC consortium

October 2020

Dear TUC2020 delegates,

It is a great pleasure for me to introduce this online proceeding of the 2020 TELEMAC User Conference.

Indeed, 2020 has been a very special year forcing the open TELEMAC-MASCARET to adapt as we all had to do in our families and in our companies. This meant holding the scientific committee in a webinar format and postponing the TUC to 2021.

The TUC is a key moment for the open TELEMAC-MASCARET community: sharing results, discovering latest release and development, expressing needs and also meeting up with friends sharing the same interests. Hence, postponing the TUC to 2021 was a difficult decision to take, that was unanimously agreed facing the situation.

The webinar held at the date of the TUC allowed the new functionalities of the upcoming TELEMAC-MASCARET release (v8p2) to be presented. An overview of the present online proceedings was also shared. It was really a pleasure to share these moments with nearly 200 participants from all over the world.

It was felt that all the interesting material should not be kept apart for a year and that all the hard work to prepare these communications should really be rewarded by publishing this online proceeding.

On behalf of the open TELEMAC-MASCARET consortium, I want to sincerely thank all the IMDC team for preparing this proceeding with all reviewers, in particular Alexander Breugem for his dedicated coordination. All this would not be possible without the implication of all the authors who choose to share the findings and project results among the TELEMAC people : thank you, as this is what makes our community active and so interesting.

Excellent reading of these paper!  
Let's meet-up in 2021

Dr Sébastien DUPRAY

Chair-person of the open TELEMAC-MASCARET consortium  
Deputy Director Risks, waters and sea @Cerema

## Contents

---

### River, estuaries, maritime, coastal sediment processes

Implementation of a novel approach accounting for the influence of vegetation on sediment transport in GAIA, <i>Jiaze Li, Nicolas Claude, Pablo Tassi, Florian Cordier, Alessandra Crosato, Stéphane Rodrigues</i> .....	2
Numerical Modelling of Sediment Transport at Weirs, <i>Antonia Dallmeier, Markus Reisenbüchler, Minh Duc Bui, Peter Rutschmann</i> .....	9
Implementation of non-Newtonian rheological models in TELEMAC-2D, <i>Pierre-Louis Ligier</i> .....	14
Investigation on ETM response to the change of boundary forcing using 3CPBE flocculation model, <i>Qilong Bi, Xiaoteng Shen, Byung Joon Lee, and Erik Toorman</i> .....	26
Fine sediment deposits in gravel bed rivers: sensitivity analysis to particle properties using a 2D hydrodynamic and sediment model, <i>H. Haddad, M. Jodeau, N. Claude &amp; G. Antoine, C. Legout</i> .....	35
Numerical modelling of the effects of change in river channel morphology on flooding frequency in the Dijle valley, Belgium, using TELEMAC-2D modelling system, <i>Sardar Ateeq-Ur-Rehman, Jutta Meylemans, Ward Swinnen, Nils Broothaerts, Gert Verstraeten</i> .....	40
Development of a hydro-morphodynamic model for simulation of bed load and morphological changes of flash-floods (Têt River, France), <i>Sebastien Pinel, Fatma Cherif, Florian Meslard, Camille Labrousse, François Bourrin</i> .....	46
Comprehensive morphodynamical analysis of the Drava River, <i>Zoltán Árpád Liptay, Alexandra Gradwohl-Valkay, Johanna Ficsor, Ákos Halmi, Ervin Pirkohoffer, Szabolcs Czigány</i> .....	53
Simulation of natural levee laboratory experiments with TELEMAC-2D/SISYPHE, <i>Rebekka Kopmann, Niklas Sokol, Till Branß, and Jochen Aberle</i> .....	61
Modelling scour around submerged objects with TELEMAC3D - GAIA, <i>Irinios Yiannoukos, Katrien Van Landeghem, Michael Roberts, Barney Smyth, and Jacob Morgan</i> .....	68

### Data assimilation, optimization, risks and uncertainties

Sensitivity of tidal modelling in coastal configurations: an uncertainty study based on field-measurement reduction, <i>Rem-Sophia Mouradi, Cédric Goeury, Pablo Tassi, Fabrice Zaoui, Olivier Thual</i> .....	75
--	----

Assessing uncertainties in flood forecasts using a mixture of generalized polynomial chaos expansions, <i>Siham El Garroussi, Sophie Ricci, Matthias De Lozzo, Nicole Goutal, Didier Lucor</i>	84
---	----

Pumping station design based on shape optimization process, <i>Florent Taccone, Cédric Goeury, Fabrice Zaoui, Adrien Petralia</i>	91
--	----

Benefits of a metamodel for automatic calibration of 1D and 2D fluvial models, <i>Rui Yang, Luc Duron, Guillaume Benefice, Pierre Nunes</i>	99
--	----

## **Numerical methods, code coupling and high performance computing**

Simulating, Storing and Accessing TELEMAC Simulations with AWS Cloud Computing Technologies, <i>Julien Cousineau</i>	108
---	-----

Ongoing developments in TELEMAC and TOMAWAC at IMDC, <i>WA Breugem</i>	115
---	-----

A Multi-class Frazil Ice Model for Shallow Water Flows, <i>Fabien Souillé, Florent Taccone, Chaymae El Mertahi</i>	122
---	-----

A newly implemented upwind scheme and numerical benchmark for the resolution of the Exner equation in GAIA, <i>Sacha Revillon, Florent Taccone and Fabien Souillé</i>	130
--	-----

## **Coastal surges, tsunami waves and extreme events**

Development of a detailed tide and storm surge forecast system for the South West Coast of Ireland, <i>Nigel Tozer, Kate Day, Nigel Bunn, Edmund Bridge, Jim Casey, Thomas Duffy</i>	139
---	-----

Improvement of a Continental Shelf Model of the North Sea, <i>Kai Chu, Alexander Breugem, Thom Wolf, Boudewijn Decrop</i>	146
--	-----

Introducing the VIMM toolbox for the (re)calibration of the SCALDIS model, <i>J. Vanlede, K. Chu and E. Fonias</i>	153
---	-----

Two-dimensional computations of Stokes drift and undertow at the near coast region, <i>Qinghui Zhang, Sebastian Escobar, Erik Toorman, Jaak Monbaliu</i>	159
---	-----

**River, estuaries, maritime, coastal sediment processes**

# Implementation of a novel approach accounting for the influence of vegetation on sediment transport in GAIA

Jiaze Li<sup>1,2,5</sup>, Nicolas Claude<sup>3</sup>, Pablo Tassi<sup>1,2</sup>, Florian Cordier<sup>1</sup>, Alessandra Crosato<sup>4</sup>, Stéphane Rodrigues<sup>5</sup>

<sup>1</sup> National Hydraulics and Environment Laboratory (LNHE), EDF R&D, Chatou, France

<sup>2</sup> Saint-Venant Hydraulics Laboratory (LHSV), ENPC, Cerema, EDF R&D, Chatou, France

<sup>3</sup> Centre d'Ingénierie Hydraulique, EDF, La Motte Servolex, France

<sup>4</sup> Department of Water Resources and Ecosystems, IHE-Delft, Delft, Pays-Bas

<sup>5</sup> UMR CNRS 7324 CITERES – Polytech Tours, Tours, France

**Abstract** — The influence of vegetation on flow and sediment transport is commonly accounted in 2D, horizontal, depth-averaged (2DH) models through the parameterization of a friction coefficient or by a drag force term in the momentum equations. In this study, we propose to implement a novel approach based on the work of Armanini and Cavedon (2019) and Bonilla Porras *et al.* (2020) to consider the effects of vegetation on flow and sediment transport. Combined with a drag force term implemented in the hydrodynamics equations, the initiation of motion parameter (Shields) was modified in the brand new sediment transport module GAIA to directly incorporate the effects of vegetation on sediment transport. A 2DH model is set-up and calibrated based on the flume experiments of Armanini & Cavedon (2019). Numerical results agree with the experimental data, but with less accuracy for high vegetation density. To validate the performance of this new approach, more numerical tests should be carried out on the basis of an independent set of physical experiments.

## I. INTRODUCTION

Anthropic activities such as channelization, sediment dredging, and dam building have affected many river systems worldwide. As a result of anthropogenic activities, channelized rivers generally show an increase of their base flow and a decrease of their flood frequency and magnitude. Consequently, reduced bar submersion and riverbed reworking have been observed in numerous regulated rivers worldwide, which might favor the expansion of vegetation over bars and inside channels (Figure 1). Vegetation increases the local hydraulic roughness as well as fine sediment deposition and reinforces the bed cohesion by the presence of roots systems [1]. Water levels increase due to the higher flow resistance and the smaller channel width, leading to an increased flood risk.

Numerous numerical models have been recently developed to consider the effects of vegetation on river morphodynamics. The commonly adopted approach to account for vegetation effects on flow resistance in two-dimensional, horizontal, depth-averaged models (2DH) is to define either a friction coefficient [2, 3, 4], or a drag force  $F_d$  added as a friction source term in the momentum equation [5, 6]. By doing so, the effect of vegetation on sediment transport is accounted indirectly by a reduced depth-averaged velocity. However, Yager & Schmeeckle [7] found that existing formulas commonly adopted

to parameterize the bedload flux are inaccurate to reproduce observed solid discharge values in vegetated reaches.

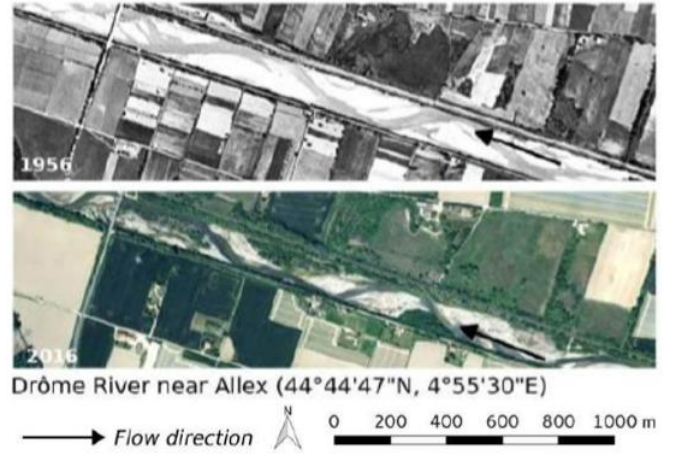


Figure 1: Examples of channelized gravel bed rivers located in the French Alpine region between 1956 and 2016, showing the development of vegetation on alternate bars (source: IGN) [5]

In their recent study, Armanini & Cavedon [8] proposed a novel approach that considers the effects of emergent vegetation on bedload transport by modifying Einstein's flow intensity parameter  $\Psi$  (Equation 5) with a correction factor that includes the plant characteristics. As a follow-up to the work of [8], Bonilla Porras *et al.*, [9] proposed an extension of this parameter to include submerged vegetation effects (Equation 6).

In this study, a modification of the dimensionless incipient grain mobility parameter is implemented in the sediment transport and bed evolution module GAIA. A 2DH model is set up using the open TELEMAC-MASCARET system. This consists of the hydrodynamic module TELEMAC-2D coupled with GAIA. The numerical results are compared with the experimental observations by Armanini & Cavedon [8] to test the implementation.

## II. SEDIMENT TRANSPORT THROUGH VEGETATION

Two dimensionless parameters are usually proposed to describe the fundamental principles of most commonly bed-load

transport equations [10], namely the dimensionless sediment transport rate,  $\Phi$ ,

$$\Phi = \frac{q_s}{d\sqrt{g\Delta d}} \quad (1)$$

and the flow intensity parameter,  $\Psi$ ,

$$\Psi = \frac{g\Delta d}{u_*^2} \quad (2)$$

where  $q_s$  is the sediment transport rate per unit width ( $\text{m}^2/\text{s}$ );  $d$  is the representative sediment particle size (m);  $\Delta = (\rho_s - \rho_w)/\rho_w$  is the submerged relative density of sediment (-), with  $\rho_s$  and  $\rho_w$  respectively the sediment and fluid density;  $g$  is the gravitational acceleration ( $\text{m/s}^2$ ); and  $u_*$  is the shear velocity ( $\text{m/s}$ ).

The dimensionless sediment transport rate  $\Phi$  can be expressed as a function of the flow intensity parameter:

$$\Phi = f(\Psi) = f(\theta^{-1}) \quad (3)$$

where  $\theta$  is the Shields parameter and  $\theta = \frac{1}{\Psi}$ .

#### A. Bedload through emergent vegetation

Derived from momentum balance analysis, a modification of Equations (1) and (2) is proposed by Armanini & Cavedon [8] to include the effects of emergent vegetation.

The dimensionless sediment transport rate in vegetated beds is defined as follows:

$$\Phi_v = \frac{q_s}{d\sqrt{g\Delta d}} (1 - \alpha_\Omega \Omega_v) \quad (4)$$

where  $\Omega_v$  is the areal density of plant (-) and  $\alpha_\Omega$  is a calibration factor (-). This modification takes account of the reduction of the active exchange surface between the bed and the flow [8].

The flow intensity parameter in vegetated beds is computed as follows:

$$\Psi_v = \Psi \left( 1 + \beta_v \Omega_v \frac{h}{D_v} \left( \frac{h}{d} \right)^{b_v} \right) \quad (5)$$

where  $h$  is the water depth (m),  $D_v$  is the plant stem diameter (m), and  $\beta_v$  and  $b_v$  are calibration parameters (-).

#### B. Bedload through submerged vegetation

Bonilla Porras *et al.*, [9] reworked the momentum balance analysis with submerged vegetation and proposed an updated version of the flow intensity parameter that adapts both to emergent and submerged vegetation, as follows:

$$\Psi_v = \Psi \left( 1 + \beta_v \Omega_v \frac{h_v}{D_v} \left( \frac{h}{d} \right)^{b_v} \left( \frac{h_v}{h} \right)^{\gamma_v} \right) \quad (6)$$

where  $h_v$  (m) is the effective plant height (equals to water depth for emergent vegetation),  $\gamma_v$  is calibration factor (-).

The calibration of parameters  $\beta_v$ ,  $b_v$  and  $\gamma_v$  is based on a series of flume tests carried out at the Hydraulics Laboratory at the University of Trento (Italy). The line of best fit equation is:

$$\Psi_v = \Psi (1 + K_v \Omega_v \frac{h_v}{D_v}) \quad (7)$$

in which  $K_v = 49.38 \left( \frac{h_v}{h} \right)^{-0.92} - 10.97 \left( \frac{h_v}{h} \right)^{-1.92}$ .

### III. NUMERICAL IMPLEMENTATION

In this study, we implemented the approach of Armanini & Cavedon's [8] and Bonilla Porras *et al.* [9] into GAIA to consider the direct effect of vegetation on sediment transport. As shown in Figure 2, the implementation can be achieved by adding a drag force in shallow water equations to account for the effect of vegetation on hydrodynamics and by modifying the Shields parameter  $\theta$  to incorporate the effect of vegetation on morphodynamics.

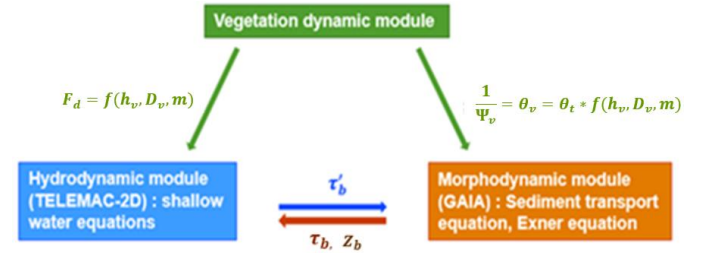


Figure 2: Schematization of the way we account for the interactions between vegetation, water flow and sediment transport for the morphodynamic modeling,  $\tau_b$  is the bed shear stress,  $\tau'_b$  is the shear stress due to skin friction,  $Z_b$  is the bed elevation.

Both the drag force and the modified Shields parameter are functions of the flow parameters and the vegetation parameters (i.e., plant diameter, height, and density).

#### A. Drag force in TELEMAC-2D

The effects of vegetation on hydrodynamics can be represented by a friction coefficient. However, Hervouet [11] indicated that by simply giving a specific friction coefficient to simulate the effect of vertical structures like vegetation, the last is not applied correctly. Hence, to represent the effect of vegetation, a drag force is added to the momentum equations according to [5], as follows:

$$F_d = -\frac{1}{2} C_d \rho_w \alpha_v m D_v \min(h_v, h) |U_v| U_v \quad (8)$$

where  $F_d$  is the drag force (N),  $C_d$  is the drag coefficient (-),  $\rho_w$  is the water density ( $\text{kg/m}^3$ ),  $\alpha_v$  is a shape factor equal to 1 for rigid cylinders (-),  $U_v$  is the flow velocity acting on vegetation ( $\text{m/s}$ ),  $m$  is the number of stems per unit area (-),  $D_v$  is the stem diameter (m), and  $h_v$  is the plant height (m).

For emergent vegetation,  $U_v$  is equal to the depth-averaged velocity. For submerged vegetation,  $U_v$  is determined by the formula of Stone and Shen [12] as follows:

$$U_v = \eta_v U \left( \frac{h_v}{h} \right)^{\frac{1}{2}} \quad (9)$$

where  $\eta_v$  is a coefficient and  $\eta_v = \frac{(1 - Dm^{0.5})}{(1 - \frac{h_v}{h} Dm^{0.5})}$

A sketch of the Fortran code implemented to compute the drag force is presented in Figure 3.

```

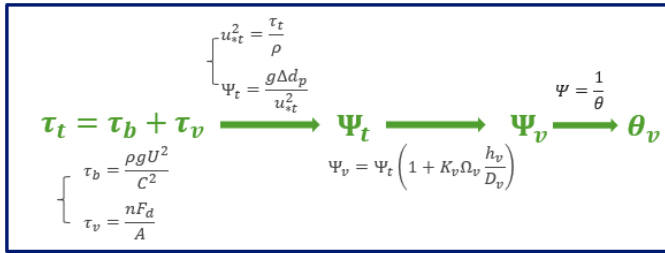
*****
! NPOIN: Number of computational nodes
! INPOLY: Function to determine whether a given point is inside the polygon
! HN: Water depth
! UN: Velocity along X
! VN: Velocity along Y
! H_VEG: Vegetation height
! D_VEG: Stem diameter
! M_VEG: Number of stems per unit area
! FUDRAG: Drag force along X
! FVDRAG: Drag force along Y
! CD: Drag coefficient
*****
DO I=1,NPOIN
  IF (HN%(I).GT.0D0) THEN
    RATIO_VEG = MIN(HN%(I),H_VEG)/HN%(I)
    ETA_VEG = (1.0-D_VEG*SQR(M_VEG))/(1.0-D_VEG*SQR(M_VEG)*RATIO_VEG)
    UNORM = SQR(UN%(I)**2+VN%(I)**2)*ETA_VEG*SQR(RATIO_VEG)
    FUDRAG%(I) = -0.5D0*D_VEG*M_VEG*CD*UNORM*RATIO_VEG
    FVDRAG%(I) = -0.5D0*D_VEG*M_VEG*CD*UNORM*RATIO_VEG
  ENDIF
ENDDO

```

Figure 3: Sketch of Fortran code used to calculate the drag force (dragfo.f)

### B. Modification of the Shields parameter $\theta$ in GAIA

The implementation of equation (7) is accomplished through the modification of the Shields parameter  $\theta$ . Figure 4 presents a conceptual diagram with the procedure followed to compute the modified Shields parameter  $\theta_v$ .

Figure 4: Chronological steps for the calculation of  $\theta_v$ 

For each symbol, the subscripts  $b, v, t$  stand for “bed”, “vegetation” and “total”, respectively. From the momentum balance analysis, the total shear stress  $\tau_t$  is equal to the sum of the bed shear stress  $\tau_b$  and the drag stress of vegetation exerted on the fluid  $\tau_v$ , which is calculated from the drag force (Equation 8). The total flow intensity parameter  $\Psi_t$  is then computed from the total shear velocity  $u_{*t}$ , which is in turn a function of  $\tau_t$ . By using equation (7), the modified flow intensity parameter for vegetated beds  $\Psi_v$  is obtained.

A sketch of the Fortran code implemented to compute the modified Shields parameter is presented in Figure 5.

```

*****
! NPOIN: Number of computational nodes
! INPOLY: Function to determine whether a given point is inside the polygon
! HN: Water depth
! UN: Velocity along X
! VN: Velocity along Y
! H_VEG: Vegetation height
! D_VEG: Stem diameter
! M_VEG: Number of stems per unit area
! DEN_VEG: Areal density of vegetation
! FUDRAG: Drag force along X
! FVDRAG: Drag force along Y
! CD: Drag coefficient
! MU: Skin friction coefficient
! TOB: Total bed shear stress
! XMVE: Fluid density
*****
DO I=1,NPOIN
  IF (HN%(I).GT.0D0.AND.AND.UNORM%(I).GT.0D0) THEN
    !-----Calculation of Tau v/water density-----
    RATIO_VEG = MIN(HN%(I),H_VEG)/HN%(I)
    ETA_VEG = (1.0-D_VEG*SQR(M_VEG))/(1.0-D_VEG*SQR(M_VEG)*RATIO_VEG)
    PART_V = 0.5D0*CD*D_VEG*M_VEG*MIN(HN%(I),H_VEG)
    & *(UNORM%(I)**2)*(ETA_VEG**2)*RATIO_VEG
    !-----Calculation of Tau b/water density-----
    PART_S = MU%(I)*TOB%(I)/XMVE
    !-----Calculation of total shear velocity-----
    USTAR_T2 = (PART_V+PART_S)
    !-----Calculation of total flow intensity parameter Psi_t-----
    PSI_T = CONS2/USTAR_T2
    !-----Calculation of modified flow intensity parameter Psi_v-----
    KV = 49.38*(RATIO_VEG**(-0.92))-10.97*(RATIO_VEG**(-1.92))
    FACTOR = 1.0+KV*DEN_VEG*MIN(HN%(I),H_VEG)/D_VEG
    PSI_V = PSI_T*FACTOR
    !-----Calculation of modified Shields-----
    TETAP%(I) = 1.0/PSI_V
  ENDIF
ENDDO

```

Figure 5: Sketch of Fortran code used to compute the modified Shields parameter

## IV. NUMERICAL MODEL TESTING

To verify the numerical implementations in GAIA, a 2D morphodynamic model is set-up and run to reproduce the flume experiments by Armanini & Cavedon [8].

### A. Flume experiment of Armanini & Cavedon [8]

Physical experiments were carried out in a 15 m long and 0.50 m wide rectangular flume. Two types of cylindrical elements were used to represent vegetation: aluminium cylinders with an average diameter of 1 cm; and rigid plastic cylinders with an average diameter of 3 cm, set in staggered configurations. Four distinct zones divide the channel longitudinally, as shown in Figure 6. The first three zones A, B and C are associated with three different vegetation densities of 200, 100 and 50 plants/ $m^2$  respectively, and the downstream zone D corresponds to a plant-free area. Complementary scenarios with a single vegetation partition (200 plants/ $m^2$ ) and totally plant-free area were also carried out.



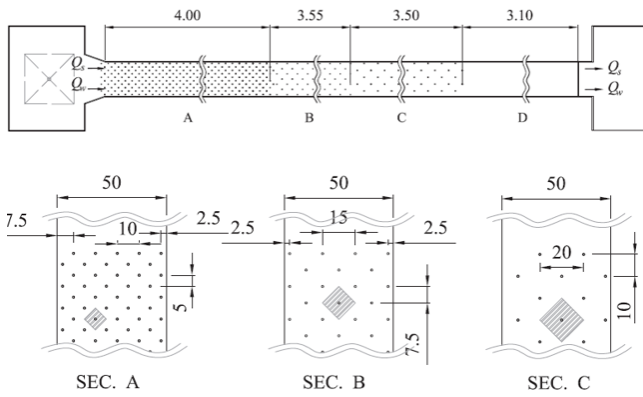


Figure 6: Flume vegetation areas: (A) reach with dense configuration (200 plants/m<sup>2</sup>), (B) reach with intermediate density (100 plants/m<sup>2</sup>), (C) reach with sparse configuration (50 plants/m<sup>2</sup>), (D) vegetation-free reach. (reproduced from Armanini & Cavedon (2019) [8])

The experiments were run under stationary conditions (constant water discharge and constant sediment discharge). Two types of sediments were used: fine uniform sand ( $\rho_s = 2591 \text{ kg/m}^3$  and  $d_{50} = 0.5 \text{ mm}$ ) and artificial spherical plastic particles ( $\rho_s = 1050 \text{ kg/m}^3$  and  $d_{50} = 0.55 \text{ mm}$ ). The water discharge  $Q$ , the sediment transport rate  $Q_s$ , the water surface and the bed level were measured during the experiment. All the experiments were carried out under steady and uniform flow conditions, in which the morphodynamic equilibrium was guaranteed at the end of the experimental runs.

In this work, only experimental runs with subcritical flows regime ( $Fr < 1$ ) and uniform sediment (sand) were selected, as shown in Tables 1 and 2.

Name	Number of stem per m <sup>2</sup>	Vegetation density (-)	Water discharge $Q$ (m <sup>3</sup> /s)	Sediment discharge $Q_s$ (m <sup>3</sup> /s)	Plant diameter $D_p$ (m)	Water depth $h$ (m)	Free surface slope $i$ (-)
1.R20	200	0.0157	0.020	1.45E-06	0.01	0.155	0.0080
	100	0.0073			0.01	0.136	0.0044
	50	0.0039			0.01	0.127	0.0037
	0	0			0	0.102	0.0014
2.R9	200	0.0157	0.009	4.68E-08	0.01	0.115	0.0049
	100	0.0073			0.01	0.097	0.0026
	50	0.0039			0.01	0.093	0.0018
	0	0			0	0.080	0.0008
3.R10	200	0.0157	0.010	1.96E-07	0.01	0.111	0.0056
	100	0.0073			0.01	0.099	0.0028
	50	0.0039			0.01	0.098	0.0023
	0	0			0	0.076	0.0010
NP1-NV	200	0.0157	0.010	3.65E-08	0.01	0.112	0.0050
	100	0.0073			0.01	0.096	0.0026
	50	0.0039			0.01	0.088	0.0020
	0	0			0	0.078	0.0011
NP2-NV	200	0.0157	0.020	1.30E-06	0.01	0.132	0.0101
	100	0.0073			0.01	0.110	0.0056
	50	0.0039			0.01	0.100	0.0037
	0	0			0	0.092	0.0019

TABLE 1: EXPERIMENTAL CONDITIONS OF THE SCENARIOS WITH 4 DISTINCT VEGETATION AREAS RETAINED FOR THE NUMERICAL SIMULATIONS (ADAPTED FROM ARMANINI & CAVEDON [8])

Name	Number of stem per m <sup>2</sup>	Vegetation density (-)	Water discharge $Q$ (m <sup>3</sup> /s)	Sediment discharge $Q_s$ (m <sup>3</sup> /s)	Plant diameter $D_p$ (m)	Water depth $h$ (m)	Free surface slope $i$ (-)
1.F20.8	200	0.0157	0.021	1.91E-06	0.01	0.157	0.0092
1.M20-FITTA	200	0.0157	0.020	2.33E-05	0.01	0.091	0.02668
2.M25-FITTA	200	0.0157	0.025	5.20E-05	0.01	0.099	0.03452
3.M23-FITTA	200	0.0157	0.023	8.68E-05	0.01	0.081	0.04275
4.F25	200	0.0157	0.025	6.35E-05	0.01	0.092	0.03823
4.M20-2-FITTA	200	0.0157	0.020	3.28E-06	0.01	0.138	0.0112
4.R25	200	0.0157	0.025	9.84E-05	0.01	0.090	0.0454
5.F20	200	0.0157	0.020	8.32E-05	0.01	0.070	0.04223
6.F20-2	200	0.0157	0.020	1.60E-05	0.01	0.105	0.02071

TABLE 2: EXPERIMENTAL CONDITIONS OF THE SCENARIOS WITH A SINGLE VEGETATION AREA RETAINED FOR THE NUMERICAL SIMULATIONS (ADAPTED FROM ARMANINI & CAVEDON [8])

### B. Model set-up and testing

The numerical model scales 1:1 the prototype. An unstructured triangular numerical mesh of 0.05 m is used, consisting of 3360 nodes and 6072 elements. A vegetation-free zone was assigned from 0 to 0.825 m along the x-axis. The upstream boundary conditions correspond to the experimental constant flow and solid discharges, and the imposed downstream water level is estimated from the measured water surface slope. The drag coefficient is set equal to 1 according to the shape and rigidity of the cylinders. Only the bedload sediment transport mechanism is considered in this study. The van Rijn [13] sediment transport formula is adopted here as it is valid for finer material in the range  $d = (0.2 - 2) \text{ mm}$ . The critical Shields parameter is calculated according to Brownlie [14], as:

$$\theta_{cr} = 0.22 * D_*^{-0.9} + 0.06e^{-7.73D_*^{-0.9}} \quad (9)$$

where  $D_* = d(g\Delta/\nu^2)^{1/3}$  is dimensionless particle diameter (-), with  $\nu$  the kinematic viscosity (m<sup>2</sup>/s).

The Strickler coefficient is used as friction coefficient to account for the bottom roughness. The adopted value is based on three no-vegetated scenarios shown in Table 3, where the average value of 61 m<sup>1/3</sup>/s is retained from the calibration procedure.

Name	Water discharge $Q$ (m <sup>3</sup> /s)	Sediment discharge $Q_s$ (m <sup>3</sup> /s)	Sediment density (kg/m <sup>3</sup> )	Particle size $d_p$ (m)	Water depth $h$ (m)	Free surface slope $i$ (-)	Calibrated Strickler K (m <sup>1/3</sup> /s)
6.F20-2	0.020	1.60E-05	2591	0.0005	0.060	0.00525	69
2.M25	0.020	5.20E-05	2591	0.0005	0.056	0.00897	59
4.M20-2	0.020	3.28E-06	2591	0.0005	0.091	0.00144	57

TABLE 3: STRICKLER COEFFICIENT CALIBRATION BASED ON THREE NO-VEGETATION SCENARIOS

### C. Numerical results

Figure 7 shows an example of bed elevation obtained at the end of the numerical simulation of scenario 1.R20 without and with the implementation of the modified Shields parameter  $\theta_v$ .

The abrupt changes of bed elevation observed in the Armanini & Cavedon's experiences are well reproduced by the newly implemented model (Figure 8). This behaviour observed in the transition zones between three vegetated areas and one vegetation-free area were unable to be captured by the original model.



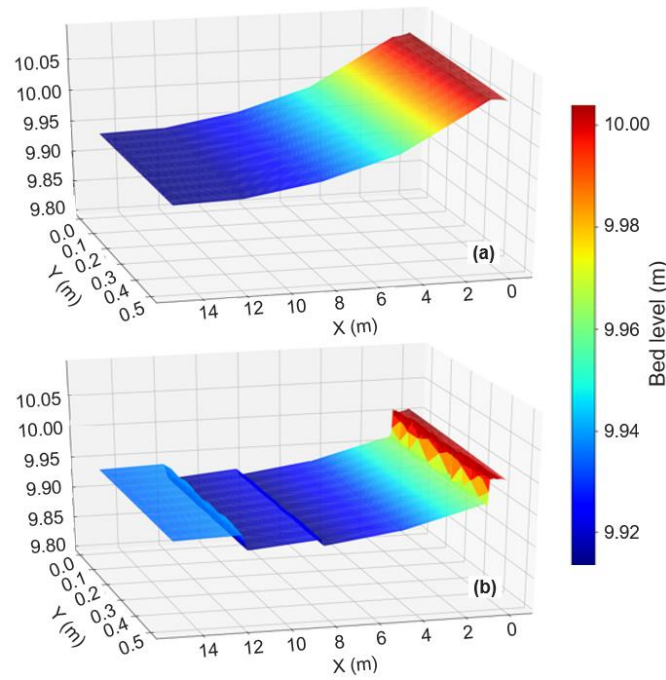


Figure 7: Bed elevation obtained at the end of simulation 1.R20: (a) original model without implementation of  $\theta_v$ , (b) modified model with implementation of  $\theta_v$  (arrow indicates flow direction).

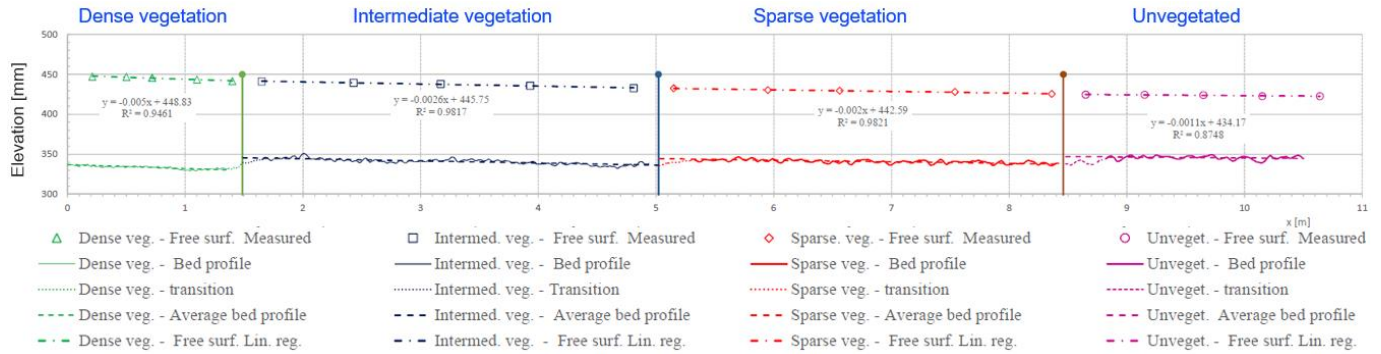


Figure 8: Measured longitudinal profiles of bed elevation and free surface of scenario NP1 (source: Armanini & Cavedon [8])

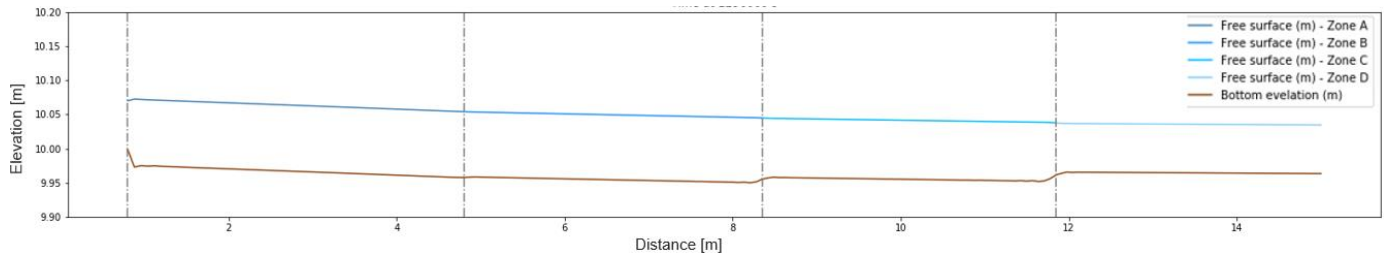


Figure 9: Numerical longitudinal profiles of bed elevation and free surface of scenario NP1 (extracted along  $y=0.25$  m)

Figures 8 and 9 present the measurements and numerical results of the longitudinal profile of free surface and bed elevation at steady-state conditions, respectively. The free surface profile and bed level slope being parallel in each vegetated area indicates that the numerical model is under steady

and uniform conditions, same than the experiment [15]. For high vegetation density,  $\Omega_v$ , the numerical results show an increase in water depth,  $h$ , and an increase in the free surface and bed slopes,  $i$ , which is consistent with observations.

Scenario	Number of stem per $m^2$	Measured water depth (m)	Simulated water depth (m)
1R20	200	0.155	0.137
	100	0.136	0.137
	50	0.127	0.125
	0	0.102	0.096
2R9	200	0.115	0.085
	100	0.097	0.084
	50	0.093	0.076
	0	0.080	0.065
3R10	200	0.111	0.086
	100	0.099	0.084
	50	0.098	0.076
	0	0.076	0.065
NP1	200	0.112	0.097
	100	0.096	0.095
	50	0.088	0.086
	0	0.078	0.071
NP2	200	0.132	0.140
	100	0.110	0.139
	50	0.100	0.127
	0	0.092	0.097

TABLE 4: COMPARISON OF MEASURED AND SIMULATED WATER DEPTH OF THE SCENARIOS WITH 4 DISTINCT VEGETATION AREAS

However, the distinction between dense (200 plant/ $m^2$ ) and intermediate vegetation (100 plant/ $m^2$ ) are not as evident as observed in experiments. Table 4 shows the experimental data and the numerical results of water depth for all the scenarios with 4 distinct vegetation areas. The average difference in water depth between dense and intermediate vegetation areas is 0.017 m in the experiments, but only 0.001 m in the model, which barely show distinction.

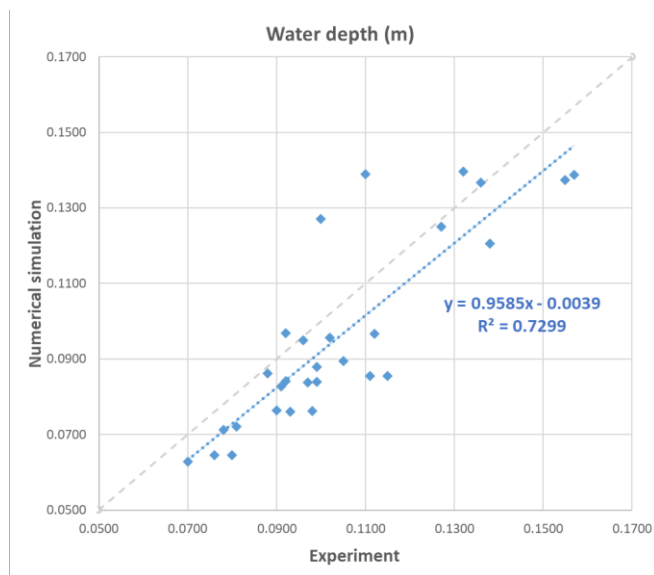


Figure 10: Comparison of the water depths obtained in the numerical model vs. in the experiment at morphodynamical equilibrium

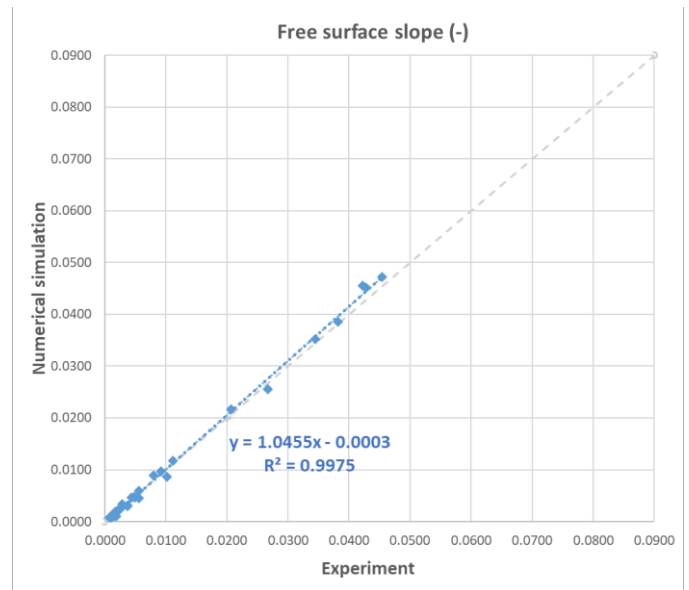


Figure 11: Comparison of the free surface slope (same as bed slope) obtained in the numerical model vs. in the experiment at morphodynamics equilibrium

Figures 10 and 11 show the comparison of numerical results and experimental observations in terms of water depth and free surface (bed) slope, for all scenarios (Tables 1 and 2). The model is able to reproduce correctly the experimental observations, which is represented by a high correlation coefficient  $R^2$  of 0.73 and 0.99, a linear function slope of 0.958 and 1.0455, respectively.

## V. CONCLUSIONS AND PERSPECTIVES

Derived from the momentum balance analysis, Armanini & Cavedon [8] proposed a novel approach to include the effects of emerging vegetation on bed load rates by adapting the dimensionless sediment transport rate  $\Phi_v$  and the flow intensity parameter  $\Psi_v$ . Subsequently, Bonilla Porras *et al.* [9] extended this modification to include also submerged vegetation.

The present study implemented this latter approach in GAIA by modifying the Shields parameter  $\theta$ . The numerical model was tested on the basis of the flume experiment of Armanini & Cavedon [8], with the aim of verifying its implementation in the TELEMAC-MASCARET modelling system. Each simulation reached morphodynamic equilibrium, well reproducing the experiments. By comparing water depth and free surface slopes, numerical results agree with the experimental observations. However, the numerical model seems to have limitations for dense vegetation (200 plants/ $m^2$ ). More numerical tests should be carried out on independent data sets to validate the performance of this approach for high-density and emergent/submerged vegetation conditions.

## ACKNOWLEDGEMENT

The present work is based on previous research of Armanini & Cavedon (2019) and Bonilla Porras *et al.*, (2020). The authors kindly acknowledge Prof. Aronne Armanini, Valentina Cavedon and José Antonio Bonilla Porras for the rich discussions and for providing the experimental data used in this work.

## REFERENCES

- [1] Gurnell, A. M., Bertoldi, W., & Corenblit, D. (2012). Changing river channels: The roles of hydrological processes, plants and pioneer fluvial landforms in humid temperate, mixed load, gravel bed rivers. *Earth-Science Reviews*, 111(1-2), 129-141.
- [2] Baptist M.J. 2005. Modelling floodplain biogeomorphology. PhD Thesis, Delft University of Technology, ISBN 90-407-2582-9.
- [3] Crosato, A., & Saleh, M. S. (2011). Numerical study on the effects of floodplain vegetation on river planform style. *Earth Surface Processes and Landforms*, 36(6), 711-720.
- [4] Vargas-Luna, A., Crosato, A., & Uijttewaal, W. S. (2015). Effects of vegetation on flow and sediment transport: comparative analyses and validation of predicting models. *Earth Surface Processes and Landforms*, 40(2), 157-176.
- [5] Jourdain, C., Claude, N., Tassi, P., Cordier, F., & Antoine, G. (2020). Morphodynamics of alternate bars in the presence of riparian vegetation. *Earth Surface Processes and Landforms*, 45(5), 1100-1122.
- [6] C.A.M.E. Wilson, O. Yagci, H. - P. Rauch & T. Stoesser (2006) Application of the drag force approach to model the flow - interaction of natural vegetation, *International Journal of River Basin Management*, 4:2, 137-146, DOI: 10.1080/15715124.2006.9635283
- [7] Yager, E. M., & Schmeeckle, M. W. (2013). The influence of vegetation turbulence and bed load transport. *Journal of Geophysical Research: earth Surface*, 118(3), 1585-1601.
- [8] Armanini, A., & Cavedon, V. (2019). Bed-load through emergent vegetation. *Advances in Water Resources*, 129, 250-259.
- [9] Bonilla Porras, J.A., Armanini, A., & Crosato, A., (2020) Sediment transport through submerged vegetation. *River Flow 2020* (Delft, Netherlands) In: Uijttewaal et al. (Eds), *River Flow 2020*, Taylor & Francis Group: London2020, p. 1-8
- [10] Einstein, H. A. (1950). *The bed-load function for sediment transportation in open channel flows* (No. 1026). US Government Printing Office.
- [11] Hervouet, J. M. (2007). *Hydrodynamics of free surface flows: modelling with the finite element method* (Vol. 360). Chichester, UK: Wiley.
- [12] Stone, B. M., and H. T. Shen (2002), Hydraulic resistance of flow in channels with cylindrical roughness, *Journal of Hydraulic Engineering*, 128(5), 500-506.
- [13] Van Rijn, L. C. (1984). Sediment transport, part I: bed load transport. *Journal of hydraulic engineering*, 110(10), 1431-1456.
- [14] Brownlie, W. R. (1981). Prediction of flow depth and sediment discharge in open channels.
- [15] Bolla Pittaluga, M., Luchi, R., and Seminara, G. (2014), On the equilibrium profile of river beds, *J. Geophys. Res. Earth Surf.*, 119, 317–332, doi:10.1002/2013JF002806.

# Numerical Modelling of Sediment Transport at Weirs

Antonia Dallmeier, Markus Reisenbüchler, Minh Duc Bui, Peter Rutschmann  
Chair of Hydraulic and Water Resources Engineering  
Technical University of Munich (TUM)  
Munich, Germany  
antonia.dallmeier@tum.de

**Abstract**—A weir is a barrier across the width of a river or stream, which is commonly used to measure or regulate flow and water elevation. Constructing a weir can alter the characteristics of the flow and sediment transport in the river reach. In order to capture complex local patterns of the flow and sediment transport near structures, three-dimensional (3D) modelling is needed. However, two-dimensional (2D) morphological simulations are frequently carried out to investigate the long-term effect of such structures on morphological alterations at larger scales due to their lower computational effort. It is thereby important that the physical processes around such hydraulic structures need to be simulated with a reasonably accurate model in these situations. At present, the clear water module TELEMAC-2D of the model system TELEMAC-MASCARET has only offered the possibility to simulate water flow at unregulated weirs in a computationally efficient manner. The present paper shows, how the sediment transport module SISYPHE of the system is adapted and extended in order to integrate weirs in hydromorphological simulations with minimal modelling effort. Analogous to the implementation in TELEMAC-2D, the boundary condition at the weir nodes is defined internally in the main program sisyphe.f as liquid boundary in a way that bedload flux can be considered. Subsequently, the bedload flux coming from the upstream side of the weir is transferred to the downstream one by modifying the subroutine conlit.f according to the proportion of each grain fraction. Conducting simulations in a study case verifies the correctness of the new implementation, where the sediment fluxes are compared as well as the total volumes of the present sediment evaluated.

## I. INTRODUCTION

Watercourses worldwide have been shaped by numerous hydraulic engineering interventions over the last decades or even centuries. However, river regulations and the construction of transverse structures for riverbed stabilization have fundamentally changed the transport of sediment in terms of quantity and quality. For better understanding the patterns of large-scale hydromorphological processes in large model areas with transverse structures, the use of numerical simulations is necessary [1]. As flow and sediment transport at or close to hydraulic structures in rivers have complex three-dimensional (3D) features, 3D numerical models provide in general more accurate results than two-dimensional (2D) approaches [2]. However, since these hydromorphological processes are very complex to model and 3D-models are computationally expensive, an easy-to-implement 2D approach for sediment transport at weirs should be developed.

The open source TELEMAC-MASCARET modeling environment only offers the possibility to simulate water flow over unregulated weirs in the clear water module TELEMAC-2D. Hereby, the weir is not constructed directly in the grid mesh. Thus, the water fluxes are calculated using empirical equations instead of using the depth-averaged SWEs [3]. Therefore, the water flow in large scale modeling areas with several weirs can be simulated accurately with little modeling and calculation effort. The present paper shows, how the sediment transport module SISYPHE is adapted and extended in order to integrate the bedload transport at weirs in hydromorphological simulations. This approach ensures minimal modelling effort of bedload transport for large consecutive domains, delimited by weirs.

The main idea for modifying the sediment transport module SISYPHE is somehow in an analogous manner to the implementation of flow calculation at weirs in the clear water module TELEMAC-2D. The boundary conditions of sediment transport at the nodes of the weir, upstream and downstream, are adjusted internally in the main program sisyphe.f as liquid boundaries, so that a bedload flux can take place there. Subsequently, the bedload flux coming from the upstream side of the weir is transferred 1:1 to the downstream one according to the proportion of each grain fraction by modifying the subroutine conlit.f. The correctness of the new implementation is verified by simulations in a study case, where the bottom elevation at different time steps is compared as well as the total volumes of the present sediment evaluated.

## II. WEIR TREATMENT IN TELEMAC-2D

The water flow over weirs is calculated in the clear water module TELEMAC-2D using the subroutines clsing.f and clhuvf.f. The process is described below.

The discharge  $Q$  is calculated using the Poleni formula in the subroutine clsing.f. Then the flow velocity perpendicular to the weir UNORM on both sides of the weir is determined based on the discharge and the flow depth known at each node. This flow velocity is transferred to the subroutine clhuvf.f. Here the tangential flow velocity at each node of the weir is calculated. Using the orthogonal and tangential flow velocity, the components of the flow velocity in x- and y-direction at the boundaries UBOR and VBOR are then calculated for both sides of the weir. These values act as transfer parameters at the new boundaries.

The boundary conditions for flow depth LIHBOR and flow velocities LIUBOR and LIVBOR at the weir are defined in the Subroutine clhuvf.f in such a way that water flow over these boundaries is possible. Per default, the boundary conditions at the border of the domain and thus at the weirs are defined as solid wall (boundary code = 2). At the weir nodes, the subroutine adjusts the boundary condition of the flow depth as a free boundary condition (KSORT = 4), while the flow velocity is assigned a boundary condition with prescribed value (KENTU = 6). Thus, the water level on the upstream and downstream side of the weir is variable. The components of the flow velocity in x- and y-direction are assigned the fixed values UBOR and VBOR, which are calculated in the previous. The orthogonal flow velocity UNORM present at the weir serves as a decision criterion for the implementation of permeable boundary conditions at the weir. Only when the flow velocity perpendicular to the weir is greater than zero, the boundary conditions at the weir are defined as permeable and a flow over the weir takes place.

Since the boundary conditions at the weir are not registered as liquid boundaries, the flux over these boundaries is not included in the mass balance. Therefore, it must be ensured that the mass flux added to the model area downstream of the weir corresponds to the absolute value of the mass flux leaving the upstream model area. The calculation and correction of the fluxes across the boundaries of the weir are handled in the subroutine propag.f. In order to ensure continuity, the fluxes over the boundaries of weir are balanced in such a way that their amounts are equal. Water masses are not generated artificially at the weir.

### III. NEW IMPLEMENTATION IN SISYPHE

In this work, the modified morphological version of SISYPHE developed by Reisenbüchler et al. (2016, TUC) [4] is used. The implementation of sediment transport over weirs is carried out in an analogous manner to the treatment of the clear water flow in TELEMAC-2D. For this purpose, both an appropriate place of embedding the code as well as a suitable transfer variable have to be identified. In SISYPHE, sediment is separated in two components, namely bedload and suspended load. It should be noted that only bedload transport over weirs is considered in this paper, which is explained in the following.

#### C. Boundary Conditions

The boundary conditions of the sediment transport rate LIQBOR and the bed evolution LIEBOR at weirs are defined in the main program sisyphe.f before calling the subroutine front2.f. The subroutine front2.f is used to identify and number liquid and solid boundaries of a model area. Consequently, the boundary conditions at the weir are also registered as liquid boundaries. Thus, a bedload flux can take place across these boundaries, which is automatically included in the mass balance. If the boundary conditions were defined in another subroutine after calling the subroutine front2.f, no bedload flux can take place across the boundaries and the bedload would therefore not be able to leave the upstream model area.

If the model area contains a weir, which is defined in the steering file, the boundary conditions for the sediment

transport rate LIQBOR and the bed evolution LIEBOR are redefined at each node of the weir. At the nodes on the upstream side of the weir, free boundary conditions are assumed for both the sediment transport rate and the bed evolution. This allows the bedload to leave the area upstream of the weir freely. However, at the nodes on the downstream side of the weir, the bedload transport rate LIQBOR is defined as a Dirichlet boundary condition, while the bed evolution LIEBOR is assigned by a free boundary condition. This ensures that an imposed value of bedload is added to the downstream side of the weir. The exact allocation can be found in table I.

TABLE I. ALLOCATION OF BOUNDARY CONDITIONS ACCORDING TO THE WEIR SIDE

	Upstream Boundary	Downstream Boundary
LIQBOR	4 = KSORT	5 = KENT
LIEBOR	4 = KSORT	4 = KSORT

#### D. Bedload Transport

As the implementation of the clear water flow over a weir in TELEMAC-2D shows, either a mass flow over a boundary must be transferred or the continuity must be ensured later. In SISYPHE, the sediment balance is ensured by solving Exner's equation for sediment transport.

Considering only bedload transport, the subroutine bedload\_solvs\_fe.f is applied to calculate the bed elevation change due to gradients of the mass fluxes of the fractional bedload flux FLBCLA. As can be seen in the subroutine, these fluxes are defined based on the bedload discharges at boundaries QBOR as well as flow directions there. At Dirichlet boundary conditions, which are usually used for inlet boundaries, the fractional bedload flux FLBCLA is calculated as a negative value of QBOR for each grain class and at each time step. Since the boundary conditions at the weir are registered as liquid boundaries, the bedload flux FLBCLA is calculated for each grain class and at each time step at the outlet boundary condition upstream of the weir. As the bedload fluxes at the upstream side of the weir are fully transferred to the imposed solid transport rate QBOR at the downstream side of the weir, the sediment conservation is ensured without any additional extension of the code.

First, the subroutine conlit.f is modified for implementing bedload transport over a weir. Assuming that the upstream side of the weir contains NPSING nodes, we define the fractional bedload flux  $Q_{CLOUT}(K)$  through this cross section as follows:

$$Q_{CLOUT}(K) = \sum_{IA=1}^{NPSING} FLBCLA(K, IA) \quad (1)$$

Where  $FLBCLA(K, IA)$  is the fractional bedload flux for grain class K through node IA.

The total bedload flux  $Q_{OUT}$  through the upstream side of the weir is then calculated by summing up the fractional bedload fluxes  $Q_{CLOUT}(K)$  of all grain classes (NSICLA):

$$Q_{OUT} = \sum_{K=1}^{NSICLA} Q_{CLOUT}(K) \quad (2)$$



To determine the fractional bedload fluxes through the downstream side of the weir, we define the ratio of the fractional bedload flux  $Q_{CLOUT}(K)$  to the total bedload flux  $Q_{OUT}$  at the upstream side of each weir:

$$RATIO(K) = \begin{cases} 0, & \text{if } Q_{OUT} = 0 \\ \frac{Q_{CLOUT}(K)}{Q_{OUT}}, & \text{otherwise} \end{cases} \quad (3)$$

Assuming that this ratio is constant along the weir, the continuity of sediment transport over the weir can be ensured.

In the subroutine `conlit.f` the function `QGL(IFRLIQ,AT)` is applied to prescribe the sediment discharges for imposed liquid boundaries, where bedload rate `SOLDIS(IFRLIQ)` is defined externally. In the subroutine `disimp.f` the total bedload rate is then distributed to the nodes at the downstream boundary of the weir. The bedload rate for each node is passed to the subroutine `conlit.f`, where the variable `QBOR` is determined considering the values of `RATIO` and sediment discharge.

This concept of modelling bedload transport can be applied for a number of weirs constructed along a river reach.

#### IV. RESULTS

The functionality of the implementation of bedload transport at weirs is verified by a hydromorphological simulation for a simple test case. The simulation area comprises a 304 m long and 30 m wide trapezoidal flume, in which two weirs are constructed (see figure 1). The first weir is located 100 m downstream of the model inlet, which indicates the left side of figure 1. The height of the channel bed at the inlet of the model area is 10.0 m while the height of the channel bed in front of the first weir is 9.9 m. The weir crest is at 13.0 m and the channel bed immediately after the first weir is at 8.9 m. The second weir is located 97 m downstream of the first weir. The channel bed in front of the second weir is at a height of 8.8 m, the weir crest at 12.0 m

and the channel bed immediately after the second weir at 0.0 m. The bottom slope of both the first canal section and the canal section between the two weirs is therefore 0.1 %, while there is no inclination of the third channel section between the second weir and the outlet. The numerical mesh consists of 2381 nodes and 4510 elements with an average edge length of 2 m. This setup allows a fast simulation in approximately 1 h and 26 min on a normal work station using one processor given a time step of 1 s and a total simulation period of 9 days.

For the hydrodynamic simulation, a stationary discharge at the inlet of 50 m<sup>3</sup>/s and a constant water elevation at the outlet of 10 m are chosen. The first weir has its crest at 13 m and the second at 12 m. The runoff-coefficient for both weirs amounts to 0.7. Initially the riverbed is defined completely as non-erodible, without any movable sediments. The morphological boundary condition at the inlet is defined as a constant sediment rate of 0.006 m<sup>3</sup>/s (without porosity). There is no sediment transport at the outlet. This ensures, that the material does not leave the model area. Thus, the bedload present in the area at the end of the simulation corresponds to the bedload added over the simulation period, which is important for the code validation. The simulation is conducted using two mobile grain fractions and a third non-movable grain class. Due to the use of several grain classes, the functionality of the code is also shown for the transport of multiple grain classes. Table II shows the sediment diameters and the fraction for the particular size classes.

TABLE II. INITIAL SEDIMENT COMPOSITION

Size class i	1	2	3
Diameter $d_{m,i}$ [m]	0.001	0.002	0.003
Fraction [-]	0.40	0.60	0.00

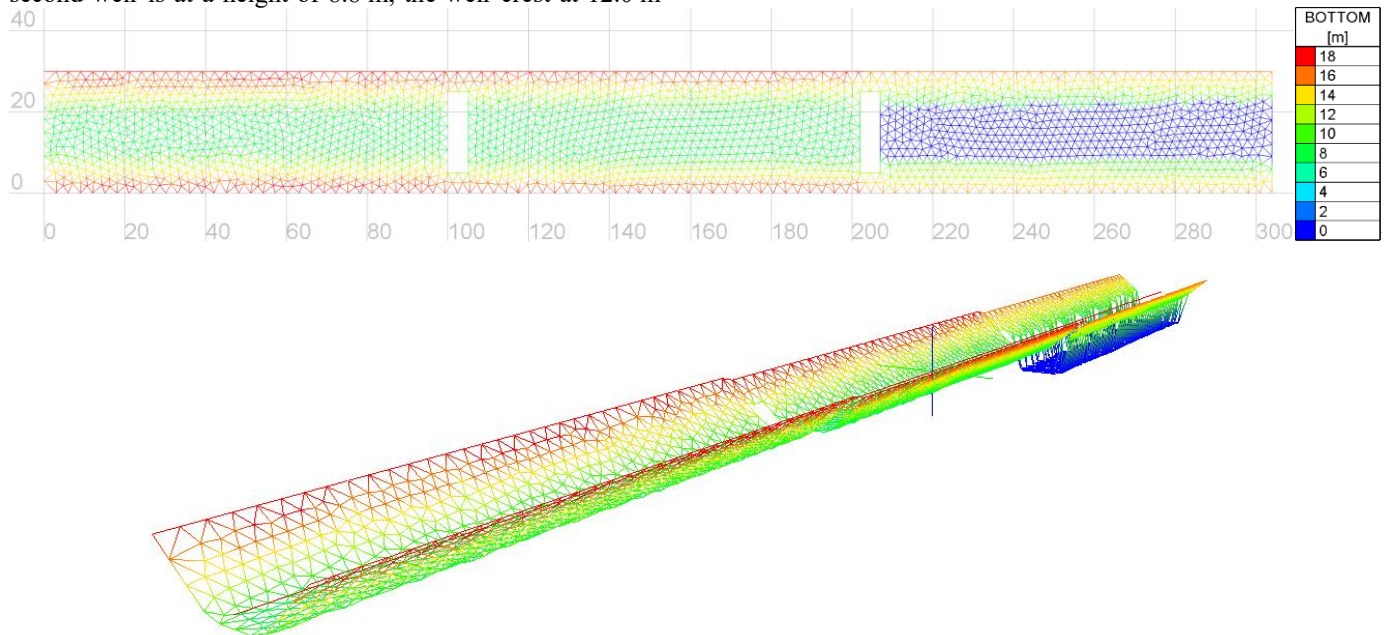


Figure 1. Plan view and 3D view of the test model area

The simulation results are analyzed regarding the development of the bottom elevation along a longitudinal section at the center of the channel, the bedload rate over a cross-section, which is located 150 m downstream of the inlet of the model area between the first and second weir, and the bedload volume present in the model area.

Figures 2a-2c show the development of the bottom elevation along a longitudinal section at the center of the channel per channel section every 24 hours of simulation time. With the help of this illustration, the development of the channel bed over the entire simulation period is clearly visible. Thus, the sediment transport and the development of the river bed can be traced. The sediment is transported over the two weirs and deposited in the third channel section between the second weir and the outlet with progressing simulation time (see figure 2c). In this settling zone, the expected deposition takes place due to the large water depth (up to 10 m) and due to the missing outlet boundary for sediment discharge. In the respective areas in front of the two weirs, stationary conditions of the channel bed are established (see figure 2a and 2b). An equilibrium of sedimentation and erosion is created here. This state is reached before the first weir after two days of simulation time and in the section between the weirs after approximately three days of simulation time.

In addition, the average bedload rate that passes a cross section in midway between the two weirs is evaluated over the simulated time. The course presented in figure 3 is maintained by a moving average analysis of the original result data. The bedload rate significantly increases after about one day of simulated time. After about 2.5 days of simulated time, the bedload rate behaves almost stationary. The development of the bedload rate corresponds to the development of the river bed in this area. As already mentioned, after a simulation period of about three days an equilibrium state of the river bed is reached in this section. The constant bedload rate at this cross section also corresponds to the constant sediment discharge at the inflow boundary of the channel.

Finally, the accumulated sediment volume in the model area at the end of the simulation is calculated and compared with the sediment rate added over the simulated time (see figure 4). At the model inlet, a constant sediment rate of  $0.006 \text{ m}^3/\text{s}$  is added over a simulation time of 9 days (777,600 s). Including the porosity of 0.4, a sediment volume of  $7,776 \text{ m}^3$  must therefore be present in the model area at the end of the simulation, since no outlet boundary exist for the sediment transport at the channel outlet. The graph of the accumulated volume in the model area shows the expected linear increase and the total accumulated volume at the end of the simulation. This amounts to  $7,776 \text{ m}^3$  as expected. An additional analysis of the grain composition of the total sediment volume shows the same grain composition as the grain fraction of the added bedload shown in table 2. Here, the volume of the first grain class makes up 40 % and the second grain class 60 % of the total volume. This evaluation shows that sediment volume is neither destroyed nor artificially generated when transported over the weirs. The mass balance is thus maintained.

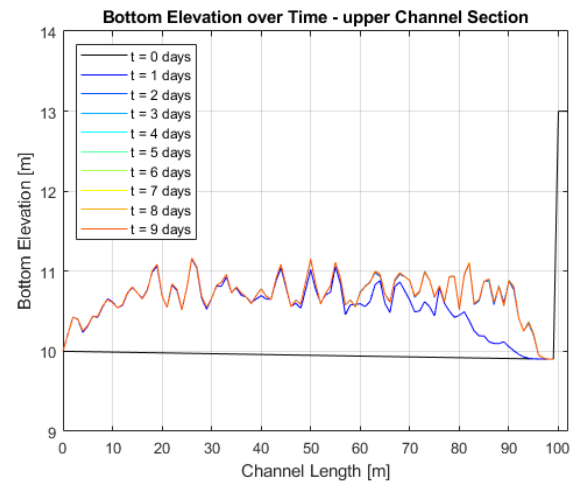


Figure 2a. Development of bottom elevation over time in the first channel section

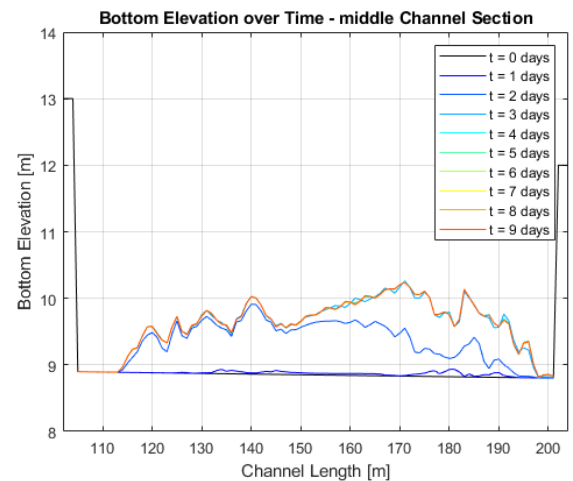


Figure 2b. Development of bottom elevation over time in the second channel section

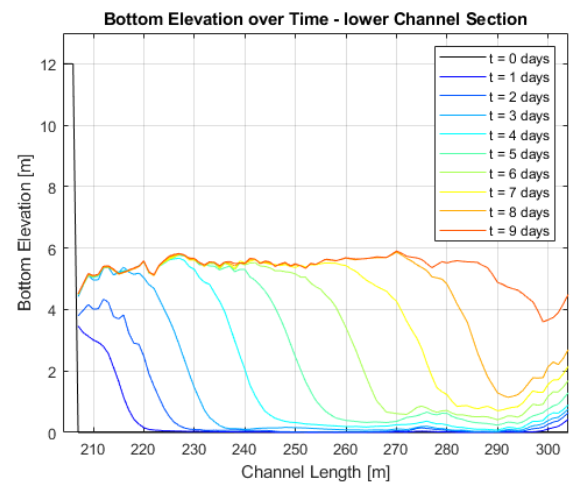


Figure 2c. Development of bottom elevation over time in the third channel section

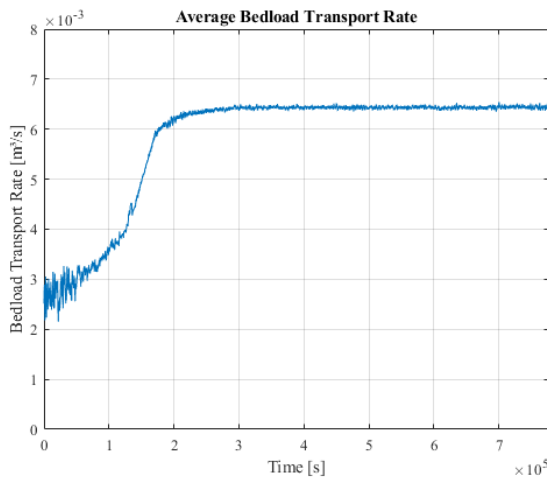


Figure 3. Average bedload transport rate over a cross section 150 m downstream of the inlet between the first and second weir over time

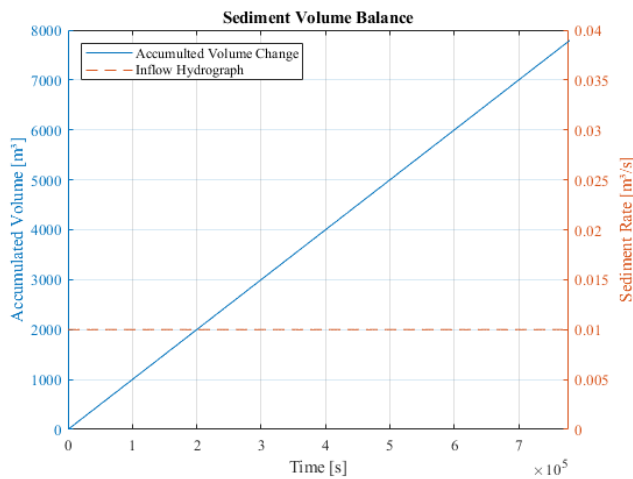


Figure 4. Comparison of the accumulated sediment volume over time and the sediment inflow hydrograph

Since the code of the bedload transfer from upstream to downstream of the weir is structured in such a way that the added bedload flux downstream is always offset by one computational time step from the bedload flux at the upstream boundary, a certain amount of bedload flux is buffered for one time step. However, this intermediate storage does not affect the correctness of the calculation results. In fact, the temporarily stored bedload quantity is only lost in the last simulation time step. For the preceding steps, the bed load quantity downstream of the weir only lags behind the bed load flow upstream by one time step, which does not lead to a distortion of the mass balance. It should also be noted that numerical models always picture only a simplified representation of reality and in no case a 100 % realistic representation of nature is possible. Within the overall accuracy of numerical models, we assume that this lag is acceptable.

## V. CONCLUSION

Until now, no numerical method has been available in the TELEMAC-MASCARET modelling environment to simulate sediment transport at weirs in a time and modelling efficient way. The new developed code offers an easy to implement, realistic and computationally efficient way to calculate sediment transport in large scale, numerical model areas. The code was verified by a simple test area, where the results regarding the deposition of bedload over time and the sediment balance were very satisfactory and met the expectations. The code can, therefore, be applied to real model areas. It will allow the combination of previously disconnected river reaches and models into one consecutive model [5]. This extension of the sediment transport module SISYPHE represents an important tool for the investigation of large-scale hydromorphological transport processes both over long runoff periods and during flood events.

The implementation of sediment transport at weirs refers to the coupling of TELEMAC-2D with SISYPHE. For the application of the above presented method for 3D simulations of the existing code has to be further modified, since a different handling of structures in the flow model is necessary.

## REFERENCES

- [1] Gmeiner, Philipp; Liedermann, Marcel; Haimann, Marlene; Tritthart, Michael; Habersack, Helmut (2016): Grundlegende Prozesse betreffend Hydraulik, Sedimenttransport und Flussmorphologie an der Donau. In: Österreichische Wasser- und Abfallwirtschaft 68 (5-6), S. 208–216. DOI: 10.1007/s00506-016-0308-5.
- [2] Wu, Weiming (2008): Computational River Dynamics. New York, London: Taylor & Francis.
- [3] Ata, Riadh (2018): Telemac2d. User Manual. Version v8p0. EDF.
- [4] Reisenbüchler, Markus; Bui, Minh Duc; Rutschmann, Peter. (2016): Implementation of a new Layer-Subroutine for fractional sediment transport in SISYPHE. Proceedings of the XXIIIrd Telemac-Mascaret User Conference, Paris, France, p: 215-220.
- [5] Aguirre Iñiguez, Diego Vladimir; Bui, Minh Duc; Giehl, Stefan; Reisenbüchler, Markus; Rutschmann, Peter (2019): Development of a hydro-morphodynamic Model for Sediment Management in the Rosenheim Reservoir. Proceedings of the XXVth Telemac-Mascaret User Conference, Toulouse, France.



# Implementation of non-Newtonian rheological models in TELEMAC-2D

Pierre-Louis Ligier  
Power Generation and Dams Department  
Sweco Energy AB  
Stockholm, Sweden  
[pierre-louis.ligier@sweco.se](mailto:pierre-louis.ligier@sweco.se)

**Abstract**—Sediment transport modelling in hydrodynamic models is based on the assumption that the sediment concentration remains sufficiently low so that the flow behaviour remains Newtonian, i.e. that the fluid is assumed to keep the same properties as water. This assumption is valid for sediment volumetric concentrations up to approximatively 20-30%. For larger concentrations, the flow behaviour can no longer be assumed to remain Newtonian and non-Newtonian rheological flow models are required to provide a more accurate modelling of the fluid behaviour. This article presents the implementation of such models in the two-dimensional hydrodynamic model TELEMAC-2D. The considered field of application is primarily the modelling of mudflows such as tailings dam failures with release of liquefied tailings in which the sediment volumetric concentrations are commonly larger than 40%. Two models have been implemented: the classic Bingham viscoplastic model and the more general Herschel-Bulkley model. Both models exhibit a plastic behaviour through the yield stress parameter that acts as a threshold for the onset of fluid motion. Once the shear stress exceeds the fluid's yield stress, the flow behaviour becomes viscous and governed by a simple constant viscosity assumption for the Bingham model whereas in the Herschel-Bulkley model, viscosity is described with a power-law. The resulting shear stress is treated as a friction slope source term applied to the two-dimensional momentum equations. The implementation offers the possibility to model the non-Newtonian rheological properties either constant in space and time (i.e. non-Newtonian fluid with constant rheological properties) or variable in space and time using a pseudo-biphasic, variable-density formulation in which the rheological properties (density, yield stress and viscosity) are computed from the local sediment volumetric concentration. Validation and application examples are presented in order to highlight the capabilities and limitations of the implemented models. The article also contains an application example of the Brumadinho tailings dam failure that occurred in Brazil in January 2019 with comparison against field observations as well as results from simulations performed with other software.

## I. INTRODUCTION

Modelling of classic sediment transport in hydrodynamic models is based on the assumption that the sediment concentration remains sufficiently low so that the flow behaviour remains Newtonian, i.e. that the fluid is assumed to keep the same properties as water. This assumption is valid for sediment volumetric concentrations up to approximatively 20-30% [1] [2]. For larger concentrations, the flow behaviour can

no longer be assumed to remain Newtonian and non-Newtonian rheological flow models are required to provide a more accurate modelling of the fluid behaviour. The behaviour of a Newtonian fluid is defined by a linear relationship between the shear (viscous) stress  $\tau_0$  [Pa] and the shear rate  $\dot{\gamma}$  [s<sup>-1</sup>]:

$$\tau_0 = \mu \dot{\gamma} \quad (1)$$

with  $\mu$  the fluid's dynamic viscosity [Pa·s]. For non-Newtonian fluids, the relationship between the shear stress and the shear rate is no longer linear and can exhibit complex behaviours (plastic, dilatant, contractant...). The rheological properties of non-Newtonian fluids can generally be described by their density, their viscosity which can vary depending on the actual strain and shear stress rates and, for some non-Newtonian models, by a yield stress. For such models, the fluid starts to flow when the actual shear stress exceeds the fluid's yield stress, otherwise the fluid stops moving and behaves as a solid. The yield stress is often referred to as a threshold value for the onset of motion. Examples of several types of Newtonian and non-Newtonian fluid behaviours are presented in Fig. 1 in a so-called shear rate-shear stress diagram.

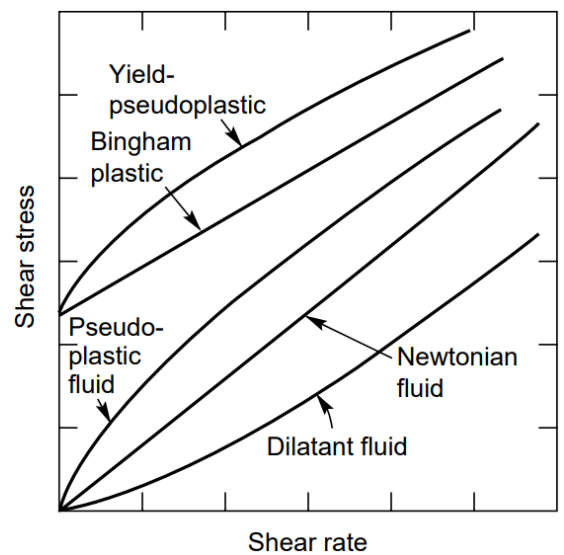


Figure 1: Examples of Newtonian and non-Newtonian fluids behaviour in a shear rate-shear stress diagram (taken from [6]).

One of the most classical non-Newtonian fluid models is the so-called Bingham or “Bingham plastic” fluid model. This model is well suited for homogeneous suspensions of fine particles, particularly mudflows, under low rates of deformation [2] and is also commonly accepted for modelling flowing tailings [3] [4]. A more generic non-Newtonian model is the Herschel-Bulkley model (yield-pseudoplastic) which combines the effects of the Bingham model with a yield stress and power-law behaviour. This model is suitable for modelling shear-thinning behaviour that some tailings slurries exhibit (loss of shear strength with increasing shear rates) [5]. Both models have been implemented in TELEMAT-2D. This article presents the theoretical background behind these two models as well as their implementation into the software. Finally, validation and application examples are provided.

## II. THE BINGHAM MODEL

### A. Formulation

The equation of the Bingham model reads:

$$\begin{cases} \dot{\gamma} = 0 & \text{if } \tau_0 \leq \tau_y \\ \tau_0 = \tau_y + \mu \dot{\gamma} & \text{if } \tau_0 > \tau_y \end{cases} \quad (2)$$

with  $\tau_y$  the fluid's yield stress [Pa]. Within the 1D and 2D modelling framework, it is common to use the quadratic rheological model proposed by O'Brien and Julien (1985) which defines the total shear stress of the flow  $\tau$  as the sum of the yield and viscous stresses induced by the non-Newtonian behaviour (i.e.  $\tau_0$ ) and of the turbulent stresses induced by bottom friction [2] [7] [8]. One assumption of the quadratic rheological model is that the shear rate  $\dot{\gamma}$  is defined as  $du/dz$ , that is the velocity gradient in the vertical direction, neglecting gradients in the horizontal plane. Assuming that the flow is laminar, the shear rate can then be approximated as [8]:

$$\dot{\gamma} = du/dz = 3U/h \quad (3)$$

with  $u$  the components of the three-dimensional velocity vector [m/s],  $U$  the depth-averaged flow velocity [m/s] and  $h$  the flow depth [m]. Another approach consists in expressing the last term of (3) as follows [7]:

$$\dot{\gamma} = \frac{KU}{8h} \quad (4)$$

with  $K$  a resistance parameter for laminar flow [-]. Its value lies in the range 24-108 for smooth surfaces (concrete, asphalt) but can increase significantly with irregular geometry and roughness (highest values of approximately 50 000) [7]. It can be observed that with the lowest value, of 24, (4) is reduced to (3). This resistance parameter has been proposed within the framework of overland runoff by Woolhiser (1975) (see also [9]) and should therefore be used in accordance with the underlying assumptions. When modelling turbulent flows, the lowest value of 24 is therefore recommended. However, the resistance parameter can also be used as an empirical coefficient in order to adjust the theoretical “laminar” shear rate to take 2D and 3D effects into account (stronger vertical velocity gradient, horizontal subgrid-gradient, etc.).

Even though the Bingham model's mathematical expression is relatively simple, the discontinuity generated by the yield stress parameter at very low shear rates is a

disadvantage and can lead to numerical instabilities. To solve this issue, several solution methods have been proposed in the literature, aiming at replacing the discontinuity by a continuous relationship between shear stress and shear rate. Three of such methods, called “Options” in this article, have been implemented, and are described in the next section.

### B. Solution methods

#### Option 1: exponential regularization

This method is based on the exponential regularization method proposed by Papanastasiou (1987) [10] [11]. An exponential term is added to the yield stress parameter making it possible to introduce a continuous relationship for low shear rates:

$$\tau_0 = \tau_y(1 - e^{-m\dot{\gamma}}) + \mu\dot{\gamma} \quad (5)$$

with  $m$  a so-called regularization parameter [s] used to control the exponential growth of shear stress for low shear rates. The effect of the regularization parameter is illustrated in Fig. 2 in which the shear stress is normalized by the yield stress. For high values of  $m$ , the classical Bingham model is retrieved whereas as  $m$  tends towards zero, the model reduces to a linear, Newtonian fluid behaviour. The value of  $m$  has been set to 1000 s as proposed in [11]. The shear rate is computed using (4) based on a user-defined value for the resistance parameter for laminar flow  $K$  (default value is 24).

#### Option 2: effective viscosity

This method is based on the effective viscosity concept by rewriting the Bingham model (2) as:

$$\tau_0 = \mu_{eff}\dot{\gamma} \quad (6)$$

with  $\mu_{eff}$  the effective viscosity [Pa·s], defined by the following set of equations, based on the so-called Cross formulation [8] [12]:

$$\mu_{eff} = \frac{\mu_0 + \mu_K B \dot{\gamma}}{1 + K_B \dot{\gamma}} \quad (7)$$

$$K_B = \mu_0 / \tau_y \quad (8)$$

$$\mu_0 = 10^3 \mu \quad (9)$$

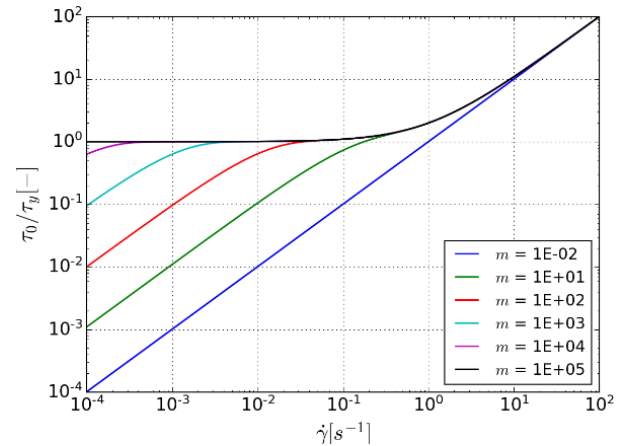


Figure 2: Bingham model, Option 1 (exponential regularization). Influence of the regularization parameter  $m$ .

The shear rate is computed using (4) based on a user-defined value for the resistance parameter for laminar flow  $K$  (default value is 24).

#### Option 3: Bingham cubic equation

This method is based on a cubic equation for the non-Newtonian shear stress that is obtained from the integration of the classical Bingham equation for laminar flow in a wide open channel, and then solving for the depth-averaged flow velocity as proposed by Rickenmann [13] and cited in [14] and [15]. The resulting cubic equation reads:

$$2\tau_0^3 - 3\tau_0^2(\tau_y + 2\mu U/h) + \tau_y^3 = 0 \quad (10)$$

This equation is solved using the CUBEEQUATION subroutine available in the TELEMAC-2D library (.sources\telemac2d), keeping the positive root closest from the theoretical value of  $\tau_0$  defined by (2).

#### Comparison between the three different options

The flow behaviour curves for the three options implemented described above are illustrated in Fig. 3 in which

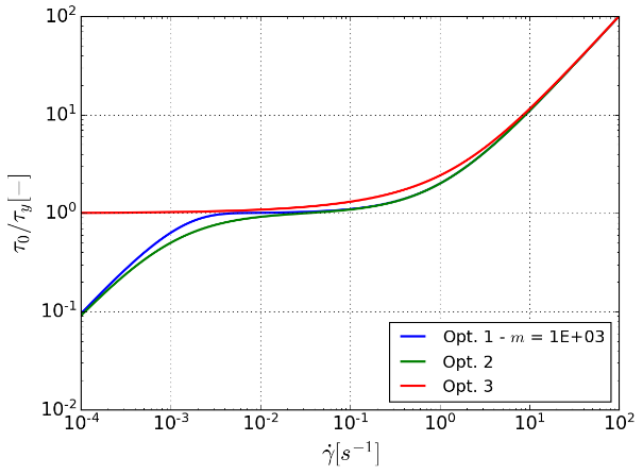


Figure 3: Bingham model, comparison between the three options implemented.

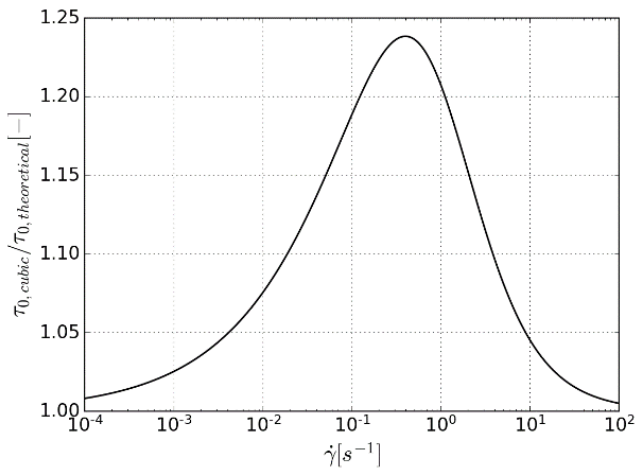


Figure 4: Bingham model, comparison between shear stress computed with cubic equation (Option 3) and theoretical values.

the shear stress is normalized by the yield stress. For Options 1 and 2, the resistance parameter for laminar flow  $K$  is set to its default value of 24. It can be observed that Options 1 and 2 correspond to a similar flow behaviour with only minor differences being observed at very low shear rates. The flow behaviour obtained with Option 3 is the closest to the theoretical Bingham model (2) at very low shear rates but yields an approximatively 5%-25% larger shear stress for shear rates in the range  $10^{-2}$ - $10^1$  s<sup>-1</sup>, which corresponds to usual values (see also Fig. 4).

### III. THE HERSCHEL-BULKLEY MODEL

#### A. Formulation

The equation of the Herschel-Bulkley model reads:

$$\begin{cases} \dot{\gamma} = 0 & \text{if } \tau_0 \leq \tau_y \\ \tau_0 = \tau_y + K_{HB}\dot{\gamma}^n & \text{if } \tau_0 > \tau_y \end{cases} \quad (11)$$

with  $K_{HB}$  the consistency parameter [Pa·s] and  $n$  the power-law index [-]. The Bingham model can be retrieved if  $K_{HB} = \mu$  and  $n = 1$ .

#### B. Solution method

The Herschel-Bulkley model has been implemented using the exponential regularization method also used for the Bingham model (Option 1), as proposed in [10]:

$$\tau_0 = \tau_y(1 - e^{-m\dot{\gamma}}) + K_{HB}\dot{\gamma}^n \quad (12)$$

As for the Bingham model, the value of the regularization parameter  $m$  has been set to 1000 s (see section II-B). The shear rate is computed using (4) based on a user-defined value for the resistance parameter for laminar flow  $K$  (default value is 24).

### IV. IMPLEMENTATION IN TELEMAC-2D

The non-Newtonian shear stress computed by the non-Newtonian models is expressed as a friction slope using the following equation:

$$S_0 = \frac{\tau_0}{\rho gh} \quad (13)$$

with  $S_0$  the friction slope [-] corresponding to the non-Newtonian shear stress,  $\rho$  the fluid's bulk density [kg/m<sup>3</sup>] and  $g$  the gravity acceleration [m/s<sup>2</sup>]. The friction slope term  $S_0$  is then multiplied by  $g$  and inserted in the momentum equations' source terms  $S_x$  and  $S_y$  [m/s<sup>2</sup>]. The source terms are treated semi-implicitly to ensure numerical stability even in regions with strong gradients (e.g. wave front). A drawback of this treatment is numerical diffusion which can lead to a loss of accuracy especially in regions where the non-Newtonian stresses are dominant. For a thorough overview of the two-dimensional equations solved by TELEMAC-2D, please refer to [16] and [17].

In its current status, the non-Newtonian models have only been implemented in the Finite Volume version of TELEMAC-2D. The non-Newtonian source term is treated semi-implicitly, as for bottom friction, in a new subroutine called NONNEWTON\_FV called from SOURCE\_MOMENT.

Tests have also been performed in Finite Elements but showed poor results with instabilities in areas with strong gradients, i.e. with small mesh sizes and/or for large values for yield stress and dynamic viscosity. However, reasonable results that compared well with Finite Volume have been obtained on dam break simulations with very large mesh sizes. Further work is required before the non-Newtonian models can also be included in TELEMAC-2D's Finite Element version.

#### V. PSEUDO-BIPHASIC, VARIABLE DENSITY FORMULATION

In practical applications for tailings dam break studies, the assumption of non-Newtonian rheological parameters constant in time and space can be limiting especially if the flood wave flows into lakes and/or rivers. In order to take mixing effects into account, a simplified pseudo-biphasic, variable density formulation has been implemented.

The principle of this formulation is to determine the fluid density and the rheological parameters (yield stress and dynamic viscosity) from the local sediment volumetric concentration  $C_V$  [-]. The sediment volumetric concentration typically ranges between 0.0-0.2 for water floods with suspended sediment, 0.2-0.45 for mud floods, 0.45-0.55 for mudflows, flowing tailings and 0.55-0.8 for landslides [1] [2]. Furthermore, this formulation is based on the underlying assumption that the sediment is transported in suspension through advection and dispersion with a nil settling velocity and without interaction with the bed (no erosion/deposition).

The type of fluid can therefore be defined by the local sediment volumetric concentration  $C_V$ . The local fluid's bulk density is then computed as:

$$\rho = \rho_W + (\rho_S - \rho_W)C_V \quad (14)$$

with  $\rho_W$  the water density [ $\text{kg/m}^3$ ] and  $\rho_S$  the sediment specific density (grains) [ $\text{kg/m}^3$ ].

In this formulation, the local sediment volumetric concentration  $C_V$  is to be defined by the user via a passive tracer (with initial and boundary conditions). The mixing between the different fluid mixtures defined by different values of  $C_V$  is therefore governed by the advection and diffusion of the passive tracer. The main limitation of this method is that diffusion at the interface between two fluids, and therefore mixing, is overestimated.

Empirical relationships have been proposed to express the yield stress and the dynamic viscosity as functions of the sediment volumetric concentration  $C_V$  [2]:

$$\tau_y = a10^{bC_V} \quad (15)$$

$$\mu = c10^{dC_V} \quad (16)$$

The values of the coefficients  $a$ ,  $b$ ,  $c$  and  $d$  are mainly function of the nature and percentage of fine particles in the mixture. Experimental values have been proposed in the literature ([2] [7] [18]).

When the pseudo-biphasic formulation is used, (15) and (16) are applied at every wet node regardless of the local value of  $C_V$ . In practical cases, the values of the coefficients  $a$ ,  $b$ ,  $c$  and  $d$  are such that the resulting yield stress and dynamic

viscosity computed with low  $C_V$  values can be considered representative of a Newtonian fluid (i.e. the corresponding non-Newtonian shear stress is negligible). The values of the coefficients  $a$ ,  $b$ ,  $c$  and  $d$  should be defined in subroutine NONNEWT\_FV.

#### VI. VALIDATION EXAMPLES

##### A. Deposition of a thickened tailings slurry

The first case used to test the non-Newtonian models implemented is the reproduction of the deposition of a thickened tailings slurry. The case used is taken from [4] for which an analytical solution is available. The set-up consists of releasing a tailings slurry with a constant discharge of 26.46 l/min in a 150 mm wide flume with a flat and smooth bottom. The slurry discharge is applied for 12 s before the fluid deposits and reaches an equilibrium profile. In the case, the slurry is released from a 21 mm x 21 mm opening and falls vertically on the bottom of the plume. In the simulation, the discharge is instead applied through a 25 mm-wide lateral open boundary centered on the flume axis at  $X = 0$  m. The computational mesh is 150 mm wide and 2000 mm long with a mesh size of 5 mm. The fluid properties are taken from measurements and are as follows: bulk density  $\rho = 1315 \text{ kg/m}^3$ , yield stress  $\tau_y = 18.6 \text{ Pa}$  and dynamic viscosity  $\mu = 0.32 \text{ Pa}\cdot\text{s}$ .

The simulations have been performed with the Bingham model for the three options implemented using the kinetic finite volume scheme (FINITE VOLUME SCHEME = 1) [19]. Bottom friction has been simulated with a Strickler coefficient of  $70 \text{ m}^{1/3}/\text{s}$  to mimic the smooth plume bottom. The standard slip condition on the lateral solid boundaries was used in order to comply with the assumptions used in the Slow Sheet Flow (SSF) model and the "Case 3" from the CFD simulations performed in [4]. It is worth noting that the SSF model is based on the assumption that the inertial effects of the flow are negligible [4]. The slow flow conditions used in the flume test are assumed to comply with this assumption.

The results are presented as flow profiles at three different times (after 12 s, 14 s and 20 s) and compared with the analytical solution of the SSF model in Fig. 5. The first observation from the results is that in the simulation, the fluid never reaches a true equilibrium profile unlike what can be observed in the experiments and assumed in the SSF model. The analysis of the simulated flow profiles shows that the shape of the slurry is well reproduced with a well-defined and steep wave front up to 14 s. After this time, the front starts to spread out in the downstream direction while the overall profile shape remains nearly constant. The cause of the lack of equilibrium state in the simulation is linked to the numerical method used to model the flow shear stress (semi-implicit treatment of the non-Newtonian source term, see section IV), in which flow velocity, although being very small, never reaches zero. A similar behaviour was observed in the CFD simulations from [4]. The comparison between the three different Bingham model options implemented shows that the Options 1 and 2 give very similar results, which is expected (see section II-B). The flow profiles after 12 s match well the



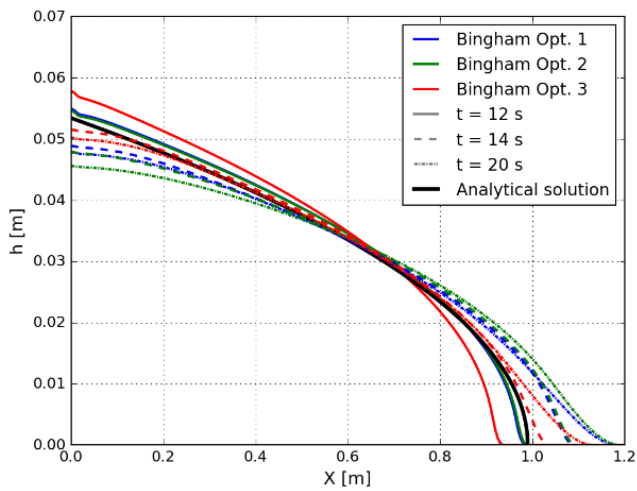


Figure 5: Deposition of thickened tailings, results of Bingham model after 12 s, 14 s and 20 s and analytical solution.

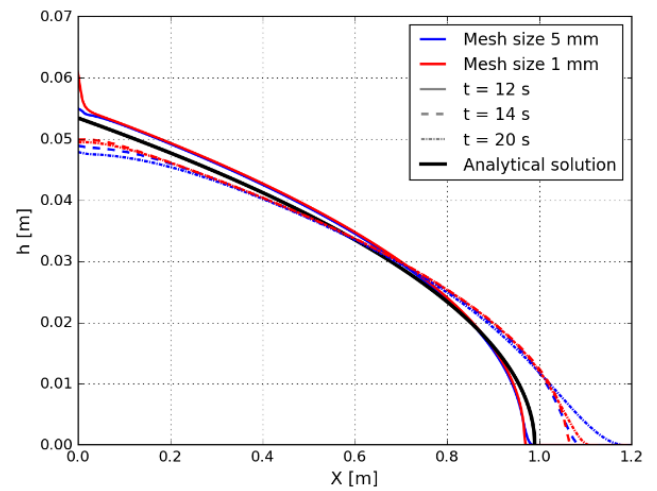


Figure 8: Deposition of thickened tailings, influence of mesh size (Bingham Option 1).

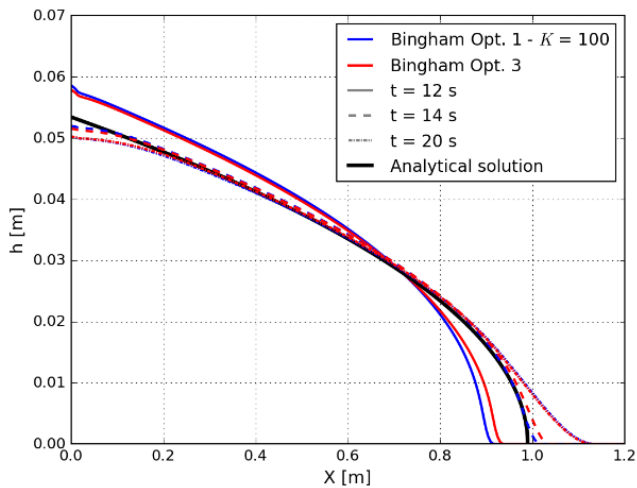


Figure 6: Deposition of thickened tailings, influence of the resistance parameter for laminar flow  $K$ .

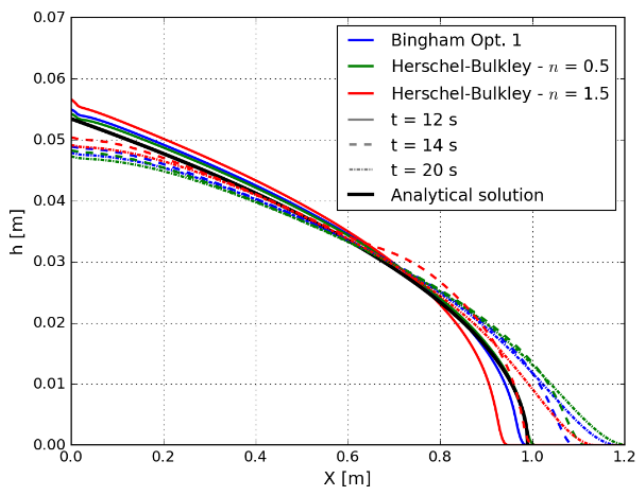


Figure 7: Deposition of thickened tailings, comparison between Bingham and Herschel-Bulkley models.

analytical solution but the profiles continue to stabilize until approximately 14 s where they reach a pseudo-equilibrium excepted for the front that continues to spread out. The flow profiles at 14 s lie within approximately 10% of the analytical solution (front distance overestimated, flow depth at  $X = 0$  m underestimated). The Option 2 shows however more spreading than Option 1 at 14 s, which is also expected as this option has a smoother transition towards the yield stress at low shear rates than Option 1. The Option 3 shows the best agreement with the analytical solution, with flow profiles located less than 5% from the SSF model. The more resistive behaviour of the Option 3 compared to Options 1 and 2 was expected as the Bingham cubic equation yields shear stresses that are 5-25% larger than theoretical values at usual shear rates (see section II-B). In comparison, the CFD simulation “Case 3” from [4] shows a flow profile with a front location approximately 5% shorter than the analytical solution.

In order to test the sensibility of the Option 1 to the resistance parameter for laminar flow  $K$ , a simulation was performed with  $K = 100$  which corresponds to the upper range for smooth surfaces. The result shows that the larger viscous stresses induced by this set-up steepens up the flow profile which lies very close from the analytical solution and from the result of Option 3 once pseudo-equilibrium is reached at 14 s (Fig. 6).

This case has also been simulated with the Herschel-Bulkley model in which the consistency parameter  $K_{HB}$  was taken equal to the dynamic viscosity used in the Bingham simulations. Two simulations were performed with power-law index values of  $n = 0.5$  and  $n = 1.5$ . The results are compared qualitatively with the Bingham Option 1 in Fig. 7 for the flow profiles at 14 s. As expected, a power-law index smaller than 1 ( $n = 0.5$ ) shows a flatter, less resistive, profile whereas a power-law index larger than 1 ( $n = 1.5$ ) shows a steeper, more resistive, profile.

Finally, the case has been run on a finer mesh to analyse the influence of mesh size on the results. The finer mesh has a 1 mm node spacing in the flow direction. Results for Bingham

Option 1 with mesh sizes 1 and 5 mm are presented in Fig. 8. The finer mesh gives very similar results than the original mesh for the flow profiles corresponding to 12 and 14 s, with a slight improvement of the front region which becomes steeper. However, a noticeable improvement is visible on the flow profile at 20 s where the finer mesh significantly limits the spreading of the front (10% shorter distance and front slope well preserved).

The results presented above show that the non-Newtonian models implemented in TELEMAC-2D can reproduce the behaviour of tailings slurry until a pseudo-equilibrium state is reached in a satisfactory way. Results compare well with the analytical solution and results from CFD simulations (for further details, please refer to [4]). Result analysis should take the numerical spreading occurring after pseudo-equilibrium is reached into account.

### B. One-dimensional dam break

The one-dimensional dam break case presented in [20] is used to test the implemented non-Newtonian models for such applications. This dam break case has also been used as a validation case for the numerical code DFEM-1D in which several non-Newtonian models have been implemented [14]. The dam break case corresponds to the instantaneous release of a non-Newtonian fluid defined by a volume of 305 m in length (in the flow direction) and 30.5 m in height on a flat, dry and smooth bottom. The fluid properties used in [14] are a fluid density  $\rho = 1835 \text{ kg/m}^3$ , a yield stress  $\tau_y = 1500 \text{ Pa}$  and a dynamic viscosity  $\mu = 100 \text{ Pa}\cdot\text{s}$ . The theoretical solution of this case provided by Hungr [20] and based on the assumption that the flow profile after reaching equilibrium is parabolic, gives a front location of  $X = 1896 \text{ m}$  counted from  $X = 0 \text{ m}$ , which corresponds to a runout distance of 1591 m counted from the dam location ( $X = 305 \text{ m}$ ).

This case was simulated using a two-dimensional triangular mesh with an element size of 3 m in both X and Y directions. The model is 3000 m long in the X direction and 12 m wide in the Y direction. The simulations have been performed with the Bingham model for the three options implemented using the HLLC finite volume scheme (FINITE VOLUME SCHEME = 5) [21]. Bottom friction has been simulated with a Strickler coefficient of  $70 \text{ m}^{1/3}/\text{s}$  to mimic the smooth and plane bottom.

The results are presented as flow profiles extracted along the longitudinal axis (defined by  $Y = 6 \text{ m}$ ) once the fluid has reached a pseudo-equilibrium state, which occur after approximately three minutes (Fig. 9). The flow profiles corresponding to the three different Bingham options implemented are compared with the result from the same simulation performed with MIKE21's Bingham fluid model (which is based on the same cubic equation as for Option 3) as well as with the analytical solution from [20]. The first observation that can be made is that results from all the simulations, including MIKE21, give fluid profiles characterized by a steep front and tail whereas the flow slope diminishes in the middle part of the fluid volume. Such flow profiles do not match with the theoretical parabolic shape of the analytical solution. Similar flow profiles were obtained

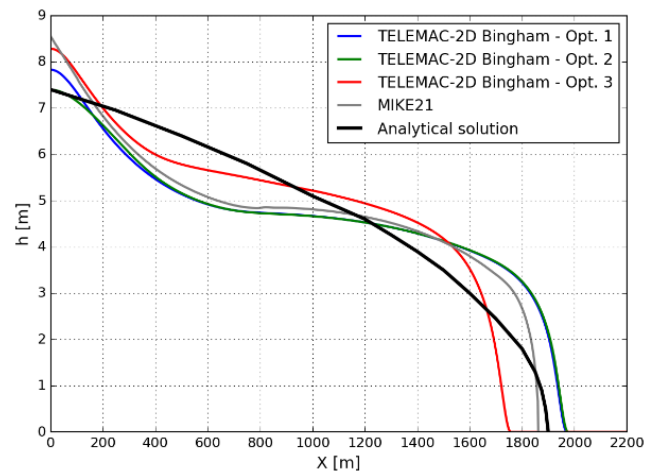


Figure 9: One-dimensional dam break, results of Bingham model compared with MIKE21 and analytical solution at pseudo-equilibrium state.

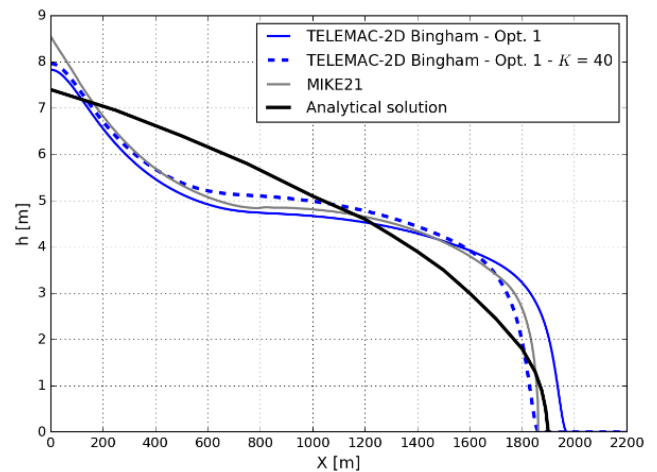


Figure 10: One-dimensional dam break, influence of the resistance parameter for laminar flow  $K$  at pseudo-equilibrium state and comparison with MIKE21 and analytical solution.

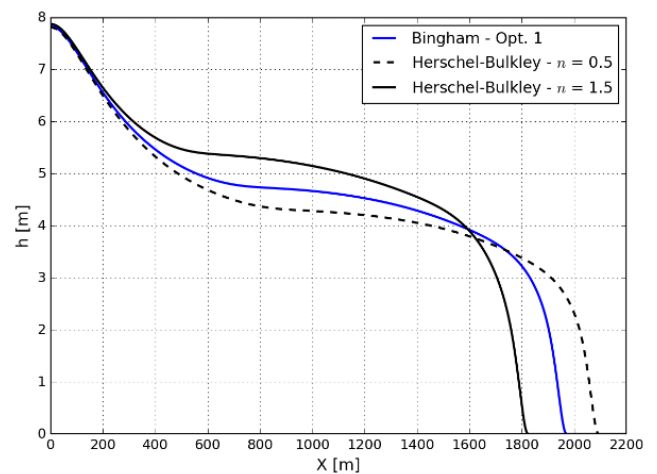


Figure 11: One-dimensional dam break, comparison between Bingham and Herschel-Bulkley models.

with the numerical code DFEM-1D for all the non-Newtonian models implemented [14]. It can be noted that in [20], it is highlighted that the assumption of a parabolic profile may not be valid in certain cases. In comparison with the flume test of thickened tailings described above, for which parabolic flow profiles were obtained, the inertial effects involved in the dam break case are not negligible which might explain the shape of the simulated flow profiles.

As for the thickened tailings case, the flow profiles obtained with the Bingham Options 1 and 2 are very close to each other, which is an expected result (see sections II-B and VI-A). The wave front is located at  $X = 1970$  m, which corresponds to a runout distance of 1665 m that is approximately 4.7% larger than the theoretical value. The flow profile obtained with Option 3 (Bingham cubic equation) shows a more resistive behaviour than Options 1 and 2 with a wave front located at approximately 1750 m which corresponds to a runout distance of 1445 m that is approximately 9.2% smaller than the theoretical value. The more resistive behaviour of the Option 3 is also an expected result (see sections II-B and VI-A). The flow profile obtained with MIKE21's Bingham model is located between the flow profiles obtained with Options 1-2 and 3, with a runout distance of approximately 1555 m, that is 2.3% smaller than the theoretical value. The differences obtained between Option 3 and MIKE21, based on the same mathematical formulation, are likely caused by different numerical methods used in the implementation (no information regarding the numerical implementation used in MIKE21 is available [15]).

In order to test the sensibility of the Option 1 to the resistance parameter for laminar flow  $K$ , a simulation was performed with  $K = 40$  which corresponds to an intermediate value for smooth surfaces. The result shows that the larger viscous stresses induced by this set-up steepens up the flow profile which lies very close to MIKE21's flow profile and from the theoretical solution (Fig. 10).

This dam break case has also been simulated with the Herschel-Bulkley model in which the consistency parameter  $K_{HB}$  was taken equal to the dynamic viscosity used in the Bingham simulations. Two simulations were performed with power-law index values of  $n = 0.5$  and  $n = 1.5$ . The results are compared qualitatively with the Bingham Option 1 in Fig. 11 for the flow profiles corresponding to the pseudo-equilibrium state (after 3 minutes of simulation). As expected and in accordance with the results obtained for the thickened tailings case, a power-law index smaller than 1 ( $n = 0.5$ ) shows a flatter, less resistive, profile whereas a power-law index larger than 1 ( $n = 1.5$ ) shows a steeper, more resistive, profile.

In a similar way as for what is observed for the thickened tailings case, the front location spreads out in the downstream direction after that the pseudo-equilibrium state is reached due to the semi-implicit treatment used for the source term. Analysis of flow profiles obtained after 10 minutes of simulation shows that the front has migrated approximately 70 m compared to its location after 3 minutes of simulation (when pseudo-equilibrium state is reached).

Some simulations have been run with the kinetic volume scheme (FINITE VOLUME SCHEME = 1). No significant differences were observed compared with the HLLC scheme.

The results presented above show that the non-Newtonian models implemented in TELEMAT-2D can reproduce the flow runout generated by a dam break in a satisfactory way. Inertial effects can have a significant influence on the flow profile shape. A detailed analysis of the results is recommended to identify the time at which the pseudo-equilibrium state is reached, which can be of importance for runout and flood propagation analysis.

### C. Mixing between non-Newtonian and Newtonian fluids

To illustrate the pseudo-biphasic, variable-density formulation, a simple test case is used. The computational domain is composed of a mean channel reach and of a side channel discharging into the main channel with a 90-degree angle. The main channel is 90 m long and the side channel is 21 m long. Both channels are 10 m wide. The bathymetry is defined as a constant level in all the model. The computational mesh is composed of triangles with an edge side of approximately 1 m. Two inflow boundaries are defined at the upstream end of both channels. One outflow boundary is defined at the downstream end of the main channel with a flow depth of 1 m.

Inflow of the non-Newtonian fluid is applied at the upstream end of the side channel by prescribing a discharge of  $4 \text{ m}^3/\text{s}$  and a sediment volumetric concentration  $C_V$  of 0.5 through a passive tracer. The non-Newtonian fluid density is computed by the model based on a sediment specific density  $\rho_s = 3000 \text{ kg/m}^3$  and the specified sediment volumetric concentration  $C_V$  according to (14). At the inflow boundary, the fluid's bulk density is  $\rho = 2000 \text{ kg/m}^3$ . Inflow of Newtonian fluid is applied at the upstream end of the main channel by prescribing a discharge of  $2 \text{ m}^3/\text{s}$  and a nil sediment volumetric concentration through a passive tracer. The Newtonian fluid density is set to  $\rho_w = 1000 \text{ kg/m}^3$ . The non-Newtonian parameters, yield stress and dynamic viscosity, are computed by the model with power laws (15) and (16) based on the local sediment volumetric concentration  $C_V$  with the following coefficients:  $a = 0.025$ ,  $b = 8.0$ ,  $c = 0.001$ ,  $d = 8.0$  (see section V). For the non-Newtonian fluid defined with  $C_V = 0.5$ , those coefficients yield a yield stress and dynamic viscosity of 250 Pa and 10 Pa·s, respectively while the Newtonian fluid ( $C_V = 0$ ) is consequently described with a yield stress and dynamic viscosity of 0.025 Pa and 0.001 Pa·s, respectively, which is a reasonable approximation.

The model is run with the Option 1 of the Bingham model using the HLLC finite volume scheme. Bottom friction has been simulated with a Strickler coefficient of  $70 \text{ m}^{1/3}/\text{s}$ . Results illustrating the steady state conditions for free surface, velocity field, sediment volumetric concentration, fluid density, yield stress and dynamic viscosity are presented in Fig. 12. It can be observed that the pseudo-biphasic, variable-density formulation enables the modelling of the mixing between non-Newtonian and Newtonian fluids under the assumption that mixing is modelled through advection and diffusion of a

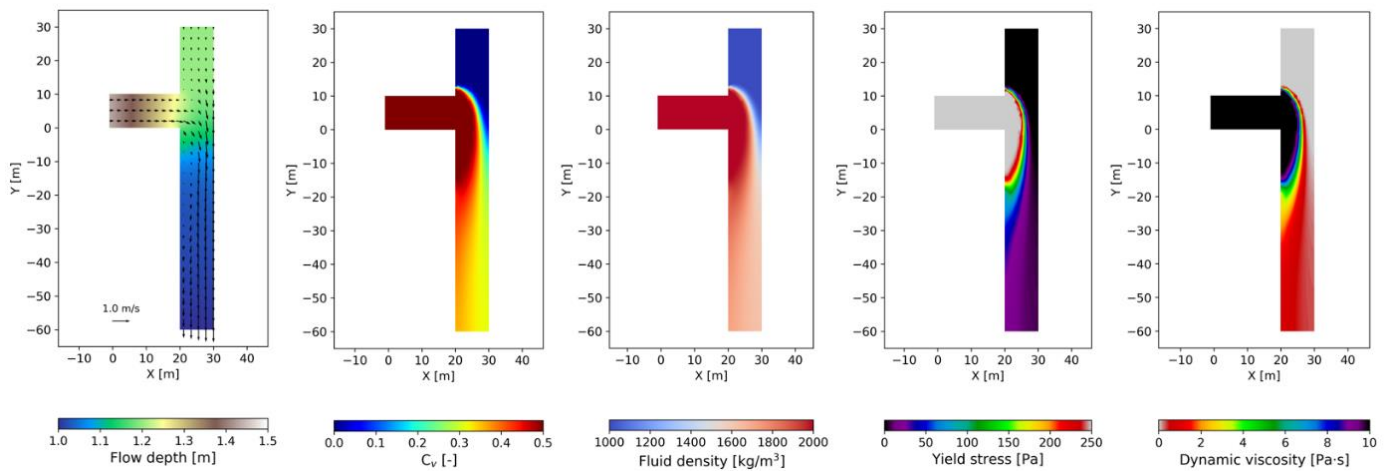


Figure 12: Mixing between non-Newtonian and Newtonian fluids, results illustrating flow conditions and rheological parameters.

passive tracer representing the sediment volumetric concentration  $C_v$  (see section V).

#### VII. APPLICATION EXAMPLE: BRUMADINHO TAILINGS DAM FAILURE

On January 25, 2019, Dam I of the Córrego do Feijão mine located approximately 9 km north-east of the city of Brumadinho (Brazil) suffered a sudden failure, caused by static liquefaction, releasing approximately  $9.7 \cdot 10^6 \text{ m}^3$  of liquefied tailings within five minutes. The outflow volume represents approximately 75% of the total storage volume of  $12.7 \cdot 10^6 \text{ m}^3$  (tailings and fill). The dam was approximately 80 m high and the crest was approximately 700 m long. The flood wave caused over 250 casualties and severe damages to the environment and infrastructure downstream of the dam site [22].

The flood wave resulting from the failure has been simulated by several teams from all over the world using different modelling tools, for example in [3], [23], [24] or [25]. Sweco has undertaken a similar work as part of an internal R&D project using the 2D hydrodynamic models MIKE21 and TELEMAT-2D. The topographical data used consists in the ALOS PALSAR RTC Digital Elevation Model (DEM) from the NASA (Alaska Satellite Facility) which describes the terrain with a 12.5 m resolution [26]. The elevation data has been acquired in 2011. Significant topographical changes occurred until the failure in the train terminal area (location A in Fig. 13) which was built after 2011 [3].

Two unstructured triangular meshes composed of 313 254 and 302 587 elements with an average edge length of 10 m was built in MIKE21. The first mesh covers the valley from upstream of the dam location down to the junction with Paraopeba River located approximately 9 km downstream of the dam while the second mesh only covers the valley from the dam toe. TELEMAT-2D simulations are based on the exact same computational meshes, converted into Selafin format with the software BlueKenue. The first mesh has been used to model the failure by letting the tailings volume be freely released at the beginning of the simulation while the

second mesh was used to model the failure with an outflow hydrograph.

For the first mesh, the DEM has been processed at the dam location in order to recreate the post-failure topography so that the liquefied tailings released during the failure event could be modelled by recreating the initial dam profile defined as initial condition for free surface in the hydrodynamic simulations. The simulated outflow volume is of approximately  $10.4 \cdot 10^6 \text{ m}^3$ , which is 7% larger than the estimated outflow volume [22].

For the second mesh, the outflow hydrograph determined by HR Wallingford in [23] using the EMBREA-MUD tailings dam breach model has been set as a boundary condition. The hydrograph volume corresponds to the estimated released volume of  $9.7 \cdot 10^6 \text{ m}^3$  [22]. The peak discharge, of  $90\,000 \text{ m}^3/\text{s}$ , is reached 5 s after the failure and progressively diminishes in steps until reaching  $0 \text{ m}^3/\text{s}$  after 300 s (see Fig. 13).

For the simulations in which the failure is modelled by letting the tailings volume be freely released, two hypotheses were considered: *i)* the liquefaction is supposed to be instantaneous through the overall tailings volume, *ii)* the liquefaction is supposed to be time-dependent and to propagate from the dam body towards the reservoir over time. For the first hypothesis, the simulation is performed with the nominal rheological properties of the liquefied, flowing tailings at simulation start (i.e. constant in space and time). For the second hypothesis, the tailings' rheological properties within the reservoir are defined as a function of time and location with respect to dam body, starting with very large values for yield stress and dynamic viscosity to "freeze" the fluid and progressively converging to their nominal, post-liquefaction, values. This hypothesis was modelled in TELEMAT-2D only as MIKE21 does not allow to define space and time-varying fluid properties. According to the analysis of the event detailed in [22], the failure quickly propagated from the dam body towards the reservoir while observations from surveillance cameras showed that liquefaction in the furthest parts of the reservoir occurred after approximately 6 to 8 minutes. The instant at which



liquefaction occurs  $t_L$  [s] (i.e. when the tailings' rheological values reach their nominal values) has been modelled across the reservoir as:

$$t_L = d^\alpha \cdot t_{L,final} \quad (17)$$

With  $d$  a dimensionless distance [-] defined linearly between the dam body (0.0) and the outer reservoir limit (1.0),  $\alpha$  a shape parameter [-] and  $t_{L,final}$  the instant at which the furthest tailings liquefy, defined as 7 minutes (420 s). The spatial and time distribution for the liquefaction time has been modelled with a shape parameter coefficient of  $\alpha = 2$ . This value has been chosen arbitrarily to mimic the observed release sequence [22] and the simulated outflow hydrograph [23]. It should be noted that this method is a two-dimensional simplification of the liquefaction process, that is significantly more complex [22].

Bottom friction was modelled using a Strickler coefficient of  $20 \text{ m}^{1/3}/\text{s}$  in both MIKE21 and TELEMAT-2D and in both meshes and no turbulence model was used.

The available documentation regarding the rheological properties of released tailings is scarce and sometimes very different values have been used in previous works ([3] [23] [24] [25]). The bulk density of the flowing liquefied tailings used in previous studies ranges between  $1800$  and  $3000 \text{ kg/m}^3$ . Information from the Expert Panel Report [20] indicates that the average material's bulk density stored in the dam was about  $2650 \text{ kg/m}^3$ . Simulations have been performed with density values of  $\rho = 1800$  and  $2650 \text{ kg/m}^3$ . A value of  $1800 \text{ kg/m}^3$  has also been used in the MIKE21 modelling performed in [23].

According to the geotechnical data available in the Expert Panel Report [22], the tailings stored contained approximately 50% of fine particles. The sediment volumetric concentration within the storage has been estimated to approximately  $C_V = 0.47$ . By combining this information with the available empirical relationships for yield stress (15) and dynamic viscosity (16) available in the literature ([2] [7] [18]), the yield stress and the dynamic viscosity have been assumed to lie between  $100$ - $1000 \text{ Pa}$  and  $10$ - $100 \text{ Pa}\cdot\text{s}$ , respectively. Simulations have been performed with yield stress values of  $\tau_y = 100, 500, 750$  and  $1000 \text{ Pa}$ . Dynamic viscosity was set to  $\mu = 50 \text{ Pa}\cdot\text{s}$  in all the simulations. Tests have shown that this parameter has limited influence on the flood wave propagation.

Available calibration data regarding water levels and flood wave propagation is scarce. The quality of the DEM is not good enough to allow for a good calibration of flow depths. According to the information available in previous studies, flood arrival time can be estimated at three locations:

- Canteen (location B in Fig. 13): ca. 2 min.
- Railway bridge (location C in Fig. 13): 10 to 12 min.
- Paraopeba River (location D in Fig. 13): 1 h 30 min to 2 h 10 min.

TELEMAT-2D simulations have been performed with the non-Newtonian Bingham model with all three implemented

Options tested. Results from Options 1 and 2 are very close from each other, therefore only results from Option 1 are presented. Simulations were performed with both kinetic and HLLC finite volume schemes, no significant differences were observed. MIKE21 simulations were performed with the Bingham flow model.

Analysis of model results with respect to flood extent and flood propagation time showed that the best results were obtained with the outflow hydrograph model, a bulk density of  $\rho = 1800 \text{ kg/m}^3$ , a yield stress of  $\tau_y = 750 \text{ Pa}$  and  $\mu = 50 \text{ Pa}\cdot\text{s}$  for the dynamic density.

To illustrate the differences between the different software and modelling assumptions with respect to outflow methods, flood wave's arrival times and flood extents the following model runs are analysed:

- T-a1 = TELEMAT-2D, outflow volume freely released, Bingham Option 1.
- T-a3 = TELEMAT-2D, outflow volume freely released, Bingham Option 3.
- T-b1 = TELEMAT-2D, outflow volume freely released with time-dependent liquefaction, Bingham Option 1.
- T-b3 = TELEMAT-2D, outflow volume freely released with time-dependent liquefaction, Bingham Option 3.
- T-c1 = TELEMAT-2D, outflow hydrograph, Bingham Option 1.
- T-c3 = TELEMAT-2D, outflow hydrograph, Bingham Option 3.
- M-a = MIKE21, outflow volume freely released.
- M-c = MIKE21, outflow hydrograph.

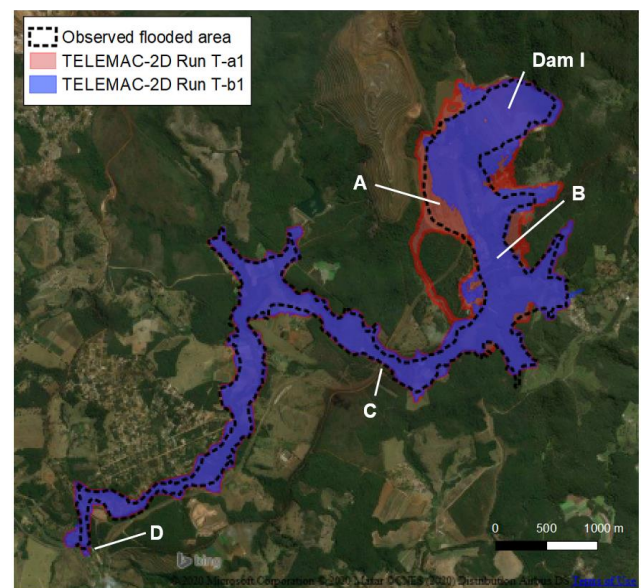


Figure 13: Brumadinho tailings dam failure, comparison of flood extents for runs T-a1 and T-b1.

TABLE 1: BRUMADINHO TAILINGS DAM FAILURE. ARRIVAL TIME AT THREE DIFFERENT LOCATIONS OBTAINED WITH THE BEST SET OF RHEOLOGICAL PARAMETERS ( $\rho = 1800 \text{ KG/M}^3$ ,  $\tau_y = 750 \text{ PA}$ ,  $\mu = 50 \text{ PA}\cdot\text{S}$ ) AND OBSERVATIONS

Run	Canteen (B)	Railway bridge (C)	Paraopeba River (D)
T-a1	00:01:15	00:04:15	01:42:00
T-a3	00:01:15	00:04:30	01:59:00
T-b1	00:01:30	00:07:00	01:43:00
T-b3	00:01:30	00:07:15	02:00:00
T-c1	00:02:15	00:09:15	02:35:00
T-c3	00:02:15	00:09:30	02:55:00
M-a	00:01:15	00:03:45	01:51:00
M-c	00:02:00	00:07:15	02:40:00
Obs.	ca 00:02:00	ca 00:10:00-00:12:00	ca 01:30:00-02:10:00

Flood wave's arrival times are presented in Table 1 with a 15 s precision. It can be seen that the outflow release method used has a large influence flood wave propagation times, with the scenarios based on an instantaneous liquefaction ("a" runs) giving an overestimation of flood wave's celerity, especially upstream of the railway bridge (location C in Fig. 13). Scenarios based on a time-dependent liquefaction ("b" runs) or on the outflow hydrograph obtained by HR Wallingford with EMBREA-MUD [23] ("c" runs) are in better agreement with observations. Concerning the latter runs, it is worth noting that the longer propagation times obtained with TELEMAC-2D are linked to the fact that the flow regime at the inflow boundary is subcritical thus underestimating the outflow velocities and overestimating the flow depths. Comparison between MIKE21 ("M" runs) and TELEMAC-2D ("T" runs) shows that propagation times obtained with MIKE21 are slightly shorter than with TELEMAC-2D at the railway bridge but lie between TELEMAC-2D's Options 1 and 3 at the junction with Paraopeba River. The overall agreement between both software is good. Comparison between Bingham Options 1 and 3 implemented in TELEMAC-2D shows that the Option 3 give slightly slower propagation times, which is an expected result based on the more resistive behaviour of this option (see section II-B, VI-A and VI-B).

A map illustrating the maximal flood extents obtained with TELEMAC-2D with an instantaneous liquefaction (run T-a1) and with a time-dependent liquefaction (run T-b1) is presented in Fig. 13. Differences between MIKE21 and TELEMAC-2D with respect to flood extent are not significant, therefore are only results from TELEMAC-2D depicted in the map, for clarity. Results from the simulation performed with a time-dependent liquefaction are in better agreement with observations. Differences on flood extents observed between observations and model results in the railway terminal area (location A in Fig. 13) are influenced by differences between the DEM data and the actual topography when failure occurred [3]. It is worth noting that the quality of the DEM is globally poor, especially in the lower part of the flood path where high grounds are present across the valley thus creating a

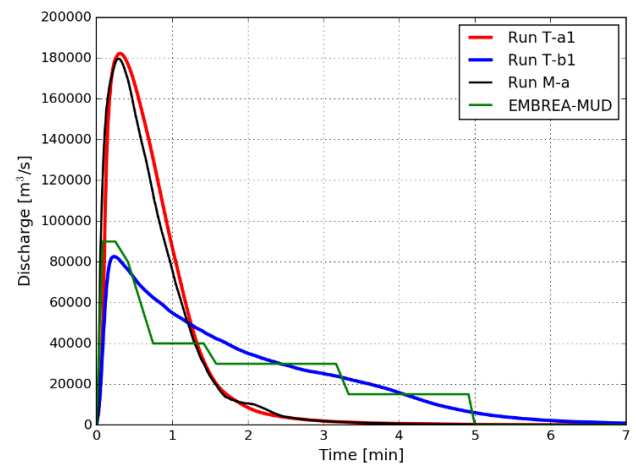


Figure 14: Brumadinho tailings dam failure, comparison of outflow hydrographs for runs T-a1 and T-b1, M-a and comparison with the hydrograph proposed by HR Wallingford using EMBREA-MUD [23].

succession of pools along the flood path which contributes to increase flow levels as well as slowing down the flood wave.

The influence of the instant at which liquefaction occurs on outflow hydrographs when modelling the release of the stored tailings is analysed by comparing the runs T-a1, M-a (instantaneous liquefaction) and T-b1 (time-dependent liquefaction), see Fig. 14. Differences between Bingham Options 1 and 3 are very small, hence only results from Option 1 are presented. The results indicate that outflows generated by an instantaneous liquefaction is characterized by a peak flow value ( $\sim 180\,000 \text{ m}^3/\text{s}$ ) approximately 2.25 times greater than with a time-dependant liquefaction ( $\sim 80\,000 \text{ m}^3/\text{s}$ ) and consequently by a shorter outflow duration ( $\sim 3$  and  $7$  minutes, respectively). The hydrographs obtained with TELEMAC-2D (T-a1) and MIKE21 (M-a) for an instantaneous liquefaction are in good agreement. The outflow hydrograph generated with a time-dependent liquefaction (T-b1) is in good agreement with the hydrograph obtained by HR Wallingford with EMBREA-MUD [23].

Analysis of the simulations performed with  $\rho = 2650 \text{ kg/m}^3$  and for other values of yield stress  $\tau_y$  between 100 and 1000 Pa, not detailed here, shows very small differences on propagation times between the dam and the railway bridge. Along this reach, the valley slope is steep (3-4% in the two first kilometres) and progressively decreases towards the railway bridge (approximately 1%), indicating that inertial effects are likely to have a much larger influence than non-Newtonian viscous stresses on flood propagation for such configuration. On the other hand, significant differences are observed downstream of the railway bridge down to the junction with Paraopeba River where the valley slope is less pronounced (0.8-1%). For example, a density of  $\rho = 2650 \text{ kg/m}^3$  in combination with a yield stress  $\tau_y = 750 \text{ Pa}$  leads to approximately 60% faster propagation time at this location compared with  $\rho = 1800 \text{ kg/m}^3$ .

This case study has shown that the non-Newtonian Bingham model implemented in TELEMAC-2D in combination with a time-dependent liquefaction gives

satisfactory results for the Brumadinho tailings dam break simulation. Results compare well with similar simulations performed with MIKE21 when modelling an instantaneous liquefaction. This case study also highlights the fact that flood propagation of flowing tailings is sensitive to several key assumptions involved in such a work: dam failure mode and outflow scenario, rheological parameters (especially the fluid's density and yield stress) and quality of topographical data used. A good estimation of these parameters and their associated uncertainties is a crucial step in a tailings dam break and emergency plan study.

### VIII. CONCLUSIONS AND PERSPECTIVES

In this article, the non-Newtonian Bingham and Herschel-Bulkley models implemented in the Finite Volume version of TELEMAT-2D have been presented. In addition, a simplified pseudo-biphasic, variable density formulation has also been implemented in order to make it possible to model the mixing between Newtonian and non-Newtonian fluids. The validation examples presented show that these models can be used to model non-Newtonian behaviour in a satisfactory manner and compared reasonably well with results from other studies performed with other numerical codes as well as with analytical solutions. The application example of the Brumadinho tailings dam failure shows that TELEMAT-2D can be used in tailings dam break studies.

Tests have been performed in Finite Elements but showed poor performance with instabilities linked to strong source term gradients. Further work is required before the non-Newtonian models can be incorporated in TELEMAT-2D's Finite Element version. Other possible improvements would be to *i*) reduce the spreading observed in the front region once a pseudo-equilibrium state is reached, *ii*) introduce a new method for computing the shear rate by taking horizontal velocity gradients into account and *iii*) to couple the pseudo-biphasic formulation with GAIA in order to include effects of settling velocity and allow the modelling of morphological changes.

This development can be used as a base for implementing other non-Newtonian models, for example Coulomb-based models that are often used in debris-flows modelling.

This development will be included in an upcoming release of the openTELEMAT-MASCARET suite.

### ACKNOWLEDGEMENT

This work has been partly funded by Sweco as part of an internal R&D project performed together with colleague Non Okumura who was in charge of the GIS work and MIKE21 modelling involved in the Brumadinho tailings dam failure study.

The author would like to thank Riadh Ata for his support and technical guidance as well as Florent Taccone at EDF R&D for his help in incorporating this development into the openTELEMAT-MASCARET suite.

### REFERENCES

- [1] Martin, V., Al-Mamun, M., & Small, A., CDA technical bulletin on tailings dam breach analysis, ICOLD symposium, 2019.
- [2] Julien, P.-Y., Erosion and sedimentation, 2nd edition, Cambridge University Press, 2010.
- [3] Yu, D., Tang, L., Chen, C., Three-dimensional numerical simulation of mud flow from a tailing dam failure across complex terrain, *Natural Hazards and Earth System Sciences*, Vol. 20, 727-741, 2020.
- [4] Gao, J., Fourie, A., Using the flume test for yield stress measurement of thickened tailings, *Minerals Engineering*, Vol. 81, 116-127, 2015.
- [5] Blight, G. E., Bentel, G. M., The behaviour of mine tailings during hydraulic deposition, *Journal of the South African Institute of Mining and Metallurgy*, 1983.
- [6] Chhabra, R.P., Richardson, J.F., Non-Newtonian Flow in the Process Industries. Fundamentals and Engineering Applications, Butterworth-Heinemann, 1999.
- [7] FLO-2D, Simulating Mudflows, White paper available at <https://flo-2d.com/downloads/> (last visit 2020-05-02).
- [8] Martinez, C., Miralles-Wilhelm, F., Garcia-Martinez, R., Verification of a 2D finite element debris flow model using Bingham and cross rheological formulations, *WIT Transactions on Engineering Sciences*, Vol. 60, 61-69, 2008.
- [9] Ajayi, A. E., Surface runoff and infiltration processes in the Volta Basin, West Africa: Observation and modeling, *Ecology and Development Series*, No. 18, ZEF Bonn, 2004.
- [10] Mitsoulis, E., Flows of viscoplastic materials: models and computations, *Rheology Reviews* 2007, 135-178, 2007.
- [11] Soto, H. P., et al., A Numerical Investigation of Inertia Flows of Bingham-Papanastasiou Fluids by an Extra Stress-Pressure-Velocity Galerkin Least-Squares Method, *Journal of the Brazilian Society of Mechanical Sciences and Engineering*, Vol. XXXII, No. 5, December-Special Issue, 2010.
- [12] Shao, S., Lo, E.Y., Incompressible SPH method for simulating Newtonian and Non-Newtonian flows with a free surface, *Advances in Water Resources*, Vol. 26, 787-800, 2003.
- [13] Rickenmann, D., Bedload transport capacity of slurry flows at steep slopes, PhD Thesis, ETH Zürich, 1990.
- [14] Naef, D., et al., Comparison of flow resistance relations for debris flows using a one-dimensional finite element simulation model, *Natural Hazards and Earth System Sciences*, Vol. 6, 155-165, 2006.
- [15] DHI, MIKE 21 Flow Model FM, Hydrodynamic Module, User Guide, 2017.
- [16] EDF R&D, TELEMAT-2D, User manual, Version v8p1, 2019.
- [17] Hervouet, J.-M., Hydrodynamics of free surface flows, John Wiley & Sons, 2007.
- [18] Oboni, F., Oboni, C., Tailings dam management for the twenty-first century. What mining companies need to know and do to thrive in our complex world, Springer International Publishing, 2020.
- [19] Audusse, E., Bouchut, F., Bristeau, M. O., Klein, R., & Perthame, B. T., A fast and stable well-balanced scheme with hydrostatic reconstruction for shallow water flows, *SIAM Journal on Scientific Computing*, 25(6), 2050-2065, 2004.
- [20] Hungr, O., A model for the runout analysis of rapid flow slides, debris flows, and avalanches, *Canadian Geotechnical Journal*, Vol. 32, 610-623, 1995.
- [21] Toro, E. F., The HLL and HLLC Riemann solvers, In *Riemann solvers and numerical methods for fluid dynamics* (pp. 315-344), Springer, Berlin, Heidelberg, 2009.
- [22] Robertson, P. K., et al., Report of the Expert Panel on the Technical Causes of the Failure of Feijão Dam I, 2019.
- [23] Lumbroso, D., et al., Modelling the Brumadinho tailings dam failure, the subsequent loss of life and how it could have been reduced, Preprint version dated 2020-06-04, *Natural Hazards and Earth System Sciences*, 2020.

- [24] Garcia, R., Tribst-Correa, A., Two-dimensional runout evaluation of the Brumadinho Tailings dam failure in Brazil, Conference presentation, Dam Safety, 2019.
- [25] Liu, S., Back analysis of the Feijao failure, Conference presentation, Tailings and mine waste, 2019.
- [26] NASA's Alaska Satellite Facility, ALOS PALSAR RTC Digital Elevation Model, <https://asf.alaska.edu/data-sets/derived-data-sets/alos-palsar-rtc/alos-palsar-radiometric-terrain-correction/> (last visit 2020-05-02).



# Investigation on estuarine turbidity maximum response to the change of boundary forcing using 3CPBE flocculation model

Qilong Bi<sup>1,2</sup>, Xiaoteng Shen<sup>3</sup>, Byung Joon Lee<sup>4</sup> and Erik Toorman<sup>2</sup>

<sup>1</sup> Flanders Hydraulics Research, Antwerp, Belgium.

<sup>2</sup> Hydraulics Section, Department of Civil Engineering, KU Leuven, Leuven, Belgium.

<sup>3</sup> College of Harbour, Coastal and Offshore Engineering, Hohai University, Nanjing, China.

<sup>4</sup> Department of Construction and Environmental Engineering, Kyungpook National University, Sangju, South Korea.

Email: [qilong.bi@mow.vlaanderen.be](mailto:qilong.bi@mow.vlaanderen.be)

**Abstract**—Seasonal variation in suspended particular matter (SPM) is often observed in the Scheldt estuary. As part of it, the estuarine turbidity maximum (ETM) zone also exhibits different characteristics in different periods of a year. There are many reasons behind this complex phenomenon, the change of boundary forcing and the biological effects. This study tries to understand the ETM response to the change of boundary forcing in a seasonal scale. For this purpose, a schematic model of the Scheldt estuary is created, and a 3-class population balance equation based (3CPBE) flocculation model is incorporated. The model results reveal that the flocculation process is crucial for reproducing the ETM, and more importantly, its seasonal variation.

## I. INTRODUCTION

The Sea Scheldt is an upper part of the Scheldt Estuary. Unlike the downstream part of the estuary, i.e. the Western Scheldt (0–60 km), the Sea Scheldt (60–160 km) can be considered as a single channel system with tidal influence, stretching from the Dutch/Belgian border to the upstream boundary at Gent (Schepers et al. 2018). Although three main tributaries, i.e. the Dender, the Durme, and the Rupel, join the Sea Scheldt at its upstream (Figure 1), their contributions to the total discharge is usually limited.

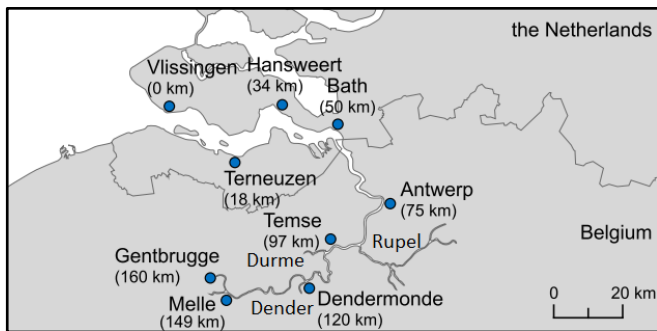


Figure 1 – Overview of the Scheldt estuary (Dijkstra et al., 2017)

Two estuary turbidity maximum (ETM) zones are often observed in the Sea Scheldt, the first one is located near

Oosterweel, which is downstream of the city of Antwerp, and the second one about 100 km to 140 km from Vliissingen (Vandenbruwaene et al. 2018). The first ETM is heavily influenced by the human interventions, e.g. dredging/dumping activities, while the second ETM is usually more subjected to the tidal forcing and the upstream discharges. This study only focusses on the second ETM in the Sea Scheldt.

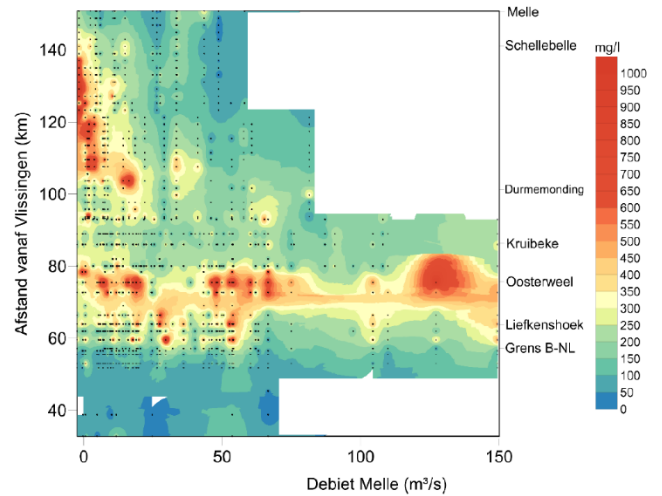


Figure 2 - Near surface sediment concentration at half-tide ebb along the Sea Scheldt in relation to the flow discharge at Melle based on all measurements since the year 2009 (source: Vandenbruwaene et al. 2018).

The long-term observation confirms that the second ETM tends to move landward and extends its length towards the upstream boundary during summer when the daily-averaged discharge is low ( $< 20 \text{ m}^3/\text{s}$ ), whereas it moves towards the downstream with shorter length during winter when the daily-averaged discharge becomes larger ( $> 35 \text{ m}^3/\text{s}$ ) (Figure 2). This seasonal variation of spatial patterns also comes with other changes in the water column. Some other field measurements show that the sediment density varies between summer and winter conditions. To be more specific, the sediment particles observed at Schellebelle (about 140 km

from Vlissingen) exhibit smaller density and larger size, hence, larger settling velocity during summer. This implies that flocculation may play a role in the seasonal variation in suspended particulate matter (SPM) in the Sea Scheldt, especially in the second ETM.

There could be many reasons for the seasonal variations of the ETM observed in the Sea Scheldt. One of the reasons is the changes of boundary forcing from winter to summer, especially the discharge at the upstream boundary. The boundary forcing could influence the hydrodynamics in several ways, e.g. alter the tidal asymmetry, shift the convergence point between the tide-energy and river-energy, and change the local flow conditions. In reality, as one of the important properties of cohesive sediments, flocculation is inevitably subject to these hydrodynamic changes as well since turbulent shear is one of the main factors controlling aggregation and breakage of flocs. This will further affect the settling velocity and density of these cohesive particles, hence, the transport process and SPM distribution, which could influence the flocculation in a feedback loop. Another possible reason for the seasonal variation of the ETM is the biological activities, which are usually high in summer and low in winter. The biomass in the water system, therefore, is under influence of the biological activities, and could be linked to the aggregation and breakage of flocs through a so-called bio-mediated flocculation (Lee et al. 2017).

Traditional sediment transport models usually have difficulties in capturing the seasonal variation of the ETM in riverine and estuarine systems due to simplified assumptions of sediment properties, e.g. uniform and constant particle size density, and settling velocity. This restricts the models reacting to the changes of boundary forcing and other conditions in a more dynamic and realistic way. Some models employ flocculation models to overcome this issue. However, the flocculation models used are either based on empirical formulas or assumptions under equilibrium conditions, which are still not ideal.

This study employs a dynamic approach for modelling flocculation process. This approach is based on a set of multiple population balance equations (MPBEs), with carefully designed source and sink terms for capturing flocculation kinetics (Lee et al. 2011; Shen et al. 2018). Instead of only tracking the floc size, this approach considers 2 classes (2CPBE) or 3 classes (3CPBE) of flocs, and utilizes a set of coupled PBEs for describing the aggregation and breakage of flocs due to Brownian motion, turbulent shear and differential settling. In this case, the number concentration of each floc class is tracked, as well as the composition of the particles. Based on this approach, a schematic model of Scheldt estuary is created and used for investigating the seasonal variation of SPM and the ETM response to the boundary forcing. The biological effects are not considered in this study for simplicity.

## II. METHODOLOGY

A 3D schematic model for the Scheldt estuary is created in this study using a customized version of the openTELEMAC modelling suite, in which multiple versions of the MCPBE flocculation model (2CPBE model and two variations of

3CPBE models) have been implemented, with additional optimizations for large-scale applications (Bi et al. 2019). The code development allows complex 3D sediment transport modelling, e.g. mixed sediment transport with multiple cohesive and/or non-cohesive classes. Transport of cohesive sediment (with two or three floc size classes) can be modelled as suspended load with flocculation kinetics enabled, while transport of non-cohesive sediment is modelled as bedload.

A 3-class cohesive sediment transport model is coupled with hydrodynamics, in which the interactions between the 3 sediment (floc) classes are accounted through the aggregation and breakage processes modelled by the 3CPBE flocculation model (Shen et al. 2018). Sediment properties, e.g. particle density and settling velocity, can be altered due to various control parameters, such as flow strength, local sediment size distribution and SPM concentration. This would allow the modelled system reacting to the boundary forcing in a more realistic way and provide the possibility of capturing the seasonal variations of SPM often observed in nature.

### A. Hydrodynamics

The hydrodynamics in TELEMAC-3D is modelled with the 3D incompressible Reynolds-averaged Navier-Stokes equations. The Navier-Stokes equations for incompressible flows consist of two equations: the continuity equation and the momentum equation. Assuming that the fluid density is constant, and applying the Boussinesq eddy viscosity approximation to the Reynolds stress term, the mass and momentum conservation equations read:

$$\nabla \cdot \mathbf{u} = 0 \quad (1)$$

$$\frac{\partial \mathbf{u}}{\partial t} + (\mathbf{u} \cdot \nabla) \mathbf{u} = -\frac{1}{\rho} \nabla p + \nabla \cdot [(\nu + \nu_T) \nabla \mathbf{u}] + \mathbf{g} + \mathbf{F} \quad (2)$$

where  $\mathbf{u}$  is the Reynolds-averaged mean velocity field,  $t$  is the time,  $\rho$  is the fluid density,  $p$  is the mean pressure,  $\nu$  is the kinematic viscosity of the fluid,  $\nu_T$  is the turbulence eddy viscosity,  $\mathbf{g}$  is the gravitational force and  $\mathbf{F}$  represents the other external forces, e.g. Coriolis force and centrifugal force.

Several turbulence models are available in the TELEMAC-3D. The most commonly used ones are the  $k - \epsilon$  model, the Smagorinski model and the mixing-length model. It is also possible for the users to define constant eddy viscosity for horizontal and vertical, respectively. In this study the  $k - \epsilon$  model is adopted in all the simulations.

### B. Sediment transport with flocculation

This study adopts the 3CPBE flocculation model (Shen et al. 2018), which is an improvement to the 2CPBE flocculation model (Lee et al. 2011) and applies it to a 3D application. Similar to the 2CPBE flocculation model, by including one more sediment class, the 3CPBE flocculation model is able to describe the flocculation dynamics with the representative sizes and mass fractions of microflocs ( $\leq 30 \mu\text{m}$ ), macroflocs ( $30 - 300 \mu\text{m}$ ) and megaflocs ( $\geq 300 \mu\text{m}$ ).

In the 3CPBE flocculation model, the microflocs belongs to the smallest class among the three. Because of its compact structure, microflocs are relatively stable in the environment and difficult to be further broken-up. Thus, it acts as the basic

building block for the other two sediment classes. Usually a fixed particle size derived from the field measurements is assigned to the microflocs, therefore, its particle density also remains constant.

The megaflocs are categorized as the largest class among the three and usually have variable sizes and densities depending on their compositions. For simplicity, in this study the megaflocs are also considered as a fixed-sized class. A representative particle size based on the field measurements is assigned to this class.

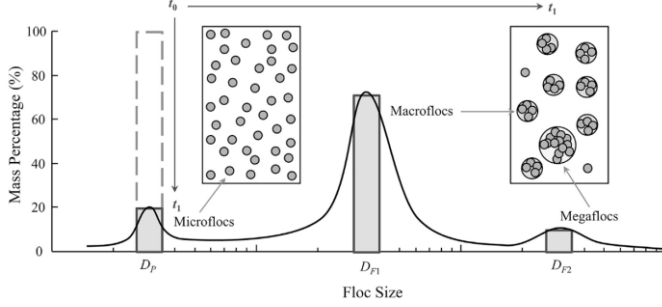


Figure 3 - Schematic diagram of the FSDs before and after flocculation (Shen et al. 2018). At time  $t_0$ , all particles are concentrated on microflocs. With time, macroflocs and megaflocs have appeared because of aggregation and breakage processes.

The governing equations of the 3CPBE flocculation model in 3D are described as follows:

$$\frac{\partial N_i}{\partial t} + (\mathbf{u} \cdot \nabla) N_i = \nabla \cdot (D_T \nabla N_i + \mathbf{w}_{s,i} N_i) + (A_i + B_i) \quad (3)$$

where  $N_i$  is the number concentration of class  $i$  ( $i=P, FI, TI$  or  $T2$ ),  $\mathbf{u}$  is the Reynolds-averaged mean velocity vector,  $t$  is the time,  $D_T$  is the turbulent diffusion coefficient,  $\mathbf{w}_{s,i}$  is the settling velocity vector of class  $i$  pointing downward,  $A_i$  and  $B_i$  are aggregation and breakage source and sink terms. Eq.(3) is a system of coupled transport equations that track (1) the number of microflocs and macroflocs in suspension per unit volume, with symbol  $N_P$  and  $N_{FI}$  respectively, (2) the total number of microflocs in all macroflocs per unit volume  $N_{T1}$ , and (3) the total number of microflocs in all megaflocs per unit volume  $N_{T2}$ .

It is worth mentioning that the eq.(3) is slightly modified when implemented in the openTELEMAT. The main reason is that the number concentration  $N_i$  is usually much larger than the other variables and could cause instability when solved in a coupled way with other unknown variables in TELEMAT-3D. The solution is to rescale  $N_i$  by multiplication both side of with the mass of one microfloc  $m_p$  (a constant value), thus, eq.(3) can be written as:

$$\frac{\partial C_P}{\partial t} + (\mathbf{u} \cdot \nabla) C_P = \nabla \cdot (D_T \nabla C_P + \mathbf{w}_{s,i} C_P) + m_p (A_P + B_P) \quad (4)$$

$$\frac{\partial C_{F1}}{\partial t} + (\mathbf{u} \cdot \nabla) C_{F1} = \nabla \cdot (D_T \nabla C_{F1} + \mathbf{w}_{s,i} C_{F1}) + m_p (A_{F1} + B_{F1}) \quad (5)$$

$$\frac{\partial C_{T1}}{\partial t} + (\mathbf{u} \cdot \nabla) C_{T1} = \nabla \cdot (D_T \nabla C_{T1} + \mathbf{w}_{s,i} C_{T1}) + m_p (A_{T1} + B_{T1}) \quad (6)$$

$$\frac{\partial C_{T2}}{\partial t} + (\mathbf{u} \cdot \nabla) C_{T2} = \nabla \cdot (D_T \nabla C_{T2} + \mathbf{w}_{s,i} C_{T2}) + m_p (A_{T2} + B_{T2}) \quad (7)$$

with  $C_P = m_p N_P$ ,  $C_{F1} = m_p N_{F1}$ ,  $C_{T1} = m_p N_{T1}$  and  $C_{T2} = m_p N_{T2}$ . By definition,  $C_P$ ,  $C_{T1}$ , and  $C_{T2}$  are equivalent to the mass concentration of microflocs, macroflocs, and megaflocs, respectively, while  $C_{F1}$  does not have a specific physical meaning. Note that eqs.(4) – (7) not only describe the flocculation process, i.e. aggregation and breakage of flocs, but also the transport of microflocs, macroflocs and megaflocs.

TABLE 1 - AGGREGATION AND BREAKAGE PROCESSES OF SUSPENDED PARTICLES WITH THREE SIZE GROUPS (SHEN ET AL. 2018).

Processes (j) ↓	Description
(1) Aggregation Microflocs & Microflocs	$\bullet + \bullet \rightarrow \left[ \frac{N_{C1}-2}{N_{C1}-1} \bullet + \frac{1}{N_{C1}-1} \bullet \right]$
(2) Aggregation Microflocs & Macroflocs	$\bullet + \bullet \rightarrow \bullet$
(3) Aggregation Microflocs & Megaflocs	$\bullet + \bullet \rightarrow \bullet$
(4) Aggregation Macroflocs & Macroflocs	$\bullet + \bullet \rightarrow \bullet$
(5) Aggregation Macroflocs & Megaflocs	$\left[ \frac{N_{C2}/N_{C1}-2}{N_{C2}/N_{C1}-1} \bullet + \frac{1}{N_{C2}/N_{C1}-1} \bullet \right]$
(6) Breakage Macroflocs	$\bullet \rightarrow \underbrace{\bullet \dots \bullet}_{f_{F1}} + \underbrace{\bullet \dots \bullet}_{1-f_{F1}} \quad K_1$
(7) Breakage Megaflocs	$\bullet \rightarrow \underbrace{\bullet \dots \bullet}_{f_{F2}} + \underbrace{\bullet \dots \bullet}_{f_{F2}} \quad K_2$

The flocculation processes included in this 3CPBE flocculation model are summarized in Table 1, with five aggregation processes and two breakage processes (Shen et al. 2018). The flocculation processes are modelled in the source and sink terms as follows.

$$(A_P + B_P) = -\frac{1}{2} \alpha_{PP} N_P N_P \left( \frac{N_{C1}}{N_{C1}-1} \right) - \alpha_{PF1} N_P N_{F1} - \alpha_{PF2} N_P N_{F2} + f_{P1} N_{C1} a_{F1} N_{F1} + f_{P2} N_{C2} a_{F2} N_{F2} \quad (8)$$

$$(A_{F1} + B_{F1}) = \frac{1}{2} \alpha_{PP} N_P N_P \left( \frac{1}{N_{C1}-1} \right) - \frac{1}{2} \alpha_{F1F1} N_{F1} N_{F1} \left( \frac{N_{C2}/N_{C1}}{N_{C2}/N_{C1}-1} \right) - \alpha_{F1F2} N_{F1} N_{F2} + (K_1 - 1) a_{F1} N_{F1} + K_2 a_{F2} N_{F2} \quad (9)$$

$$(A_{T1} + B_{T1}) = \frac{1}{2} \alpha_{PP} N_P N_P \left( \frac{N_{C1}}{N_{C1}-1} \right) + \alpha_{PF1} N_P N_{F1} - \frac{1}{2} \alpha_{F1F1} N_{F1} N_{F1} \left( \frac{N_{C2}/N_{C1}}{N_{C2}/N_{C1}-1} \right) - N_{C1} \alpha_{F1F2} N_{F1} N_{F2} - f_{P1} N_{C1} a_{F1} N_{F1} + (1 - f_{P2} - f_{F2}) f_{P2} N_{C2} a_{F2} N_{F2} \quad (10)$$

$$(A_{T2} + B_{T2}) = \alpha_{PF2} N_P N_{F2} + \frac{1}{2} \alpha_{F1F1} N_{F1} N_{F1} \left( \frac{N_{C2}/N_{C1}}{N_{C2}/N_{C1}-1} \right) + N_{C1} \alpha_{F1F2} N_{F1} N_{F2} - (1 - f_{P2}) N_{C2} a_{F2} N_{F2} \quad (11)$$

where  $P$ ,  $F1$ ,  $F2$ ,  $T1$  and  $T2$  are the indices for microflocs, macroflocs, megaflocs, microflocs in macroflocs and microflocs in megaflocs,  $N_i$  is the number concentration ( $i=P, F1, F2, T1$  or  $T2$ ),  $\alpha$  is the collision efficiency,  $\beta_{ij}$  is the collision frequency ( $i, j=P, F1, F2, T1$  or  $T2$ ),  $a_i$  is the breakup frequency concentration ( $i=F1$  or  $F2$ ),  $N_{C1}=N_{T1}/N_{F1}$  the number of microflocs bonded in a macrofloc,  $N_{C2}=N_{T2}/N_{F2}$  the number of microflocs bonded in a megafloc (for fixed size of megaflocs,  $N_{C2}$  is a constant),  $f_{P1}$  is the mass fraction of created microflocs when a macrofloc breaks up,  $f_{P2}$  is the mass fraction of created microflocs when a megafloc breaks up,  $f_{F2}$  is the mass fraction of the remaining megafloc when a larger megafloc breaks up,  $K_1$  is the number of created macroflocs when a larger macrofloc breaks up,  $K_2$  is the number of generated macroflocs when a megafloc breaks up.

The collision efficiency  $\alpha$  is a fitting parameter, and the collision frequency  $\beta_{ij}$  can be expressed as (Thomas et al., 1999; Maggi, 2005) with a linear combination of three mechanisms (terms):

$$\beta_{ij} = \frac{1}{6} G (D_i + D_j)^3 + \frac{\pi}{4} (D_i + D_j)^2 |w_{s,i} - w_{s,j}| + \frac{2 K_B T (D_i + D_j)^2}{3 \mu D_i D_j} \quad (12)$$

where  $G$  is the shear rate,  $w_s$  is the settling velocity,  $K_B$  is the Boltzmann constant,  $T$  is the absolute temperature and  $\mu$  is the fluid dynamic viscosity,  $D$  is the particle diameter,  $w_s$  is the settling velocity given by a fractal-corrected Stokes equation with hindered settling corrections (Winterwerp and van Kesteren, 2004),  $i$  and  $j$  are the indices  $P, F1, F2, T1$  or  $T2$ . Given the fixed size of microflocs, the sizes of macroflocs and megaflocs can be determined as (Matsoukas and Friedlander, 1991):

$$D_{Fi} = D_P N_{Ci}^{1/\eta f_i}, \quad i = 1, 2 \quad (13)$$

where  $\eta f$  is the fractal dimension of flocs, and  $D_P$ ,  $D_{F1}$  and  $D_{F2}$  are the characteristic sizes of microflocs, macroflocs and megaflocs, respectively. In the 3CPBE flocculation model used in this study,  $D_{F2}$  is also assumed as a constant to reduce the number of tracers. This assumption can be supported by field data used in Shen et al. (2018).

It is important to note that the effect of turbulent shear (the first term in eq.(12)) is the main mechanism in natural environments (Winterwerp, 1998). The effect of differential settling (second term in eq.(12)) is important during slack tide when turbulence is low (Lick et al., 1993), while the effect of Brownian motion (the third term in eq.(12)) is generally low for large particles (Winterwerp, 1998).

The breakup frequency  $a$  can be written as (Winterwerp, 1998):

$$a_i = E_b G \left( \frac{D_i - D_P}{D_P} \right)^{3-\eta f} \left( \frac{\mu G}{F_y / D_i^2} \right)^{1/2} \quad (14)$$

where  $E_b$  is the breakage coefficient. The floc strength  $F_y$ , although not a constant (Kranenburg, 1999), is assumed  $10^{-10}$  Pa in this study (Maggi et al., 2007; Verney et al., 2011).

The erosion and deposition fluxes have to be computed at the interface between bed layer and water column in order to provide the necessary bottom boundary conditions for the governing equations of 3CPBE flocculation model (eq.(4) – (7)). This is done in GAIA, which is a sediment transport module in the openTelemac suite. Therefore, in order to have a complete 3D sediment transport model, TELEMAC-3D has to be coupled with GAIA.

The following equation is used as the boundary condition near the bed for the suspended sediment transport equation (taken at a reference height  $z_b$  above the bed):

$$-D_v \frac{\partial C_i}{\partial z} - w_{s,i} C_i = (E_i - D_i)_{z_b} \quad (15)$$

where  $D_v$  is the vertical eddy diffusivity,  $C_i$  is the sediment mass concentration of class  $i$  ( $i=P, F1, T1$  or  $T2$ ),  $z$  is the vertical coordinate,  $w_s$  is the settling velocity,  $E_i$  is the erosion flux of class  $i$  and the deposition flux of class  $i$   $D_i = w_{s,i} C_i$ .

In the 3CPBE flocculation model, it is assumed that macroflocs and megaflocs are destroyed by large shear near the bottom and broken down into microflocs when deposited to the bed. In this case, the bed material only consists of microflocs, which will be the only floc class that can be eroded. Hence, the bottom boundary conditions for eq.(4) – (7) become:

$$-D_v \frac{\partial C_i}{\partial z} \Big|_{z_b} = \begin{cases} E_i & \text{if } i = P \\ 0 & \text{if } i = F1, T1 \text{ or } T2 \end{cases} \quad (16)$$

This is a Neumann type boundary and it states that the diffusive flux is balanced by the erosion flux at the bottom. In TELEMAC-3D, the erosion flux of microflocs is given by:

$$E_p = \max \left( 0, M \left( \frac{\tau_b}{\tau_c} - 1 \right) \right) \quad (17)$$

where,  $M$  is the erosion parameter,  $\tau_b$  is the bed shear stress and  $\tau_c$  is the critical shear stress for erosion.

### III. SCHEMATIZED SCHELDT MODEL

For better understanding the seasonal variation of SPM and the ETM response to the boundary forcing in the Sea Scheldt, and finding out the influence of flocculation processes on the ETM dynamics, a 3D schematized model with six vertical layers based on the measured estuary width and bottom elevation was created.

The 3CPBE flocculation model proposed by Shen et al. 2018 is adopted in this study for modelling the flocculation kinetics. There are two variations of the 3CPBE model, a simplified version assuming a fixed-sized megaflocs, and a more complex version that allows the properties of megaflocs evolving dynamically. The former is applied in the current model for simplicity, while the latter is more suitable for incorporating biological effects, which could also be important processes for the seasonal variation of SPM observed in rivers and coasts (Lee et al. 2017; Fettweis et al. 2017).

In this study, the geometry of the Scheldt Estuary has been schematized by a funnel-shaped domain as in Dijkstra et al.



(2017) and Brouwer et al. (2018), based on observations. As shown in Figure 4, the schematized geometry is derived by fitting an exponential function of a ratio of two polynomials against observed width along the Scheldt estuary. Similarly, the bottom in the schematized domain is obtained by fitting a smooth function to the measured cross-sectionally averaged depth along the estuary. To better approximate the tidal propagation in the estuary, the tidal prism is kept as close as possible to the real estuary. The estuary width is used for deriving the schematized geometry, the bottom is kept flat in cross-channel direction but with longitudinal slope. This synthetic bathymetry is then derived using the measured wet-sections along the estuary, so that the tidal prism will not be altered.

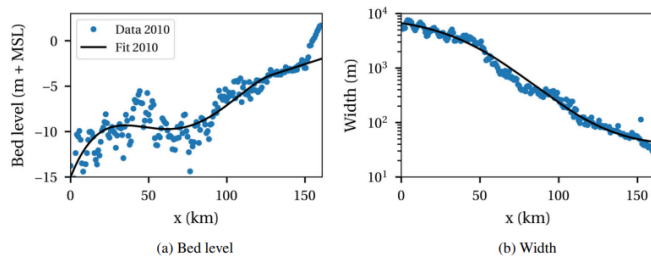


Figure 4 - The measured and fitted geometry of the Scheldt Estuary (Dijkstra et al., 2017)

The schematized domain starts at Vlissingen the estuary mouth and ends all the way up to the Gentbrugge where tidal locks were installed. The total length is 160km. The width is about 13.3km at the mouth and about 90m at the upstream boundary. It is worth mentioning that due to the simplified geometry, the tidal flats are not included, which may result in overestimation of tidal amplitude.

In order to have a lightweight triangular mesh that allows the model running efficiently for long period, the grid size is defined as a function of the width along the estuary (Bi et al. 2020). This results in a mesh that is symmetric about the x-axis. There are always four elements distributed along the y-axis at each kilometre, and those elements are aligned with the streamlines from downstream until the very upstream. The final mesh size ranges from about 4000 m in the estuary mouth to about 30 m in the upstream boundary (Figure 5).

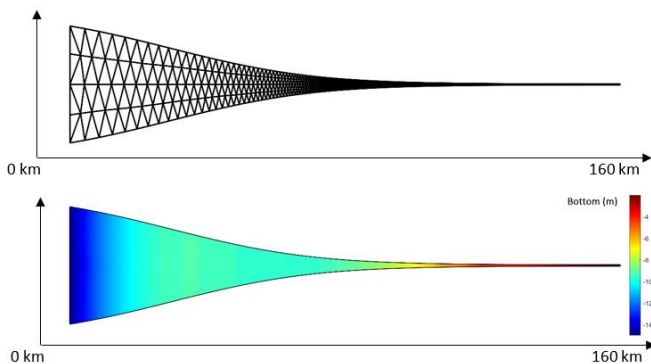


Figure 5 - The Telemac grid and bathymetry of the schematized Scheldt estuary

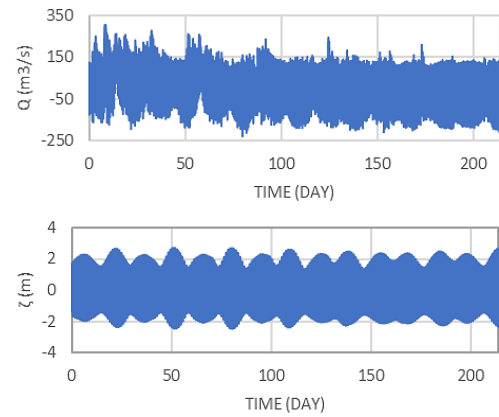


Figure 6 – Boundary conditions of the model (upper: upstream discharge measured at Melle, lower: downstream water level measured at Cadzand)

For the hydrodynamics, the boundary conditions are based on the field measurements in order to provide a better approximation of the tidal forcing. The continuously measured timeseries of water level at Cadzand and freshwater discharge at Melle in 2015 is imposed at downstream (km 0) and upstream (km 160) boundaries, respectively (Figure 6).

For the sediment transport, due to the lack of continuous data at the downstream boundary, the model assumes a so-called equilibrium boundary condition for sediment concentration. Instead of using fixed values, the imposed SPM concentrations at both upstream and downstream boundaries are time-dependent and computed based on the equilibrium condition at the reference level near the bottom, under which the erosion rate is assumed to be the same as the deposition rate. The equilibrium concentration is derived from the 1DV transport equation, in which the eddy diffusivity has a parabolic profile given by the mixing length theory. The concentration profiles imposed at both boundaries are given by Rouse profiles:

$$C(z) = c_b \cdot \left( \frac{z}{H - z} \frac{H - z_b}{z_b} \right)^{-w_s/\kappa u_*} \quad (18)$$

$$c_b = E/w_s \quad (19)$$

in which,  $\nu_t$  is the eddy viscosity,  $H$  is the water depth,  $z_b$  is the reference level for the near-bed concentration  $c_b$ ,  $w_s$  is the settling velocity,  $\kappa$  is the von Karman constant and  $u_*$  is the shear velocity. The erosion rate  $E$  can be computed in a similar way as described in eq.(17). It is worth mentioning that the SPM concentration is only imposed when the water flux pointing inward (coming into the domain), whereas the zero gradient of concentration is imposed when the water flux pointing outward. This type of boundary treatment is called the Thatcher-Harleman boundary condition, which aims to suppress unphysical SPM concentration gradient near open boundaries (Thatcher and Harleman, 1972).

In order to reveal the influence of the flocculation process on the SPM distribution and ETM dynamics, the model is compared with a reference case without flocculation. The other model settings and parameters are listed in Table 2.

TABLE 2 – OVERVIEW OF THE MODEL SET-UPS

Model set-up	Reference case	Model with flocculation
<b>Turbulence model</b>	$k-\varepsilon$ model	$k-\varepsilon$ model
<b>SPM concentration at boundaries</b>	Eqs.(18) and (19) with $z_b=1$ cm	The total mass concentration is given by eqs.(18) and (19) with $z_b=1$ cm, and it is distributed to microflocs (10%), macroflocs (80%) and megaflocs (10%).
<b>Sediment type</b>	cohesive	cohesive
<b>Particle size (<math>\mu\text{m}</math>)</b>	60	Microflocs: 15 Macroflocs: variable Megaflocs: 350
<b>Sediment density (<math>\text{kg/m}^3</math>)</b>	1800	Microflocs: 2500 Macroflocs: variable Megaflocs: 1064 (from fractal theory)
<b>Settling velocity (<math>\text{mm/s}</math>)</b>	1	Microflocs: 0.18 Macroflocs: variable Megaflocs: 4.1
<b>Critical shear stress for erosion (Pa)</b>	0.4	0.4
<b>Partheniades constant</b>	$1.0\text{e-}04$	$1.0\text{e-}04$

Both the reference model and the model with flocculation start from 01/01/2015 00:00:00 and runs for a period of 7 months covering winter to summer conditions.

#### IV. RESULTS AND DISCUSSION

The winter and summer conditions in the model is mainly induced by the boundary forcing, which is based on the field measurements. It is known from the data that mean discharge, as shown in Figure 7, is usually much lower in summer (Vandenbruwaene et al. 2018). This change of upstream forcing will further affect tidal asymmetry, flow field, and sediment input from boundaries. If considering the flocculation process, it is no surprise that the floc properties could also react to these changes, exhibiting different characteristics between winter and summer, hence, influencing the SPM distribution under tidal motions.

The model results show that both the reference run and the run with 3CPBE flocculation model could capture the location shift of the second ETM. However, without flocculation, the reference run predicts lower SPM concentration during the entire simulation period, especially in winter condition, and fails to capture the longitudinal growth of the ETM during summer (Figure 2), which is well reproduced in the run with 3CPBE model as seen in Figure 8.

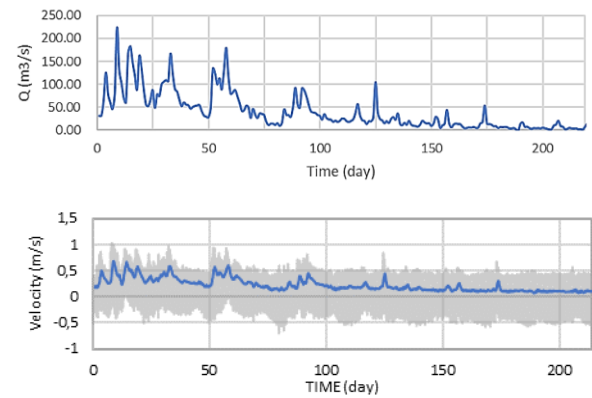


Figure 7 – Daily-averaged upstream discharge measured at Melle in 2015 (upper) and depth-averaged velocity at the upstream boundary with positive values pointing downstream (lower)

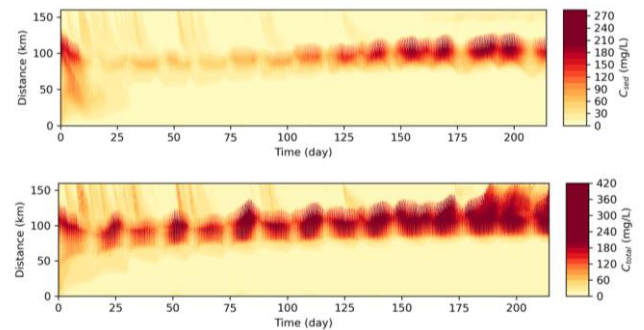


Figure 8 – Evolution of depth-averaged SPM concentration along thalweg of the model from winter to summer (Upper: reference model, lower: model with flocculation)

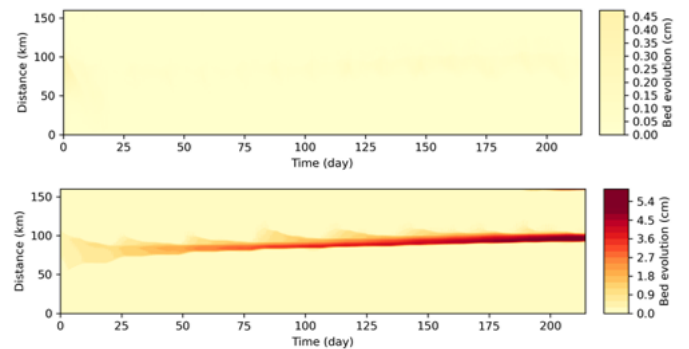


Figure 9 – Bed evolution along thalweg of the model from winter to summer (Upper: reference model, lower: model with flocculation)

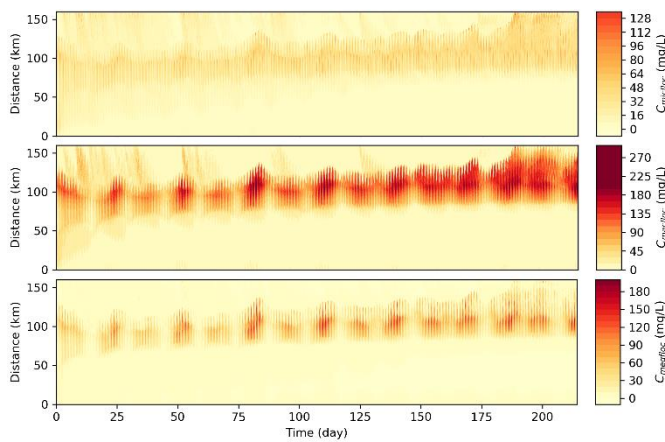


Figure 10 – Evolution of SPM concentration along thalweg from the model with flocculation (Upper: microflocs, middle: macroflocs, lower: megaflocs)

Moreover, higher sedimentation rates are found in the model with flocculation, and the accumulation of bed material occurs in the ETM zone (Figure 9). The bed evolution shows that this bed layer moves towards upstream when ETM zone moves. According to the previous study (Bi et al. 2020), the cumulative bed layer occurs at the location, where the landward net transport rate decreases sharply, it is also where the tidal energy from downstream meets the river energy from upstream (Chen et al. 2005). In the reference model without flocculation, the sedimentation still happens during slack tides, likely forming a weak fluid mud layer, but the deposited sediment is eroded when flow becomes stronger, hence the bed layer is barely accumulated over long period. This suggests that the net sediment transport is altered by the flocculation model, resulting in a higher sediment trapping efficiency in the ETM zone compared to the reference case.

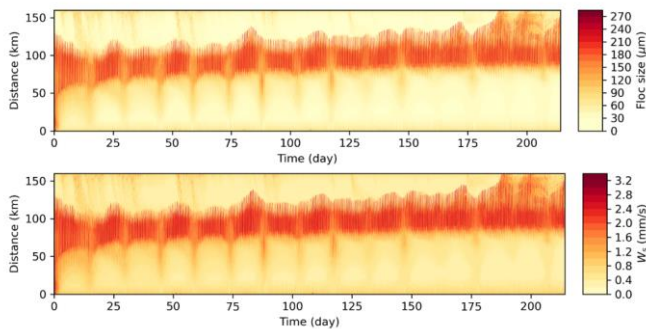


Figure 11 – evolution of mean floc size (upper) and settling velocity (lower) along thalweg of the model with flocculation

One of the advantages of the 3CPBE flocculation model is that it can provide detailed information about how the different sediment groups evolve spatially and temporally in the system and their relations. Figure 10 shows the modelled SPM concentrations of three sediment groups, microflocs, macroflocs and megaflocs, among which the macroflocs are the majority. Further analysis reveals that, with the 3CPBE flocculation model, larger flocs with higher settling velocity can be formed in the ETM zone, whereas outside of this region the smaller flocs with lower settling velocity are found. It also can be seen in Figure 11 that the location of the area with large

flocs reacts to the boundary forcing in the same way as the location of ETM zone does, showing the variations during spring-neap cycles as well as in longer period from winter to summer.

The depth-averaged SPM concentrations of three floc size groups along the thalweg of the modelled domain are further analysed by averaging over the winter and summer period, respectively (Figure 12). In winter, the peak SPM concentration is located at 100 km from the estuary mouth. The ETM zone has narrower extent towards upstream and the megaflocs are negligible in the region from 120 km to 160 km. In summer, the peak SPM concentration shifts about 10 km towards upstream and the ETM zone has larger extent towards upstream. The megaflocs also appear in the upstream region, changing the composition of the sediment particles.

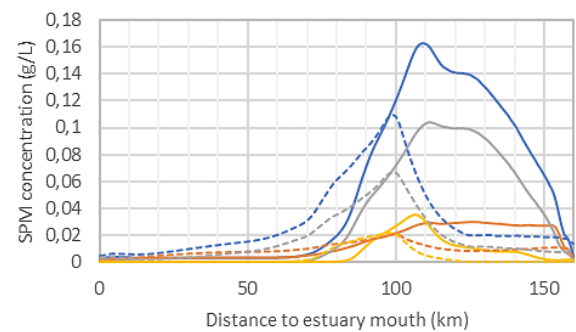


Figure 12 – Depth-averaged SPM concentration along thalweg averaged over winter (dash lines) and summer (solid lines) (blue: total SPM, orange: microflocs, grey: macroflocs, yellow: megaflocs).

In order to understand the seasonal variation of SPM captured by the 3CPBE flocculation model, an upstream boundary node is selected for further examination. The depth-averaged velocity and the SPM concentration is extracted from the model results (Figure 13 and Figure 14).

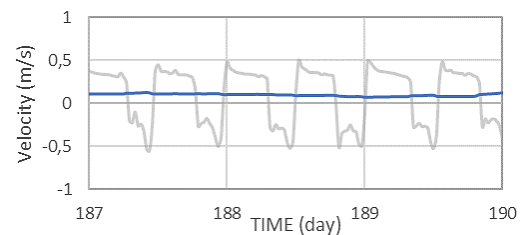


Figure 13 – depth-averaged velocity at upstream boundary in a short period in summer with positive values pointing downstream (grey: instantaneous value, blue: 24H moving average)

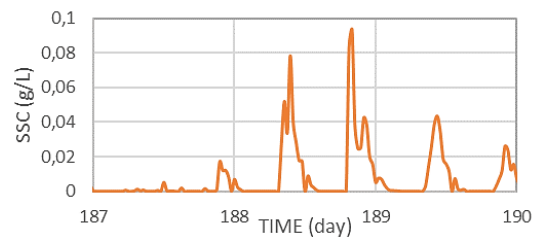


Figure 14 – Depth-averaged total SPM concentrations at the upstream boundary

As seen in the evolution of the depth-averaged velocity at the upstream boundary (Figure 7), the magnitude decreases and the tidal asymmetry changes from winter to summer, with a trend of becoming less ebb dominant. This is one of the reasons that the ETM location shifts towards upstream. In the zoom-in view of a short period in summer (Figure 13 and Figure 14), one can find that the SPM imposed at the upstream boundary only show peaks when the velocity points upstream. Since the Thatcher-Harleman boundary condition is adopted in the model, the SPM concentration can only be caused by advective transport from downstream.

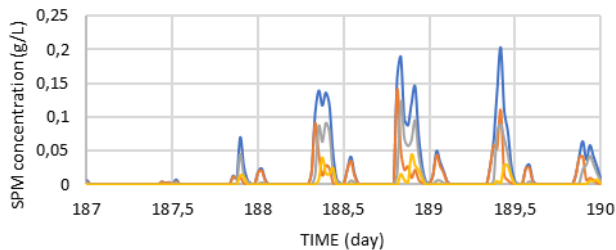


Figure 15 – SPM concentrations of microflocs (orange), macroflocs (grey), megaflocs (yellow) and total SPM concentration (blue) at 159 km

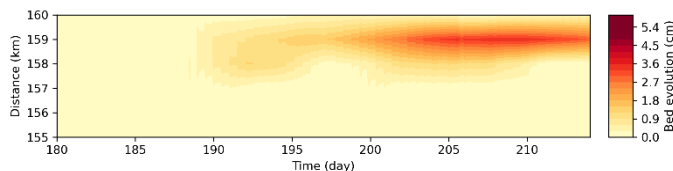


Figure 16 – The zoom-in view of bed evolution near the upstream boundary in a short period in summer

At a location near the upstream boundary (159 km from the estuary mouth), the SPM concentrations of the three floc groups are shown in Figure 15. The change of the boundary forcing results in an environment more favourable for aggregation of flocs. The larger flocs start forming when the sediments being transported from downstream to this location. It is also clear that microflocs appear first during the peak flood velocity, then they form larger flocs during the transition to slack tide and settle down to the bed. This also explains the cause of the sedimentation near the upstream boundary in the same period (Figure 16). It is possible, when the upstream discharge becomes larger, that this cumulated bed layer will be eroded again, providing extra sediment input to the system.

## V. CONCLUSION

The analysis of the model results reveals that the flocculation process modelled by the 3CPBE flocculation model is crucial for capturing the seasonal variations of SPM in the upstream region. The modelled system response is close to the field observations.

The results also link the zone with higher settling velocities to the zone with higher SPM concentration in the schematized domain. The comparison with the reference model indicates that only the flocculation model could reproduce reasonable settling velocities in the high concentration area in winter, which are important for maintaining the ETM zone under higher upstream discharge.

From winter to summer, the ETM zone shifts its location towards upstream and increase its extent. This is only reproduced by the model with flocculation. This dynamic behaviour of the ETM is possibly due to several reasons. The change of boundary forcing (lower upstream discharge) leads to a less ebb dominant system, which allows the sediment being transported more landward. The flocculation process enhances this trend by justifying the settling velocity to the local flow conditions and SPM concentrations. The increase of the extent of the ETM zone is only reproduced combining the effect of tidal asymmetry and flocculation process in the model. And this cannot be achieved by using a single value of settling velocity as in the traditional sediment model.

However, it is worth pointing out that due to the lack of tidal flats in the domain, it is unclear how the intertidal area would influence the results. This will be investigated in the future study.

## ACKNOWLEDGEMENT

This work is supported by the Flanders Hydraulics Research and Sediment Dynamics group at KU Leuven.

## REFERENCES

- [1] Bi, Q., Joon Lee, B., Shen, X., Toorman, E., Smolders, S., Vanlede, J. (2019). Implementing MCPBE flocculation models in TELEMAC and investigating the influence of flocculation on large scale sediment transport, in: 15th international conference on cohesive sediment transport processes 13 – 17 October 2019, Istanbul, Turkey (INTERCOH 2019): abstract book. pp. 116-118.
- [2] Bi, Q.; Kaptein, S. J.; Schramkowski, G.; Smolders, S.; Mostaert, F. (2020). The iFlow inspired TELEMAC-3D model: Sub report 1 – Comparing ETM dynamics with the iFlow model. Version 2.0. FHR Reports, 19\_025\_1. Flanders Hydraulics Research: Antwerp.
- [3] Brouwer, R. L., Schramkowski, G. P., Dijkstra, Y. M., & Schuttelaars, H. M. (2018). Time evolution of estuarine turbidity maxima in well-mixed, tidally dominated estuaries: The role of availability-and erosion-limited conditions. *Journal of Physical Oceanography*, 48(8), 1629-1650.
- [4] Chen, M. S., Wartel, S., Van Eck, B., & Van Maldegem, D. (2005). Suspended matter in the Scheldt estuary. *Hydrobiologia*, 540(1-3), 79-104.
- [5] Dijkstra, Y. M., Brouwer, R. L., Schuttelaars, H. M., & Schramkowski, G. P. (2017). The iFlow modelling framework v2. 4: a modular idealized process-based model for flow and transport in estuaries. *Geoscientific Model Development*, 10(7).
- [6] Fettweis, M., & Lee, B. J. (2017). Spatial and seasonal variation of biomineral suspended particulate matter properties in high-turbid nearshore and low-turbid offshore zones. *Water*, 9(9), 694.
- [7] Kranenburg, C. (1999). Effects of floc strength on viscosity and deposition of cohesive sediment suspensions. *Continental Shelf Research*, 19(13), 1665-1680.
- [8] Lee, B. J., Toorman, E., Molz, F. J., & Wang, J. (2011). A two-class population balance equation yielding bimodal flocculation of marine or estuarine sediments. *Water research*, 45(5), 2131-2145.
- [9] Lee, B. J., Hur, J., & Toorman, E. A. (2017). Seasonal variation in flocculation potential of river water: Roles of the organic matter pool. *Water*, 9(5), 335.
- [10] Lick, W., Huang, H., Jepsen, R., 1993. Flocculation of fine-grained sediments due to differential settling. *J. Geophys. Res.: Oceans* 98, 10279-10288.
- [11] Maggi, F., 2005. Flocculation Dynamics of Cohesive Sediment (Ph.D. Dissertation). Delft University of Technology, Netherlands.

- [12] Maggi, F., Mietta, F., Winterwerp, J.C., 2007. Effect of variable fractal dimension on the floc size distribution of suspended cohesive sediment. *J. Hydrol.* 343, 43-55.
- [13] Matsoukas, T., Friedlander, S.K., 1991. Dynamics of aerosol agglomerate formation. *J. Colloid Interface Sci.* 146, 495-506.
- [14] Schepers, L., Maris, T., Meire, P., & Temmerman, S. (2018). The Scheldt estuary: an overview of the morphodynamics of intertidal areas. In *Landscapes and Landforms of Belgium and Luxembourg* (pp. 281-296). Springer, Cham.
- [15] Shen, X., Lee, B. J., Fettweis, M., & Toorman, E. A. (2018). A tri-modal flocculation model coupled with TELEMAT for estuarine muds both in the laboratory and in the field. *Water research*, 145, 473-486.
- [16] Thatcher, M. L., and D. R. F. Harleman (1972), A mathematical model for the prediction of unsteady salinity intrusion in estuaries, Tech. Rep. 144, Dep. of Civ. Eng., Mass. Inst. of Technol., Cambridge.
- [17] Thomas, D.G., Judd, S.J., Frawcett, N., 1999. Flocculation modeling: a review. *Water Res.* 33, 1579-1592.
- [18] Vandenbruwaene, W., Hertoghs, R., Michielsens, S., Van De Moortel, I., Brackx, M., Claeys, S., Plancke, Y., Vereecken, H., Meire, D., Deschamps, M. & Mostaert, F. (2019). Monitoring Effecten Ontwikkelingsschets (MONEOS)–Jaarboek monitoring 2018: factual data rapportage van monitoring waterbeweging en fysische parameters in de Zeeschelde in 2018. WL Rapporten.
- [19] Verney, R., Lafite, R., Brun-Cottan, J.C., Le Hir, P., 2011. Behaviour of a floc population during a tidal cycle: laboratory experiments and numerical modelling. *Contin. Shelf Res.* 31, S64-S83.
- [20] Winterwerp, J. C. (1998). A simple model for turbulence induced flocculation of cohesive sediment. *Journal of hydraulic research*, 36(3), 309-326.
- [21] Winterwerp, J. C., & Van Kesteren, W. G. (2004). *Introduction to the physics of cohesive sediment dynamics in the marine environment*. Elsevier.



# Fine sediment deposits in gravel bed rivers: sensitivity analysis to particle properties using a 2D hydrodynamic and sediment model

H. Haddad, M. Jodeau, N. Claude & G. Antoine

National Hydraulics and Environment Laboratory (LNHE)  
EDF R&D  
Chatou, France  
hanna.haddad@edf.fr

C. Legout

Université Grenoble Alpes, CNRS, IRD, Grenoble INP,  
IGE, Grenoble, France

**Abstract**— Fine sediment dynamics in mountainous rivers are poorly understood. However, high suspended sediment concentrations during natural events or reservoir flushing are known to be an issue further downstream. Numerical models are frequently used to predict sediment behavior, but measurements of cohesive sediment properties are rarely available. This study investigates the sensitivity of a numerical model to parameters describing cohesive sediment behavior. The study case is a 3-km reach of the Isère River in the Alps with alternate gravel bars. The simulated outputs are the surfaces and volumes of fine sediment deposits over control areas. These outputs are analyzed to assess the sensitivity to the parameters describing erosion and sedimentation in order to identify on which measurements and in which areas measurements efforts should be focused. For two simulated flushing events, disparities between various deposition areas are observed, depending on their locations on the gravel bar and the local hydraulic conditions.

## I. INTRODUCTION

Fine sediments exhibit various stages of deposition and erosion during their transport from hillslopes to the ocean [1]. In alpine gravel bed rivers, massive deposits can occur, leading to bar elevation, riparian vegetation growth and consequently to bar stabilization, which in turn increases flooding risks and alters the river ecological quality [2]. Hydropower dams modify fine sediment fluxes in downstream rivers. While the presence of cohesive sediment deposits is highly visible in such environments, the processes leading to their deposition and potential resuspension is poorly understood. This is particularly due to the high spatial and temporal variability of fine sediment deposits characteristics [3] in preferential deposition areas [4].

Distributed numerical models are interesting tools to better understand cohesive sediment dynamics and to predict sediment propagation, transport and deposition during a period of interest. Multiple studies investigated the efficiency of various operations on the river, including flushing flows [5], [6] and dredging operations [7]. A few of them focused on spatial and temporal variations of fine sediment properties [8], [9]. However, in many numerical studies, measurements of cohesive sediment properties are not available [10]. Thus, one has to use values from the literature often obtained for different conditions or to perform calibrations. The aim of this

study is to assess i) the capability of a 2D numerical model to reproduce fine sediment deposits on gravel bars, ii) which parameters describing erosion and sedimentation of cohesive particles are the most sensitive and iii) to which extent the results of sensitivity analysis are controlled by global boundary and local hydrodynamic conditions.

## II. MATERIAL AND METHODS

### A. Study site

#### 1) Fréterive reach on the Isère river

The Isère River is a gravel bed river located in the southern French Alps. The modeled area is a 3 km reach located 38 km downstream the Aigueblanche dam and 200 m upstream of the Isère-Arc confluence. It is embanked, rectilinear and about 100 m wide, with a bed slope of 0.0016 m/m. Bed material is composed of coarse sediment ( $d_{50} = 24$  mm), non-cohesive fine sediment ( $d_{50} = 180$   $\mu$ m) and cohesive sediment ( $d_{50} = 40$   $\mu$ m). The average suspended sediment concentration (SSC) is less than 1 g/l most of the time but can reach more than 10 g/l during runoff or flushing events of the Aigueblanche dam.

During the 2017 winter, the area was subject to restoration works that consisted of mechanically removing vegetation and fine sediments from gravel bars as well as remodeling the gravel bars. These operations were performed to reduce the flooding risk and restore the bar mobility.

#### 2) The 2017 and 2018 flushing events of the Aigueblanche dam

The Aigueblanche dam is flushed once a year if the spring discharges are high enough. This operation allows to remove fine sediment in the reservoir to limit the transfer of sand to the turbine and the elevation of the bed river upstream of the reservoir. The 2017 and 2018 flushing events were characterized by distinct maximal liquid discharge and sediment concentration. Thus, these two events were selected to investigate differences in terms of deposition and erosion.

The 2017 flushing event (fig 1.a) lasted 3 days (28/05 to 31/05), with a liquid discharge peak of 200 m<sup>3</sup>/s and a SSC peak of 12 g/l with a 1-day delay compared to the peak discharge.

The 2018 flushing event starting from 06/05/2018 (fig 1.b) lasted 3 days and reached higher discharges (peak discharge around  $300 \text{ m}^3/\text{s}$ ) with smaller SSC. The modelled event includes the flushing and can be decomposed in three parts. The main SSC peak, around  $2.5 \text{ g/l}$  was reached 8 hours after the peak discharge. In a second part, a flood event (starting from 09/05/2018) corresponds to a rinsing test that was performed to try to limit the fine sediment deposits after the flushing event. The goal of these high discharges was to re-suspend eventual deposits on downstream gravel bars. These events were followed by a natural runoff event with high discharges.

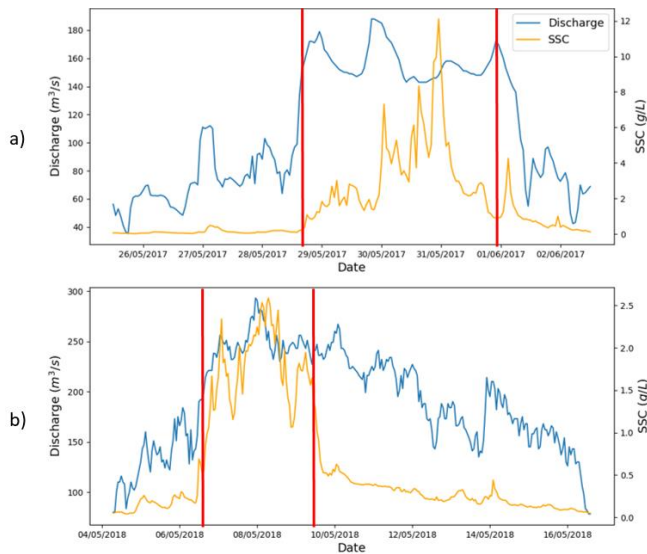


Figure 1. Discharge and suspended sediment concentrations (SSC) for two flushing events in (a) 2017 and (b) 2018. Vertical red lines correspond to the flushing period for each modelled event.

### 3) Bed elevation data and aerial pictures

Topography and bathymetry surveys were performed between January and April 2017 as well as a LIDAR (Light Detection and Ranging) measurements in 2014. They were used to create the digital elevation model (DEM) of the Frériverie reach. Four aerial photos, two in April and May before the 2017 flushing event and two in June and July after the 2017 flushing, are available. The comparison of manually digitized contours of fine deposit patches on the photos allows to obtain the surfaces of fine sediment deposits before and after the flushing event on the gravel bars for a given discharge.

While the modeled reach is 3km long, the sensitivity analysis focuses only on 2 bars (fig 2) representative of the whole reach. In this zone, multiple areas of deposits are identified from aerial photography: a secondary channel (named SC), 5 marginal deposits on the right bank of the central bar (RBMDi with i from 1 to 5), 3 on the left bank (LBMDi with i from 1 to 3) and 2 bar tail deposits, BT14 and BTU4. Control areas were chosen for each of these areas.

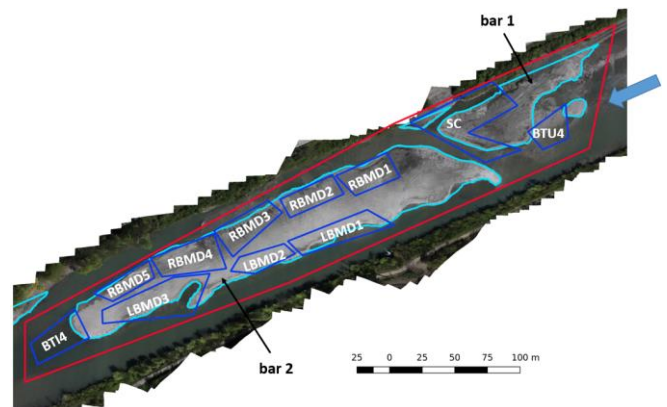


Figure 2. Area of interest illustrated by a photography taken in April 2017 ( $Q=35 \text{ m}^3/\text{s}$ ) after the restoration works and before the flushing event of 2017. Bars are digitized in light blue. The blue arrow indicates the water direction from right to left. The contour in red covers the whole area and the blue ones are the areas of various patches: right bank marginal deposit (RBMD), left bank marginal deposit (LBMD), bar tails (BT14 and BTU4) and secondary channel (SC).

### B. Modeling of the Frériverie site

The numerical simulations were run using the release 8.0 of TELEMAC-2D and SISYPHE from the open source TELEMAC-MASCARET hydro-informatics system coupled with SISYPHE [11]–[13]. The model includes 526,653 nodes and 1,042,620 triangular mesh elements. The mean node distance is about 1.6m. The model simulation time step has been set to 1 s in order to respect the Courant-Friedrichs-Lewy (CFL) condition.

For all the calculations, the initial bed elevation corresponds to the configuration before the 2017 flushing event (remodeled bars without fine sediment deposits).

#### 1) Hydraulics and calibration of the Strickler coefficient

The boundary conditions for the hydraulics are the following: for a prescribed liquid discharge at the inlet of the domain, a Manning-Strickler law is used to compute the water level at the outlet of the modeled area, with the approximation of a wide rectangular canal. The mean slope is obtained from the measured bathymetry. The Strickler coefficient was calibrated to  $40 \text{ m}^{1/3}/\text{s}$  allowing to reproduce at best the modeled surfaces of non-immersed gravel bars obtained with aerial photography observations for two steady states ( $Q=35 \text{ m}^3/\text{s}$  in April and  $Q=53 \text{ m}^3/\text{s}$  in May).

#### 2) Sediment transport

In this study case, two main hypothesis were taken, given the configuration of the study site: (1) bed load is not taken into account, for the 2017 flushing event, data show that the bed evolution due to bed load is negligible. (2) It should be stressed that the input SSC shown in figure 1 is a mixture of all sediments. Since no data on the suspended sediment classes is available, the sedigraph is modeled considering a unique class of cohesive sediment with given properties (settling velocity, critical erosion and deposition shear stresses and erosion rate). The Partheniades and Krone formulae are used to compute the erosion and deposition flux:

$$E = \begin{cases} M \left[ \left( \frac{\tau_b}{\tau_{ce}} \right) - 1 \right] & \text{if } \tau_b > \tau_{ce} \\ 0 & \text{otherwise} \end{cases} \quad (1)$$

$$D = \begin{cases} w_s C \left[ 1 - \frac{\tau_b}{\tau_{cd}} \right] & \text{if } \tau_b < \tau_{cd} \\ 0 & \text{otherwise} \end{cases} \quad (2)$$

where  $E$  is the erosion flux [ $\text{kg/m}^2/\text{s}$ ],  $M$  the Partheniades constant [ $\text{kg/m}^2/\text{s}$ ],  $\tau_b$  the bottom shear stress [ $\text{Pa}$ ],  $\tau_{ce}$  the critical erosion shear stress [ $\text{Pa}$ ].  $D$  is the deposition rate [ $\text{kg/m}^2/\text{s}$ ],  $w_s$  the settling velocity [ $\text{m/s}$ ],  $C$  the depth-averaged concentration [ $\text{kg/m}^3$ ] and  $\tau_{cd}$  the critical shear stress for deposition [ $\text{Pa}$ ].

### 3) Sensitivity study methodology

Multiple field and laboratory measurements were conducted previously on the Isère River and other similar gravel bed rivers in the Alps. They were used to define the range of values for each parameter describing the sediment properties. Table 1 shows the chosen values for the reference simulation. The settling velocity and the critical erosion shear stress were derived from mean values extracted from the measurements [3]. The values of the critical deposition shear stress and the erosion rate  $M$  were chosen as an approximation since no measurement is available.

First of all the aerial photos after the 2017 flushing event are used to check if the model correctly reproduced the locations and surfaces of deposits for the reference simulation. Then, one parameter at a time is modified and values are tested for multiple orders of magnitude in order to test the sensitivity of the modeled outputs. The 2017 and 2018 flushing events are simulated in order to assess the effect of different upstream boundary conditions.

TABLE 1. LIST OF SIMULATIONS FOR THE COHESIVE SENSITIVITY STUDY. EACH PARAMETER WAS VARIED FOR A WIDE RANGE OF VALUES (COLUMNS 3) TO TEST ITS INFLUENCE OVER MULTIPLE ORDERS OF MAGNITUDE.

Parameter	Reference simulation	Min and Max values for the sensitivity analysis
$w_s$ [ $\text{m/s}$ ]	$0.17 \cdot 10^{-3}$	$[10^{-5} \rightarrow 10^{-2}]$
$\tau_{cd}$ [ $\text{Pa}$ ]	0.4	$[10^{-3} \rightarrow 40]$
$\tau_{ce}$ [ $\text{Pa}$ ]	1	$[0.1 \rightarrow 6]$
$M$ [ $\text{kg/m}^2/\text{s}$ ]	$10^{-3}$	$[10^{-4} \rightarrow 1]$

To evaluate the model sensitivity for given boundary conditions, the volume of deposit is calculated for each control area (fig 2) or for the whole area. Plotting the dimensionless volume  $Y$  against the dimensionless parameter  $X$  shows the sensitivity. A higher gradient indicates a more sensitive parameter.

$$X = \frac{\text{parameter value}}{\text{reference value of the parameter}} \quad (3)$$

$$Y = \frac{\text{deposit volume}}{\text{reference deposit volume}} \quad (4)$$

## III. RESULTS AND DISCUSSION

### A. Evaluation of the sediment model

The first step was to evaluate the model's capability to reproduce fine sediment deposits. Thus, the model was tested for the 2017 flushing event for cohesive sediments using the reference simulation configuration. The observed surfaces of deposits are derived from the aerial photography taken in July 2017 at low discharge after the flushing event. Figure 3 represents the observed and simulated deposits over the two gravel bars.

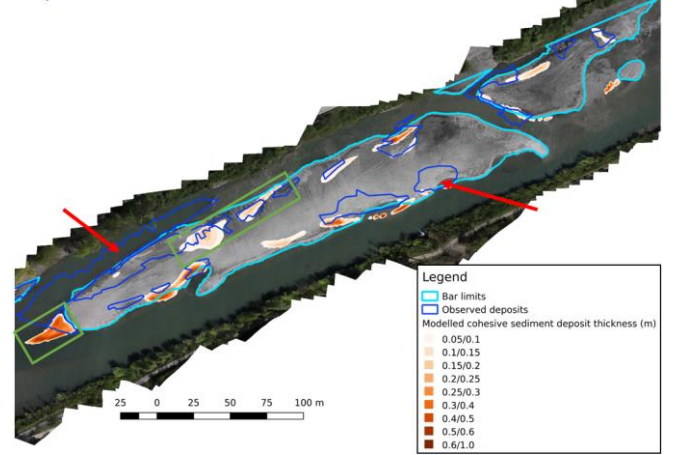


Figure 3. Map of observed and modeled deposits in the area with the reference configuration for cohesive sediment. For the modeled outputs, the legend starts for a deposit value of 0.05m: a deposit is only considered if it is higher than 0.05 m. Red arrows indicate numerical errors in locations related to interpolation and lack of topography measurements. Green rectangles show bar tail deposits thicker than superficial deposits.

The total surface of the observed deposits in the area is  $5400 \text{ m}^2$  and the numerical model reproduces  $2550 \text{ m}^2$ . About half of the observed deposits are not reproduced by the model. However, aerial photography observations include sandy areas as well as cohesive deposits and cannot be distinguished. The model focuses only on cohesive sediment and it is therefore normal to reproduce less deposits than the observed ones. Furthermore, some numerical errors are related to interpolation of topography on the central bar as well as a lack of measurements in the channel on the right of the central bar (red arrows on figure 3).

Nevertheless, marginal deposits, bar tail deposits, secondary channel deposits as well as superficial deposits, can be identified. This is coherent with the description of deposits given by Wood and Armitage [14] and observed by Gregory et al. [4].

The thickness of different deposits is not available. However, the numerical model is in agreement with field observations that show that bar tail deposits are thicker than marginal and superficial ones. The reference simulation leads to a maximum of more than 40 cm of deposits on the bar tail and less than 10 cm in some superficial areas (green rectangles on figure 3).

It is thus fair to say that the model reproduces quite well cohesive sediment deposits in the zone.

### B. Global sensitivity analysis

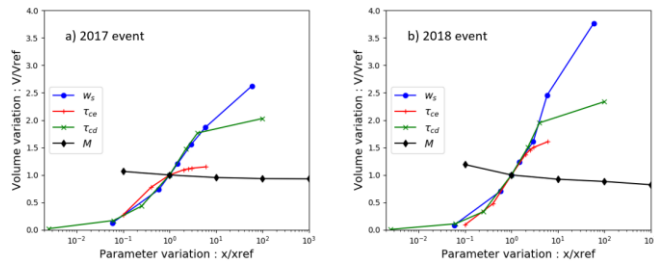


Figure 4. Sensitivity to cohesive sediment parameters in the whole area for the (a) 2017 flushing event and (b) 2018 flushing event.

For the global sensitivity analysis, the dimensionless volumes are plotted according to the four dimensionless parameters (fig 4).

For the 2017 flushing event, the reference deposit volume in the zone is 423.04 m<sup>3</sup> (table 2). This volume is multiplied by 2.6 when the settling velocity is 2 orders of magnitude higher and divided by 8 when the settling velocity is one order of magnitude lower (fig 4.a, blue line, and table 2). The plot for the critical shear stress for deposition (fig 4.a, green line) follows the same slope except for the last point. For this event, these parameters are the most sensitive ones. The critical erosion shear stress is less sensitive than  $w_s$  and  $\tau_{cd}$  but plays a non-negligible role: the minimum volume obtained is 115 m<sup>3</sup> and the maximum 486 m<sup>3</sup>. This suggests that the higher the value of  $\tau_{ce}$  is, the more fine sediments are re-suspended. A threshold is reached for the high values of  $\tau_{ce}$ , which suggests that the highest values for bed shear stress obtained for these boundary conditions are lower than the threshold.

For the 2018 flushing event, the reference simulation leads to a total volume of deposit of 401.5 m<sup>3</sup> which is 5% lower than the volume simulated with the 2017 event (table 2). The 2018 flushing event exhibits higher discharges and thus globally higher shear stresses. This leads to less deposits. The

settling velocity and critical shear stress for deposition are also very sensitive for the 2018 event. But also, for the 2018 boundary conditions, the outputs are more sensitive to the critical erosion shear stress than for the other event (fig 4.b, red line): the maximum and minimum volumes are respectively 644 m<sup>3</sup> and 37 m<sup>3</sup>, values which are more spread out than for the 2017 event and the slope of the line is higher.  $\tau_{ce}$  is a very sensitive parameter for higher discharges and is as sensitive as  $w_s$  and  $\tau_{cd}$  for the second scenario tested.

TABLE 2. DEPOSITED REFERENCE VOLUME FOR EACH EVENT AND MIN AND MAX DEPOSITED VOLUME FOR EACH PARAMETERS

Deposited volume (m <sup>3</sup> )	2017		2018	
	min	max	min	max
Reference	423.04		401.5	
$w_s$	54	1110	35	1512
$\tau_{cd}$	10	859	4	938
$\tau_{ce}$	115	486	37	644
$M$	393	451	330	478

### C. Effect of local hydraulic conditions

These conclusions derived at the bar scale might exhibit spatial variations depending on the location in the bar. Thus, the sensitivity was investigated at smaller scales corresponding to various facies of deposition areas, i.e. RBMD1, BTI and SC.

For the 2017 flushing event, in RBMD1 (fig 5.a) and SC (fig 5.c) the reference volumes are respectively 28 m<sup>3</sup> and 36 m<sup>3</sup>. In RBMD1  $\tau_{cd}$  is the most sensitive parameter (volume multiplied by 3 when  $\tau_{cd}$  is multiplied by 4) followed by  $w_s$  (volume multiplied by 3 when  $w_s$  is multiplied by 100). In the SC area (fig 5.c), the settling velocity is the most sensitive parameter (volume multiplied by 5 for maximum value, outside graph) while  $\tau_{ce}$  and  $\tau_{cd}$  are equally sensitive.

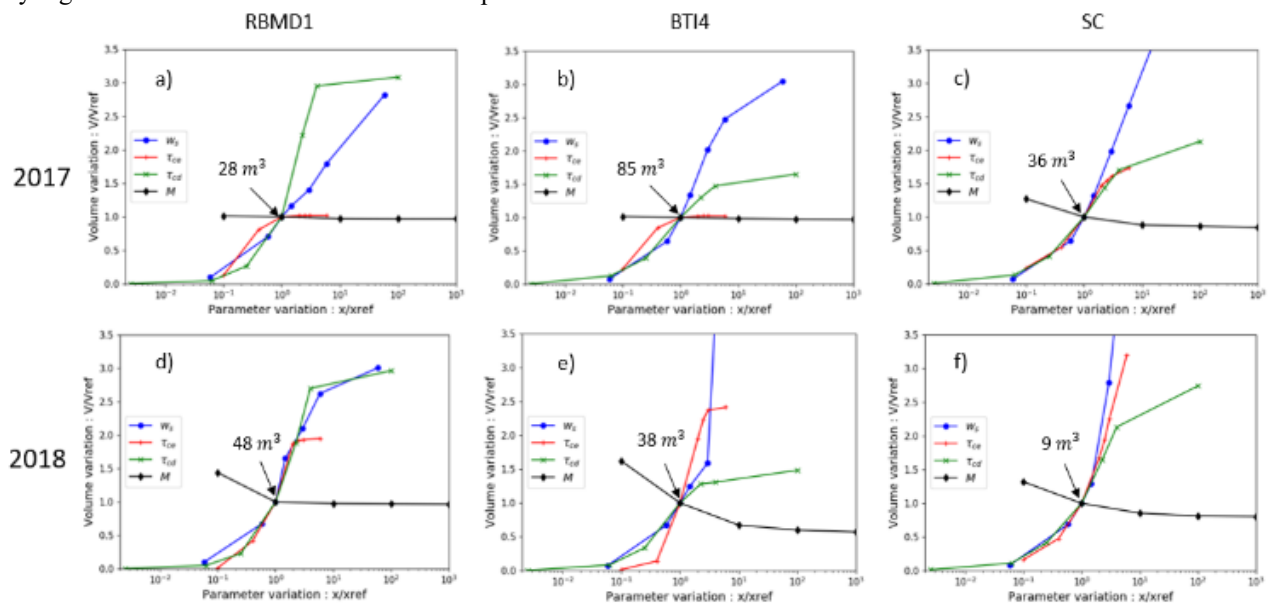


Figure 5. Sensitivity on different control volumes for the (a,b and c) 2017 and (d,e and f) 2018 events. The y axis is limited between 0 and 3.5 in order to compare the different figures, maximum values don't appear on the plots (e) and (f).



The results can be compared to two studies. Hostache et al. [9] looks at general sensitive parameters on a large floodplain scale and evidence the fact that the most sensitive parameter is the settling velocity which is coherent with figure 4. Our study's objectives are however closer to the ones aimed by Milan et al. [15] where they look at spatial patterns in sediment deposit related to hydraulic conditions and velocities. Indeed, the spatial differences observed in figure 5 can be explained by local hydraulic conditions related to gravel bed topography. For the same global boundary conditions, local velocities are controlled by topography and can favor one parameter of the sediment over another. The results suggest that on high altitudes (superficial part of gravel bars), shear stresses are low and therefore  $\tau_{cd}$  is a very sensitive parameter. On low altitudes  $w_s$  and  $\tau_{ce}$  gain more importance.

By comparing the 2017 and 2018 flushing events, we can notice that the global boundary condition can sharpen the difference in sensitivity in different areas. For the 3 control volumes in figure 5, the critical erosion shear stress is much more sensitive for the 2018 boundary conditions than for the 2017 ones. In the bar tail area for example,  $\tau_{ce}$  is the most sensitive parameter for the 2018 event (volume multiplied by 2.5 and divided by 9 when the parameter is respectively multiplied by 3 and divided by 2), at least before the threshold is reached.

Figures 4 and 5 show that the critical shear stress for deposition is a very sensitive coefficient. This can be a source of uncertainty in modeling studies since direct measurement of this quantity is not possible in situ. However, in the community, the existence of this variable is debated [16]. Indeed, some authors argue that deposition and erosion occur at the same time [17]. In fact, on the plots in figures 4 and 5, a "break" in the slope of the green line is clearly visible when  $\tau_{cd}$  becomes larger than  $\tau_{ce}$ , which corresponds to a change of paradigm and deposition and erosion are allowed at the same time.

#### IV. CONCLUSIONS

The aim of this study was to better understand the behavior of fine sediment deposits in a 2D morphodynamic numerical model for two different flushing events in a gravel bed river.

The main results are: (1) the simulated deposition map exhibits good agreement with observed fine sediment deposits with parameters estimated from previous in situ measurements. (2) An event with higher discharges intensifies the sensitivity to the critical erosion shear stress. (3) Local topography and hydraulic conditions are important factors to the sensitivity of the modeled deposits to cohesive sediment parameters.

These results highlight the importance of knowing sediment origins and their properties and will be considered during future field monitoring seeking to supply the numerical model.

#### ACKNOWLEDGEMENTS

The authors would like to thank the French National Research Agency (ANR) under the grant ANR-18-CE01-0020 (DEAR project) and EDF CIH for their support.

#### REFERENCES

- [1] K. Fryirs, "(Dis)Connectivity in catchment sediment cascades: a fresh look at the sediment delivery problem" *Earth Surface Processes and Landforms*, vol. 38, no. 1, pp. 30–46, Jan. 2013, doi: 10.1002/esp.3242.
- [2] C. Jourdain, N. Claude, P. Tassi, F. Cordier, and G. Antoine, "Morphodynamics of alternate bars in the presence of riparian vegetation," *Earth Surface Processes and Landforms*, Dec. 2019, doi: 10.1002/esp.4776.
- [3] C. Legout, I. G. Droppo, J. Coutaz, C. Bel, and M. Jodeau, "Assessment of erosion and settling properties of fine sediments stored in cobble bed rivers: the Arc and Isère alpine rivers before and after reservoir flushing: Erosion and settling dynamics of fine sediments in cobble bed rivers," *Earth Surf. Process. Landforms*, vol. 43, no. 6, pp. 1295–1309, May 2018, doi: 10.1002/esp.4314.
- [4] B. Camenen, M. Jodeau, and M. Jaballah, "Estimate of fine sediment deposit dynamics over a gravel bar using photography analysis," *International Journal of Sediment Research*, vol. 28, no. 2, pp. 220–233, Jun. 2013, doi: 10.1016/S1001-6279(13)60033-5.
- [5] A. Gregory, R. R. Morrison, and M. Stone, "Assessing the Hydrogeomorphic Effects of Environmental Flows using Hydrodynamic Modeling," *Environmental Management*, vol. 62, no. 2, pp. 352–364, Aug. 2018, doi: 10.1007/s00267-018-1041-6.
- [6] T. Esmacili, T. Sumi, S. Kantoush, Y. Kubota, S. Haun, and N. Rüther, "Three-Dimensional Numerical Study of Free-Flow Sediment Flushing to Increase the Flushing Efficiency: A Case-Study Reservoir in Japan," *Water*, vol. 9, no. 11, p. 900, Nov. 2017, doi: 10.3390/w9110900.
- [7] M. Haimann et al., "Monitoring and modelling concept for ecological optimized harbour dredging and fine sediment disposal in large rivers," *Hydrobiologia*, vol. 814, no. 1, pp. 89–107, Jun. 2018, doi: 10.1007/s10750-016-2935-z.
- [8] M. Tritthart, M. Haimann, H. Habersack, and C. Hauer, "Spatio-temporal variability of suspended sediments in rivers and ecological implications of reservoir flushing operations," *River Res Appl.*, vol. 35, no. 7, pp. 918–931, Sep. 2019, doi: 10.1002/rra.3492.
- [9] R. Hostache, C. Hissler, P. Matgen, C. Guignard, and P. Bates, "Modelling suspended-sediment propagation and related heavy metal contamination in floodplains: a parameter sensitivity analysis," *Hydrol. Earth Syst. Sci.*, vol. 18, no. 9, pp. 3539–3551, Sep. 2014, doi: 10.5194/hess-18-3539-2014.
- [10] R. C. Grabowski, I. G. Droppo, and G. Wharton, "Erodibility of cohesive sediment: The importance of sediment properties," *Earth-Science Reviews*, vol. 105, no. 3–4, pp. 101–120, Apr. 2011, doi: 10.1016/j.earscirev.2011.01.008.
- [11] R. Ata, "Telemac user manual." Dec. 2018.
- [12] P. Tassi, "Sisyphe user manual." Dec. 2018.
- [13] C. Villaret, J.-M. Hervouet, R. Kopmann, U. Merkel, and A. G. Davies, "Morphodynamic modeling using the Telemac finite-element system," *Computers & Geosciences*, vol. 53, pp. 105–113, Apr. 2013, doi: 10.1016/j.cageo.2011.10.004.
- [14] P. J. Wood and P. D. Armitage, "Sediment deposition in a small lowland stream-management implications," p. 12, 1999.
- [15] D. Milan, G. Heritage, N. Entwistle, and S. Tooth, "Morphodynamic simulation of sediment deposition patterns on a recently stripped bedrock anastomosed channel," *Proc. IAHS*, vol. 377, pp. 51–56, Apr. 2018, doi: 10.5194/piahs-377-51-2018.
- [16] J. P.-Y. Maa, J.-I. Kwon, K.-N. Hwang, and H.-K. Ha, "Critical Bed-Shear Stress for Cohesive Sediment Deposition under Steady Flows," *J. Hydraul. Eng.*, vol. 134, no. 12, pp. 1767–1771, Dec. 2008, doi: 10.1061/(ASCE)0733-9429(2008)134:12(1767).
- [17] J. C. Winterwerp, W. G. M. van Kesteren, B. van Prooijen, and W. Jacobs, "A conceptual framework for shear flow-induced erosion of soft cohesive sediment beds" *J. Geophys. Res.*, vol. 117, no. C10, p. n/a-n/a, Oct. 2012, doi: 10.1029/2012JC008072.



# Numerical modelling of the effects of change in river channel morphology on flooding frequency in the Dijle valley, Belgium, using TELEMAC-2D modelling system

Sardar Ateeq-Ur-Rehman<sup>1,3</sup>, Jutta Meylemans<sup>1</sup>, Ward Swinnen<sup>1,2</sup>, Nils Broothaerts<sup>1</sup>, Gert Verstraeten<sup>1</sup>

<sup>1</sup> KU Leuven, Division of Geography and Tourism, Department Earth and Environmental Sciences, Celestijnenlaan 200E, B-3001 Heverlee, Belgium

<sup>2</sup>Research Foundation Flanders (FWO), Egmontstraat 5, B-1000 Brussels, Belgium

<sup>3</sup>Corresponding author email address: [sardar.ateeq@kuleuven.be](mailto:sardar.ateeq@kuleuven.be)

**Abstract**— Climate and land use changes can have an important impact on the channel discharge regime and consequential river morphology. As a consequence, flood frequency and flood depth in the river valley will be impacted. This relationship remains, however, poorly understood for many rivers. Nevertheless, such information is needed to understand ecological and hydrological processes in river channels and adjoining floodplains. It requires information on the complex interlinkage between channel morphology and discharge as well as on flood frequency and flood depth at high spatio-temporal resolutions. This study uses the TELEMAC-2D model in the Dijle valley, Belgium. Due to substantial urbanization in the Dijle catchment over the last few decades, discharge peaks in the river channel have continuously been increasing. The TELEMAC-2D model shows, however, that widening and deepening of the Dijle river channel has been reducing the flood frequency, flooding water depth and area in the valley.

## I. INTRODUCTION

Flood frequency and duration can affect groundwater level and ecology in floodplains. On the other side, flood frequency and duration is influenced by climate change, hydraulic structures or changes in river and floodplain morphology. Climate change is contributing to more extreme hydrological events, which are also triggered by long lasting or heavy floods [1]. Hydraulic structures are normally used to mitigate downstream flooding by creating damming effect, however, some hydraulic structures such as ramps or bridges can also create obstacles for river flow and can cause upstream flooding by changing river morphology alone or together with climate change [2]. To deal with sediment deficiency downstream due to hydraulic structures, normally sediments are added artificially. In the absence of hydraulic structures, excessive sediments are dragged out. Poorly managed sediment addition or dredging can change riverbed morphology, which subsequently can affect flood frequency, water depth, and flood duration. This can also further affect groundwater levels and ecological processes in the floodplain.

For example under the effect of climate change, urbanization in the catchment together with artificial removal of sediments, channel morphology within the main Dijle river channel (located in central Belgium) has changed over the last decades

[3]. The modified river channel may accommodate (without bank-full discharges) high flows which consequently can reduce flooding frequencies and increases hyporheic groundwater loss into the channel. This phenomenon can be more pronounced during low discharges with implications for the ecological state of the riparian zone and surrounding floodplain. Although the effect of land-cover and land-use change on river hydrology has been studied [4, 5], no study has been done to evaluate the effect of changing river morphology on the flooding frequencies and flooding areas in the valley which is also needed in groundwater and ecological modelling.

[3] made use of topographic surveys of the river channel in 1969 and compared it to LiDAR elevation data (collected from 2001 to 2003) to compute changes in river channel morphology. They found that approximately 9,000 m<sup>3</sup> of sediments have been eroded from a 10 km river reach upstream of Leuven (Fig. 1). Similarly, [6] applied the Pettitt test [7] to detect the qualitative and quantitative changes in discharge series collected from 1974 to 2002 at Sint-Joris-Weert and found a statistically significant increasing trends in peak discharges and their frequencies. However, there is a research gap in literature with respect to impact of the rate of increase in peak discharges and incising on the flooding frequencies: either they are balancing each other or they have disproportional relationship.

Therefore, to quantify the combined effect of changes in discharge and river morphology, we applied the TELEMAC-2D model as this tool not only provides high spatio-temporal resolution information about water depths, velocities and bank-full discharges, but also that its source code can be modified according to local conditions [8]. The modelling environment can also be launched on parallel processing which significantly reduces computation time. Therefore, we applied the TELEMAC 2-D hydrodynamic model to a relatively naturally maintained area between Korbeek Dijle and Sint-Joris-Weert (Fig. 1). We used simulated discharges as upstream boundary conditions which were calculated using the STREAM hydrological model [9]. The model can simulate the discharge of rivers based on input data of climate (precipitation and temperature), soil and land-use and has also previously been applied on the Dijle river [4]. The STREAM model also provides us with an opportunity to quantify the flooding

frequencies on a larger time scale by providing discharges of missing periods.

## II. STUDY AREA AND DATA

The Dijle river is a typical meandering lowland stream, located at the northern side of the Western European loess belt in central Belgium (Fig. 1). The main river channel is well connected with a drainage network in the floodplains that facilitates water flows during raising or lowering of flooding water depth. The river reach between Sint-Joris-Weert and Korbeek Dijle has a length of 6 km with an average slope of 0.0457 m/100 m and is a relative naturally maintained area where four tributaries join the main river channel. The cumulative discharge of these tributaries is approximately 12.3% of the total river discharge. Since 1973 and 1982 daily water levels at Sint-Joris-Weert and Korbeek Dijle have been recorded and are freely available on the website of the Flemish Environmental Agency (VMM): [waterinfo.be](http://waterinfo.be). Discharge at Sint-Joris-Weert can be calculated using a stage-discharge rating curve developed by the Flemish government. Discharges of the tributaries have not been measured, however, after estimating their discharges, a stage-discharge (HQ) rating curve for Korbeek Dijle can also be developed. To obtain discharge time series for missing days, the STREAM model is used. Like other Belgian rivers, the Dijle has peak flows during winter months which can exceed 26 m<sup>3</sup>/s. The gauge station at Sint-Joris-Weert can measure discharges up-to maximum 29.38 m.a.s.l. Even though the river discharge has been showing an increasing trend in both high frequency and peak discharge magnitude [4, 6].

Bathymetric surveys of the Dijle river from Grez-Doiceau to Heverlee have been conducted in 1969 and 1999 at an average longitudinal sampling interval of 21 m. The sampling interval between cross sections is lower where the river curves or is strongly meandering and vice versa. Surveys conducted in 1999 and 2018 are projected in the Belgian Lambert 72 coordinate system, while the non-digitalized survey in 1969 can be converted into the same coordinate system using geospatial software such as ArcGIS or MATLAB or python, etc. A very detailed 1.0 m x 1.0 m resolution light detection and ranging (LiDAR) surface elevation survey of the whole Dijle floodplain conducted in 2014 is also available. More details about LiDAR surveys and their application at the Dijle river can be found in [3].

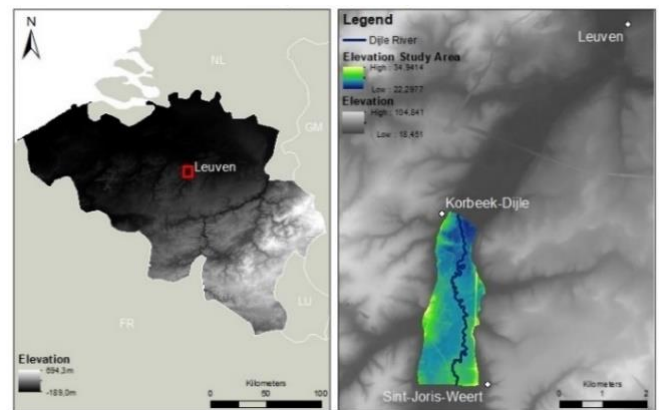


Fig. 1: Location of the study area within the Dijle floodplain (right) and within Belgium (left).

## III. METHODS

There are strong evidences that together with incising/widening of the channel, discharges in the Dijle river channel have also been increasing [3, 6]. However, there remains a research gap with respect to the impact of increase in discharge on the different types of channel geometries in our study area. Therefore we simulated four different geometries using the STREAM model's estimated discharges at Sint-Joris-Weert (SW), at four tributaries, and at Korbeek Dijle (KD) as shown in Fig. 2. Although measured discharges at Sint-Joris-Weert and water levels at Korbeek Dijle are available since 1973 and 1982, respectively, ([waterinfo.be](http://waterinfo.be)), we want to analyze the flooding frequency over a larger time span. The STREAM model provides us an opportunity to quantify the flooding frequencies on a larger time scale by providing the discharges of missing period, i.e. before 1973 or 1982. The STREAM model simulate the discharges record using climate (precipitation and temperature), soil and land-use (Fig. 2) and has also previously been applied on the Dijle river [4]. In the modelling process we use discharges at Sint-Joris-Weert and at four tributaries as upstream boundary conditions while using stage-discharge rating curve (QH) calculated in eq. (3) we converted discharge at Korbeek Dijle into water levels and used as downstream boundary conditions (Fig. 2)

The river surveys of 1969 and 1999 were used to develop two meshes for calculating bank-full discharges. The bank-full discharges were used as boundary conditions for the floodplain meshes developed using the river bathymetric surveys and the 2014 LiDAR survey. Since no major land use changes took place in the floodplain itself, [10], we used the 2014 survey for the area outside of the main river channel for both the 1969 and 1999 periods. Similarly, a higher resolution (1 m x 1 m) LiDAR survey also provides us with an opportunity to precisely represent the small channels and ditches within our floodplain. These small anthropogenic channels act as drainage networks to help with spreading of bank-full discharges and draining water during the lowering of water level in the river channel. We have no indication that these drainage channels have been adjusted in the past decades.

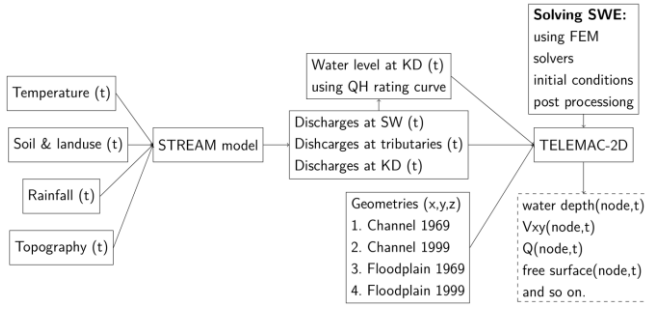


Fig. 2: Schematic diagram of the modelling process. The STREAM model predicts discharges and water levels from 1955 to 2018 using environmental input data, whereas, TELEMAC-2D outputs flooding frequency and flooding water depths for different morphologies of Dijle river channel and floodplain.

Using USBR guidelines, we specified a higher Manning roughness (0.05) for the whole floodplain as it has vegetation [11]. For the main river channel and all other draining networks, we use a Manning coefficient equal to 0.028. The river channel has vegetative banks that acts to increase the lateral roughness; therefore, we used a higher Manning value of 0.032 for both left and right river banks. To obtain discharge boundary conditions before 1973 we use a well calibrated STREAM model. The calibration period was from 1973 to 2018 with a Nash-Sutcliffe model efficiency of 0.35 for the daily discharges and  $R^2$  was at 0.51 for the monthly discharges.

To simulate flooding, we used TELEMAC-2D model on the supercomputing machines of the Vlaams Supercomputer Centrum (VSC). The TELEMAC model is compiled on the VSC cluster (Leuven site) using the Intel compiler version 18.0.1 and CentOS 7.7 operating system. Our simulations are launched on compute nodes with Intel SkyLake or CascadeLake processors. The explicit MPI launching command that is used in the systel.cfg file is: `mpi_cdmexec: mpirun --hostfile $PBS_NODEFILE -np <ncsize> <exename>`, where, at runtime, the \$PBS\_NODEFILE environment variable expands to the list of all hostnames and cores used to run the compute job.

As our study objective was to analyse the impact of geomorphological changes on flooding, we used the constant eddy viscosity model in our computations which can provide us stable solutions at a lower computational cost. To avoid negative depths in our study domain we specified the minimum value of water depth equal to 1.0 cm. To efficiently utilize memory and computational time, we saved our results after each 12 hours using variable time step option. We fix courant number equal to 0.9 while using upwind scheme with the modified SUPG method [12]. The detail of computation grid, boundary conditions, model setup, and modelling parameters is given below.

#### A. Construction of channel and floodplain meshes

Initially we delineated the main river and drainage channels in the floodplain using the official hydrological atlas of Flanders. To precisely represent the river channel and its connectivity with the drainage channels, we constructed meshes with resolution ranging from 0.5 to 10.0 m. Mesh nodes in 0.5 m resolution are four times more than 1.5 m, however, there is a slight different in their fitness with the measured elevation points (Fig. 3). At

both resolutions the drainage channels are better represented, therefore, we selected a 1.5 m mesh resolution. For the entire floodplain (excluding drainage channels) we also constructed meshes with resolution ranging from 1.0 to 20.0 m, however, the floodplain was more precisely represented with 5.0 m resolution. Although, BlueKenue is an efficient tool for creating selafin format files for TELEMAC-2D computation, its processing time for finalizing sub-mesh and island edges connectivity was approximately 3 to 5 hours for our study area. Details of our all four computational grids is tabulated in Table 1.

TABLE 1: INFORMATION ABOUT CHANNEL AND FLOODPLAIN MESHES

Computational grids	No of nodes	Maximum elevation (m)	Area ( $10^6 \text{ m}^2$ )
Channel morphology in 1969	1,13,116	35.50	0.22
Channel morphology in 1999	1,12,764	35.48	0.22
Floodplain morphology in 1969	4,48,580	31.45	4.16
Floodplain morphology in 1999	4,52,056	31.29	4.16

#### B. Initial and boundary conditions

As an initial condition we filled all four of our computational domains slightly higher (0.1 m) then their maximum bottom level (Table 1), so that the models can attain stable conditions at the beginning. The daily discharges obtained using the STREAM model at Sint-Joris-Weert and four tributaries were applied as upstream boundary conditions while the daily water levels were kept as the downstream boundary condition at Korbek Dijle. The modelling flow chart used in the study is shown in Fig. 2. The climate data (mean daily temperature and total daily precipitation) used in the STREAM model was collected at six gauging stations, Ukkel, Zaventem, Beauvechain, Chastre, Marbais and Braine L'alleud, all located around the study area (Fig. 4). The soil input data is derived from the Belgian soil map along with the European dataset "Soil Hydrogrids" for the hydrological properties of the soil such as soil moisture storage. The land use input data is obtained from the European scale CORINE-land cover map from 1990 [13]. The land elevation within the floodplain (from Sint-Joris-Weert to Korbek Dijle (Fig. 1)) has barely been changed from 1990 until 2008 [10, 13]. This means that during the last 30 years the elevation would have a negligible impact on changes in flood frequencies in the study area.



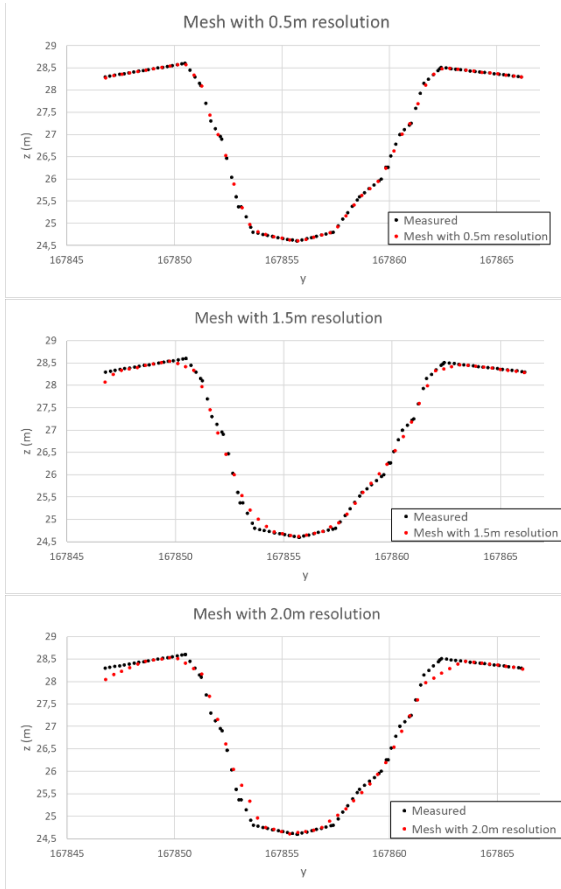


Fig. 3: Measured and modelled river channel cross sections, with a mesh resolution of 0.5 ( $R^2=0.999$ ), 1.5 ( $R^2=0.994$ ), and 2 ( $R^2=0.990$ ); for the Dijle river channel between Sint-Joris-Weert and Korbeek-Dijle.

Discharges at Sint-Joris-Weert are calculated using the following stage-discharge rating curves developed by the Flemish Environmental Agency (VMM):

$$\text{Until } 1/1/1985: Q_{SW} = 9.5 * (H_{SW} - 27.21) \text{ for } H_{SW} < 27.21 \quad (1)$$

$$\text{From } 2/1/1985: Q_{SW} = 10.97 * (H_{SW} - 27.0) \text{ for } H_{SW} < 27.0 \quad (2)$$

whereas  $Q_{SW}$  and  $H_{SW}$  are discharges ( $\text{m}^3/\text{s}$ ) and water levels (m) at Sint-Joris-Weert, respectively. Next, a relation between the water level at the gauging stations at Sint-Joris-Weert ( $H_{SW}$ ) and Korbeek Dijle ( $H_{KD}$ ) could be fitted, which has an  $R^2=0.77$ :

$$H_{KD} = 0.975 * H_{SW}^{0.973} \quad (3)$$

This formula can be used to calculate the water level at Korbeek-Dijle for missing days (between 1973 and 1982) and for a longer time span (from 1953). Although the gauge station at Korbeek Dijle does not record water levels above 26.28 m.a.s.l., hypothetically we extrapolated it with eq. (3) for 42 discharge events above  $27.9 \text{ m}^3/\text{s}$  in our time series (Fig. 5). Using formula (3) we also defined downstream boundary conditions while our upstream boundary conditions were the STREAM estimated discharges from 1953 to 2018 (Fig. 5). The STREAM model estimated maximum and minimum discharge of  $140.21$  and  $1.73 \text{ m}^3/\text{s}$  at Sint-Joris-Weert, respectively. The maximum and minimum water levels at Korbeek Dijle were  $24.22$  and  $35.11 \text{ m}$ , respectively (Fig. 5). As we are simulating flooding events, we used discharges slightly above mean

estimated discharge at Korbeek Dijle, i.e.  $7.0 \text{ m}^3/\text{s}$  which corresponds to 1,028 days or 4.3% of the total time series. In both channel meshes, 36 processors of VSC machines can simulate approximately 70 days in one day while in floodplain meshes 180 processors can simulate approximately 18 days in one day.

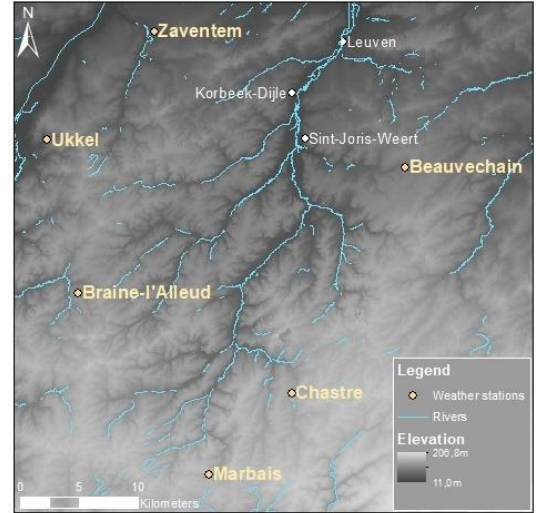


Fig. 4: Location of the rain gauge stations nearby the study area used in STREAM model for discharge calculations. For location, see Fig. 1.

#### IV. RESULTS AND DISCUSSION

With the 1969 channel' geometry a  $7.02 \text{ m}^3/\text{s}$  reached the bank-full level while in 1999 a  $9.54 \text{ m}^3/\text{s}$  discharge was required. Therefore, with the 1999 geometry we observed only 24 events of bank-full discharges compared to 173 events in 1969' geometry indicating that more than 80% reductions in the occurrences of bank-full discharges over 30 years.

Using the 1969 channel bank-full discharges as boundary conditions for both the 1969 and the 1999 floodplain meshes, the TELEMAC model shows that the average flooding area and water depth remains low in the 1999's floodplain mesh (Fig. 6). For the highest hypothetical exceptional flood event ( $142.42 \text{ m}^3/\text{s}$  at Korbeek Dijle- (Fig. 5)) mean water level in the 1969 floodplain was approximately at  $37.5 \text{ m.a.s.l.}$  while it is simulated  $1.5 \text{ m}$  lower for the 1999 floodplain. Similarly in all flooding events, the average flooding water depth was also approximately  $0.5$  to  $1.0 \text{ m}$  lower in 1999 floodplain. For example on  $28^{\text{th}}$  August 1996 at discharge of approximately  $90 \text{ m}^3/\text{s}$  and water level of  $28.0 \text{ m}$  at Korbeek Dijle, the flood water depth at cross section AA in 1999's river mesh was  $8.0 \text{ cm}$  lower compared to the river form in 1969 (Fig. 5 and Fig. 7 to Fig. 9). Similarly, the area under flood was also approximately  $10$  to  $20 \%$  less in 1999 river mesh. Comparing both river geometries at cross section AA shows that the riverbed elevation in 1999 floodplain was  $24 \text{ cm}$  lower compared to 1969. Therefore, it can accommodate higher discharges in the river channel. Comparison of both river channel beds shows that widening and deepening of the river channel from 1969 to 1999 resulted in a total increase of channel volume for the  $6 \text{ km}$  reach amounting to  $52,236 \text{ m}^3$  (Fig. 7 to Fig. 9). This volume corresponds to an average channel erosion rate of  $146.6 \text{ g/s}$  since 1969. Although the average channel erosion rate is very low compared to an

average suspended sediment load (approximately 5.50 kg/s) at Korbeek Dijle calculated by [14] (from 1998 to 2000), it nevertheless has increased the threshold of over-bank discharges from 7.02 m<sup>3</sup>/s to 9.54 m<sup>3</sup>/s.

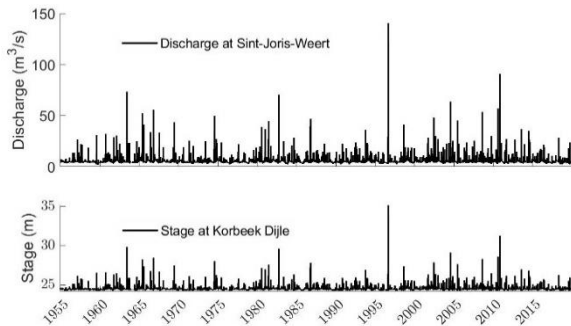


Fig. 5: Discharge data at Sint-Joris-Weert and stage data at Korbeek-Dijle, for the period 1955 -2018

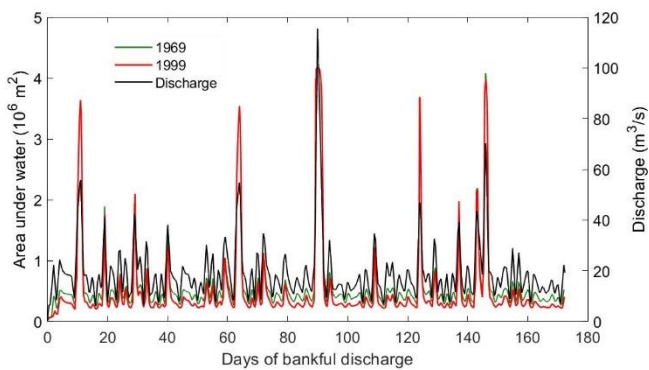


Fig. 6: Floodplain area under water while applying 1969' channel bank-full discharges.

On the same boundary conditions (Fig. 6). our modelling results shows that an average 2.0 m decrease in riverbed elevation may reduce the flooding frequencies up to 10 to 20% in the Dijle Valley (Fig. 10). Similarly the lower riverbed elevation can reduce the flooding water depth up to 0.5 to 1.0 m in the floodplain. However, the river channel has also been changing, due to change in discharges and sediment supply, over the time which has not been included in the modelling process. Additionally, the hydrodynamic calculations, without a hydrodynamic calibration, are very much simplified and can only be used for evaluation purpose of different topographic scenario before moving to morphodynamic modelling. Inclusion of morphodynamic modelling can precisely estimate the rate of change in flooding frequencies with respect to change in discharges and river morphology.

Nevertheless the deeper river channel which is well connected with huge drainage network can also increase groundwater loss into the channel. Most of the studies relate groundwater depletion with urbanization, land use change [15] However, less ground water recharge can also be relevant to decrease flooding in the valley. Moreover, entry of groundwater through the drainage channels and riverbanks can not only effect ecology (by depleting groundwater level) but can also increase pore water pressure which may also have been contributing in bank erosion. Therefore, the current findings can aid our

understanding how a complex web of controlling factors such as the frequency of peak discharges, urbanization, land-use/cover, and changes in catchment surface sediment supply are affecting channel morphology which are consequently altering flooding and perhaps the groundwater dynamics in the floodplain. Similarly, our findings can help to understand the impact of channel morphological changes on flooding and its impact on groundwater and ecology in the valley.

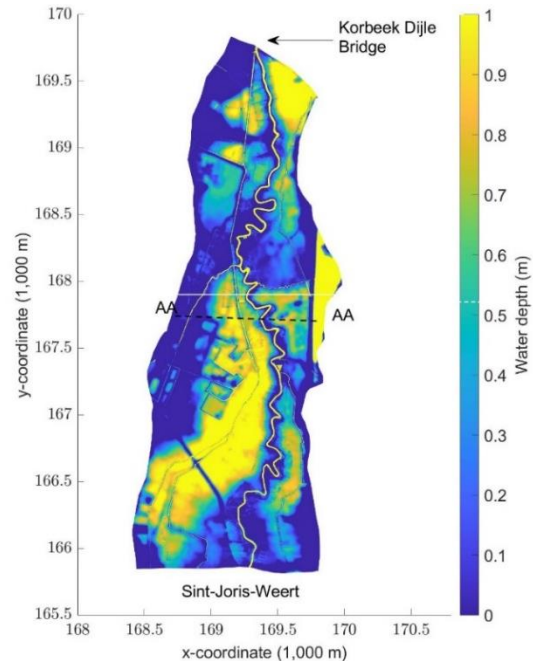


Fig. 7: Flooding on 28 August 1996 in floodplain of 1969. Transect AA shows location of Fig. 9.

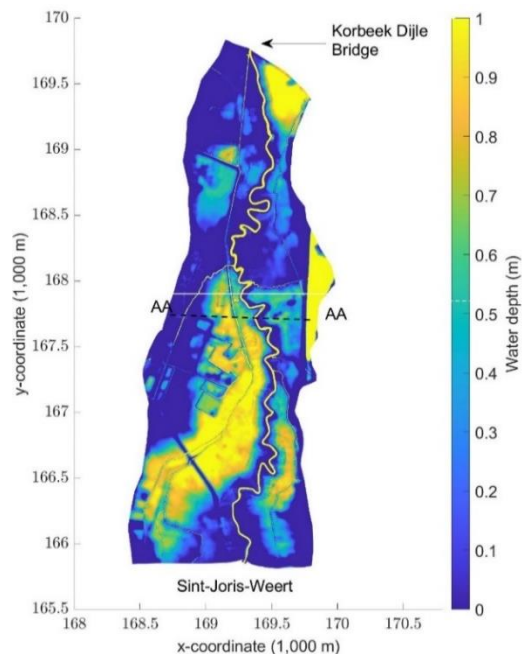


Fig. 8: Flooding on 28 August 1996 in floodplain of 1999. Transect AA shows location of Fig. 9.



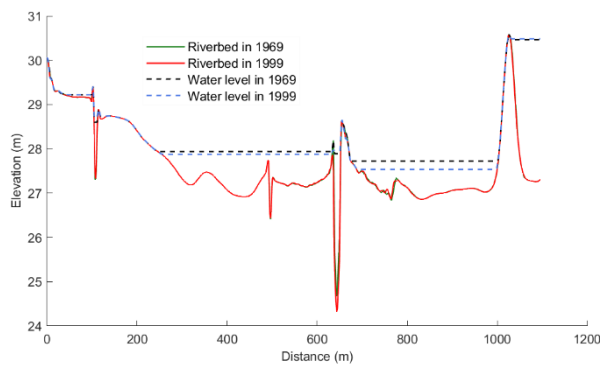


Fig. 9: Riverbed and water level in 1969 and 1999 for a transect perpendicular on the Dijle river. For location, see Fig 7 and Fig. 8.

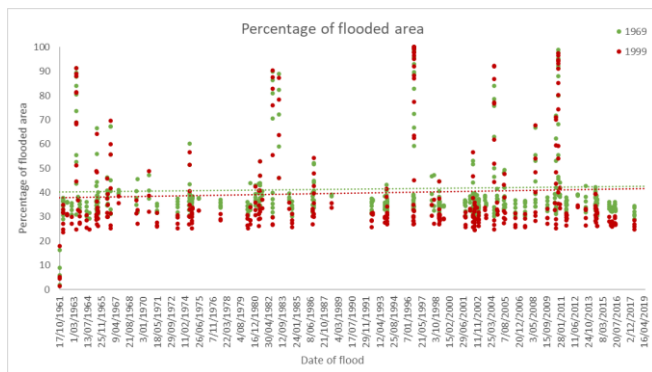


Fig. 10: Percentage of floodplain area flooded in 1969 and 1999 floodplain meshes showing low flooding in 1999 due to incising and widening of the river channel.

## V. CONCLUSION

The TELEMAC-MASCARET modelling environment is a very power tool to analyse flooding problems. High spatio-temporal resolution outputs of water depth, velocity, and discharge at any desired location can provide an opportunity for researchers to not only analyse flooding in a more detailed way but TELEMAC's output can also be used as an input in groundwater or ecological models. The finding that flooding frequency and flooding water depths have been decreasing since 1969 due to widening and deepening of the Dijle river channel contrast with the observed increase in high discharge events. Thus, our modelling results show that local channel morphological changes have a stronger impact on local flood risk than changes in discharge. Although together with incising, channel discharge has been increasing, it is still unclear whether sediment supply was also influenced and played a role in incising and widening of the river channel.

## ACKNOWLEDGEMENT

This research was partly financed by the Fonds Wetenschappelijk Onderzoek (S003017N - Future Floodplains - Ecosystem Services of Floodplains under socio-ecological changes). This research has also been supported by the Fonds Wetenschappelijk Onderzoek (grant no. 1167019N). The resources and services used in this work were provided by the VSC (Flemish Supercomputer Center), funded by the Research Foundation - Flanders (FWO) and the Flemish Government

## REFERENCES

- [1] A. Bronstert, "Floods and climate change: Interactions and impacts," *Risk Anal.*, 23 (2003), p 545-557.
- [2] M. Reisenbüchler, M.D. Bui, D. Skublics, P. Rutschmann, "An integrated approach for investigating the correlation between floods and river morphology: A case study of the Saalach River, Germany," *Sci. Total Environ.*, 647 (2019), p 814-826.
- [3] B. Notebaert, G. Verstraeten, G. Govers, J. Poesen, "Qualitative and quantitative applications of LiDAR imagery in fluvial geomorphology," *Earth Surf. Process. Landf.*, 34 (2009), p 217-231.
- [4] B. Notebaert, G. Verstraeten, P. Ward, H. Renssen, A. Van Rompaey, "Modeling the sensitivity of sediment and water runoff dynamics to Holocene climate and land use changes at the catchment scale," *Geomorphology*, 126 (2011), p 18-31.
- [5] B. Notebaert, "Sensitivity of river systems to human actions and climatic events across different environments: A holocene perspective," PhD thesis, Department of Earth and Environmental Sciences, KU Leuven, Leuven, 2009.
- [6] V.H. Michiel, "Analyse van de fluviatiele dynamiek in het Dijlebekken (1969-2008) op basis van veldgegevens en modellering," M.Sc. thesis, Faculteit Wetenschappen, KU Leuven and Free University of Brussels-VUB, Leuven, 2009.
- [7] A.N. Pettitt, "A non-parametric approach to the change-point problem," *J. Roy. Stat. Soc. C-App.*, 28 (1979), p 126-135.
- [8] S. Ateeq-Ur-Rehman, M.D. Bui, S.u. Hasson, P. Rutschmann, "An innovative approach to minimizing uncertainty in sediment load boundary conditions for modelling sedimentation in reservoirs," *Water*, 10 (2018), p 1-27.
- [9] J. Aerts, M. Kriek, M. Schepel, "STREAM (Spatial Tools for River Basins and Environment and Analysis of Management Options): 'Set up and requirements'," *Phys. Chem. Earth Pt B-Hydrol. Oceans Atmos.*, 24 (1999), p 591-595.
- [10] L. Poelmans, A. Van Rompaey, V. Ntegeka, P. Willems, "The relative impact of climate change and urban expansion on peak flows: a case study in central Belgium," *Hydrol. Process.*, 25 (2011), p 2846-2858.
- [11] G.J. Arcement, V.R. Schneider, "Guide for selecting Manning's roughness coefficients for natural channels and flood plains," *Water Supply Paper*, 1989.
- [12] R. Ata, "TELEMAC v7.2 User Manual," Open TELEMAC-MASCARET, Chatou, France, 2007.
- [13] European Environmental Agency, "CORINE Land Cover Project, published by the Commission of the European Communities," 1995.
- [14] A. Steegen, "Sediment deposition in and export from small agricultural catchments," PhD thesis, Department of Geography and Geology, KU Leuven, Belgium, 2001.
- [15] F. De Smedt, O. Batelaan, "Investigation of the human impact on regional groundwater systems," in: E. Tiezzi, C.A. Brebbia, J.L. Uso (Eds.) *Ecosystems and Sustainable Development Iv*, Vols 1 and 2, Wit Press, Southampton, 2003, p. 1145-1153.

# Development of a hydro-morphodynamic model for simulation of bed load and morphological changes of flash-floods (Têt River, France)

Sebastien Pinel<sup>1</sup>, Fatma Cherif<sup>1</sup>, Florian.Meslard<sup>1</sup>, Camille Labrousse<sup>1</sup>, François Bourrin<sup>1</sup>

<sup>1</sup> 1 Centre of education and research on Mediterranean environments (CEFREM), University of Perpignan, 52 avenue Paul Alduy, 66860, Perpignan, France;

[sebastien.pinel@univ-perp.fr](mailto:sebastien.pinel@univ-perp.fr); [sebpinel@gmail.com](mailto:sebpinel@gmail.com);  
[fatma.cherif@etudiant-enit.utm.tn](mailto:fatma.cherif@etudiant-enit.utm.tn); [florian.meslard@univ-perp.fr](mailto:florian.meslard@univ-perp.fr); [camille.labrousse@univ-perp.fr](mailto:camille.labrousse@univ-perp.fr); [fbourrin@univ-perp.fr](mailto:fbourrin@univ-perp.fr).

**Abstract**— Mediterranean coastal rivers are subject to the climate hazards. Most of the year, they present low water levels with low flows and during intense and short rainy events, their flow increases sharply. These "flash-floods" comprise an intense advancing water wave that induce considerable sediment loads. Most of the solid flows through coastal rivers take place during these brief events. Besides, the materials transported by the river significantly impact the river morphology. These changes may promote floods, destabilize hydraulic structures and disrupt their operations. To analyse the amounts of sediment bed loaded by the Têt River (Gulf of Lions, France) and their effects on the river morphological changes during floods events, we implemented a hydro-sedimentary model (hydrodynamic and sediment transport processes, TELEMAC-2D-GAIA) over the last 12.5 km reach (up to the river mouth). Hydrodynamics calibration was performed on two recent floods events over Manning coefficients. Validation on a third event led to a NSE (coefficient of Nash–Sutcliffe efficiency) of 0.66. Despite several simplifications, the morpho-dynamics model provided reasonable performance regarding the bed load transport. A test of sensitivity on the transport formulae conducted to choose the Meyer-Peter and Müller formula. After investigations on model limitations, we examined the morphological impact of a flash flood on the river. Further researches will focus on simulation of the 100-year flood induced by the 2020 Gloria event.

## I. INTRODUCTION

River floods are essential processes in the land-to-sea transfer of sediment. They can be classified into two different types: seasonal floods and flash-floods. The former are generally associated with large systems such as the Amazon and characterised by a seasonal flood pulse [1]. Occurring during several weeks or months, meteorological conditions that have caused these floods are not directly linked with coastal conditions. Conversely, flash-floods are short and intense events occurring during a few hours or days, and provoked under intense meteorological conditions. Flash-floods are common features in Mediterranean watersheds. They are associated with small mountainous catchments influenced by brief meteorological marine storm events during which depressions over the sea induce rapid and extreme rainfall over coastal relief. The result is a sudden river discharge of fresh water and sediment to the coastal zone. In

this case, hydrology in the inner-shelf are closely linked with local meteorological conditions.

Due to the event-driven nature of the discharge in small rivers, most sediment reaching the sea from them usually does so during flash-floods. Small rivers are estimated to account for more than the half the annual suspended sediment load to the Mediterranean Sea [2]. Hence, it is important for global sediment flux studies to investigate flash-floods in which steep basin topography can give rise to a high potential sediment discharge [3]. Sediment delivered to the sea during such floods may be stored in prodeltas or bypass these to reach the canyon region and then the abyssal plain [4].

Due to their small spatio-temporal scale, flash-floods require specific sampling and modelling strategies. Hence, studies about flash-floods have focused on the dynamics and the fate of sudden river inputs to the coastal zone [4], the river system (runoff, fresh water and solid fluxes) [5], suspended sediment balance [6]. Coupling hydrodynamics and transport sediment models allows investigating the sediment dynamics [7], the link between flash-floods and river morphology [8]. However, researcher face major shortcomings: i) morpho-dynamics model are very sensible to sediment transport law [8], ii) unlike suspended load, bed load has been hardly estimated.

The aim of the study is to model the bed load and morphological changes that occurred during three major recent floods over the Têt River (southwestern Gulf of Lions, France). We firstly present the study zone, the modelled reach and events. The following section describes the material (models and data) and methods. The results and discussion sections include model reliability, modelling limitations, bed load estimation and morphological evolution.

## II. STUDY ZONE AND MODELLED HYDROLOGIC EVENTS

The Têt River discharges into the south-western part of the Gulf of Lions (Figure 1). The Têt catchment (1396 km<sup>2</sup>) has a mean altitude of 1023 m and a mean slope of 12 [9]. Its maximum headwater elevation is at 2100 m and the river length is about 100 km [10]. Over the 1980–2000 period, the averaged annual precipitation for the entire basin is 757 mm.

The rainfall pattern is characterised by long dry periods interrupted by short, violent marine events that can result, within a few hours, in flood events. The average liquid discharge at the gauging station at Perpignan, 12.5 km upstream from the mouth, is  $10.82 \text{ m}^3 \cdot \text{s}^{-1}$ . Instantaneous discharge can reach more than  $1000 \text{ m}^3 \cdot \text{s}^{-1}$  during major floods associated with extreme rainfall events [11]. Extreme floods with a discharge peak of  $540 \text{ m}^3 \cdot \text{s}^{-1}$  have a 5-year return interval, whilst relatively smaller flood events with a discharge peak of  $180 \text{ m}^3 \cdot \text{s}^{-1}$  have a return interval of 2 years. To reduce the intensity of peak floods, a retention dam was built in 1978 at Vinça, 50 km upstream from the mouth, on the border between the mountainous part and the alluvial plain.

In the present study, modelled domain is a 12.5-km reach from Perpignan up to 500 m from the Têt River mouth (Figure 1). The study period (2018-2019) encompasses three extreme flood events whose main characteristics are resumed in Table 1.

TABLE 1. CHARACTERISTICS OF STUDIED FLOOD EVENTS

Event	Dates (beg*- end)	Peak d** (m <sup>3</sup> /s)	Peak date	Return period (years)
Flood1	2018/10/14	237	2018/10/15	2-5
	2018/10/21			
Flood2	2018/11/17	159	2018/11/18	2-5
	2018/11/22			
Flood3	2019/10/22	241	2019/10/24	2-5
	2019/10/26			

Beg\*=beginning; d\*\* = discharge.

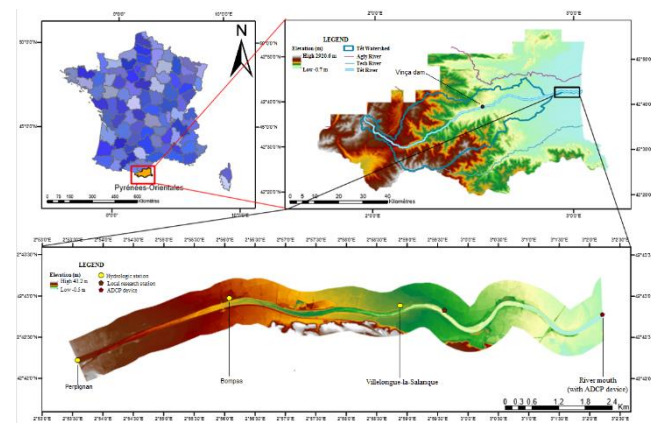


Figure 1. Study zone

### III. MATERIAL AND METHODS

The TELEMAC-MASCARET SYSTEM is freely available at [www.opentelemac.org](http://www.opentelemac.org) and was designed for computational fluid dynamics [12] and associated processes. The morpho-dynamics modelling consists in coupling an hydrodynamic model with a module of sediment transport and riverbed evolution.

#### A. Hydrodynamics modelling and settings

The two dimensional (2D) hydrodynamic module (TELEMAC-2D v8p1) simulates free-surface flows in the two dimensions of horizontal space. For more details, readers are referred to the TELEMAC-2D user manual [13].

TELEMAC-2D model offers several numerical options for calculation. Here, we chose the method of characteristics to simulate velocity advection for its stability and the propagation step is solved by the conjugate gradient method with a diagonal preconditioning which ensures numerical stability. We used default values for viscosity ( $10^{-6} \text{ m}^2 \cdot \text{s}^{-1}$ ) and water density ( $1000 \text{ kg} \cdot \text{m}^{-3}$ ). For reasons of model stability, we set the hydrodynamic time step to 2 s. Bottom friction was based on the Manning coefficient map. We used the Blue Kenue software [14] to generate a mesh of 71733 triangular elements with sides ranging from 10 m to 100 m. Channel sub-mesh presents higher resolution (10 m) (Figure 2).

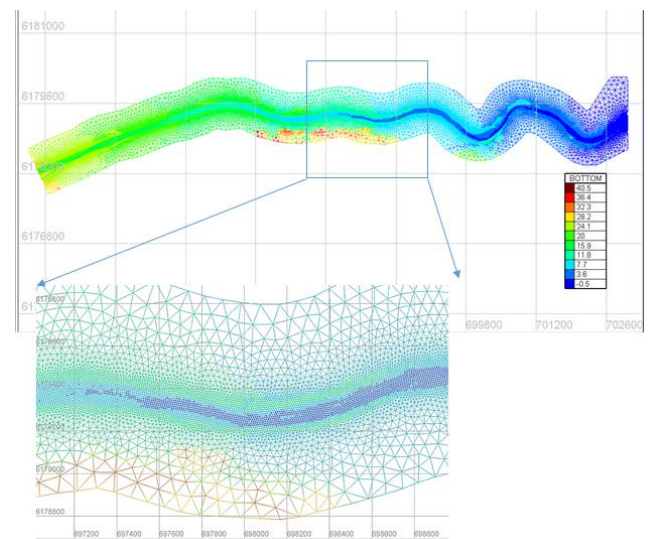


Figure 2. Mesh for modelling

The hydrodynamic model requires three boundary conditions: at upstream two water-inflow boundary conditions and at downstream a water level boundary condition. The two former are the *in situ* Perpignan and Basse discharges. The water level is the one observed at river mouth. The model also included rain and evaporation during simulations.

The hydrodynamic model was run during all the floods events (Table 1). It was initialized by a pre-simulation over a period of 10 days starting with constant water level (29 m), and constant velocity ( $0 \text{ m} \cdot \text{s}^{-1}$ ). The selected constant water level corresponded to the river bottom elevation at the upstream boundary condition with a shift of +3 m.

#### B. Morpho-dynamics modelling settings

Based on the historical sediment transport module SISYPHE, GAIA [15] is a recently developed module of the TELEMAC-MASCARET SYSTEM for modelling of sediment transport and bed evolution. It simulates a large number of complex physical processes (different sediment classes, sand-mud mixtures) commonly found in river and



estuarine modelling. It offers several formulae available for sediment transport and solves riverbed evolution with the sediment mass conservation equation. Second currents and effect of bed slope associated with the influence of gravity can be included. In addition, vertical stratification of sediments and non-erodible riverbed is possible to set up in the model. For more details, readers are referred to the GAIA user manual [15].

The boundary conditions for the fractional sediments were modified to allow a prescribed constant solid discharge at the inlets of the domain, as well as free open boundary for the sediments at the outlet. The prescribed constant solid discharge was derived from literature estimation of annual discharges ( $1.5 \times 10^{-6} \text{ kg.s}^{-1}$ ) [6].

For estimating the sediment transport of two classes of non-cohesive sediments (D50 of 200  $\mu\text{m}$  and 500  $\mu\text{m}$ ), several formulae for bed load (Meyer-Peter and Müller, Van Rijn) and total load (Engelund-Hansen, Engelund-Hansen modified by Cholley-Cunge) were tested. The bed structure was discretized in two layers: an active sediment layer (thickness of 0.15 m) and erodible layer (thickness of 2 m). Sediment slide, secondary currents, skin friction and slope effects were excluded with the aim of simplify the model.

### C. Calibration and validation assessment

A first calculation with the hydraulic model TELEMAT 2D was conducted to determine the variations of hydraulic parameters during the floods events. We calibrated the hydrodynamics model in terms of water height and velocity from both first floods event (i.e. Flood1 and Flood2) adjusting Manning coefficients in the channel by a trial-and-error method. Accuracy is controlled against reference datasets: water level measured at Bompas and Villelongue-la-Salanque, and velocity recorded by the ADCP at the river mouth. Once the model calibrated, we performed the hydrodynamics model validation. Accuracy is controlled at same locations than the calibration.

Regarding morpho-dynamics, due to control data lack, model calibration and validation consisted in sensibility tests in relation with sediment transport law, bed structure and sediment distribution (fraction and  $D_{50}$ ). Within the view to calibrate the model, for each simulation, we computed the simulated quantity of sediment transported by bed load, and compared it with estimations of annual total load of sediment from literature.

Several classical statistics served to appraise model accuracy: the Pearson correlation coefficient, the RMSE (m), the Nash-Sutcliffe efficiency (NSE, [16]).

### D. Available datasets

#### Hydrologic data

At upstream, the French Ministry of Ecology, Sustainable Development and Energy provides hourly water discharges of the Têt River at the Perpignan gauging station, 12.5 km upstream from the river mouth ( $42^{\circ}42'13''\text{N}$ ,  $02^{\circ}53'32''\text{E}$ ). Data are available at <http://www.hydro.eaufrance.fr/>. Due to the lack of data and according to [6], discharges of the Basse

Affluent of Têt River has been computed as 10% of the measured discharge at Perpignan gauging station.

Along the studied reach, the same institution provides hourly time series of levelled water level at Bompas ( $42^{\circ}42'58''\text{N}$ ,  $2^{\circ}56'4''\text{E}$ ) and Villelongue-de-la-Salanque ( $42^{\circ}42'53''\text{N}$ ,  $2^{\circ}58'53''\text{E}$ ) gauging stations.

At downstream, an Acoustic Doppler Current Profiler (ADCP Aquadopp Profiler 2 MHz, Nortek) provides 10-minutes times series of vertical-averaged velocity (intensity and direction) and depth. This device is located 500 m from the river mouth ( $42^{\circ}42'47''\text{N}$ ,  $3^{\circ}02'13''\text{E}$ ). Pre-processing necessitate to turn depth data into water level. It is noteworthy that depending that depending on hydrologic condition, this gauge receive both marine and inland influence.

#### Rainfall and evaporation data

Hourly rainfall data are originate with two sources: *in situ* and satellites. The French national meteorological service (Météo-France, <https://donneespubliques.meteofrance.fr/>) provides the observed local rain at Perpignan airport ( $45^{\circ}44'14''\text{N}$ ,  $2^{\circ}52'22''\text{E}$ ). Gaps in the data (<2%) are filled with remote sensing rainfall. The product PERSIANN-Cloud Classification System is a real-time global high resolution (4km) satellite precipitation product developed by the Center for Hydrometeorology and Remote Sensing (CHRS) at the University of California, Irvine (UCI) [17]. Satellite data are available at <http://chrsdata.eng.uci.edu/>.

The local meteorological station does not provide evaporation. We use hourly evaporation issued from 8-km gridded dataset SAFRAN. It is a mesoscale atmospheric analysis system for surface variables [18]. In this dataset, both observations from meteorological stations and surface analyses from numerical weather prediction systems are used. Data are freely available at Météo-France portal.

#### Bottom friction map

We use the Corine Land Cover Edition 2018 to define zones with same cover assumed to reflect similar friction properties. The European Environment Agency provides this product through the Copernicus Land Monitoring Service (<https://land.copernicus.eu/>). From a 44-items classification, we built a simplified land cover map: riverbed, crops, and urban. Following literature advises [19], different values of Manning roughness coefficient were assigned: 0.09 for the crops area, and 0.01 for the urban. Over the riverbed, we tested several manning coefficients within the range 0.03-0.05.

#### Topography data

The French National Geographic Institute provides a Digital Terrain Model at <https://geoservices.ign.fr/>. This raster (RGE ALTI), derived from LiDAR data, has a 5 m spatial resolution and 15 cm vertical accuracy. It is noteworthy that that this DTM rely on data acquired before the studied event (unknown date). Topographic features (cross-sections, slope map) are collected from the digital elevation model.

#### Sediment data

Literature review provides estimations of annual load of suspended sediment for the Têt River. Knowing that, for Mediterranean rivers, the total transported sediments can be

divided into 80% suspended sediments and 20% bed-loaded sediments [8], we can estimate the amount of bed-loaded sediments during one year.

TABLE 2. SUSPENDED AND BED-LOADED SEDIMENT QUANTITY FOR THE TÊT RIVER.

Study	Study period	Transported suspended sediment (t.yr <sup>-1</sup> )	Transported bed-loaded sediment (t.yr <sup>-1</sup> )
[20]	1980-1999	53 546 ± 15 796	13386 ± 3160
[4]	1977-2004	61 000 ± 18 000	15250 ± 4500
[6]	1977-2013	45 000 ± 35 000	11250 ± 8750

#### IV. RESULTS

##### A. Hydrodynamics model performance

The hydrodynamic model was poorly sensitive to the choice of the Manning parameter when exploring the whole range of Manning values in the riverbed. We finally selected the channel value giving the lowest RMSE: 0.04 s.m<sup>-1/3</sup>.

Regarding the hydrodynamics validation (Figures 3a-b), the simulated and observed water levels are in good agreement at all gauges. Averaged RMSE, NSE and correlation coefficient at the both stations were 0.76 m, -1.2 and 0.96, respectively. The velocity comparison (Figure 3c) leads to RMSE of 0.19 m.s<sup>-1</sup>, NSE of 0.57 and correlation coefficient of 0.96. Difference between the indicators at both location suggests that model accuracy has spatial variations. Visual investigation of graphics shows that vertical and velocity accuracies have temporal variations. RMSE, NSE and correlation coefficient presented the lowest values at the beginning of flushing, respectively. Best scores should be obtained during rising waters.

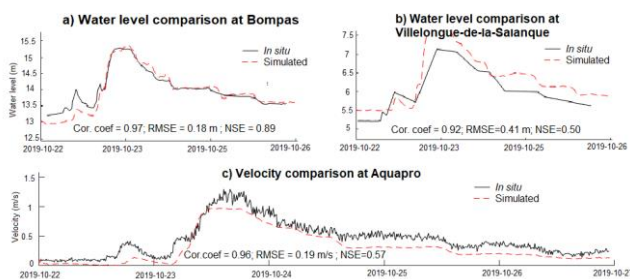


Figure 3. Hydrodynamics validation (Flood3)

##### B. Sediment transport

###### Bed load estimation

We performed several simulations tests to investigate the influence of the different transport laws in bed load estimation. Figure 4 presents the simulated bed load discharges at downstream location for Flood1. We can observe that difference between simulated discharges are important. Apart from the bed load induced from Van Rijn formula, the simulated bed load discharges are closely related.

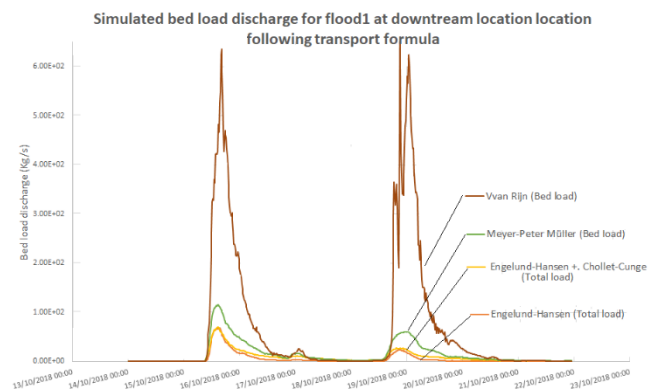


Figure 4. Bed load discharge for Flood1 at the downstream boundary condition according different transport formulae.

Table 3 gives an overview of the simulated quantity of the bed-loaded sediment during the Flood1 according to the transport formula. As expected, the quantity of sediment is highly variable. Both original and improved Engelund-Hansen formulas seems to underestimate the bed load, while Van Rijn formula likely overestimates the bed-load. Comparing with literature-derived quantity of annual bed-loaded sediment (Table 2), best accuracy is obtained with the Meyer-Peter and Müller formula. Hence, all the following results have been performed using this formula.

TABLE 3. SIMULATED QUANTITY OF BED-LOADED SEDIMENT DURING FLOOD1 FOR THE TÊT RIVER ACCORDING TO THE TRANSPORT FORMULA.

Formula	Transported bed-load sediment (t)
Meyer-Peter and Müller	10321
Van Rijn	45587
Engelund-Hansen	3454
Engelund-Hansen+Cholley-Cunge	5617

###### Bed evolution

We present here the bathymetry evolution during the Flood1 (Figures 5a-c). For comparison facility, vertical scale have be limited from -1 m to 1m. However, Figure 5c presents erosion and deposition values superior to 4 m. The analysis shows a spatio-temporal alternation between both processes of erosion and deposition. Between the peak and the end of the peak (Figures 5b-c), there is a notable difference in the magnitude and the zone of erosion/deposition. At the end of the event (Figure 5c), erosion is more important in the upstream reach, while deposition occurs in the downstream part of the river.



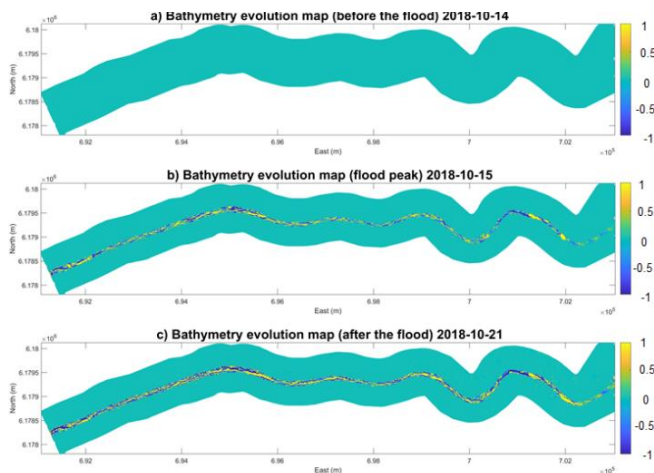


Figure 5. Maps of bathymetry evolution

To analyse the morphological evolution, a comparative analysis of several cross-sections (Bompas, Villelongue-de-la-Salanque and the downstream reach) was conducted before the floods, one day after the peak and at the end of the floods. In this study, for clarity reasons, we only present these results for the Flood1 (Figure 6). The temporal superposition of the cross-sections at the same zone indicates silted sections (deposition) and erosion sections.

We observe that changes in cross-sections are not spatially and temporally uniform. Indeed, upstream cross-sections are subject to intensified phenomena of erosion and deposition. Hence, after Flood1 simulated deposition and erosion can respectively reach 2.0 m and 1.1 m (Figure 6a), while at downstream location erosion is null and averaged deposition remains low ( $<0.5$  m) (Figure 6c). Depending on the cross-section location, erosion and deposition do occur on the same way (Figures 6a-b). At last, we also observe that between the peak flow and Flood1, there are notable bed evolution.

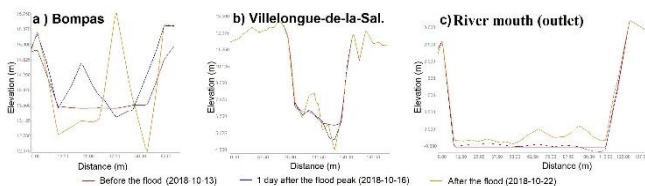


Figure 6. Simulated morphological evolution of the perpendicular cross-sections during the Flood1 at a) Bompas, b) Villelongue-de-la-Salanque, c) River mouth.

The investigation of the evolution of longitudinal riverbed profile reveals large variations of deposition ( $>4$  m) and erosion ( $>2$  m). Overall reach slope remains the same, despite large local variations.

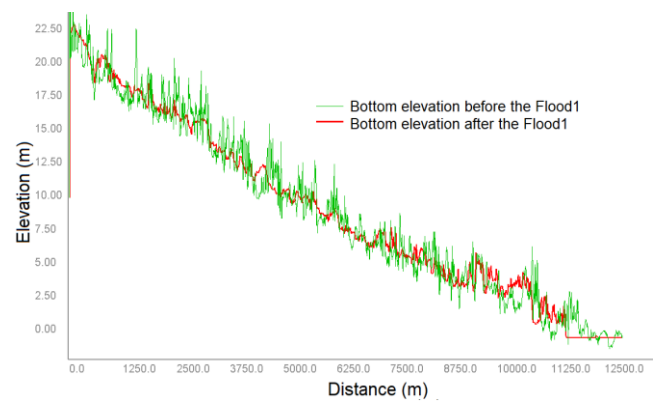


Figure 7. Simulated morphological evolution of the longitudinal profile during the Flood1

## V. DISCUSSION

### A. Model reliability

#### *Hydrodynamics model performances*

The validation performed on Flood3 event showed that simulated water levels were in good agreement with the observations. Comparing with the amplitude of the flood wave (3 m at Perpignan), the RMSE ( $<0.41$  m) value remained low. At Villelongue-de-la Salanque, accuracy is lower and we can note there is a continuous shift of nearly 0.50 m. This suggests that gauge reference could be false. Indeed, gauges can be subject of landslide that can be induced by flash-floods.

The model was able to simulate the river velocity variations with a slight under-estimation. It also reproduces the flow reversion during marine floods (i.e. when sea water level rise before inland waters at the beginning of a floods). Apart from Manning coefficient uncertainty, the velocity underestimation can be linked with unadjusted topography errors. Indeed, several years (without knowing how many) separate topographic surveys and modelled events. Hence, the numerous annual floods have redesigned the braided river. Hence, 2018 riverbed could actually be narrower and higher than in the used RGE-Alti riverbed.

Study results highlights that accuracy is lower during flushing waters. This is mostly due to uncertainty propagation [21], an under-representation of the inner-drainage channels and moreover the importance of actual morphological changes. Indeed, they are essential to reproduce flash-floods events [8].

#### *Morpho-dynamics model performances*

Morpho-dynamics model performance has only been assessed by comparing bed load discharge at the river outlet with bed load estimations derived from suspended discharges values encountered in the literature (limitations of this method are discussed hereafter)

#### *Model limitations*

The analysis of the hydrodynamics model performance showed the importance of topographic controls. Hence, modellers should take into account both the accuracy and the resolution of input topography. Here, UAV orthoimages

evidence a braided bed whose channels width remains inferior to the minimum mesh edge size (10 m). In addition, greenfield banks and river bed with a pronounced micro-topography (hummocks and hollows) and hydraulic structures (weirs) should affect the local water velocity field. With a 10m-mesh resolution, the model does not capture such fine-scale topographic controls. However, these features are taken into account through the roughness coefficient that is adjusted during the model calibration.

Calibration and validation steps suffer from a lack of control data. Indeed, regarding hydrodynamics, horizontal accuracy (flood extent) has not been controlled and velocity fields cannot be fully spatially checked.

Control and input data for the morpho-dynamics suffer from a lack of sediment and bed evolution information. Phillips traps that capture bed load sediment were difficult suitable for assessment. Indeed, simulation and period of sampling collection were different. During a flood event, the traps were filled or sandbagged. Entrance of the Philips traps were also clogged. Further field works and connection with local collectivity (that own cross-section elevation datasets) are needed to increase the data exchanges and the *in situ* knowledge in terms of bed-evolution, bed load, sediment distribution, cover and layers (thickness, number).

Models could have been more sophisticated. By instance, TELEMAT-2D can include wind effect. Depending on the type of the rainy event (marine or inland), local wind magnitude can vary. However, regarding the floods velocity magnitude, if winds may have impact on our results, the topography, sediment layers characteristics and transport law remain the primary sources of models uncertainty. Several options in GAIA have not been activated: sediment slide, slope effect and secondary currents. The latter could explain misrepresentation of the riverbed at the bends. *In situ* device (LISST-Streamside) shows the presence of non-cohesive sediments that we did not take into consideration.

Model calibration and validation are assessed through three classical statistics. However, using these parameters to determine the model performance in predicting riverbed evolution might not be appropriate. New skill scores, such as Brier Skill Score [22], should be computed.

Despite these limitations, the good agreement between observed and simulated data suggests the morpho-dynamics model is sufficient to capture the flow and the sediment transport within the river.

### B. Sediment transport

The use of several sediment laws highlights the model sensibility to this parameter. Both of total load methods (Engelund-Hansen, Engelund-Hansen modified by Chollat-Cunge) overestimate bed load transport. Engelund-Hansen equation [23] overestimates the transport of the finest sediments in comparison with other sediments. It may also be because these equations are designed for grain of larger size. Meyer-Peter and Müller, Van Rijn methods are adapted methods regarding the size of the simulated sediment.

### C. Morphological evolution

The process of sediment transport (erosion, transportation and sedimentation) may change the riverbed topography [22]. Erosion agents include flowing water, waves, wind or gravity. Eroded material is eventually dropped at another location (deposition). Low waters are associated with deposition and slowly modify the landform [24], whereas during flash-floods both phenomena intensively occur causing changes on the river morphology.

Our results suggest that once the flood wave passed, erosion and deposition continue. During the flood, there is always an alternation between both processes. Spatial repartition of these phenomena depends on local conditions: slope, meanders, presence of hydraulics structures or vegetation [8]. These conditions explain why we observed at the end of the Flood I a higher erosion in the straight upstream reach (Figures 5c, 6a and 7) and a higher deposition in the downstream meandering and over the flat part of the river (Figures 5c and 7). Looking at the longitudinal and perpendicular profiles of the outlet (Figures 6c-7), one may note low deposition at the outlet and enhanced deposition and erosion in the first part of the reach. Above-mentioned local conditions together with the increase of the river width (+166 % between Bompas and the river mouth) could explain such an organisation of phenomena.

## VI. CONCLUSION

In this study, we implement a hydro-sedimentary model within the view to analyse the amounts of sediment bed loaded by the Têt River (Gulf of Lions, France) and their effects on the river morphological changes during recent flash-floods (three in all).

Hydrodynamics model is successfully calibrated against the two floods and validated against the third one (NSE of 0.66). Water velocity are slightly under-estimated.

Despite several simplifications, the morpho-dynamics model provides reasonable performance regarding the estimation of bed load transport. A test of sensitivity on the transport formulae conducts to choose the Meyer-Peter and Müller formula. After investigation on model limitations, we examine the morphological impact of a flash flood on the river.

In January 2020, the Gloria storm generated a 100-year floods event. The downstream device could not recorded the full event and has been taken out during the flood. Further researches will focus on i) improving the current morpho-dynamics model ii) using neural network to reconstruct the downstream water level condition to simulate sediment transport during this 100-year floods event.

### ACKNOWLEDGEMENT

The authors thank the DEM'EAUX project for the funding of this work. Special thanks goes to Nicolas Aleman, Bruno Charrière, Mahrez Sadhaoui, Nicolas Akil, Mahmoud Moussa and Xavier Durrieu De Madron for their advices.

## REFERENCES

1. Junk, W.; Wantzen, K.M. The flood pulse concept: new aspects, approaches and applications - an update. In Proceedings of the Proceedings of the Second International Symposium on the Management of Large Rivers for Fisheries; 2004; Vol. II, pp. 117–149.
2. Sadaoui, M.; Ludwig, W.; Bourrin, F.; Romero, E. The impact of reservoir construction on riverine sediment and carbon fluxes to the Mediterranean Sea. *Prog. Oceanogr.* **2018**, *163*, 94–111.
3. Milliman, J.D.; Syvitski, J.P.M. Geomorphic/tectonic control of sediment discharge to the ocean: the importance of small mountainous rivers. *J. Geol.* **1992**, *100*.
4. Bourrin, F.; Durrieu de Madron, X. Contribution to the study of coastal rivers and associated prodeltas to sediment supply in Gulf of Lions (NW Mediterranean Sea). *Vie Milieu* **2006**, *56*, 307–314.
5. Gaume, E.; Livet, M.; Desbordes, M.; Villeneuve, J.P. Hydrological analysis of the river Aude, France, flash flood on 12 and 13 November 1999. *J. Hydrol.* **2004**, *286*.
6. Sadaoui, M.; Ludwig, W.; Bourrin, F.; Raimbault, P. Controls, budgets and variability of riverine sediment fluxes to the Gulf of Lions (NW Mediterranean Sea). *J. Hydrol.* **2016**, *540*, 1002–1015.
7. Khosronejad, A.; Kang, S.; Flora, K. Fully coupled free-surface flow and sediment transport modelling of flash floods in a desert stream in the Mojave Desert, California. *Hydrol. Process.* **2019**, *33*, 2772–2791.
8. Gharbi, M.; Soualmia, A.; Dartus, D.; Masbernat, L. Floods effects on rivers morphological changes application to the Medjerda River in Tunisia. *J. Hydrol. Hydromechanics* **2016**, *64*, 56–66.
9. Ludwig, W.; Serrat, P.; Cesmat, L.; Garcia-Esteves, J. Evaluating the impact of the recent temperature increase on the hydrology of the Têt River (Southern France). *J. Hydrol.* **2004**, *289*.
10. Garcia-Esteves, J.; Ludwig, W.; Kerhervé, P.; Probst, J.L.; Lespinas, F. Predicting the impact of land use on the major element and nutrient fluxes in coastal Mediterranean rivers: The case of the Têt River (Southern France). *Appl. Geochemistry* **2007**, *22*.
11. Lespinas, F.; Ludwig, W.; Heussner, S. Impact of recent climate change on the hydrology of coastal mediterranean rivers in Southern France. *Clim. Change* **2010**, *99*.
12. Moulinec, C.; Denis, C.; Pham, C.T.; Rougé, D.; Hervouet, J.M.; Razafindrakoto, E.; Barber, R.W.; Emerson, D.R.; Gu, X.J. TELEMAC: An efficient hydrodynamics suite for massively parallel architectures. *Comput. Fluids* **2011**, *51*, 30–34.
13. Hervouet, J.M.; Ata, R. *User manual of opensource software TELEMAC-2D*; www.opentelemac.org, 2019;
14. Canadian Hydraulics Centre Blue Kenue Available online: <http://www.nrc-cnrc.gc.ca/eng/ibp/chc/software/kenue/bluekenue.html> (accessed on Sep 1, 2018).
15. Tassi, P.; Hervouet, J.M. *User manual of opensource software GAIA*; www.opentelemac.org, 2019;
16. Nash, J.E.; Sutcliffe, J. V River flow forecasting through conceptual models part I - A discussion of principles. *J. Hydrol.* **1970**, *10*, 282–290.
17. Nguyen, P.; Shearer, E.J.; Tran, H.; Ombadi, M.; Hayatbini, N.; Palacios, T.; Huynh, P.; Braithwaite, D.; Updegraff, G.; Hsu, K.; et al. The CHRS data portal, an easily accessible public repository for PERSIANN global satellite precipitation data. *Sci. Data* **2019**, *6*.
18. Quintana-Seguí, P.; Le Moigne, P.; Durand, Y.; Martin, E.; Habets, F.; Baillon, M.; Canellas, C.; Franchisteguy, L.; Morel, S. Analysis of near-surface atmospheric variables: Validation of the SAFRAN analysis over France. *J. Appl. Meteorol. Climatol.* **2008**, *47*.
19. Arcement Jr, G.J.; Schneider, V.R. Guide for Selecting Manning's Roughness Coefficients for Natural Channels and Flood Plains. *Tech. Report, Geol. Surv. Water-Supply, United States Gov. Print. Off. Washington, U.S.A* **1989**, 38.
20. Serrat, P.; Ludwig, W.; Navarro, B.; Blazi, J.L. Variabilité spatio-temporelle des flux de matières en suspension d'un fleuve côtier méditerranéen: La Têt (France). *Comptes Rendus l'Academie Sci. - Ser. Ila Sci. la Terre des Planetes* **2001**, *333*.
21. Teng, J.; Jakeman, A.J.; Vaze, J.; Croke, B.F.W.; Dutta, D.; Kim, S. Flood inundation modelling: A review of methods, recent advances and uncertainty analysis. *Environ. Model. Softw.* **2017**, *90*, 201–216.
22. Sutherland, J.; Peet, A.H.; Soulsby, R.L. Evaluating the performance of morphological models. *Coast. Eng.* **2004**, *51*.
23. Engelund, F.; Hansen, E. A monograph on sediment transport in alluvial streams. *Monografia* **1967**.
24. Goff, J.R.; Ashmore, P. Gravel transport and morphological change in braided sunwapta river, Alberta, Canada. *Earth Surf. Process. Landforms* **1994**, *19*.

# Comprehensive morphodynamical analysis of the Drava River

Zoltán Árpád Liptay  
Hungarian Hydrological Forecasting Service  
General Directorate of Water Management  
Budapest, Hungary  
[liptay.zoltan@ovf.hu](mailto:liptay.zoltan@ovf.hu)

Ákos Halmai, Ervin Pirkohoffer, Szabolcs Czigány  
Institute of Geography and Earth Sciences  
University of Pécs, Faculty of Sciences  
Pécs, Hungary  
[halmaia@gamma.ttk.pte.hu](mailto:halmaia@gamma.ttk.pte.hu), [pirkhoff@gamma.ttk.pte.hu](mailto:pirkhoff@gamma.ttk.pte.hu),  
[sczigany@gamma.ttk.pte.hu](mailto:sczigany@gamma.ttk.pte.hu)

Alexandra Gradwohl–Valkay, Johanna Ficsor  
Doctoral School of Earth Sciences  
University of Pécs, Faculty of Sciences  
Pécs, Hungary  
[valkays2@gamma.ttk.pte.hu](mailto:valkays2@gamma.ttk.pte.hu), [johannaficsor@hotmail.com](mailto:johannaficsor@hotmail.com)

**Abstract**— The Drava River is located in southern Central Europe, it is a major tributary of the lower Danube River. It has been the subject for a couple of sediment studies in the recent years, but comprehensive morphodynamical studies have not been done yet. During this study, an extensive field measurement was carried out to survey all the necessary data from river bathymetry to channel morphology. A recreational-grade sonar system was assembled and mounted on a double-hull vessel and connected with a geodetic Global Navigation Satellite System (GNSS) device. Field data were completed with ADCP measurements and suspended sediment sampling with laboratory evaluation. Seven characteristic river bed compositions were separated based on the field data, each representing a different mixture of grains from medium sand to coarse gravel ( $d_{50} = 0.125\text{--}16\text{ mm}$ ). Fine particles were completely absent in the upper layer of the armoured river bed. Previous studies shown that 50% of the annual sediment transport occurs during high flows due to this phenomenon. We analysed the reach from Órtilos to Drávaszabolcs, the length of approximately 160 km with internally coupled TELEMAC-2D and SISYPHE models using the Wilcock–Crowe formula for bed-load and the Bijker formula for suspended load. Three scenarios of different temporal characteristics and numerical approaches were selected to get an overview of the long- and short-term morphological processes. Short-term bed-load and suspended load transport, long-term bed-load transport and morphology, and finally the cohesive transport (measured concentration, double and half concentrations, equilibrium concentration). Results showed that at the streamflow of  $363\text{ m}^3/\text{s}$  bed-load is less than 20% of the total sediment transport reaching its highest values at the steepest reaches of the upper part and suspended transport is generally two magnitudes higher. Significant changes in the bed also occur on the steeper upper part, gradually widening narrow sections and moderating steep slopes. Annual bed-load is estimated to be around 40 kt at Barcs and annual suspended load is approximately 2.5 Mt, these are in the range of previous studies of the same flow regime. Modelling only cohesive sediment resulted in erroneous results

due to the important role of coarser grains. Finally, higher discharges were simulated on a smaller scale in order to analyse the development of a natural flood plain channel at Heresznye and the possible effects of dredging. Results showed the slow migration of the river bed and the erosion of the artificially modified flood plain channel, returning itself to a naturally stable condition.

## I. INTRODUCTION

The major rivers of Central Europe in general have undergone heavy anthropogenic influences since navigational and power driven utilizations become important issues. These influences result in changing hydrological and morphological regimes without exception. The Drava River is located in southern Central Europe, it is a major tributary of the lower Danube River originating from Northeastern Italy. Several dams and reservoirs are located along the river for hydropower generation that led to a heavily modified behavior both in hydrological and morphological manner [1, 4]. It has always been a subject for sediment studies [5, 6] and also for sediment modeling in the recent years [2]. In the current study we analyzed the reach between Órtilos and Drávaszabolcs (Fig. 1.) the length of approximately 160 km, where the river serves as the basis of the border between Hungary and Croatia. The same reach was studied in [1] and a significant decrement of the water levels was presented based on long-term (1875-2006) water level time-series due to upstream reservoirs. Reference [8] shows about 65% decrement in suspended sediment concentration at Botovo station (beginning of our study area) and 81% at Donji Miholjac station (end of our study area) between the 1960 and 2017 caused by construction and operation of reservoirs. These reservoirs trap the particles approximately above coarse pebbles so only finer sediment arrives to the study area, but the confluence with Mura River at Órtilos returns coarser sediment. The river is still rich in sediment thus it reacts very dynamically to hydrological circumstances as it is discussed in [4]. The annual average



discharge on the studied reach was  $521 \text{ m}^3/\text{s}$  in the past 10 years, while the lowest value was  $151 \text{ m}^3/\text{s}$  and highest was  $2305 \text{ m}^3/\text{s}$ .



Figure 1. The study area.

An extensive field measurement campaign was carried out to survey all the necessary data. These data included detailed river bathymetry, channel morphology, sediment properties and hydrological parameters such as water level and discharge. The used equipment was a recreational-grade sonar system assembled and mounted on a double-hull vessel and connected to a geodetic Global Navigation Satellite System (GNSS) device. Field data were completed with ADCP measurements and suspended sediment sampling at numerous locations for laboratory evaluation. The database of the processed data served as an input for numerical modelling. We used the TELEMAC-2D model for two dimensional hydrodynamic analysis and later coupled it internally with the SYSIPHE morphodynamic model.

## II. METHODS

### A. Analysis of the measured data

The output of the river bed scanning was a digital terrain model of  $1 \times 1 \text{ m}$  resolution with the error less than  $0.1 \text{ m}$  in altitude. This DTM served as the geometric input for the numerical modelling. The detailed process of assembling the equipment, the collection of data and the post-processing of the surveyed information is described in [3].

The sampling of the river bed material on the studied reach resulted in 40 particle distribution curves shown on Fig 2. The curves represent approximately seven characteristic river bed compositions that are well separated in the range of medium sand to coarse pebble ( $d_{50} = 0.125\text{--}16 \text{ mm}$ ). Fine particles were completely absent in the upper layer due to armouring of the river bed. The armoured bed surface consist of coarser particles trapping fine particles and is unlikely to present significant sediment transport during lower flow conditions. Previous studies shown that 50% of the annual sediment transport occurs during high flows due to this phenomenon. The seven characteristic curves were used as initial bed compositions in the morphodynamical modelling. Nine sediment fractions were introduced in these compositions with the diameters of  $0.125, 0.375, 0.75, 1.5, 2.4, 3.4, 6, 12$  and  $16 \text{ mm}$ .

Samples of water containing suspended sediment particles with the diameter of less than  $63 \text{ microns}$  were analysed in

laboratory by laser scanning. Concentration distributions were obtained for 10 diameters from  $1.5$  to  $60 \text{ microns}$ .

### B. The hydrodynamic model: TELEMAC-2D

The TELEMAC-2D model was selected to perform the modelling tasks due to its stable, reliable and fast solution algorithm and its capability of modelling sediment processes through SYSIPHE. A fully dynamic simulation was required on a relatively fine TIN of  $10 \text{ meters}$ . This resolution allowed the model to represent a realistic cross-section shape even in narrow sections, the fine shape of islands and the rough outline of bridge piers yet allowed manageable simulation time and size of result files. The TIN (as shown on Fig. 3.) consisted of  $563755$  calculation points and  $1091411$  triangles.

Steady-state simulations were carried out with the inflow discharge of  $363 \text{ m}^3/\text{s}$  at Órtilos. The lower boundary condition was  $87 \text{ m a.s.l.}$  at Drávaszabolcs. The uniform roughness of  $0.028 \text{ s/m}^{1/3}$  was defined based on previous studies and current validation runs. This value represented an average roughness of the river bed giving satisfactory results in previous hydrodynamic studies and flood plain inundation modelling, thus this value is assumed to represent an average bed material of the study area.

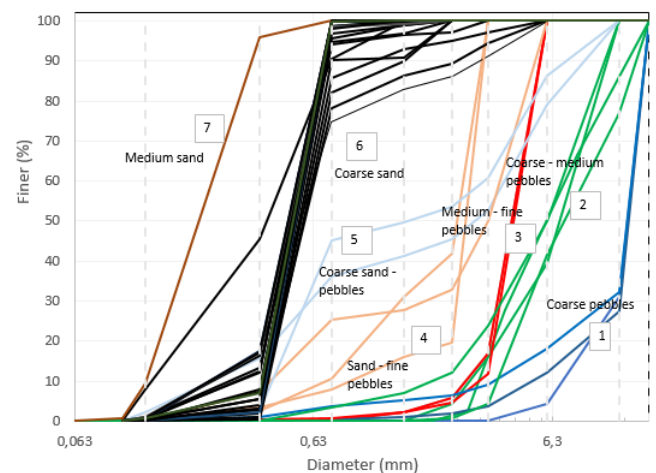


Figure 2. River bed composition ( $0.125, 0.375, 0.75, 1.5, 2.4, 3.4, 6, 12$  and  $16 \text{ mm}$  diameters as dashed lines)

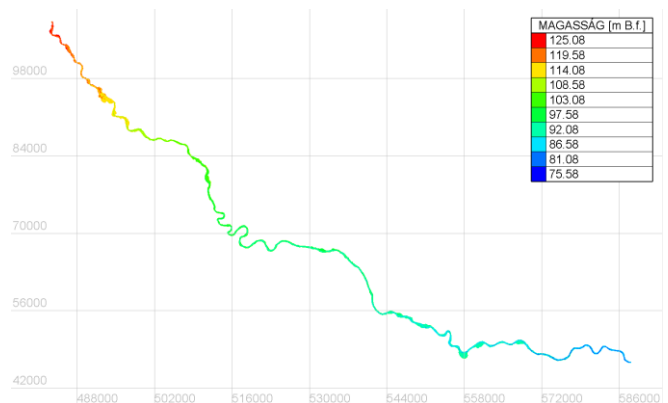


Figure 3. TIN model for TELEMAC-2D



### C. The morphodynamic model: SYSIPHE

We coupled the validated hydrodynamic model internally with SYSIPHE. Three versions of the model were created to estimate short-term and long-term non-cohesive, and cohesive sediment processes. All morphodynamic simulations used a heterogeneous fraction distribution as initial condition, so the measured sediment mixtures were loaded into each calculation points at the beginning by an external FORTRAN subroutine. The hydrodynamic initial conditions were derived from previous hydrodynamic simulations to have a hot start and avoid extreme initial results.

The Wilcock-Crowe formula [7] was used for bed-load due to the promising results in other studies while dealing with armoured bed and wide range of sediment sizes. The suspended load was modelled in the short-term simulation by the Bijker formula. SYSIPHE assumes an exponential distribution of suspended sediment in the water column. This assumption is valid in our case as the lowest Rouse number is app. unity for the smallest particles and higher values for coarser particles. Equilibrium initial and boundary condition were used everywhere. A temporal ratio of 120 was used to stretch the 5 second hydrodynamic time step to 10 minutes and the entire simulation period to 70 and later to 365 days for long-term morphodynamic evaluations.

Cohesive sediment was modelled with two different set of boundary and initial conditions. First based on the measured concentrations and then using the Van Rijn equilibrium concentration. Both of the simulations resulted in very high concentrations on the steep sections and heavy deposition elsewhere. We assume that the bed armouring and the interaction of cohesive and non-cohesive sediments have a significant role on the concentration of particles below 63 microns. These particles might get trapped by coarse particles thus not causing significant erosion and deposition. A severe concentration deficit is assumed during the simulated flow conditions originating from upstream parts of the Drava River. Setting the Krone-Partheniades constant to zero would lead to zero erosion in the Exner equation. This approach gives relatively constant simulated concentration profile along the model domain in the range of measured values, however is a theoretic setup with unacceptably strong simplifications. Therefore the results of these simulations are not discussed in the Results section. The proper approach in case of Drava River would be the modelling of mixed sediment with several classes in both the non-cohesive and the cohesive size range.

Local simulations were also carried out based on the results of the comprehensive simulations. One of the studies was the analysis of a flood plain channel at Heresznye at higher discharges and on a finer TIN. Hydrodynamic simulation were done with HEC-RAS 2D at 1 meter resolution based on diffusive wave approximation to select the necessary model variants. Finally morphodynamic simulation were done on 5 meters with 800 and 1500 m<sup>3</sup>/s main channel discharges. These long-term steady-state simulations are hypothetical because such discharge values do not have the assumed duration, but they allowed us to analyse the flood plain and the stability of artificial canals in the natural environment under inundation.

## III. RESULTS

### A. Short-term simulations

Short-term analysis of bed-load and suspended load transport showed that bed-load is less than 20% of overall sediment transport on the steeper upper parts. On the lower parts of the river bed-load is less than suspended load with two magnitudes (Fig. 4.). Regarding the size of particles smaller diameters are present in higher quantity, such as 0.125 mm and 0.375 mm. The bed evaluation shows an intensive trend from the interpolated geometry to a smoother and more natural bed shape in the first half of the simulation mostly on the steeper parts, and after these major changes are done the slower and more expected changes remain in operation. For example the narrow sections are getting deeper and the washed-out sediment is depositing in the downstream wide section as it is shown at Vízvár on Fig. 5.

A frequently referred section of the Drava River is the upstream cross-section of the bridge at Barcs (154.1 river km). Annual bed-load is estimated to be around 40 kt at this cross-section and annual suspended load is approximately 2.5 Mt. These values are in the range of previous studies of the same flow regime.

The traveling speed of major bed formations was also estimated based on the results. It ranges from 1 m/day on the steeper upper part to 5 m/s at the lower part. A short section of the river bed in the initial and the simulated state is presented on Fig. 6.

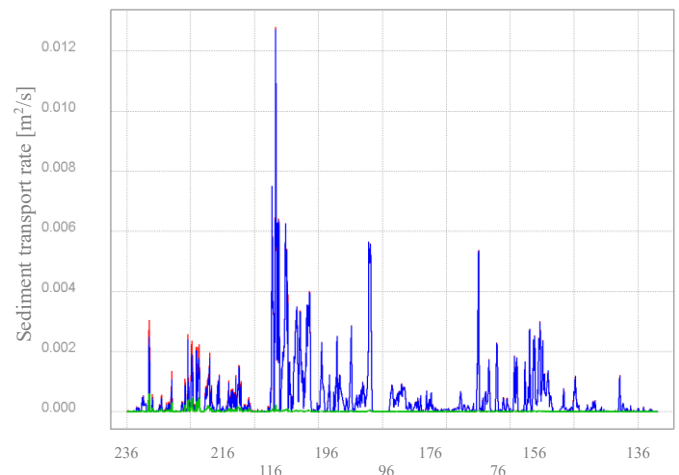


Figure 4. Total sediment transport (red), suspended load transport rate (blue), bed-load transport rate (green) [m<sup>2</sup>/s]

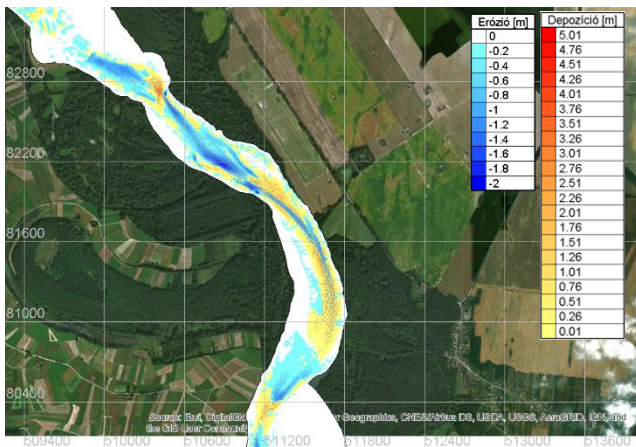


Figure 5. Erosion and deposition at Vízvár after 12 hours of simulation start.

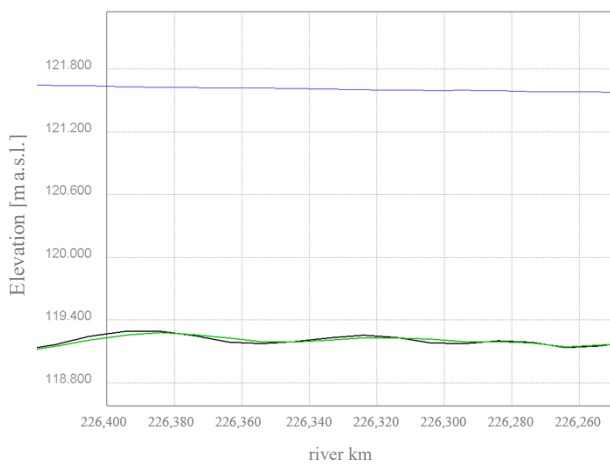


Figure 6. Moving bed formations before (black) and after (green) 12 hours of simulation.

### B. Long-term simulations

Long-term simulations based only on bed-load showed the same trends and magnitudes as the short-term ones. High bed-shear stresses occurred in the first few days of the simulation leading to significant bed changes. The longitudinal profile of bed-shear stress is shown on Fig. 7. The steeper upper part (app. the first 50 km) is represented with higher initial and also final values, while the lower part is relatively constant. Fig. 8. and 9. also show the significant drop of bed-shear stress to 0 to 70 days.

The travelling of major bed formations also showed the same magnitude as the previous simulations. Highest speeds occurred on the upper part up to 5 m/day. A section of the longitudinal bed profile is shown on Fig. 10. The initial bed level is compared to the changed bed after 70 days of simulation. However the river bed undergone significant changes some characteristic points are easily recognisable and their travelling speed can be assessed.

Bridge piers were represented in the model with minor simplifications so their impact on the river bed is visible in the

results. The bridge at Barcs is shown on Fig. 11. with a lesser and a greater scour hole downstream of the piers. Velocity and bed-load transport vectors show a bit of divergence close to these bed formations due to the major changes in the bed slopes. Fig. 12. shows the evolution of the river bed around the bridge piers. Downstream scour holes are slowly filled while upstream scours are deepened.

Long-term analysis generally showed the tendencies of river bed evolution. Major changes are experienced on the steeper upper part (Fig. 13.) and generally less significant changes on the lower part (Fig. 14.) except locally at bridge piers.

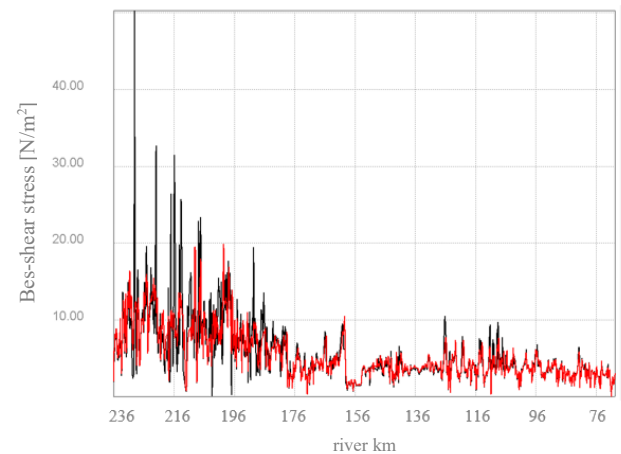


Figure 7. Longitudinal profile of bed-shear stress before (black) and after (green) 70 days of simulation.

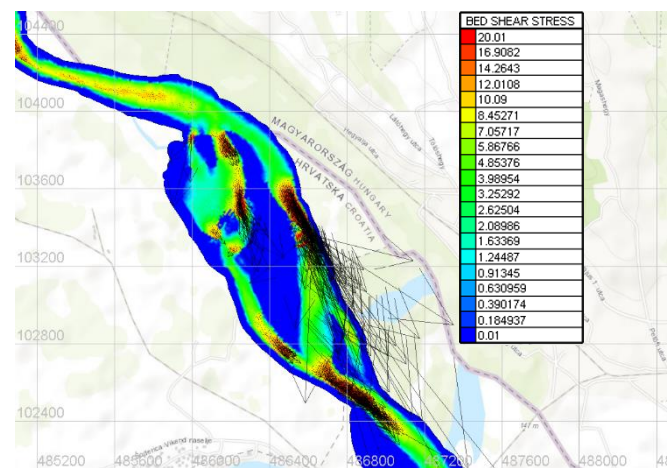


Figure 8. Initial bed-shear stress and bed-load transport rate vectors.

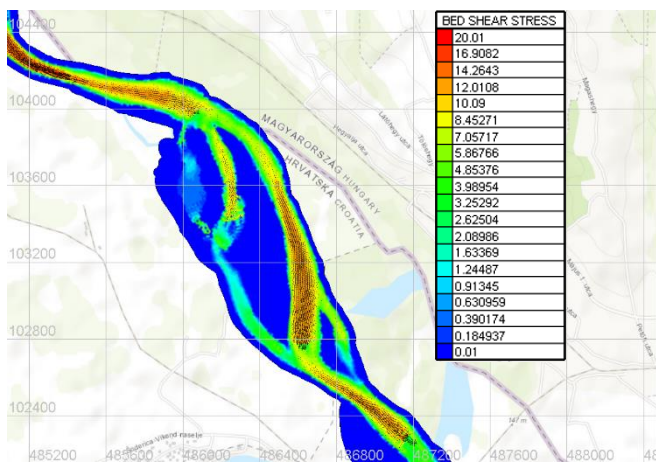


Figure 9. Final (70 days) bed-shear stress and bed-load transport rate vectors.



Figure 10. Moving bed formations before (grey) and after (after) 70 days of simulation.

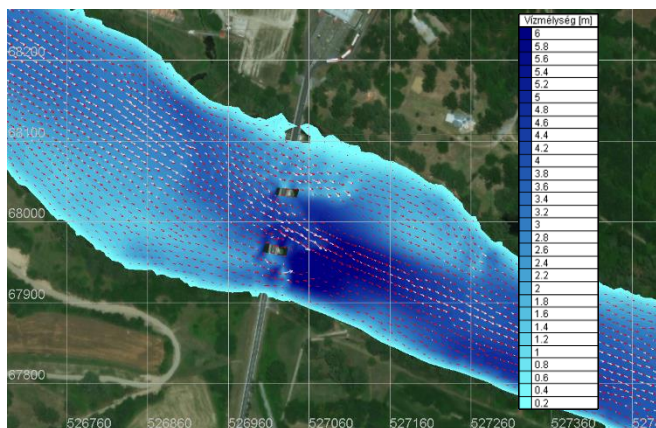


Figure 11. Water depth at Barcs with velocity (white) and bed-load transport (red) vectors.

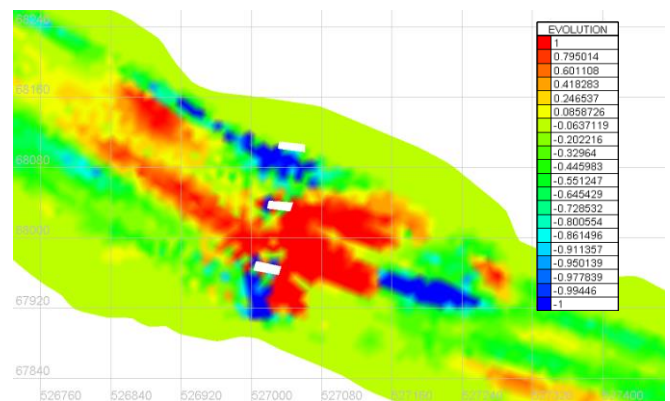


Figure 12. Bed evolution at Barcs after 365 days.

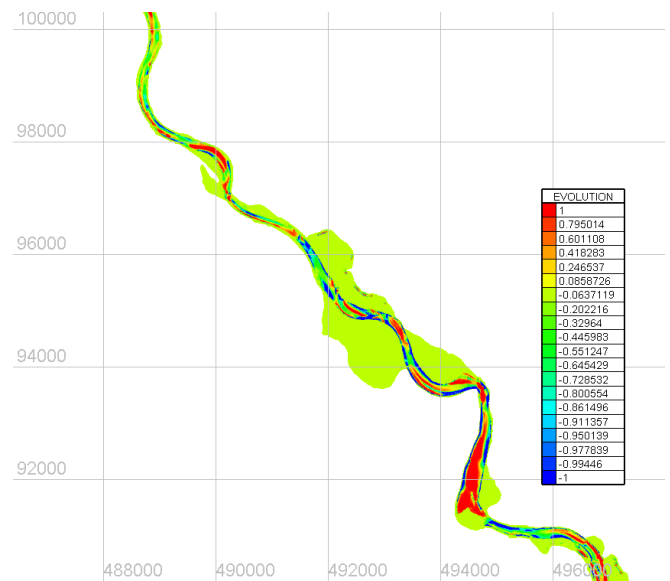


Figure 13. Major changes on the upper part after 365 days.

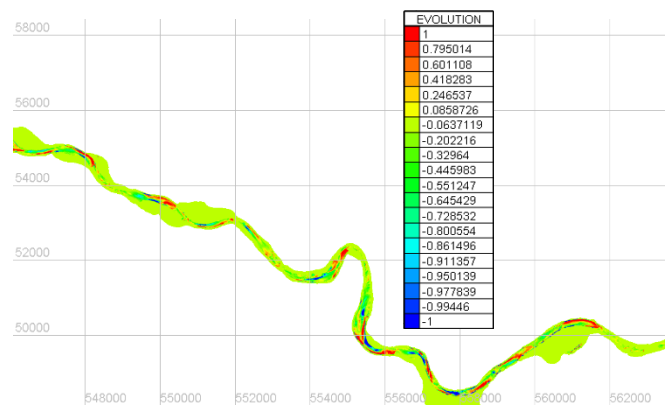


Figure 14. Minor changes on the lower part after 365 days.

### C. Local simulations

Local simulations were also carried out at selected river reaches to analyse local tendencies in greater details. Such a simulation was the modelling of a flood plain channel at Heresznye in its natural and planned status (Fig. 15-16.). The planned measures included the widening and deepening of the channel to return it to its former role during floods. The flood plain channel is flooded at discharges above 700 m<sup>3</sup>/s in its



natural state and after the measures this threshold is lowered to 100 m<sup>3</sup>/s.

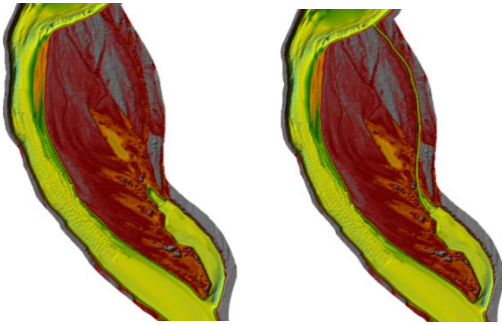


Figure 15. Natural and planned state of the flood plain channel.



Figure 16. Natural and planned cross-profile of the flood plain channel (the cell size of the calculation grid was 1 meter).

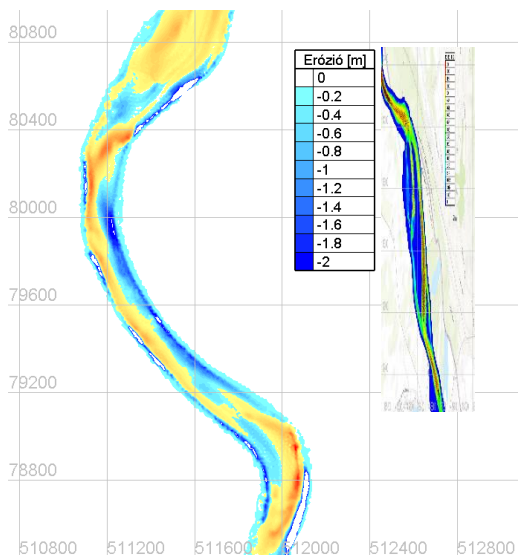


Figure 17. River bed evolution after 365 days at 363 m<sup>3</sup>/s.

The previous simulations also included this site so bed evolution results were available on the 10 meter based TIN for 363 m<sup>3</sup>/s discharge shown on Fig. 17. These low-flow results indicate slight deposition along the main channel and erosion along the convex bend.

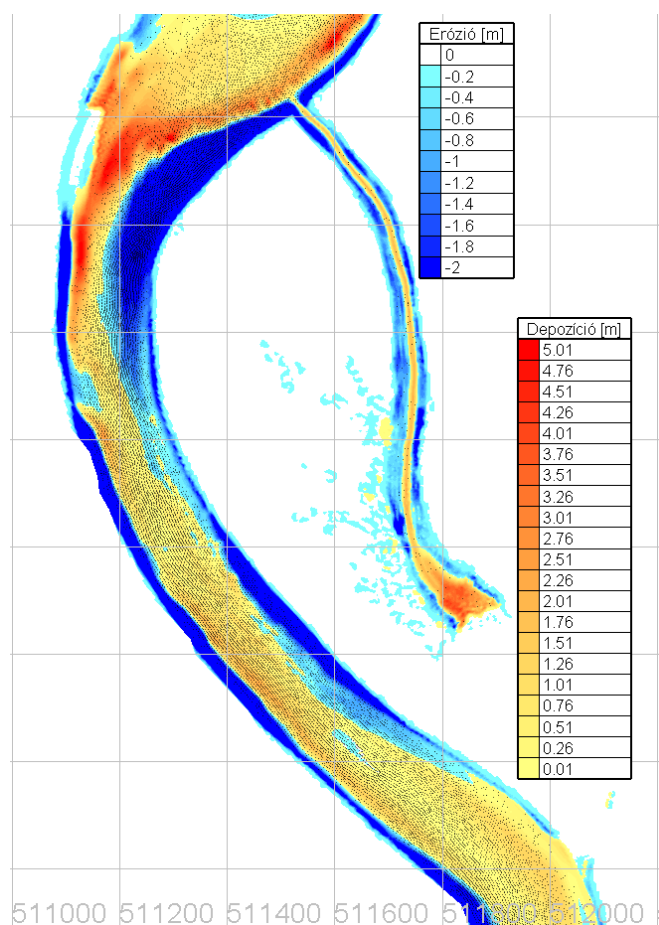
Two dimensional HEC-RAS simulations were done on a 1x1 m cell-sized grid to estimate inflow discharges at different flow conditions. Results are shown in the table below:

INFLOW AT DIFFERENT FLOW REGIMES

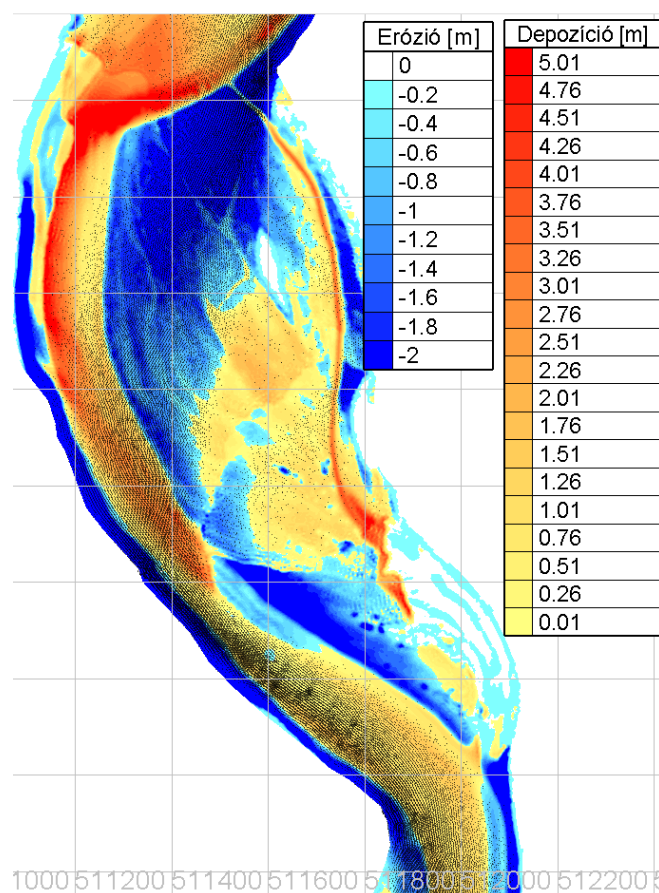
<i>Discharge in Drava [m<sup>3</sup>/s]</i>	<i>Inflow to flood plain channel [m<sup>3</sup>/s]</i>
100	0.8
200	4
400	15
800	42
1000	60
1500	120

As the simulation used the diffusion wave approximation validation runs were done with fully-dynamic setup as well. These indicated that inflow discharges are slightly (~10%) overestimated due to higher velocities in the model. Finally two of the above listed situations were selected for morphodynamic simulation.

One of variants was to simulate 800 m<sup>3</sup>/s on the Drava River for 550 days based on the planned state of the flood plain channel (Fig. 18.). This discharge is 153% of the average annual discharge of the past 10 years, so a relatively high value lower than any of the maximum discharges in these years. The main river bed presented erosion on the convex bend and deposition of sediment on the concave bend. The flood plain channel however suffered much more dramatic changes. The cross-section has broadened and filled up intensively, resulting in heavy sediment load arriving to the lower part of the channel. High bed-shear stress values (~10 N/m<sup>2</sup>) are present initially but they gradually decreased to 5 N/m<sup>2</sup> after 10 days. These values represent a drag force capable of moving coarse pebbles ( $d < 32$  mm) while coarser gravels and artificial surfaces withstand it easily.

Figure 18. River bed evolution after 550 days at 800m<sup>3</sup>/s.

The second simulation was done at 1500 m<sup>3</sup>/s which is well representing the high-flow conditions, it was surpassed 3 times in the past 10 years. The simulation lasted for 180 days but it is important to note that such high discharges only occur during floods and usually last for a few days. It means that the tendencies may be right but the magnitudes are overestimated at the end of the simulation. While analysing the results (Fig. 19.) we see as the water straightens its flow path by eroding the island between the main and flood plain channels. The inflow area of the flood plain channel is also heavily affected and an even greater sediment load is washed downstream along the channel. At the end of the simulation the geometry of the flood plain channel almost returned to its current natural status.

Figure 19. River bed evolution after 180 days at 1500m<sup>3</sup>/s.

#### IV. DISCUSSION

Several model variants were run during the current study and all showed acceptable numerical performance both in speed and stability. Sediment transport models generally started with increased transport rates and converged to the measured magnitudes after the first few days depending on the temporal ratio between the hydrodynamic and morphodynamic models. After these initial run-up periods all results fell in the range measured and previously published values of this reach of the Drava River.

The cohesive models were not successful due to the significant interaction of the sediment classes and river bed armouring. The proper approach in case of Drava River would be the modelling of mixed sediment with several classes in both the non-cohesive and the cohesive size range.

The local study on a fine TIN of 5 meters gave valuable results regarding the intervention to a naturally stable status of the Heresznye flood plain channel. The simulated variants showed heavy deformation of the artificial cross-section taking into account only locally available bed material. Simulated bed-shear stress values highlighted the need for coarser bed cover.



## ACKNOWLEDGEMENT

This research was funded by the Higher Education Institutional Excellence Program of Ministry of Human Capacities (Hungary), grant number “20765-3/2018/FEKUTSTRAT” at University of Pécs; and the Hungarian Scientific Research Fund (project GINOP-2.3.2-15-2016-00055).

The authors are grateful to the South-Transdanubian Water Management Directorate for providing various datasets (LiDAR, orthoimagery, geometry of artificial objects) and their devoted assistance during the measurement campaigns.

## REFERENCES

- [1] Bonacci, Ognjen & Oskoruš, Dijana. (2010): The changes in the lower Drava River water level, discharge and suspended sediment regime. *Environmental Earth Sciences*. 59. 1661-1670. 10.1007/s12665-009-0148-8.
- [2] Cikojević, A., Gilja, G., Baranya, S., Kuspilić, N., and Pomázi, F. (2020): Sediment transport modelling of the Drava River confluence, EGU General Assembly 2020, Online, 4–8 May 2020, EGU2020-3873, <https://doi.org/10.5194/egusphere-egu2020-3873>
- [3] Halmi, Á.; Gradwohl–Valkay, A.; Czigány, S.; Ficsor, J.; Liptay, Z.Á.; Kiss, K.; Lóczy, D.; Pirkhoff, E. (2020): Applicability of a Recreational-Grade Interferometric Sonar for the Bathymetric Survey and Monitoring of the Drava River. *ISPRS Int. J. Geo-Inf.* 2020, 9, 149.
- [4] Kiss, T., András, G. (2015): Kanyarulatfejlődés sajátosságai és antropogén hatások vizsgálata két drávai kanyarulat példáján. *Tájékológiai Lapok* 13 (1): 73-88.
- [5] Szekeres J. (2003): A Dráva hordalékjárásának vizsgálata a legfrissebb adatok figyelembevételével, Összefoglaló jelentés, Budapest, VITUKI
- [6] Tamás, Enikő Anna. (2019). Sediment Transport of the Drava River: *Environmental Problems and Solutions*. 10.1007/978-3-319-92816-6\_7.
- [7] Wilcock, P. & Crowe, C., J. (2003): Surface-based Transport Model for Mixed-Size Sediment. *Journal of Hydraulic Engineering-asce - J HYDRAUL ENG-ASCE*. 129. 10.1061/(ASCE)0733-9429(2003)129:2(120).
- [8] Zhu, S., Bonacci, O. i Oskoruš, D. (2019): Assessing sediment regime alteration of the lower drava river. *Electronic Journal of the Faculty of Civil Engineering Osijek-e-GFOS*, 10 (19), 1-12. <https://doi.org/10.13167/2019.19>.

# Simulation of natural levee laboratory experiments with TELEMAC-2D/SISYPHE

Rebekka Kopmann  
Hydraulic Engineering in Inland Waterways  
Bundesanstalt für Wasserbau (BAW)  
Karlsruhe, Germany  
Rebekka.kopmann@baw.de

Niklas Sokol, Till Branß, Jochen Aberle  
Leichtweiß-Institut für Wasserbau  
Technische Universität Braunschweig  
Braunschweig, Germany

**Abstract**—Natural levees are wedge-shaped sediment deposits which are formed along the banks of alluvial channels. They define a longitudinal borderline between the main channel and the floodplain and impact the interaction of the flow between the main channel and floodplains. They are hence of importance for river management, e.g. in terms of flood protection, overbank sedimentation, and transport of pollutants. The processes involved in levee formation were investigated in flume experiments performed by the Leichtweiß-Institut für Wasserbau (LWI) within the BMBF-project “In\_StröHmunG”. In the framework of a Master thesis conducted at the LWI in cooperation with the BAW, data of these experiments were used to investigate the capabilities of the TELEMAC-MASCARET system to simulate the evolution of these morphological features. In particular, the aim of the master thesis was to figure out which processes can be reproduced with a depth-averaged model and which parameters are significant to reproduce levee formation. A total of six experiments with different sediment transport rates and configurations of vegetation on the floodplain were simulated with TELEMAC-2D/SISYPHE considering both suspended and bed load sediment transport. Numerical results showed that levee masses could be successfully calibrated and validated. The simulated levee geometry had the typical shape characteristics, but the deposition locations differed from those observed in the physical model. This preliminary investigation showed that depth-averaged models are able to capture the main levee formation processes.

## I. INTRODUCTION

Flood events can lead to considerable sediment deposits on the floodplains and form so-called natural levees. Natural levees define a longitudinal borderline between the main channel and the floodplain and are hence impacting the interaction of the flow between the main channel and floodplains. Such interactions are important for river management, e.g. in terms of flood protection, overbank sedimentation, and transport of pollutants. The processes governing natural levee formation are of ongoing research. Therefore, flume experiments were carried out in the framework of the BMBF-project at LWI laboratories in Braunschweig (Germany) to get insight into the formation of natural levees [1].

According to [2] the formation of natural levees can be related to two different lateral sediment transport mechanisms, through which suspended sediment from the main channel is conveyed onto the adjacent floodplains. Fig. 1 compares both

concepts: a) transport of sediments to the floodplains induced by a shear layer between the channel parts due to different flow velocities, and b) advective transport resulting from water level differences between the main channel and the floodplains.

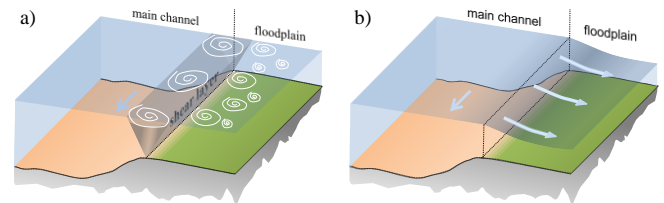


Figure 1: Turbulence induced sediment transport (a), advective sediment transport (b). (according to [2])

The laboratory experiments focused on the turbulence induced transport mechanism which is influenced by the shear layer between the main channel and the floodplain. This shear layer leads to a rapid decrease of turbulence over the floodplain. As a consequence, sediment cannot longer remain in suspension and deposits at the floodplain edge so that natural levees are formed exhibiting a steep slope towards the main channel and a milder slope towards the floodplains [2].

Natural levee formation can also be observed on Federal waterways and is therefore of interest for the Bundesanstalt für Wasserbau BAW. First investigations about modelling of natural levees were carried out in the framework of a master thesis [3] and are presented in this paper. The laboratory experiments were simulated with TELEMAC-2D and SISYPHE ([www.opentelemac.org](http://www.opentelemac.org)). The aim of the master thesis was to investigate which processes can be simulated with a depth averaged model (TELEMAC-2D coupled with SISYPHE) and which parameters are most sensitive.

## II. Laboratory experiments

The laboratory experiments were conducted in a 2 m wide and 30 m long, sediment recirculating tilting flume in the hydraulic laboratory at LWI. A 20 m long section of a half trapezoidal compound channel was built in the flume starting at a distance of 4 m from the flume inlet (Fig. 1). The section had a 10 cm high floodplain with a width of 130 cm and a channel bed width of 60 cm connected to the floodplain via a 1:1 sloped bank. Artificial grass mats of 3 cm height were used to simulate roughness on both the bank and the floodplain. The

main channel bed was built from film faced plywood plates with a single layer of fixed polystyrene granulate grains as roughness ( $d_{50} = 2.06$  mm). The granulate was also used as surrogate sediment in the experiments to accelerate morphodynamical development. The polystyrene grains were of cylindrical shape and had a solid density of  $\rho_s = 1058$  kg/m<sup>3</sup>. The sediment was recirculated using the sediment recirculation circuit of the flume.

Data of six experimental runs were utilised for the numerical simulations. The experiments were conducted in two experimental series, hereafter referred to with the same names as used in [1]. All experiments were carried out with a discharge of 32 l/s, a water stage of 16 cm in the main channel, a constant bed slope of  $S = 0.0005$ , quasi uniform flow conditions and over a period of 19.5 h. Sediment transport rates were controlled by the amount of sediment in the flume and monitored via calibrated turbidity meters installed in the recirculation circuit. It is important to note that sediment was mainly transported in suspension, i.e. no bedforms were

developed. After each experiment the final levee configuration was documented. The material forming the levee deposits was collected in 60 cm long sections over the measurement section and weighted to determine the mass of deposited sediment. Further details of the model setup and experimental program can be found in [1].

Experiments of the “T-series” used herein were initially designed to investigate the impact of bedforms on levee formation but also featured two experiments without bedforms as reference used in this study. Experiments of the “MB-series” used herein focused on the effect of additional emergent vegetation simulated by a 12 cm wide strip of rigid cylinders with a diameter of 3 mm arranged in staggered arrays with a spacing of 2 x 2 cm, placed along the floodplain edge. This strip of vegetation was investigated in a continuous and in an intermitted configuration. For the latter the vegetation strip was reduced to vegetation patches of 120 cm length separated by gaps of 180 cm length in between. Fig. 2 gives an overview of the model setup and geometry.

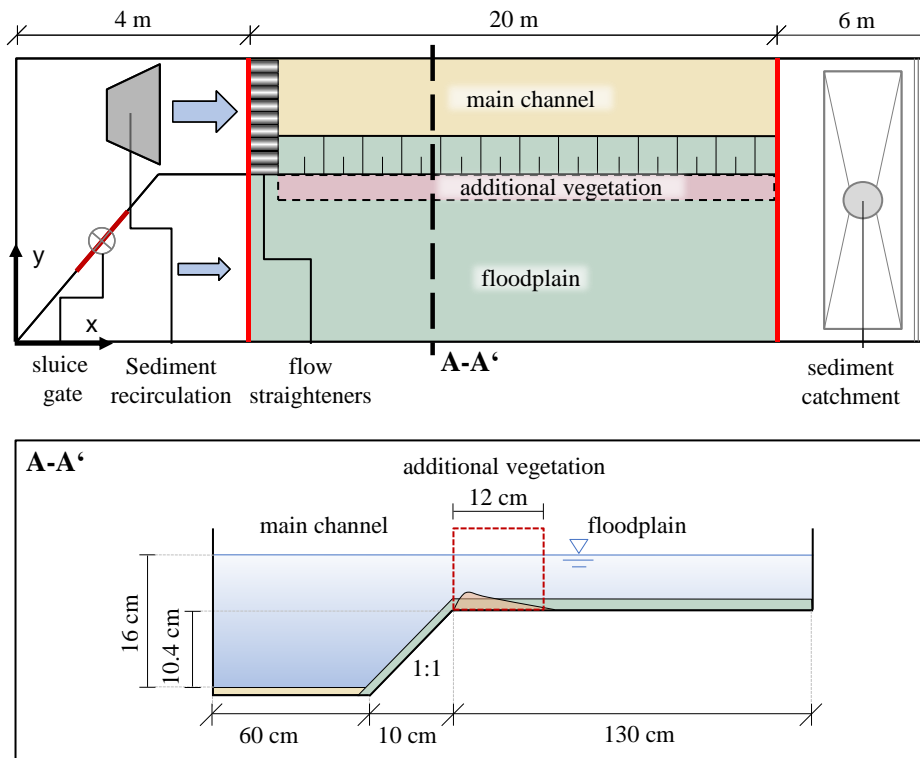


Figure 2: Top view and cross section of the flume model ([1]).

### III. NUMERICAL SIMULATIONS

For the numerical simulations the modules TELEMAC-2D and SISYPHE were chosen. The aim was to investigate which processes of the natural levee formation can be simulated with a depth averaged model as well as to investigate the limitations of the approach.

Initially, the hydrodynamic simulation was performed with the BAW's standard steering-file configuration, which includes the N-type MURD advection scheme, Nikuradse roughness law and as turbulence model either the horizontal mixing length model or k- $\epsilon$  model [4]. This parameterization was later enriched with the Baptist's roughness law to account for vegetation-induced friction [5].

The model domain was discretised with a fine unstructured finite element mesh with typical size of approx. 3 cm, resulting in 57412 nodes and 112564 elements (Fig. 3). Due to instabilities at the start of the simulation period, a very small time step of 0.05 s was set for some configurations which led to Courant numbers of approx. 0.5 in the main channel.

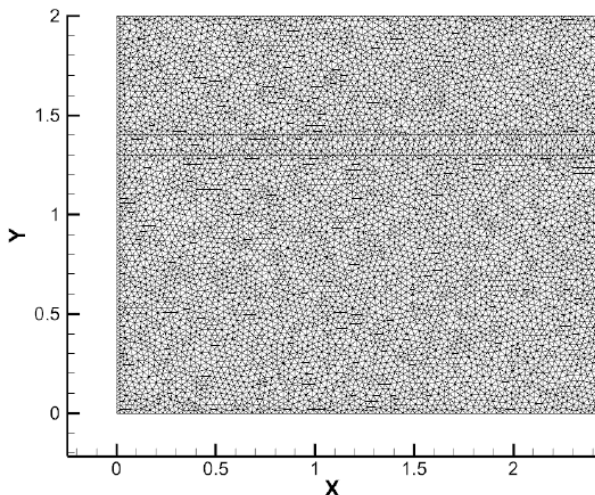


Figure 3: Mesh detail at the inlet. (from [3] page 19)

#### A. Hydraulic calibration

The hydraulic calibration was performed by comparing the model results with velocity measurements conducted in laboratory experiments without sediments. Uniform flow conditions were reached by the boundary conditions shown in Fig. 4. During the calibration process the roughness parameters for the two roughness zones (main channel and floodplain) and the turbulence model were selected.

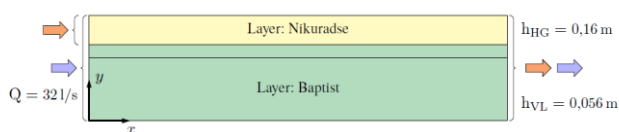


Figure 4: Boundary conditions and roughness layers for the hydraulic calibration. (from [3] page 20)

For the glass walls of the flume the Nikuradse roughness was set to 1 mm. At the floodplains the vegetation formulation from Baptist [5] is used as the grass height is about half of the water depth. The bottom roughness was chosen to 5 mm, the vegetation height to 2.5 cm and the vegetation diameter to 0.8 mm. The roughness coefficient in the main channel was calibrated to 6.18 mm which equals 3 times the median grain diameter. In order to ensure a proper velocity distribution at the inlet the velocity distribution was taken from the outlet for a fully developed flow.

Fig. 5 shows the comparison of the measured and simulated depth averaged velocities. At the floodplains the velocity could only be measured above the artificial grass which means that values in between the grass blades are missing. The velocity profile inside the blades of grass is assumed to decrease linear to zero. Nevertheless, the values at the floodplains are not as reliable as in the main channel.

Using the original k- $\epsilon$  model the roughness coefficients at the main channel needed to be increased to  $k_s = 5 \cdot d_{50} = 10.3$  mm. If the turbulence is mainly caused by bottom roughness and not by geometry structures, experiences at BAW indicate that the k- $\epsilon$  model produces lack of turbulent viscosity. Adding additional turbulent viscosity of  $10^{-3} \text{ m}^2/\text{s}$  to the calculated values from the k- $\epsilon$  model the new values are in the same order like the turbulent viscosities from the horizontal mixing length model. With this, the smaller roughness coefficient ( $k_s = 3 \cdot d_{50}$ ) can be used. The steep velocity gradients in the shear zone were better captured by the original k- $\epsilon$  model than by the horizontal mixing length model or the modified k- $\epsilon$  model. But as shown in Fig. 5 the overall agreement of all models is very similar. The modified k- $\epsilon$  model was chosen for further use because the roughness coefficients in the main channel were in a better agreement with roughness prediction formulas and the more complex turbulence model promised a better representation of the turbulent flow.

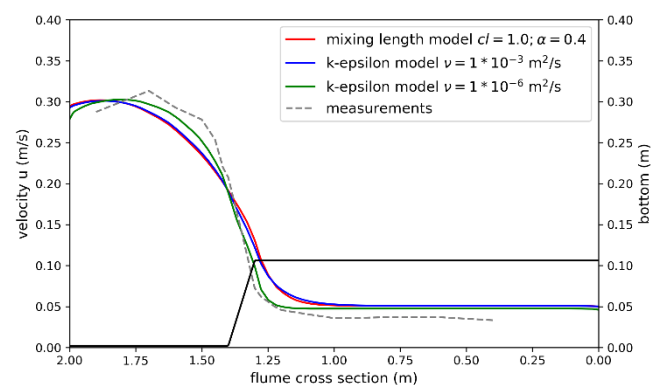


Figure 5: Comparison of measured and simulated time and depth averaged velocity along the cross section at 15m.

#### B. Morphodynamic configuration

As there was no experience in modelling natural levee formation the general configuration and the numerical parameters needed to be investigated. First it had to be decided

whether bedload and/or suspended load should be considered. In literature the initiation of suspension is assumed if the ratio of the critical bed-shear velocity  $u_{cr}^*$  and the settling velocity  $w_s$  equals 0.25 (Engelund), 0.4 (van Rijn) or 1.0 (Bagnold) [6]. According to this the sediments in the flume experiments should be in suspension for shear velocities above 0.0075 ... 0.031 m/s. The bed-shear velocity in the main channel  $u^* = \sqrt{\frac{\rho g h_{HG} I}{\rho}}$  can be calculated from the water depth  $h_{HG}$  and the bed slope  $I$  to 0.028 m/s. As the value is nearly at the top of the range for initiation of suspension it is most likely that most of the material in the main channel will be transported in suspension.

Deposits at the floodplains only occur if sediment was transported as suspended load. Thus, the calibration of the levee masses could only be done with parameters of the suspended load. Without bedload the sediments tended to aggregate in the main channel. Therefore, the combination of bedload and suspended load worked best. For the bed load transport Meyer-Peter & Müller bed load formula with MPM factor of 3 is used.

Defining the sediment boundary condition was not trivial. According to the laboratory model the sediment transport concentration was uniformly imposed at the main channel. In the model this boundary condition led to sediment aggregation over time at the inlet. Therefore, a concentration distribution along the inlet was calculated from the equilibrium concentration. With this procedure no deposition occurred in close proximity to the inlet.

Another challenge was that the vegetation height on the floodplain could not assumed to be constant over time due to high sediment deposition in the artificial grass (see Fig. 6). This was solved by a modification that corrected the vegetation height used in the vegetation formulation by the height of the deposited sediments.

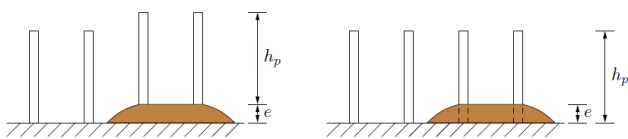


Figure 6: Vegetation height ( $h_p$ ) without (left) and with (right) adaption to sediment aggregation( $e$ ). (from [3] page 35)

### C. Morphodynamic calibration

For the morphodynamic calibration the laboratory experiment T4 was chosen. The boundary conditions (water ( $Q$ ) and sediment discharge ( $Q_{sed}$ ) and water depth at the main channel ( $h_{HG}$ ) and the deposited levee mass ( $m_{levee}$ ) are summarised in table 1. The calibration was only done with the levee mass, whereas the width and position of the levees were compared afterwards.

TABLE 1: MEASUREMENT DATA FOR LABORATORY EXPERIMENTS T4 AND T5

	Q (l/s)	$h_{HG}$ (m)	$\Delta t$ (h)	$Q_{sed}$ (m <sup>3</sup> /s)	$m_{levee}$ (g/m)
T4	32	0,16	19.5	$2.38185 \cdot 10^{-5}$ = 42 g/(sm)	56.4
T5	32	0,16	19.5	$3.10208 \cdot 10^{-5}$ = 54.7 g/(sm)	117.1

The settling velocity, the porosity and the density, were set to the values of the sediment used in the flume experiments (respectively equal to  $w_s=0.031$  m/s,  $p=0.379$ ,  $\rho_s=1058$  kg/m<sup>3</sup>). The critical Shields parameter  $\Theta_c$  and the reference height  $z_{ref}$  were calculated according to the formulas from van Rijn [6,7] using the dimensionless grain diameter  $D^*=15$ , the water depth  $h$  and the equivalent roughness coefficient  $ks$ .

$$\Theta_c = 0.04 D_*^{-0.1} = 0.04 15^{-0.1} = 0.0305 \quad (1)$$

$$z_{ref} = 0.01 h < 0.5 ks < 0.2 h = 3.09 \text{ mm} \quad (2)$$

After all other parameters were determined from measurements, the only calibration parameter left was the sediment dispersion. In SISYPHE three calculation options are available to account for dispersion: setting a constant value, using the turbulent viscosity calculated by the turbulence model of the hydrodynamics or using the Elder approach. Setting a constant value was not investigated as it seems too simple. Using the turbulent viscosity values from the hydrodynamic calculation resulted in very low natural levee masses. For the Elder approach [4] two parameters can be calibrated which define the longitudinal  $\alpha_l$  and transversal  $\alpha_t$  dispersion together with the friction velocity  $u_*$  and the water depth  $h$ .

$$\epsilon_t = \begin{cases} \alpha_l u_* h \\ \alpha_t u_* h \end{cases} \quad (3)$$

Elder determined the longitudinal parameter to 6 and the transversal to 0.23, but with this parameter combination levee masses were largely overestimated. With a much smaller transversal parameter of 0.06 the levee masses were in perfect agreement to the measurements. The longitudinal parameter had nearly no influence on the resulting masses as the lateral sediment transport to the floodplains is decisive.

The validation was done with a similar laboratory experiment T5, which featured a 30% higher sediment concentration than in T4 (see Table 1). With the same parameter configuration, the computed levee masses ( $m_{levee}=95.9$  g/m) were underestimated by 18%.

In the flume experiment the masses were determined in the 6 m long evaluation section in order to avoid influences from the inlet and outlet. The behaviour at the inlet and outlet was not comparable between flume experiment and numerical model. For the hydrodynamics of the numerical model the boundary conditions were chosen in such a way that the flow conditions did not vary significantly with flume length. The



inlet boundary condition for the suspended sediment was also defined with the help of the equilibrium concentration which also minimised the influence of the inlet. Therefore, levee masses were computed over the whole domain. In Fig. 7 the distributions of the simulated levee masses along the flume are presented. It can be seen that the levee masses decreased over the flume length. This trend was in general also observed in the laboratory model (see Fig. 9) despite this cannot be shown with T4 and T5 as in these experiments only a mean value for levee mass was measured. The evaluation section of the laboratory model was located nearer to the outlet than to the inlet which would lead to smaller masses. This must be due to the different evaluation procedures the numerical model underpredicts the masses per flume length.

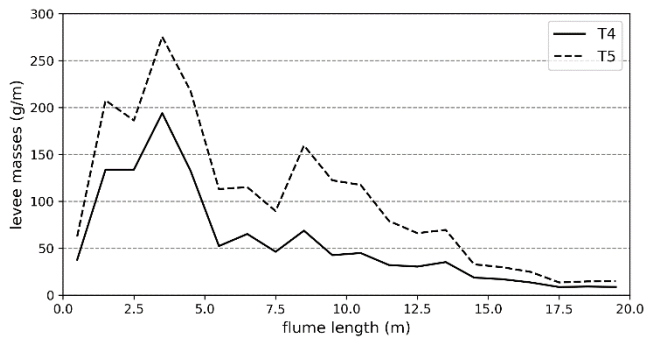


Figure 7: Development of levee masses along the flume for T4 and T5.

The evaluation of the simulated levee geometries was performed between the flume section 10 to 15 m. Fig. 8 presents the simulated levee cross sections for T4 and T5. In general, the typical geometry of natural levees with a steep slope towards the main channel and a slowly descend towards the floodplain can be observed. Along the flume length the height of the levees decreased, whereas the width was more or less constant. Additionally, levees were higher for T5 due to higher sediment input. In the laboratory model only sediment deposits higher than the artificial grass were able to be measured reliable. For that reason, the comparison between laboratory and numerical model for T4 and T5 was limited to levee width, position and mass.

The maximal levee width of about 10 cm is in good agreement to the measured ones (11.1 cm for T4 and 11.7 cm for T5). The position of the simulated levees was 10 cm from the edge of the slope. In the measurements the levees were located directly at the floodplain edge. With a better representation of the shear zone able to capture the 3D flow field, an improvement of the solution would be expected.

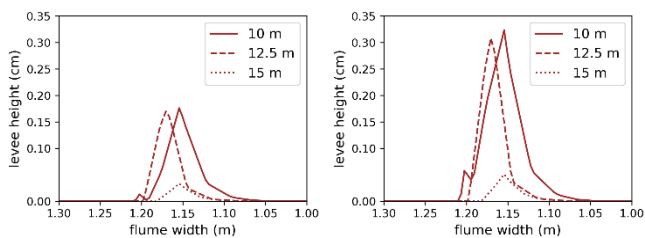


Figure 8: Form and width of simulated levees for T4 (left) and T5 (right).

The simulated masses increased over time and asymptotically approached a maximum value, which, however, was not reached even after 19.5 hours. This behaviour has been observed in similar experiments performed in the laboratory model.

#### D. Sensitivity to sediment parameters

The sensitivity of the settling velocity  $w_s$  and the critical Shields parameter  $\Theta_c$  to the calculation of the natural levee masses were investigated. Because the settling velocity is precisely known from measurements it should therefore not be modified during the calibration process. Nevertheless, it is important to understand its influence to the natural levee formation.

Table 2 shows the parameter values, their investigated ranges and their influence on the levee masses. Lower settling velocities but higher critical Shields values produce increasing levee masses. Both parameters have a considerable impact to the levee masses although even for small parameter value changes. In the last table row a scaled sensitivity  $S$  is calculated with the mass change  $\Delta m$  divided by the parameter change  $\Delta w_s$  resp.  $\Delta \Theta_c$  and multiplied by the calibrated parameter  $w_s$  resp.  $\Theta_c$ .

$$S = \frac{\Delta m}{\Delta w_s} w_s \quad (4)$$

TABLE 2: SENSITIVITY DUE TO  $w_s$  AND  $\Theta_c$

	$w_s$ (m/s)	$\Theta_c$
calibrated value	0.031	0.0305
investigated range	0.028 – 0.033	0.02 – 0.04
difference to reference value	-0.003 / +0.002	-0.0105 / +0.0095
mass change $\Delta m$ (g/m)	+42.2 / -18.1	-48.3 / +101.7
scaled sensitivity $S$ (g/m)	+654.1 / -187	-140.3 / +326.5

With the scaled sensitivity the influence of both parameters to the levee masses can be compared. All values are in the same range which means that both parameters have approximately the same influence. The largest value was reached for the decreased settling velocity value.

#### E. Experiments with medium vegetation

Four further experiments were simulated which investigated the influence of additional vegetation strips on levee formation. Two experiments (MB10, MB11) featured continuous vegetation strips while the vegetation strip was intermitted in the other two experiments (MB23, MB25).

In Table 3 the boundary conditions and the resulting levee masses of the laboratory experiments featuring additional vegetation are summarised.

TABLE 3: MEASUREMENT DATA FOR THE VEGETATION LABORATORY EXPERIMENTS

	Q (l/s)	$h_{HG}$ (m)	$\Delta t$ (h)	$Q_{sed}$ (m <sup>3</sup> /s)	$m_{levee}$ (g/m)
MB10 continuous vegetation	32	0,16	19.5	$1.9905 \cdot 10^{-5}$ =35.1 g/(sm)	54.6
MB11 continuous vegetation	32	0,16	19.5	$2.4953 \cdot 10^{-5}$ = 44 g/(sm)	110.2
MB23 intermittent vegetation	32	0,16	19.5	$3.10208 \cdot 10^{-5}$ =54.7 g/(sm)	117.1
MB25 intermittent vegetation	32	0,16	19.5	$2.38185 \cdot 10^{-5}$ =42 g/(sm)	56.4

Simulation results of the levee masses along the flume at the end of the experiment are compared to the measurements in Fig. 9 and Fig. 10. For the continuous vegetation the simulated levee masses fit well to the measurements. But the behaviour at the inlet is completely different between the laboratory model and the numerical model. It seems that after approx. 10 m flume length the differences due to the inlet can be neglected.

For the intermittent vegetation the development of the levee masses along the flume exhibit a pulsating behaviour. Obviously, the numerical model reacted to the vegetation sections with increasing levee formation. The higher roughness due to the vegetation roughness immediately decreased the velocity and thus led to sediment deposition.

For the laboratory model it is the other way around. The levee masses are higher in the sections without vegetation. This can be related to gradually decreasing flow velocities in the particular vegetated sections where the minimum velocity was reached at the downstream end. As a consequence, the vegetated sections sheltered parts of the downstream unvegetated gaps, too, and thus more sediment deposited in these sections. Probably only a three-dimensional model is able to reproduce the complex flow situation due to this intermittent vegetation.

Comparing Fig. 9 and 10 it can be seen that with intermittent vegetation the levee masses are decreased. Experiment MB11 and MB25 had approximately the same sediment input. The levee mass measured in MB25 (intermittent vegetation) was only the half of the mass measured in MB11 (continuous vegetation). In the numerical

model the levee mass was stronger reduced due to intermittent vegetation to approx. 40%.

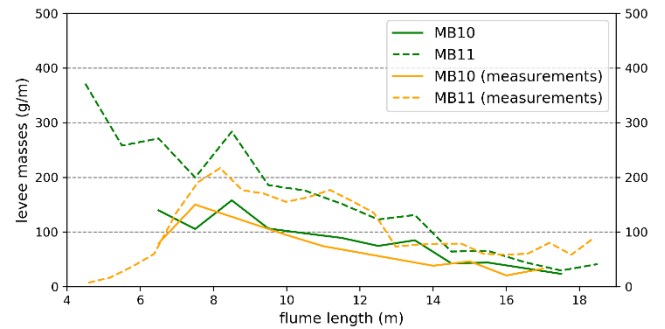


Figure 9: Comparison of the development of levee masses along the flume for the continuous vegetation experiments.

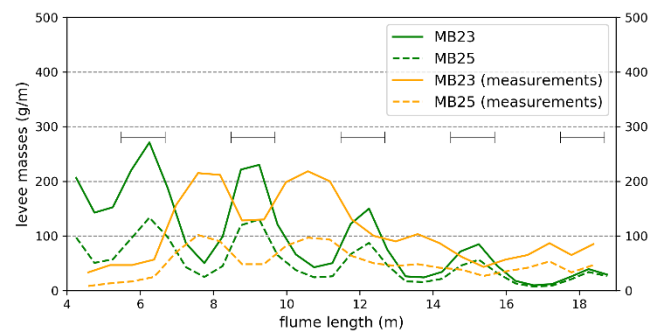


Figure 10: Comparison of the development of levee masses along the flume for the intermittent vegetation experiments.

#### IV. CONCLUSIONS

The numerical simulation of natural levee formation laboratory experiments with TELEMAT-2D and SISYPHE showed promising results. By calibrating only the sediment dispersion parameter, the levee masses could be simulated in a good agreement to the measurements. The simulated levee geometry showed a typical steep slope towards the main channel and a slowly descent towards the floodplains, whereas the position of the levees was shifted onto the floodplain. This difference can be related to the artificial grass used in the laboratory model which behaved like a sediment trap and explains the earlier deposition of the sediments. However, the maximal width of the simulated levees was comparable with the measured ones.

The numerical simulation of the physical experiments accounting for vegetation showed good results as long as the vegetation was continuously arranged. For intermittent vegetation the flow and transport processes were too complex to be captured with a depth-averaged model. Nevertheless, the general behaviour of pulsating levee masses along the flume was simulated satisfactorily.

Further investigations are planned with TELEMAT-3D coupled to SISYPHE (or the brand-new sediment transport module GAIA). This should allow a better reproduction of the shear zone and consequently a more precise capture of earlier sediment deposition processes.

## REFERENCES

- [1] T. Branß, J. Aberle and A. Dittrich. „In StröHmunG (Innovative Systemlösungen für ein transdisziplinäres und regionales ökologisches Hochwasserrisikomanagement und naturnahe Gewässerentwicklung) - Teilprojekt: Modellversuche zur Rehenbildung“, Bericht Nr. 1088, Leichtweiß-Institut für Wasserbau Technische Universität Braunschweig, 2018.
- [2] P.N. Adams, R.L. Slingerland and N.D. Smith, “Variations in natural levee morphology in anastomosed channel flood plain complexes”, *Geomorphology* 61(1-2), 127-142, doi: 10.1016/j.geomorph.2003.10.005, 2004.
- [3] N. Sokol, “Numerische Modellierung von Laborversuchen zur Rehenbildung”, Master thesis at Leichtweiß-Institut für Wasserbau Technische Universität Braunschweig, 2020.
- [4] TELEMAT-MASCARET consortium, „User manual telemat2d Version V8P1“, [http://wiki.opentelemat.org/doku.php?id=documentation\\_v8p1r1](http://wiki.opentelemat.org/doku.php?id=documentation_v8p1r1)
- [5] M.J. Baptist, V. Babovic, J. Rodríguez Uthurburu, M. Keijzer, R.E. Uittenbogaard, A. Mynett, A. Verwey, “On Inducing Equations for Vegetation Resistance”, *Journal of Hydraulic Research*, 45(4), 435-450. 2007.
- [6] L.C. van Rijn, “Sediment transport - Part II: suspended load transport. *Journal of Hydraulic Engineering*, 110 (11), 1613-1641, 1984.
- [7] L.C. van Rijn, “Principles of sediment transport in rivers, estuaries and coastal seas”, (Bd. 1006), Aqua publications Amsterdam, 1993.

# Modelling scour around submerged objects with TELEMAC3D - GAIA

Irinios Yiannoukos  
School of Ocean Sciences  
Bangor University  
Bangor, UK  
[i.yiannoukos@bangor.ac.uk](mailto:i.yiannoukos@bangor.ac.uk)

Katrien Van Landeghem; Michael Roberts; Barney Smyth; Jacob Morgan  
Bangor University, Bangor, UK  
Amelia Couldrey; Thomas Benson; Richard Whitehouse; Connor McCarron  
HR Wallingford, Wallingford, UK  
Rory Quinn  
Ulster University, Coleraine, UK

**Abstract**— The ever-increasing need for seabed infrastructure enabling offshore centralised storage and renewable energy extraction requires accurate predictions of erosion and deposition of surrounding seafloor sediments. As offshore surveys are prohibitively expensive and time-consuming, improved flow simulations around seabed objects are preferred. In this study, a coupled TELEMAC3D-GAIA model is developed to help understand the interaction of the enhanced diverted flow around a submerged cylinder with the surrounding bed in a controlled laboratory environment. The present study focuses mainly at the shape of the object in the computation domain. The performance of TELEMAC3D-GAIA for simulating scour in the wake of the object is assessed in terms of the accuracy of the hydrodynamic simulation and the morphodynamics of the bed evolution. Preliminary results from the simulations show a potential of using TELEMAC3D-GAIA to simulate the flow and bed dynamics around submerged objects.

## I. INTRODUCTION

The introduction of an object to the seabed changes the flow regime around the object's immediate environs, leading to flow contraction. Horseshoe vortices form immediately around the structure and lee-wake vortices form further away (Figure 1). This enhanced flow increases the forces on the bed by a factor of four (Quinn and Smyth, 2018), causing erosion of sediment (scour) from the bed near the object which is transported and deposited further downstream.

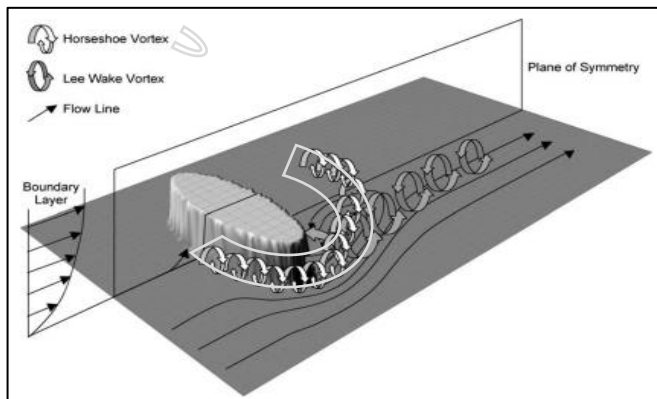


Figure 1: Schematic of vortex development and flow patterns around a submerged wreck site (modified from Quinn, 2006).

The scour and deposition of seabed sediment can have implications for species compositions between hard and soft substrata (McArthur et al., 2010). The ability to predict the associated seabed dynamics is therefore of importance for seabed management. Seabed dynamics around submerged objects are currently difficult to model accurately when the bed is mixed and coarse (e.g. sand and gravel), both due to uncertainties in flow dynamics and sediment transport. The orientation of the object to the flow is an important parameter defining the extend and shape of the scour marks (Coston, 1979; Saunders, 2005; Quinn, 2006; Quinn et al., 2016).

To investigate bed dynamics around a submerged object, a laboratory experiment was conducted using a 10m long by 30 cm wide Armfield recirculating flume tank (Figure 2). A 9.4 cm submerged cylinder with a 4.4 cm diameter was embedded on a sandy bed and a unidirectional flow of  $0.26 \text{ m}\cdot\text{s}^{-1}$  was applied, experimentally tested to mobilise the sand. 3-dimensional bed scans were made using an array of SeaTek 5 MHz ultrasonic transducers (Jette, 2005) at several stages in the experiment.

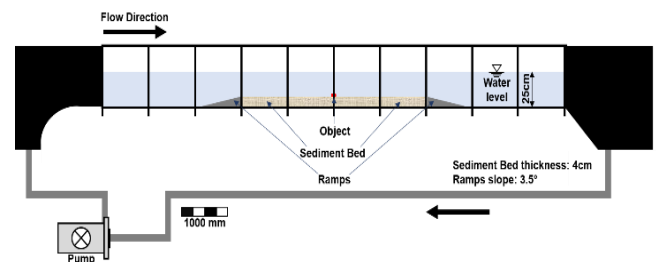


Figure 2: Schematic illustration of the experimental setup

The outputs of the coupled TELEMAC3D-GAIA simulations of the laboratory experiments highlighted the potential for accurate simulation of flow and bed dynamics around submerged objects. A number of numerical difficulties arise, however, when dealing with sediment transport around submerged objects at this scale. These difficulties and the suggested ways to resolve them are presented below through comparisons of model results with the laboratory experiments.

Although ripples were generated upstream and downstream of the object during the experiment, this study focuses solely on modelling the scour formation and depositional features formed in the immediate vicinity of the object.

## II. NUMERICAL MODEL TO SIMULATE FLUME TANK EXPERIMENTS

### A. Hydrodynamic simulations

The discharge,  $Q$ , used in the simulations was calculated using Equation 1:

$$Q = a \times b \times u, \quad (1)$$

where  $a$  and  $b$  are the water depth and flume width respectively, and  $u$  is the depth averaged flow speed measured in the flume tank using a 4MHz MET-FLOW Ultrasonic Doppler Velocimetry Profiler (UDVP).

The reference height,  $z_R$ , of the UDVP transducer above the bed at which the depth-averaged velocity was measured in the flume tank, assuming a logarithmic velocity profile (Ma et al., 2019) was calculated using equation 2:

$$z_R = \frac{h}{e}, \quad (2)$$

where  $h$  is the water height above the bed and  $e$  is the Napier's constant (2.71828...). This depth-averaged velocity was used for the validation of the modelled flow speeds.

A key feature of flow around objects, is the conversion of linear flow to turbulent flow, due to the existence of an obstacle (object) to the flow (Smyth and Quinn, 2014). Thus, the  $k$ - $\varepsilon$  model was used in TELEMAC, as it is the most common model used to simulate mean flow characteristics associated with turbulent flow conditions.

### B. Morphodynamic simulations

The TELEMAC-MASCARET module GAIA was chosen for the simulation of the sediment transport and bed evolution within the domain and around the submerged object. Upgraded from the SISYPHE module, GAIA allows for a better simulation of the sedimentary processes in the water-bottom interface. GAIA can also manage different sediment classes, and several transport models, which is ideal not only for this study, but also for the case of mixed bed dynamics. In GAIA, suspended sediment transport processes are mainly dealt with by the hydrodynamic module (TELEMAC), while the near-bed, stratigraphic and bedload processes are led by GAIA (Audouin et al., 2019).

### C. Governing equations

In this study, TELEMAC3D was used to simulate the impact of a submerged cylinder on the flow. Navier Stokes equations were solved using the Boussinesq approximation for momentum.

The  $k$ - $\varepsilon$  model used to calculate the Turbulent Kinetic Energy (TKE) at the computation domain includes the equation for the TKE- $k$ , by solving the balance equations of turbulence for  $k$  (energy production) and  $\varepsilon$  (energy dissipation) (Goll, 2016).

The TKE- $k$  of the model is calculated using Equation 3:

$$\frac{\partial k}{\partial t} + u \cdot \nabla k = \nabla \left( \nu + \frac{\nu_t}{\sigma_k} \right) \nabla k + P - \varepsilon \quad (3)$$

and the accompanying equation of  $\varepsilon$  is Equation 4:

$$\frac{\partial \varepsilon}{\partial t} + u \cdot \nabla \varepsilon = \nabla \left( \nu + \frac{\nu_t}{\sigma} \right) \nabla \varepsilon + C_{1\varepsilon} \frac{\varepsilon}{k} P - C_{2\varepsilon} \frac{\varepsilon^2}{k} \quad (4)$$

TELEMAC3D coupled with GAIA calculates the bed shear stress,  $\tau_0$ , using the velocity of the first  $\sigma$ -layer above the bed using Equation 5 (Tassi and Villaret, 2014):

$$\tau_0 = \rho \left( \frac{1}{\kappa} \ln \frac{z'}{z_0} \right)^{-2} u(z')^2, \quad (5)$$

where  $\rho$  is the water density  $\kappa$  is the unitless Von Kármán constant (0.41),  $z'$  is the first  $\sigma$  layer height above the bed (m),  $z_0$  is a hypothetical level with 0 velocity (m) and  $u(z')$  is the velocity at the first  $\sigma$ -layer above the bed ( $\text{m} \cdot \text{s}^{-1}$ ).

As previously mentioned, TKE in the model is calculated using the  $k$ - $\varepsilon$  model. The TKE at the first  $\sigma$ -layer above the bed (plane 2), can be included in the calculation of the bed shear stress,  $\tau_0$ , in the form of Equation 6:

$$\tau_0 = \max(\rho u_*^2, \rho r k), \quad (6)$$

where  $u_*$  the friction velocity,  $r$  a proportionality coefficient and  $k$  the TKE.

The use of Equation 6 means that the coupled model uses the standard TELEMAC model shear stress result away from the structure, where closer to the object, it is assumed that the TKE dominates the bed shear stress.

The van Rijn (1984, 2007) equations were used to calculate the suspended load and bed load transport as they are suitable for material in the range of 0.2 – 2 mm. The van Rijn equations are based directly on the bed shear stress for the simulation of the sediment mobilisation, whereas other formulas within the GAIA source code are based on near bed velocities. The bedload transport rate is predicted using (van Rijn, 2007; Equation 7):

$$\Phi_b = 0.053 D_*^{-0.3} \left( \frac{\theta - \theta_{cr}}{\theta_{cr}} \right)^{2.1}, \quad (7)$$

where  $\Phi_b$  is the dimensionless current-induced sediment transport,  $D_*$  the non-dimensional sediment particle diameter and  $\theta$  and  $\theta_{cr}$  the bed shear stress and critical Shields parameter for sediment motion respectively. The equilibrium concentration,  $C_{eq}$  used to calculate the suspended load transport is predicted using (van Rijn, 1984; Equation 8):

$$C_{eq} = 0.015 d_{50} \left( \frac{\theta' / \theta_{cr} - 1}{z_{ref} D_*^{0.3}} \right)^{3/2}, \quad (8)$$

where  $\theta_{cr}$  is the critical Shields parameter and  $\theta' = \mu \theta$  the bed shear stress due to skin friction. The reference height  $z_{ref}$  is related to the total bed roughness,  $k_s$  with  $z_{ref} = 0.5 k_s$ .

Friction was applied on the bed using a Chézy coefficient,  $C$ , which was controlled by applying the Nikuradse formula (Leroy, 2019; Equation 9):



$$C = 7.83 \ln \left( \frac{12h}{k_s} \right), \quad (9)$$

where  $h$  is the water depth and  $k_s$  is the total bed roughness (0.005-0.02). For simulation of non-quasi-horizontal flows, the method above is preferred over other depth-averaged models (Leroy, 2019). The Nikuradse formula was also chosen as it makes it possible for friction to be prescribed based on a logarithmic velocity profile, for a given bed roughness, without any averaging of the velocity on the vertical axis.

#### D. Methods to validate the model

The test case presented here is for pure sand with a median grain size  $d_{50}$ , of 0.259 mm and the simulation time was 2 hours (the same as the laboratory experiment run time). The simulations were conducted assuming one uniform layer of sediment with a thickness of 4 cm. The mesh resolution away from the object was set at 2 cm, increasing to 0.25 cm close to the object. The time step for the runs was set to 0.00625 s. The final bed elevation from the simulation was compared with the final bed elevation of the laboratory experiments.

Depth-averaged flow velocities from the TELEMAC2D simulation were compared with the corresponding measurements from the laboratory experiments (Figure 3). Due to the presence of the UDVP transducer affecting the flow and causing subsequent scour, it was not possible to collect a time series of UDVP measurements during the laboratory experiments without affecting the final result. Therefore, UDVP measurements were collected at the end of the experimental runs. The experimental velocities at 3 locations upstream and 4 locations downstream of the object, provide a mean value of  $317 \text{ mm}\cdot\text{s}^{-1}$  where the mean value of the modelled velocities at the same locations, provide a mean value of  $324 \text{ mm}\cdot\text{s}^{-1}$  (Figure 3a). Therefore, although the model seems to overestimate the flow speed by  $\sim 2\%$ , the discrepancy is within the error margin of the UDVP instrument used for the experimental measurements (0.4-5%). Thus, as the measured flow speeds fall within the instrument's accuracy the modelled depth averaged flow velocities can be trusted and the coupling of the hydrodynamics and sediment transport models is deemed successful.

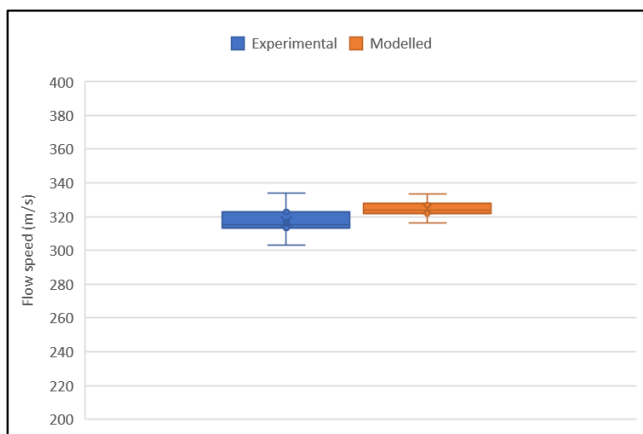


Figure 3: a) Comparison of experimental and modelled depth averaged flow speeds (The horizontal line in the box plots represents the median value of the measurements. The values at the whiskers of the plots represent the extreme values).

#### E. Problems encountered

As previously mentioned, a number of numerical difficulties arose and are presented in this section.

##### 1. Shocks in the simulation

Applying the full discharge at the beginning of the simulation caused instabilities and shocks to the flow, resulting in simulation failure. This was overcome by using a liquid boundary file in which the discharge was increased linearly (i.e. ramped) from  $0 - 0.2 \text{ m}^3\cdot\text{s}^{-1}$  within the first 5 minutes of the simulation, while allowing the morphological development of the bed.

The time step and mesh resolution values were also tested, to check if shocks and instabilities can be controlled by using different values. Both the time step and the mesh resolution were reduced but made no significant difference in reducing the instabilities and shocks in the simulation. Therefore, the aforementioned values for time step and mesh node size were selected for time saving purposes.

##### 2. GAIA treating object as sediment

Another limitation arose because the object was submerged and placed on the bed. When running the simulation, GAIA treated the object as erodible sediment, causing the complete erosion of the object within the first 90 seconds of the simulation (Figure 4).

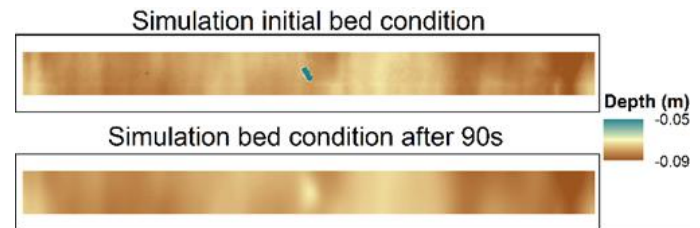


Figure 4: Model prior to and after 90s of flow applied to the computation domain.

To resolve this problem, the object was treated as a raised bed feature with the shape of the object (cylinder) by modifying the user\_bed\_init.f subroutine in the GAIA source code to include:

```
! Only apply sediment in areas
WreckLevel = -0.074
DO IPOIN=1,NPOIN
! Set the sediment to be thick enough to reach the bottom
of the flume
  if (zf%R(ipoin).ge.WreckLevel.and.
    & x(ipoin).gt.1.9.and.x(ipoin).lt.2.0) then
    ESTRATUM(1,IPOIN) = 0.D0
  else
    ESTRATUM(1,IPOIN) =
SED_THICK(1)+(zf%R(ipoin)+0.08)
  endif
! set the availability of each class
  RATIO_INIT(1,1,IPOIN) = 1.0
ENDDO
```

This modification applied sediment only at areas deeper than -7.4 cm from the transducers (the sedimentary bed level).

### 3. Ultrasonic transducers not identifying exact object shape

Another limitation was caused by the limited resolution of the 3D bed scans during the laboratory experiments. The ultrasonic transducers could not identify the object used in the experiments as a cylinder, due to horizontal accuracy limitations (Figure 5).



Figure 5: Initial laboratory scan of the object using SeaTek 5MHz ultrasonic transducers prior to flow.

The irregular shape of the object caused instabilities (due to turbulent flows) to the downstream flow, causing changes to the magnitude in the vertical (Figure 6).

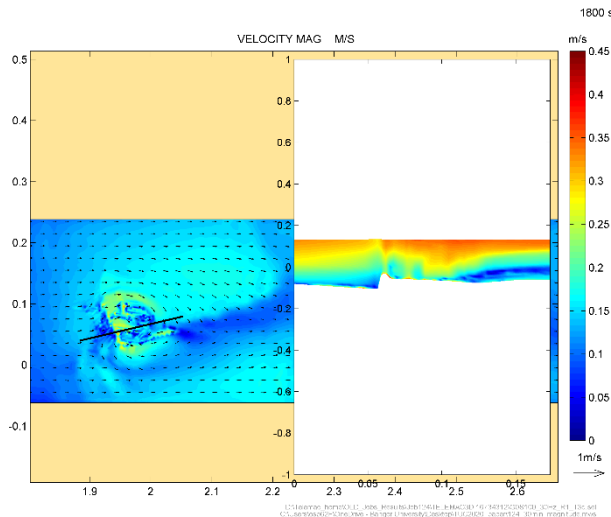


Figure 6: Magnitude of the flow after 30 minutes of simulation taken at the first horizontal plane above the bed ( $j=2$ )

The instabilities in the simulated flow caused errors in estimations of bed shear stress, generating deeper scour marks in the model than the scour marks observed in the laboratory experiments (Figure 7; Table 1). In general, the overall modelled scour length was comparable with the length of the experimental data, but the experimental data showed a shallower mean depth value of the scour mark and shorter depositional feature than the modelled data. Also, the scour mark in the simulations was offset northwards compared to the experimental data. The depositional feature in the model was longer than the formed in the experimental data and had a higher mean thickness value. This was expected due to the larger volume of eroded sediment.

TABLE 1: NUMERICAL COMPARISON OF EXPERIMENTAL AND MODELLED SCOUR MARK CHARACTERISTICS.

	Modelled data	Experimental Data	% Difference
'North' side of scour length (m)	0.32	0.30	6.7
'South' side of scour length (m)	0.21	0.21	0
Depositional feature length (m)	0.49	0.31	58.1
Scour mark mean depth (m)	-0.08	-0.09	-12.1
Depositional feature mean thickness (m)	-0.07	-0.07	0

In Figures 7d and 8d, negative values (red) represent areas where the simulated bathymetry was deeper than the laboratory experiments, where positive values (blue) represent areas where the simulated depth is shallower than the experimental depth.

To resolve the instabilities in the model caused by the irregular shape of the object, an artificial half-cylinder simulated the object (Figure 8).

The aforementioned instabilities in the simulation caused the maximum number of iterations to be exceeded. To reduce the instabilities and prevent shocks, the **FREE SURFACE GRADIENT COMPATIBILITY** keyword value was kept below 1. This made it possible to delete spurious oscillations of the free surface and alter the consistency of the water depth and the velocities in the continuity equation slightly, thus increased the numerical stability of the simulation.

Good correlations are noted for lengths and average elevations of depositional feature and scour mark between the modelled and experimental data, especially at the 'North' side of the scour mark (Figure 8; Table 2). The scour mark present upstream in the laboratory experiments and not in the model, is probably caused because of the shape of the object. In the model, the flow is diverted over the object and turbulence is not created upstream in order to form the scour mark. Similar observations were made by Hatipoglu and Avci (2002).

TABLE 2: NUMERICAL COMPARISON OF EXPERIMENTAL AND MODELLED SCOUR MARK CHARACTERISTICS FOR THE TEST CASE OF THE OBJECT IN THE SIMULATION AS A HALF-CYLINDER.

	Modelled data	Experimental Data	% Difference
'North' side of scour length (m)	0.31	0.30	3.3
'South' side of scour length (m)	0.12	0.21	-57.1
Depositional feature length (m)	0.32	0.31	3.2
Scour mark mean depth (m)	-0.09	-0.09	0
Depositional feature mean thickness (m)	-0.08	-0.07	14.3

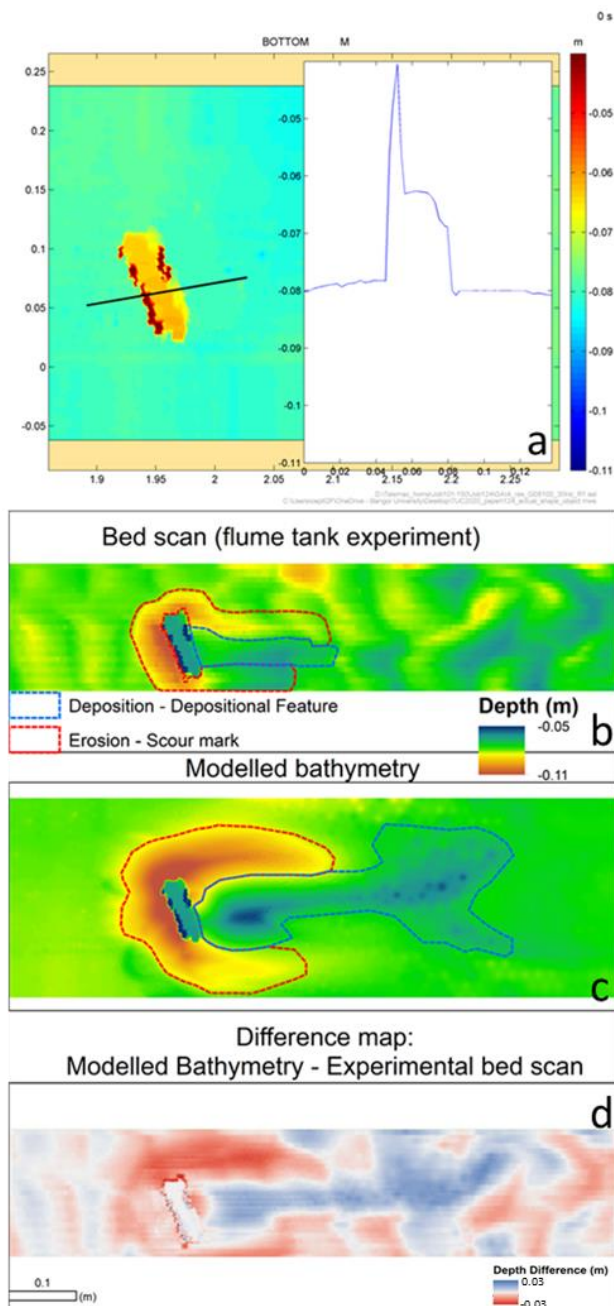


Figure 7: Profile showing the shape of the object as captured by the 3D SeaTek bed scan transducers (7a) Experimental bed scan (7b) compared with Modelled bathymetry (7c) and Difference map of the modelled and the experimental bathymetry (7d).

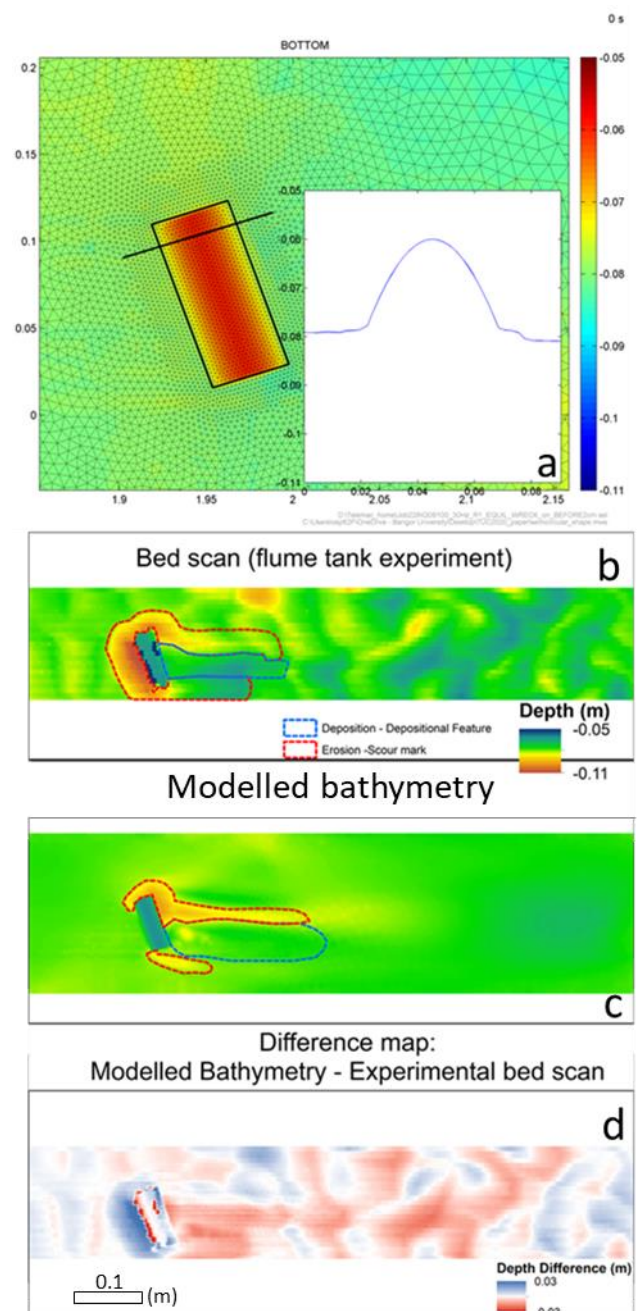


Figure 8: a) 2D representation of the half-cylinder in the computation domain (profile created from the horizontal line in the middle of the object) and representation of the geometry (mesh) of the computation domain around the object 8b) Experimental bed scan 8c) Modelled bathymetry and 8d) Difference map of the difference between the modelled and the experimental data.



Although the object in the simulation was treated as half-cylinder raised above the bed, the actual shape of the object above the bed is shown in Figure 9 where only the lower ~20% of the cylinder was actually buried.

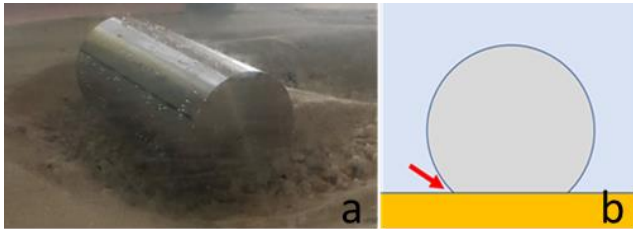


Figure 9: Picture of the cylinder in the laboratory experiments at the end of the test (9a) and schematic illustration of how the cylinder was placed on the bed at the start of the experiment (9b).

### III. RECOMMENDATIONS FOR FUTURE RESEARCH

Significant steps were made towards simulating the flow and bed dynamics around objects using coupled TELEMAT3D – GAIA. Preliminary results show real potential for the coupled model being an effective method to simulate experimental data and help understand the physical processes behind the laboratory observations. Further research is needed to accurately calculate the bed shear stress from the modelled flow speed and incorporate that into morphodynamic simulations.

The curvature of the cylinder is probably the parameter causing the largest discrepancies between the experimental and modelled data. The cylinder needs to also be treated as solid below the bed at the start of the simulation. Hatipoglu and Avci (2002), modelled the flow around submerged cylinder using a Computational Fluid Dynamics (CFD) model. Their observations compare well with the observations presented in the present study. We therefore need to address the curvature of the object above the bed and the solidity of the object below the bed in future simulations. The results from this study and from Hatipoglu and Avci (2002), suggest that covering the sides of offshore cables and pipelines would cause less scour, something that is worth investigating.

The ultimate aim of this ongoing research is to accurately simulate the flow and bed dynamics around submerged objects on mixed coarse beds. In mixed sand and gravel beds, the shear stress needed to mobilise the gravel fraction can be up to 64% less compared to the shear stress needed to mobilize the gravel in a well-sorted gravel bed (McCarron et al., 2019). To investigate bed dynamics around a submerged object on mixed coarse beds (sand and gravel), similar laboratory experiments were conducted with the cylinder embedded on different sand and gravel mixtures, with the gravel percentage varying between 0% and 20% in steps of 5%. Laboratory experiments were also conducted at 7.5% gravel and 12.5% gravel. Two unidirectional flow speeds were applied to the bed, experimentally tested to mobilize either just the sand (flow speed of  $0.26 \text{ m}\cdot\text{s}^{-1}$ ) or both the sand and the gravel fractions (flow speed of  $0.40 \text{ m}\cdot\text{s}^{-1}$ ). There is therefore availability of experimental data and there is also the potential of using TELEMAT3D – GAIA to achieve the accurate

simulation of flow and bed dynamics around submerged objects placed on mixed coarse beds.

### REFERENCES

- [1] Audouin, Y. et al. (2019). Introducing GAIA, the brand new sediment transport module of the TELEMAT-MASCARET system. 26th Telemat User Conference. (October). Toulouse, France.
- [2] Caston, G. (1979). Wreck marks: indicators of net sand transport. *Marine Geology*, 33, pp. 193–204.
- [3] Goll A. (2016). 3D numerical modelling of dune formation and dynamics in inland waterways. *Mechanics of the fluids* [physics.class-ph]. Université Paris-Est. English. <NNT : 2016PESC1119>.
- [4] Hatipoglu, F., & Avci, I. (2002). Flow around a partly buried cylinder in a steady current. *Ocean Engineering*, 30(2), 239–249.
- [5] Jette, C. (2005). SeaTek 5 MHz Ultrasonic Ranging System. Technical report, 10.
- [6] Leroy, A., TELEMAT-3D Theory guide, 2019
- [7] McArthur, M. A., Brooke, B. P., Przeslawski, R., Ryan, D. A., Lucieer, V. L., Nichol, S., McCallum, A. W., Mellin, C., Cresswell, I. D. and Radke, L. C. (2010). On the use of abiotic surrogates to describe marine benthic biodiversity. *Estuarine, Coastal and Shelf Science*, 88, 21–32.
- [8] McCarron, C. J., Van Landeghem, K. J., Baas, J. H., Amoudry, L. O. and Malarkey, J. (2019). The hiding-exposure effect revisited: A method to calculate the mobility of bimodal sediment mixtures. *Marine Geology* 410, 22–31.
- [9] Quinn, R and Smyth, TAG, (2018). Processes and patterns of flow, erosion, and deposition at shipwreck sites: a computational fluid dynamic simulation, *Archaeological and Anthropological Sciences*, 10(6): 1429-1442.
- [10] Quinn, R. (2006). The role of scour in shipwreck site formation processes and the preservation of wreck-associated scour signatures in the sedimentary record - evidence from seabed and sub-surface data. *Journal of Archaeological Science*, 33(10), 1419–1432.
- [11] Quinn, R., Saunders, R., Plets, R., Westley, K., Dix, J. (2016). Marine Scour of Cohesionless Sediments. Chapter 4 in *Site Formation of Submerged Shipwrecks*, University Press of Florida.
- [12] Saunders R (2005). Seabed scour emanating from submerged three-dimensional objects; archaeological studies; Chapter 1. Unpublished PhD Thesis, University of Southampton
- [13] Smyth, T. A. G., & Quinn, R. (2014). The role of computational fluid dynamics in understanding shipwreck site formation processes. *Journal of Archaeological Science*, 45(1), 220–225.
- [14] van Rijn L.C. (1984). Sediment transport - Part II: suspended load. *Journal of Hydraulic Division*, HY11:1631–1641.
- [15] van Rijn L.C. (2007). Unified view of sediment transport by currents and waves. 1. initiation of motion, bed roughness, and bed-load transport. *Journal of Hydraulic Engineering*, 133 (6):64.



## **Data assimilation, optimization, risks and uncertainties**

# Sensitivity of tidal modelling in coastal configurations: an uncertainty study based on field-measurement reduction

Rem-Sophia Mouradi<sup>1,2</sup>, Cédric Goeury<sup>1</sup>, Pablo Tassi<sup>1</sup>, Fabrice Zaoui<sup>1</sup>

<sup>1</sup>National Laboratory for Hydraulics and Environment (LNHE)  
Electricité De France (EDF) R&D  
6 Quai Watier, Chatou, France  
[remsophia.mouradi@gmail.com](mailto:remsophia.mouradi@gmail.com)

Olivier Thual<sup>2</sup>

<sup>2</sup>Climate, Environment, Coupling and Uncertainties research unit (CECI)  
Université de Toulouse, CERFACS/CNRS  
Toulouse, France

**Abstract**—Hydrodynamic models are increasingly used in operational industrial contexts for prediction and analysis purposes, including risk assessment and design optimization. In the modelling phase, expertly made choices can have consequences on either computational cost (i.e. mesh resolution, domain size, etc.), or closures to unknowns and their parameters (friction, turbulence, etc.). These choices are examples of epistemic uncertainty in hydrodynamic applications. Simultaneously, in the last few years, field measurements have become more accessible, giving the opportunity to deepen validation processes, and to challenge standard modelling practices based on expert judgement.

In this study, a sensitivity analysis to modelling choices such as domain extent and friction closure formulas is assessed in the context of tidal forcing in a coastal area. Comparison to field measurements of free surface and velocity components is performed using Dimensionality Reduction (DR), by means of Proper Orthogonal Decomposition (POD).

Firstly, numerical simulations with small, medium and large scale computational domains and two different friction parameterizations (i.e. Strickler and Colebrook-White), are performed and statistically compared. For this purpose, Monte Carlo (MC) simulations are launched for each modelling configuration, using samples of uncertain friction parameters and tidal boundary conditions. The different behaviors are therefore analyzed using comparative statistics on the available measurement points (average, confidence intervals, etc.).

Secondly, using POD, the behavior of each configuration, over the space of all possible events, is reduced to few representative components, commonly called modes or patterns. These modes are mutually compared for the different configurations, as well as to POD modes deduced from a distinct analysis on field measurements. A sensitivity analysis on POD modes using Sobol' indices shows that the chosen configurations can have different sensitivities to the same uncertain input parameters. This suggests that a calibration procedure might respond to different control parameters depending on the modelling choices. Consequently, the optimal estimates found from one configuration to the other, may differ.

## I. INTRODUCTION

Shallow Water Equations (SWE) are commonly used in coastal applications as good compromise between precision and computational cost. However, modelling a real case application is not always trivial. For example, the influence of the computation domain extension on the results is in general poorly evaluated, and the uncertainty implied by source terms closures, for example friction, is often overlooked. In the absence of alternatives, these choices are determined by expert opinion. In particular, calibration of the model on measurements is used to justify the model's capacity to provide physically coherent information, and therefore its predictive capability. The fitted model is then used to analyze the flow between calibration points. However, the equivalence between good-fit and accuracy can be questioned. For example, friction is often calibrated to fit measurements at different stream points, spatially or temporally distributed, as in [4, 10]. It is then assumed that the bed and the flow characteristics are uniformly distributed between the calibration points, and that the model is trusted for the other choices, namely domain size. This of course is a strong assumption.

The goal of the present study is to analyze the uncertainty resulting from common modeling choices: domain size and friction closure. For this purpose, four domain extents are compared, and two friction formulas are confronted. Different challenges are however encountered. Firstly, realistic hydrodynamic cases are high dimensional, i.e. they involve numerous parameters, and the response is spatio-temporal, which makes pointwise analysis difficult. Secondly, measurements are also spatio-temporal fields and are sometimes noisy. Proper Orthogonal Decomposition (POD) is therefore used to reduce the dimensionality of the numerical output on one hand, and to reduce and smoothen the observation on the other hand. This makes the comparison of uncertainties resulting from different model choices easier. Indeed, POD is respectively applied on the numerical model results and on observations. The resulting patterns are confronted. Then, the coefficients associated to the numerical POD patterns are learned using PCE (Polynomial Chaos

Expansion), to provide a meta-model that helps perform low cost Sensitivity Analysis (SA) [13, 14], and can be used to replace the model for fast calibration.

Last, besides patterns comparison, the most influencing parameters for each modeling configuration are optimally calibrated and compared. A 3DVAR algorithm is used [15], even though measurements are distributed in time. This is made possible thanks to POD that reduces the temporal behavior over the simulation window to few scalars instead of a high dimensional time series.

An example of a power plant's cooling intake, located in a coastal area is studied as an application case. The intake provides the plant with water via a pumping system. The study of the intakes hydrodynamics is of industrial interest, but the external currents should be trustworthy. Hydrodynamic uncertainty should therefore be quantified. Five measurement points are available off the coast, and 48 hours simulations are launched for the uncertainties investigation.

This paper is organized as follows. Firstly, theoretical background on hydrodynamic modeling, Uncertainty Quantification (UQ), using PCE, POD, SA and 3DVAR are shortly described in Section II. Secondly, modeling uncertainties are investigated in Section III, using four domain extents and two friction closures. Thirdly, optimal calibration results are compared for the modeling settings in Section IV. Lastly, a conclusion is given in Section IV.

## II. MATERIALS

### A. Shallow Water Equations

Shallow Water Equations (SWE) are obtained by depth-averaging the three-dimensional Reynolds-averaged free-surface Navier-Stokes equations, allowing the representation of almost-horizontal, two-dimensional (2D), shallow flows [1]. The mass and momentum conservation equations are defined in (1), where the system unknowns are the velocity components  $\mathbf{u} = (u, v)^T$  along the Cartesian coordinates  $(x, y)$  and the free surface elevation  $\eta := h + b$ , with  $h$  the water depth and  $b$  the bottom elevation. The gravitational acceleration  $g$  and the water density  $\rho$  are considered constant. Vector  $\boldsymbol{\tau}_b$  denotes the bottom shear stress, vector  $\mathbf{F}$  represents external forces (Coriolis, surface tension, wave radiation, etc.), and  $\nu_e$  is the effective viscosity accounting for kinematic, eddy and "dispersion" viscosity, the latter resulting from the vertical integration.

$$\begin{cases} \frac{\partial h}{\partial t} + \nabla \cdot (h\mathbf{u}) = 0 \\ \frac{\partial (h\mathbf{u})}{\partial t} + \nabla \cdot (h\mathbf{u} \otimes \mathbf{u}) = -g\nabla\eta - \frac{\boldsymbol{\tau}_b}{\rho} + \frac{h\mathbf{F}}{\rho} + \nabla \cdot (h\nu_e\nabla\mathbf{u}) \end{cases} \quad (1)$$

In this work, the external forces are omitted and the effective viscosity is set to water's kinematic viscosity for simplicity. While this is practical for a first investigation of the model's behaviour in a UQ framework, it is worth mentioning that the omitted terms are physically important and must, in principle, be considered. The bottom shear stress and the hydrodynamic Boundary Conditions (BC) need closure.

Physical parameterizations are generally used, here considered uncertain, and discussed in the following in Subsection B.

### B. Uncertain friction and boundary conditions

1) *Friction*: Bed shear stress is unknown and needs closure. It is capital for environmental applications, as it has considerable influence on the flow because of the energy dissipation it induces [2]. Its exact formulation remains unknown, but many formulas can be found in literature, with specific calibration parameters. It is generally expressed as in (2), where  $C_f$  is a dimensionless friction coefficient.

$$\boldsymbol{\tau}_b = \frac{1}{2}\rho C_f |\mathbf{u}| \mathbf{u}, \quad (2)$$

Literature formulas for  $C_f$  are either empirical or semi-empirical [2]. One of the most widely used empirical formulas is Strickler's model (3) (or Manning-Strickler in the Anglo-Saxon terminology, as explained in [3]). Coefficient  $B$  takes values in the range [21.1, 26.613]  $m^{1/2}s^{-1}$  and  $k_s$  is the bed roughness height, often set to the median bed grain size [3]. The formula is usually written as a function of the so-called Strickler coefficient  $K := B/k_s^{1/6}$ . It can be noted that equivalence with Nikuradse is assured for the particular value  $\frac{k_s}{h} = 0.037$ , if and only if  $B=26.613$  (developments in [19]).

$$C_f = \frac{2g}{B^2} \left(\frac{k_s}{h}\right)^{1/3}. \quad (3)$$

Semi-empirical formulas express the impact of near-bed turbulence on bed resistance to the flow. Indeed, not only turbulence modifies the currents in the water column, but the turbulence regime also changes the bed resistance [3]. For example, Colebrook-White's implicit formula (4) can be used, where  $B_1$ ,  $B_2$  and  $B_3$  are dimensionless, with values respectively in the ranges [2, 2.14], [0, 7.17] and [8.888, 14.83], as reported by Yen [5].

$$C_f = \frac{\lambda}{4} = \frac{1}{4 \left( -B_1 \log \left( \frac{1}{B_2} \frac{k_s}{h} + \frac{B_3}{Re\sqrt{\lambda}} \right) \right)^2}. \quad (4)$$

For both formulas,  $k_s$  must be defined. This variable is often adopted as a calibration parameter, although being physically complex to describe, as it results from different contributions (e.g. skin friction, bed forms dissipation, etc.) [6]. For coastal applications, van Rijn [6] proposes the

formula  $k_s = \sqrt{(k_s^c)^2 + (k_s^{mr})^2 + (k_s^d)^2}$ , where the total roughness  $k_s$  is induced by ripples  $k_s^c$ , mega-ripples  $k_s^{mr}$  and dunes  $k_s^d$ . Using the bounds reported in [6] for each component, the variation interval  $k_s \in [0.00064, 1.023] m$  is obtained.

2) *Tidal Boundary Conditions*: Tidal forcing are usually imposed as BC in coastal applications. In this study, the TPXO data-base is used [7], particularly the European Shelf (ES) local model within TELEMAT-2D [8]. The hydrodynamic unknowns at the boundary are modelled as a superposition of harmonic components, as in (5) and (6),

$$\mathbf{F}(\mathbf{p}, t) = \sum F_i(\mathbf{p}, t), \quad (5)$$

$$F_i(\mathbf{p}, t) = f_i(t) A_{F_i}(\mathbf{p}) \cos\left(\frac{2\pi t}{T_i} - \phi_{F_i}(\mathbf{p}) + u_i^0 + v_i(t)\right), \quad (6)$$

where the term  $F$  at point  $\mathbf{p}$  and time  $t$  represents the unknown (velocity component and/or water depth),  $F_i$  a harmonic component with constant period  $T_i$ , amplitude  $A_{F_i}$ , phase  $\phi_{F_i}$ , phase at origin of times  $u_i^0$ , and temporal nodal factors  $f_i(t)$  and  $v_i(t)$ . Thompson's method is then used to prescribe BC [9], and three parameters, denoted  $CTL$  (Coefficient of Tidal Level),  $MTL$  (Mean Tidal Level) and  $CTV$  (Coefficient of Tidal Velocity), can be used to calibrate the BC on measurements, as in (7) and (8). For example,  $MTL$  allows to account for seasonal variability (effect of thermal expansion, salinity variations, air pressure, etc.) in addition to long-term sea level rise resulting from climate change [17].

$$h(\mathbf{p}, t) = CTL \times \sum h_i(\mathbf{p}, t) - z_f + MTL, \quad (7)$$

$$\mathbf{u}(\mathbf{p}, t) = CTV \times \sum \mathbf{u}_i(\mathbf{p}, t). \quad (8)$$

In this study,  $MTL$  variation interval is deduced from measurements (Section III.A) as [4.0 m CM, 6.0 m CM], whereas the non-dimensional parameters  $CTL$  and  $CTV$  are expertly determined and respectively set to [0.8, 1.2] and [0.8, 3.0]. Using these bounds, the measurements fall within the simulated min-max interval (see Fig. 3). Coefficients  $MTL$ ,  $CTL$  and  $CTV$  can be used to compensate the effects of storm and surge (atmospheric and wave setup), as the latter are not modelled and not taken into consideration in the TPXO database.

### C. Uncertainty Quantification

The objective of UQ studies is to determine the impact of uncertain inputs or model on the uncertainty of simulated output. Firstly, an identification and quantification of uncertainty sources should be performed, as done in Subsection B. Here, in the absence of other information, Uniform densities are deduced from literature value ranges for each variable (Subsection B). Secondly, Monte Carlo (MC) simulations are realized. A random sample of the uncertain inputs of size 1000 is generated with the Uniform laws, and corresponding calculations are launched. Thirdly, MC outputs are analysed. Statistics such as mean and standard deviation can be calculated, and the overall behaviour can be analysed, for example by reducing the output's space to representative components using Proper Orthogonal Decomposition (POD), described in Subsection D.1. Additionally, Sensitivity Analysis (SA) is performed to rank the uncertain inputs by their influence on the output. For this purpose, Polynomial Chaos Expansion (PCE) can be used to calculate Sobol' indices, as explained in Subsections D.2 and D.3.

Lastly, once the most influencing parameters are identified, they can be used to fit the model on measurements. For example, optimal methods like 3DVAR, shortly described in Subsection D.4, can be used. This gives a best estimation for parameters as well as associated confidence intervals. The latter are generally much narrower than the initial UQ intervals, which reduces uncertainty.

1) *Proper Orthogonal Decomposition*: The goal of POD is to extract patterns of a continuous bi-variate function. These patterns, when added and multiplied by adequate coefficients, explain the main dynamics. Let  $\mathbf{u}: \Omega \times \mathbb{T} \rightarrow \mathbb{D} = Im(\mathbf{u})$  be a continuous function of two variables  $\epsilon, \delta \in \Omega \times \mathbb{T}$ . The following relationships and

properties hold for any  $\Omega \times \mathbb{T}$  and Hilbert space  $\mathbb{D}$  characterized by its scalar product  $(\cdot, \cdot)_{\mathbb{D}}$  and induced norm  $\|\cdot\|_{\mathbb{D}}$ . For example, this could concern the reduction of a temporal series, controlled by stochastic parameters ( $\epsilon = \{t_1, \dots, t_n\}$  and  $\delta = \{\theta_1, \dots, \theta_V\}$ ), where  $\mathbb{D}$  is a set of scalar real values or vector real values (e.g.  $\mathbb{R}$  or  $\mathbb{R}^2$ ). POD consists then in an approximation of  $\mathbf{u}(\epsilon, \delta)$  at a given order  $d \in \mathbb{N}^*$  [11] as in (9),

$$\mathbf{u}(\epsilon, \delta) \approx \sum_{k=1}^d v_k(\delta) \sigma_k \boldsymbol{\varphi}_k(\epsilon), \quad (9)$$

where  $\{v_k(\delta)\}_{k=1}^d \subseteq \mathcal{C}(\mathbb{T}, \mathbb{R})$  and  $\{\boldsymbol{\varphi}_k(\epsilon)\}_{k=1}^d \subseteq \mathcal{C}(\Omega, \mathbb{D})$ , with  $\mathcal{C}(\mathbb{A}, \mathbb{B})$  denoting the space of continuous functions defined over  $\mathbb{A}$  and arriving at  $\mathbb{B}$ , and  $\{\sigma_k\}_{k=1}^d \subseteq \mathbb{R}$ . The objective is to identify  $\{\boldsymbol{\varphi}_k(\cdot)\}_{k=1}^d$  that minimizes the distance of the approximation to the true value  $\mathbf{u}(\cdot, \cdot)$ , over the whole  $\Omega \times \mathbb{T}$  domain, with an orthonormality constraint for  $\{\boldsymbol{\varphi}_k(\cdot)\}_{k=1}^d$  using the scalar product  $(\cdot, \cdot)_{\mathbb{D}}$ . This can be defined, in the least-squares sense, as a minimization problem.

The minimization problem is defined for all orders  $d \in \mathbb{N}^*$ , so that the members  $\boldsymbol{\varphi}_k$  are ordered according to their importance. The family  $\{\boldsymbol{\varphi}_k(\epsilon)\}_{k=1}^d$  is called the POD basis. The solution to this problem is well established [11, 12]: the POD basis of  $\mathbb{D}$  of order  $d$  is the set of orthonormal eigenvectors of an operator  $\mathcal{R}: \mathbb{D} \rightarrow \mathbb{D}$  defined as  $\mathcal{R}(\boldsymbol{\varphi}) = \langle (\mathbf{u}, \boldsymbol{\varphi})_{\mathbb{D}} \times \mathbf{u} \rangle_{\mathbb{T}}$ , if the eigenvectors are taken in decreasing order of corresponding eigenvalues, which are  $\{\lambda_k = \sigma_k^2\}_{k=1}^d$ . An accuracy rate, also called Explained Variance Rate (EVR), can be calculated as  $\sum_{k \leq d} \lambda_k / \sum_{k=1}^{+\infty} \lambda_k$ , which tends to 1 (perfect approximation) when  $d$  tends to  $+\infty$ . Each  $\lambda_k$  represents the variance proportion carried by mode  $k$ . When a given  $d \ll \min(\dim(\mathbb{D}), \dim(\mathbb{T}))$  corresponds to a high accuracy rate, we speak of dimensionality reduction.

2) *Polynomial Chaos Expansion*: The idea behind Polynomial Chaos Expansion (PCE) is to formulate an explicit model that links a variable (output) to conditioning parameters (inputs), both living in a probability space. The interest variable denoted  $\mathbf{y}$  and the input parameters denoted  $\boldsymbol{\theta} = (\theta_1, \theta_2, \dots, \theta_V)$  are characterized by a given density. The models response can be approximated as in (10),

$$\mathbf{y} = \mathcal{M}(\boldsymbol{\theta}) = \mathcal{M}_0 + \sum_{i=1}^V \mathcal{M}_i(\theta_i) + \sum_{1 \leq i < j \leq V} \mathcal{M}_{i,j}(\theta_i, \theta_j) + \dots + \mathcal{M}_{1,\dots,V}(\theta_1, \theta_2, \dots, \theta_V), \quad (10)$$

where  $\mathcal{M}_0$  is the mean of  $\mathbf{y}$  and  $\mathcal{M}_{I \subseteq \{1, \dots, V\}}$  is the common contribution of variables  $I \subseteq \{1, \dots, V\}$  to  $\mathbf{y}$ . For PCE, these contributions have a polynomial form, as in (11),

$$\mathbf{y} = \mathcal{M}(\boldsymbol{\theta}) = \sum_{|\underline{\alpha}| \leq P} c_{\underline{\alpha}} \zeta_{\underline{\alpha}}(\theta_1, \theta_2, \dots, \theta_V), \quad (11)$$

with  $\underline{\alpha} = \{\alpha_1, \dots, \alpha_V\}$  and  $|\underline{\alpha}| = \sum_{i=1}^V \alpha_i$ , defining a multivariate polynomial basis  $\{\zeta_{\underline{\alpha}}, \underline{\alpha} \in \mathbb{N}^V \text{ and } |\underline{\alpha}| \in \{0, \dots, P\}\}$  as  $\zeta_{\underline{\alpha}}(\theta_1, \theta_2, \dots, \theta_V) = \prod_{i=1}^V \xi_{\alpha_i}^{(i)}(\theta_i)$ . For each parameter  $\theta_i$ ,  $\{\xi_{\alpha_i}^{(i)}, \alpha_i \in \{0, \dots, P\}\}$  is an orthonormal polynomial basis, and  $P \in \mathbb{N}$  is a chosen polynomial degree.  $c_{\underline{\alpha}}$  are deterministic coefficients that can be estimated using different methods. In this work, the Least Angle Regression Stagewise method (LARS) is used to construct an adaptive



sparse PCE. Further details on PCE in general and LARS in particular can be found in [20].

3) *Sensitivity Analysis*: PCE can be used with variance decomposition [13, 14] to analyse the influence of the inputs variances on the output's variance [14]. For the general case of a multivariate model written as in (10), the contribution of the polynomial indexed by  $\underline{\alpha}$ , to the output  $\mathbf{y}$  can be computed in terms of variance, as in (12),

$$S_{\underline{\alpha}} = \frac{\text{var}[c_{\underline{\alpha}} z_{\underline{\alpha}}]}{\text{var}[\mathbf{y}]} = \frac{c_{\underline{\alpha}}^2}{\sum_{|\underline{\beta}| \leq P} c_{\underline{\beta}}^2}, \quad (12)$$

where  $S_{\underline{\alpha}}$  are the well-known Sobol' indices [14]. Adding them for all the polynomials that contribute to  $\mathbf{y}$  equals 1. They allow to rank all terms by their relative contribution to  $\mathbf{y}$ . The contributions can either be: (i) analysed for each polynomial; (ii) used to compute the 1<sup>st</sup> order contribution of a variable  $\theta_i$  alone (1<sup>st</sup> Sobol' index denoted  $S_i$ ) by adding the monomial contributions only; (iii) or used to compute the total contribution of  $\theta_i$  (total Sobol' index denoted  $S_i^T$ ) by adding the contributions of all polynomials involving  $\theta_i$ .

4) *Optimal Calibration using 3DVAR*: An automatic algorithm is here used for inverse parameters estimation from observations and a numerical model. On the first hand, observations are not perfect. On the other hand, one may have a first guess for the parameters (physical knowledge, previous simulations, etc.), but the latter is uncertain. In order to find the best compromise between measurements errors and parameters first guess errors, the optimization takes the form of a minimization problem, for the function defined in (13),

$$J(\boldsymbol{\theta}) = \frac{1}{2}(\boldsymbol{\theta} - \boldsymbol{\theta}_b)^T \mathbf{B}^{-1}(\boldsymbol{\theta} - \boldsymbol{\theta}_b) + \frac{1}{2}(\mathbf{y} - \mathcal{H}(\mathcal{M}(\boldsymbol{\theta})))^T \mathbf{R}^{-1}(\mathbf{y} - \mathcal{H}(\mathcal{M}(\boldsymbol{\theta}))), \quad (13)$$

where  $\mathbf{y}$  is the observation,  $\mathcal{M}$  the numerical model,  $\mathcal{H}$  an operator from the simulation to the observation space,  $\boldsymbol{\theta}$  the set of unknown parameters and  $\boldsymbol{\theta}_b$  a background knowledge (or first guess) of the parameters. The background and observation errors are represented by error covariance matrices, respectively denoted  $\mathbf{B}$  and  $\mathbf{R}$ . This is commonly known as a data assimilation variational problem, where  $J$  is called cost function, and minimizing it is referred to as 3DVAR [15, 16].

Here, the observation and simulation are the same variables expressed on the same locations and times, i.e.  $\mathcal{H}$  is identity. The observation can be POD reduced and approximated as a matrix product  $\mathbf{y} \approx \boldsymbol{\Phi}_Y \boldsymbol{\Sigma}_Y \tilde{\mathbf{y}}$ , where a finite number of POD modes is stored in  $\boldsymbol{\Phi}_Y$ , the corresponding square roots of eigenvalues are stored in  $\boldsymbol{\Sigma}_Y$  and  $\tilde{\mathbf{y}}$  contains the multiplicative coefficients, which are a reduced form of  $\mathbf{y}$ . Next, the simulation result  $\mathcal{M}(\boldsymbol{\theta})$  can be POD reduced and the coefficients learned using PCE as a function of  $\boldsymbol{\theta}$ , which is written as  $\mathcal{M}(\boldsymbol{\theta}) \approx \boldsymbol{\Phi}_X \boldsymbol{\Sigma}_X \tilde{\mathcal{M}}(\boldsymbol{\theta})$ , where  $\tilde{\mathcal{M}}(\boldsymbol{\theta})$  is a vector storing PCE models for the reduced version of simulation result. The cost function can then be approximated as in (14).

$$J(\boldsymbol{\theta}) \approx \frac{1}{2}(\boldsymbol{\theta} - \boldsymbol{\theta}_b)^T \mathbf{B}^{-1}(\boldsymbol{\theta} - \boldsymbol{\theta}_b) + \frac{1}{2}(\tilde{\mathbf{y}} - \tilde{\mathbf{H}} \tilde{\mathcal{M}}(\boldsymbol{\theta}))^T \tilde{\mathbf{R}}^{-1}(\tilde{\mathbf{y}} - \tilde{\mathbf{H}} \tilde{\mathcal{M}}(\boldsymbol{\theta})), \quad (14)$$

where  $\tilde{\mathbf{H}} = (\boldsymbol{\Phi}_Y \boldsymbol{\Sigma}_Y)^{-1} \boldsymbol{\Phi}_X \boldsymbol{\Sigma}_X$  is a new linear operator (matrix) that links the reduced observation to the PCE model of reduced simulation  $\tilde{\mathcal{M}}(\boldsymbol{\theta})$ , and  $\tilde{\mathbf{R}}^{-1} = (\boldsymbol{\Phi}_Y \boldsymbol{\Sigma}_Y)^T \mathbf{R}^{-1} (\boldsymbol{\Phi}_Y \boldsymbol{\Sigma}_Y)$ . The new minimization problem is an approximation of the original, but is less costly. Indeed, reduction implies that the dimension of  $\tilde{\mathbf{y}}$  is much lower than the full observation's, and that of  $\tilde{\mathcal{M}}(\boldsymbol{\theta})$  is much lower than the numerical model's. Additionally, PCE performs in seconds while the numerical model needs hours, making the model evaluation time negligible.

In the following, the uncertainties resulting from modelling choices (domain extension, friction closure) are investigated using the previously described theoretical elements.

### III. UNCERTAINTIES RELATED TO MODELING CHOICES

Firstly, a description of the study case and available data is given in Subsection A. The case is used to investigate the differences that come from domain extent choice in Subsection B, and friction formula choice in Subsection C.

#### A. Case study

The study site is located on the eastern English Channel coast in northern France. The study zone is mega-tidal and dominated by a semi-diurnal circulation, with moderate wave activity. In particular, a power plant's cooling intake is of interest. Its upstream boundary is connected to the sea, and a pumping system ensures the plant's cooling. Hydrodynamic models of different extents, as shown in Fig. 1-a, can be used to represent the flow in the intake. The choice of domain extent and other simulation parameters (Section II) is considered uncertain. Consequently, four domain extensions are compared in Subsection B and two friction formulas confronted in Subsection C. For validation, five measurement points (indicated in Fig. 1-a) of  $(u, v)^T$  and  $\eta$  over a two-month period are available. In addition to tidal effects, possible occurrence of storms, surges and resulting non-linear interactions with the tides influence these measurements. However, it is difficult to isolate their effect in the measured quantities as highlighted in [17]. The tidal BC coefficients introduced in Subsection B.2 will therefore be used to calibrate the total signal.

Firstly, domains of different sizes, centred on the cooling intake, are created. Four domains in particular, of sizes 800 m, 2 km, 7 km and 8 km, are compared in Section B. These denominations correspond to the distance from the intake entrance to the offshore, and equal distance on either side of the intake, to the east and to the west alongshore. Secondly, mesh convergence is assessed on the 2 km domain, and results in elements of size 50 m at the sea, 2.5 m at the intake walls and 0.5 m at the intake pumps. This configuration is kept for all domain sizes, and the resulting geometries share the same mesh in the common zones. The mesh is shown in Fig. 1-b, where the intake is coloured in red, and the growth of elements size from the intake to the sea is visible. The corresponding

meshes contain 28 188, 31 814, 74 079 and 87 617 nodes for the four domain extensions respectively. Thirdly, bathymetries are retrieved from different sources: a Digital Elevation Model (DEM) composed of global and local bathymetries [18], an interpolation of topographic beach profiles and a nearshore multi-beam bathymetry inside the intake and at its vicinity. The same bathymetries are applied for all domain sizes, and the resulting geometries share the same bathymetry in the common zones. It should be mentioned that the used data are not necessarily available at measurement date, and are spatially interpolated. This results in an epistemic uncertainty. Additional sources of uncertainty, namely measurement errors should be noted. However, this is not explicitly dealt with. For the sake of simplicity, calibrating friction is considered to compensate, in average, for the uncertainty in the right hand side terms of SWE.

Lastly, for all domain extensions, the BC are directly interpolated from the TPXO data-based. As all domain sizes keep smaller than a TPXO element size, the differences in the BC only result from linear interpolation due to the distance of boundary elements from the TPXO nodes. The idea is to evaluate the sensitivity of the simulations to pure extension of the calculation domains and not to changes in the BC nature. For the same reasons, BC of the smaller domains are not interpolated from larger domains because this would compensate for the difference of extension, which is exactly what we want to analyse.

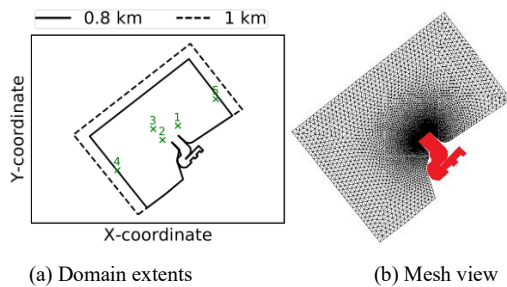


Figure 1 - Examples of domain extents with representation of measurement points outside the intake and view of the mesh.

Measurements of tidal periods are extracted and superposed as in Fig. 2.

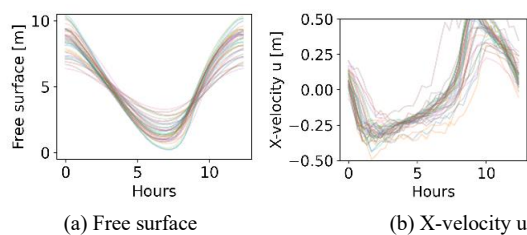


Figure 2- Superposition of field measurements in front of the intake on point 1, for two hydrodynamic variables.

The different periods are considered as realizations of a temporal series, and POD is performed. The behaviour over two months is therefore reduced to a few components. The associated EVR are shown in Fig. 3. Velocity components  $u$  and  $v$  show the same behaviour. The two-months measurements, from which 38 periods were extracted for each

variable, can therefore be reduced to 2 components, giving 99% of captured variance for free surface, and over 96% for the velocity components.

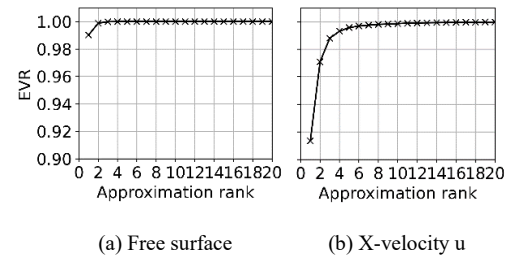


Figure 3- EVR for the free surface and X-velocity  $u$  after measurement based POD reduction on Point 1.

### B. Domain size implications

As introduced in Section I and represented in Fig. 1, the comparison of hydrodynamic computations with domains of different sizes, centred on the cooling intake, is attempted. The four domains of sizes respectively denoted 800 m, 2 km, 7 km and 8 km, presented in Subsection A, are compared.

In this section the Strickler formula is used for all domain extensions. The following uncertain parameters are considered for UQ: three for BC calibration ( $MTL$ ,  $CLT$ ,  $CTV$ ) and two Strickler coefficients at the intake ( $K_1$ , red zone in Fig. 1-b) and at sea ( $K_2$ ). The inputs bounds are described in Section II.B. In particular, the exact calculation for  $K_1$  and  $K_2$  using the formula  $K = B/k_s^{1/6}$  and the bounds from Section II.B for  $B$  and  $k_s$  gives the interval  $[21.02, 90.66] m^{1/3}s^{-1}$ .

A number of 1000 MC simulations is launched on each domain. The min-max values of velocity  $u$  and examples of MC realizations are shown in Fig. 4 for two domains. The 2 km domain reaches higher velocities than the 7 km domain, with the same uncertain parameters and bounds. Simulation examples (plots in colours in Fig. 4) show abrupt variations at low tides with the 2 km domain. Conversely, the 7 km one shows a smoother behaviour. For both domains, measurements fall within the modelled interval. Last, whatever the modelling domain, a slight time-lag between measurements and numerical simulations is observed.

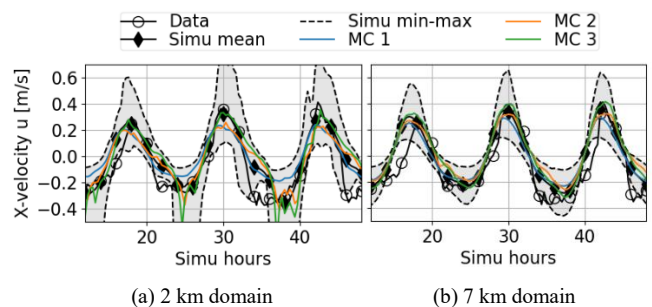


Figure 4- MC min-max envelope of x-velocity  $u$  extracted at Point 5, for domains of size 2 km and 7 km, and examples of MC realizations in colours.

Investigation of the 2 km domain shows the presence of tidal flats at BC, which might be the cause of velocity oscillations. Indeed, an extraction of the hydrodynamic variables on the 2 km contour at low tide is performed in Fig. 5. It shows that the velocity extremums are much higher for

the 2 km domain (Fig. 5-b) than for bigger extents. These higher velocities are due to the negligible water depths on the same locations (Fig. 5-a). Indeed, the velocity BC provided by the TPXO data base are not directly  $(u, v)^T$ , but transport fluxes  $(uh, vh)^T$ . Division by water depth  $h$  causes the velocity BC to be infinite when  $h$  is negligible. An often used practical engineering solution is to deepen the bathymetry at BC. Nevertheless, this solution is not used to avoid additional uncertainties and the impact of propagation of this error at BC is studied and compared to other domains.

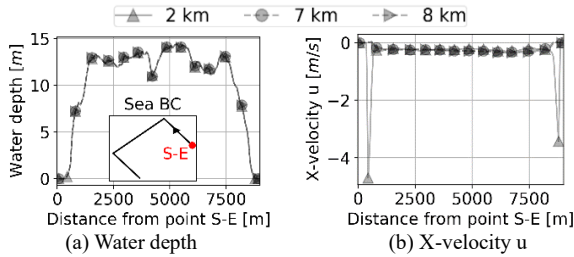


Figure 5- Hydrodynamic variables extracted on the 2 km sea BC at low tide for three different domain extents.

POD is used in order to analyse the full time series variations at a given point. The EVR is shown for example on Point 1 in Fig. 6. The problem is highly reducible. Free surface elevation reaches 99% variance with two modes, for all domain sizes. The relative RMSE (Root Mean Squared Error) between the simulation results and a 2-Mode POD reduction, averaged over the MC sample, is around 0.3%. Velocity components show different behaviours for different domains. For example, the y-velocity  $v$  is much less reducible for the 2 km domain, probably linked to the numerical error at the BC. The average relative RMSE, between the simulations and a 2-Mode POD, is around 5.8% with the 8 km domain, while it reaches 8.4% with the 800 m domain. It can also be noticed that the 800 m, 7 km and 8 km domains EVRs are ordered by domain size and 99% of the variance is captured with 2 modes, except for 2 km.

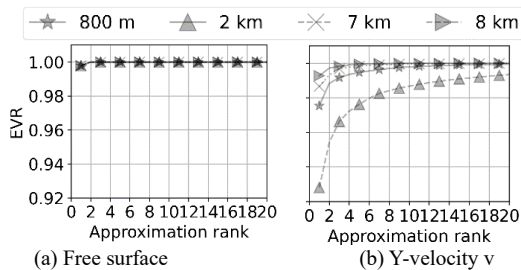


Figure 6- EVR for two hydrodynamic variables after MC simulations POD reduction on Point 1.

Next, free surface modes are shown in Fig. 7 for Point 1, where numerical and measurements modes are compared. Both modes are identical for all domains, and their shapes are comparable to measurement modes. However, the amplitudes of numerical Mode 1 are smaller than measurements. This difference can be explained by the represented information. Measurements Mode 1 is characterized by larger amplitudes, because measurements tidal coefficient varies, whereas the numerical Mode 1 only represents MC stochastic variation around the same tide. Furthermore, Mode 1 is always strictly

positive, be it for the numerical or real mode. When multiplied by a positive coefficient (corresponding to a given MC realization or a given measurement period), it stays positive and translates vertically, i.e. the mean tidal level changes. Mode 2 oscillates from negative to positive, but not symmetrically. Adding it to Mode 1 corrects both tidal range and mean. It can be noticed that the periods of Mode 1 and 2 are approximately semi-diurnal, which can for example be compared to the principal lunar and solar semidiurnal tidal components (M2 and S2). It should be noted however that POD modes have no theoretical reason to recover the tidal harmonics, as would be the case with a Fourier decomposition. This is rather related to the statistical importance of such harmonics in the global variance of the system. Lastly, a phase shift is observed between simulations and reality, for both modes. This phase is more important at ebb than at flood. It may correspond to the un-modelled effect of tide-surge interactions. Indeed, as explained in [17], the latter can lead to more surge at low than at high tide, resulting in a phase lag where the surge precedes the high water by few hours.

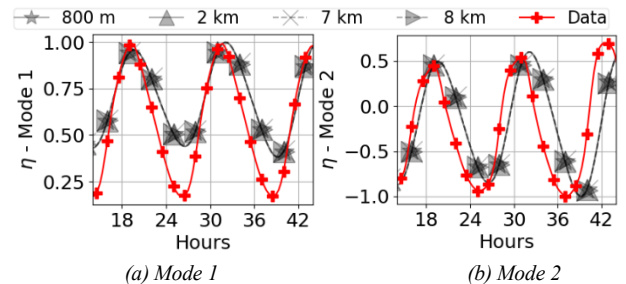


Figure 7- Comparison of the first two modes of free surface to reality, after reduction on point 1, for all tested domain sizes.

Comparison of X-velocity modes is shown in Fig. 8. First, differences between domains can be observed, and are bigger in Mode 2 than in Mode 1. Once again, the domain of size 2 km behaves differently even for Mode 1 (oscillations). This is a numerical artefact, as no oscillations are noticed in the measurements.

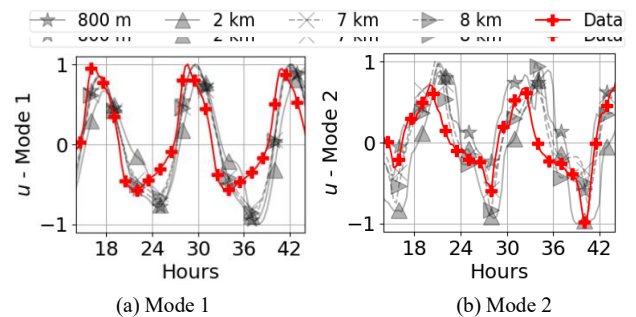


Figure 8- Comparison of the first two modes of x-velocity  $u$  to reality, after reduction on point 1, for all tested domain sizes.

Secondly, no model succeeds in reproducing the asymmetry observed at the extremums of measurements for Mode 1. Something is missing in the modelling that cannot be corrected by domain extent (Coriolis force, turbulence, waves, storm and atmospheric surges, non-linear interactions of tides with the latter, more precise bathymetry, etc.). For Mode 2, the overall numerical behaviour is comparable to the real one. It seems however that the domain of size 2 km fails at



reproducing the sharp minimal peaks (for example at Hour 40 in Fig. 8-b) that the other models capture better. The same conclusions hold for Y-velocity  $v$ , with oscillations at the minimum noticed with the numerical simulations, and not present in the real mode. For modes of higher rank, no similarity between the numerical results and the measurements is observed.

Next, Sobol' indices of the inputs are compared for all domain sizes. They are calculated using degree 3 PCE models of the POD temporal coefficients, as explained in Section II.C.3. The MC sample is separated to a training set (80%) and a test set (20%) and PCE models are learned on the training set. For example, with the 8 km model, it can be noted that the 90<sup>th</sup> percentile of the relative RMSE, between the simulations and a 2-Mode POD-PCE meta-model, calculated on the test set, remains below 0.3% for the free surface, and below 6.1% for the velocities. Sobol' indices results for free surface and X-velocity  $u$  are shown in Fig. 9. For free surface, the only influencing variable for Mode 1 is  $MTL$  (Mean Tidal Level). For Mode 2, the influence of coefficient  $CTL$  is dominant, and  $MTL$  is in second position. This is coherent with previous interpretation of free surface modes. No differences between domain sizes are noticed. For the velocity components, influences change with domain sizes. For Mode 1, the most influencing variable is  $CTV$  for all domain extents, followed by the Strickler coefficient  $K_2$ . This tendency is inverted for Mode 2. However,  $CTV$  is more important for the smallest domain of 800 m, whereas  $K_2$  is less important, probably due to the spatial proximity of the BC to the analysed Point 1. For the 2 km domain,  $K_2$  is much more important than for the other extents for both modes. This can be explained by the higher velocity values, as  $K_2$  interacts with velocity in the shear stress formula (2). An interaction between  $K_2$  and  $CTV$  is noticed (undashed portion), also explained by the shear stress formula.

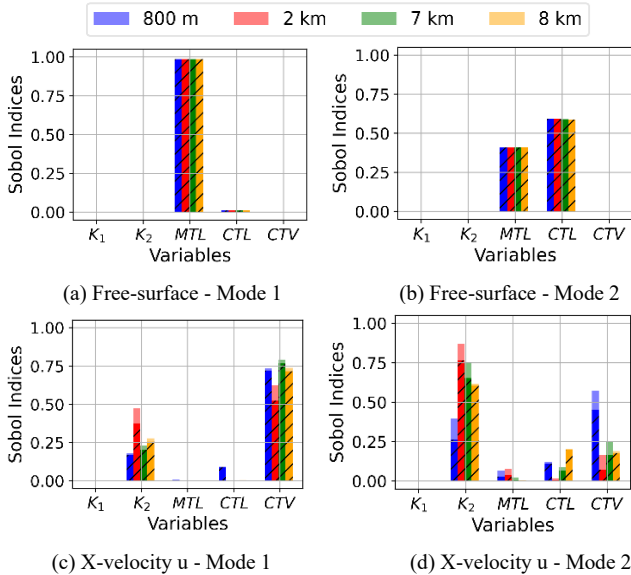


Figure 9- Sobol' indices for the two first modes of free surface and x-velocity  $u$  on Point 1, with the different domain sizes. Full bar plot represents total Sobol' indices. The dashed portion corresponds to the 1<sup>st</sup> order Sobol' index, and the remaining to the interaction with other variables.

Slight differences are observed between the 7 km and 8 km domains, namely more importance in Mode 1 for  $K_2$  and  $CTV$  with 7 km, which could be explained by higher proximity of the BC. The differences are larger for Mode 2, but the latter is associated to less variance percentage. Moreover, the Strickler coefficient dominance for Mode 2 means that the observed velocity peaks in Fig. 8 can be moderated by friction, except for the smallest domain, where BC is dominant. The smallest the domain, the more controllable it is with BC only. Last, intake's friction  $K_1$  has no influence outside. Calibration outside can hence be performed without controlling  $K_1$ .

### C. Friction closure influence

The same analysis strategy is adopted to study the Strickler and Colebrook friction formulas, introduced in Section II.B. The same domain of size 8 km with the bathymetry and mesh described in Subsection III.A are used. Eight uncertain parameters are used for Colebrook's UQ: three for BC ( $MTL$ ,  $CTL$ ,  $CTV$ ), roughness heights at the intake ( $k_s^1$ ) and at sea ( $k_s^2$ ) and three structural uncertainty parameters ( $B_1$ ,  $B_2$  and  $B_3$ ). With the Strickler formula, six uncertain parameters are used: three for BC, two roughness heights, and one structural parameter  $B$ . All inputs and corresponding bounds are described in Section II.B. Temporal responses at the five measurement points are reduced using POD. No differences can be observed in terms of EVR, all variables can be reduced to 2 modes for over 99% of variance. The modes shapes are compared, and no differences are observed in the free surface first two modes. Slight differences can be seen in the velocity modes, as shown in Fig. 10, particularly for Mode 2 for which small oscillations appear with Strickler's model and not with Colebrook's. No formula succeeds however in reproducing the observed asymmetry of measurements Mode 1, and a phase can be noticed for both modes. Apparently, this lack of asymmetry representation cannot be corrected with friction closure modification either.

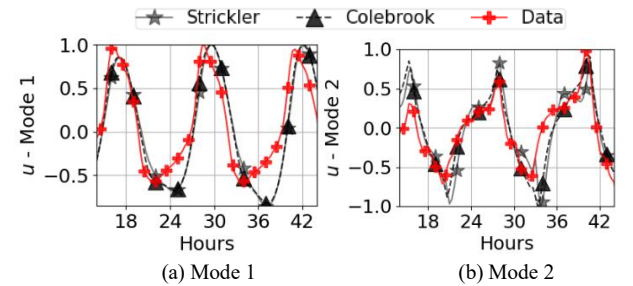


Figure 10- Comparison of the first two modes of x-velocity  $u$  to reality, after reduction on point 1, for two friction formulas.

SA is performed and no differences are observed for the free surface modes. Sobol' indices of the X-velocity  $u$  modes are shown in Fig. 11. Naturally, Sobol' indices of  $B$  are plotted only for Strickler's model, and those of  $B_1$ ,  $B_2$  and  $B_3$  are plotted only for Colebrook's. Slight differences are observed in Fig. 11.



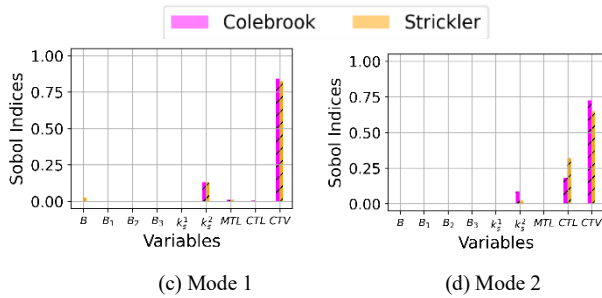


Figure 11- Sobol' indices for the two first modes of free surface and x-velocity  $u$  on Point 1, with different friction formulas. Full bar plot represents total Sobol' indices. The dashed portion corresponds to the 1<sup>st</sup> order Sobol' index, and the remaining to the interaction with other variables.

For Mode 1 there is a slight influence of the structural parameter  $B$  for the Strickler model, whereas the parameters of Colebrook's model show no influence. Additionally, the velocity BC correction denoted  $CTV$  gains influence with Colebrook, whereas the sea rugosity  $k_s^2$  loses impact. The increase of influence for  $CTV$  with Colebrook's model is more important for Mode 2. The ranking of variables is however the same, even though the proportion of influence changed.

#### IV. IMPLICATIONS OF EXPERTLY MADE CHOICES ON OPTIMAL CALIBRATION

An example of the uncertainty of optimal calibration is shown on the domain extents variation. A 3DVAR algorithm is used, with the same configurations, parameters and bounds, for all domains. The measurement is reduced to 2 modes, and the calibration is performed on the learned 2-modes POD-PCE meta-models for each numerical simulation, by minimizing the cost function in (14). This allows the observation to be simpler (smoothing) and the problem dimension to be lower (2 coefficients per each variable, instead of 48 hours temporal series). The observation's error covariance matrix  $\mathbf{R}$  is considered diagonal (no error correlations) and calculated from measurement errors (5 cm for free surface and 1 cm/s for velocity). The background of each input parameter is set to the average of its variation interval, and the background's error covariance matrix  $\mathbf{B}$ , also considered diagonal, is estimated from the interval's variance (squared maximum distance from mean). Calibration results are shown in Fig. 12.

Firstly, it can be noticed that while oscillations are slight with the domain of size 2 km at point 4, they become more and more important when approaching the intake, at Point 3 where they gain amplitude and at Point 1 when the response becomes completely uncontrolled. Without specific correction, this domain is therefore of no interest in operational conditions. Secondly, the velocities represented with size 800 m are of lower amplitudes than with the largest domains of sizes 7 and 8 km. For Point 3 for example in Fig. 12-b, the 800 m domain fits better the minimum velocities than the biggest domains, and vice-versa at the maximum velocities. However, it can be seen in Fig. 12-c that the velocity shapes and amplitudes modelled by the biggest domains are more realistic than with the smallest ones. Lastly, even though domains of sizes 7 and 8 km show similar behaviour, slight differences can be observed. For Point 3 for example in Fig. 12-b, the extrema reached by domain of size 8 km are higher than with the 7 km

domain. Hence, even with similar choices for domain extent (7 and 8 km), the best fit could be uncertain. Physical analysis and prediction are therefore also uncertain.

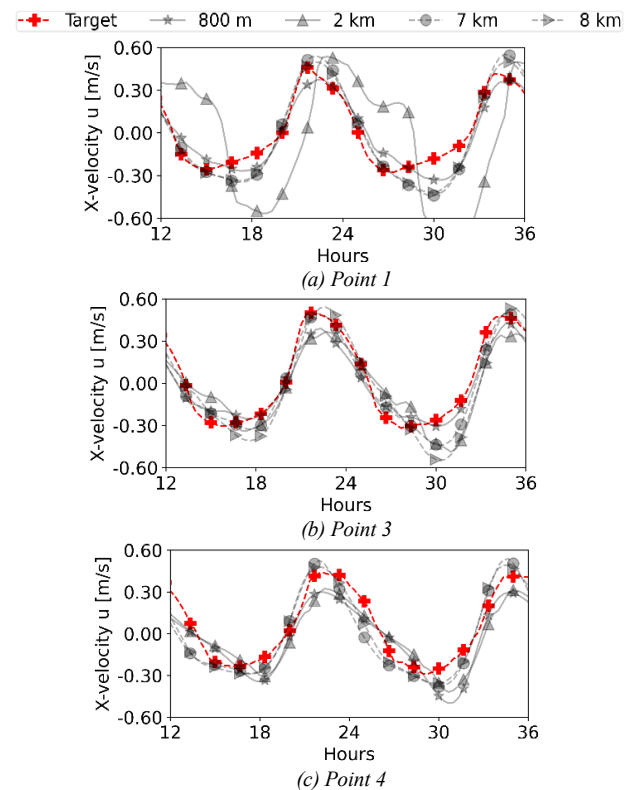


Figure 12- Example of optimal calibration with the tested domain extents, for x-velocity  $u$  at points 1, 3 and 4.

In particular, a comparison of X-velocity  $u$  profile at the intake's entrance for domains of sizes 7 and 8 km, at half ebb tide, is given in Fig. 13, after 3DVAR calibration. As a reminder, no calibration point is available on this profile. It can be noticed that differences are bigger and analysis is even more uncertain in locations where no measurement is available, even though both domains were calibrated.

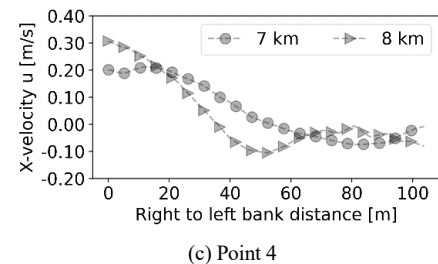


Figure 13- Intake's entrance cross-sectional profile of x-velocity at half ebb tide after 3DVAR calibration.

Last, the optimal parameterizations are different with the four domain sizes. For example, the Strickler coefficient at the sea equals  $33.9 \text{ m}^{1/3} \text{ s}^{-1}$  for the domain of size 8 km whereas it is equal to  $55.85 \text{ m}^{1/3} \text{ s}^{-1}$  for the domain of size 800 m, when  $CTV$  equals 4.16 for the 8 km domain and 4.38 for the 800 m domain. This shows that, in a coastal configuration, the generalization of such parameters, friction

coefficient for example, is hardly possible, without further investigations about their meaning, as optimal values are strongly related to the numerical choices that precede calibration. Additionally, the optimal values for such parameters (e.g. friction coefficient) can be time-varying. Therefore, a dynamic optimal-fitting procedure may be necessary.

## V. CONCLUSION

In this study, uncertainties resulting from standard modelling choices in hydrodynamics, i.e. domain size and closure choice for friction were studied.

Firstly, measurements were POD reduced, and their patterns compared to numerical POD patterns resulting from different modelling configurations in a UQ framework. While similarities between observations and simulations are identified, some particularities present in the measurements, such as tidal velocity asymmetry, could not be modelled with the chosen configurations. This emphasizes the need of additional physics to be incorporated into the model, for example the Coriolis force, turbulence, waves, storm and atmospheric surges, non-linear interactions of tides with surge, or more precise bathymetric information. Noticing the lack of accord between the numerical and measurement-based patterns might help saving High Performance Computing resources: it is vain to try calibrating these configurations to capture particularities of the measurements when their modes behave differently, i.e. when the corresponding physical process is missing in the model.

Secondly, SA was performed on each modelling configuration. Differences were noticed, in terms of importance ordering and influence magnitude. It also indicates that the smaller the domain, the more important BC are, which is a coherent conclusion. This could have consequences on calibration processes. Indeed, as a last investigation, a 3DVAR algorithm was tested, using the same parameters, on all modelling configurations. In this context, POD reduction on both measurements and simulations along with PCE meta-models were used to dramatically reduce the computational time required by the 3DVAR algorithm. The results show that the obtained optimal states and associated optimal parameters may differ, even with close modelling choices (e.g. close domain extents), which highlights on uncertainties inherent to common modelling choices.

## ACKNOWLEDGEMENT

The authors acknowledge the French National Association of Research and Technology (ANRT) for funding, and are grateful to the TELEMAT-MASCARET (hydrodynamics), OpenTURNS (uncertainty quantification) and ADAO (data assimilation) developer communities.

## REFERENCES

- [1] J.-F. Gerbeau and B. Perthame. *Derivation of Viscous Saint-Venant System for Laminar Shallow Water; Numerical Validation*. Research Report RR-4084, INRIA, 2000.
- [2] H. Morvan, D. Knight, N. Wright, X. Tang and A. Crossley. *The concept of roughness in fluvial hydraulics and its formulation in 1d, 2d and 3d numerical simulation models*. Journal of Hydraulic Research, 46: 191-208, 03 2008.
- [3] M. Marriott and R. Jayaratne. *Hydraulic Roughness – links between manning's coefficient, nikuradse's equivalent sand roughness and bed grain size*. Proc. 5<sup>th</sup> Annual Conf. on Advances in Computing and Technology, 01 2010.
- [4] H. H. Barnes. *Roughness characteristics of natural channels*. Number 1849. US Government Printing Office, 1967
- [5] B.C. Yen. *Open channel flow resistance*. Journal of hydraulic engineering, 128(1) : 20-39, 2002.
- [6] L. C. van Rijn. *Unified view of sediment transport by currents and waves. I: Initiation of motion, bed roughness, and bed-load transport*. Journal of Hydraulic Engineering, 133(6) : 649-667, 2007.
- [7] G. D. Egbert and S. Y. Erofeeva. *Efficient Inverse Modeling of Barotropic Ocean Tides*. Journal Atmospheric and Oceanic Technology, 19 (2) : 183-204, 02 2002.
- [8] C.-T. Pham and F. Lyard. *Use of tidal harmonic constants databases to force open boundary conditions in telemac*. In Proceedings of the XIXth TELEMAT-MASCARET User Conference 2012.
- [9] J.-M. Hervouet. *Hydrodynamics of Free Surface Flows : Modeling with the Finite Element Method*. John Wiley & Sons, Ltd : Hoboken, NJ, USA, 2007.
- [10] K. Fisher and F. Dawson. *Reducing uncertainty in river flood conveyance: Roughness review*. 07 2003.
- [11] Lumley, J. L. (1967). *The Structure of Inhomogeneous Turbulent Flows*. Proceedings of the International Colloquium on the Fine Scale Structure of the Atmosphere and Its influence on Radio Wave Propagation, edited by A. M. Yaglam, and V. I. Tatarsky, Doklady Akademii Nauk SSSR, Nauka, Moscow.
- [12] L. Sirovich. *Turbulence and the dynamics of coherent structures: I, II and III*. Quarterly Applied Mathematics, 45: 561, 1987.
- [13] Y. Caniou. *Global sensitivity analysis for nested and multiscale modelling*. PhD thesis, 2012.
- [14] B. Sudret. *Global sensitivity analysis using polynomial chaos expansions*. Reliability Engineering & System Safety, 93(7): 964-979, 2008.
- [15] A. Carrassi, M. Bocquet, L. Bertino and G. Evensen. *Data assimilation in the geosciences: An overview of methods, issues and perspectives*. Wiley Interdisciplinary Reviews: Climate Change, 9(5):e535, 2018.
- [16] J.-P. Argaud. *User Documentation in SALOME 7.5 platform of the ADAO module for Data Assimilation and Optimization*. EDF R&D report, 2016.
- [17] Idier, D., Bertin, X., Thompson, P. and Pickering, M.D., 2019. *Interactions between mean sea level, tide, surge, waves and flooding: mechanisms and contributions to sea level variations at the coast*. Surveys in Geophysics, 40(6), pp.1603-1630.
- [18] Shom. *MNT Bathymétrie de façade Atlantique (Projet Homonim)*. 2015.  
[http://dx.doi.org/10.17183/MNT\\_ATL100m\\_HOMONIM\\_WGS84](http://dx.doi.org/10.17183/MNT_ATL100m_HOMONIM_WGS84)
- [19] Machiels, O., Erpicum, S., Archambeau, P., Dewals, B. and Pirotton, M., 2009. *Bottom friction formulations for free surface flow modeling*. In 8th NCTAM Congress
- [20] Blatman, G. and Sudret, B., 2011. Adaptive sparse polynomial chaos expansion based on least angle regression. *Journal of computational Physics*, 230(6), pp.2345-2367.

# Assessing uncertainties in flood forecasts using a mixture of generalized polynomial chaos expansions

Siham El Garroussi<sup>1</sup>, Sophie Ricci<sup>1</sup>, Matthias De Lozzo<sup>2</sup>, Nicole Goutal<sup>3</sup>, Didier Lucor<sup>4</sup>

<sup>1</sup>CECI, CERFACS/CNRS, 42 Avenue Gaspard Coriolis, 31057 Toulouse Cedex 1

<sup>2</sup>IRT Saint Exupéry, CS34436, 3 Rue Tarfaya, 31400 Toulouse

<sup>3</sup>EDF, LNHE, 6 quai Watier, 78400 Chatou

<sup>4</sup>LIMSI, Campus Universitaire bâtiment 507, Rue John Von Neumann, 91400 Orsay  
siham.elgarroussi@cerfacs.fr

**Abstract**—Surrogate modelling based on generalized polynomial chaos expansion has emerged as a suitable alternative to standard Monte Carlo based methods that are accurate but computationally cumbersome. However, if there are non-linearities in the relationship between model inputs and model output, building a single generalized polynomial chaos expansion model leads to poor predictions. This paper investigates a Mixture-of-Experts approach based on machine-learning methods to divide the input space into subspaces that do not feature non-linearities. Then, generalized polynomial chaos expansions are built on each of these regions. This approach is applied to a reach of the Garonne River where the floodplain water height is non-linear with respect to the uncertain inputs (bottom roughness and upstream discharge), especially in locations where the topography features a strong gradient.

## I. INTRODUCTION

Real-time forecasting is an important component of flood risk management, but it is subject to multiple uncertainties caused by model inputs, initial states, model structures, and model parameters [9]. Knowledge of the type and magnitude of these uncertainties is crucial to understand and interpret the model's results.

The key part of an uncertainty quantification (UQ) analysis is the propagation of the uncertainties through the simulation model [8]. Due to the high computational cost of two-dimensional hydrodynamic simulators, the direct use of methods based on Monte Carlo sampling is excluded. Surrogate models are thus used to overcome this issue [4] [16].

From the class of surrogate models, generalized polynomial chaos expansions (gPCE) has proven useful in a wide range of applications for emulating responses of computational models with random input, quantifying output uncertainty, and providing sensitivity indices with, in particular, an analytical formula for expectation, variance and Sobol' indices [3]. This surrogate model relies on a functional representation of output random variables as an expansion in terms of orthonormal basis functions and is built on an efficient space-filling sampling of the uncertain parameter space. However, the gPCE model tends to struggle when applied to problems related to unsteadiness, stochastic discontinuities, long-term integration, and large perturbation [25].

Different approaches with varying degrees of complexity have been proposed in the literature to address this kind of behavior. Examples include multi-resolution / multi-element polynomial chaos expansions [20] [25], regression trees [10] [17], multivariate adaptive regression splines [13], among others. They rely on the idea of partitioning the input parameter space into (often disjoint) subspaces, followed by the use of regression-based surrogates in each subspace with an intrusive approach. In this paper, we propose a non-intrusive Mixture-of-Experts (MoE) approach based on machine-learning tools to handle non-linearities in a gPCE-UQ workflow that stands on the “divide-and-conquer” principle. The general outlines of gPCE modeling are first introduced. This is followed by a description of the different blocks of the MoE. Finally, the Garonne River (Southwest France) hydrodynamic test case, where the floodplain water height is non-linear due to the combination of random model inputs (bottom roughness and upstream discharge) and properties of the terrain, is used to show the effectiveness of the proposed approach.

## II. PROBLEM SPECIFICATION

### A. Study area

The study area extends over a 50 km reach of the Garonne River (France) between Tonneins (upstream), downstream of the confluence with the River Lot, and La Réole (downstream). This part of the valley was equipped in the 19<sup>th</sup> century with infrastructure to protect the Garonne flood plain from flooding events. A system of longitudinal dykes and weirs was progressively constructed after the 1875-flood to protect the floodplains and organize submersion and flood retention areas.



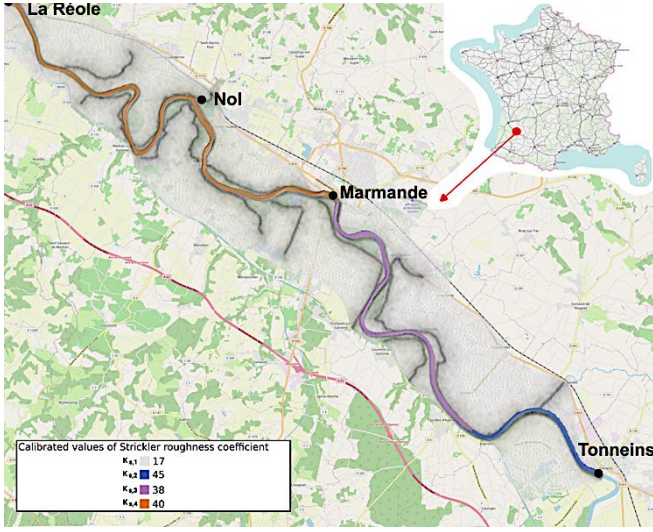


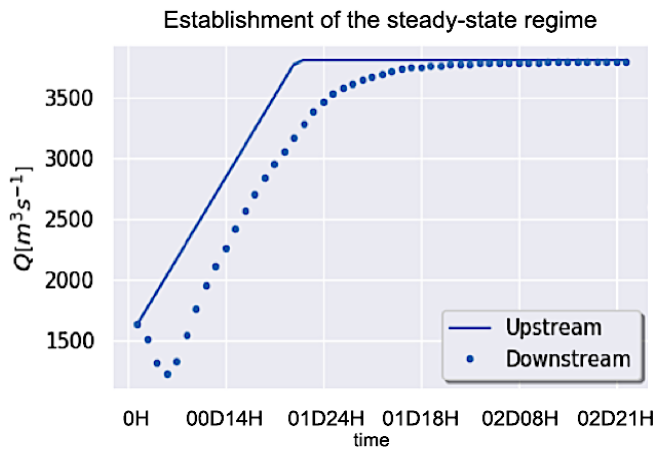
Figure 1: Zoning of the roughness coefficient over the study area.

### B. Hydraulic modeling

The TELEMAC-2D (T2D) model, constituted by a triangular mesh of the study area of some 41 000 nodes with a refined mesh size near the dykes (see Fig. 1), has an upstream discharge imposed at Tonneins, and downstream, a stage-discharge rating curve corresponding to the stream gauge at La Réole. This hydraulic model has been realized by Besnard and Goutal (2008) [1]. The dynamic is solved by the 2D solver of the TELEMAC software [11] based on the resolution of the shallow water equations in the non-conservative form using the finite element method. The results of the simulation are water height and mean velocity on the vertical axis at each node in the mesh [14]. In this paper, a focus will be given to the water height in node 35067 (NoI) located on a ditch downstream of a dyke (see Fig. 1) in Sainte-Bazeille commune.

### C. Model uncertainties characterization

In this study, we consider the effect of two sources of uncertainty on water height  $h$  for flood events, respectively Strickler roughness coefficient  $K_s$  which characterizes the

Figure 2: The uncertain input variable  $Q_{up}$  is a steady-state value reached through a ramp function.

roughness of the river bottom, and the upstream discharge  $Q_{up}$  resulting from the establishment of the steady-state regime, as shown in Fig. 2 for the node NoI. The ramp lasts one day and the constant hydraulic inflow two days at  $Q_{up}$ .

The Strickler roughness coefficient  $K_s$  is defined according to 4 areas, as shown in Fig. 1: grey for the floodplain ( $K_{s,1}$ ), and blue, purple, and orange for the upstream ( $K_{s,2}$ ), middle ( $K_{s,3}$ ), and downstream ( $K_{s,4}$ ) parts of the main channel respectively. Its distribution is assumed to be uniform, and its range is set to cover the calibration values. The upstream discharge is assumed to follow a Gaussian distribution centered around the biennial flood at Tonneins  $3\,300\text{ m}^3\text{s}^{-1}$ , of a standard deviation of  $1\,100\text{ m}^3\text{s}^{-1}$ . Moreover, to avoid too high or too low values, the probability density is truncated at  $600\text{ m}^3\text{s}^{-1}$ , corresponding to the annual mean discharge, and  $6\,000\text{ m}^3\text{s}^{-1}$ , corresponding to the vicennial flood at Tonneins. Tab. 1 summarises the distribution of uncertain model inputs.

TABLE 1: PROBABILITY DISTRIBUTION OF THE UNCERTAIN INPUT VARIABLES

Uncertain variable	Calibration values	Distribution
$K_{s,1} [\text{m}^{1/3}\text{s}^{-1}]$	17	$\mathcal{U}[5, 20]$
$K_{s,2} [\text{m}^{1/3}\text{s}^{-1}]$	45	$\mathcal{U}[40, 50]$
$K_{s,3} [\text{m}^{1/3}\text{s}^{-1}]$	38	$\mathcal{U}[33, 43]$
$K_{s,4} [\text{m}^{1/3}\text{s}^{-1}]$	40	$\mathcal{U}[35, 45]$
$Q_{up} [\text{m}^3\text{s}^{-1}]$	—	$\mathcal{N}(3\,300, 1\,100)$

### D. Computing environment

CERFACS's cluster has been used to run T2D simulations. Simulating the river and the floodplain dynamics takes about 6 minutes on 15 cores, for the study case presented in Sect. II. A over three days. This cost is not practical in the context of the UQ framework requiring thousands of T2D simulations to estimate statistics. Hence the importance of replacing the numerical simulator with a surrogate model [18].

## III. GENERALIZED POLYNOMIAL CHAOS EXPANSION-BASED UNCERTAINTY PROPAGATION

### A. Generalized Polynomial Chaos Expansion

Let us consider a computational model  $\mathcal{M}: x \in \mathcal{D}_x \subset \mathbb{R}^d \mapsto y = \mathcal{M}(x) \in \mathbb{R}$ . Suppose that the uncertainty in the input parameters is modeled by a random vector  $X$  with prescribed joint probability density function (PDF)  $f_X(x)$ . The resulting (random) quantity of interest  $Y = \mathcal{M}(X)$  is obtained by propagating the uncertainty in  $X$  through  $\mathcal{M}$ . Assuming that  $Y$  has a finite variance (which is a physically meaningful assumption when dealing with hydrodynamical systems), it belongs to the so-called Hilbert space of second-order random variables, which allows for the following spectral representation to hold [7]:

$$Y = \sum_{j=0}^{\infty} y_j Z_j. \quad (1)$$



The random variable  $Y$  is therefore cast as an infinite series, in which  $\{Z_j\}_{j=0}^{\infty}$  are multivariate orthonormal polynomials in the input vector  $X$ , i.e.,  $Z_j = \Psi_j(X)$ .

We assume that the input variables are statistically independent so that the joint PDF is the product of the  $d$  marginal distributions:  $f_X(x) = \prod_{i=1}^d f_{X_i}(x_i)$ , where the  $f_{X_i}(x_i)$  are the marginal distributions of each variable  $\{X_i, i = 1, \dots, d\}$  defined on  $\mathcal{D}_{X_i}$ . It can be proven that the set of all multivariate polynomials in the input random vector  $X$  forms a basis of the Hilbert space in which  $Y = \mathcal{M}(X)$  is to be represented [7]:

$$Y = \sum_{\alpha \in \mathbb{N}^d} y_{\alpha} \Psi_{\alpha}(X), \quad (2)$$

where  $\Psi_{\alpha} = \prod_{i=1}^d \phi_{\alpha_i}$  and  $(\phi_{\alpha_i})_{i \geq 0}$  is an orthonormal basis for  $X_i$ .

For standard uncertain input distributions, the associated families of orthonormal polynomials are well known [5]. Given the set of these polynomial bases  $(\Psi_{\alpha}(X))$ , the next step is to compute the gPCE coefficients  $(y_{\alpha})$ . In this study, we focus on a particular non-intrusive approach based on the least-square analysis to compute the coefficients of gPCE from repeated evaluations of the existing model  $\mathcal{M}$  considered as a black-box function. By selecting an orthonormal basis with respect to the input parameter distributions, the corresponding coefficients can be given a straightforward interpretation: the first coefficient  $y_0$  is the mean value of the model output, whereas the variance is the sum of the squares of the remaining coefficients [5]. Similarly, the Sobol' indices, commonly used for sensitivity analysis study, are obtained by summing up the squares of suitable coefficients [3].

#### A. Error metrics

In the present study, two standard metrics are used to measure the quality of the gPCE surrogate model: the  $Q_2$  predictive coefficient and the Root Mean Squared Error (RMSE). The validation is carried out over an input-output validation database  $D_v$  of size  $N_v$ .

At the  $k^{\text{th}}$  mesh node, the  $Q_2$  predictive coefficient reads:

$$Q_2 = 1 - \frac{\sum_{i=1}^{N_v} (h_k^{(i)} - \bar{h}_k^{(i)})^2}{\sum_{i=1}^{N_v} (h_k^{(i)} - \bar{h}^{(i)})^2},$$

Where  $\bar{h}^{(i)} = \frac{1}{N_v} \sum_{k=1}^{N_v} h_k^{(i)}$ .

#### B. Hydrodynamic uncertainty propagation using gPCE

[19] showed that, in a two-dimensional hydrodynamic steady regime, the gPCE model drastically reduces the number of runs needed for propagating uncertainty and could be applied to more complex studies. Moreover, [23] highlights that considering the large dimension of the water height, combining the surrogate model with a space reduction method allows good learning at a reduced computational cost.

In that respect, a reduced gPCE is used here to replace the T2D model to propagate uncertainty at a reduced cost for the transitional flow regime. Learning and validation databases of size 1 000 and 500 respectively are considered. The inputs are sampled according to an optimized LHS [26] following their

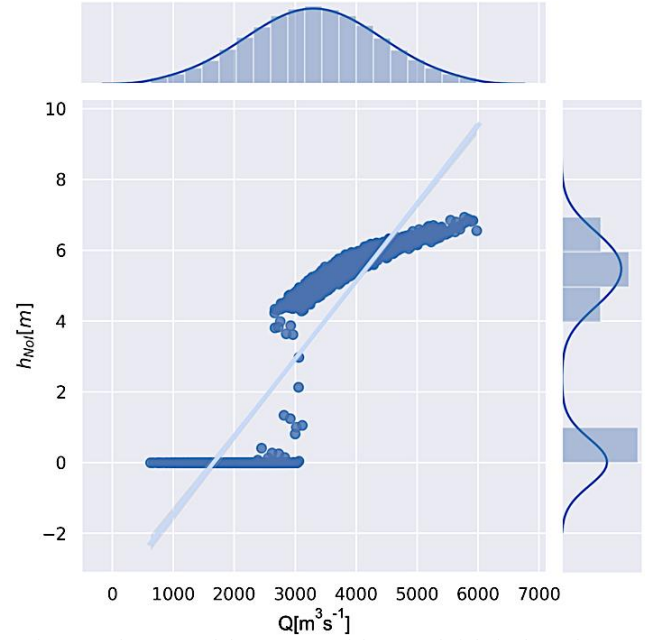


Figure 3: The PDF and the response of the water height in the node NoI to the upstream discharge.

PDF defined in Tab. 1. The gPCE surrogate is computed for each time step of the integration from time  $t_{\text{initial}} = 0$  second corresponding to the time of injection of the flow discharge upstream of the study area, to time  $t_{\text{final}} = 3$  days corresponding to the setting up of the steady-state regime. While the predictive coefficient  $Q_2$ , evaluated on the validation database considering all mesh nodes for  $t_{\text{final}}$  is equal to 1, it is significantly smaller than 1 during the transition phase before setting up the steady-state regime. In order to understand why the gPCE surrogate model does not correctly predict the water height  $h$  simulated with the T2D during the transient phase, a time of this latter has been chosen  $t_{\text{intermediate}} = 1$  day 2 hours, and only one mesh node has been selected which is the NoI node. This is the configuration where the worst RMSE value has been recorded. The gPCE degree  $P$  was varied between 0 and 24. The optimal  $P$  in this case is 4 allowing to have a  $Q_2$  of 0.54, and an  $RMSE$  of 0.92 m, which is statistically not satisfactory.

Furthermore, as shown in Fig. 3, the PDF of  $h$  at node NoI is bimodal and the response function according to  $Q_{\text{up}}$  is non-linear. Indeed, as the node NoI is on a ditch, upstream discharge values that are lower than 3 000  $\text{m}^3\text{s}^{-1}$  lead to almost zero water depth. And upstream discharge values higher than 3 000  $\text{m}^3\text{s}^{-1}$  lead to water depth values higher than 4 m. Thus, the gPCE surrogate model is not a good choice to approach non-linear functions because of its inherent smoothness.

Advanced strategies should then be applied. In this study, a Mixture-of-Experts (MoE) approach is used in order to improve gPCE performance. This approach is based on machine-learning methods allowing to decompose the random inputs space into subspaces over which the solution varies smoothly and consequently build a global representation as a collection of smooth representations defined over subspaces.

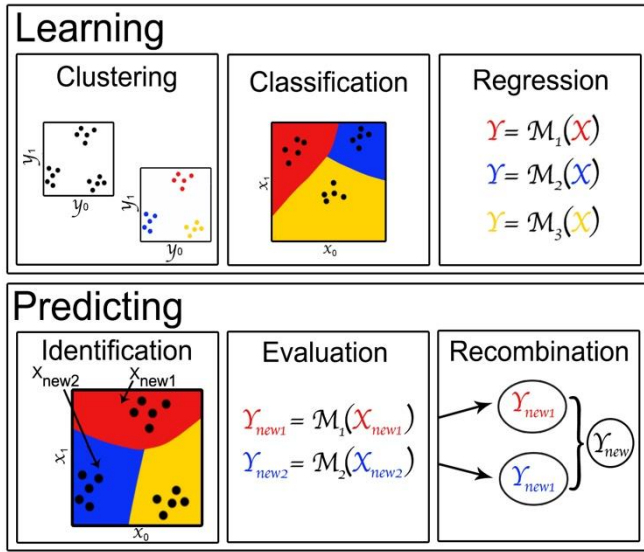


Figure 4: Illustration of the Mixture-of-Experts approach.

#### IV. MIXTURE OF GPCE EXPERTS FOR UQ

##### A. Workflow of the MoE

The proposed approach for handling non-smooth functions consists of the following steps, as illustrated in Fig. 4:

- **Learning:**

- 1) *Clustering*: this is the first step of the approach when the analyst attributes to each output observation  $y^{(i)}, i = \{1, \dots, N\}$  a class that corresponds to an identified behavior of the system. In the ideal case, this can be done manually using expert knowledge.

In the general case, it is more convenient to rely on an automated approach where the  $K$  classes are directly learned from the data using unsupervised learning algorithms [6] as K-Means [2] and DBSCAN [15].

- 2) *Classification*: once the classes are identified, they are mapped to the input space. This latter is then split according to the labels resulting from the clustering of the output space. This can be done via the SVM algorithm [12] [24].
- 3) *Regression*: the dataset is split into the different groups identified in the previous two steps. For each group, a local gpCE  $\{\hat{M}_k, k = 1, \dots, K\}$  is built.

- **Predicting:**

Once the local models are built, it is necessary to recombine them when evaluating a new point from the input space. This is achieved in three steps:

- 1) *Identification*: this involves identifying the class to which belongs the new point. The previously built classifier can be used in that respect.
- 2) *Evaluation*: the new point is then projected in the output space using the appropriate gpCE model.

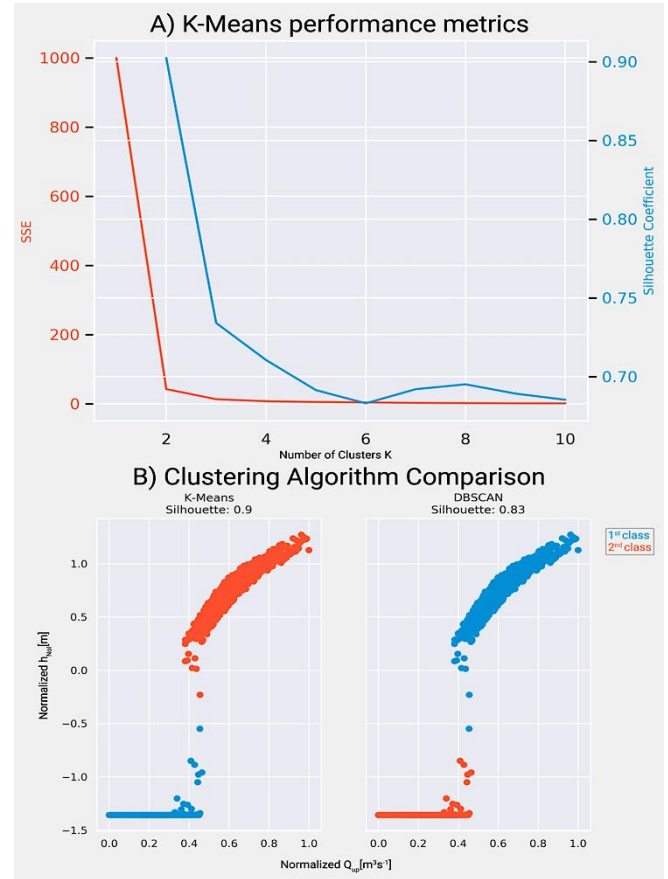


Figure 5: A) The top curve represents the evolution of the two metrics: the sum of squared errors in red, and the silhouette coefficient in blue for the K-Means clustering method. B) The result of the clustering of the water height according to the upstream discharge, left: K-Means; right: DBSCAN. In blue, the first class detected by the algorithm and in red the second class.

- 3) *Recombination*: the final approximation is obtained by combining the different predictions as follows:

$$\hat{M}(x) = \sum_{k=1}^K w_k(x) \hat{M}_k(x), \quad (3)$$

$w_k(x)$  are weight functions defined such that  $\sum_{k=1}^K w_k(x) = 1$ . There are two main types of weight functions: binary approach and weighting approach. In the present study, only the first approach was investigated.

##### B. Validation of the MoE on the hydraulic test case

For the K-Means clustering algorithm, data are split into  $K$  clusters. Two methods are commonly used to evaluate the appropriate number  $K$ : The elbow method [22] and the silhouette coefficient [21].

For the elbow method, the  $x$ -value of the elbow point is thought to be a reasonable trade-off between error and the number of clusters. The red curve in Fig. 5. A. shows the evolution of the sum of squared errors (SSE) of classification according to the number of clusters  $K$ , and it indicates that the elbow point in the SSE curve is located at  $K = 2$ .

The silhouette coefficient is a measure of cluster cohesion and separation. It quantifies how well a data point fits into its assigned cluster based on two factors:

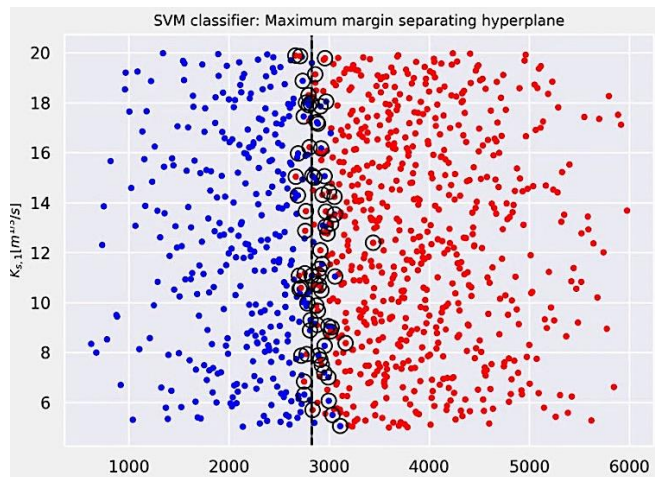


Figure 6: SVM-based classification.

- How close the data point is to other points in the cluster,
- How far away the data point is from points in other clusters.

A high value of this coefficient indicates that samples are closer to their clusters than they are to other clusters. In Fig. 5. A., the blue curve represents the silhouette coefficient and shows that the best choice for  $K$  is 2 since it has the maximum score. Thus, the best number of classes for the K-Means based on the results of those two metrics is  $K = 2$ . The resulting clustering is shown in Fig. 5. B as well as the clustering of the DBSCAN algorithm. Although the two algorithms do not process in the same way, their results are similar, with more cluster refinement for K-Means (silhouette = 0.9). Therefore, the clustering algorithm retained is K-Means with  $K = 2$ .

Once these 2 clusters are defined according to the K-Means clustering labels, these latter are mapped to the input space as shown in Fig. 6. The input space is then divided into two classes, blue and red. The separation hyperplane is mainly dependent on the upstream discharge injected at Tonneins and corresponds to a value of  $Q = 2700 \text{ m}^3/\text{s}$ . This value is physically significant; it matches the bank-full discharge in the main channel. Thus, a possible interpretation of the hyperplane plotted in a black line in Fig. 6, is the stage at which the main channel and floodplain become connected.

The next step is the construction of an appropriate gPCE surrogate model in each class. To have a good gPCE model, it is necessary to have an optimal degree  $P$ , and thus to loop to get the best  $P$ . For that purpose, the polynomial degree  $P$  was varied between 1 and 9, and the optimal degree selected is the one that gives an optimal  $RMSE$  and  $Q_2$  calculated on the validation database. The proposed approach improves the prediction, as shown in Tab. 2.

TABLE 2: COMPARISON OF THE RESULTING ERRORS

Surrogate models' performance	gPCE	MoE-gPCE
RMSE [m]	0.92	0.02
$Q_2$	0.54	0.98

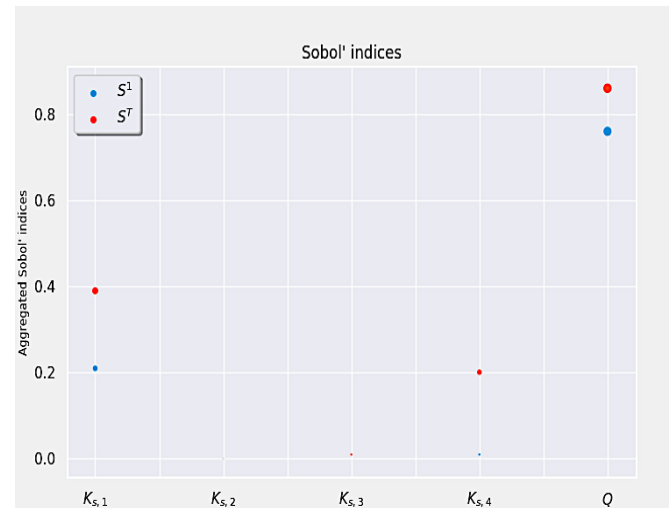
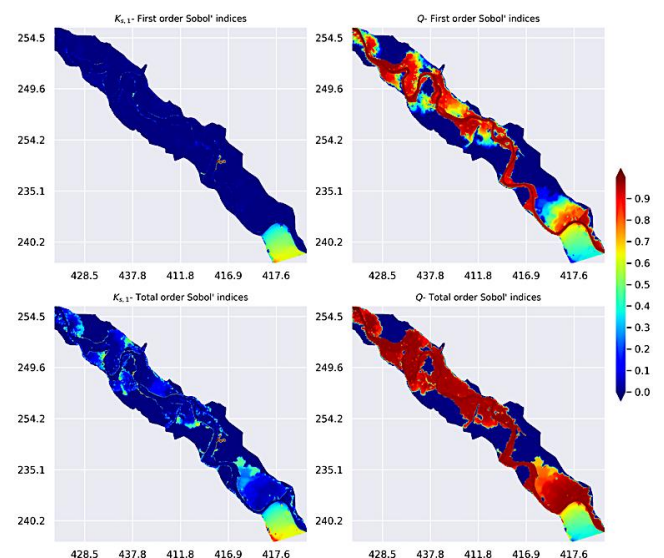


Figure 7: Sobol' indices for water height at node NoI.

Indeed, the  $RMSE$  of the MoE-gPCE model is 2 cm, contrary to the  $RMSE$  of the general model based on a single gPCE surrogate model, which is approximatively equal to 1 m, and the  $Q_2$  of the MoE-gPCE is 0.98 whereas it is 0.54 for the classic gPCE.

The computation of spatially aggregated first-order Sobol' indices for sensitivity analysis from the gPCE coefficients shows that the water height at the node NoI is mainly governed by the upstream discharge injected at Tonneins (76%) and is weakly governed by the roughness at the bottom of this node (21%) as illustrated in Fig. 7. The total order Sobol' indices highlight the interaction of the variables  $K_{s,1}$  and  $Q$  with the other variables. Indeed, the total order Sobol' indices of  $K_{s,1}$  is 39%, which means a contribution of the interaction of this variable with the other variables on the variability of the water height at this node.

Figure 8: Spatial aggregated Sobol' indices, first at the top and total in the bottom, for the water height discretized over the mesh following the uncertain inputs:  $K_{s,1}$  on the left, and  $Q$  on the right.

The MoE-gPCE proved to be robust for the NoI node where the water height is non-linear, so it was applied for all other points where the *RMSE* is greater than 0.3 m by applying a single reduced gPCE. This modeling over the whole mesh allowed to have the different statistics over the study area, in particular the mean, the upper quartile, the variance, and Sobol' indices displayed for the uncertain variables  $K_{s,1}$  and  $Q$  in Fig. 8. This figure shows that, for the transitional regime studied here, the variance of the water height over the study area is mostly explained (84% on average) by the upstream discharge  $Q$ . Moreover, the water height variability in the floodplain near the liquid boundary condition at the upstream part of the numerical model is shared between the influence of the floodplain roughness coefficient  $K_{s,1}$  and the upstream discharge  $Q$ , which is consistent with the numerical artefact of the T2D modeling mentioned in [1] and related to the neighbourhood of the upstream liquid boundary. The large areas next to the edges of the study area show no influence either from the upstream discharge  $Q$  either from the floodplain roughness coefficient because they are not wet at the time  $t_{intermediate}$ . Otherwise, the roughness coefficients of the bottom of the main channel  $K_{s,2}$ ,  $K_{s,3}$  and  $K_{s,4}$  have almost no influence on the variability of the water depth over the study area.

Total order Sobol' indices highlight the multivariate effects of the different input variables. Note that the results of the sensitivity analysis are dependent on the distribution of the uncertain input variables and the degree of truncation of polynomial expansion.

## V. CONCLUSION AND PERSPECTIVES

This paper presents the Mixture of generalized polynomial chaos expansion experts approach (MoE-gPCE) allowing to deal with local non-linearities and to take advantage of the benefits of generalized polynomial chaos expansion (gPCE) model. Focus is given to the particular hydrodynamic case when multiple behaviors of the water height can be observed. The proposed approach consists of first identifying such behaviors and then classifying them using a support vector machine algorithm. The resulting prediction is obtained by building local gPCE in each subspace and then recombining them using a binary scheme. When applied to the water height at a node downstream of a dyke (NoI), this approach has led to the emergence of two classes in which the water height behaves differently depending on whether the upstream discharge is less or more the bank-full discharge in the main channel. The different statistical moments as well as the Sobol' indices were computed via MoE-gPCE. The proposed approach has been extended to all points when a single gPCE gives poor predictions.

However, the accuracy of the resulting predictions relies on the accuracy of the classification step. This step can be improved using adaptive sampling to better define the boundary between the two subspaces. Furthermore, improving the performance of gPCE for all mesh nodes using the proposed approach is equivalent to construct 72 000 gPCE (3 000 nodes where a single gPCE is not accurate, 8 values of the gPCE degree  $P$ , 3 potential number of classes) which is

relatively expensive, hence the need to find a method allowing the execution of MoE-gPCE at a reduced cost in the context of high output dimension.

## ACKNOWLEDGEMENT

We would like to thank EDF R&D's PRISME department for their support in using OpenTURNS. We thank all these people for the enriching discussions we were able to have on uncertainty methods for two-dimensional river hydraulics issues.

## REFERENCES

- [1] A. Besnard, N. Goutal, "Comparison between 1D and 2D models for hydraulic modeling of a floodplain: case of Garonne River", *Houille blanche, Revue internationale de l'eau*, 2011, pp.42-47.
- [2] A. Likas, N. Vlassis and J. Verbeek, "The global k-means clustering algorithm", *Pattern Recognition*, 36, 2003, pp. 451-461.
- [3] B. Sudret, "Global sensitivity analysis using polynomial chaos expansion". In P. Spanos and G. Deodatis (ed), *Proc. 5<sup>th</sup> Int. Conf. on Comp. Stoch. Mech. (CSM5)*, 2006.
- [4] B. Sudret, S. Marelli and J. Wiart, "Surrogate models for uncertainty quantification: An overview", 11<sup>th</sup> European Conference on Antennas and Propagation (EUCAP), Paris, 2017, pp.793-797.
- [5] B. Sudret, "Uncertainty propagation and sensitivity analysis in mechanical models", *Contributions to structural reliability and stochastic spectral methods*, Tech. rep., Université Blaise Pascal, Clermont-Ferrand, 2007, France.
- [6] C. M. Bishop, "Pattern recognition and machine learning", Springer, 2016.
- [7] C. Soize, R. Ghanem, "Physical systems with random uncertainties: chaos representations with arbitrary probability measure", *SIAM J. Sci. Comput.*, 2004, 26(2), pp.395-410.
- [8] E. de Rocquigny, et al., "Uncertainty in industrial practice: A guide quantitative uncertainty management", January 2008.
- [9] E. M. Mockler, K. P. Chun, G. Sapirza-Azuri, M. Bruen Gonzalo and H. S. Weather, "Assessing the relative importance of parameter and forcing uncertainty and their interactions in conceptual hydrological model simulations," *Adv. in Water Resources*, 2016.
- [10] H. A. Chipman, E. I. George and R.E. McCulloch, "BART: Bayesian Additive Regression Trees", *Annals of Applied Statistics*, 2010, 4(1), pp.266-298.
- [11] J. C. Galland, N. Goutal, J. M. Hervouet, "Telemac: A new numerical model for solving shallow water equations", *Advances in Water Resources*, 1991, 14(3), pp.138-148.
- [12] J. C. Platt, "Probabilistic outputs for support vector machines and comparisons to regularized likelihood methods", 1999.
- [13] J. H. Friedman, "Multivariate adaptive regression splines", *Annals of Statistics*, 1991, 19(1), pp.1-67.
- [14] J. M. Hervouet and P. Bates, "The TELEMAT Modelling System", 2000, Wiley.
- [15] K. Khan et al., "DBSCAN: Past, present and future", *ICADIWT*, 2014.
- [16] K. Sargsyan, "Surrogate models for uncertainty propagation and sensitivity analysis". In: R. Ghanem, D. Higdon, H. Owahdi (ed) *Handbook of uncertainty quantification*. Springer, Cham, 2015.
- [17] L. Breiman, J. Friedman, C. J. Stone, and R. A. Olshen, "Classification and regression trees", 1984, CRC press.
- [18] M. De Looze, "Surrogate modeling and multifidelity approach in computer experimentation", *Journal de la Société Française de Statistique*, 2015, 156(3).
- [19] N. Goutal, et al., "Uncertainty quantification for river flow simulation applied to a real test case: The Garonne valley", *SimHydro*, 2017.
- [20] O. L. Maitre, H. Najm, R. Ghanem, and O. Knio, "Multi-resolution analysis of Wiener-type uncertainty propagation schemes", *Journal of Computational Physics*, 2004, 197(2), pp.502-531.



- [21] P. J. Rousseeuw, "Silhouettes: a graphical aid to the interpretation and validation of cluster analysis", *Journal of computational and applied mathematics*, vol. 20, 1987, pp.53-65.
- [22] R. I. Thorndike, *Psychometrika*, vol. 18, 1953, pp.266-267.
- [23] S. El Garroussi, M. De Lozzo, S. Ricci, D. Lucor, N. Goutal, C. Goeury, "Uncertainty quantification in a two-dimensional river hydraulic model", UNCECOMP 2019, 3<sup>rd</sup> ECOCOMAS Thematic Conference on uncertainty quantification in computational sciences and engineering. Crete, Greece, 24-26 June 2019.
- [24] V. N. Vapnick, "The nature of statistical learning theory", Springer-Verlag, 1995.
- [25] X. Wan and G. E. Karniadakis, "Multi-element generalized polynomial chaos for arbitrary probability measures", *SIAM J. Sci. Comput.*, 2006, 28(3), pp.901-928.
- [26] G. Damblin, M. Couplet and B. Iooss, "Numerical studies of space filling designs: optimization algorithms and subprojection properties", *Journal of Simulation*, 2013, 7, pp.276-289.

# Pumping station design based on shape optimization process

Florent Taccone, Cédric Goeury, Fabrice Zaoui  
National Laboratory of Hydraulics and Environment  
EDF R&D  
Chatou, France  
florent.taccone@edf.fr

Adrien Petralia  
Polytech' Lyon / EDF R&D  
Lyon, France  
Chatou, France

**Abstract**— Optimization applications with TELEMAC are increasing due to interoperability development of the system module. The present work is based on a shape optimization process apply to a real problem: the optimization of the streamline trajectories in front of a pumping station intakes. Deflectors have been designed in the model upstream of the intakes to drive the flow as perpendicular as possible to the intake entrances. The deflector's shape is defined based on two parameters controlling the size and the orientation respectively.

In a first step, a cost function evaluating the orientation of the streamlines was defined. Then, a study was carried out on these two parameters to estimate, for each deflector, which configuration minimizes the cost function based on TELEMAC-2D runs. Finally, a statistical emulator was used to link the input parameters with the cost function residual. Indeed, this metamodeling technique allowed a simplification of the TELEMAC-2D study, drastically reducing computational times. This was particularly useful to apply an optimization process on the parameters of the shapes, requiring many TELEMAC-2D study runs.

The results of this study allowed identifying an optimal shape for each deflector, while ensuring a certain robustness of the solution.

## I. INTRODUCTION

TELAPY, the API interface of the TELEMAC-MASCARET platform [1], allows the application of transverse mathematical tools for hydraulic studies with TELEMAC-2D. Its python interface offers the possibility to encapsulate a TELEMAC-2D run in OpenTURNS algorithms ([www.openturns.org](http://www.openturns.org)). Thus, [2] shows an example of uncertainty quantification on the input parameters of a TELEMAC-2D model. This type of method has also been applied for optimization processes in [3], in particular with automatic calibration applied on the bottom friction coefficient and tidal parameters, in comparison with measured data. [4] presents a schematic case of shape optimization on which the optimization process is applied. This is a fish pass for which shapes are defined to maximize the flow velocity in the central compartment. These shapes are introduced into the contour of the mesh and a cost function is evaluated on the TELEMAC-2D run to assess the relevance of the shapes to the targeted problem. As these shape optimization processes require a lot of evaluation of the numerical model, it is important, in this study with a large domain, to be interested in the metamodeling techniques developed in [5]. Indeed, the creation of a statistical model allows a quasi-instantaneous evaluation of an approximation of the

TELEMAC-2D model, where the approximation error can be estimated.

The aim of this study is to optimize the efficiency of pumps in a water intake station by modifying the streamlines upstream. In this framework, this work designs deflectors in the channel, before the intakes, to allow the flow to enter perpendicularly. The deflector shape should therefore allow the best possible response to the problem, while respecting the physical constraints of the pumping station channel.

After presenting the tools used in this study in section II, the first step in this work is to carry out a parametric study. This study is organized as follow:

1. The construction of the TELEMAC-2D model and the associated hydrodynamic parameters are presented in section III.A.
2. The location and shape of the deflectors, the physical constraints associated with its shapes and the parameters describing them will be defined in III.B
3. The cost function to evaluate the perpendicularity of the current lines at the inlet of the intakes is described in III.C.
4. Finally, a large number of TELEMAC-2D simulations are run with randomly drawn deflector parameters to determine which shape minimizes the cost function, as presented in III.D.

In a second step, described in section IV, a statistical model linking the shape definition parameters and the residuals calculated during the parametric study will be created. By applying an optimization algorithm to this statistical model, it is possible to obtain optimal shapes to respond to the problem of perpendicularity of the water lines. The study of the statistical model will also give the possibility to evaluate the smoothness of the solution in order to have an idea of the robustness of the solution (how a small change in the shape parameter influence the cost function evaluation).

## II. PRESENTATION OF THE TOOLS

### A. TELEMAT-MASCARET Python tools

#### 1) TelApy

TelApy [1] is a Python module that is part of the TELEMAT system. It is an API, Application Programming Interface, which allows the user to interact with the core of the TELEMAT system coded in FORTRAN using Python scripts. This module allows for example to control the execution of a simulation carried out with TELEMAT-2D by retrieving information at each time step.

#### 2) Postel

Postel [8] is a Python module that is also part of the TELEMAT system. It allows to do post-processing by extracting data from the results file obtained from a simulation. It can be used as a visualization tool to plot the studied domain and the scalar fields representing the state variables of a simulation. In this case, it is mainly used to extract data for the cost function evaluation.

### B. Tools used in the SALOME platform

#### 1) GEOM

SALOME's GEOM module is a design software that allows you to create geometric objects (curves, surfaces, points, etc.) in 2D and 3D. This module can be used with the SALOME graphical interface or by using the associated Python library by calling GEOM class functions in a script. This module has been used to define the contour of the calculation domain and the mesh refinement zones.

#### 2) MESH

The MESH module of SALOME is used to mesh objects created in the GEOM module. It contains several algorithms to generate uniform but also more complex meshes. For example, it allows to mesh a domain by defining properties of sub-meshes.

#### 3) YDEFIX

Ydefix is a C++ library of the SALOME platform that allows distributing a series of calculations on the resources of a machine. In this study, it allows us to distribute the calculations of the simulations on a computing cluster. This library can be used through the SALOME platform as a Python module. It allows to execute a Python script sequentially on a large number of processors in at the same time. It is therefore possible, for example, to launch a large number of TELEMAT-2D calculations via the module TelApy simultaneously. However, technical limitations of this module does not permit to run several TELEMAT-2D computations with the internal parallelism of the code.

#### 4) OpenTURNS

OpenTURNS (Open source initiative to Treat Uncertainties, Risks'N Statistics) is a C++ library developed by EDF R&D, Airbus Group, IMACS Engineering, ONERA and PHIMECA allowing the treatment of uncertainties. This library can be controlled via a Python module or via the graphical interface of the SALOME platform. It allows a large number of applications, from data analysis to the creation of

statistical models. It also contains several optimizers to solve minimization problems.

## III. PARAMETRIC STUDY

### A. TELEMAT-2D model

The pumping station studied pumps its water from the sea and is subject to tides. The domain represents the sea offshore over a 3 km zone with a 200 m mesh size, then in the channel the mesh size is 2 m. A third refinement zone is defined along the wall on which the pumps are located with a mesh size of 20 cm. A new mesh is generated for each TELEMAT-2D run, keeping these characteristics, including the deflectors in the outline. A single mesh generation takes approximately 20 seconds.

The area of interest for the study is at the end of the channel where there are 20 intakes. The suction flow rate in the pumps are distributed as follows:

- 2 pumps with a flow discharge of 1.1 m<sup>3</sup>/s;
- 8 pumps with a flow discharge of 8.125 m<sup>3</sup>/s;
- 2 pumps with a flow discharge of 1.1 m<sup>3</sup>/s;
- 8 pumps with a flow discharge of 8.125 m<sup>3</sup>/s.

Regarding boundary conditions, there are two types in the model. The sea boundary conditions, allowing the representation of the tide in the model, and the pump boundary conditions. Concerning the tidal boundary conditions, in order to have a good representation of both the free surface dimension in the model and the the current velocity, a water height on the edge facing the channel entry and velocities, uniform over the depth, on the lateral edges are imposed. The imposed values are computed using the TPXO database and represent schematic tide of coefficient 120. For the boundary conditions of the pumping station, the suction flow rate imposed is constant, corresponding to the values described previously. In TELEMAT-2D the processing of boundary conditions is done in such a way that the velocity field is imposed perpendicularly to the boundary condition segments. As the objective is to study the direction of the flow at the entrance of the intakes a slight indentation has been created for each intake. They represent the beginning of the openings so that the entrance is not completely forced to be perpendicular. Figure 1 shows the position of boundary conditions and the definition of boundary conditions in the limits for the first 10 intakes (the last 10 being similar).

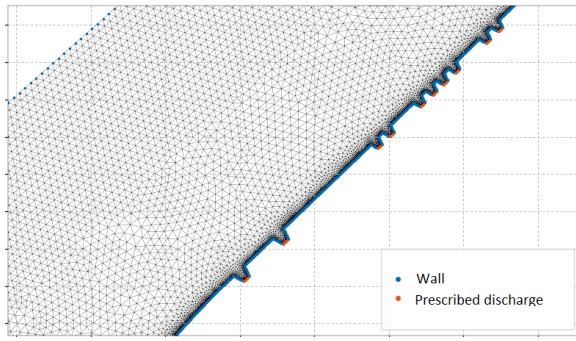


Figure 1: Visualization of the imposition of the pumping station intakes in the model

The calculation starts in a high sea state and lasts one and a half tidal cycle, i.e. 18 hours, and thus 64800 seconds. The beginning of the simulation, during the first half cycle, allows the establishment of the model to be independent from the initial condition. The results are therefore taken into account over the entire tide, in the last two-thirds of the simulation. To represent the friction effects of the bottom, a Manning-Strickler friction law is used, with a Strickler's coefficient set at  $57.6 \text{ m}^{1/3}/\text{s}$ . This value has been calibrated in a precedent study using velocity flow measurements with on several ADCP profiles.

#### B. Definition of the deflector shapes

In order to have a shape that is more adjustable than a simple circle, one opts for the catenary curve equation, a function well known in physics that describes the shape taken by a heavy and flexible cable. This shape is governed by the equation:

$$f(x) = a \cdot \cosh\left(\frac{x}{a}\right),$$

where the parameter  $a$  has the dimension of a length, and can be interpreted in its physical sense as the length of the suspended cable.

This function has been modified in this study to represent the orientation of the catenary curve. It becomes:

$$f(x) = a' \cdot \cosh\left(\frac{x+b}{a'}\right) + c,$$

with:

$$a' = -ab^2 \text{ and } c = a \cosh\left(\frac{b}{-a}\right) \text{ if } b \in [0.5; 1],$$

$$a' = -a(1+b)^2 \text{ and } c = a \cosh\left(\frac{1+b}{-a}\right) \text{ if } b \in [0; 0.5].$$

Figure 2 shows how the length parameter  $a$  influences the shape of the deflector. This parameter represents the amplitude of the shape, and it is used to define whether it will take up more or less space in the channel. It is important to note that the smaller is  $a$ , the larger is the shape.

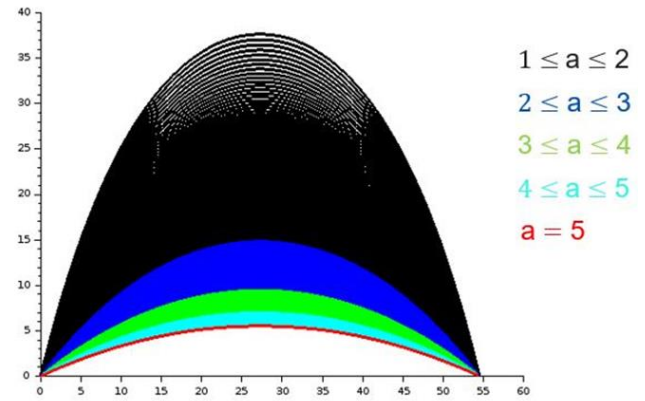


Figure 2: Illustration of the influence of the  $a$  parameter on the deflector shape ( $b=0.5$ ).

The second parameter  $b$  influences the orientation of the deflector. Figure 3 illustrates its shape, depending on the value of  $b$ .

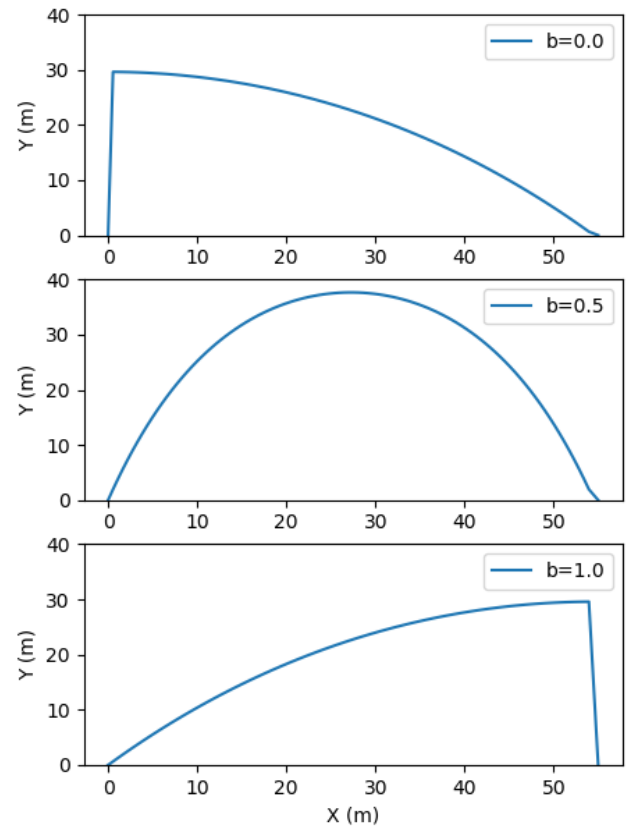


Figure 3: Illustration of the influence of the  $b$  parameter on the deflector shape ( $a=1$ ).

These deflectors are inserted in the mesh contour, on the segment preceding each group of 10 pumps. Figure 4 shows their location in the domain.



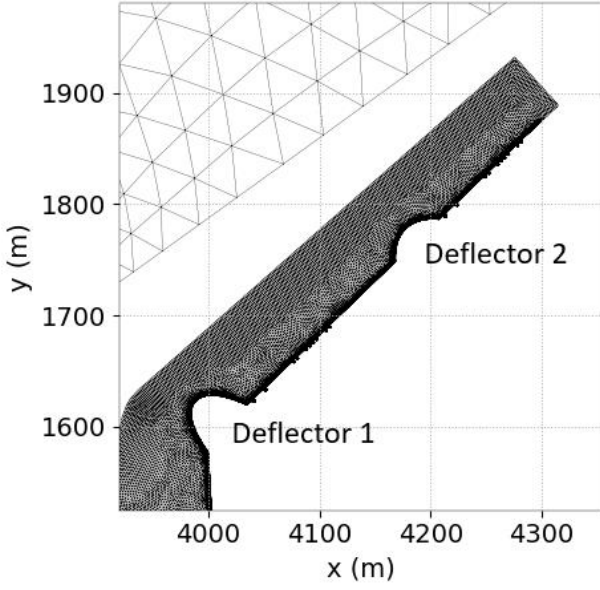


Figure 4: Location of the deflectors in the domain, here with the parameters ( $a_1 = 1, b_1 = 0.5, a_2 = 2, b_2 = 0.5$ ).

Finally, we have four parameters that govern the optimization problem. Thus, we have two parameters  $a$  and  $b$  and two deflectors, so the entry points of the study are written as  $X = [a_1, b_1, a_2, b_2] \in [1; 5] \times [0; 1] \times [2; 5] \times [0; 1]$ .

### C. Cost function

In order to optimize the pumping station efficiency, the streamlines should run as perpendicular as possible to the inlet of the intakes. The aim is to reduce the  $\alpha$  angle, shown by the black arc in Figure 5, between the normal line at the inlet and the line defined by the water velocity vectors. For every simulation, the goal is to give a single value of the residual to be able to classify the shapes of the deflectors and evaluate which one is the most appropriate for this physical issue.

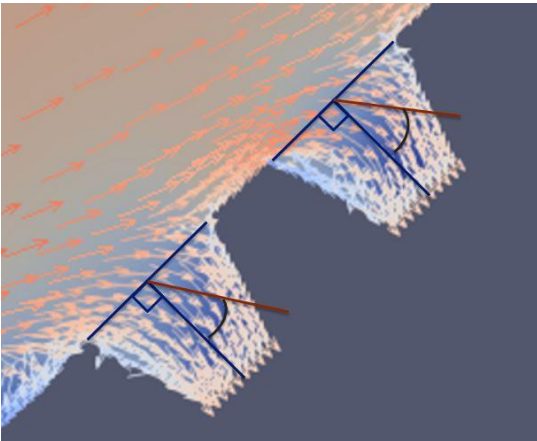


Figure 5: Schematic representation of the optimization problem.

One defines the function  $\text{atan2}(y, x)$ , with the formula:

$$\text{atan2}(x, y) = 2\arctan\left(\frac{y}{\sqrt{x^2 + y^2} + x}\right),$$

with  $x \neq 0$ . The interest of using this function lies in the fact that it allows to calculate the angle between two vectors.

With a reference system  $(\vec{i}, \vec{j})$  defined at the intake, as shown in Figure 6, one can note  $\vec{V} = \begin{pmatrix} x \\ y \end{pmatrix}$ ,  $\overrightarrow{AB} = \begin{pmatrix} x_0 \\ y_0 \end{pmatrix}$  and  $\phi = \text{atan2}(y - y_0, x - x_0)$ . We thus have  $\phi$  the angle between  $\vec{V}$  representing the velocity vector at the entrance of the intake and  $\overrightarrow{AB}$ , where A and B are the two points located at the intake entrance extremities.

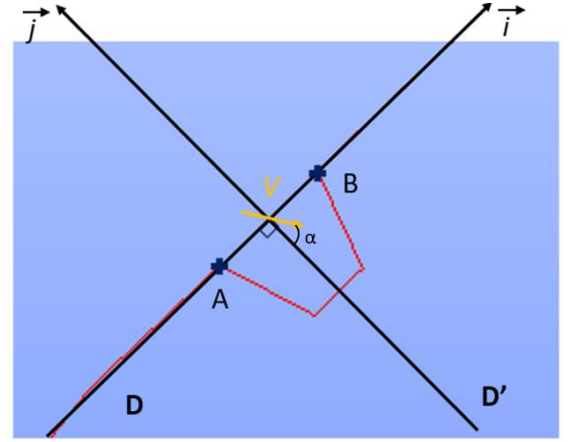


Figure 6: Illustration of the notation to define the cost function.

One then distinguishes two cases:

- If  $\phi < 0$ , the velocity vector enter the intake and we set  $\alpha = \left| \phi \right| - \frac{\pi}{2}$ ;
- If  $\phi \geq 0$ , the velocity vector enter the intake and we set  $\alpha = \pi - \left| \phi - \frac{\pi}{2} \right|$ .

We therefore have a residual angle  $\alpha$  between 0 and  $\pi$  which takes into account the direction of arrival of the vector. The minimum 0 is reached when the vector enters perpendicularly into the intake. The maximum is  $\pi$  and it is reached when the vector exits perpendicularly from the intake.

For a fixed simulation, for a time iteration in the TELEMAC-2D computation  $i$  and an intake  $j \in [1, n]$ , with  $n = 20$ , we calculate for each of the  $N$  interpolated vector  $V_{i,j}^k$  on the segment  $[A, B]_j$ , the angle between the vector  $V_{i,j}^k$  and the line normal to the segment  $[A, B]_j$ . Averaging on the  $N$  interpolated vector, one have:

$$S_{i,j} = \frac{\sum_{k=1}^N \alpha_{i,j}^k}{N},$$

with:

- $\alpha_{i,j}^k = \left\| V_{i,j}^k \right\| \left| \phi_{i,j}^k - \frac{\pi}{2} \right|$  si  $\phi_{i,j}^k < 0$ ;
- $\alpha_{i,j}^k = \left\| V_{i,j}^k \right\| \left( \pi - \left| \phi_{i,j}^k - \frac{\pi}{2} \right| \right)$  si  $\phi_{i,j}^k > 0$ .

Averaging then over the iteration number during all the computational time, and over all the intakes, one obtain the final residual estimation:

$$Res = \frac{\sum_{j=1}^n \frac{\sum_{i=0}^{n_{iter}} S_{i,j}}{n_{iter}}}{n}.$$

#### D. Sampling and results

In order to carry out the parametric study, it was necessary to sample the shape parameters in an optimal way. Indeed, it is necessary to obtain as much information as possible on the behaviour of the model output for each point  $X = [a_1, b_1] \times [a_2, b_2]$  evaluated by the TELEMAT-2D numerical model.

There are several ways to explore a given domain: divide it in a regular way (all the points in the domain are equally distributed), sampling it randomly or using quasi-random methods, known as "space filling". Given that the domain has 4 dimensions, using a regular grid would require a lot of points to evaluate in order to hope to explore the domain in an optimal way. On the other hand, the use of a random sampling method such as the Monte-Carlo method following a probability law would not allow to cover the whole space, some areas would remain unexplored. This is due to the independent nature of each point draw. There are therefore several quasi-random methods for obtaining an optimized sampling allowing exploring the domain in an optimal way without having to generate a too large sample. In our case, the LHS method (Latin Hypercube Sampling) has been used. This method is based on a uniform probability law, in our case, for each parameter. Each sample is then positioned based on the precedents so that they do not have common coordinates between them.

In order to further optimize the space coverage, 500 LHS samples are drawn and the one with the best space coverage is selected, minimizing the centered  $L_2$  discrepancy [7]. The OpenTURNS module was used to sample the shape parameters. To carry out the parametric study, a sampling of 720 points was carried out.

All 720 TELEMAT-2D runs to obtain the results files were launched using the YDEFIX module of the SALOME platform. Each calculation is carried out on a processor and the duration of a calculation is between 12 and 15 hours. The YDEFIX module also allows calculating the residuals associated with each simulation, by launching both the post-processing of the results files using Postel [8] and the evaluation of the cost function. This process takes about 2 h 30 min on 36 processors with YDEFIX, compared to more than 10 times more if the results had been evaluated sequentially. Indeed, this post treatment process is very costly because it requires the extraction of the results on 20 intake entries, for 720 results file, each one containing more than 200 frames.

Once for each calculation, a residual is identified. The minimum residual the cost function is retained and the parameters of the forms that make it possible to obtain this minimum residual is extracted. The shape obtained is described by the point  $(a_1=2.47, b_1=0.15, a_2=2.65,$

$b_2=0.15)$ . Figure 7 shows the shapes with the smaller residual. Both shapes are large and oriented towards the upstream side of the channel. This causes an acceleration of the flow on the opposite side of the channel. This also creates a small recirculation after the shapes, orienting the flow in the desired direction in the two first intakes with low suction rate. The minimum residual is 0.259345 and the maximum residual is 0.5120612 obtained for the shapes with the parameter set  $(a_1=4.43, b_1=0.53, a_2=4.36, b_2=0.53)$ .

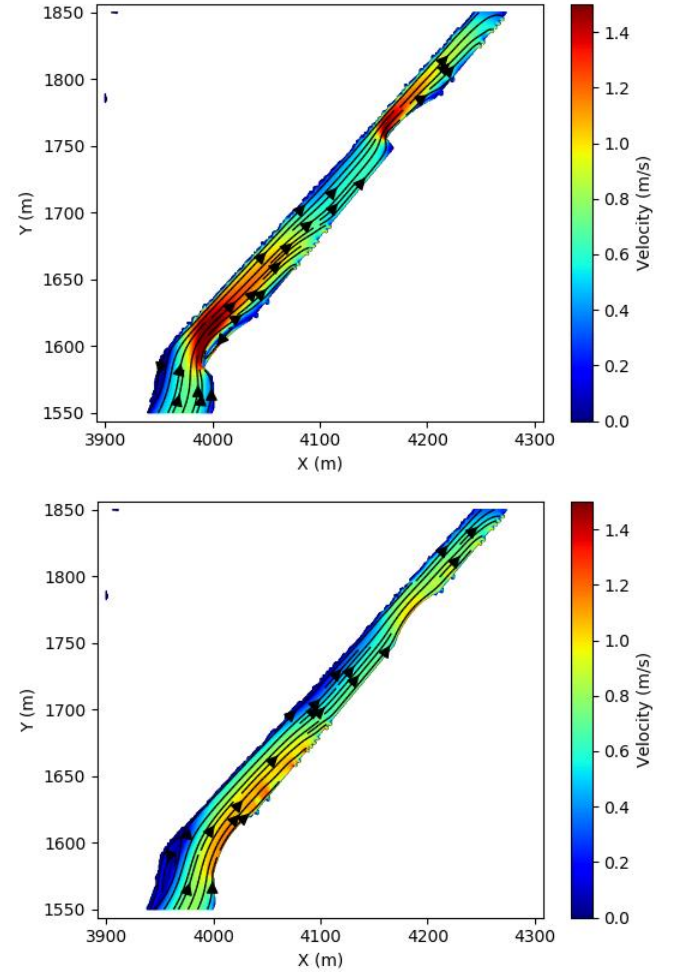


Figure 7: Shapes of the deflector minimizing (top) and maximizing (bottom) the cost function.

## VII. METAMODELING AND OPTIMIZATION

### A. Creation of the metamodel

A metamodel, is a mathematical function that allows replacing a very time-consuming model. It makes it possible to approximate the answers of a complex model, while having a very negligible calculation cost in comparison. In our case, a metamodel has been created to approximate the residuals of the cost function defined above. To generate a metamodel, the 720 points already evaluated by the TELEMAT-2D model are used as a learning data base.

As input for the model, one defines  $X_s \in \mathbb{R}^{720 \times 4}$ , all the points of the LHS experimental design. At the output, one

defines  $Y_s \in \mathbb{R}^{720}$ , the set of values of the residuals of a cost function. One then can note:

$$X_s = \begin{pmatrix} X^1 \\ \vdots \\ X^{720} \end{pmatrix} = \begin{pmatrix} a_1^1 & b_1^1 & a_2^1 & b_2^1 \\ \vdots & \vdots & \vdots & \vdots \\ a_1^{720} & b_1^{720} & a_2^{720} & b_2^{720} \end{pmatrix};$$

$$Y_s = \begin{pmatrix} Y^1 \\ \vdots \\ Y^{720} \end{pmatrix} = \begin{pmatrix} G(X^1) = Res^1 \\ \vdots \\ G(X^{720}) = Res^{720} \end{pmatrix},$$

which is the learning database for the metamodel.

The metamodel interpolation has been done with the kriging method via OpenTURNS. It consists in considering the deterministic output  $G(X^i) = Y^i, i \in [1, N]$  and  $N = 720$  obtained using the TELEMAT-2D model as the production of the random field described as:

$$G(X^i) = \beta F(X^i) + W(X^i),$$

where  $\beta F$  is the regression part of the model and  $W$  the stochastic part. The regression function used is linear. Thus, it reads:

$$\beta F(x) = \beta_0 + \sum_{i=1}^N \beta_i x_i.$$

$W$  is also called Gaussian process and one can write  $W \sim N(0, c)$  where  $c$  is a covariance function such that  $c = \sigma^2 r$  with  $R$  the correlation function. The Matérn covariance function is used. It is described as:

$$c(x, u) = \sigma^2 \frac{2^{\alpha-1}}{\Gamma(\alpha)} - \left( \sqrt{2\alpha} \left\| \frac{x-u}{\theta} \right\|_2 \right)^\alpha K_\alpha - \left( \sqrt{2\alpha} \left\| \frac{x-u}{\theta} \right\|_2 \right),$$

with  $\Gamma$  the gamma function,  $K_\alpha$  the modified Bessel function of the second kind and  $\alpha, \theta$  and  $\sigma$  three strictly positive parameters respectively set to 1.5, 1 and 1.

Let  $x^*$  be a new unsampled point, to determine its value using the metamodel. The result by Gaussian kriging is given by the Best Linear Unbiased Prediction:

$$\hat{G}(x^*)_{|X_s, Y_s} \sim N(\mu(x^*), \hat{\sigma}^2(x^*)),$$

with:

$$\mu(x^*) = \beta F(x^*) + r(x^*) R_s^{-1} (Y_s - \beta F(X_s)),$$

$$\hat{\sigma}^2(x^*) = \sigma^2 (1 - r(x^*)^T R_s^{-1} r(x^*)),$$

where one has:

$$r(x) = (R(x_1, x), \dots, R(x_N, x))^T,$$

$$(R_s)_{i,j} = R(x_i, x_j),$$

with:

$$R(x, u) = \frac{c(x, u)}{\sigma^2}.$$

[9] shows that, with a kriging interpolation, a sample size of a few hundred is sufficient to get a good estimation of the metamodel, even with high dimensional inputs (superior to 10). The size of the learning sample chosen here then appears to be sufficient. In this study, a convergence study showed that a sample of less than 100 inputs is enough in this case.

### B. Validation

In order to assess the predictivity of the metamodel, the criterion  $Q2$  is used. It requires a test database from the numerical model that was not used to create the metamodel. We therefore use 90% of the database to learn the metamodel and 10% to validate it through the  $Q2$  estimation. This coefficient quantifies the part of variance of  $\bar{Y}$ , which is the set of output values of the test database, described by the metamodel. The criterion writes:

$$Q2(Y, \hat{Y}) = 1 - \frac{\sum_{i=1}^N (Y_i - \hat{Y}_i)^2}{\sum_{i=1}^N (\bar{Y} - Y_i)^2},$$

where:

- $Y_i$  are the observed values from the test database,
- $\hat{Y}_i$  are the values predicted by the metamodel,
- $\bar{Y}$  is the calculated average of the observed values from the test database.

The closer the  $Q2$  coefficient is to 1, the better the fit of the model to the observations in the test database.

For the metamodel constructed with the cost function above presented, the predictivity criterion  $Q2$  obtained is 0.859. Figure 9 shows the differences between the evaluation by the model and the metamodel on the validation sample. It can be seen that the metamodel reproduces the TELEMAT-2D model well in most cases.

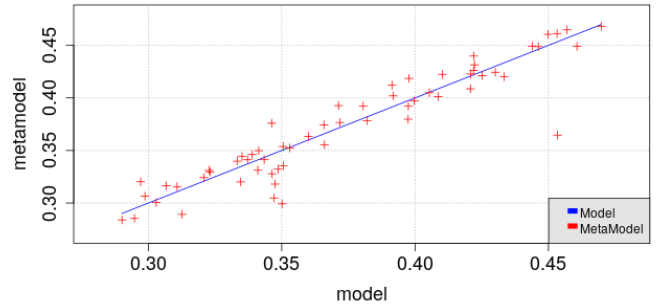


Figure 8: Validation test of the metamodel.

### C. Sensitivity analysis

Sobol analysis is a sensitivity analysis technique based on variance decomposition. Given  $X_i^k$  a random vector,  $i \in [1, n]$  with  $n$  the number of input parameters per evaluation, 4 in our case, and  $k$  the model dimension. Let  $Y^k$  be the output random variable of the model obtained with the input vector  $X_i^k$ . Then for a fixed  $k$ , one quantifies the dependence of the parameter  $Y$  on the input variables of the vector  $X_i$ . One considers the numerical model  $G$  such as:

$$Y^k = G(X_i^k).$$

Using the Sobol index method, one therefore tries to evaluate the part of the variance of the vector  $Y^k$  due to the different components of the vector  $X_i^k$ . To do this, the method is based on a decomposition of the variance  $\text{Var}[Y]$  using the Sobol-Hoeffding formula [10]:

$$\text{Var}[Y] = \sum_{i=1}^n V_i + \sum_{i<j} V_{i,j} + \sum_{i<j<l} V_{i,j,l} + \dots + V_{1,2,\dots,n},$$

with  $V_i = \text{Var}[E[Y|X_i]]$  and  $V_{i,j} = \text{Var}[E[Y|X_i, X_j]] - \text{Var}[E[Y|X_j]]$ , where  $E$  represents the expected value.

One can then define the Sobol indices:

- the first-order Sobol index, denoted  $S_i$ , which quantifies the impact caused by the variable  $X_i$  on the variance  $\text{Var}[Y]$ , independently of the interactions that  $X_i$  can exert on the other variables  $X_j$ ,  $j \neq i$ . It is expressed as:

$$S_i = \frac{\text{Var}[E[Y|X_i]]}{\text{Var}[Y]};$$

- the total Sobol index, denoted  $ST_i$ , which defines the sum of all interactions in which variable  $X_i$  is involved. It is written:

$$ST_i = \frac{\text{Var}[E[Y|X_{-i}]]}{\text{Var}[Y]},$$

with  $X_{-i}$  the vector  $X$  without its  $i^{\text{th}}$  component.

The Sobol sensitivity analysis is applied to the metamodel constructed with the cost function evaluating the orientation of the flow at the intakes. 5000 evaluations of the metamodel are used to estimate the Sobol's indices. Figure 9 shows the influence of each parameter defining the shapes by displaying their first-order and total Sobol indices. Note that the most influential parameter is parameter  $b_1$  representing the orientation of the first deflector. It can therefore be thought that this parameter is very influential in minimizing the residual of the cost function through recirculation created by this orientation, greatly influencing the direction of flow at the two first intakes. The second most important variable is the size of the first deflector, which can be explained by the fact that a shape that is too small does not generate sufficient recirculation to have a significant effect at the first intakes. Finally, it can be seen that the parameters of second deflector have little influence on the residuals. This little influence on the residuals can be explained by the fact that the second deflector is the closest to the end of the channel. The pumping here is playing a bigger role in hydraulic forcing and thus less flow is drawn to the end of the channel. The flow is therefore less likely to be parallel to the intakes and a deflector has less influence on the flow orientation.

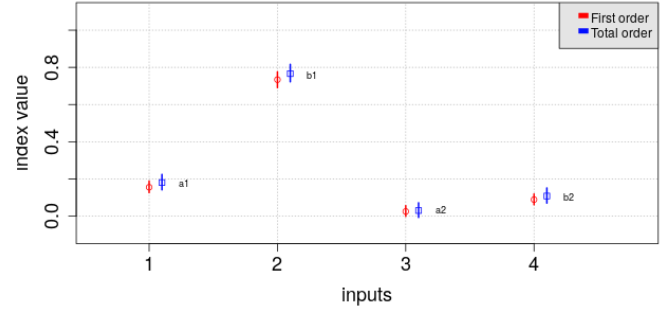


Figure 9: Sensitivity analysis of each shape parameter using Sobol indices.

#### D. Optimizer

The COBYLA optimizer is used via OpenTURNS [6]. This algorithm works on an incrementally principle: for each  $x$ , the optimizer evaluates  $f(x)$  then, from an  $x_i$  such that  $|x - x_i| < \rho$ ,  $\rho \in \mathbb{R}$ , calculates  $f(x_i)$  and compares its value to  $f(x)$ . If the new value  $x_i$  gives  $|f(x_i)| < |f(x)|$  then  $x = x_i$  is the new starting point for the next iteration. The control distance  $\rho$  is decreased during iterations in order to evaluate the minimum of the function as accurately as possible. Optimization algorithm finishes when the control radius  $\rho$  becomes less than a predefined value  $\rho_{\text{end}}$  (fixed to  $10^{-5}$ ). In other words, the initial input of the algorithm are a starting point  $x_0$ , a control radius initial  $\rho_{\text{beg}}$  and a target radius  $\rho_{\text{end}}$ . The diagram in Figure 10 can schematize it.

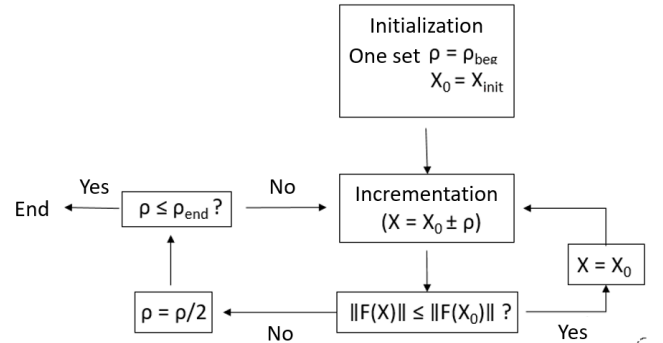


Figure 10: scheme of the COBYLA optimizer algorithm.

The main weakness of this algorithm is its inability to distinguish a local minimum from a global minimum. To overcome this disadvantage, it is necessary to make a multistart. This consists in running the algorithm several times with different starting points evenly distributed in space. The number of starting points is fixed to 500 in this study.

The optimizer has been applied to the metamodel created from the cost function. Its application gives an optimal point of  $(a_1=2.4, b_1=0.16, a_2=2.2, b_2=0.16)$ . The shape found with the parametric study thus gives a lower residual than the one found with the optimizer. However, the values of the parameters obtained are close  $((a_1=2.47, b_1=0.15, a_2=2.65, b_2=0.15)$  and  $(a_1=2.4, b_1=0.16, a_2=2.2, b_2=0.16))$  and the residuals are low for both configurations 0.259345 and 0.292294. In particular, the parameters  $b_1$  and  $a_1$ , which are the parameters identified as having the most influence during the sensitivity analysis are close. This seems to show that a small perturbation of the parameters of the first form leads to a small increase of the residual and therefore this could be a



sign that the obtained solution is robust. Figure 11 shows that the streamlines in the channel obtained with the shape from the optimizer are quite close to those observed with the shape from the parametric study in Figure 7.

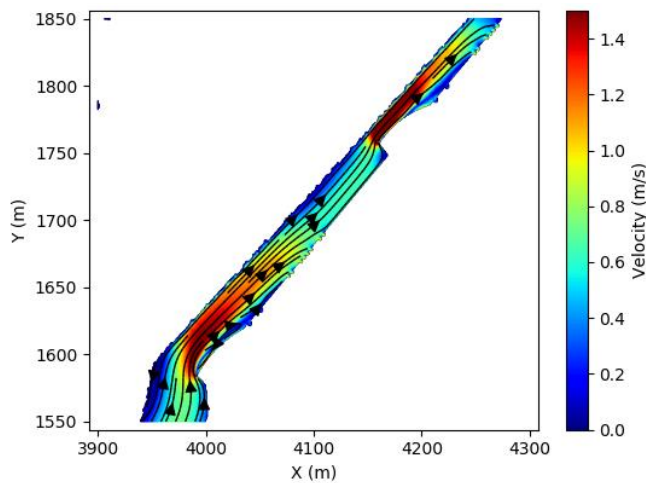


Figure 11: Velocities and streamlines for the shape obtained with the COBYLA optimizer.

### VIII. CONCLUSION

This paper presents an optimization study of the shape of deflectors in a pumping station in order to orient the flow as well as possible in its intakes.

First, after having built the TELEMAC-2D model, the shapes of the two deflectors had to be described with two parameters each, allowing to control their size and orientation. Then, a cost function was defined to evaluate the orientation of the flow lines at the intakes entrance. Then, automatic mesh generation methods to run 720 calculations with shape parameters drawn randomly, and to calculate a residual for each run. It was then possible, to identify for which parameters the minimum residual was observed. In this case, the deflectors obtained are of medium size, with a shape oriented upstream, creating a recirculation small the first one.

Then, a metamodel was created with a kriging method, to interpolate the input parameters of the database of the 720 calculations and the output residuals. This model was evaluated by a quality criterion, Q2, to ensure that the metamodel represents the responses of the numerical model. It then allowed a sensitivity analysis to be performed on the input parameters, giving the orientation of the first deflector and, to a lesser extent, its size, as the most important parameter. An optimization of the deflector parameters was then carried out on the metamodel and the results gave parameters close to those obtained with the minimum of the parametric study. A TELEMAC-2D calculation with the parameters resulting from the optimization also gave a low residual, close to the minimum of the parametric study. The solution found during the parametric study is therefore retained, and its robustness has been demonstrated by an optimization study giving very similar results.

One perspective considered in this work is to evaluate a second cost function assessing the sedimentation potential in

the channel, and to define the shapes of the deflectors by optimization on multi-objective criteria.

### REFERENCES

- [1] TelApY User Manual, V8P1
- [2] C. Goeury, T. David, R. Ata, S. Boyaval, Y. Audouin, N. Goutal, A.-L. Popelin, M. Couplet, M. Baudin, R. Barate, "Uncertainty Quantification on a real case with TELEMAC-2D", Proceedings of the 22nd Telemac-Mascaret User Club, 2015
- [3] C. Goeury, A. Ponçot, J.-P. Argaud, F. Zaoui, R. Ata, and Y. Audouin, "Optimal calibration of TELEMAC-2D models based on a data assimilation algorithm", 24 th Telemac-Mascaret User Conference, Graz, Austria, pp. 73- 80, 2017
- [4] C. Goeury, F. Zaoui, Y. Audouin, P. Prodanovic, J. Fontaine, P. Tassi, R. Ata, "Finding Good Solutions to Telemac Optimization Problems with a Metaheuristic", XXV th Telemac & Mascaret User Club, 2018
- [5] Amsallem, D., Zahr, M., Choi, Y., & Farhat, C. (2015). Design optimization using hyper-reduced-order models. *Structural and Multidisciplinary Optimization*, 51(4), 919-940.
- [6] OpenTURNS documentation, <http://openturns.github.io/openturns/latest/index.html>
- [7] Fang, K. T., Ma, C. X., & Winker, P. (2002). Centered  $L_2$ -discrepancy of random sampling and Latin hypercube design, and construction of uniform designs. *Mathematics of Computation*, 71(237), 275-296.
- [8] Audouin Y., Fontaine J., Fouquet T., Goeury C., Leroy A., Pham C.-T., Souillé F., Taccone F., Duron, L., Daou, M.-P. and Sécher, M. "A new Python3 module for TELEMAC-MASCARET dedicated to post-treatment: Postel" XXVI th Telemac & Mascaret User Club, 2019
- [9] Maurel, A., Iooss, B., Van Dorpe, F., & Volkova, E. (2008). An efficient methodology for modeling complex computer codes with Gaussian processes. *Computational Statistics & Data Analysis*, 52(10), 4731-4744.
- [10] Olivier Roustant. Sobol-Hoeffding decomposition: bounds and extremes. 2018. hal-01953080

# Benefits of a metamodel for automatic calibration of 1D and 2D fluvial models

Rui YANG<sup>1,2</sup>

<sup>1</sup> Ecole Centrale de Lyon

36 Avenue Guy de Collongue, 69134 Écully, France

Luc DURON<sup>2</sup>, Guillaume BENEFIGE<sup>2</sup>, Pierre NUNES<sup>2</sup>

<sup>2</sup> Compagnie Nationale du Rhône

2 rue André Bonin, 69009 Lyon, France

[l.duron@cnr.tm.fr](mailto:l.duron@cnr.tm.fr)

**Abstract**— Construction of hydraulics models are often time-consuming in terms of calibration, which is an essential step. In this paper, two methods (kriging and XGBoost) are used to build intermediate metamodels for 1-D and 2-D hydraulic models to calibrate friction coefficients defined by zones. The resulting metamodels were hereafter applied for sensitivity analysis and other applications. The benefits of an intermediate metamodel were assessed on multiple real applications and this method was compared to the other semi-automatic calibration method (meta-heuristic method, see [12]). The developed approach involving a metamodel appears to be highly computationally less intensive and leads to similar results.

## I. INTRODUCTION

The calibration of a hydraulic model is an essential phase, which consists typically in adjusting friction coefficients. The common Strickler coefficients are indeed often hard to estimate, because they depend on the materials of the riverbed, the shape of the riverbed, etc. and they may account for different terms of energy losses depending of the flow rate. That's why it is necessary to calibrate it to minimize the error between simulations and observations. Usually for channel with simple cross section geometry, if the error of water level between hydraulic model and observations is around a few centimetres and the error of discharge is 5 to 10% of the nominal discharge, the hydraulic model is considered as correctly calibrated. But if the error is too large at some locations, it is possible that the model parameters are wrong, the observations are wrong, or it is necessary to add new features to the hydraulic model [13]. In this paper, it is assumed that observations and discharges are correct. Moreover, it only focuses on 1D and 2D steady flow models.

The classic calibration approach needs to repeat hydraulic calculations which is a time-consuming process. An interesting method is to build an intermediate and abstract metamodel and apply it to multiple purposes, as presented by Zaoui et al. (see [1]). This methodology is presented in detail in the next section.

This automatic calibration was applied firstly on a 1D simple test case with multiple design of experiments (DOE) methods and metamodels, as presented in section IV.A. Once the method was validated, it has been applied and compared to a more complex model in 1D and 2D. The computations

have been performed on a 1D computation model named Crue10 (property of CNR) and a TELEMAC-2D model. Moreover, some sensitivity analysis have been conducted in order to consolidate the calibrated parameters and give some complementary information for the modeler.

The developed scripts are done with Python and are based on the scikit-learn module. They consist of a set of functions which the modeler can combined.

## II. METHODOLOGY

This paper proposes to use an intermediate metamodel to realize the calibration. Figure. 1 shows the general workflow for the automatic calibration.

Firstly, the input space is sampled to create a matrix called design of experiments (DOE). There are several DOE methods (LHS, PhiP, MinDist and C2), which are described hereafter. Then hydraulic computations are performed for each sample. Input variables are Strickler coefficients for different zones of a river and output variables are water levels at different sections and discharges. Intervals of Stricker coefficient are chosen by experience without further information, based on the principle of maximum entropy the uniform law is used [14].

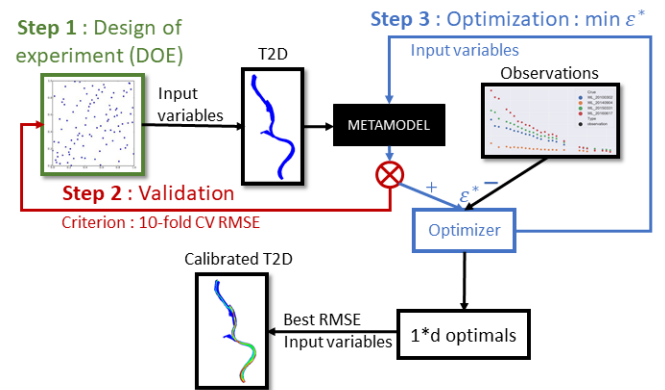


Figure 1. Workflow of the automatic calibration

The second step is the construction of the metamodel and its validation. For the metamodel definition, the DOE and the output variables are used, and multiple methods can be applied

(e.g. kriging, XGBoost etc.). The validation process consists in a cross-validation to define the accuracy of the metamodel. If the error criteria is too high it is recommended to increase the size of the DOE or adjust the hyperparameters of the metamodel.

Finally, the third step is the optimization step, which is based on a minimization approach of root-mean-square error between metamodel predictions and observations. Water level elevation measurements are realized at different stations and one discharge corresponds to one water line.

Because of the equifinality problem and the use of a meta-heuristic method, this process is repeated  $1*d$  ( $d$  is the number of input variables) times, which lead to the best configuration of input variables. We observed that  $d$  repetitions is a good compromise and leads in practice to around 10-20 repetitions.

#### A. Design of experiment (DOE)

The definition of the DOE is an essential step, because it determines calculation costs. There are mainly three types of DOE methods [3]:

- Classical DOE (factorial, composite, etc.),
- Law-discrepancy sequences,
- Latin Hypercube Design (LHS).

When using a non-parametric metamodel (the number of parameters can grow with the sample size), there are only two criteria to assess a DOE [3]:

- No redundancy by projection,
- Space filling designs.

In our study cases, the hydraulic model often depends on more than ten Strickler coefficients. But the water level measured at a station only depends on a few of them. That's why we expect the experiment points won't be confused when we make the projection onto the subspace constructed by a few of Strickler coefficients. That's also the reason that the property of no redundancy by projection is important [4]. Otherwise, if we assume that we don't have any prior knowledge about the response surface, the only thing we can do is to explore the input space. It corresponds to the space filling designs [3].

For engineering applications, the classical DOE is not convenient because the size of the DOE will be huge when the number of input variables is large (e.g. the factorial design needs  $2^d$  points where  $d$  is the number of inputs) [4]. For the Law-discrepancy sequences, when the number of input variables is large, it performs badly on the projection [6]. The Latin Hypercube Design (LHS) can guarantee the property of no redundancy but it is often poor on the space filling [4]. That's why we need LHS and space filling designs. The objective is to generate a DOE created by LHS method  $X_d^N = (x_j^{(i)})_{(i=1\dots N, j=1\dots d)}$  where  $N$  is the size of DOE,  $d$  is the number of input variables and  $x_j^{(i)}$  represents the  $j$ -th input of the  $i$ -th experiment), that minimizes a space filling

criterion  $\phi$ . For example, the space filling criterion  $\phi$  can be [7]:

- The minimum average distance between 2 elements according to L2 norm:

$$\phi(X) = \min |x^{(i)} - x^{(j)}|_{L^2}, \forall i \neq j = 1, \dots, N \quad (1)$$

- PhiP: The p-moment of the xi distribution

$$\phi_p(X) = (\sum_{1 \leq i < j \leq N} |x^{(i)} - x^{(j)}|_{L^2}^{-p})^{\frac{1}{p}}, p = 50 \text{ by default} \quad (2)$$

- C2: The centred L2-discrepancy

$$C^2(X_d^N) = \left(\frac{13}{12}\right)^d - \frac{2}{N} \sum_{i=1}^N \prod_{k=1}^d \left(1 + \frac{1}{2} \left|x_k^{(i)} - 0.5\right| - \frac{1}{2} \left|x_k^{(i)} - 0.5\right|^2\right) + \frac{2}{N^2} \sum_{i,j=1}^N \prod_{k=1}^d \left(1 + \frac{1}{2} \left|x_k^{(i)} - 0.5\right| + \frac{1}{2} \left|x_k^{(j)} - 0.5\right| - \frac{1}{2} \left|x_k^{(i)} - x_k^{(j)}\right|\right) \quad (3)$$

After sampling, we can have a sample matrix:

$$K = \begin{pmatrix} K_{s11} & \dots & K_{s1d} \\ \vdots & \ddots & \vdots \\ K_{sN1} & \dots & K_{sNd} \end{pmatrix}_{N \times d} \quad (4)$$

$K_{sij}$  represents the  $j$ -th Strickler coefficient of the  $i$ -th sample.

Then we pass it to the hydraulic model to get a response matrix with  $n$  stations and  $m$  water lines:

$$Z = \begin{pmatrix} Z_{11} & \dots & Z_{1(n \times m)} \\ \vdots & \ddots & \vdots \\ Z_{N1} & \dots & Z_{N(n \times m)} \end{pmatrix}_{N \times (n \times m)} \quad (5)$$

$Z_{ik}$  represents the  $k$ -th water level of  $i$ -th sample.

A water line is a set of observed water elevations at different stations for the same boundary conditions (assumed to be steady flow).

#### B. Metamodel

Understanding of the dataset structure is very useful for metamodeling. The properties of our dataset:

- Tens input variables that are continue and assumed to be non-correlated and independent,
- Hundreds of output variables that are continue and correlated,
- The size of dataset is ten times the number of input variables.

In terms of data science, it's a typical regression problem with small dataset.

It is not recommended to use parametric model (e.g. linear regression, polynomial, exponential etc.) because these models are often too simple to recognize.

In the field of mechanics, we use often kriging which is a powerful method for metamodeling when the size of dataset is not too large. In fact, the prediction of kriging interpolates the real output and is probabilistic so that one can compute empirical confidence intervals. But they lose efficiency in high dimensional spaces (when the number of input variables exceeds a few dozens) and they use whole samples information to perform the prediction [8].

Generally, the only thing we need to define is the kernel matrix which describes the covariance of the Gaussian process (i.e. kriging). In our case, the output (water level) comes from a hydraulic model, therefore the response surface is smooth (i.e. not noisy). Additionally, it is not periodic. The common choice for the kernel matrix is Matérn 5/2 [2].

Another method is XGBoost (Extreme Gradient Boosting). It's very popular and powerful in the field of machine learning [9]. XGBoost method is based on the decision tree ensembles. The tree ensemble model consists of a set of classification and regression trees (CART). Usually, a single tree is not enough to make a prediction. That's why an ensemble model which calculates weighted average of multiple trees is used [9]. It has been proved very powerful over the Kaggle competition [9]. But there exists a lot of hyperparameters for the training process. In practice, we need to tune the XGBoost to fit better our dataset. Based on our study cases, a fine-tuned XGBoost metamodel can perform at least as well as kriging.

In fact, we do not make a complete model for all outputs but one single model for one output and then combine all of them. Thus, we used univariate metamodels because:

- The sample size is not large, and the number of outputs variables is acceptable.
- We don't know exactly the correlation among the outputs. If we create one complete model this can't help us to increase the quality of model [10].

Of course, we can make some transformations over outputs to decrease the number of outputs. For example, we can calculate the RMSE error between metamodel predictions and observations [1]. But some information will be lost. It's better to make a single model for each output.

$$M(K_{s1}, \dots, K_{sd}) = \begin{cases} M_1(K_{s1}, \dots, K_{sd}) \\ \vdots \\ M_{n \times m}(K_{s1}, \dots, K_{sd}) \end{cases} \quad (6)$$

where:

- $M_l$  is the metamodel for the first output;
- $K_{sl}$  is the first input variable.

### C. Validation

In the field of machine learning, k-fold cross-validation is commonly used to estimate the performance of machine learning models. Because it doesn't take any additional data

and generally results in a less biased or less optimistic estimate of the model skill than other methods [8].

Usually, if the size of dataset is less than 100, we take  $k = 20$ , else we take  $k = 10$ .

In the hydraulic field, the criteria below are often used:

$$\text{Mean signed error (MSE): } \frac{\sum_{i=1}^N \sum_{j=1}^{n \times m} (M_j(K_{s1}, \dots, K_{sd}) - Z_{ij})}{N \times n \times m} \quad (7)$$

$$\text{Mean absolute error (MAE): } \frac{\sum_{i=1}^N \sum_{j=1}^{n \times m} |M_j(K_{s1}, \dots, K_{sd}) - Z_{ij}|}{N \times n \times m} \quad (8)$$

Root-mean-square error (RMSE):

$$\sqrt{\frac{\sum_{i=1}^N \sum_{j=1}^{n \times m} (M_j(K_{s1}, \dots, K_{sd}) - Z_{ij})^2}{N \times n \times m}} \quad (9)$$

Where:

- $M$  is the metamodel
- $Z$  is the value of the initial hydraulic model
- $K$  is the Strickler coefficient

### D. Optimization

In this part, we compare metamodel predictions with observations and minimize the error between them. The cost function is a RMSE:

$$\sqrt{\frac{\sum_{j=1}^{n \times m} (M_j(K_{s1}, \dots, K_{sd}) - O_j)^2}{n \times m}} \quad (10)$$

$O$  is the corresponding observation.

We use a common optimization algorithm named particle swarm optimization (PSO). it belongs to the metaheuristic optimization methods. It can converge fast, has short computational time and has high probability and efficiency in finding the global optimum [11].

## III. HYDRAULIC MODELS AND STUDY AREAS

There are totally three study cases or hydraulic models: Chautagne (CE) 1D, Bourg-lès-Valence (BV) 1D and BV 2D. The 3 models are in two different parts of the Rhône river: in the upper Rhône for Chautagne and lower Rhône for Bourg-lès-Valence (lower bottom slope, larger cross-sections).

A 1D computation code named Crue10 (property of CNR) is used for the sake of methodology investigations, as it computes fast. But the main test cases are in the region of Bourg-lès-Valence and involves 2 different computations codes: Crue and TELEMAT-2D. The 2 hydraulic models are using a different discretization of shallow water equations. They can both be used to calculate the water level at different sections under different boundary conditions.

In our study cases, we use minor-river bed and major-river bed Strickler coefficient over different parts of the hydraulic models as input variables. The models do not include any storage area.



### A. Chautagne (1D) [CE]

Chautagne's model covers about 59 km<sup>2</sup> around a run-of-river dam. The hydraulic model (1D) used in this paper contains hundred sections and covers 7 km long. 2 water level profiles correspond to different boundary conditions (see discharge values in Table IV), the water level is measured at 15 locations for each water line. There are 12 input variables (6 minor-river bed and 6 major-river bed Strickler coefficient) and 30 (15\*2) output variables.

TABLE I. CHAUTAGNE MODEL MAIN CHARACTERISTICS

Number of sections	100
River length	6.7 km
Number of water lines	2

### B. Bourg-lès-Valence (1D and 2D) [BV]

The model of BV is located along the Rhône river, upstream the dam of La Roche-de-Glun. It covers nearly 16 km and has been separated into multiples zones, as presented on figure 2. The 2 hydraulic models (Crue and TELEMAC-2D) are covering the same domain and have a similar bathymetry.

4 water lines are available and the water level are measured at 32 locations. Overall, there are 14 input variables and 128 (32\*4) output variables.

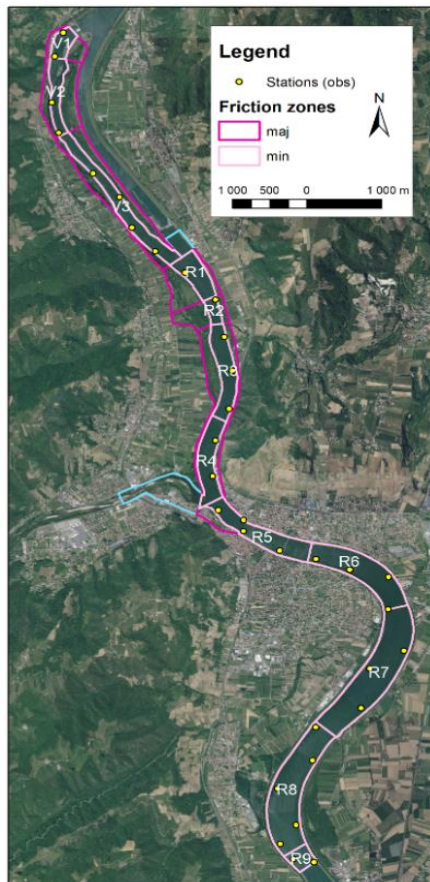


Figure 2. Overview of BV domain and zoning

TABLE II. BOURG-LÈS-VALENCE MODELS MAIN CHARACTERISTICS

	1D	2D
Number of sections/nodes	248	32 000
River length	15.6 km	
Number of water lines	4	

## IV. APPLICATIONS

Normally, XGBoost parameters need to be fine-tuned for each case. But in practice, XGBoost method is compared with kriging. If the validation RMSE of XGBoost method is much better than kriging method (about a half), there is no need to fine-tune XGBoost parameters. When we deal with similar problems (response surfaces are similar) or data structures, the hyperparameters do not need to be adapted.

And in our study cases, the hyperparameters of XGBoost are fine tuned in the BV 1D model, and they work for two another cases. Therefore, the same hyperparameters of XGBoost were used for all subsequent tests.

### A. Chautagne 1D model

#### (1) Benchmark of DOE – validation step

For the Chautagne 1D, 10 DOEs were repeated for each size and each method (4 sizes \* 4 methods = 16 combinations). The size tested are (3\*d, 5\*d, 7\*d, 10\*d) where  $d$  ( $d=12$ ) is the number of input variables. There are four methods in total: non-optimized LHS, LHS + Space filling C2, LHS + MinDist, LHS + PhiP. Finally, two metamodel methods are compared: kriging and XGBoost, with a 10-fold cross-validation RMSE for all DOEs (160 in total). This benchmark corresponds to a convergence study.

Figure 3 is a box plot and each box consist of 10 DOEs.

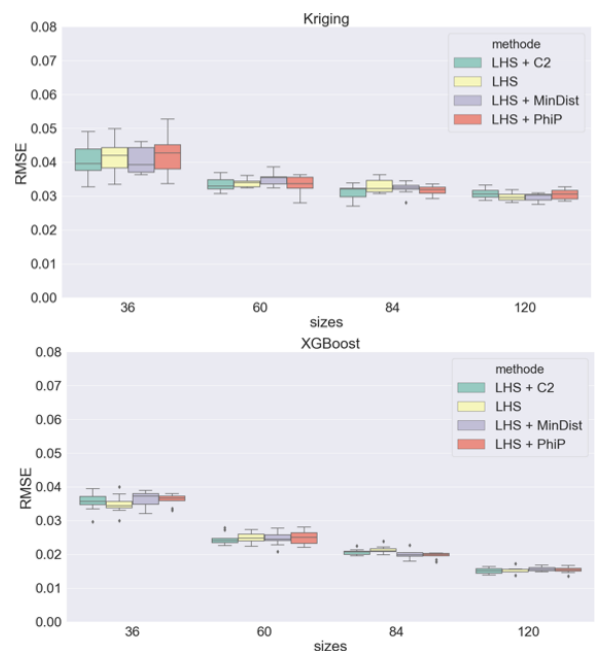


Figure 3. The 10-fold CV RMSE of XGBoost and Kriging in different designs of experiment with different sizes and methods

We find:

- As the  $N$  (size of DOE) increases, both RMSE and variance (the height of box) are decreasing.
- When the size of DOE reaches  $10*d$ , there is almost no difference between the four methods.
- XGBoost method is slightly better than kriging with lower RMSE and lower variance. Additionally, the RMSE of XGBoost method decrease more rapidly than using kriging with  $N$  increasing.

In this study case, the relationship between one output and inputs is not too complicated. Generally, one output is only related to three or four inputs and the relation is like a combination of second or third order polynomials. A DOE with size  $10*d$  is enough.

There is no obvious difference between the four methods. So, we prefer to use LHS optimized by MinDist which is very simple and can optimize the property of space filling.

Because XGBoost method is not guaranteed that it is always performing better than kriging and it takes only a few seconds to construct a metamodel, both metamodels are used. Then the recommendation is to use directly the one giving the best RMSE.

### (2) Benchmark of metamodels for optimization

For the optimization process a metaheuristic method, called PSO, is used. Hence the process is not reproducible and the solution not fixed. In this comparison, the PSO process was applied  $1*d$  ( $d=12$  input variables) times for each metamodel. The optimization seeks to minimize the RMSE between hydraulic model and observations. The DOE in this part has a size of  $10*d$  created by LHS+MinDist.

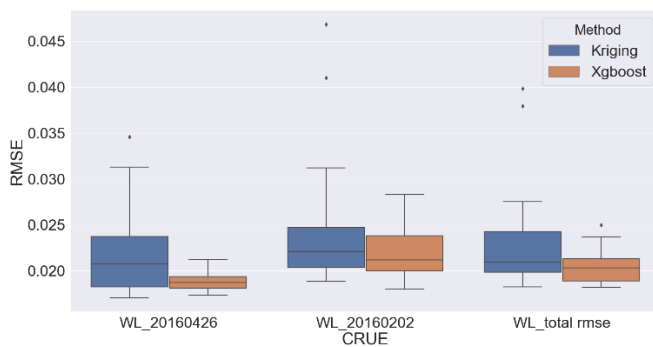


Figure 4. RMSE between hydraulic model and observations

Figure 4 presents box plots and each box contain  $1*d$  experiments. It shows the RMSE between hydraulic model simulations and observations for two water lines and the total RMSE of them.

In terms of optimization, XGBoost method is slightly better than kriging method, with lower variance and lower average of total RMSE. For kriging method, the average of total RMSE is 0.023 m and the standard deviation is 0.006 m.

For XGBoost method, the average is 0.021 m and the standard deviation is 0.002 m.

The minimum RMSE for kriging and XGBoost methods are very close, values are respectively 0.019 m and 0.018 m. Therefore, their performances are similar in terms of calibration but results with the XGBoost method have a better repeatability.

Based on the result of optimization step, we prefer to do  $1*d$  times optimization processes by using XGBoost method and choose the best RMSE. This configuration is investigated in depth in the following part.

### (3) Results for the best configuration

The selected configuration is based on:

- Metamodel: XGBoost method,
- Size of DOE:  $10*d$ ,
- Type of DOE: LHS + MinDist.

The validation criteria are presented in Table III. The metamodel is not biased (MSE close to 0) and has an absolute error (MAE) less than 1cm. Furthermore, the total validation RMSE (0.014m) is close to the optimisation RMSE (0.018m).

TABLE III. VALIDATION STEP FOR CE 1D

	RMSE	MAE	MSE
Value (m)	0.014	0.009	-0.0005

Fig. 5 plots the water level of hydraulic model, metamodel prediction and observation at different sections (axis label "sect\_id" corresponds to the section number) and different water lines. We get 0.019 m RMSE for water line (1), 0.018 m RMSE for water line (2). This result is basically equivalent to the traditional calibration method.

Fig. 6 plots the value of input variables (Strickler coefficients) for the optimal point, the upper and lower boundary for each input. Here, *Maj* means major-river bed, *Min* means minor-river bed and *Rf* corresponds to a friction zone. The optimal values correspond to the typical values that the modeller could reach with the traditional method.

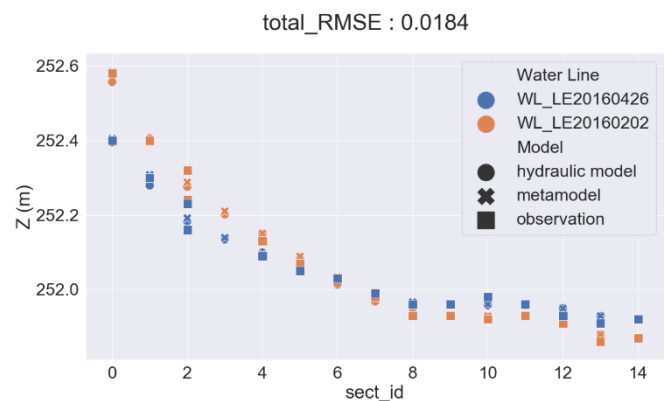


Figure 5. Water lines for Chautagne 1D

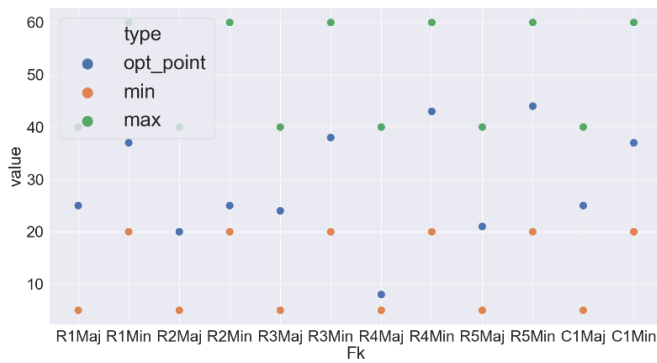


Figure 6. Input values (Strickler coefficients) range (min/max) and optimal configuration (opt\_point) for Chautagne

TABLE IV. WATER LINES REFERENCES

Waterline	2016-02-02 (1)	2016-04-26 (2)
Discharge (m <sup>3</sup> /s)	900	646
RMSE Optimization (m)	0.0186	0.0182

#### (4) Sensitivity Analysis

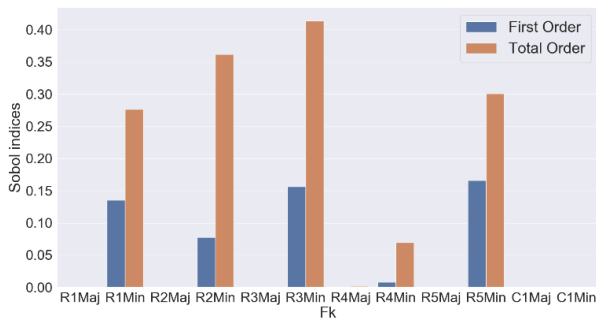


Figure 7. Sobol' indices (total and first order) of RMSE between metamodel predictions and observations for Chautagne.

Fig. 7 shows only 5 parameters are significant and they are all Strickler coefficients located in the minor riverbed. This observation results of the selected events since discharges are not high enough to flood the major bed.

#### B. Bourg-lès-Valence 1D model

The methodology defined on Chautagne test case has been conducted on the more complex model, named BV. In a similar manner, a DOE of size  $10 \times d$  ( $d=14$  inputs variables) created by LHS+MinDist is used.

##### (1) Validation

In the validation step, we create two metamodel by using respectively kriging and XGBoost methods.

TABLE V. KRIGING'S VALIDATION STEP FOR BV 1D

	RMSE (m)	MAE (m)	MSE (m)
<b>Kriging</b>	0.025	0.014	-0.0002
<b>XGBoost</b>	0.022	0.013	-0.0002

For the BV 1D, in the validation step, a fine-tuned XGBoost method gives a 0.022 m RMSE that is still better than 0.025 m given by kriging method. This result corresponds to what was obtained with Chautagne 1D.

##### (2) Optimization

Like the study case Chautagne 1D, we use PSO method to find 1\*d ( $d=14$  inputs variables) optimal Strickler coefficient by minimizing the RMSE between hydraulic model and observations. The value of the minimum RMSE was used as criterion to compare the performance of the two metamodels.

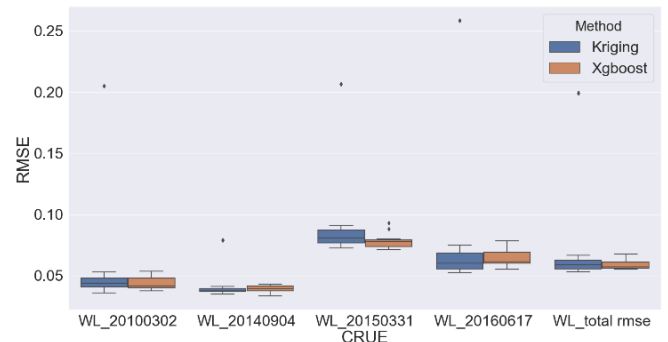


Figure 8. Optimization step for BV 1D

In terms of optimization, XGBoost method is better than kriging method, with lower variance and lower average of total RMSE. For kriging method, the average of total RMSE is 0.079 m and the standard deviation is 0.040 m. For XGBoost method, the average is 0.059 m and the standard deviation is 0.004 m.

The minimum RMSE of kriging is 0.053 m and the minimum RMSE of XGBoost method is 0.055 m. The RMSE of optimization step is about twice as much as the RMSE of validation step.

BV 1D model gives similar results compared with CE 1D model. In the validation step, XGBoost method is always better than kriging method. In the optimization step, their performances are similar for calibration and XGBoost method has better repeatability.

#### C. Bourg-lès-Valence 2D model

As for BV 1D model, a DOE of size  $10 \times d$  ( $d=14$  inputs variables) created by LHS+MinDist is used in this part.

##### (1) Validation

In the validation step, we create two metamodels by using respectively kriging and XGBoost methods.

TABLE VI. KRIGING'S VALIDATION STEP FOR BV 2D

	RMSE (m)	MAE (m)	MSE (m)
<b>Kriging</b>	0.115	0.071	-0.0008
<b>XGBoost</b>	0.066	0.040	0.0002

For the BV 2D model, in the validation step, a fine-tuned XGBoost method gives a 0.066 m RMSE which is much better than 0.115 m given by Kriging method. We get a RMSE much larger than Chautagne 1D and BV 1D models. Nevertheless,

R-square in the three cases are very close. Therefore, the variance in the water level in BV 2D model is larger than in the two another cases.

### (2) Optimization

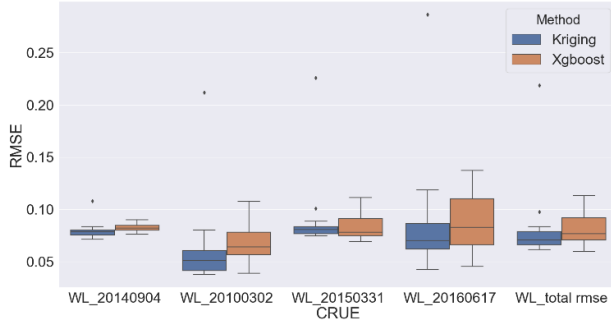


Figure 9. Optimization step for BV 2D

In terms of optimization, for Kriging method, the average of total RMSE is 0.083 m and the standard deviation is 0.040 m. For XGBoost method, the average is 0.082 m and the standard deviation is 0.016 m. The minimum RMSE of Kriging method is 0.061 m and the minimum RMSE of XGBoost method is 0.060 m.

We find all these three study cases give a similar result. XGBoost method is always better than Kriging method in the validation step. In the optimization step, XGBoost method is more stable (lower variance), especially in 1D. But the minimum RMSE of both methods is very close.

So, only one optimal point is considered, XGBoost method is better. But if  $1*d$  optimal points are computed and the minimum of them used, the performance of both methods is close.

### D. BV 1D vs BV 2D models

All results are based on the following configuration:

- Metamodel: XGBoost method,
- Size of DOE:  $10*d$ ,
- Type of DOE: LHS + MinDist,
- 10-fold cross-validation for validation step.

#### (1) Water lines

total\_RMSE : 0.0552

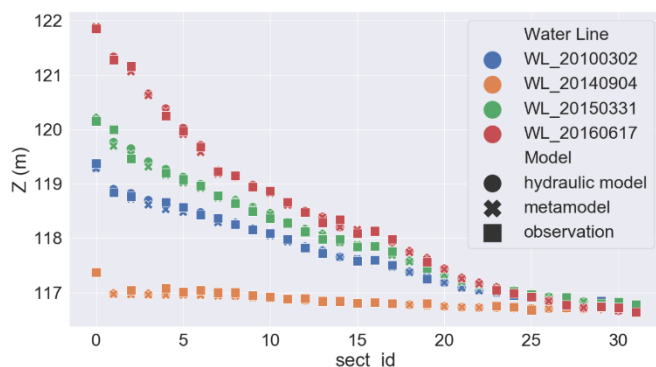


Figure 10. Water lines of BV 1D

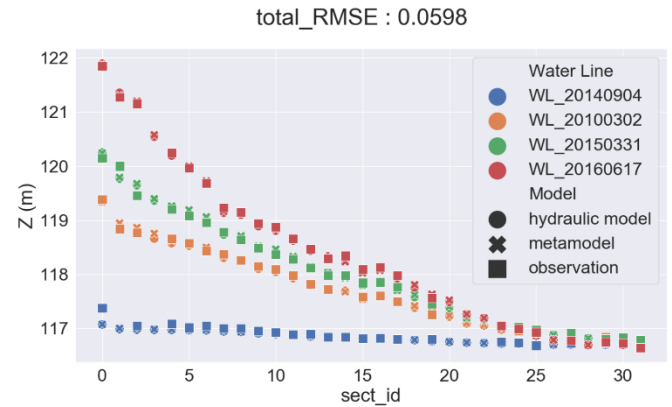


Figure 11. Water lines of BV 2D

In this section, we use the minimum RMSE of  $1*d$  optimal points for each model (either 1D or 2D). In both cases, the Strickler coefficients used in the model are those calibrated with the metamodel built thanks to XGBoost method with the method LHS + MinDist. For BV 1D model, the RMSE between observations and simulations is 0.055 m. For BV 2D model, the RMSE is 0.060m. We find also that the points with large error are concentrated in the upper part (section id 0,1,2,4).

### (2) Strickler coefficients

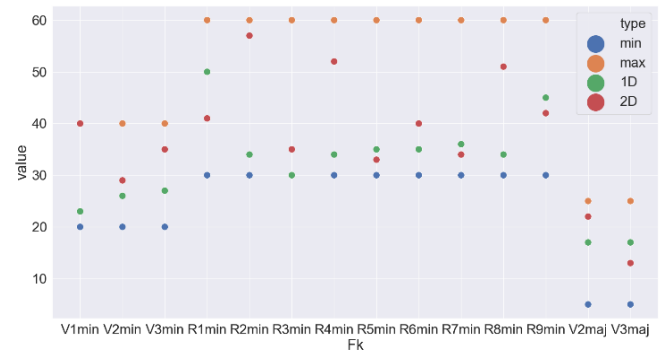


Figure 12. Strickler coefficients: BV 1D vs BV 2D

Figure 12 shows the value of Strickler coefficient for BV 1D and BV 2D models at the optimal point. *Min* and *Max* correspond to the domain of Strickler coefficients. Strickler coefficients are overall higher in 2D than in 1D, which is what is expected. In the details, the Strickler coefficients for 1D and 2D in V1min, R2min, R4min and R8min are much different. Whereas the values are closer for the other.



(3) Sobol' indices

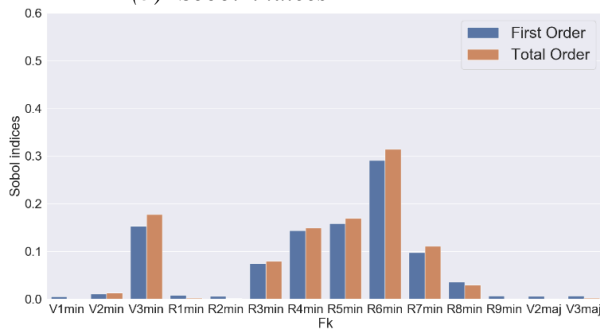


Figure 13. Sobol' indices (total and first order) of BV 1D

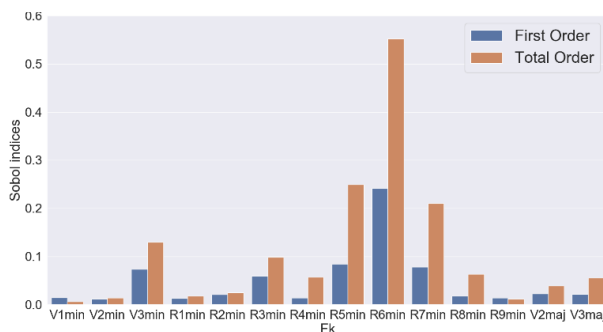


Figure 14. Sobol' indices (total and first order) of BV 2D

Figure 13 shows the Sobol' indices of BV 1D model, the first order is close to the total order. It means there is no much interaction effects between inputs. These inputs mainly affect outputs independently. But in BV 2D model, the total order is larger than first order. It means the interaction effects are much more important. The outlines of 1D and 2D are basically similar, except that V3min and R4min in the BV 1D are more important. In the Figure 12, the K-value in V1min, R1min, R2min and R8min is much different between 1D and 2D models. And we also find that in the Sobol' indices of these Strickler coefficients have no effect to the output neither in 1D model nor in 2D model. So, the value of these coefficients is not important. This also the case for V2min, R9min and major-river bed zones. But for 1D model, values of Strickler coefficient in parts V3min and R4min play a significant role in the outputs. Therefore, the dispersion around the mean K-value is expected to be lower in those groups of sections than in other parts of the river. But for 2D model, the role played by those two coefficients is not so important. So, in the process of optimization, the value of these two coefficients will be more random and the discrepancy is expected to be larger.

## V. CONCLUSION

This paper shows it's relevant to build an intermediate metamodel and it has been applied to various test cases (1D and 2D). Based on three study cases, in the validation step, XGBoost method always performs better than kriging method, with lower RMSE.

In the optimization step, because of the use of a meta-heuristic and the equifinality problem, it is recommended to repeat the optimization  $1 \times d$  times and choose the best

solution. We find the best RMSE of XGBoost method is close to the best RMSE of kriging method in this step.

Finally, when we apply this approach to other study cases, we might need to adjust the hyperparameters of XGBoost method. This choice of the hyperparameters should be investigated and automated.

The perspectives include some more advanced applications on the calibrated metamodel, such as uncertainty quantification. In addition, when the hydraulic model or the uncertainty definition slightly changes, updating old metamodel, without reconstructing a new one, is also an interesting problem.

## REFERENCES

- [1] Fabrice Zaoui, Cédric Goeury and Yoann Audouin. "A Metamodel of the Telemac Errors", XXVIth TELEMAT-MASCARET User Conference, October 2019, Toulouse.
- [2] Mohammed Reza Kianifar and Felician Campean. "Performance evaluation of metamodeling methods for engineering problems: towards a practitioner guide", Structural and Multidisciplinary Optimization, July 2019.
- [3] Mona Abtini. "Plans prédictifs à taille fixe et séquentiels pour le krigeage". Thèse de doct. August 2018.
- [4] Jessica Franco. "Planification d'expériences numériques en phase exploratoire pour la simulation des phénomènes complexes". Thèse de doct. 2008.
- [5] Loic Le Gratiet and Claire Cannamela. "Kriging-based sequential design strategies using fast cross-validation techniques with extensions to multi-fidelity computer codes." 2012. arXiv:1210.6187 [math.ST].
- [6] Razi Sheikholeslamiet Saman Razavi. "Progressive Latin Hypercube Sampling: An efficient approach for robust sampling-based analysis of environmental models". In: Environmental Modelling Software93 (2017), p. 109-126.issn: 1364-8152.
- [7] Airbus-EDF-IMACS-Phimeca, "Reference Guide - OpenTurns 1.15," 2020.
- [8] F. Pedregosa et al. "Scikit-learn: Machine Learning in Python". In: *Journal of Machine Learning Research* 12 (2011), p. 2825-2830.
- [9] Carlos Guestrin Tianqi Chen. "XGBoost: A Scalable Tree Boosting System". Proceedings of the 22nd ACM SIGKDD International Conference on Knowledge Discovery and Data Mining (2016).
- [10] Jack P.C. Kleijnen, Ehsan Mehdad "Multivariate versus univariate Kriging metamodels for multi-response simulation models" Volume 236, Issue 2, 2014, Pages 573-582.
- [11] Abdmouleh, Zeineb & Gastli, Adel & Ben-Brahim, L. & Haouari, Mohamed & Al-Emadi, Nasser. (2017). "Review of optimization techniques applied for the integration of distributed generation from renewable energy sources." *Renewable Energy*.
- [12] Meta-heuristic Optimization Method for the Calibration of Friction Coefficients in 1-D Open Surface Channel Modeling, Pierre-Loïc Rothé et al., *Advances in Hydroinformatics*, 2018
- [13] P.O. Malaterre, J.P. Baume, N. Jean-Baptiste, J. Sau. Calibration of open channel flow models: a system analysis and control engineering approach. *SimHydro 2010: Hydraulic modeling and uncertainty*, Jun 2010, Sophia-Antipolis, France. 10 p., 2010. <hal-00783013>
- [14] Mouradi, Rem-Sophia & Audouin, Yoann & Goeury, Cédric & Claude, Nicolas & Tassi, Pablo & el Kadi Abderrezak, Kamal. (2016). Sensitivity analysis and uncertainty quantification in 2D morphodynamic models using a newly implemented API for TELEMAT2D/SISYPHE.

## **Numerical methods, code coupling and high performance computing**

# Simulating, Storing and Accessing TELEMAC Simulations with AWS Cloud Computing Technologies

Julien Cousineau  
National Research Council Canada  
Ottawa, Canada  
[julien.cousineau@nrc.ca](mailto:julien.cousineau@nrc.ca)

**Abstract**— The rise of cloud computing and on-demand availability of computer system resources brings new opportunities for TELEMAC users, potentially including big data analysis, data and process automation, and machine learning. The paper presents a new application programming interface (API) module to simulate, store and access TELEMAC simulations with Amazon Web Services (AWS) cloud computing technologies. One of the main goals of the API is to create a means for users to quickly create models, solve TELEMAC simulations, automate low level processes and easily share results with a wide range of users (e.g. scientists, engineers, stakeholders, and the public); thus enabling faster and more informed decision-making.

## I. INTRODUCTION

In the simplest terms, cloud computing services, such as AWS, can provide computational resources to support the typical workflow associated with TELEMAC hydrodynamic simulation: creating a steering file, storing the input files on a local/network drive and run the simulation on the local/network drive. This can be easily achieved using the AWS EC2 service which allows users to access computing resources and control operations on one or a cluster of virtual machines. StarCluster [1] is a good toolkit for creating and managing distributed computing clusters hosted on AWS EC2. This approach, however, does not offer functionality for users to quickly create models, solve TELEMAC simulations, automate low level processes and easily share results with a wide range of users. Without a suitable API to support integration, users must have knowledge of both TELEMAC and AWS environments (i.e. installation/setup, simulation processes, storage, credentials) and this makes the process difficult with a steep learning curve.

A new API, henceforth referred as AWS TELEMAC API (ATAPI), was develop with the TELEMAC TelApy module and AWS services. ATAPI simplifies the integration of TELEMAC simulation with AWS resources, alleviating the knowledge prerequisites of low level processes that would otherwise be required. The ATAPI allows users to focus their energy on the project at hand, enabling faster and more informed decision-making. ATAPI is part of a larger framework which includes data storage, data analysis/simulation and data visualization. Fig 1 shows how a user can interact with the framework and how ATAPI is intergraded in it. Although the user can use a website or API

tools (e.g. Postman) to access ATAPI through services such as API Gateway and Lambda, only the direct access route with a python interface is presented in this paper.

ATAPI is divided into three main components:

- Storing input and output files for TELEMAC simulations;
- Creating simulation cases; and,
- Simulating TELEMAC models.

Each component uses different AWS services to achieve their goal: AWS S3 is used to store and access data; AWS DynamoDB is used to store scenarios and track simulation progress; AWS Batch and AWS EC2 are used to simulate the cases. This paper describes the methodology for each of these components; an example is also presented to showcase the process and technology. Fig 2 shows the architecture diagram of ATAPI.

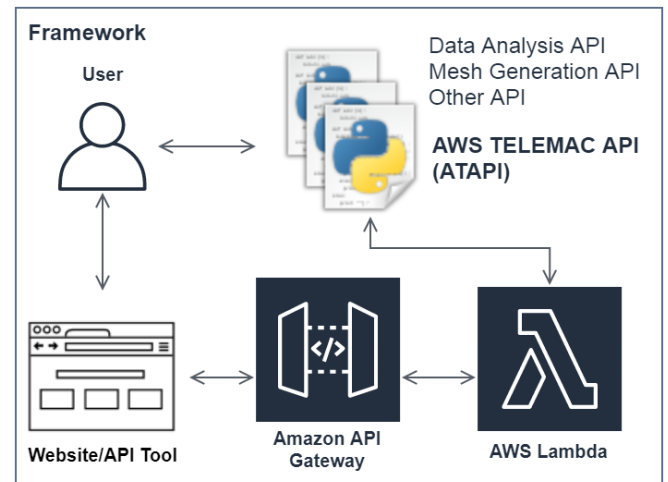


Fig 1: User interaction with ATAPI and other API services in the framework. A user can interact with ATAPI using a python interface or a website/API tool

## II. STORING AND ACCESSING DATA

Storing and accessing data is an important component since decision-making is often based on data and data visualization. With the exception of steering files (.cas), all

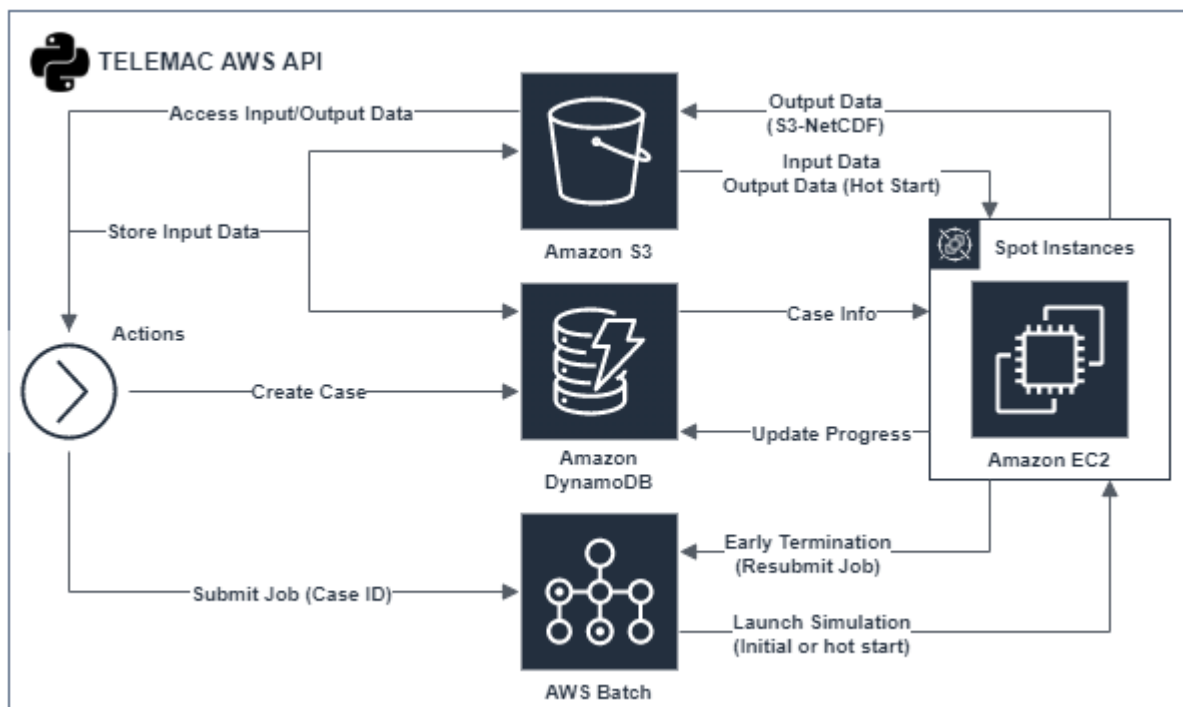


Fig 2: The architecture diagram of ATAPI. It allows storage of, and access to, data using AWS S3 and stores its metadata using AWS DynamoDB; create and store simulation cases, and track simulation progress using AWS DynamoDB; and, simulate cases using AWS Batch and AWS EC2.

input data (i.e. geometry file, boundary condition file) and result files are stored on Amazon Simple Storage Service or AWS S3: an object storage service that offers industry-leading scalability, data availability, security, and performance. Files are stored as objects in a specific S3 Bucket, which can be shared with the public or specific users. Amazon Elastic Block Store (EBS), another type of storage service, is used only temporarily during simulations with the virtual machines.

To increase efficiency in querying files in a S3 Bucket, metadata is created for each file and stored in AWS DynamoDB: a key-value and document database. The metadata consist of information such as name, file type, username, date created, date modified, and name of S3 Bucket.

Fig 3 shows an example of data and metadata stored in AWS S3 and AWS DynamoDB, respectively. The ATAPI currently saves files under the project name and under either *Input* or *Output* folders as shown in the figure. The input folder contains input files required to run TELEMAT (e.g. Geo\_M2.slf, ocean.M2.cli) and the output folder contains the model output files. The only exception is the steering files (.cas). Steering information (i.e. keywords and values) is stored on AWS DynamoDB as shown in the architecture diagram (Fig 2) since metadata, such as simulation progress, date created, date modified, and created by, are also saved.

Typically, simulation results are saved in a results file: a binary Selafin file (.slf). However, most result files contain a few hundred Megabytes to Terabytes of data. Unfortunately, AWS S3 does not allow partial download of binary files and this makes accessibility and enquiries difficult. For example,

extracting a time-series at one node (e.g. less than 1MB data) would require download of the entire results file from AWS S3. The solution for this is to create partition files that contain the model results using the S3-NetCDF package.

#### A. Model Results and S3-NetCDF

The S3-NetCDF package [2] was developed during the study to partition/split large array or TELEMAT results file into smaller file/object fragments for AWS S3. For example, instead of storing a one Terabyte Selafin file, the S3-NetCDF package can partition the file into thousands of files, each containing a slice of the data. This makes accessibility and enquires more efficient and less expensive for AWS S3.

Packages such as S3-netcdf-python [3] already exist but are mainly targeted at climate data products discretized over a structured mesh. Therefore, existing packages are incompatible with TELEMAT simulations that use an unstructured mesh.

The S3-NetCDF package uses the NetCDF (Network Common Data Form) binary format file (.nc) instead of the Selafin file (.slf). NetCDF has become standardized and supported in the scientific community, and has better interoperability with other formats. Netcdf4-python [4] is a python wrapper and was used during development to create and read NetCDF files. NetCDF also has the capability of data compression, which is a big advantage, cost-wise, in storing large datasets on AWS S3.

The S3-NetCDF package works by creating a master file (.nca), also known as the header, and partition files (.nc). The master file contains the definitions of variables (i.e. name of



variable, units), dimensions (i.e. size of array), metadata, groups and partition indices. The partition file contains the data. The files are partitioned by group, by variable and then by temporal and spatial sub-domains. The size of the subdomains (# of temporal and spatial nodes) depends on the size requested by the user. By default, the size of each partition file is 10 MB.

Files in S3 Bucket				
Amazon S3 > taramodel > TARA > input				
<input type="checkbox"/> Name ▾	Last modified ▾	Size ▾	Storage class ▾	
<input type="checkbox"/> surge	--	--	--	
<input type="checkbox"/> surge_user_fortran	--	--	--	
<input type="checkbox"/> Geo_M2.slf	Jul 1, 2020 1:13:25 PM GMT-0400	12.5 MB	Standard	
<input type="checkbox"/> oceanH.M2.cli	Jul 1, 2020 1:13:26 PM GMT-0400	7.0 MB	Standard	

File metadata in DynamoDB				
id ⓘ	createdAt ▾	name	type	updatedAt ▾
TARA/input/Geo_M2.slf	1593623...	Ge...	slf	15936236...
TARA/input/oceanH.M2.cli	1593623...	oc...	cli	15936236...
TARA/input/surge/rcp85.GFDL-ESM2i	1593623...	rcp...	slf	15936236...
TARA/input/surge/rcp85.GFDL-ESM2i	1593656...	rcp...	slf	15936569...
TARA/input/surge_user_fortran/bord.f	1593623...	bord	f	15936236...
TARA/output/rcp85.GFDL-ESM2M.20	1593646...	rcp...	nca	15936467...
TARA/output/rcp85.GFDL-ESM2M.20	1593656...	rcp...	nca	15936569...

Steering info and metadata in DynamoDB				
id ⓘ	iframe ▾	keywords ▾	module ▾	nframe ▾
TARA/rcp85.c	25921	{ "AIR PRESSUR...	telemac2d	25921
TARA/rcp85.c	26065	{ "AIR PRESSUR...	telemac2d	26065
TARA/rcp85.c	25921	{ "AIR PRESSUR...	telemac2d	25921
TARA/rcp85.c	25921	{ "AIR PRESSUR...	telemac2d	25921

Fig 3: Example of file, file metadata and steering info stored on AWS

Fig 4 shows an example of model results with different partitioning options. The master file contains three dimensions: number of nodes (nnode), number of elements (nelem) and number of frames (nframe). It also contains four groups and numerous variables that contain data. Each variable under a group has the same array shape. For example, every variable under Group A contains nnode values (1D array). Variables under Group C/D contain nframe by nnode values (2D array).

The datacubes in Fig 4.1-3 illustrate different ways that the data from Group C can be partitioned between temporal and spatial domains by varying the partitioning size. The

partitioning size is by the user. In this example, the first cube is partitioned with a file size of 10 MB, which contains data for one frame and for all nodes. The second cube is partitioned with a file size of 20 MB and partition files contain the two frames with all nodes. The third cube is partitioned with a file size of 5MB and partition files contain data from 1 frame and half the nodes.

Group C is perfect for querying spatially mapped variables for a given frame since it only needs to download 1 file (2 files for the third cube). However, Group C data are not conducive to extracting time-series information as this requires each partition file to be read. The solution for this is to duplicate and transpose the data in Group D, as shown in Fig 4.4. Although the data are saved twice, it is relatively cheaper to store data than to download the entire dataset from AWS S3 for every enquiry.

### III. CREATING STEERING CASE

Steering case information (i.e. keywords and values), typically saved in steering files (.cas), is stored in AWS DynamoDB as an object (under the *keywords* column). The simulation progress, type of TELEMAT module (e.g. telemac2d, telemac3d) and other metadata are saved in the database. A database is easier to maintain and update compared to writing/reading a file from AWS S3.

Fig 3 shows an example of cases in AWS DynamoDB. The simulation progress is identified by nframe and iframe, which are the total number of frames in the simulation and current frame position in the simulation, respectively. The simulation is complete when iframe is equal to nframe.

There are two ways of saving steering information: using a steering file (.cas) or using a JSON file/object that contains keywords and values. All local input files in a steering file (e.g. GEOMETRY FILE) are automatically uploaded and the local paths are replaced by the S3 paths.

### IV. SIMULATING SCENARIOS

Simulations are executed using virtual machines with Amazon Elastic Compute Cloud (Amazon EC2). EC2 is an AWS service that provides secure, resizable compute capacity in the cloud. These virtual machines are used to run TELEMAT simulations and can be automatically scaled and sized based on the number of simulations using AWS Batch.

#### A. AWS Batch and EC2 Spot Instances

AWS Batch provides functionality to create computer environments, assign a job queue and specify the type of job. In this case, the job is running TELEMAT and saving model results to AWS S3. AWS Batch dynamically provisions the optimal quantity and type of compute resources (e.g., CPU or memory optimized instances) based on the volume and specific resource requirements of the batch jobs submitted.

During ATAPI development, the Amazon EC2 Spot Instances was used instead of EC2 On-Demand Instances. This allows the ATAPI to take full advantage of unused EC2 capacity in the AWS cloud. Spot Instances are available at up to a 90% discount compared to On-Demand prices.

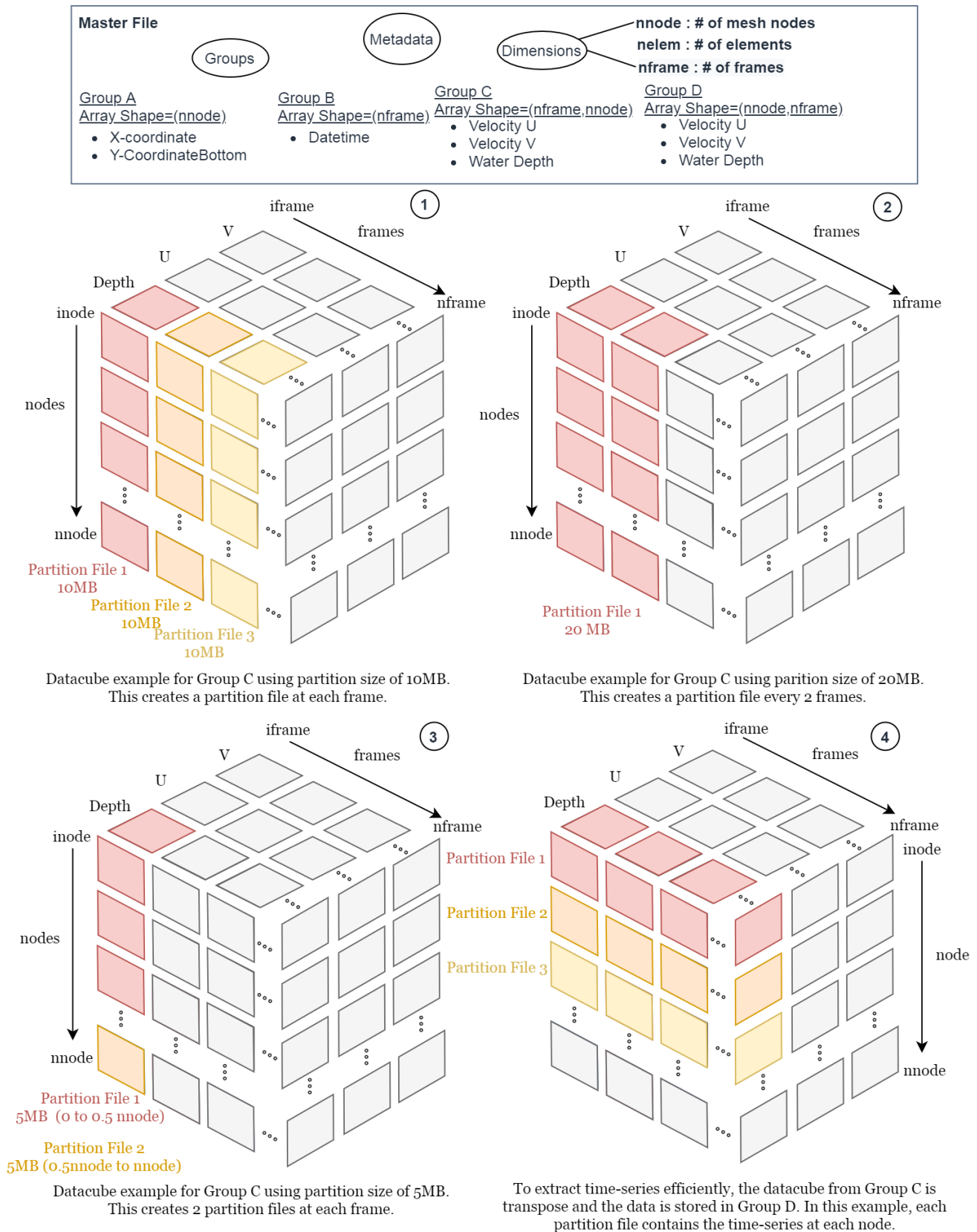


Fig 4: Examples of different partitioning options based on the variables, temporal and spatial domains, and the size of the partitions.

The downside of using Spot Instances is early termination. Users can bid on spare Amazon EC2 instances to reduce computational costs but if the Spot price increases above the users bid price, then the Spot Instance can be terminated with two minute warning. This can be an issue for TELEMAT using the typical python launch scripts (i.e. `telemat2d.py`) since there's no communication between TELEMAT and AWS, and no way of determining early termination.

Amazon EC2 has different types of instances but the compute optimized series (C-series) is recommended for TELEMAT simulations since they are made for scientific computing. Most C-series use the latest Intel and AMD cores (e.g. 2nd generation Intel Xeon Scalable Processors – Cascade Lake). A cluster of virtual machines with AWS Batch for one simulation is currently not supported with ATAPI - it only runs on a single virtual machine (up to 48 cores) per simulation.

### B. Job and Docker Container Image

Docker container images are used to run jobs on AWS Batch. A Docker container image is a lightweight, standalone, executable package of software that includes everything needed to run an application: code, runtime, system tools, system libraries and settings. Multiple Docker container images can exist on the same virtual machine.

A Docker image was develop using ATAPI, TELEMAT V8P1R0 and its software dependencies on an Alpine 3.11 Linux template image. The Docker file, used to create the Docker image, is available in the GitHub repository [5]. When launching, the image automatically starts a simulation script from ATAPI.

It is important to note that the default Docker image container size is 22 GB and virtual machine size is 100 GB - multiple Docker containers can exist on a single virtual machine. The 22GB container size offers enough storage to contain software packages and scripts. However, large input files (>22 GB) can cause issues if the default container size is not changed.

### C. Simulation Script and TELEMAT TelApy

The simulation script from ATAPI runs TELEMAT simulations with the help of TELEMAT TelApy [6] – it allows full control of the simulation while running a case. This allows users to:

- download input data from AWS
- create a new or continuing simulation steering file using case info from AWS DynamoDB
- Create a S3-netcdf output file or prepare a previous computation file
- prepare the study using TelApy
- simulate the case step-by-step
- save model results instantly with S3-NetCDF (Group C),
- save the simulation progress by changing iframe in DynamoDB; and,

- determine Spot Instances termination and resubmit the job, if necessary

The logical flow diagram of the script is shown in Fig 5.

Starting a new simulation case creates a new S3-NetCDF file automatically. By default, ATAPI creates the essential variables to continue a simulation. For example, for TELEMAT2d, it creates velocity  $u$ , velocity  $v$  and free surface elevation variables.

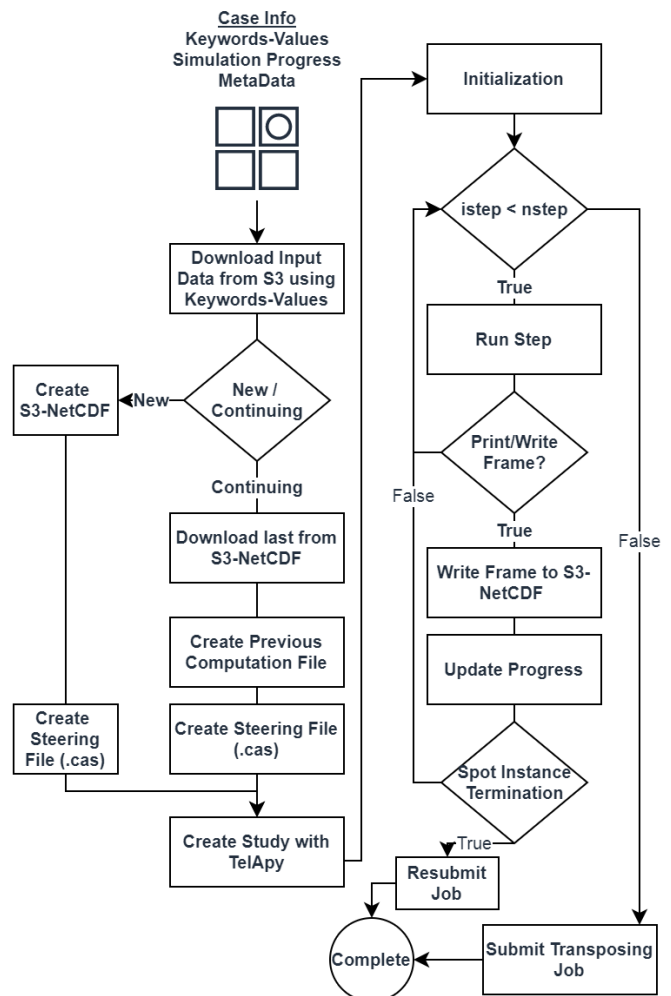


Fig 5 – Flow chart of the simulation script

The  $nframe$  is computed during the initialization step using the GRAPHIC PRINTOUT PERIOD keyword and the number of time steps (i.e. MODEL.NTIMESTEPS). The  $iframe$  value is updated every time simulation output data are saved to S3-NetCDF.

Cases with early termination are resubmitted to AWS Batch as a continuing job. Keywords such as PREVIOUS COMPUTATION FILE and COMPUTATION CONTINUED are added to the steering file. Data from the last saved frame are automatically downloaded from S3-NetCDF and are saved as the previous computation file.

To prevent simulated data from being unnecessarily written to the Docker container results file, the keyword `NUMBER OF FIRST TIME STEP FOR GRAPHIC PRINTOUTS` is specified equal to the number of time steps in the simulation. This prevents exceedance of the 22GB container limit.

Once the simulation is complete, it submits another job to transpose the dataset from Group C to Group D.

#### D. Transposing Script

ATAPI includes a short script to transpose the data array from Group C ( $nframe, nnode$ ) to GroupD ( $nnode, nframe$ ). This permits quick and efficient extraction of time-series information. As mentioned in the previous section, extraction of time-series information from Group C data would be computationally inefficient and expensive, as it would require download of every partition file. Fig 6 shows a flow chart diagram summarizing the script procedure. The memory-map functionality from the Numpy package was used to transpose the array. Numpy memory-map improves computational efficiency by allowing the data array to be stored as a binary file on the disk, as opposed to keeping the data in memory.

### V. APPLICATION EXAMPLE

ATAPI was used to simulate surge on the west coast of Canada using 3-hourly atmospheric and wind data from ECMWF ERA5. The model was used to simulate 35 scenarios from October to March from 1980 to 2015. Model and simulation characteristics are shown in TABLE 1.

TABLE 1: MODEL AND SIMULATION CHARACTERISTICS OF THE EXAMPLE

Number of nodes (nnode)	352,464
Number of elements (nelement)	618,205
Number of scenarios	35
Number of frames (nframe)	25921 26065 - leap year
Input atmospheric and wind data @ 3hr	~ 6 GB per scenario
Output model results (U,V,FS) @ 10min	~110 GB per scenario

#### A. Create steering case info and storing input files

For this project, the atmospheric and wind data input files were created on a local machine. A steering file (.cas) was created for each scenario on a local machine and then uploaded using ATAPI. Each scenario case was created using the syntax shown below:

```
1. from awstelemacapi import AwsTelemacApi
2. atapi=AwsTelemacApi ()
3. case1Info=atapi.upload('case1.cas')
4. ...
5. Case35Info=atapi.upload('case35.cas')
```

AwsTelemacApi is the main class object in ATAPI. The class contains AWS information such as Dynamo Table Ids, S3 Buckets Id, local folder, number of cores during simulation,

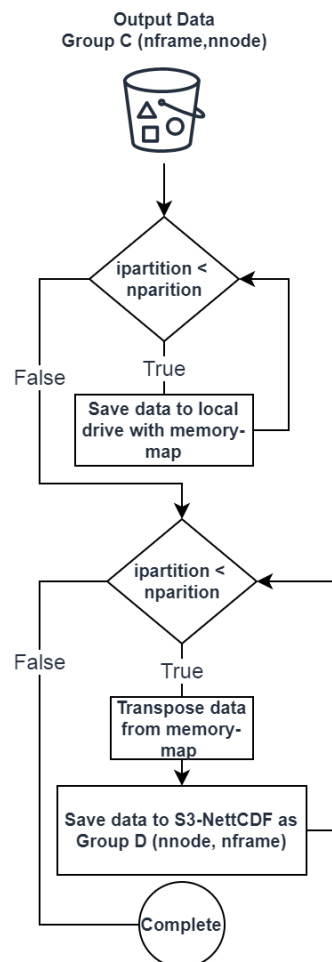


Fig 6: Flow chart of the transposing script

credentials, etc. Default values in the class can be changed by specifying keys-values as arguments (at line 2). The upload function provides functionality to read a steering file (.cas), convert the content to a steering object, check if local input files exist, upload input files to AWS S3, change the input paths in the steering object to S3 Path and upload the steering object to AWS DynamoDB.

#### B. Submit job and Simulate

The simulation jobs were submitted as shown below:

```
1. atapi.submitJob("case1")
2. ...
3. as atapi.submitJob("case35", cpu=24)
```

This syntax will send the jobs to the AWS batch queue. Once the environment is ready, it will run the simulation until completion. When calling the function, users must specify the case ID; no additional user-input is required. However, the number of CPUs employed can be changed by adding a key-value argument. The default number of CPUs is 48. If the simulation is already complete (i.e. *iframe* is equal to *nframe*), it will raise a warning.



For this example, the AWS account used during the runs had a limited access of 160 total CPUs. It took approximately 3 days to simulate all 35 scenarios with a price tag of approximately \$200 CAD at a 60% discount. Had On-Demand Instances been employed, the cost would have been approximately \$350CAD.

### C. Reading and Exporting

There are multiple ways of reading simulation data from AWS S3. A few example commands to extract the data are presented below, including descriptive comments:

```
1. # Extract u @ frame 0 for all nodes
2. u=atapi.query("case1", "u", frames=0)
3. # Extract u @ frame 1 and first 3 nodes
4. u=atapi.query("case1", "u", frames=0, nodes=[0, 1, 2])
5. u=atapi.query("case1", "u", frames=0, nodes=slice(0, 3))
6. # Extract u time-series @ node 0
7. u=atapi.query("case1", "u", nodes=0)
```

The code automatically selects the best group from which to extract data depending on the specifications of the enquiry. For example, the first 3 commands select data from Group C since the queries request data across a spatial range during a single time step. The fourth command selects data from Group D since the query requests data across a temporal range at a single location.

Data can be exported in a variety of formats including NetCDF, SelaFin, CSV, JSON and Shapefiles. There are some limitations associated with specific formats, and these limitations will be raised by Python should they be encountered (e.g. cannot export spatial and temporal data in a CSV file). A few example commands to export data are presented below, including descriptive comments:

```
1. # Export to netCDF (default): frame 0 for all nodes
2. atapi.export("case1", "u", frames=0)
3. # Export to SelaFin
4. atapi.export("case1", "u", frames=0, format="slf")
5. # Export to csv: node 0 for all frames
6. atapi.export("case1", "u", nodes=0, format="csv")
```

## VI. CONCLUDING REMARKS

This paper introduces the ATAPI, a new application programming interface that simplifies the integration of TELEMAT software and AWS resources. ATAPI is part of a framework that allows users to simulate, store and access TELEMAT simulations using AWS Cloud Computing Technologies. This capability permits automation of low level processes and allows users to easily share results with a wide range of users (e.g. scientists, engineers, stakeholders, and the public); thus enabling faster and more informed decision-making.

ATAPI was developed, built and tested on a Linux virtual machine using Python3. The API has only a few dependencies including:

- TELEMAT TelApy: Interact with TELEMAT simulations
- S3-NetCDF: read/write partition NetCDF files to S3
- SlfPy: Read/Write SelaFin files
- BOTO3: Communicate with AWS services
- Numpy, Scipy and Matplotlib: Scientific python packages

Documentation, installation, examples and tutorials (work in progress) are available on Github [5]. An AWS account is required to try ATAPI with the python interface.

### ACKNOWLEDGEMENT

The development of ATAPI was indirectly funded through multiple projects including “A New Tool and Database of Storm Surges and Waves in British Columbia Coastal Waters for Assessing Climate Risks to Federal Transportation Infrastructure” and “Inventory and Assessment of Tidal Energy Resources near Northern Communities”, financed by Transport Canada and POLAR Knowledge Canada, respectively. I thank Sean Ferguson from the National Research Council Canada for reviewing the manuscript and providing constructive feedback.

### REFERENCES

- [1] MIT, “StarCluster”, 2020, <http://web.mit.edu/stardev/cluster/>.
- [2] Cousineau, J, “s3-netcdf”, 2020, GitHub repository <https://github.com/meracan/s3-netcdf>.
- [3] Massey, Neil; Hassell, David; Lawrence, Bryan (2018): Semantic storage of climate data on object stores. Zenodo. Presentation. <https://doi.org/10.5281/zenodo.2597531>
- [4] Unidata, “netcdf4-python”, 2020, GitHub repository, <https://unidata.github.io/netcdf4-python>.
- [5] Cousineau, J, “aws-telemat-api”, 2020, GitHub repository <https://github.com/meracan/aws-telemat-api>.
- [6] Goeury, Cédric; Audouin, Yoann; Zaoui, F.; Ata, Riadh; El Idrissi Essebtay, S.; Torossian, A.; Rouge, D. (2017): Interoperability applications of TELEMAT-MASCARET System. In: Dorfmann, Clemens; Zenz, Gerald (Hg.): Proceedings of the XXIVth TELEMAT-MASCARET User Conference, 17 to 20 October 2017, Graz University of Technology, Austria. Graz: Graz University of Technology. S. 57-64.

# Ongoing developments in TELEMAC and TOMAWAC at IMDC

W. A. Breugem  
IMDC NV  
Antwerp, Belgium  
abr@imdc.be

**Abstract**—In this paper, various ongoing developments in TELEMAC and TOMAWAC are presented. The presented developments are:

- 1.) Two-way coupling between TELEMAC-2D and TELEMAC-3D.
- 2.) Implementation of surface rollers in TOMAWAC.
- 3.) The implementation of a functionality to export history files (data on a limited number of locations in the computational domain, such that typically a much higher output frequency can be used) in TELEMAC, TOMAWAC and GAIA
- 4.) Implementations to switch off horizontal diffusion in TELEMAC-3D, which lead to large speed-up of calculations with advected tracers.

## I. COUPLING BETWEEN TELEMAC-2D AND TELEMAC-3D

### A. Background and motivation

In many engineering applications, one has to deal with problems that involve three-dimensional flow effects in large areas. However, the three-dimensional flow effects are often important in only a part of the model domain. An example is the Scheldt estuary in Belgium (Fig.1). In this estuary, the effect of density currents due to the variation in salinity is important, especially in the area around Antwerp, for which the use of three-dimensional calculations is necessary. In these areas, an estuarine turbidity maximum (ETM) occurs, and also for the correct simulation of such an ETM, three-dimensional calculations are necessary. However, in the upstream parts of the estuary, which still have a large tidal variation, three-dimensional effects are less important. Instead, the tributaries are narrower, leading to the need of smaller mesh sizes and smaller time steps, such that the upstream part has a large impact on the calculation time of the model. Because of this, a large speed-up could in principle be obtained by performing simulations using a two-way coupled TELEMAC-2D and TELEMAC-3D model, where the TELEMAC-2D model is used in the upstream part of the estuary, and TELEMAC-3D in the downstream part.



Fig.1 Overview of the Scheldt Estuary (from VNSC communications).

### B. Objective and limitations

The objective is to develop a two-way coupling between TELEMAC-2D and TELEMAC-3D. This coupling has the following requirements:

- The coupling must work in parallel.
- Each sub-model can use different parameters. Especially, each model must have its own time step, which must be a multiple of each other.
- The coupling should be able to handle meshes with different extends (i.e. some overlap between the meshes must be possible).
- The changes to the existing TELEMAC-2D and TELEMAC-3D code should be as limited as possible.

### C. Implementation

The coupling between TELEMAC-2D and TELEMAC-3D is implemented in the Fortran version of the TELEMAC-API (the file `homere_api.F`). Many of the ideas for the coupling are inspired by the previous work coupling TELEMAC-2D to MASCARET [1]. Based on the finding in that work, it was opted for a method, in which both models are run consecutively (i.e. a multiplicative Schwartz method). Hence first TELEMAC-2D is run for one or more sub-steps, followed by TELEMAC-3D. The number of sub-steps for each of the models depends on the ratio of time steps in TELEMAC-2D and TELEMAC-3D. At the last sub-step, water levels and velocities at the location of the open boundaries are collected and communicated to the other model using the TEL2TOM

functionality [2]. TEL2TOM is a parallel coupling facility, developed originally to couple TELEMAC and TOMAWAC on different meshes. It provides parallel communication, as well as spatial interpolation using weighting coefficients that have to be determined during the pre-processing stage. Time interpolation or extrapolation is performed on the communicated water levels and velocities. The information that is applied on the boundaries are water levels ( $\eta$ ) and flow rates ( $q=Hu$ ), with  $H$  the water depth and  $u$  the flow velocity. Here, the flow rate is applied at an inflow boundary and the water level at an outflow boundary. These two variables were chosen, because some experiments showed that using these two variables, substantially more stable results were obtained than using water levels and velocities on the boundaries.

#### D. Limitations of the implementation.

The use of the TELEMAC-API leads to the limitations, that only one TELEMAC-2D model can be coupled with only one TELEMAC-3D model. Such a model can however consist of many different, unconnected domains. These domains must have the same physical and numerical parameters (such as the time step). Further, the coupling of additional TELEMAC modules (such as GAIA or WAQTEL) seems only possible with one of the two models (either TELEMAC-2D or TELEMAC-3D), but not to both of them. In the current implementation, coupling of tracers (e.g. temperature or salinity) is not implemented, but this could be done with relatively limited effort. Finally, in the existing TELEMAC code, there are a couple of functionalities, where the code of TELEMAC-2D and TELEMAC-3D are interlinked. The most important of these functionalities are the use of tidal boundary conditions (TPXO) and the use of meteorological data (wind and atmospheric pressure). Therefore, in the current implementation of the 2D-3D coupling, these features can only be used in TELEMAC-2D. Note that this limitations could be solved with relatively limited efforts by some cleaning of the code for these specific functionalities.

#### E. Preliminary results

A first test is performed to verify the correct implementation of the coupling. In this test, a TELEMAC-2D model, with two disconnected sections (an inflow section and an outflow section) is coupled to a TELEMAC-3D model with 20 vertical nodes in between (Fig. 2). The model represents a river (with flow from left to right), with some connected branch in the middle of the domain. The total length of the domain is 100 km, with a mesh size of 50 m, leading to 24169 nodes in the 2D domain and 3865 nodes in the 3D domain. The overlap between the two domains is 1 km at each side. The mesh in the overlap is the same in both meshes (although this is not strictly necessary for the coupling), except from a few small changes, to prevent overconstrained triangles at the boundaries of the subdomain. At the transitions between the domains, a water level boundary condition is used downstream, and a velocity boundary condition upstream. A slowly varying discharge boundary condition was applied at the upstream boundary of the 2D domain.

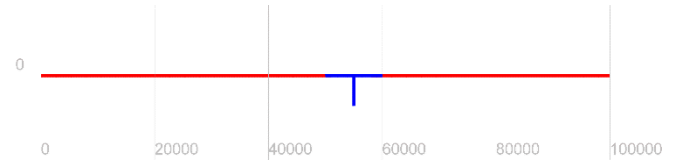


Fig. 2 Overview of the model domain. The TELEMAC-2D model is red, the TELEMAC-3D domain is blue.

The preliminary results of the water levels of the two models are shown in Fig. 3. It can be seen in this figure that the water levels coincide at the location where of the downstream boundary of the subdomains, thus showing that the implementation is correct. The water level in the 3D domain is however rather noisy. This becomes much worse when the time step is increased (in this test a rather small time step of 1 s was used). The cause of these instabilities is currently being investigated.

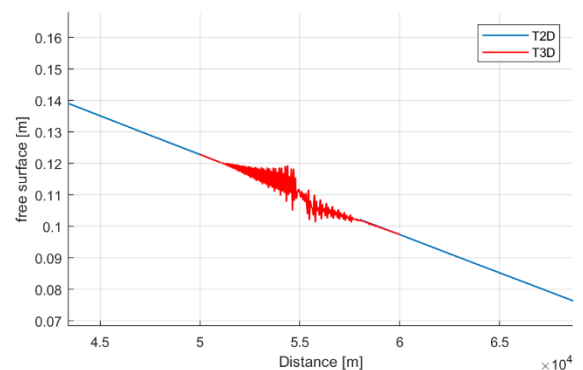


Fig. 3 Preliminary results of the water level in the two models after three hours of simulations.

#### F. Future work

The current implementation is limited to unidirectional flow, because the type of the boundary conditions (water level or velocity boundary) at the connections between the TELEMAC-2D domain and the TELEMAC-3D domain is currently set in the .cli files. The first step that will be performed is a functionality to change the type of the boundary condition depending on the flow conditions (flow direction and Froude number), such that also problems with changing flow directions (such as tides) can be simulated.

Further, in the current implementation, each model performs one iteration (i.e. there is no real Schwarz loop) per time step. While this is beneficial for calculation times (especially multiple iterations with TELEMAC 3D do not seem desirable), performing multiple iterations when needed, may make the model more stable. This will be investigated.

The results of the preliminary tests showed that the results can be influenced substantially by reflections at the (downstream) boundaries. Test using Thompson boundary conditions did not show any improvements. For the good functioning of the coupling, it seems necessary to develop non-reflective boundary conditions. Different options exist for this. One option, is to perform nudging (e.g. [5]). With this

option, the momentum equations are changed, such that the flow velocities are nudged toward the externally prescribed boundary conditions. Another option is to use Flather boundary conditions (e.g. [5]), which use a radiation condition on outflow boundaries to prevent reflections. It is to be investigated, which of these is the most appropriate option. It is noted that the development of non-reflective boundary conditions would be beneficial for many other applications as well.

Finally, further testing of the functionality needs to be performed.

## II. SURFACE ROLLERS IN TOMAWAC

### A. Background and motivation

When waves break, a part of the wave energy is transferred to surface rollers. These propagate shoreward, thus causing a delay between the point, where the waves begin to break and the point, where wave setup and longshore currents develop. In addition the surface rollers transfer mass towards the coast, thus influencing the return current that occurs. Finally, they can influence the stirring up of sediment

### B. Objective and limitations

The objective is to implement a model for the evolution of the energy of the surface rollers, and its influence on the long-shore currents. The effect of surface rollers on the stirring up of sediment and on the Stokes drift are currently neglected.

### C. Implementation

In the implementation, we follow the work by Zenner [8]. More information can also be found in for example [6]. According to these references, the surface roller energy  $E_r$  per unit of mass is given by:

$$E_r = \frac{1}{2} A \frac{\overline{U_{roller}^2} + \overline{W_{roller}^2}}{L}$$

Here,  $L$  is the wave length,  $A$  is cross-sectional area of the surface roller, and  $U_{roller}$  and  $W_{roller}$  the velocity components in the horizontal and vertical direction respectively. The overbar denotes averaging over a roller. The evolution of the surface roller energy is given by the following differential equation:

$$\frac{\partial E_r}{\partial t} + \frac{\partial c_x E_r}{\partial x} + \frac{\partial c_y E_r}{\partial y} = D_w - D_r$$

Here  $c_x$  and  $c_y$  are the x and y components of the phase velocity of the waves.  $D_w$  is the energy dissipation due to breaking of the waves (which is calculated in TOMAWAC using the depth induced breaking routines, e.g. using the formulation of Battjes and Jansen), and  $D_r$  is the energy dissipation of the surface rollers, which is parametrized as:

$$D_r = 2 \frac{\beta_s}{\beta_2} \frac{g}{c} E_r$$

Here,  $\beta_s$  and  $\beta_2$  are calibration parameters, and  $g$  is the gravitational acceleration.

The effect of the surface rollers of the current comes from its effect on the radiation stresses, which are given by:

$$S_{xx} = S_{xx,waves} + \cos^2 \theta E_r$$

$$S_{xy} = S_{xy,waves} + \cos \theta \sin \theta E_r$$

$$S_{yy} = S_{yy,waves} + \sin^2 \theta E_r$$

Here,  $S_{xx}$ ,  $S_{xy}$  and  $S_{yy}$  are the different components of the radiation stress tensor,  $S_{xx,waves}$ ,  $S_{xy,waves}$ ,  $S_{yy,waves}$  the radiation stress components from the surface waves (as calculated in TOMAWAC), and  $\theta$  the mean wave direction.

This differential equation is implemented in TOMAWAC using a fractional step method. The advection step is solved first using the method of characteristics. The velocity field is determined every time step from the peak period, water depth and mean wave direction calculated by TOMAWAC (for the moment ignoring the effect of wave-current interaction). After the advection step, the source and sink terms are applied. Here,  $D_r$  is calculated using an implicit numerical discretisation while  $D_w$  uses an explicit discretisation.  $D_w$  is exported directly from the calculation of the depth induced breaking term of Battjes-Janssen in TOMAWAC. Currently, this is only implemented in a new version of the breaking source term (which can be switched on by setting the keyword DEPTH-INDUCED BREAKING DISSIPATION=10). This new implementation of the source term speeds up the calculation of the depth-induced breaking significantly by the following modifications:

- The use of an implicit numerical scheme with Newton-Raphson iteration. This additionally has the advantage that it makes the computation more robust and that the user does not need to specify the number of time steps for the breaking iterations; the number of iterations is determined automatically using a convergence criterion.
- The use of threshold to make sure the depth-induced breaking is only calculated on the mesh points, where depth induced breaking is important (i.e. shallow points).
- The calculation of the energy dissipation for the mean action density only, because the source term of Battjes-Janssen leads to an energy dissipation that is constant for each component in the spectrum. Only after all the iterations for breaking are performed, the energy dissipation is applied over the spectrum.

### D. Preliminary results

A first test was performed in the littoral test case. In this test case, waves, with an offshore significant wave height of 1.0 m propagate toward the coast under an angle. While propagating, towards the shore, they refract and start breaking thus generating a longshore current. The results of two test calculations, one without surface roller and one with surface rollers are shown in Fig. 4. This figure shows clearly that the surface rollers cause the wave-driven current to be moved closer to the shore. This is as expected from theory, and this is one of the main motivations for including the effect of surface rollers. Further, it causes the maximum longshore to increase. Interestingly, a current in the opposite direction is generated at



the start of the breaking zone. The reason for this is not yet clear.

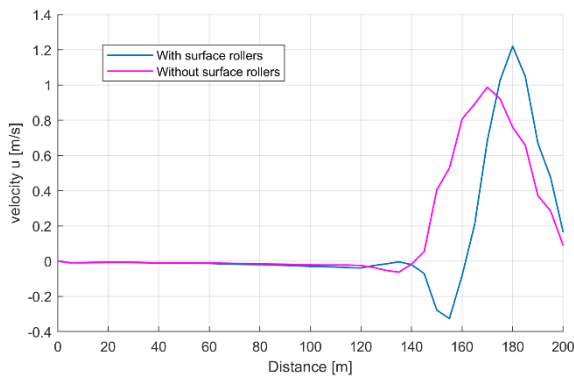


Fig. 4 The wave-generated longshore current in the littoral test case with and without surface rollers. The beach is on the right side of the figure

### E. Future work

In the next phase, more extensive testing of this functionality is needed, in both schematic test cases and real applications, as well as using parallel computations. It seems especially needed to compare the results in a schematic test case, with some reference solution. Also, the implications of ignoring the effect of wave-current interaction need to be studied. Further, the effects of surface rollers on return currents and the stirring up of sediment may be implemented to improve the cross-shore modelling facilities in TELEMAC-TOMAWAC-GAIA. Finally, some work need be done on the IO with respect to this routine, such as adding keywords to the .CAS file and adding the possibility to export the surface roller energy to the TOMAWAC result files (this is currently done using a private array).

## III. IMPROVEMENTS IN INPUT/OUTPUT

### A. Background and motivation

When working with TELEMAC, input and output are important to provide correct data to the model as well as to export the results of the simulations for postprocessing. Different computational environments provide different limitations in this respect. On HPC clusters, the storage space may be limited for the individual users, and hence the need arises to limit the amount of storage space taken by the input and output data in the model. Other advantages of limiting these data consist of shorter pre-processing and post-processing times, and shorter times needed to download data. Especially on older infrastructure, the time spend on IO may be a bottleneck for the duration of the computation.

### B. Objective and limitations

The objective is to provide more flexibility in the TELEMAC-IO. More specific, the aim is to develop the functionality to make so called “history files”, which are files which export time series of point-data or 1-d vertical profiles (for example at the location of a measurement station), but with a much higher time resolution than is typically used in the normal TELEMAC output files. Further, it is the objective

to improve the *find\_variable* subroutine, to limit the amount of IO in this routine.

### C. Implementation

The functionality for exporting history files is implemented. This functionality reads coordinates of the required output points from a text file, performs linear interpolation on the data (using weight factors computed during the initialization of the model in order to have a fast performance; these weights are calculated such that they correspond to the P1 discretisation used in TELEMAC; the weight factors are saved for the entire calculation in order to save calculation time) and then stores the data using the existing HERMES IO-module. Finally, some adaptations to GRETEL were done, in order to be able to merge the generated output files of a parallel computation to a single output file.

In order to generate the history files, the following keyword were added to TELEMAC-3D (and similar in TOMAWAC, GAIA and TELEMAC-2D)

**HISTORY COORDINATES FILE** : the name of the file with the required output coordinates

**2D HISTORY FILE**: 2D results file with time series of depth-averaged point data

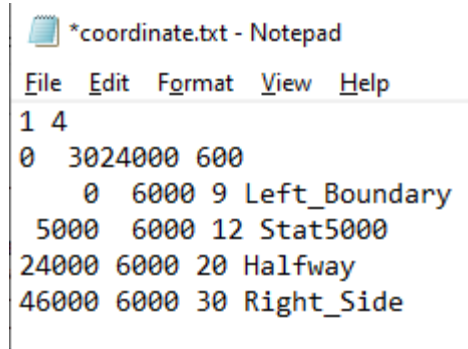
**3D HISTORY FILE**: 3D results file with time series of 1DV profile data

The format of the HISTORY COORDINATE FILE is as follows:

- On the first line, there are two numbers indicating:
  - The number of time periods for which data is written to the HISTORY FILE
  - The number of coordinates for which output is generated
- On the next lines, for each output period, three numbers indicating:
  - Start of the output period (in seconds since the start of the model)
  - End of the output period (in seconds since the start of the model)
  - Output time interval (in seconds)
- For each coordinate, three numbers and a string:
  - X-coordinate of the output point
  - Y-coordinate of the output point
  - Unique ID of each station (in order to easily encounter the output data in the output files). This ID will be written to the IKLE-array in the output file, which has a size [NPOINTSx1]. Note that the history files have different points. There is no mesh information, thus explaining that the length of the IKLE array is the same as the number of points in the history file.

- The name of the station (for better readability of the coordinate file)

An example is shown in Fig. 5.



```
*coordinate.txt - Notepad
File Edit Format View Help
1 4
0 3024000 600
0 6000 9 Left_Boundary
5000 6000 12 Stat5000
24000 6000 20 Halfway
46000 6000 30 Right_Side
```

Fig. 5 Example of a HISTORY COORDINATE FILE

Finally, an updated version of *find variable* was made. This function is used to read data from input files (e.g. for meteo data), including the time interpolation of the data. However, this function reads data from the previous and future moments in the input file, at each time step. This leads to a large amount of IO, in case the time step in the input file is much larger than the time step in the model. In the updated version, data from the previous and future time steps in the input files are stored in memory, thus limiting the amount of IO considerably.

#### IV. IMPROVEMENTS IN 3D SCALAR TRANSPORT AND STRATIFIED FLOW

##### A. Background and motivation

In many practical problems, the transport of scalars is important. For example, these tracers can be different sediment fractions when using GAIA, or different water quality parameters when using WAQTEL maybe in combination with AED2. In many situations, these scalars vary strongly over the vertical, meaning that it is important to perform 3D simulations using TELEMAT-3D. Using these modules can lead to problems with large number of advected tracers (in AED2, this can be up to at least 24). However, using many scalar variables can lead to large calculation times. Some of these tracers (like sediment salinity or temperature) are so called active tracers. This means that their concentration influences the density, and hence can change the flow due to the generation of baroclinic pressure gradients or stable vertical stratifications, which damp turbulence.

##### B. Objective and limitations

The objective is to improve the transport of scalars in TELEMAT-3D, in particular with the objective to decrease the calculation time of the simulation, and to diminish the artificial vertical mixing present in TELEMAT-3D.

##### C. Implementation

Profiling was done, in order to determine the bottlenecks with respect to the transport of tracers. From this it was found that diffusion formed a bottleneck, which is apparently because a large matrix needs to be solved to calculate the

diffusion. This matrix is substantially larger than the matrix in the flow calculations, which contains only the 2D points, whereas the tracer diffusion is calculated using a matrix containing all 3D points. It was then realized that for many (but certainly not all) typical problems (e.g. dispersion of sediment plumes), the horizontal diffusion is not very important physically (in contrast to vertical diffusion, which is very important). This is particularly so, because the advection schemes that are typically used in TELEMAT (like NERDS) lead to a substantial amount of numerical diffusion, which seems to be of a similar magnitude as the horizontal diffusion calculated by the advection-diffusion solver. Also note that horizontal diffusion in large scale flows (such as in coasts or oceans) is a process that is physically not very well understood, making the values for the coefficients that need to be specified by the user rather uncertain.

It was then realized that for sediment, it is possible to switch off the horizontal diffusion and apply the vertical diffusion (with a fully implicit scheme), using the subroutine *set\_diff* by setting these two settings in the .cas file:

```
SCHEME FOR DIFFUSION OF TRACERS = 0
ADVECTION-DIFFUSION SCHEME WITH
SETTLING VELOCITY : 1
```

These settings only work in combination with residual distribution schemes (such as NERD or LIPS). This is not a big disadvantage, as these are the most suited advection schemes for the transport of tracers in practical applications anyway.

In order to speed up calculation of tracers, the code was adapted (by specifying settling velocities and erosion/depositions terms with a default value of zero), such that horizontal diffusion can be switched off, and vertical diffusion is calculated for any tracer (not just sediment), by setting the previously shown keywords. In order to have all important physical processes, the surface boundary conditions and the explicit and implicit source terms were added to the *set\_diff* subroutine, such that they can also be taken into account for those tracers that need it.

Note that in those cases where horizontal diffusion is important, one could set IMPLICITATION FOR DIFFUSION = 0.0 in order to have the horizontal diffusion explicit. This is different from using SCHEME FOR DIFFUSION OF TRACERS = 2, because when using *set\_diff*, an implicit scheme is still used vertically. In this way, the horizontal diffusion is taken into account for a fraction of the computation cost. There is a time step criterion involved:

$$\Delta T < \frac{\Delta X^2}{D_H}$$

Here,  $\Delta X$  is a measure of the mesh spacing (e.g. the square root of the area of the triangle)  $\Delta T$  is the time step and  $D_H$  is the horizontal diffusivity. For typical, engineering applications, this criterion allows rather large time steps, which are typically larger than the time step actually used in the model. Note that the use of *set\_diff* ensures that the vertical diffusion is solved implicitly, which is important, because the time restriction for vertical diffusion is much more stringent

due to the fact that in typical applications, the vertical mesh spacing is much finer than the horizontal one.

#### D. Preliminary results

The settings prescribed in the previous section have been applied in many different model simulations. Indeed, a large speed up is obtained. Switching off horizontal diffusion appeared to have the following additional advantages:

- Simulations appear to be more stable (especially on tidal flats).
- The mass balance seem to be more correct (even when decreasing the accuracy of the solver to  $10^{-12}$ ).
- In case of stratified flow, horizontal diffusion can lead to some extra vertical mixing (especially when the vertical layers are not completely horizontal, e.g. when using sigma or double-sigma layers. This diminishes the stratification, leading to incorrect results (such as errors in the penetration of a salt wedge).

Two examples are presented here. First a schematic case was run using AED-2 with phytoplankton in a square basin with 133 nodes, with a time step of 60 s. This test case has 22-advected tracers. The calculation time with the traditional TELEMAC settings was 49 s for a simulation period of one day. Switching the horizontal diffusion off, the calculation time reduced to 20 s, giving a speed-up of a factor 2.5, while the results remained the same. In this case, the speed-up is still rather modest, which is due to the fact that the case is homogeneous, and hence the number of iterations of the matrix solver when solving horizontal diffusion of the tracers appears to be very low (either 0 or 1).

As a second example, a test case is run, in which the Rouse profile is calculated for a single sediment fraction using 10 vertical nodes. In this test case, the standard TELEMAC settings (with the default solver for the diffusion of tracers, which is conjugate gradient on a normal equation) resulted in a calculation time of 25 s, which reduced to 12 s in case the horizontal diffusion was switched off. In this case, the speed up is much larger. The reason is that in this case, the flow field and the concentration profile were not homogeneous, hence leading to a larger number of iterations to solve the implicit horizontal diffusion (the typical number of iterations for the matrix solver was around 10). Also in this case, the results were very similar for the cases with and without horizontal diffusion.

#### E. Future work

In the next phase, it is intended to change the first-order advection scheme in the *set\_dif* subroutine to a second order scheme, in order to limit the numerical diffusion. Further, more attention will be paid to the stratified flow. Specifically, two issues are addressed. Hodges and Rueda [4] study the inclusion of density driven flows in a numerical algorithm rather similar to the wave-equation approach used in TELEMAC-3D [3]. They show that adding the baroclinic pressure gradient directly (such as done in TELEMAC-3D)

leads to a system of equations that is unstable without any further dissipation. This means, that artificial currents can be created, when active tracers are present. Although these artificial currents are typically weak (a few cm/s), this may be a serious problem, particularly in situations where the flow is weak, such as in lakes or in the deep ocean. As a solution, they propose a prediction-corrector scheme, which is stable.

Further, it is important to calculate the baroclinic pressure gradient accurately. This can be very difficult, particularly in case the elevation of vertical layers vary in space such as when using sigma-coordinates or close to the bottom using z-double-sigma coordinates. Wang et al [7] proposed to use cubic-spline interpolation to perform accurate vertical interpolation to equal levels, in order to calculate the baroclinic pressure gradient more accurately.

It is intention to implement these two techniques in TELEMAC-3D and study whether these prevent artificial mixing of stratification in an idealized case.

## V. SUMMARY AND CONCLUSIONS

In this paper, various ongoing developments in TELEMAC and TOMAWAC are presented. The presented developments are:

1.) Two-way coupling between TELEMAC-2D and TELEMAC-3D. In this task, TELEMAC-2D and TELEMAC-3D are coupled with the objective to decrease the calculation time substantially, by only applying TELEMAC-3D in the areas where three-dimensional processes are physically important. At the moment, a first test case is set up, which still shows instabilities that need to be addressed.

2.) Implementations of surface rollers in TOMAWAC. Here, an extra physical process is implemented in TOMAWAC. A first test in the littoral test case shows that the implementation changes the longshore current in a way as expected from theory.

3.) The functionality to export history files (data on a limited number of locations in the computational domain, such that typically a much higher output frequency can be used) in TELEMAC, TOMAWAC and GAIA

4.) the possibility to switch off horizontal diffusion in TELEMAC-3D, which lead to large speed-up of calculations with advected tracers.

## REFERENCES

- [1] Barthélémy, S., Ricci, S., Morel, T., Goutal, N., Le Pape, E., & Zaoui, F. (2018). On operational flood forecasting system involving 1D/2D coupled hydraulic model and data assimilation. *Journal of Hydrology*, 562, 623-63
- [2] W.A. Breugem, E. Fonias, L. Wang, A. Bolle, G. Kolokythas and B. De Maerschalck, "TEL2TOM: coupling TELEMAC2D and TOMAWAC on arbitrary meshes," XXVth TELEMAC-MASCARET User Conference, Toulouse, 15-17 October 2019
- [3] Hervouet, J. M. (2007). *Hydrodynamics of free surface flows: modelling with the finite element method* (Vol. 360). Chichester, UK: Wiley.
- [4] Hodges, B. R., & Rueda, F. J. (2008). Semi-implicit two-level predictor-corrector methods for non-linearly coupled, hydrostatic, barotropic/baroclinic flows. *International Journal of Computational Fluid Dynamics*, 22(9), 593-607.

- [5] Marchesiello, P., McWilliams, J. C., & Shchepetkin, A. (2001). Open boundary conditions for long-term integration of regional oceanic models. *Ocean modelling*, 3(1-2), 1-20.
- [6] Roelvink, D., Reniers, A. J. H. M., Van Dongeren, A., Van Thiel de Vries, J., Lescinski, J., & McCall, R. (2010). XBeach model description and manual. Unesco-IHE Institute for Water Education, Deltares and Delft University of Technology. Report June, 21, 2010.
- [7] Wang, Q., Danilov, S., & Schröter, J. (2008). Finite element ocean circulation model based on triangular prismatic elements, with application in studying the effect of topography representation. *Journal of Geophysical Research: Oceans*, 113(C5).
- [8] Zenner, S. (2018) Numerieke simulatie van golven, stromingen en sedimenttransport in de strand- en strandnabije zone, Master thesis KU Leuven (in Dutch)



# A Multi-class Frazil Ice Model for Shallow Water Flows

Fabien Souillé, Florent Taccone

National Laboratory of Hydraulics and Environment  
EDF R&D

6 Quai Watier, Chatou, France

[Fabien.souille@edf.fr](mailto:Fabien.souille@edf.fr)

Chaymae El Mertahi

EDF R&D and  
ENSEEIH

6 Quai Watier, Chatou, France

2 rue Charles Camichel, Toulouse, France

**Abstract**— Frazil ice, consisting of suspended disk shaped crystals, is the primary form of ice encountered in turbulent water bodies. Frazil ice clogging of power plants water intakes is a risk that companies have been challenged to address in recent years. In this context, physically based modelling is a useful tool that helps predict the evolution of water temperature and frazil ice during cold events. The TELEMAC-MASCARET system, with its recently introduced module KHIONE (coupled with TELEMAC-2D), allows to predict frazil ice dynamics via a thermal growth model, considering constant crystal radii. Among the drawbacks of this approach are the difficulty of choosing a representative radius and the turbulence variation not being taken into consideration in the thermal growth process. Multi-class models, assuming a discrete radius distribution, each class being composed of particles of the same radius, are more complex but provide a comprehensive description of frazil ice formation processes. This work is aimed at bringing state of the art frazil ice models into the TELEMAC-MASCARET system in order to expand its frazil modeling capabilities. A multi-class frazil ice model is therefore developed in the present work.

Several processes are modelled to predict frazil ice formation and evolution: thermal growth and decay, consisting of phase change around crystals (increasing their size), is based on the heat transfer between turbulent water and frazil ice particles; secondary nucleation, which increases the number of nuclei, is caused by the fragmentation of particles due to collisions; flocculation, i.e. formation of larger aggregates, is assumed to be the net effect of flocculation and breakup processes; salinity is also taken into consideration as it has a significant impact on the fusion temperature. Thus, salt rejection process due to phase change is modelled as well.

The proposed model is able to simulate the evolution of depth-averaged temperature, salinity, frazil concentration in a 2D domain with time dependent atmospheric drivers. It has been confronted to laboratory experiments and is able to reproduce supercooling and temperature recovery for both fresh water and saline water under different turbulent conditions.

## I. INTRODUCTION

When water temperature diminishes below the fusion point (supercooling), small particles of ice start to develop. These disk shaped crystals, known as frazil ice, are the primary form of ice encountered in turbulent water bodies. Their growth dynamic can lead to significant impact on environment and industrial facilities during cold events by accumulation on submerged structures such as water intake trash racks.

Frazil ice physics have been studied a lot over the last decades. A general overview can be found in [5, 8]. Several models are proposed in literature to predict the evolution of frazil concentration, temperature and ice cover during freeze-up periods like [23], [12], [22] or [15]. One has been added to TELEMAC-MASCARET v8p0 through a collaboration between EDF R&D, HR Wallingford and Clarkson University that gave birth to a new module dedicated to ice modelling named KHIONE [2] (coupled with TELEMAC-2D). It is based on the long experience acquired by Clarkson University with the development of river ice models such as CRISSP2D and DynaRICE [13, 22, 24]. However, the first implementation of KHIONE only incorporates tracer transport (Eulerian part of DynaRICE) and a static model for surface ice cover (static border ice). The focus of DynaRICE, i.e. ice cover dynamics developed in [13, 22] through an SPH formulation was not integrated into KHIONE by then. The frazil ice model in KHIONE relies on one equation to describe volume fraction, assuming all particles have the same radius, and the evolution of the concentration to be mainly governed by thermal growth [19, 22]. Turbulence variation is neglected in the model and a constant Nusselt number is considered.

The multi-class model developed in this study brings new processes to KHIONE, including thermal growth (and decay), secondary nucleation, flocculation, the effect of turbulence, salinity impact on fusion point and salt rejection. Its goal is to increase KHIONE's ability to predict frazil ice evolution in the early phase of supercooling. Frazil ice crystals vary in size from about  $10^{-5}$  m to  $10^{-3}$  m and can form large flocs up to  $10^{-1}$  m [7]. Given the observed wide range of crystal radii in nature, and the sensitivity of a growth/melting model to this parameter, the use of the multi-class model provides a more physical representation of this process. Moreover, the multi-class approach allows to model a wide variety of physical processes which leads to a more comprehensive depiction of frazil crystals evolution in the flow. The multi-class description relies on a discrete distribution of radius, each class being composed of particles of the same radius. The evolution of the concentration of each class is then modelled with a set of advection-diffusion equations with source terms defined for each process. Thermal growth is based on the heat transfer between turbulent water and frazil ice crystals and consist of mass jumps between classes as proposed in [23]. However, the thermal growth model chosen in this study is the one later presented by [12] for its ability to model melting. Additionally, collisions between suspended frazil particles produce a fragmentation that creates new nuclei. This phenomenon, known as secondary nucleation, is modelled as

proposed in [20]. Collisions also produce flocculation and breakup and the formation of larger aggregates is assumed to be the net effect of these processes as suggested in [20]. Turbulence also plays an important role in the effectiveness of the heat transfer between water and the particle, and consequently in frazil ice formation as it increases thermal growth rate. It also plays a key role in estimating the collision rate between particles [8, 11, 20]. Two options are proposed in this model to estimate turbulent parameters, a k- $\epsilon$  model and a simplified depth integration of vertical k- $\epsilon$  profiles as proposed in [23]. Finally, salinity has a significant impact on frazil ice since it diminishes the fusion point. Additionally, frazil formation releases salt, increasing the local salinity. Both impact on the freezing temperature and salt rejection process are modelled in this study.

Frazil ice formation has been studied in laboratory experiments [3, 4, 10, 18] at relatively small scale. Understanding the formation of frazil in large water bodies is still challenging and is an active research topic. Some attempts to measure frazil in nature have been made as in [21]. Frazil ice concentration being the focus of our study, it has been decided to assess KHIONE's validity in the supercooling phase. The model proposed in this study is therefore confronted to experimental data from [3] for fresh water and [10] for saline water in the case of a turbulent flow in a racetrack configuration.

This paper is organised as followed. First, the model equations and numerical resolution method are presented. Then, it is confronted to experimental data [3, 10] to evaluate its representation of the temperature and frazil ice evolution. Finally, the performances and limitations of the model are discussed.

## II. MODEL FORMULATION

This study is focused on environmental flows in rivers, lakes or coastal areas. The 2D viscous Shallow Water Equations (SWE) are considered for the mean flow, and are introduced hereafter. Temperature, salinity and frazil volume fraction are considered to be passive scalars and are modelled with convection-diffusion equations with source terms. Frazil volume fraction is assumed small compared to 1 so that it does not affect water density nor viscosity. Ice cover dynamics are not taken into account in the model.

### A. Hydrodynamics

The SWE can be obtained from the incompressible Navier-Stokes equations for a Newtonian fluid, assuming that the water depth  $h$  is small compared to the longitudinal length of the domain. The conservation of mass and momentum reads:

$$\frac{\partial h}{\partial t} + \nabla \cdot (h\mathbf{u}) = 0, \quad (1)$$

and

$$\frac{\partial h\mathbf{u}}{\partial t} + \nabla \cdot \left( h\mathbf{u} \otimes \mathbf{u} + g \frac{h^2}{2} \mathbf{I} \right) = -gh\nabla z_b + \nabla \cdot (h\mathbf{D}) - \frac{\boldsymbol{\tau}_b}{\rho}. \quad (2)$$

The unknowns of the system are the depth averaged mean velocity  $\mathbf{u} = [u(x, y, t), v(x, y, t)]^T$  and the water depth  $h(x, y, t)$ . The space and time coordinates denoted  $(x, y)$  and  $t$  will be dropped in the following for clarity's sake. In Equations (1) and (2)  $z_b$  is the bottom elevation,  $\boldsymbol{\tau}_b$  is the

bottom shear stress,  $g$  is the gravitational acceleration and  $\rho$  is the density of water, assumed to be constant. The diffusion tensor  $\mathbf{D}$  is written as  $\mathbf{D} = 2(\nu + \nu_t)\boldsymbol{\epsilon}$  where  $\boldsymbol{\epsilon} = \frac{1}{2}(\nabla\mathbf{u} + \nabla\mathbf{u}^T)$  is the rate of strain tensor,  $\nu$  the kinetic viscosity of water and  $\nu_t$  the turbulent viscosity. Equations (1) and (2) need closure relations for the bottom shear stress and the turbulent viscosity. The Manning-Strickler relation is used for bottom shear stress and either a k- $\epsilon$  or a constant viscosity model is used for the estimation of  $\nu_t$ .

### B. Frazil evolution

A discrete radius distribution is used to describe suspended frazil ice. A number of  $N_c$  classes are considered. The balance equation of the frazil volume fraction for the  $k^{\text{th}}$  class is given by:

$$\frac{\partial C_k}{\partial t} + \mathbf{u} \cdot \nabla C_k = \nabla \cdot (\nu_{t,k} \nabla C_k) + S_{GM}^k + S_{SN}^k + S_{FB}^k, \quad (3)$$

where  $C_k$  is the depth averaged volume fraction and  $\nu_{t,k}$  is the turbulent diffusivity of the  $k^{\text{th}}$  frazil class. The source terms  $S_{GM}^k$ ,  $S_{SN}^k$ ,  $S_{FB}^k$  stand for thermal growth (melting), secondary nucleation and flocculation (breakup) respectively. The total frazil concentration  $C$  can be computed as  $C = \sum_{k=1}^{N_c} C_k$ . The number of particles per unit volume for each class is given by  $N_k = C_k/V_k$  with  $V_k$  the frazil crystal volume of class  $k$ .

#### 1) Thermal growth

Let us first introduce the heat flux between frazil crystals of class  $k$  and water in Equation (4):

$$q_k = \frac{K_w Nu_k}{l_k} (T_i - T), \quad (4)$$

where  $K_w$  is the thermal conductivity of water and  $T_i$  the crystal temperature assumed to be equal to the freezing temperature  $T_f(S)$  which depends on the salinity  $S$  such that  $T_f(S) = -0.0575S + 0.00171S^{3/2} - 0.00021S^2$ . Frazil crystals are supposed to have the same disk shaped geometry characterized by a radius  $r_k$  and a thickness  $e_k$ , related with a constant ratio  $R$  such that  $e_k = 2r_k/R$ .  $R$  is fixed to 8 based on [8]. The characteristic length scale  $l_k$  for the crystals of class  $k$  is supposed to be equal to  $r_k$  as suggested in [11, 12]. The Nusselt number  $Nu_k$  is defined with the parametrization initially proposed in [1] and [25] and summarized in [5] and [11]. Let us define the ratio  $m^* = r_k/\eta$  between the radius and the Kolmogorov length scale noted  $\eta$  and defined by:

$$\eta = \left( \frac{\nu^3}{\epsilon} \right)^{1/4}, \quad (5)$$

where  $\epsilon$  is the turbulent kinetic energy dissipation rate and  $\nu$  the molecular viscosity of the fluid. For small particles, heat transfer is governed by diffusion and convection, and the Nusselt number can therefore be written in Equation [6].

$$Nu_k = \begin{cases} 1 + 0.17m_k^* P_r^{1/2} & \text{if } m_k^* \leq P_r^{-1/2} \\ 1 + 0.55m_k^{*2/3} P_r^{1/3} & \text{if } P_r^{-1/2} < m_k^* \leq 10 \end{cases} \quad (6)$$

For larger particles ( $m_k^* > 1$ ), heat transfer is governed by turbulent mixing of the boundary layer around the crystal and the Nusselt number is defined by

$$Nu_k = \begin{cases} 1.1 + 0.77\alpha_T^{0.035} m_k^{*2/3} P_r^{1/3} & \text{if } \alpha_T m_k^{*4/3} \leq 1000 \\ 1.1 + 0.77\alpha_T^{0.25} m_k^{*1/3} & \text{if } \alpha_T m_k^{*4/3} > 1000 \end{cases}, \quad (8)$$

in which  $P_r$  denotes the Prandlt number, defined as the ratio between molecular and thermal diffusivity, and  $\alpha_T = \frac{\sqrt{2k}}{|u|}$  the turbulent intensity.

The thermal growth (or decay) source term  $S_{GM}^k$  represents the net rate of volume change of class  $k$  resulting from interactions with classes  $k-1$  and  $k+1$  due to freezing or melting. Following [23] for thermal growth and [12] for the introduction of melting, the net rate of volume fraction change for the frazil class  $k$  can be defined as:

$$S_{GM}^k = \frac{V_k}{\Delta V_{k-1}} [(1-H)M_k + HG_{k-1}] - \frac{V_k}{\Delta V_k} [(1-H)M_{k+1} + HG_k], \quad (10)$$

with  $H = He(T_f - T)$ , where  $He$  is the Heaviside function and  $V_k$  the volume of ice crystals. Volume ratios  $\Delta V_k = V_{k+1} - V_k$  account for the scaling of the computed volume change to the number of particles that jump from a class to another. As explained in [8], frazil crystals are supposed to grow only from their edges because of their disk shape, which leads to the production rate for thermal growth defined by:

$$G_k = \frac{K_w Nu_k}{L_i \rho_i} (T_f - T) \frac{2}{r_k^2} C_k, \quad (11)$$

whereas the melting is supposed to occur on all surfaces of the disk which leads to:

$$M_k = \frac{K_w Nu_k}{L_i \rho_i} (T_f - T) \frac{2}{r_k} \left( \frac{1}{r_k} + \frac{1}{e_k} \right) C_k, \quad (12)$$

where  $\rho_i = 916.8 \text{ kg.m}^{-3}$  is the ice density and  $L_i = 3.35 \cdot 10^5 \text{ J.kg}^{-1}$  the latent heat of ice fusion. For the first and last classes, the boundary conditions  $V_0 = V_{N_c+1} = G_0 = G_{N_c} = M_{N_c+1} = 0$  are used [12].

When only one class of frazil is selected in KHIONE, the model uses a monoclase frazil ice model, in which only thermal growth is considered. In this case, the source term for frazil ice is defined by:

$$S_{GM}^1 = (1-H)M_1 + HG_1. \quad (13)$$

### 2) Secondary nucleation

When frazil crystals collide, new nuclei are detached which increases the volume fraction of the smallest particles. This is known as the secondary nucleation process. Secondary nucleation can be modelled using an approximation of the collision frequency between particles [20]. A particle with a velocity  $w_k^r$  relative to the fluid sweeps a volume  $\delta V = w_k^r \pi r_k^2 \delta t$  during  $\delta t$ . The collision frequency can be estimated as  $f_{coll}^k \sim \tilde{n} \delta V n_k / \delta t$ , in which  $\tilde{n}$  is an estimation of the average number of particles per unit volume, defined in Equation (14) and  $n_k$  the number of particles of class  $k$  per unit volume:

$$\tilde{n} = \max \left( \sum_{j=1}^{N_c} n_j, n_{max} \right). \quad (14)$$

$n_{max}$  is a calibration parameter used to limit collisions impact. The relative velocity is estimated from the rising and turbulent velocities such that

$$w_k^r = \sqrt{U_k^t{}^2 + w_k^2}, \quad (15)$$

with  $U_k^t = 2r_k \sqrt{\frac{\varepsilon}{15\nu}}$  and  $w_k$  the buoyant rise velocity of frazil crystals. Different empirical approaches are proposed in the literature to estimate  $w_k$ , i.e. [16], [9] and [5]. In this study, we use the formulation proposed in [9] which has been confronted to lab and field data. The rise velocity is estimated with:

$$w_k = \sqrt{\frac{2ge_k(\rho - \rho_i)}{C_d \rho}}. \quad (16)$$

in which the drag coefficient  $C_d$  can be calculated with the Reynolds number of frazil crystals as described in [9]. Finally, volume fraction change rate due to secondary nucleation can be written as:

$$S_{SN}^k = \begin{cases} \sum_{j=2}^N \pi \tilde{n} w_j^r r_j^2 C_j & \text{if } k = 1 \\ -\pi \tilde{n} w_k^r r_k^2 C_k & \text{if } k \neq 1 \end{cases}. \quad (17)$$

### 3) Flocculation

Flocculation and breakup are supposed to result only in a net increase in scales [20]. The effectiveness of class jumps is supposed to be linearly dependent on radius:

$$\beta_k = a_{floc} \frac{r_k}{r_1}, \quad (18)$$

where  $a_{floc}$  represents the proportion of frazil crystals that move from class  $k$  to  $k+1$  per second. A value of  $a_{floc} = 10^{-4} \text{ s}^{-1}$  is suggested in [20] based on a size distribution spectrum. This value depends on turbulence as discussed hereafter. The flocculation source term is defined as:

$$S_{FB}^k = \beta_{k-1} C_{k-1} - \beta_k C_k. \quad (19)$$

### C. Thermal balance

The water fraction of the water-ice mixture is characterized by a temperature, subject to a heat balance defined as:

$$\frac{\partial}{\partial t} [(1-C)T] + \nabla \cdot [(1-C)\mathbf{u}T] = \nabla \cdot (v_t \nabla [(1-C)T]) + \frac{\phi}{h\rho c_p} - \frac{S_L}{\rho c_p}, \quad (20)$$

with  $c_p = 4.1855 \cdot 10^3 \text{ J.kg}^{-1} \text{ K}^{-1}$  the specific heat of water and  $\phi$  the net heat flux at the free surface in  $\text{W.m}^{-2}$ . The heat source  $S_L$  due to melting or freezing, can be written as  $S_L = \rho L_i \delta w - \rho c_p T_i \delta w$ , expressed in  $\text{W.m}^{-3}$ , where  $T_i$  the crystal temperature, assumed to be equal to the freezing temperature and  $\delta w$  is the water volume change rate ( $\text{s}^{-1}$ ) due to frazil ice evolution expressed as:

$$\delta w = -\frac{\rho_i}{\rho} \sum_{k=1}^{N_c} S_{GM}^k. \quad (21)$$

Equation (20) can be developed as:

$$(1-C) \frac{\partial T}{\partial t} + (1-C) \mathbf{u} \cdot \nabla T = (1-C) \nabla \cdot (v_t \nabla T) - 2v_t \nabla T \nabla C + \frac{\phi}{h\rho c_p} - \delta w \left( T - T_f + \frac{L_i}{c_p} \right), \quad (22)$$

Additionally, the term  $2v_t \nabla T \nabla C$  in Equation (22) can be neglected after [12], considering the hypothesis  $C \ll 1$ . Hence, the following heat balance equation is obtained:

$$\frac{\partial T}{\partial t} + \mathbf{u} \cdot \nabla T = \nabla \cdot (v_t \nabla T) + \frac{\phi}{h\rho c_p(1-C)} + \frac{\rho_i}{\rho(1-C)} \left( T - T_f + \frac{L_i}{c_p} \right) \sum_{k=1}^{N_c} S_{GM}^k. \quad (23)$$

Equation (23) can be further simplified by considering  $C \ll 1$  and  $T - T_f \ll \frac{L_i}{c_p}$ , which leads to:

$$\frac{\partial T}{\partial t} + \mathbf{u} \cdot \nabla T = \nabla \cdot (v_t \nabla T) + \frac{\phi}{h\rho c_p} + \frac{\rho_i L_i}{\rho c_p} \sum_{k=1}^{N_c} S_{GM}^k. \quad (24)$$

Both Equations (23) and (24) were implemented in KHIONE in this study.

#### D. Salinity balance

The salinity balance is given by:

$$\frac{\partial S}{\partial t} + \mathbf{u} \cdot \nabla S = \nabla \cdot (v_{t,S} \nabla S) + S_R, \quad (25)$$

in which  $v_{t,S}$  is the turbulent diffusivity and  $S_R$  is the salt rejection source term. Salt rejection was taken into account in the single class model developed in [19]. In the case of multiple classes, salt rejection can be expressed as a function of the water phase rate of volume change  $\delta w$ . Finally, the salinity rejection source can be calculated as:

$$S_R = \frac{\rho_i}{\rho} (S - S_i) \sum_{k=1}^{N_c} S_{GM}^k, \quad (26)$$

with  $S_i$  the salinity of frazil crystals assumed to be equal to zero.

#### E. Turbulence

Turbulence parameters, required to compute the different source terms above defined, are estimated using the k- $\epsilon$  solver from TELEMAT-2D. A second option, suggested in [23], has been implemented to reduce computational cost for simple applications and relies on a depth integration of k and  $\epsilon$  profiles defined as:

$$k(z) = \frac{u_*^2}{\sqrt{C_\mu}} \left( 1 - \frac{z}{h} \right), \quad (27)$$

$$\epsilon(z) = \frac{u_*^3}{kz} \left( 1 - \frac{z}{h} \right), \quad (28)$$

in which  $u_*$  is the friction velocity and  $C_\mu = 0.09$ . The profiles are integrated between the upper bound of the viscous boundary

layer and the free surface [23]. Turbulent viscosities are then computed as  $\nu_t = C_\mu k^2 / \epsilon$ .

#### F. Numerical resolution

##### 1) Time integration

Time integration of Equations (3), (24) and (25) is done with a time splitting technique. First, the convection-diffusion operators are solved using classical numerical schemes available in TELEMAT-2D. Let us note  $C_k^{n+1}$  the volume fraction of frazil and  $T^{n+1}$  the temperature at time  $t^{n+1}$ . The fields obtained after the first step are noted  $\tilde{C}_k$  and  $\tilde{T}$ . Time integration of source terms is then done as:

$$\begin{cases} C_k^{n+1} = \tilde{C}_k + \Delta t^n (S_{GM}^{k,1} + S_{SN}^k + S_{FB}^k) \quad \forall k \in \llbracket 1, N_c \rrbracket \\ T^{n+1} = \tilde{T} + \Delta t^n \left( \frac{\phi}{h\rho c_p} + \frac{\rho_i L_i}{\rho c_p} \sum_{k=1}^{N_c} S_{GM}^k \right) \end{cases}, \quad (29)$$

with  $\Delta t^n$  the time step and  $S_{GM}^{k,1}$  and  $S_{GM}^{k,2}$  defined by:

$$S_{GM}^{k,1} = (T_f^n - T^n) \left( \frac{V_k}{\Delta V_{k-1}} [(1-H^n) \chi_k^n C_k^* + H^n \psi_{k-1}^n C_{k-1}^n] - \frac{V_k}{\Delta V_k} [(1-H^n) \chi_{k+1}^n C_{k+1}^n + H^n \psi_k^n C_k^*] \right), \quad (30)$$

$$S_{GM}^{k,2} = (T_f^n - T^*) \left( \frac{V_k}{\Delta V_{k-1}} [(1-H^n) \chi_k^n C_k^n + H^n \psi_{k-1}^n C_{k-1}^n] - \frac{V_k}{\Delta V_k} [(1-H^n) \chi_{k+1}^n C_{k+1}^n + H^n \psi_k^n C_k^n] \right), \quad (31)$$

in which  $\psi_k^n$  and  $\chi_k^n$  are defined with:

$$\psi_k^n = \frac{2K_w Nu_k^n}{\rho_i L_i r_k^2}, \quad (32)$$

$$\chi_k^n = \frac{2K_w Nu_k^n}{\rho_i L_i r_k} \left( \frac{1}{r_k} + \frac{1}{e_k} \right). \quad (33)$$

Replacing  $*$  by  $n$  in Equations (30) and (31), the Euler explicit scheme is obtained and  $S_{GM}^{k,1} = S_{GM}^{k,2}$ . A semi-implicit scheme is obtained replacing  $*$  by  $n+1$  in Equations (30) and (31). The resolution is subject to time step constraints with both approaches. Note that both secondary nucleation and flocculation have been treated explicitly in this work. A semi-implicit approach similar to the one described for thermal growth is possible, but has not been tested yet. Finally, no fully implicit time scheme has been presented in this study, as it would need an overall modification of KHIONE's structure, which was out of the scope of this work.

##### 2) Stability and positivity of frazil volume fraction

For a single class of frazil in case of supercooling ( $T < T_f$ ), the numerical scheme defined in Equation (29) becomes:

$$\begin{cases} C^{n+1} = \tilde{C} + \Delta t^n \psi_1^n (T_f^n - T^n) C^* \\ T^{n+1} = \tilde{T} + \Delta t^n \frac{\phi^n}{h\rho c_p} + \Delta t^n \frac{\rho_i L_i}{\rho c_p} \psi_1^n (T_f^n - T^*) C^n \end{cases} \quad (34)$$

Neglecting advection-diffusion and supposing  $T_f = 0$ , the stability of the system and the positivity of  $C$ , in the case of the Euler explicit time scheme, lead to a constraint on time step defined by:



$$\Delta t^n \leq \min \left( 2 / \left[ \frac{\rho_i L_i}{\rho c_p} \psi_1^n C^n + \frac{\phi^n}{h \rho c_p |T^n|} \right], \frac{1}{\psi_1^n |T^n|} \right). \quad (35)$$

This constraint implies that the time step  $\Delta t^n$  at time  $t^n$ , should be sufficiently small with respect to a coefficient that is proportional to the squared radius of frazil crystals (due to the definition of  $\psi_1^n$ ).

In theory, the condition (35) is no longer valid for the numerical scheme defined in Equation (29), and the stability condition of this scheme is yet to be determined. However, numerical tests suggest that the radius of the smallest class is still the main limiting factor. In the numerical simulations presented hereafter, the time step has been adjusted to verify the stability condition and the convergence of the results.

### 3) Maximum concentration

A limiter is introduced for both mono-class and multi-class models to prevent the concentration from reaching the maximum allowed volume fraction. This limiter is mandatory since the concentration linearly increases at constant cooling rate. When concentration reaches a threshold of 1, all sources are frozen and only melting is authorized.

## III. APPLICATION

### A. Calibration

The model presented in this study has two main calibration parameters, namely  $n_{max}$  and  $a_{floc}$  respectively from Equations (14) and (18). Additionally, one has to provide a distribution of radius and initial seeding in order to run the model. In this section, the calibration method, based on previous work in the literature [20, 26] is described.

A typical distribution of radii observed in experiments is the lognormal distribution [4, 6]. Such distribution has also been recently observed in Alberta Rivers as shown in [14]. Given the difficulty of providing correct parameters for the lognormal distribution, authors often use a simplified distribution of particles, introduced in [17]. As for the radii, they typically range from 4  $\mu\text{m}$  to 5 mm [4, 17]. In this study, radius for each classes are spread out uniformly between minimum and maximum radius which are set to 10  $\mu\text{m}$  to 1 mm respectively, with a default number of classes set to 10, which gives the best compromise between precision and computational cost.

Modelling seeding and primary nucleation is still a major difficulty in frazil studies as the seeding process is not fully

understood yet. It depends on atmospheric conditions (snow, mist) and water impurities, which may considerably vary in the different experiments and in nature. Furthermore, frazil artificial seeding is carried out in experiments as in [10], which consists in releasing ice scraps in water at a controlled rate. In this study, the initial seeding is done by introducing a number of particle, noted  $N_0$ , supposed to be equally shared by all classes [20]. In order for the model to be able to properly model multiple growth and melting sequences, a minimum threshold of concentration, based on  $N_0$  is set. Below this threshold, all processes are disabled except thermal growth.

Parameters  $n_{max}$  and  $a_{floc}$  influence the evolution of particles distribution in time. The parameter  $a_{floc}$  is fixed to  $10^{-4}$  as suggested in [20]. This reduces the number of calibration parameters to two,  $n_{max}$  and  $N_0$ . Besides, [20] propose to set a common value of  $n_{max}$  for all experiences. Therefore, only  $N_0$  needs to be chosen specifically for each case. However, it has been shown in [26] that a common parameter  $n_{max}$  for all experiments is difficult to choose as it depends on turbulence. Correlations between  $n_{max}$ ,  $N_0$  and turbulent intensity, based on numerical simulations, have been proposed in [26] to overcome this difficulty. The presence of such correlations between the parameters suggests that calibrating them independently, as in [20], might not be optimal. Further investigations, for example using data assimilation methods, should be considered but are out of the scope of this paper. Consequently, the values proposed in [20] are used as a first guess, and then both parameters  $n_{max}$  and  $N_0$  are adjusted for each experiment.

### B. Carstens experiments

Carstens experiments [3] were conducted in a recirculating oval flume of 600 cm long, 30 cm deep and 20 cm wide. Water depth was set to 20 cm and temperature was recorded at approximately 5 to 10 cm deep with a mercury thermometer marked to 0.01  $^{\circ}\text{C}$ . The physical parameters of the experiment are summed up in the Table 1. Following the calibration method previously introduced, numerical simulations were carried out with a time step of 0.1 s. The evolution of temperature and total frazil volume fraction are presented in Figure 1. The characteristic time  $t_c$  corresponds to the moment when 90% of the maximum temperature depression is recovered. The calibrated parameters are presented in Table 2. Additionally, the evolution of frazil distribution is presented in Figure 2 for the first Carstens experiment.

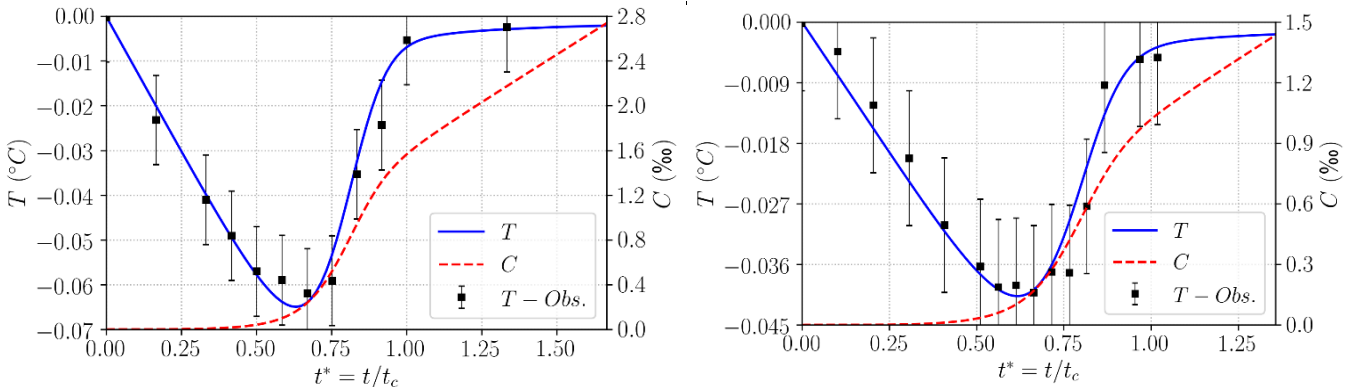


Figure 1: Simulated temperature and total frazil volume fraction with comparison to Carstens experiments I (left) and II (right).

TABLE 1: PHYSICAL PARAMETERS OF EXPERIMENTS

Case	h (m)	u (m/s)	$\Phi/h$ (W/m <sup>3</sup> )	S (ppt)	k (m <sup>2</sup> /s <sup>2</sup> )	$\varepsilon$ (m <sup>2</sup> /s <sup>3</sup> )
Carstens I	0.2	0.5	1400	0	$9.6 \cdot 10^{-4}$	$1.2 \cdot 10^{-3}$
Carstens II	0.2	0.5	550	0	$4.8 \cdot 10^{-4}$	$3.8 \cdot 10^{-4}$
Tsang & Hanley	0.11	0.15	122	29-31	-	-

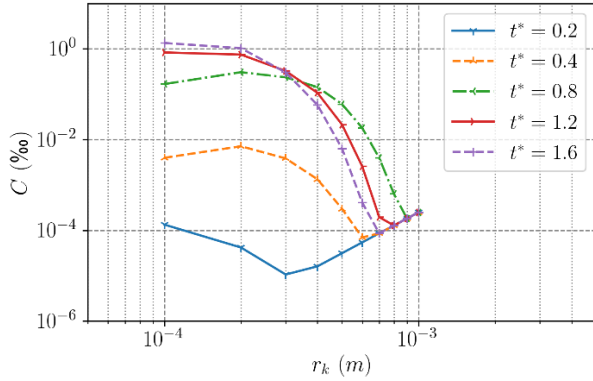


Figure 2: Evolution of simulated frazil volume fraction per class in the first Carstens experiment.

TABLE 2: CALIBRATED PARAMETERS.

Case	$a_{floc}$ (s <sup>-1</sup> )	$n_{max}$	$N_0$ (m <sup>-3</sup> )
Carstens I	$10^{-4}$	$1 \cdot 10^6$	$3.2 \cdot 10^2$
Carstens II	$10^{-4}$	$1.5 \cdot 10^6$	$1.9 \cdot 10^2$
Tsang & Hanley	$10^{-4}$	$2 \cdot 10^6$	$2 \cdot 10^3$

### C. Tsang and Hanley experiments

Tsang & Hanley experiments [10] (C) were conducted in a recirculating, racetrack shaped, flume of 65 cm long, 13 cm deep and 15 cm wide. The tank was filled with sea-water of salinity comprised between 29 and 31 ppt. The frazil concentration was estimated using temperature measurements, made with a thermometer calibrated to 0.0001 °C, with repeatability of 0.001 °C. This leads to an absolute error of  $1.25 \cdot 10^{-5}$  on frazil observations. The physical parameters of the experiment are summed up in Table 1. To reproduce experiments, a momentum source term is introduced to simulate the propeller. The source term is adjusted in order to reach a hydrodynamic steady state with a mean flow velocity of  $0.15 \text{ m} \cdot \text{s}^{-1}$ . The Manning friction law is used with friction factor of  $0.011 \text{ m}^{-1/3} \cdot \text{s}$ . Turbulent parameters were estimated with Equations (27) and (28) giving average values of  $k=7 \cdot 10^{-6} \text{ m}^2 \cdot \text{s}^{-2}$  and  $\varepsilon=2.4 \cdot 10^{-6} \text{ m}^2 \cdot \text{s}^{-3}$  in the racetrack at steady state. Figure 3 illustrates the configuration of the model and steady state mean flow velocity.

Artificial seeding described in [10] was reproduced by introducing a total number of particles  $N_0$  when temperature reaches the seeding temperature, denoted  $T_n$ . The salinity was set to 31.2 ppt for all simulations, giving a fusion temperature of

$T_f = -1.7056$  °C. Common calibration parameters were adjusted to the nine experiments, as shown in Table 2. Results are presented in Figure 6 with  $C^* = C/C_c$ , the characteristic total frazil concentration being defined by  $C_c = C(t_c)$ .

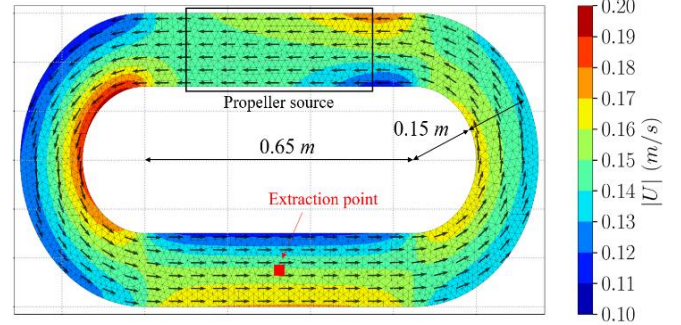


Figure 3: Racetrack geometry used in Tsang &amp; Hanley experiments (1985) and simulated hydrodynamic steady state.

### D. Sensitivity to model parameters

A sensitivity analysis is carried out on different parameters of the model. The sensitivity to the initial seeding  $N_0$  and the maximal number of collision for secondary nucleation  $n_{max}$  are presented in Figure 4 and 5 respectively.

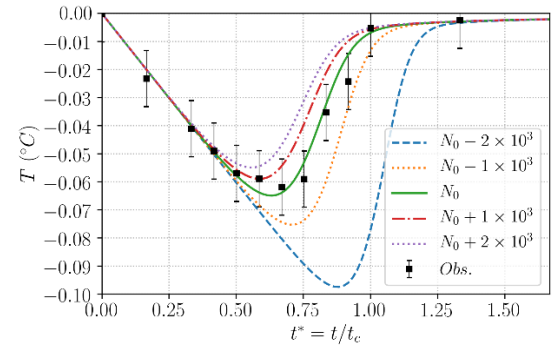
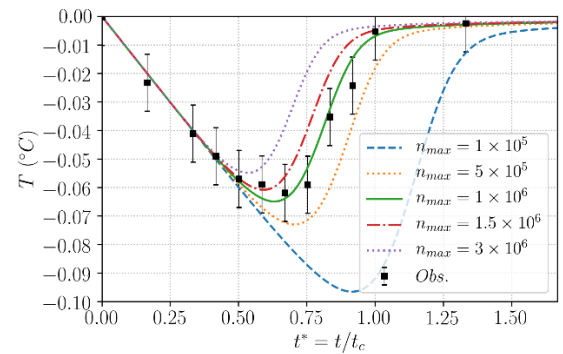


Figure 4: Sensitivity to the initial seeding for the first Carstens experiment.

Figure 5: Sensitivity to  $n_{max}$  for the first Carstens experiment.

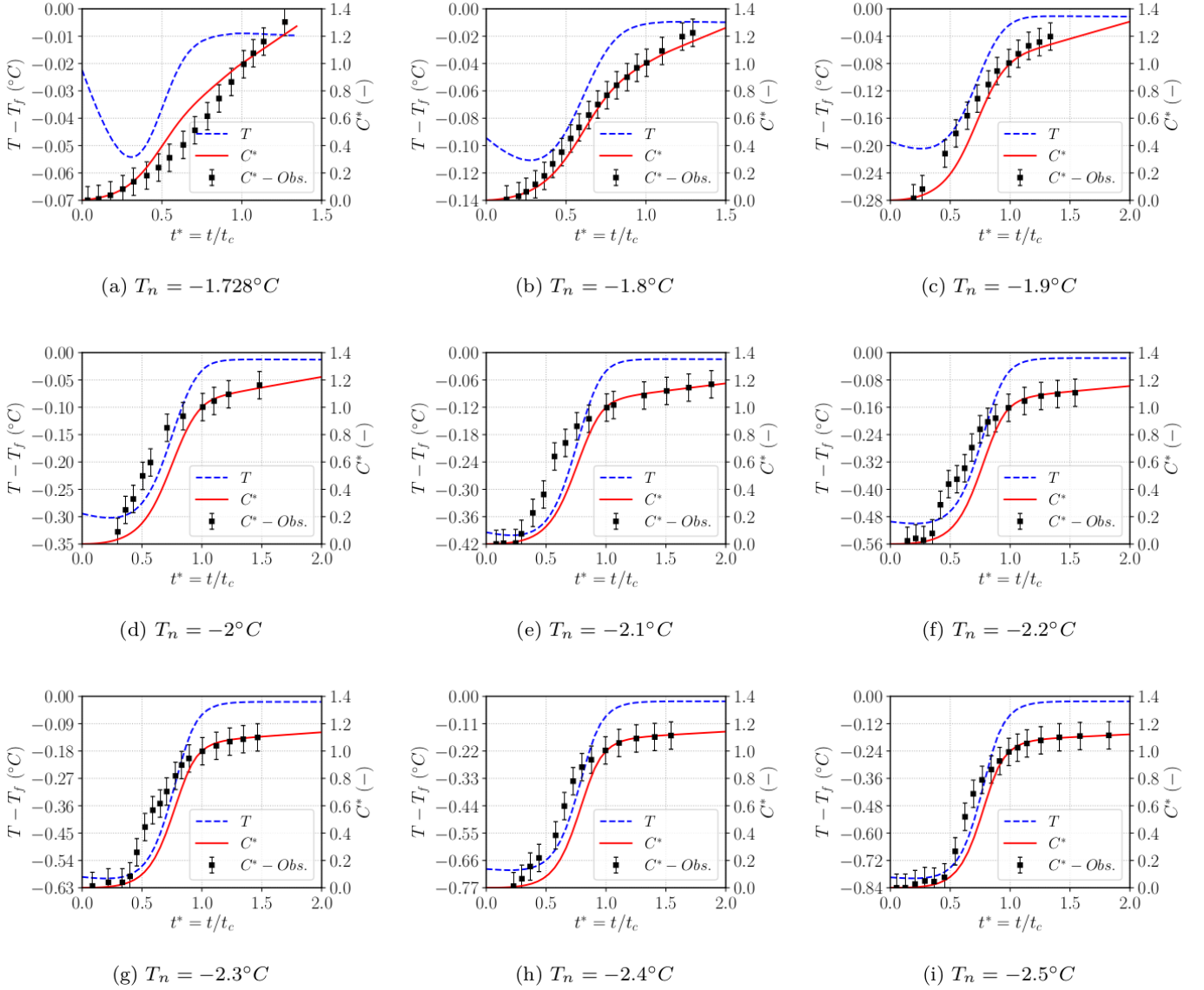


Figure 6: Simulated temperature and normalized total frazil volume fraction with comparison to Tsang & Hanley experiments for different seeding temperatures.

#### IV. DISCUSSION

The confrontation of numerical results to experimental data is encouraging as the model is able to reproduce supercooling and temperature recovery under different turbulent and salinity conditions as shown on Figure 1 and Figure 6.

The sensitivity analysis results indicate that small modifications of  $N_0$  and  $n_{max}$  have significant impact on the results. Consequently, fitting temperature or total frazil concentration may be tedious and should be done cautiously. In addition to global evolution of frazil total concentration and temperature, one has to verify the evolution of the particles' distribution against time. Unfortunately, frazil ice distribution have not been measured in Carstens and Tsang & Hanley experiments. However, distributions obtained in [4] and later used in [26] to calibrate a multi-class model, indicates that a  $n_{max}$  of  $10^6$  combined with an initial seeding of  $6.4 \cdot 10^3$  allow a good representation of frazil distribution evolution against

time. This is not the case with the present work as shown in Figure 2. The evolution of simulated distribution with  $n_{max} = 10^6$  indicates a predominance of secondary nucleation over thermal growth and flocculation, leading to higher concentration on the lower classes. This causes the model to miss the expected lognormal distribution of particles observed in [4] even though a good match is obtained on total frazil concentration and temperature. Such a difference between the results obtained in this work and [26] might come from the overestimation of thermal growth, for which the correction presented in [11] is taken into account in the present work. Other probable causes are the model chosen for the estimation of the rise velocity and the gravitational removal that is neglected in present study. Consequently, additional tuning of model parameters is required to expect a good representation of frazil ice distribution against time with the current model. Furthermore, the model convergence in terms of number of classes still needs to be studied, as well as its sensitivity to the initial conditions. For this purpose, a comprehensive sensitivity analysis should be

considered in the future. Optimal calibration methods could also provide insight on the best way to fit parameters for the present model.

The TELEMAT-MASCARET system is best suited for large-scale environmental modelling. However, the experiments reproduced in the present work were conducted on small-scale geometries of less than several meters. Despite the lack of frazil ice data in natural water bodies, additional validation on larger domains should nonetheless be considered in the future to assess the applicability of the model on large-scale geometries.

The present model has been developed in the shallow water framework, specifically for coupling with TELEMAT-2D. It should be mentioned that the shallow water assumption does not allow to describe the vertical profile of frazil concentration. This may have a significant impact in real applications where the flow is not vertically mixed and thermohaline stratification is well established. The impact would be a higher frazil concentration close to the free surface, where temperature and salinity are low. Furthermore, a 3D model would allow a better representation of the buoyancy of frazil crystals, hence increasing the vertical heterogeneity of frazil volume fraction.

## V. CONCLUSION

In this study, a multi-class model for frazil ice modelling has been developed for TELEMAT-2D/KHIONE. This work brings state of the art frazil ice model into KHIONE expanding its capabilities and allowing more advanced investigation of frazil ice processes in shallow water flows. Several processes have been implemented, including thermal growth, secondary nucleation and flocculation. Turbulence has been taken into account in the processes by a coupling with TELEMAT-2D  $k-\epsilon$  solver. Salinity has also been taken into account by means of a variable fusion temperature and a salt rejection source term. Euler explicit and semi-implicit time schemes were presented for the resolution of the coupled system. The model has been validated on two experiments from literature, one with fresh water and the other with ocean water.

The depth averaged temperature and total frazil volume fraction evolution obtained with the calibrated model are in good accordance with experimental data for both fresh and saline water. However, the model is sensitive to the calibration parameters (maximal collision number for secondary nucleation and initial seeding) which does not allow a good representation of the typical lognormal distribution of particles with standard values suggested in literature. Further investigations on the impact of each process are needed to obtain a better understanding of these parameters influence on particles' distribution. Additionally, a comprehensive sensitivity analysis would be useful in order to better describe the capabilities and limitations of the present model.

## REFERENCES

- [1] G. K. Batchelor. Mass transfer from small particles suspended in turbulent fluid. *Journal of Fluid Mechanics*, 98(3):609–623, 1980.
- [2] S. E. Bourban, H. F., H. T. Shen, and R. Ata. Introducing khione - (eulerian) part i of the ice modelling component of telemat. TUC, 2018.
- [3] T. Carstens. Experiments with supercooling and ice formation in flowing water. *Geofys. Publ. Norway*, 26(9) (3-18), 1966.
- [4] S. Clark and J. Doering. Laboratory experiments on frazil-size characteristics in a counterrotating flume. *Journal of Hydraulic Engineering*, 132:94–101, 2006.
- [5] S. F. Daly. Frazil ice dynamics. CRREL Monograph 84-1, 1984.
- [6] S. F. Daly. Frazil ice measurement in crrel's flume facility. *IAHR Ice Symp.*, Iowa City, page 427–438, 1986.
- [7] S. F. Daly. Frazil ice blockage of intake trash racks, cold regions technical digest no. 91-1. Technical report, US Army Corps of Engineers, 1991.
- [8] S. F. Daly. Report on frazil ice. Technical report, International Association for Hydraulic Research, Working Group on Thermal Regimes, Special Report 94-23, 1994.
- [9] J. Gosink and T. Osterkamp. Measurements and analyses of velocity profiles and frazil ice-crystal rise velocities during periods of frazil-ice formation in rivers. *Annals of Glaciology*, 4:79–84, 1983.
- [10] T. O. Hanley and G. Tsang. Formation and properties of frazil in saline water. *Cold Regions Science and Technology*, 8:209–221, 1984.
- [11] P. Holland, D. L. Feltham, and S. F. Daly. On the nusselt number for frazil ice growth—a correction to “frazil evolution in channels” by lars hammar and hung-tao shen. *Journal of Hydraulic Research*, page pp. 1–4, 2006.
- [12] P. R. Holland and D. L. Feltham. Frazil dynamics and precipitation in a water column with depth-dependent supercooling. *Journal of Fluid Mechanics*, 530:101–124., 2005.
- [13] L. Liu and H. T. Li, H. and Shen. A two-dimensional comprehensive river ice model. 18th IAHR International Symposium on Ice, 2006.
- [14] V. MacFarlane, M. Loewen, and F. Hicks. Measurements of the size distribution of frazil ice particles in three alberta rivers. *Cold Regions Science and Technology*, 2017. doi: 10.1016/j.coldregions.2017.08.001.
- [15] Z.-y. Mao, J. Yuan, J. Bao, X.-f. Peng, and G.-q. Tang. Comprehensive two-dimensional river ice model based on boundary-fitted coordinate transformation method. *Water Science and Engineering*, 7(1):90–105, 2014.
- [16] V. Matoušek. Frazil and skim ice formation in rivers. In *Proceedings of the IAHR Ice Symposium*, 1992.
- [17] R. Mercier. The reactive transport of suspended particles: Mechanics and modeling. PhD thesis, Joint Committee on Oceanographic Engineering, Massachusetts Institute of Technology, Cambridge, Mass., 1984.
- [18] B. Michel. Theory of formation and deposit of frazil ice. Eastern Snow Conference, Proc. Annual Meeting, Quebec., 1963.
- [19] A. Omstedt. On supercooling and ice formation in turbulent sea-water. *Journal of Glaciology*, 31(109), 1985.
- [20] A. Omstedt. Simulation of supercooling and size distribution in frazil ice dynamics. *Cold regions science and technology*, 1994.
- [21] M. Richard. Field Investigation of Freshwater Frazil Ice Dynamics. PhD thesis, Faculté des études supérieures de l'Université Laval, 2011.
- [22] H. T. Shen. Mathematical modeling of river ice processes. *Cold Regions Science and Technology*, 62 (1):pp.3–13, 2010. doi: doi:10.1016/j.coldregions.2010.02.007.
- [23] H. T. Shen and L. Hammar. Frazil evolution in channels. *Journal of Hydraulic Research*, 2010. doi: 10.1080/00221689509498572.
- [24] H. T. Shen and A. M. Wasantha Lal. A mathematical model for river ice processes. Technical report, US Army Corps of Engineers Cold Regions Research and Engineering Laboratory, 1993.
- [25] P. H. Wadia. Mass transfer from spheres and discs in turbulent agitated vessels. PhD thesis, Department of Chemical Engineering, Massachusetts Institute of Technology, Cambridge, MA., 1974.
- [26] S. M. Wang and J. C. Doering. Numerical simulation of supercooling process and frazil ice evolution. *Journal of Hydraulic Engineering*, 2005.



# A newly implemented upwind scheme and numerical benchmark for the resolution of the Exner equation in GAIA.

Sacha Revillon

Sup Galilée, LNHE, EDF R&D  
Villetaneuse, Chatou, France  
[revillon.sacha@gmail.com](mailto:revillon.sacha@gmail.com)

Florent Taccone and Fabien Souillé

LNHE, EDF R&D  
Chatou, France  
[florent.taccone@edf.fr](mailto:florent.taccone@edf.fr)

**Abstract**— Erosion and bedload transport have a high influence on industrial facilities and water quality. These phenomena can be modelled by the Saint-Venant Exner system defined by shallow water equations and a sediment mass balance equation. This system is often handled by using a splitting method which consists in developing solvers for the hydraulic part and the morphodynamic part.

However, this numerical resolution can lead to instability issues when complex flows are treated. Spurious oscillations can appear for different flow regimes, and in particular for supercritical flows. For example, [1] carried out hydrodynamic and morphodynamic simulations dealing with a torrential flow. They showed numerous oscillations and were forced to fix a non-erodible bed in high erodible zones with supercritical flows in their simulations.

In this work, we present the current numerical methods proposed in GAIA module to solve the Exner equation. We also propose an upwind scheme for the two dimensional Exner equation which is the 2D adaption of the upwind scheme proposed in COURLIS [6]. A coupled scheme [7] has been implemented in order to be compared with the splitting method.

In order to validate the different results and to highlight the various limitations of the current schemes, a numerical benchmark is set up, using test cases from the scientific literature. This benchmark is composed of several dunes evolutions under fluvial, transcritical and torrential flows in order to test the ability of the schemes to deal with regime changes and is also made of dam break cases which are relevant indicators for testing shock treatment.

It is shown that the centered scheme is stable most of the time, but fails on two tests including the full torrential one. The currently implemented upwind scheme does not work as soon as supercritical flow appears and the newly implemented is stable for almost all test cases.

## I. INTRODUCTION

Erosion and bedload transport can be modelled by the Saint-Venant Exner system. Some numerical papers [2] and recent studies [1] have shown that using splitting methods to solve this system can lead to instabilities. Oscillations often appear for different flow regimes and pollute simulations with transcritical flows apparitions.

The aim of this work is to find when these numerical oscillations appear and how to deal with it. For this purpose, we have listed the current numerical schemes developed in the GAIA module of the v8p1 version of TELEMAC-MASCARET. Moreover, we have implemented a two dimensional upwind scheme adapted from COURLIS, which is a one dimensional sedimentology module. A coupled scheme [7], which consists in considering the system as a whole, has also been studied in order to be compared with the other methods. Therefore, we have set up a numerical benchmark of test cases composed of dune evolutions under fluvial, transcritical and torrential regimes flows and dam break cases. These simulations have enabled us to test the stability of the different schemes and to highlight the outbreak of spurious oscillations.

This work is organized as follows: in Section 2, the mathematical model, the several numerical schemes and the numerical benchmark are introduced. In Section 3, the results on those tests cases are presented.

## II. METHODS

### A. Mathematical model

In this work, one considers the 2D bedload transport modelled by the Saint-Venant Exner system defined by the shallow water equations [3] and the Exner sediment mass balance equation. This system can be written as:

$$\begin{cases} \partial_t h + \operatorname{div}(hu) = 0 \\ \partial_t hu + \operatorname{div}(hu \otimes u) + \nabla \left( \frac{gh^2}{2} \right) = -gh \nabla b - \frac{\tau}{\rho_w}, \\ \partial_t b + \varepsilon \operatorname{div}(q) = 0 \end{cases} \quad (1)$$

with the water depth  $h(t, \mathbf{x})$  in m, the velocity  $\mathbf{u}(t, \mathbf{x}) = (u_1, u_2)$  in m/s and  $\mathbf{x} = (x, y)$ ,  $g$  the gravitational constant in  $\text{m}^2/\text{s}$ ,  $b(t, \mathbf{x})$  the bathymetry in m, the water density  $\rho_w$  in  $\text{kg}/\text{m}^3$ ,

$\tau = (\tau_x, \tau_y)$  the frictional stress in  $m^{1/3}.s$ , the solid discharge  $q = (q_x(x), q_y(x))$  in  $m^2/s$  and  $\varepsilon = 1/(1 - \Phi)$  with  $\Phi$  the bed porosity. In this work, Grass formula is used [4]:

$$q = (A_g u_1 (u_1^2 + u_2^2), A_g u_2 (u_1^2 + u_2^2)), \quad (2)$$

which is widely present in numerical papers due to its simplicity. The constant  $A_g$  takes values between 0 and 1 and models the intensity of the interaction between the fluid and the bed.

Meyer Peter & Muller formula [5], which is often used in industrial studies, has also been tested in order to ensure that the schemes also produce similar results in term of stability.

Solving (1) by a splitting approach consists in building a solver for the hydrodynamical part and another for the morphodynamical part that communicate together. Solving this system by a coupled approach consists in treating all three equations at the same time. This splitting method allows to add some complex physical processes and is easier to set up in an industrial context than the coupled approach. However as shown in [2], it can lead to some instabilities issues because the eigenvalues of the fluid part with a zero fixed bottom evolution are not always convenient approximations of the eigenvalues of the full system. In particular, with supercritical flows, one of the eigenvalues of the full system is always negative which can be interpreted as information propagating upstream. The use of splitting strategy in such situation cannot take into account this information since the two eigenvalues of the shallow water equations are always positive in this case.

## B. Numerical methods

### 1) Current numerical methods in GAIA

GAIA is a sediment transport and bed evolution module of the TELEMAT-MASCARET modelling system [16]. It manages different sediment classes and numerous physical processes for both 2D and 3D spatial dimensions. In this paper, we only focus on finite volumes schemes solving bedload transport without suspension. The finite elements centered scheme of GAIA has shown the same stability results as the finite volumes one.

To solve the two-dimensional Saint-Venant Exner system on an unstructured mesh, a control volume  $C_i$  is built around each node  $P_i$  as shown on Figure 1. It passes through the gravity center of each element adjacent to that node.

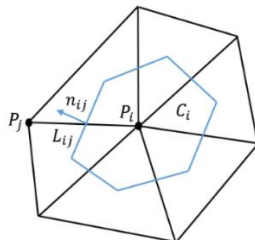


Figure 1: Control volume on an unstructured mesh [15].

Exner equation can be discretised by a finite volume method as:

$$E. \quad b_i^{n+1} = b_i^n - \Delta t \sum_{K_{ij}} \sigma_{ij} q_{ij}^n \quad (3)$$

with  $\sigma_{ij} = \frac{L_{ij} \varepsilon}{|C_i|}$  and  $\sum_{K_{ij}} \sigma_{ij} q_{ij}^n \cong \int_{C_i} \varepsilon \text{div}(q)$ .

$b_i^n$  is the bottom variable discretized at the time  $n$ ,  $C_i$  is the cell  $i$  and  $|C_i|$  its area,  $K_{ij}$  is the interface between the cells  $i$  and  $j$ ,  $L_{ij}$  its length.  $q_{ij}^n$  is the solid discharge at the interface between cells  $i$  and  $j$ .

There are two finite volumes schemes implemented in GAIA, a decentring scheme and a centered scheme.

#### 1.1) GAIA decentring scheme

The decentring is chosen according to the sign of the projected solid discharge at the interface between two cells:

$$F. \quad (q_{proj})_{ij}^n = n_{x,ij} q_{x,ij} + n_{y,ij} q_{y,ij} \quad (4)$$

G. with  $q_{x,ij}$  and  $q_{y,ij}$  the mean of the  $x$  and  $y$  solid discharge components at each side of the interface,  $n_{x,ij}$  and  $n_{y,ij}$  the components of the normal of the interface.

H. If (4) is positive i.e the solid discharge comes from the cell  $i$  so we take  $q_{ij}^n = q_i^n$ , the solid discharge at the node  $i$ . If (4) is negative i.e the solid discharge comes from the cell  $j$  so we take  $q_{ij}^n = q_j^n$ , the solid discharge at the node  $j$ .

This gives us the following scheme:

$$q_{ij}^n = \begin{cases} q_j^n, & \text{if } (q_{proj})_{ij}^n < 0 \\ q_i^n, & \text{if } (q_{proj})_{ij}^n \geq 0 \end{cases} \quad (5)$$

with  $q_i \cong \frac{1}{|C_i|} \int_{C_i} q$ .

#### 1.2) GAIA centered scheme

The numerical flux for the centered scheme is defined by:

$$q_{ij}^n = \frac{q_i^n + q_j^n}{2}.$$

### 2) Newly implemented COURLIS adapted scheme

An upwind scheme based on the same idea as one proposed in the module COURLIS has been implemented [6]. COURLIS is a 1D-sedimentology module coupled with MASCARET, the 1D hydraulic code of TELEMAT-MASCARET. The proposed numerical scheme in this module is an upwind scheme based on the Froude number. The Froude number is defined as:

$$F_r = \frac{u}{\sqrt{gh}}, \quad (7)$$

and indicates the flow regime. If the regime is fluvial the Froude number is smaller than one, otherwise the regime is torrential. In the fluvial case, the information concerning bed evolution propagates in the direction of the fluid stream so an upstream

decentring is made. In the torrential case, solid flow information propagates upstream so a downstream decentring is made. It is known that some instabilities can appear with transcritical flows [2,7] so the main idea behind this scheme is to capture regimes changes in order to adapt the stream to the flow regime. We need to construct velocities and water height at the interfaces in order to calculate an associated Froude number discretized as:

$$(F_r)_{i+\frac{1}{2}} = \frac{u_{i+\frac{1}{2}}^{Roe}}{\sqrt{gh_{i+\frac{1}{2}}^{Roe}}}, \quad (8)$$

In this one-dimensional scheme, the left cell is centered on the node  $i$ , the right cell is centered on the node  $i+1$  and  $i+\frac{1}{2}$  is the cells interface. Velocities and water heights are computed with the following Roe intermediate states:

$$h_{i+\frac{1}{2}}^{Roe} = \sqrt{h_i h_{i+1}}, \quad (9)$$

$$u_{i+\frac{1}{2}}^{Roe} = \frac{\sqrt{h_i} u_i + \sqrt{h_{i+1}} u_{i+1}}{\sqrt{h_i} + \sqrt{h_{i+1}}}, \quad (10)$$

The numerical flux is defined as:

$$q_{i+\frac{1}{2}}^n = \begin{cases} q_i^n, & \text{if } (F_r)_{i+\frac{1}{2}} < 1 \\ q_{i+1}^n, & \text{if } (F_r)_{i+\frac{1}{2}} \geq 1 \end{cases} \quad (11)$$

To extend this resolution in two dimensions, we now have to take into consideration the tangential velocity at the interface, indeed not to consider this quantity could result to an underestimation of the Froude number and to decenter in the wrong direction.

We have the new Froude number and Roe intermediate states:

$$(F_r)_{ij} = \frac{\|u_{ij}\|}{\sqrt{gh_{ij}^{Roe}}}, \quad (13)$$

$$u_{ij}^N = \frac{\sqrt{h_i} u_i^N + \sqrt{h_j} u_j^N}{\sqrt{h_i} + \sqrt{h_j}}, \quad (14)$$

$$u_{ij}^T = \frac{\sqrt{h_i} u_i^T + \sqrt{h_j} u_j^T}{\sqrt{h_i} + \sqrt{h_j}}, \quad (15)$$

with  $u_{ij} = (u_{ij}^N, u_{ij}^T)$ .

We are now able to calculate (11) with these new variables.

### 3) Coupled implemented scheme

The coupled approach has been proved to be more stable than the splitting one and can be used as a reference in terms of stability. In order to compare the stability of the two methods, two numerical schemes have been implemented. The first is an approached Riemann solver for the shallow water equations [14] and the second is its extension to the Saint-Venant Exner system [7]. They satisfy several essential properties. These schemes guaranty water depths positivity and preserve the steady state of the lake at rest, the wet-dry and dry-wet transition. Numerical fluxes are derivatives of the Harten-Lan-van Leer flux [9] with a specific discretization of source terms. The numerical scheme for the shallow waters equations will be used in TELEMAT-2D to solve the hydrodynamical part when the splitting approach will be considered for the test cases. Its extension to the whole system (1) will be used when the coupled approach will be considered.

### 4) Second order extension

A simple second order extension of the newly implemented upwind scheme has been tested. For the Saint-Venant Exner system (1), the main idea is to calculate the numerical fluxes with reconstructed variables [13]. A MUSCL reconstruction (Monotonic Upstream-centered Scheme for Conservation Laws) is made in TELEMAT-2D when second order scheme are used. It consists in replacing the piecewise constant approximation of the variables by reconstructed ones. Reconstructed left and right states are obtained by linear or parabolic approximation computed with the previous time steps states. These corrected variables are now used to calculate second order flux.

Our naïve approach has consisted in using the reconstructed variables computed by TELEMAT-2D and to send it to GAIA. They are used to calculate the Froude number and the solid discharge in the Grass formula. Unfortunately, spurious oscillations appeared even with the most diffusive flux limiter.

### C. Numerical Benchmark

The scientific literature on this subject has shown that instabilities can appear with flow regime changes and shock apparitions [1,2,14]. Therefore, we have selected test cases that include all these configurations. It will enable to link theoretical assumptions on the instabilities apparitions with practical results and to highlight the limitations of the each scheme.

### 1) Dune evolutions under various flows

Dune evolutions are classical test cases for morphodynamical simulations and deal with different flow regimes, which is interesting for our work. We have set up five dune evolution tests, two full fluvial cases with a strong and a weak interaction, two transcritical cases with and without a shock and a full torrential one.

*Fluvial flow:* These classic test cases of sedimentology model the evolution of a dune under a fluvial flow. The first one simulates a strong interaction between the flow and the bed river [7]. The second models a weak interaction [10] and results are compared with an asymptotic solution given in [11]. The channel is 1000 m long and 10 m wide, the initial data are given by:

$$\begin{cases} b(0, x) = \begin{cases} 0.1 + \sin\left(\frac{(x-300)\pi}{200}\right)^2 & \text{if } 300 \leq x \leq 500, \\ 0.1 & \text{elsewhere,} \end{cases} \\ h(0, x) = 10 - b(0, x), \\ u(0, x) = \frac{q_0}{h(0, x)}, \end{cases}$$

with  $q_0 = 10 \text{ m}^2/\text{s}$  the inflow discharge. Grass formula (2) is used with  $A_g = 1.0$  for the strong interaction and 0.001 for the weak interaction case. The asymptotic solution is valid for a low interaction of the riverbed with water,  $A_g < 0.01$  and a flow rate less than  $10 \text{ m}^2/\text{s}$ . It is given by:

$$b(t, x) = \begin{cases} 0.1 + \sin\left(\frac{(x_0-300)\pi}{200}\right)^2 & \text{if } 300 \leq x_0 \leq 500, \\ 0.1 & \text{otherwise} \end{cases},$$

with  $x_0$  solution of:

$$\begin{aligned} x &= x_0 + A_g \epsilon m_g q_0^{m_g} t \left( 10 - \sin\left(\frac{(x_0-300)\pi}{200}\right)^2 \right)^{-(m_g+1)}, \\ &\quad \text{if } 300 \leq x_0 \leq 500 \\ x &= x_0 + A_g \epsilon m_g q_0^{m_g} t 10^{-(m_g+1)}, \quad \text{otherwise} \end{aligned}$$

This solution is valid until  $t < t_0$  where  $t_0$  is the time at which the characteristics cross. It is estimated at  $t_0 = 23827912.4 \text{ s}$  with  $m_g = 3$ .

*Transcritical flow without shock:* it corresponds to the transition from a subcritical regime (Froude number  $< 1$ ) to a supercritical regime (Froude number  $> 1$ ). This test evaluates the robustness of schemes that may be sensitive to flow regime changes. The channel is 10 meters long and 1 meter wide, the initial data are given by:

$$\begin{cases} b(0, x) = 0.1 + 0.1e^{(x-5)^2} \\ h(0, x) = 0.4 - b(0, x) \\ u(0, x) = \frac{q_0}{h(0, x)} \end{cases},$$

with  $q_0 = 10 \text{ m}^2/\text{s}$  the inflow discharge..

Grass formula (2) is used with  $A_g = 0.0005$  on a 2300 elements unstructured mesh.

*Transcritical flow with a shock:* it models a hydraulic jump that is characterized by two regime flow changes, subcritical to supercritical then supercritical to subcritical. The channel is 20 m high and 2 m wide. The initial bathymetry is:

$$b(0, x) = 0.25e^{-0.5(x-10)^2}.$$

We evaluate the initial water height in a steady state with the equations in [12] with  $q(t, 0) = q_0 = 0.45 \text{ m}^2/\text{s}$  and  $h(t, 0) = 0.5 \text{ m}$ . Grass formula (2) is used with  $A_g = 0.0005$  on a 1270 elements unstructured mesh.

*Torrential flow:* Under a torrential flow, we expect the sand dune to move upstream. The initial bathymetry is given by:

$$b(0, x) = \begin{cases} 0.2 - 0.05(x-10)^2, & \text{if } 8 \leq x \leq 2 \\ 0, & \text{otherwise} \end{cases}.$$

The inflow discharge is  $q(t, 0) = 2 \text{ m}^2/\text{s}$  and  $h(t, 0) = 0.5 \text{ m}$ . The channel is 10 m long and 1 m wide and we use Grass formula with  $A_g = 0.001$  on a 2680 elements unstructured mesh.

### 2) Dam break tests

Dambreak test cases are useful to evaluate a scheme ability to deal with shock and rarefaction waves. The initial data of the wet case are:

$$\begin{cases} b(0, x) = 0, \\ h(0, x) = \begin{cases} 2 & \text{if } x \leq 5, \\ 0.125 & \text{otherwise,} \end{cases} \\ u(0, x) = 0 \end{cases}$$

with Grass formula (2) and  $A_g = 0.005$ .

For the dry bottom case, the water height now includes a dry zone:

$$b(0, x) = \begin{cases} 2 & \text{if } x \leq 5 \\ 0 & \text{otherwise} \end{cases}.$$

Moreover we include a friction term based on the Strickler formula with  $K_s = 50$ .

## III. RESULTS

In all the different test cases results, the centered scheme of GAIA will be named as CENTER, the decentring scheme of GAIA as GAIA DECENTRING, the newly implemented scheme as COURLIS\_2D and the coupled scheme as ACU.



### A. Dune evolutions under fluvial flow

Long simulations are useful to highlight diffusivity or lack of stability of a scheme. The first result on Figure 2 is obtained

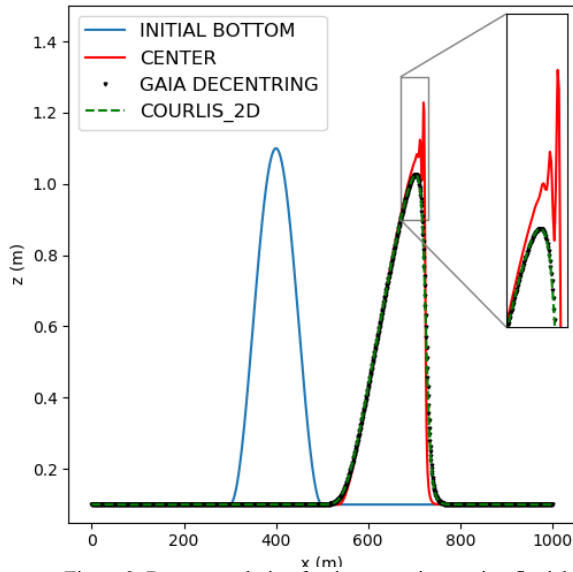


Figure 2: Bottom evolution for the strong interaction fluvial case.

1000-second simulation on the strong interaction case. We notice that GAIA DECENTRING and COURLIS\_2D give same results, which seems logical because the Froude number is always smaller than one and the solid flow is always positive. However, CENTER oscillates and is less diffusive.

The weak interaction case shown on Figure 3 is obtained with a 238 080 s simulation. Results are similar and we can see that ACU and CENTER begin to oscillate. It shows that even on weak interaction case, spurious instabilities can appear. Mesh convergence has been made on this case and a one-order accuracy has been highlighted for COURLIS\_2D on Figure 4 that explains the numerical diffusion.

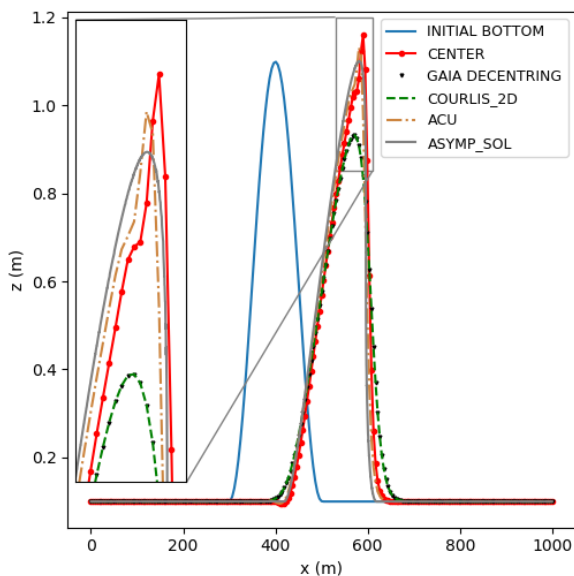


Figure 3: Bottom evolution for the weak interaction fluvial case.

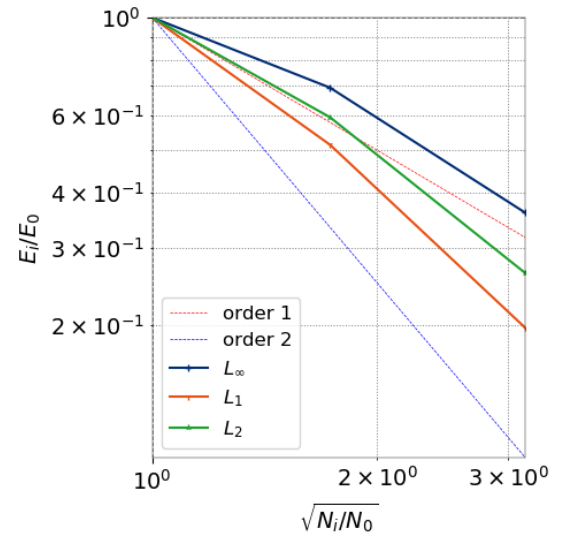


Figure 4: Strong interaction fluvial case: relative error on the bottom.

### C. Dune evolution under a shock-free transcritical flow

Figure 5 illustrates the initial and final states at  $T = 20s$ , GAIA DECENTRING is not shown for clarity sake due to its high oscillations. The inflow is subcritical and the outflow is supercritical.

Bottom evolution for all scheme can be seen on Figure 6, we notice that GAIA DECENTRING is the only one to produce oscillations in particular in the torrential zone and that CENTER shows a small bump at the critical outflow that increases with time.

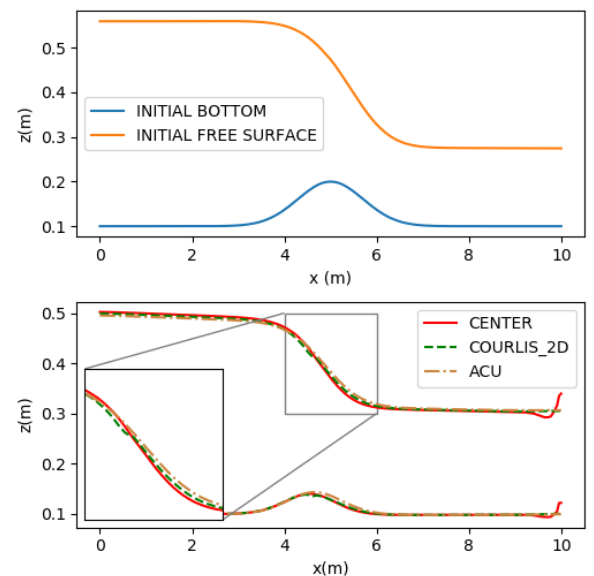


Figure 5: Free surface and bottom at initial and final time for the shock-free transcritical flow.

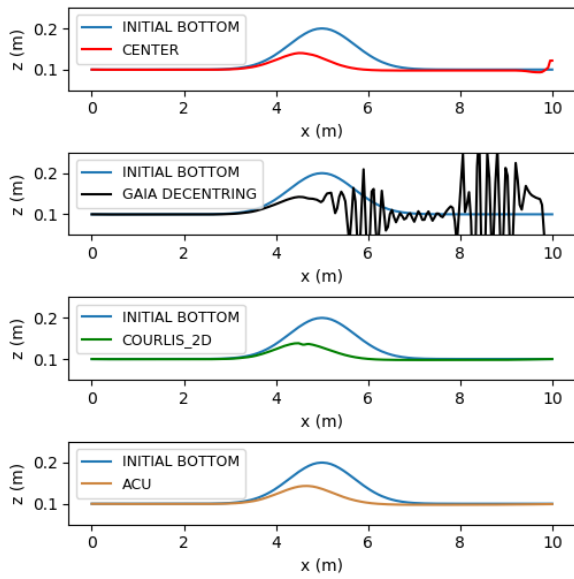


Figure 6: Bottom evolution for the shock-free transcritical flow.

### B. Dune evolution under a transcritical flow with shock

This test represents a hydraulic jump characterized by two regime changes after a 20-second simulation on Figure 7. GAIA DECENTRING is not shown for clarity sake due to its high oscillations. COURLIS\_2D and ACU seem to give smoother results than CENTER.

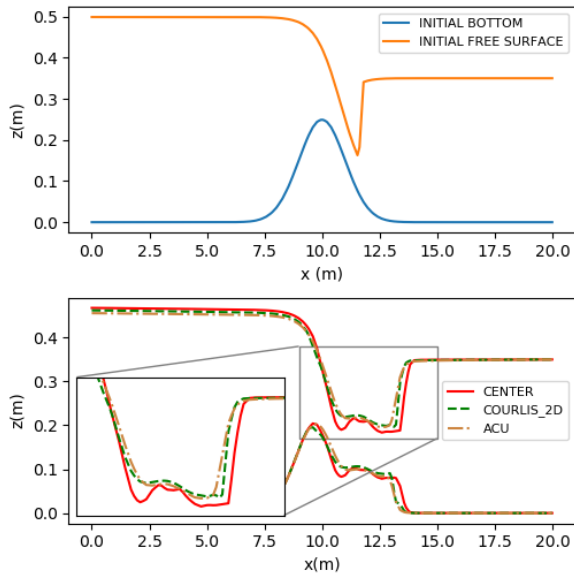


Figure 7: Free surface and bottom at initial and final time the transcritical flow with a shock case.

Once again, the upwind scheme of GAIA produces oscillations in flow regimes changes area seen on Figure 8.

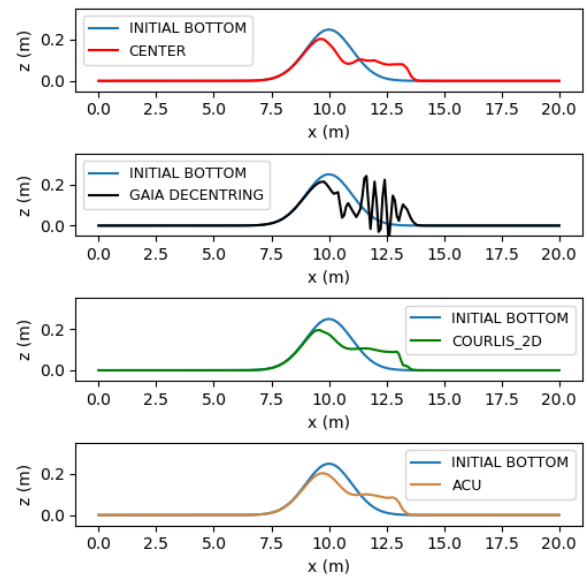


Figure 8: Bottom evolution for the transcritical flow with a shock case.

### C. Dune evolution under a full torrential flow

COURLIS\_2D and ACU are the only ones to finish the 20-second simulation without producing oscillations. GAIA DECENTRING was not able to finish it and CENTER produces a sediment abnormality at the right boundary shown on Figure 9. This abnormality increases with time that has forced us to stop the simulation after 20 seconds.

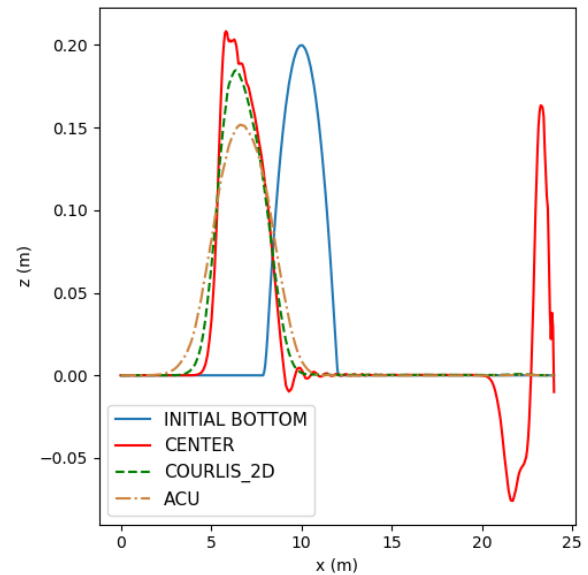


Figure 9: Bottom evolution for the anti-dune test case.

#### D. Dambreak over a wet bottom

Figure 10 illustrates the initial and final situation one second after the break.

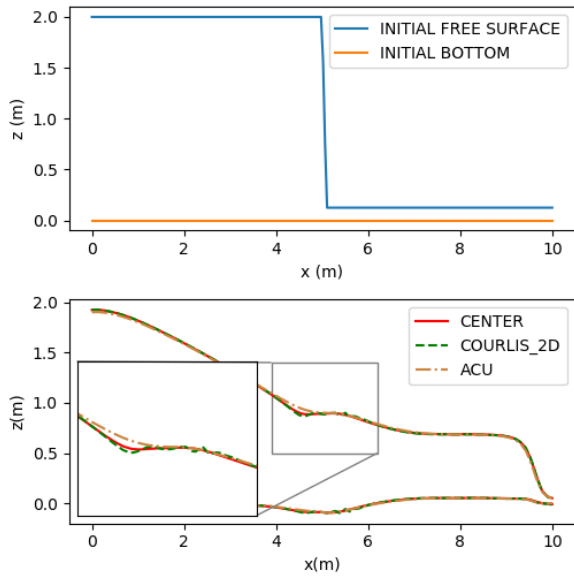


Figure 10: Free surface and bottom at initial and final time for the dambreak wet bottom case.

As shown on Figure 11, CENTER and ACU do not produce any oscillations. We notice a small peak at the shock for COURLIS\_2D and bigger ones for GAIA DECENTRING. However, COURLIS\_2D oscillations seem to be bounded and do not grow with longer simulations whereas those of GAIA DECENTRING do.

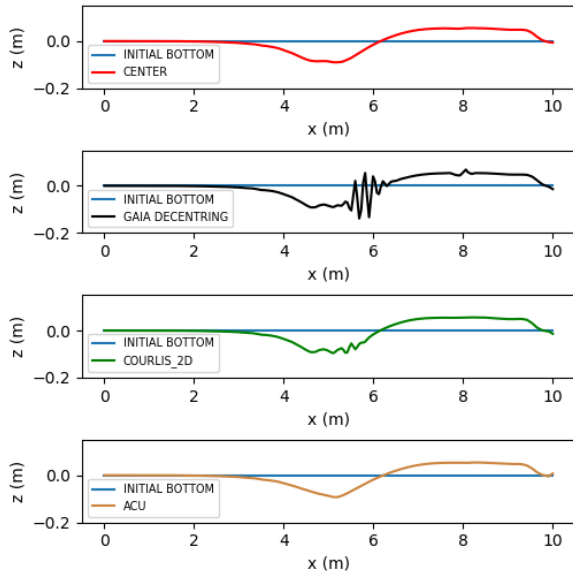
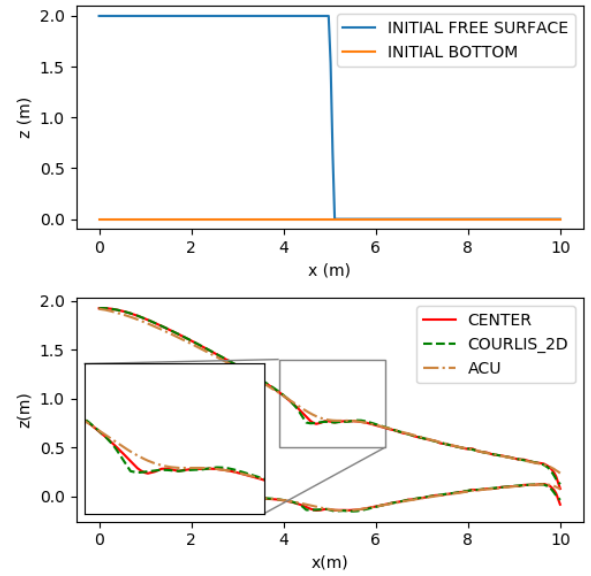


Figure 11: Bottom evolution for the dambreak wet bottom case.

#### E. Dambreak over a dry bottom

Figure 12 illustrates the initial and final situation one second after the break.



J.

Figure 12: Free surface and bottom at initial and final time the dambreak dry bottom case.

We can see on Figure 13 that GAIA DECENTRING still oscillates and ACU seems to produce the smoothest result.

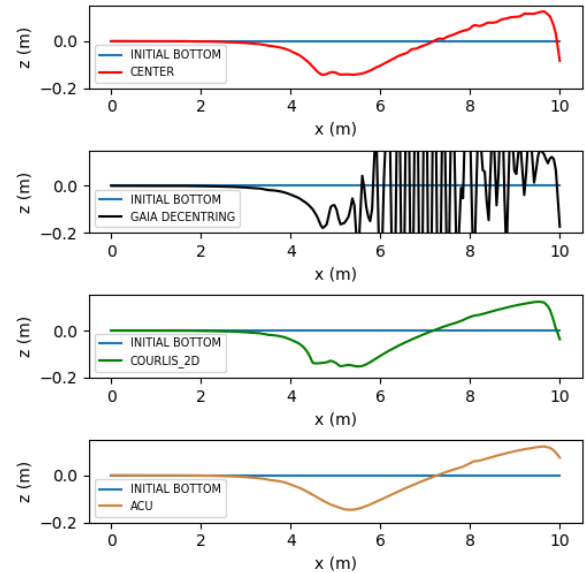


Figure 13: Bottom evolution for the dambreak dry bottom case.

## F. Discussion

All the previous results are summarized in Table 1. We can see that the decentring scheme of GAIA is not stable and has only succeeded the full fluvial test. The centered scheme fails on the two dune evolutions with no regime change but handle the two dambreak cases with no oscillations. Our newly implemented upwind scheme have passed all dune evolutions test including the full torrential one, however some small oscillations have appeared on the dambreak wet bottom test case that explains the yellow case. The coupled scheme has only failed on the fluvial test case but has handled all the other tests giving the smoothest results. For this benchmark, COURLIS\_2D seems to be the strongest approach for the splitting method but is diffusive as an order one accuracy. ACU is the most stable scheme for the treatment of shocks and rarefaction waves as shown on the dambreak tests results.

TABLE 1: SUMMARY OF RESULTS (✓: SIMULATION SUCCEEDED WITHOUT OSCILLATIONS / ≈: APPARITIONS OF SMALL BOUNDED OSCILLATIONS / ✗: PRESENCE OF SPURIOUS OSCILLATIONS)

	CENTER	GAIA DECENTRING	COURLIS 2D	ACU
Fluvial	✗	✓	✓	✗
Transcritical	✓	✗	✓	✓
Transcritical with shock	✓	✗	✓	✓
Torrential	✗	✗	✓	✓
Dambreak wet	✓	✗	≈	✓
Dambreak dry	✓	✗	✓	✓

## IV. CONCLUSION

The aim of this work was to find when instabilities appear solving bedload transport by a splitting approach and to determine how current implemented scheme or its adaptations can handle this issue.

To do this, we have presented the current finite volumes method implemented in the v8p1 version of GAIA and adapted a one-dimensional COURLIS upwind scheme based on the evaluation of the Froude number at the interfaces. An approximate Riemann solver has also been implemented [14] to solve the shallow waters equations and its extension to the Saint-Venant Exner system based on the coupled approach. [7].

A numerical benchmark has been set up, composed of cases found in the scientific literature in order to test the ability of each scheme to deal with flow regime changes and shocks.

Results have shown that the decentring scheme of GAIA was not stable and was only able to deal with full fluvial flows. As soon that regime changes or a torrential flow arise spurious oscillations appear. The centered scheme of GAIA showed oscillations on the subcritical test case and the full torrential one but was able to handle regime changes and shocks treatment. The newly implemented 2D adaptation of the COURLIS scheme seems to be stable and only produces a small oscillation on one dam break test case. The coupled scheme has only

produced instabilities on the fluvial flow test case and has presented the smoothest results. However, this approach does not allow us to use complex physical processes like managing different sediment classes, sediment slide or slope effect.

This benchmark has enabled us to highlight the apparition of oscillations in flow regime changes and torrential areas. Moreover, it has allowed us to identify the limitations of the present methods and cases where no one works. The newly implemented upwind scheme has filled in this gap by handling torrential flows and can be easily integrated into GAIA.

## REFERENCES

- [1] Michal Pavlíček and Oddbjørn Bruland, "Numerical modelling of flash flood event in steep river using Telemac 2D and Sisyphe", *TELEMAC-MASCARET User Conference*, 2019.
- [2] S. Cordier, H. Minh Le and T. Morales de Luna, "Bedload transport in shallow water models: why splitting (may) fail, how hyperbolicity (can) help", 2010.
- [3] Barré de Saint-Venant and Adémar-Jean-Claude, "Théorie du mouvement non permanent des eaux, avec application aux crues des rivières et à l'introduction des marées dans leur lit", 1871.
- [4] Anthony J.Grass and Ragaet N.M.Ayoub, "Bed load transport of fine sand by laminar and turbulent flow", *Coastal Engineering*, 1982.
- [5] E. Meyer-Peter and R. Müller, "Formulas for Bed-Load Transport", 1948.
- [6] M. Sécher, P. Ung, E. Valette, M. Jodeau and N. Goutal, "Courlis: a 1D suspension and bedload code", *E3S River Flow*, 2018.
- [7] E. Audusse, C. Chalons and P. Ung, "A simple three-wave Approximate Riemann Solver for the Saint-Venant--Exner equations", 2016.
- [8] E. Audusse "Shallow waters equations and related topics: Numerical Analysis for Sediment transports, flows on rotating domains and primitive equations", 2018.
- [9] F. Bouchut, "Nonlinear stability of finite volume methods for hyperbolic conservation laws and well-balanced schemes for sources.", *Birkhäuser Verlag, Frontiers in Mathematics*, 2004.
- [10] M.J. Castro Diaz, E.D. Fernández-Nieto, A.M. Ferreiro and C. Parés, "Two-dimensional sediment transport models in shallow water equations. A second order finite volume approach on unstructured meshes", *Computer Methods in Applied Mechanics and Engineering*, 2009.
- [11] J. Hudson, "Numerical Techniques for Morphodynamic Modelling", 2001.
- [12] O. Delestre et al., "SWASHES: a compilation of Shallow Water Analytic Solutions for Hydraulic and Environmental Studies", 2016.
- [13] E. Audusse, M-O. Bristeau, "A well-balanced positivity preserving « second order » scheme for shallow water flows on unstructured meshes.", *Journal of Computational physics*, 2004.
- [14] E. Audusse, C. Chalons and P. Ung, "A simple well-balanced and positive numerical scheme for the shallow-water system", 2015.
- [15] M-O Bristeau and B. Coussin, "Boundary Conditions for the Shallow Water Equations solved by Kinetic Schemes", 2001.
- [16] Y. Audouin and al., "Introducing GAIA, the brand new sediment transport module of the TELEMAC-MASCARET system", 2019.



## Coastal surges, tsunami waves and extreme events

# Development of a detailed tide and storm surge forecast system for the South West Coast of Ireland

Nigel Tozer, Kate Day, Nigel Bunn  
HR Wallingford  
Wallingford, UK  
[n.tozer@hrwallingford.com](mailto:n.tozer@hrwallingford.com)

Edmund Bridge, Jim Casey, Thomas Duffy  
The Office of Public Works,  
Dublin, Ireland

Eoin Sherlock  
Met Éireann  
Dublin, Ireland

**Abstract**— This paper describes the development and results of a TELEMAC-2D hydrodynamic model set up to potentially provide an operational forecast of tides and storm surges for Tralee and adjacent bays, in South West (SW) Ireland. The TELEMAC-2D model was set up using the latest bathymetry data including high resolution multibeam and LiDAR data. The model was initially forced with TPXO tidal data and wind and pressure data from ECMWF and Met Éireann and calibrated against available gauge data in SW Ireland including Tralee Bay. The initial calibration of the model showed good agreement against the measurements, with the tide and storm surge model predictions, close to, or within the specified minimum target accuracy and forecast delivery times. Following the first of two trial periods in winter 2018/2019 the model boundary tidal forcing was updated to use FES2014, which resulted in closer agreement with tidal predictions. The second live trial period was subsequently carried out during the autumn of 2019. An analysis of the results shows that the hydrodynamic model is in good agreement with measurements. Little difference was observed between the storm surge forecasts using the ECMWF or Met Éireann meteorological forcing, but it was expected that the higher resolution Met Éireann Harmonie data has the potential to provide more detail. This paper summarises the development model setup and results to date.

## I. INTRODUCTION

The Office of Public Works (OPW) in Ireland is investigating the viability of an operational tide, storm surge and wave forecast system for Tralee and adjacent bays in an area of the South West Coast of Ireland (Fig. 1).

This could potentially supplement an existing operational national storm surge forecast service and a trial regional tide, storm surge and wave forecast system on the East Coast of Ireland.

The study area of interest was Tralee and the adjacent bays (Fig 1. inset). This area is exposed to storm surges due to strong winds and low atmospheric pressure, as well as waves generated in the Atlantic Ocean that propagate from offshore and those generated more locally within the bays. Whilst the required forecast system does not yet extend to forecasting coastal inundation levels or extents due to high waves and water levels, the system is expected to provide an indication of the potential for coastal flooding.

Two continuous trial periods were carried out to forecast wave conditions, tide and surge levels at 45 points distributed

along the coastline of Tralee and the adjacent bays. This paper focusses on the tide and storm surge modelling aspects of the development project and validation against measured data.

## II. THE MODEL

To predict the tide and storm surges a TELEMAC-2D hydrodynamic model was set up and calibrated against available sources of measured water levels and wave conditions in the vicinity of Tralee Bay.

The TELEMAC-2D model was set up to cover an area extending from Blacksod Bay in the North to Bantry Bay in the South and West to the edge of the continental shelf. The model mesh comprises approximately 200,000 nodes, and close to 400,000 elements. It has a spatial resolution of the order of 10km offshore reducing to 10's of metres in the coastal regions thus providing an accurate representation of the seabed in the shallow coastal waters.

### A. Bathymetry

The accuracy of the forecasts will depend on several factors including the accuracy of the available source bathymetry, the model resolution and the model boundary conditions comprising forecast winds, surface pressure and water levels. For this pilot study a wide range of sources of bathymetry were obtained and compiled to provide the model seabed depths.



Figure 1 Location Map (Sources: Google Earth, GSHHS, ETOP01)

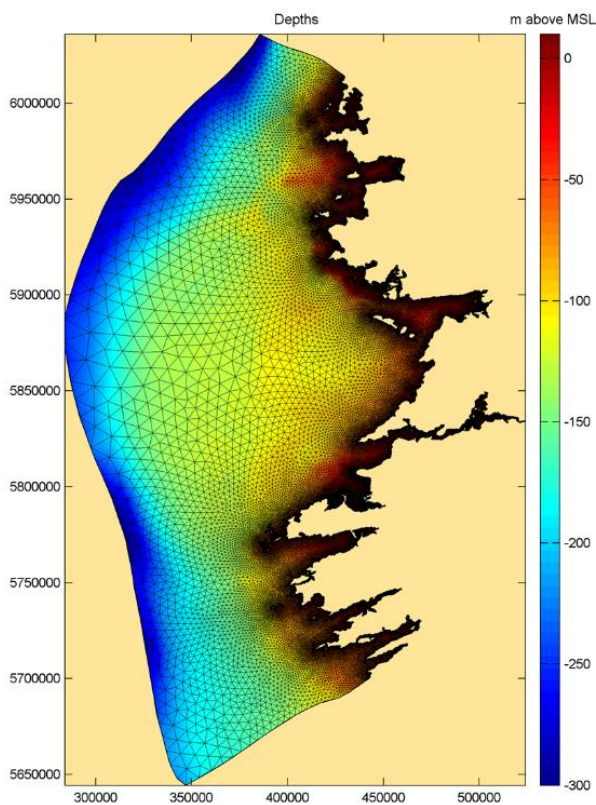


Figure 2 Model mesh and bathymetry

The main source of bathymetry was obtained from the Geological Survey of Ireland and Marine Institute joint INFOMAR project (GSI [1] and INFOMAR [2]) which hosts an extensive set of bathymetry data around the coast of Ireland compiled from a number of different sources including multibeam survey and LiDAR data. Within Tralee Bay, detailed LiDAR data from OPW, and further offshore beyond the limits of the INFOMAR data, GEBCO 2014 point data [3], were used. Within parts of Brandon Bay, charted point data was used to improve the seabed map in this area which was not well covered by the above datasets. Tralee Bay includes areas of shallow intertidal saltmarsh, so the LiDAR data was particularly useful in representing these areas in the model. Where necessary the VORF model [4] was used to transform some of the surveys to a common vertical datum.

### B. Tidal conditions

The hydrodynamic conditions are dominated by astronomical tidal effects. To represent the tidal effects, the offshore boundary of the model was initially driven by tidal levels extracted from the TPXO satellite altimetry dataset [5, 6]. TPXO provides tidal boundary conditions based on 13 tidal harmonic constituents, and has a spatial resolution of  $1/12^\circ$ .

As part of an initial trial period, model results were compared against publicly available tide gauge data from several locations [7, 8]. An analysis of the model results when run to represent only the astronomical tide effects, showed noticeable discrepancies in the model predictions. A tidal

harmonic analysis of measured data at Fenit Pier, within Tralee Bay, showed some relatively important tidal constituents were not included in the TPXO dataset.

A review of the performance of several different global tidal models given in [9], by comparison of model predictions against in-situ and satellite derived measurements of the main tidal constituents, concluded that FES2012 and TPXO08 performed best in shelf seas, with FES2012 having the highest resolution and the lowest errors for the main tidal constituents for shelf seas such as the European Continental shelf. More recently [10] show that FES2014 [11], improves upon FES2012. FES2014 has a spatial resolution of  $1/16^\circ$  and provides up to 34 constituents, including several of the important constituents evident from the harmonic analysis of the measurements.

### C. Atmospheric conditions

Storm surges are a result of atmospheric wind and pressure effects and can also be influenced by the geometry of the coast and by the tides. Two sources of atmospheric pressure and wind speed and directions were considered in this study:

- The Met Éireann Harmonie model (HIRLAM-Aladin Research in Mesoscale Operational NWP In Euromet) data [12], represents the atmosphere using the fundamental equations of meteorology and produces forecast data for a wide variety of surface parameters such as wind, rain, temperature and precipitation at a horizontal resolution of 2.5 km, with 65 levels in the vertical. A 54-hour forecast with a 1 hour temporal resolution is produced four times a day, at 00Z, 06Z, 12Z and 18Z.
- The European Centre for Medium Range Weather Forecasting (ECMWF) Operational atmospheric forecast [13] model provides a 10-day forecast and is also produced four times a day and is produced at a resolution of 0.1 degrees. The ECMWF forecasts are available in hourly timesteps from 0 to 90 hours, 3 hourly from 93 to 144 hours and 6 hourly from 150 to 240 hours.

For the present study the TELEMAC-2D model was forced with the 00Z and 12Z Harmonie forecasts providing a short-range forecast of up to 54 hours using a temporal resolution of 1 hour. The model was also run independently, using the 00Z ECMWF operational forecasts providing a short to medium range forecast, meeting the requirement of a 6-day forecast. This used ECMWF forecasts with a temporal resolution of 3 hours and spatial resolution of 0.125 degrees as this was the forecast made available at project commencement.

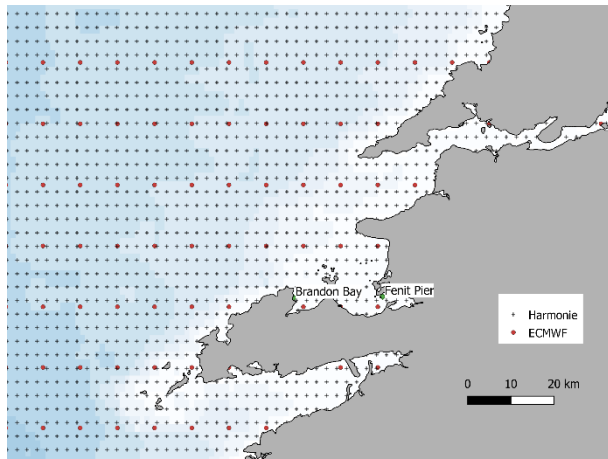


Figure 3 ECMWF and Harmonie model points

To account for surges at the model outer boundary, tidal elevations imposed were first adjusted for the hydrostatic head due to air pressure (inverse barometer effect).

The coefficient of wind influence, which takes into account to some extent the roughness of the seas and other processes, was calculated following the standard TELEMAC formulation given by the Institute of Oceanographic Sciences in the UK [17]:

$$\text{if } |U| < 5 \text{ m/s then } a = 0.565 \times 10^{-3}$$

$$\text{if } 5 < |U| < 19.22 \text{ m/s then } a = (-0.12 + 0.137|U|) \times 10^{-3}$$

$$\text{if } |U| > 19.22 \text{ m/s then } a = 2.513 \times 10^{-3}$$

where  $U$  is wind speed and  $a$  is coefficient of wind influence.

Two of the main differences between the EMCWF and Harmonie data is the spatial resolution currently available and temporal resolution as used in the present study, so one could expect that the Harmonie data should provide a more accurate representation of the wind fields, particularly any small spatial and temporal scale features such as small intense storms.

### III. MEASURED DATA

Relevant observational tide data on the West and SW coast of Ireland are available from the Irish National Tide Hydrometric Network (INTGN) [8] at Roonagh Pier, Galway Port, Inishmore, Kilrush Lough and Castletownbere Port, and from the OPW Hydrometric Network [7], including Fenit Pier and Blennerville within Tralee Bay. The INTGN data are generally available every 6 minutes (except for Castletownbere Port: every 15 minutes) and are referenced to Ordnance Datum (OD) Malin Head (OSGM15). The OPW data in Tralee Bay are currently available every 5 minutes and are also referenced to OD Malin Head (OSGM15).

Some observational tide gauge stations such as at Roonagh Pier and Kilrush Lough have only been in operation for a relatively short period. It is also worth noting that there can be long interruptions in the data, e.g. when the devices were serviced. This means that not all of the data could be used when performing tidal analysis.

A temporary tide gauge was also installed by the GSI at Brandon Quay, within Brandon Bay, providing a short term record of water levels during the second trial period.

### IV. MODEL CALIBRATION

An initial model calibration was carried out using TPXO and ERA5 wind and pressure data from ECMWF as a proxy for operational forecast wind and pressure data. ERA5 [15] is a climate reanalysis dataset, available through the Copernicus Climate Data Store [16]. The initial calibration of the tide only model predictions was based on a spring neap cycle at Fenit Pier from 2008 that is representative of an average spring neap cycle.

For the calibration of the model for tide and surge events, an analysis of the tide gauge data at Fenit Pier was carried out to identify five events between 2013 and 2017 with notable surge residuals, including the highest event recorded at Fenit Pier. It is worth noting that high surge residuals, and some of the events selected, did not necessarily occur with spring tides.

The model calibration included sensitivity tests to the bed friction, tide, and atmospheric forcing. Fig 4 shows a sample of the predicted water levels and associated currents. The tidal time series shown is for a point south of Fenit Pier and to the east of Derrymore Island.

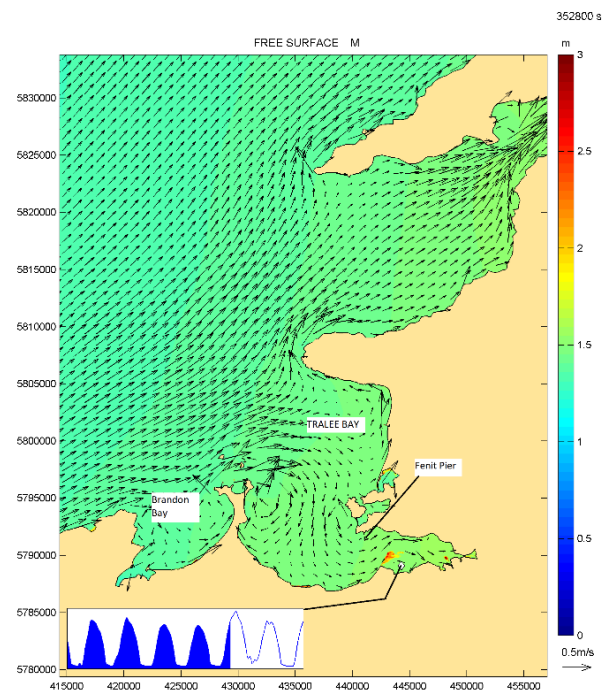


Figure 4 Model surface elevation and associated currents

Model results were subsequently validated against tide gauge data across the area including at Fenit Pier, Kilrush Lough, Galway Port and Inishmore for a representative average spring-neap cycle. The tide only results were in reasonably good agreement with average errors of between 0.02m to 0.1m in elevation and errors of between 9 to 18 minutes in the timing of high waters, but outside the target accuracy set for the system. Following the initial model calibration, a first continuous trial



period was carried out during the winter of 2018-2019. Results from this trial at the Fenit Pier tide gauge within Tralee Bay showed relatively small but nevertheless noticeable differences in the tide only predictions.

The differences between the model predictions and synthesised tides, whilst relatively small, appeared in both the phase and amplitude, and therefore were unlikely to be corrected by simple adjustments to the TPXO data, as occasionally required. The synthesised tides were based on a tidal harmonic analysis of the Fenit Pier gauge for the continuous period between February 2016 to July 2017 using T-Tide [14]. A review of the amplitudes of the harmonic constituents from this analysis showed several important constituents were not included in TPXO but were included in FES2014.

A hindcast of the first continuous trial period using FES2014 produced a noticeable improvement in model predictions, particularly at high water, and was therefore adopted for the second trial period.

## V. MODEL VALIDATION

Model validation was carried out as part of two continuous forecast trial periods. Following model recalibration after the first trial period, the second continuous trial period was carried out during the months of October to December 2019. During the second trial, as presented in this paper, the model was forced with FES2014 at the boundaries, with wind and pressure forcing from the forecasts provided by ECMWF operational forecast and Met Éireann Harmonie forecast within the model domain. The following sections present a comparison of the model results against observed data at Fenit Pier. Table 1 summarises the tide and wind/pressure forcing used during the different stages of the study.

TABLE 1. TIDE ONLY ERROR STATISTICS

Study Phase	Time period	Tide forcing	Wind/pressure forcing
Initial model calibration	Average Spring-neap cycle	TPXO	ERA5
Validation trial period 1	24-Nov-2018 to 22-Feb-2019	TPXO	Harmonie (0-54 hours) and ECMWF (0-144 hours)
Validation trial Period 2	8-Oct-2019 to 9-Dec-2019	FES2014	Harmonie (0-54 hours) and ECMWF (0-144 hours)

## A. TIDE ONLY

The model results for the tide only component are presented first. These results were generated by running the model with tide only forcing, i.e. using only FES2014 and comparing the results against the synthesised tide levels.

The model was run once a day as part of the operational forecast system to produce a 6-day tide-only prediction, i.e. without meteorological forcing. The main aim of running the tide only model was to be able to quote surge residuals at all the forecast points within Tralee and adjacent bays. The model results are presented in Fig. 5 as a timeseries of water elevations for a two-day sample period during the second two month trial period to illustrate the model predictions, when there was a noticeable surge event. Scatter plots of all high-water predictions during the trial period are also given in Fig. 6 together with the associated error statistics quoted in Table 1. The error bars in Fig 6 are  $\pm 0.15\text{m}$ , which was the target accuracy for the tide only component of the model.

The time series shows the model is in close agreement with the synthesised tide levels. Fig 6 shows that the model predictions of all high tide levels during the trial period are generally within the target accuracy, with a few high waters slightly underpredicted. The error statistics quoted in Table 2 show that the model predictions meet the target accuracy for 89% of all high waters, and for the higher high waters above Mean High Water Spring (MHWS) the target accuracy is met 100% of the time. MHWS at Fenit Pier is estimated from our tidal analysis of the gauge data to be 2.22m above Mean Sea Level (MSL). Mean errors quoted in Table 2, show a small positive bias of 1cm for all high waters and 6cm for high waters above MHWS.

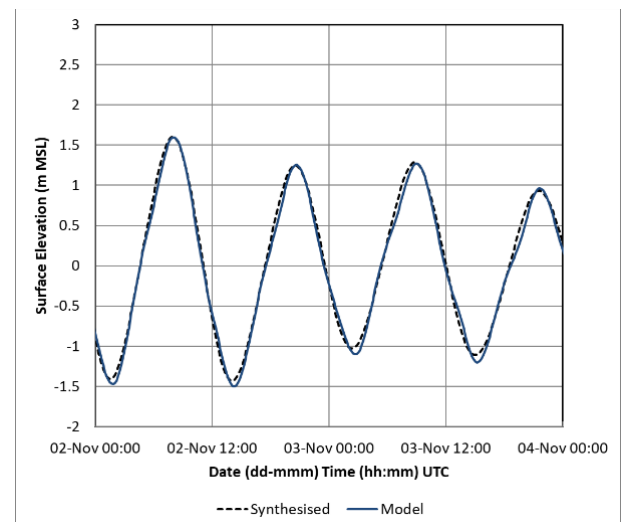


Figure 5 Tide only synthesised and model predictions at Fenit Pier

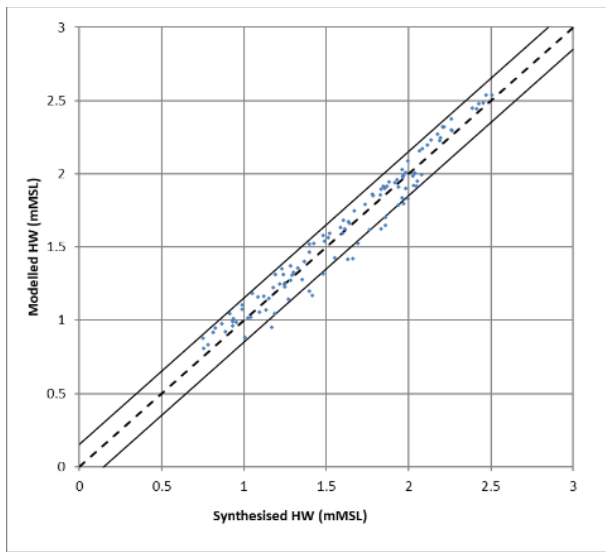


Figure 6 High tide levels model vs. Synthesised

TABLE 2 .TIDE ONLY ERROR STATISTICS

	Mean Error (m)	Mean Absolute Error (m)	Error range (m)	Target (m)	Events within target (%)
High Waters	0.01	0.08	-0.25 0.13	+/-0.15	89
High waters above MHWS	0.06	0.06	0.03 0.11	+/-0.15	100

### B. TIDE AND SURGE

The tide and surge model results presented are the first 12 or 24 hours of each forecast, based on the Harmonie or ECMWF forced model runs, respectively. The model results are presented in Fig. 7 as a sample 2-day time series of the surface elevation. A scatter plot of all the high water (HW) predictions during the trial period are shown in Fig. 8, with associated error statistics quoted in Table 2. The error bars in the scatter plot is the target accuracy measure of 0.25m.

The time series plot in Fig 7 covers the same period as in Fig. 5. Fig 7 shows that the models are in reasonably good agreement with the observations. Furthermore, there is little visible difference between the model forced by either ECMWF or Harmonie for this period.

The scatter plot in Fig 8 shows the model predictions of all high waters during the second trial period, plotted against the observed high waters. This plot shows that the model is generally well within the target accuracy of +/-0.25m with only a few high waters slightly underpredicted.

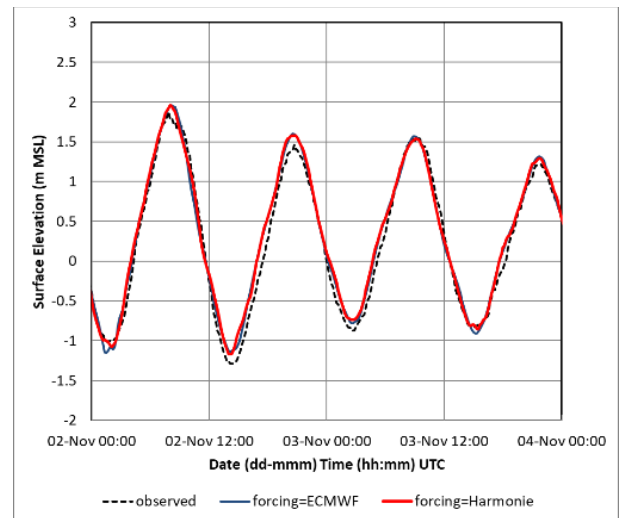


Figure 7 Tide and surge model predictions and observations at Fenit Pier

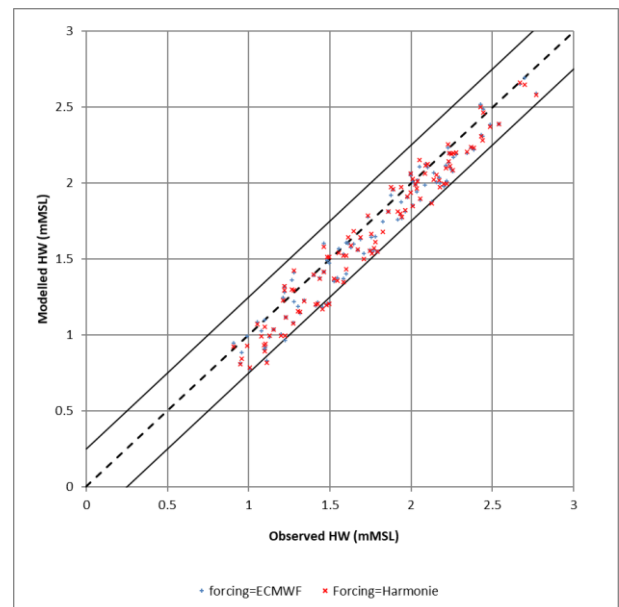


Figure 8 High total water levels: Model vs. Observed

Tables 3 and 4 summarise the error statistics of the model, forced using ECMWF and Harmonie, for all high waters and all high waters above MHWS, respectively. These tables show that there is very little difference between the model forced by Harmonie compared with ECMWF.

The scatter plot and error statistics show a small negative mean error of -9cm and -10cm for all high waters and all high waters above MHWS, respectively. It is expected that this negative bias can be corrected through small adjustments to the wind and pressure forecasts, and would be best performed and confirmed after a longer term of model simulations e.g. one year or more, in case there are inter-annual effects.

TABLE 3. TIDE AND SURGE ERROR STATISTICS – HIGH WATERS

Forcing	Mean Error (m)	Mean Abs Error (m)	Error range (m)	Target (m)	Events within target (%)
Harmonie	-0.09	0.11	-0.30 0.14	+/-0.25	96%
ECMWF	-0.09	0.11	-0.28 0.14	+/-0.25	95%

TABLE 4. TIDE AND SURGE ERROR STATISTICS – HIGH WATERS ABOVE MHWS

Forcing	Mean Error (m)	Mean Abs Error (m)	Error range (m)	Target (m)	Events within target (%)
Harmonie	-0.10	0.11	-0.22 0.07	+/-0.25	100%
ECMWF	-0.10	0.11	-0.22 0.09	+/-0.25	100%

### C. TIDE TIMINGS

The timing of the tides are also important for a real-time forecast system. Fig 5 and Fig 7 show that the timing of the tides is in good agreement with the tidal synthesis and observations, respectively. Error statistics in terms of Mean Error and Mean Absolute Error in minutes for the second month trial period are given in Table 5.

TABLE 5. TIDE AND SURGE ERROR STATISTICS – ALL HIGH WATERS

Variable	Benchmark	Model	Mean Error (Minutes)	Mean Absolute Error (Minutes)
Tide only HW	Tidal synthesis	Tide only model	3.6	10.0
Total HW	Raw Obs	Short range forecast	-7.4	17.2
Total HW	Raw Obs	Medium Range Forecast	-8.6	17.4
Skew surge	Raw Obs – tidal synthesis	Short range forecast	-10.8	15.4
Skew surge	Raw Obs – tidal synthesis	Medium Range Forecast	-11.8	15.7

## VI. REAL TIME OPERATIONAL SYSTEM

The two continuous trial periods were run as a fully automated real time operational forecast system delivering forecasts to a website within a target delivery schedule. All model runs were carried out on HR Wallingford's internal Linux computing cluster with model runs scheduled using the Linux

utility, *cron*. Hotstart files were used to initialise model runs from the previous forecast, requiring only an initial model spin up period at the beginning of each trial period. Pre and post-processing of incoming data and results used a combination of existing TELEMAT-system and bespoke python utilities to reformat, interpolate and transform boundary conditions and reformat model results. The password protected forecast website was hosted on an Amazon Web Server (AWS).

## VII. CONCLUSIONS

A TELEMAT-2D hydrodynamic model has been developed to forecast tide and storm surge conditions on the South West coast of Ireland. The model forms part of a real time forecast system under development to provide short to medium range forecasts of up to 6 days. The model was forced with boundary tide levels from FES2014 and wind and pressure forecasts (within the model domain) from the ECMWF and Met Éireann's Harmonie models.

The model has been calibrated and validated against astronomical tide levels synthesised from observed gauge data and total water levels i.e. also accounting for storm surges. The model has been shown to be in good agreement with the observations, generally meeting the target accuracy required of the system in terms of both the elevation and timing of high waters.

Further improvement to the total water levels could be made by correcting for biases in the surge predictions which could be based on the data from the two trial periods. It is recommended that if such adjustments are made, the results are reviewed e.g. on an annual basis as part of routine model system maintenance, after a longer period of operation.

For the trial periods modelled to date there was little visible difference between the model results when forced by the ECMWF and Met Éireann's higher resolution Harmonie models. Further simulations are recommended for extreme storm events for which the higher resolution Harmonie model is expected to provide a more detailed and accurate forecast of the wind conditions.

The model results presented in this paper are based on deterministic forecasts of the wind and atmospheric pressure. Both the ECMWF operational forecast model and Met Éireann's Harmonie model are also run to provide ensemble forecasts of wind and pressure. The availability of ensemble forecasts of wind and pressure means that there will be the possibility of producing corresponding ensemble forecasts i.e. probabilistic forecasts of total water levels including surge. Future development of a probabilistic forecast of water levels will involve a review of the available input data, together with consideration of the balance between accuracy and computational requirements; possible subsampling of the full ensemble and an assessment of model resolution and the potential application of meta modelling techniques.

## ACKNOWLEDGEMENT

The authors thank colleagues at HR Wallingford, in particular Noémie Durand and Alan Cooper, the Office of Public Works and Met Éireann, in particular Rosemarie Lawlor, for invaluable contributions and discussion throughout the study.

The authors also thank the Geological Survey Ireland and the Marine Institute for supplying the bathymetric data used in the model, and Sean Cullen, Niall Finn and Eoin McCraith of GSI for the temporary tide gauge deployment.

#### REFERENCES

- [1] GSI <http://www.gsi.ie>
- [2] INFOMAR <https://www.infomar.ie/>
- [3] Weatherall, P., K. M. Marks, M. Jakobsson, T. Schmitt, S. Tani, J. E. Arndt, M. Rovere, D. Chayes, V. Ferrini, and R. Wigley (2015), A new digital bathymetric model of the world's oceans, *Earth and Space Science*, 2, 331–345, doi: 10.1002/2015EA000107.
- [4] VORF. 2007. [https://www.iho.int/mtg\\_docs/com\\_wg/IHOTC/IHOTC8/UK\\_VORF.pdf](https://www.iho.int/mtg_docs/com_wg/IHOTC/IHOTC8/UK_VORF.pdf)
- [5] Egbert, Gary D., and Svetlana Y. Erofeeva. "Efficient inverse modeling of barotropic ocean tides." *Journal of Atmospheric and Oceanic Technology* 19.2 (2002): 183-204.
- [6] OSU, "OSU Tidal Data Inversion Software and Atlas," Oregon State University, 2008.
- [7] OPW [www.waterlevel.ie](http://www.waterlevel.ie)
- [8] Irish National Tide Gauge Network (INTGN).
- [9] Stammer, D., et al. (2014), Accuracy assessment of global barotropic ocean tide models, *Rev. Geophys.*, 52, 243–282, doi:10.1002/2014RG000450.
- [10] Ray R.D., B.D. Loomis, S.B. Luthcke and K.E. Rachlin (2019). Tests of ocean-tide models by analysis of satellite-to-satellite range measurements: an update. *Geophys. J. Int.* (2019) 217, 1174–1178 doi: 10.1093/gji/ggz062.
- [11] Carrere, L., Lyard, F., Cancet, M., and Guillot, A. (2015). "FES 2014, a new tidal model on the global ocean with enhanced accuracy in shallow seas and in the Arctic region," in *Proceedings EGU General Assembly Conference Abstracts* (Vienna: EGU General Assembly)
- [12] Bengtsson, L., and Co-authors, 2017: The HARMONIE–AROME Model Configuration in the ALADIN–HIRLAM NWP System. *Mon. Wea. Rev.*, 145, 1919–1935, <https://doi.org/10.1175/MWR-D-16-0417.1>.
- [13] ECMWF operational forecast ([www.ecmwf.int](http://www.ecmwf.int))
- [14] Pawlowicz, R., B. Beardsley, and S. Lentz, "Classical tidal harmonic analysis including error estimates in MATLAB using T\_TIDE", *Computers and Geosciences* 28 (2002), 929-937.
- [15] Hersbach, H., Dee, D. ERA5 reanalysis is in production. ECMWF Newsletter No. 147 – Spring 2016.
- [16] <https://cds.climate.copernicus.eu>
- [17] Flather, R.A.. 1976 Results from a storm surge prediction model of the north-west European continental shelf for April, November and December, 1973. Wormley, UK, Institute of Oceanographic Sciences, 37pp. (Institute of Oceanographic Sciences Report 24)



# Improvement of a Continental Shelf Model of the North Sea

Kai CHU, Alexander BREUGEM, Thom WOLF,  
Boudewijn DECROP  
IMDC N.V.  
Antwerp, Belgium  
[kai.chu@imdc.be](mailto:kai.chu@imdc.be)

**Abstract**— A continental shelf model (iCSM) was developed in TELEMAC-2D at IMDC. The model domain covers the North Sea, the Irish Sea, the Celtic Sea and the Bay of Biscay. This paper presents the stepwise improvement of the iCSM model. The model predictive skills on water levels are significantly improved with several new features implemented. The averaged root-mean-square-error (RMSE) at the Belgian coast is reduced to 13 cm after calibration. The Storm Xaver in December 2013 is well reproduced. The model also shows good predictive skills on velocities (both stationary and ADCP sailed) near the Belgian coast.

## I. INTRODUCTION

During the past decades the attention to global climate change and its local effects have highlighted the significance of providing accurate information on the natural evolution of coastal hydrodynamics and morphology, human intervention assessment and natural disaster predictions. The Belgian Coastal Zone has important environmental and commercial values due to the presence of large harbours and wind farms. An accurate prediction of the tidal propagation is important for both planning purposes (e.g. coastal zone management) and for the nautical accessibility (e.g. navigation to the harbour of Zeebrugge and the Scheldt river estuary). Process-based numerical models, including the most important processes and parameters for tidal predictions, have been widely adopted for this purpose. The numerical model shall be reliable to perform accurate predictions during normal conditions, in which the main forcing for the water levels and velocities are coming from the tidal wave that enters the North Sea from the Norwegian Sea in the north, with a secondary influence of the tidal wave entering through the Dover Strait from the South. In addition, the model shall also be able to produce adequate predictions during extreme conditions when strong winds and large atmospheric pressure gradients are present.

A continental shelf model (iCSM) was developed in TELEMAC-2D at IMDC [1]. The model generally showed decent tidal propagations in the North Sea, albeit room for further improvement was possible along the coast of the Southern Bight, in particular in the Belgian Coastal Zone. This paper presents the stepwise improvement of the iCSM model by including several relevant physical processes and improving the model parameter calibration. The model predictive skills on both water levels and velocities are significantly improved.

## II. MODEL SETUP

The iCSM domain covers the North Sea, the Irish Sea, the Celtic Sea and the Bay of Biscay (Figure 1).

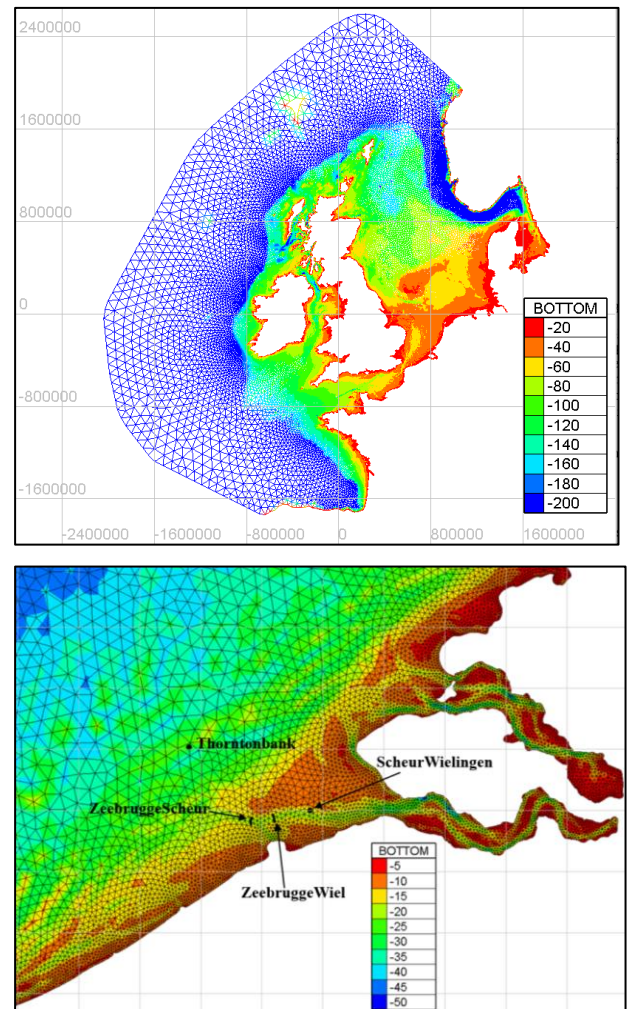


Figure 1. Upper panel: Bathymetry and computational mesh of iCSM. Lower panel: Detailed view of the Belgian Coastal Zone (horizontal system: Spherical Mercator projection. Vertical datum: MSL). The measurement locations of stationary and ADCP sailed velocities are also indicated.

The model is built in a spherical Mercator projection with Coriolis effect included. The computational mesh consists of approximately 150,000 nodes and 292,000 elements. The unstructured mesh is refined near the coastal zones, e.g. with a minimal resolution of 500 m at Belgian coast. Mesh refinement is also applied along the coastlines of UK, France and The Netherlands as well as in the Wadden Sea and the English Channel. The Scheldt river estuary is partly included in the model, thus allowing the tidal wave to propagate sufficiently up into the estuary, such that the influence of the estuary on the tide in the coastal zone is considered. The freshwater discharge from the rivers is neglected, since its magnitude is rather small compared to the discharge from the tidal flow in the estuary.

The model bathymetry is adopted from the latest EMODNET 2018 dataset with a spatial resolution of  $1/16 \times 1/16$  arc minutes (circa  $115 \times 115$  meters).

The model is driven by both tidal and nontidal forcing. The tidal water levels at the open boundaries are specified in the frequency domain with 14 harmonic constituents (M2, S2, N2, K2, K1, O1, P1, Q1, M4, MS4, MN4, MF, MM and 2N2) from the TPX09 global tidal inversion [2]. In addition, 16 minor harmonic constituents (2Q1, SIGMA1, RO1, M1, CH11, PI1, PHI1, THETA1, J1, OO1, 2N2, MU2, NU2, L2, T2, LAMBDA2) are added at the open boundaries by switching on the ‘MINOR CONSTITUENTS INFERENCE’ in TELEMAC. Although wind setup at the open boundaries are negligible due to the deep water locally, the non-tidal effect of local pressure is considered important and therefore are added at the open boundaries by means of Inverse Barometer Correction (IBC) [3]. It is an isostatic response of the oceans to atmospheric pressure, i.e. with increase in pressure the sea level goes down and vice versa. In simple terms, 100 Pa decrease in atmospheric pressure with result in 1 cm increase in sea surface height.

$$IBC(x, y, t) = \frac{-(P(x, y, t) - P_0)}{\rho_0 \times \gamma} \quad (1)$$

where  $P_0$  represents the standard atmospheric pressure of 101,325 Pascal.

The meteorological surface forcing includes the space- and time varying wind (at 10-meter height) and air pressure at MSL from the ERA5 hourly dataset provided by European Centre for Medium-range Weather Forecasting (ECMWF). The use of Flather [4] and Charnock formula [5] (Figure 2) for the wind drag coefficient are evaluated. The optimal setting is found with a dimensionless Charnock coefficient of 0.04 which accurately captures the peak high-water levels on a stormy event. Using the Flather formula leads to  $\sim 5$  cm underestimation of the water levels (details are not shown in this paper).

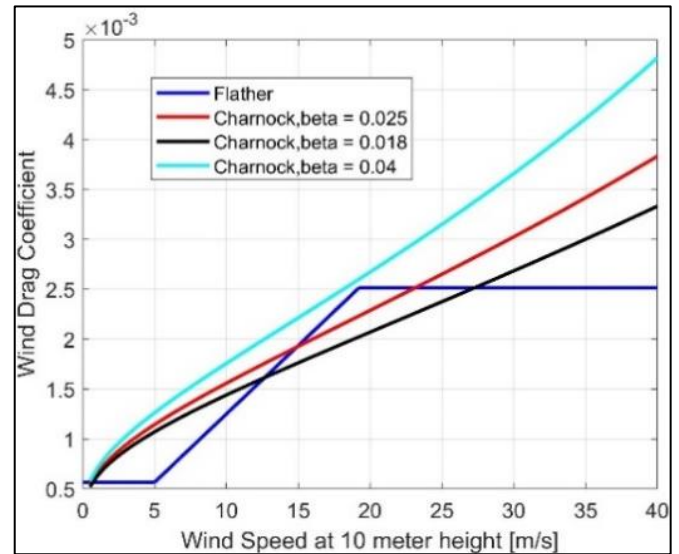


Figure 2. Relation between wind speed at 10 m height and wind drag coefficient using Flather formula and Charnock formula with different Charnock coefficients (beta).

The global tidal dissipation consists of two terms. In shallow waters the tidal dissipation through bottom friction is the primary mechanism. However, the dissipation of tidal energy through generation of internal tides is the dominant mechanism when tides propagate over steep topography in deep stratified waters. The global energy conversion rate from external to internal tides is 25-30%, amounts to about 1 TW, mainly occurs in areas of rough topography [6]. The parameterization of internal tide dissipation has been implemented to TELEMAC-2D and successfully applied to the in-house IMDC South Asian Model (iSAM) where the internal tide dissipation is a dominant process. The model predictive skill on water levels is significantly improved. Inside of the iCSM domain, Bay of Biscay is well-known for pronounced internal tidal dissipation in summer. Therefore, this process is included as well and its impact on tidal propagations in the Belgian Coastal Zone is evaluated. For a 2D barotropic model, the internal-tide stress  $\tau_{IT}$  is parameterized as below and added to the momentum equation [7].

$$\tau_{IT} = (1/2)\kappa h^2 N \mathbf{u} \quad (2)$$

The implementation is only applied in water depths greater than 200 m.  $\mathbf{u} = (u, v)$  represents the horizontal velocity vector.  $\kappa$  represents the wave number which is set to be spatially constant of  $2\pi/(10 \text{ km})$ .  $h^2$  represents the standard deviation of the bathymetry in a certain area, computed based on EMODNET 2018 dataset interpolated on a  $0.01^\circ \times 0.01^\circ$  rectangular grid. Over each grid cell, a polynomial sloping surface is fit to the bottom topography (given by  $H = a + bx + cy + dxy$ ), and the residual heights are used to compute  $h^2$  by mean-square averaging over the grid cell. The depth averaged buoyancy frequency (Brunt-Väisälä frequency)  $N$  accounts for the stratification which is calculated based on the annual means of water density adopted from World Ocean Atlas (WOA) 2013-V2 dataset provided by NOAA. The buoyancy frequency  $N$  is implemented as a spatially varying scalar field but constant both in the vertical and in time.

$$N = \sqrt{\frac{g}{\rho} \frac{d\rho}{dz}} \quad (3)$$

Another physical process often neglected in regional models but of remarkable importance at oceanic scale is the self-attraction and loading effect (SAL). This phenomenon consists of three effects: the deformation of the seafloor under the weight of the water column (Earth is an elastic body); the redistribution of Earth mass and its corresponding changes in the gravitational field; the gravitational attraction induced by the water body on itself. As SAL has a well-acknowledged impact on the tidal phases [8], therefore we included it in the iCSM using a simple beta ( $\beta$ ) approximation approach which utilizes a proportionality constant between SAL elevation and surface elevation, with typical values of  $\beta \sim 10\%$  on a global scale. One can consider it as a reduction factor of the barotropic pressure gradient. In the North Sea, the representative value of  $\beta$  is found to be 1.5% [9] which is parameterized in iCSM by reducing the gravity  $g$  by 1.5%. The full form of momentum equation applied on iCSM is expressed as:

$$\frac{\partial u}{\partial t} + u \frac{\partial u}{\partial x} + v \frac{\partial u}{\partial y} - f v = -g(1 - \beta) \frac{\partial \zeta}{\partial x} - \frac{1}{\rho} \frac{\partial P_{atm}}{\partial x} + \nu \left( \frac{\partial^2 u}{\partial x^2} + \frac{\partial^2 u}{\partial y^2} \right) - \frac{\tau_{xbot}}{h} - \frac{\tau_{xIT}}{h} + \frac{\tau_{xwind}}{h} \quad (4)$$

$$\frac{\partial v}{\partial t} + u \frac{\partial v}{\partial x} + v \frac{\partial v}{\partial y} + f u = -g(1 - \beta) \frac{\partial \zeta}{\partial y} - \frac{1}{\rho} \frac{\partial P_{atm}}{\partial y} + \nu \left( \frac{\partial^2 v}{\partial x^2} + \frac{\partial^2 v}{\partial y^2} \right) - \frac{\tau_{ybot}}{h} - \frac{\tau_{yIT}}{h} + \frac{\tau_{ywind}}{h} \quad (5)$$

To account for the effect of bottom friction, a spatially varying roughness field of Nikuradse value is determined by manual calibration (Figure 3). The calibrated bottom friction map shows higher value in the west side of the Dover Strait. However, this large variation on Nikuradse values does not lead to substantial variations on the bed drag force (logarithmic relation).

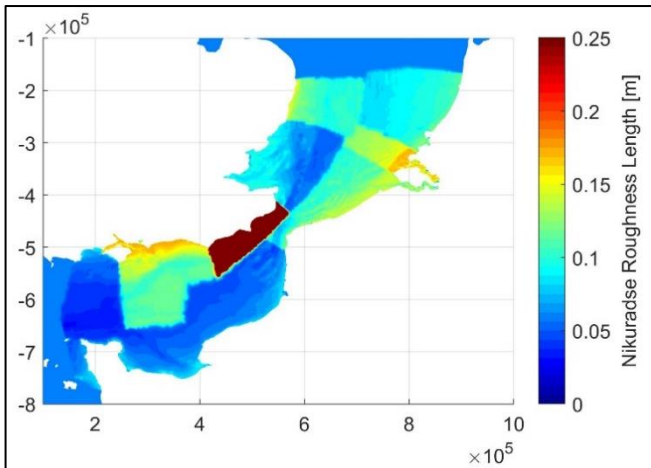


Figure 3. Spatial varying bottom friction of Nikuradse roughness length applied in iCSM.

### III. CALIBRATION RESULTS

The model is calibrated for the entire year of 2015, with time step of 2 minutes. The computation takes 3 hours with 48 cores, which is sufficiently efficient. During the calibration,

the focus is made on improving the water level representation at 28 stations along the coasts of UK, France, Belgium and the Netherlands.

The stepwise calibration is summarized in Table 1. The Reference model (Run01) includes the use of EMODNET 2018 bathymetry data; TPX09 tidal boundary with minor harmonic components switched on; ERA5 hourly wind and pressure data and Charnock coefficient of 0.04, as described in the previous section. The remaining processes are taken as separate calibration steps; thus the contribution of each step can be evaluated. Figure 4 shows the RMSE of each calibration step. The detailed statistics are averaged over each coastal region and summarized in Table 2. VIMM (Visualization of Model and Measurements) is adopted for comparison between model and measurements in this study [10].

It is noteworthy that the inverse barometer correction (Run02) effectively reduces the bias of water level in general. This is more pronounced in the Belgian Coastal Zone where it is reduced from 6.9 cm to 1.1 cm and the model accuracy holds till the end of the calibration. Subsequently the RMSE of the water level also decreases by 20% on average. An exception is found along the British coast where, according to literatures [11], the inverse barometer correction accounts for only one-third of the observed variability of MSL in UK, whereas larger-scale atmospheric or ocean processes (e.g. gyre-scale circulations) may play important roles as well. However, successful modelling of such processes is still a major challenge.

Including internal tide dissipation (Run03) hardly modify the tidal propagation in the North Sea. For instance, the RMSE of water level is reduced by less than 1 cm on average. This is probably because the tidal wave entering the North Sea is primarily coming from the North, while the tidal wave coming from the South via Dover Strait has only a secondary influence. The impact of internal tide dissipation in the Bay of Biscay requires further evaluation in future studies.

Including SAL (Run04) effectively reduces the bias of M2 tidal phase which is decreased e.g. from  $5.4^\circ$  to  $1.5^\circ$  in the Belgian Coastal Zone. Nevertheless, it shows limited improvement in the UK, which implies that the beta approximation may not be sufficient to represent the spatial characteristics of the SAL field. A more decent way of modelling the SAL effect using the spherical harmonics approach [9] will be considered in future studies.

Finally tuning the bottom roughness (Run05) leads to better predictions on M2 amplitude. This is more noticeable in the Belgian and Dutch coastal zone where the bottom roughness adjustments are focused on.

TABLE 1. OVERVIEW OF ICSM CALIBRATION STEPS.

Run ID	Description
Run01	Reference
Run02	Run01+ inverse barometer correction
Run03	Run02 + internal tide dissipation
Run04	Run03 + self-attraction and loading
Run05	Run04 + spatially-varying bottom roughness



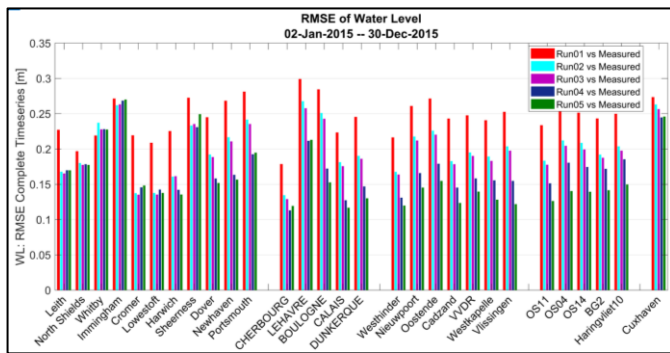


Figure 4. RMSE of water levels during model calibration.

TABLE 2. STATISTICS OF CALIBRATION RESULTS. THE VALUES ARE LINEARLY COLOR-CODED FROM red (largest errors) to green (lowest errors).

Statistics	Zone	Run01	Run02	Run03	Run04	Run05
RMSE of water level [cm]	UK	23.9	19.7	19.4	18.4	18.4
	France	24.6	20.5	19.8	15.4	14.6
	Belgium	24.7	19.7	19.2	15.6	13.3
	Netherlands	24.6	20	19.3	17.3	14
	Average	24.5	20	19.4	16.7	15.1
Bias  of water level [cm]	UK	8.1	6.6	6.5	6.6	6.7
	France	7.9	1.4	1.5	1.6	1.5
	Belgium	6.9	1.1	1.3	1.3	1.5
	Netherlands	7.8	1	1.7	1.9	2.1
	Average	7.7	2.5	2.8	2.9	3
Bias  of M2 Amplitude [cm]	UK	3.7	3.6	3.5	3.5	3.3
	France	6.2	6.5	5.9	8.4	7.2
	Belgium	13.1	13.8	12.9	13.4	8.2
	Netherlands	17.7	18.4	17.5	17.7	11.6
	Average	10.2	10.6	10	10.8	7.6
Bias  of M2 Phase [deg]	UK	4.2	4.5	4.3	4	3.7
	France	4.7	4.4	4.3	2.2	2
	Belgium	5.4	4.8	4.9	1.5	1.1
	Netherlands	5.5	4.9	5	1	1.2
	Average	5	4.7	4.6	2.2	2

#### IV. VALIDATION RESULTS

After calibration, the iCSM is validated on water level during the Storm Xaver. The model predictive skills on stationary and ADCP sailed velocities are also evaluated. The M2 tide from the model is compared to OSU/TPXO data [2]. Afterwards, the iCSM is used to force a regional model of the Scheldt Estuary via boundary nesting.

##### K. Hindcast of the Storm Xaver

The Storm Xaver is an extratropical storm that occurred from December 4<sup>th</sup> to December 10<sup>th</sup>, 2013. It formed in Greenland and grew while travelling North of Scotland up to the Baltic Sea. During the storm, the air pressures decreased to 962 mb and wind velocities up to 130 km/h were observed. The storm led to increased water levels around the North Sea and even to inundations in England and Wales.

In order to perform a hindcast of the storm, the model was run for the period 4<sup>th</sup>-10<sup>th</sup> December 2013. Figure 5 exemplifies the water level comparison at Cadzand. The peak

water level on 06-Dec-2013 is well captured by the model with a discrepancy less than 10 cm. Table 3 implies that the water level predicted by the model during the Storm Xaver is slightly worse than the calibration results (e.g. the RMSE in the Belgian Coastal Zone is increased from 13.3 cm to 17.5 cm). The meteorological surface forcing of wind and air pressure play more dominant roles during stormy events. This suggests that the use of a constant Charnock coefficient in space and time is insufficient for modelling extreme storms. The space- and time varying Charnock coefficient are available in the ERA5 dataset. This parameter accounts for increased aerodynamic roughness as wave heights grow due to increasing surface stress. It depends on the wind speed, wave age and other aspects of the sea state and is used to calculate how much the waves slow down the wind. They are computed by the ECMWF wave model and used in the air-sea boundary layer parameterization of the ECMWF meteorological model. Using these variable Charnock values could be a reasonable solution to improve the model performance for stormy periods. Hence it will be considered for future studies.

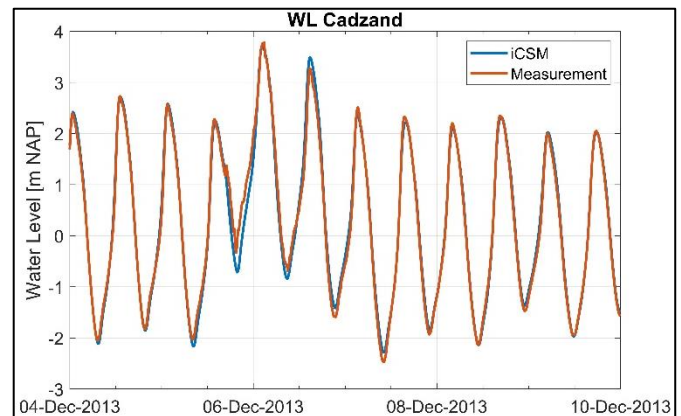


Figure 5. Modelled and measured water levels at Cadzand during the Storm Xaver.

TABLE 3. RMES AND BIAS OF THE WATER LEVEL DURING THE STORM XAVER.

Statistics	Zone	Calibration (Run05)	Validation (Xaver Storm)
RMSE of water level [cm]	UK	18.4	22.5
	France	14.6	19.3
	Belgium	13.3	17.5
	Netherlands	14	18.7
	Average	15.1	19.5
Bias  of water level [cm]	UK	6.7	8.6
	France	1.5	1.7
	Belgium	1.5	2.1
	Netherlands	2.1	3.4
	Average	3	3.9

##### L. Validation on velocities

The modelled velocities are compared with measurements at the stations Scheur/Wielingen (Figure 6) and Thorntonbank (Figure 7), the latter of which is slightly more offshore. In general, the model reproduces the flow patterns decently for both velocity magnitude and direction. The RMSE of flow magnitude are 16 cm/s and 13 cm/s at those two stations. The bias of flow magnitude is -2 cm/s and 0 cm/s respectively.



There is a slight discrepancy on the flow direction at Scheur/Wielingen, probably due to the uncertainty of the local bathymetry interpolated on relatively coarse mesh.

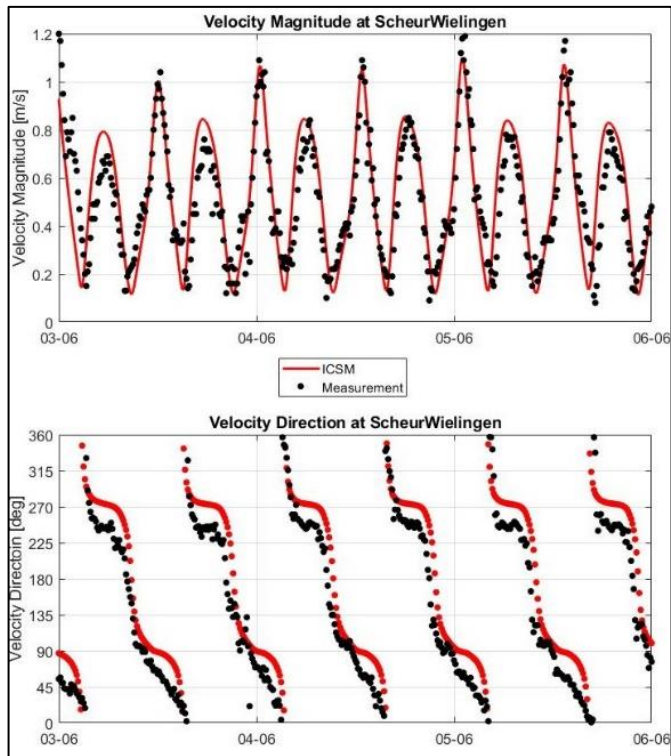


Figure 6. Modelled and measured velocity at Scheur/Wielingen.

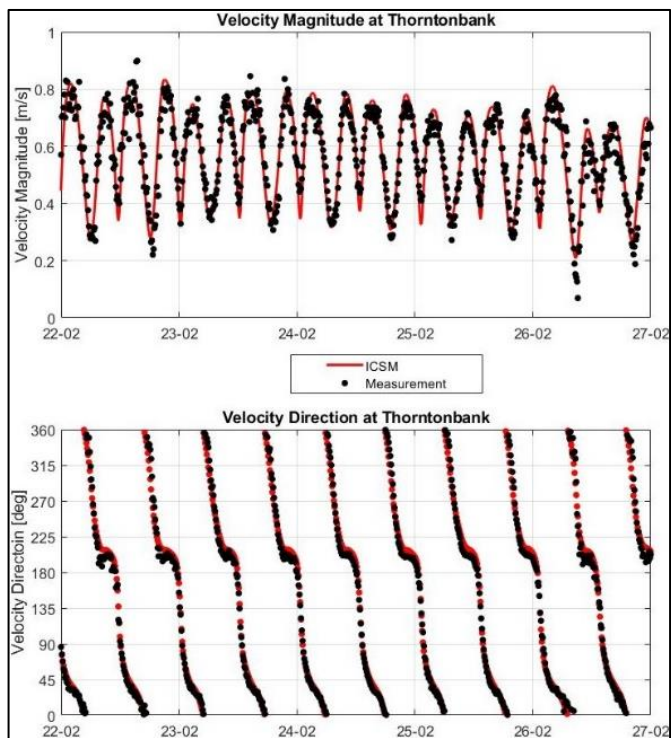


Figure 7. Modelled and measured velocity at the Thorntonbank.

The modelled flow patterns are also validated against 13-hour ADCP sailed velocities near Zeebrugge (see locations in

Figure 1). Figure 8 and Figure 9 exemplify the comparison during maximum flood. Both flow magnitude and direction are well reproduced by the model, despite of the rather coarse mesh used locally. For the complete 13-hour period, an averaged RMSE of 16.3 cm/s and 17.5 cm/s are observed at Scheur and Wielingen respectively. The corresponding relative-mean-absolute-error (RMAE) which measures the model performance on both velocity magnitude and directions, is 0.33 and 0.31 respectively. Therefore, the model performance is categorized as *good* [12].

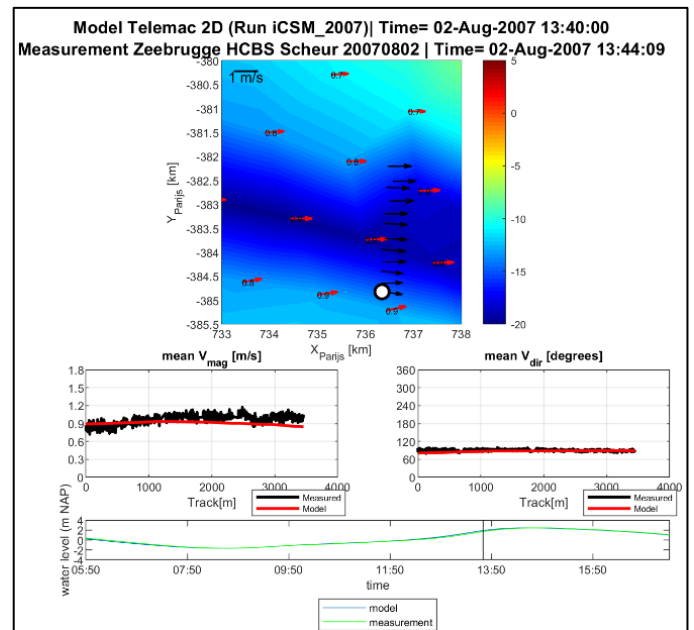


Figure 8. Modelled and measured ADCP velocity at Zeebrugge Scheur during flood.

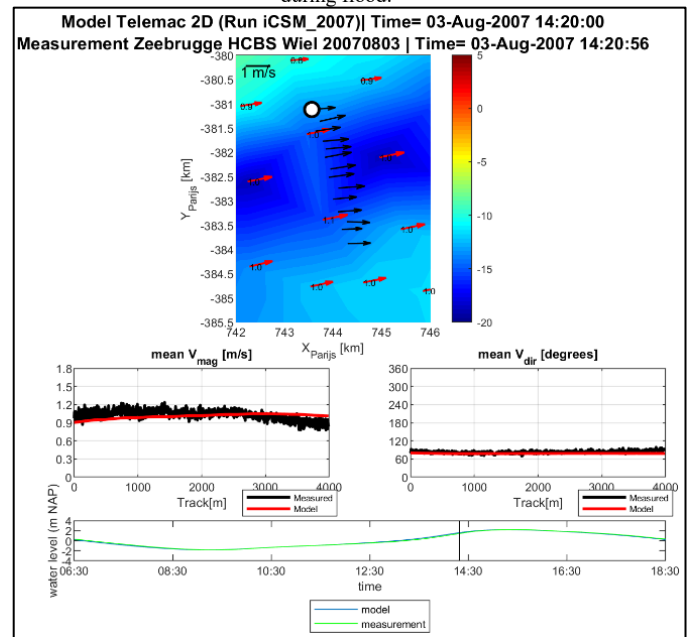


Figure 9. Modelled and measured ADCP velocity at Zeebrugge Wielingen during flood.

### M. Validation on M2 tide

The iCSM runs for the entire year of 2015 again without meteorological forcing. The tidal amplitude and phase of the tidal constituents computed by the model are then compared to those from OSU/TPXO [2]. The most dominant tidal constituent in the North Sea is the M2-tide, which is therefore the only one presented in this paper.

Figure 10 presents the map of the calculated M2 amplitude in the model area and the differences from TPXO, which are below 10 cm in a large part of the model domain. The differences tend to be larger in shallow areas and close to the coast (e.g. ~40 cm in the Southern Bight). However, the iCSM is expected to be more accurate than TPXO in these regions, because the model resolution is higher and the physical processes occurring in shallow water are better included in the model than in TPXO. The co-tidal map for the M2 component is shown in Figure 11. The lines of equal tidal phase show good agreement between the model and TPXO. The locations of the amphidromic points in the North Sea are well reproduced by the model.

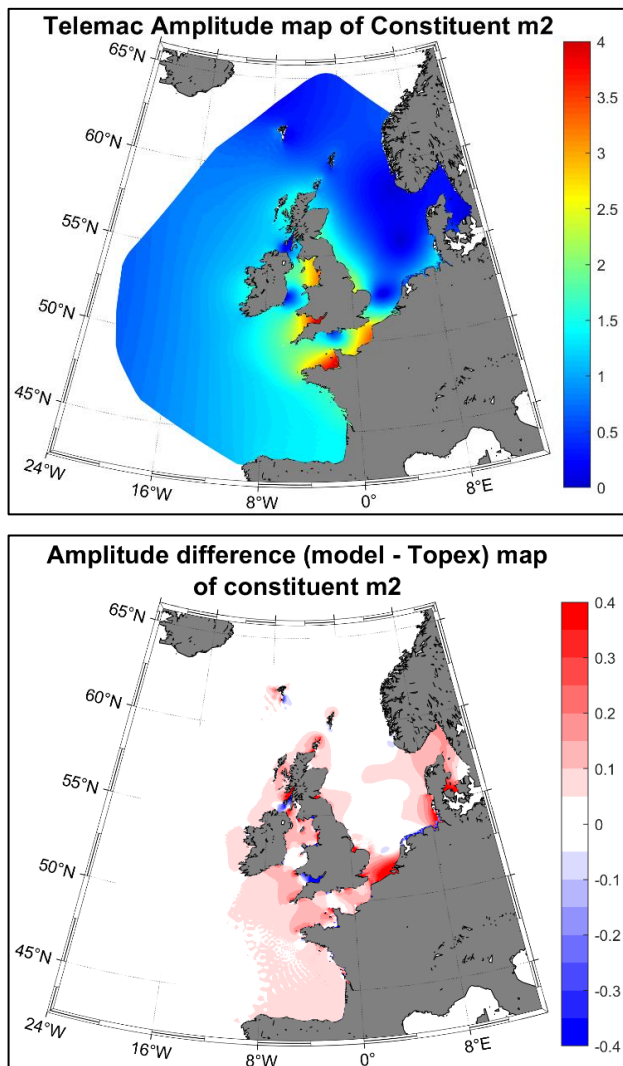


Figure 10. Co-range maps of the M2 tide from the model (top) and the difference from TPXO (bottom).

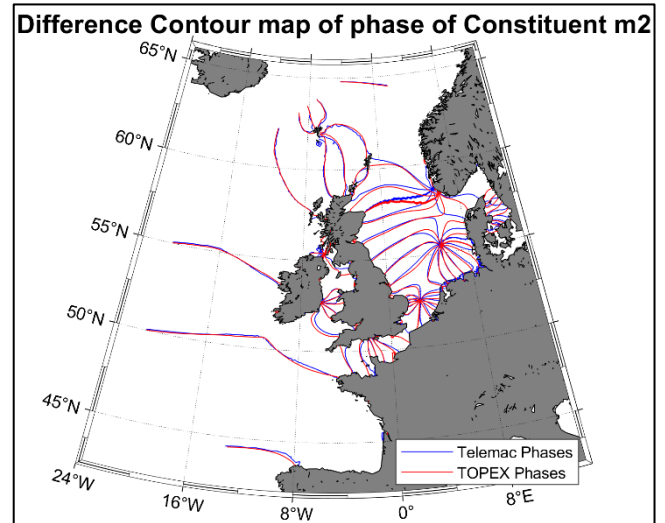


Figure 11. Co-tidal maps of M2 phase from the model and TPXO.

### N. Validation on a regional Scheldt model

Boundary nesting is a common practice for modelling phenomenon on different scales e.g. from oceanic to coastal and estuarine scale. The calibrated iCSM is a useful tool to provide boundary conditions for any model that has its boundaries inside of the iCSM domain. Figure 12 exemplifies the application of boundary nesting between iCSM and a regional model of the Scheldt Estuary. The two models are nested in the vicinity of Vlissingen, which is near the mouth the Scheldt river. The boundary nesting is performed with an in-house MATLAB toolbox which drives the calculation of flow conditions (e.g. water level and velocities) in iCSM. The results are interpolated onto the open boundary locations of the Scheldt model; thus the time-dependent flow conditions can be transported from the iCSM to the regional Scheldt model.

Figure 13 presents the RMSE of water levels in the Belgian Coastal Zone calculated from iCSM and in the Scheldt Estuary calculated from the Scheldt model. The water levels predicted by both models show decent consistency, which implies that the tidal flow is well transferred from iCSM to the Scheldt model. The averaged RMSE calculated for the Scheldt Estuary is around 10 cm. The lower RMSE at Vlissingen from the Scheldt model is obtained from the more detailed representation of the geometry and bathymetry on a finer mesh.

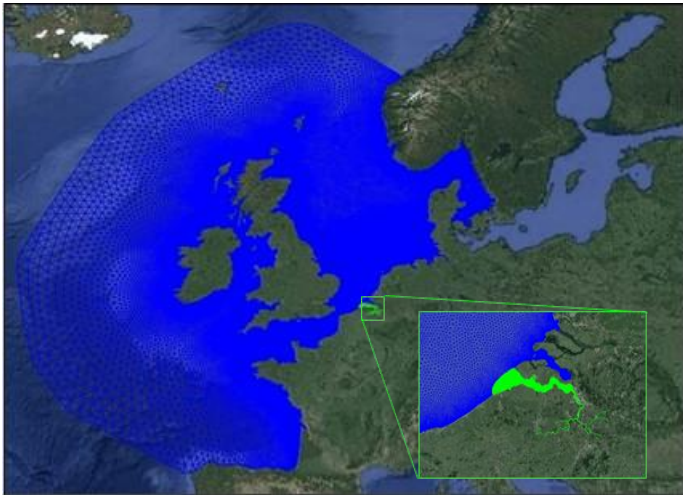


Figure 12. Boundary nesting between iCSM (blue) and the Scheldt model (green).

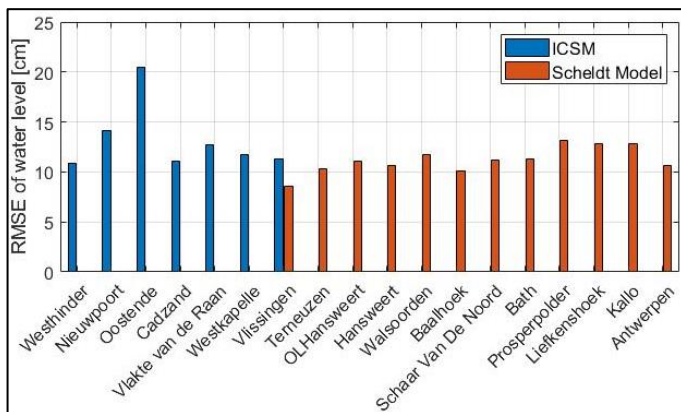


Figure 13. RMSE of water level calculated for one spring-neap cycle in 2017 from iCSM and the Scheldt Model.

## V. SUMMARY AND CONCLUSIONS

The stepwise improvement of the in-house continental shelf model of the North Sea is presented in this paper. The model is driven by the latest bathymetric and meteorological data. Using the Charnock wind drag formula with a coefficient of 0.04 leads to better predictions on peak water level during storms. Several physical processes often neglected in regional models, but of substantial importance at oceanic scale are included into iCSM.

Focusing on the Belgian coastal zone, it is noticed that the inverse barometer correction significantly reduced the bias of the water level to  $\sim 1$  cm. Including self-attraction and loading leads to a much lower bias of the M2 phase ( $\sim 1^\circ$ ). Internal tide dissipation occurring in the Bay of Biscay hardly influences the tidal characteristics. In the end, tuning the bottom roughness decreases the averaged RMSE of the water level to 13 cm.

As validation, the iCSM shows capability to predict the peak water levels during Storm Xaver. Both near-shore (near harbour of Zeebrugge) and off-shore velocities are also predicted reasonably well. The co-range and co-tidal maps generally show a good agreement with TPXO. The improved

iCSM model is used to force a regional model of the Scheldt Estuary via boundary nesting. The averaged RMSE calculated for the Scheldt Estuary is around 10 cm.

Therefore, it is concluded that the iCSM is a decent tool fulfilling both scientific and engineering needs.

## REFERENCES

- [1] Breugem, A., Verbrugge, T. and Decrop, B. (2014). A continental shelf model in TELEMAC 2D. TELEMAC User Conference, Proceedings. Presented at the TELEMAC User Conference.
- [2] Egbert, G. D., A. F. Bennett, and M. G. G. Foreman (1994). TOPEX/POSEIDON tides estimated using a global inverse model. *J. Geophys. Res.*, 99(C12), 24821–24852, doi:10.1029/94JC01894.
- [3] Zijl, F., Verlaan, M., and H. Gerritsen (2013). Improved water-level forecasting for the Northwest European Shelf and North Sea through direct modelling of tide, surge and non-linear interaction. *Ocean Dynamics*, 63, 823–847.
- [4] Flather, R. A (1984). A numerical model investigation of the storm surge of 31 January and 1 February 1953 in the North Sea. *Q. J. R. Meteorol. Soc.* 110, 591–612.
- [5] Charnock, H (1955). Wind stress on a water surface. *Q. J. R. Meteorol. Soc.* 81, 639–640.
- [6] Egbert, G. D., Ray, R. D (2000). Significant dissipation of tidal energy in the deep ocean inferred from satellite altimeter data. *Nature*. 405(6788):775–778. doi:10.1038/35015531.
- [7] Steven, R. J (2001). Parameterizing Tidal Dissipation over Rough Topography. *Geophysical Research Letters*. 28-5, 811–814.
- [8] Gordeev R. G., Kagan B A., Polyakov E. V. (1977). The effects of loading and self-attraction on global ocean tides: the model and the results of a numerical experiment. *J Phys Oceanogr* 7(2):161–170.
- [9] Apecechea, M. I., Verlaan, M., Zijl, F., Coz, C.L., Kemkamp., H. (2017). Effects of self-attraction and loading at a regional scale: a test case for the Northwest European Shelf. *Ocean Dynamics*, 67, 729–749.
- [10] Vanlede, J., Chu, K., Fonias, E. (2020). Introducing the VIMM toolbox for the (re)calibration of the SCALDIS model. TELEMAC User Conference, Proceedings.
- [11] Woodworth, P. L., Teferle, F. N., Bingley, R. M., Shennan I., Williams., S. D. P. (2009) Trends in UK mean sea level revisited. *Geophys J Int* 176(22):19–30. doi:10.1111/j.1365-246X.2008.03942.x.
- [12] Sutherland, J., Walstra, D. J., Chesher, T., Rijn, L.C., Southgate, H.N. (2004). Evaluation of coastal area modelling systems at an estuary mouth. *Coastal Engineering*. 51. 119–142.



# Introducing the VIMM toolbox for the (re)calibration of the SCALDIS model

J. Vanlede  
Flanders Hydraulics Research (FHR)  
Antwerp, Belgium  
[joris.vanlede@mow.vlaanderen.be](mailto:joris.vanlede@mow.vlaanderen.be)

K. Chu; E. Fonias  
International Marine and Dredging Consultants (IMDC)  
Antwerp, Belgium

**Abstract**— The SCALDIS model is the most recent model schematisation of the Scheldt estuary, including the Belgian Coastal Zone, the Western Scheldt (NL), the Sea Scheldt (Be.) and its tributaries. SCALDIS is implemented using TELEMAC-3D, and is being recalibrated in an ongoing project. For a reference model with a broad possible set of applications, it is important to have a calibration strategy that is sufficiently broad in scope. In order to achieve this goal, the VIMM toolbox is used for the hydraulic model. It is in-house developed at Flanders Hydraulics Research (FHR) and runs in MATLAB. It has a data model to store model results and measurements. This enables the statistical core of the code to be agnostic of model type (currently, Mike11, Delft3D, Delft-FM, Simona and TELEMAC are supported) and to be flexible with regards to measurement data sources.

## I. INTRODUCTION

The SCALDIS model [1] is a reference model on which many different applications are based. It provides the hydrodynamic input for sediment transport calculations (sand and mud). The hydrodynamic results are also used to delineate habitats in the subtidal zone of the Sea Scheldt. In particular, the maximum flood current velocity defines robust boundary values for high and low dynamic subtidal zones. This is based on an extensive validation with monitored spatiotemporal variability of benthic fauna [2]. Furthermore, the SCALDIS model is used to evaluate the effect of flood control areas on the hydrodynamics in the Scheldt estuary. Tracer dispersion experiments in the model are used to calibrate an ecosystem model. The flow fields it produces are also processed as a flow atlas, and are implemented in the shipping simulator of Flanders Hydraulics Research (FHR).

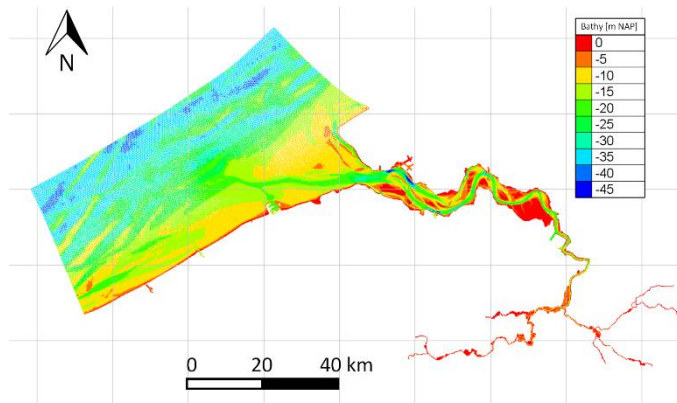


Figure 1 - Mesh and bathymetry (m NAP) of the SCALDIS 2019 model

## II. THE SCALDIS MODEL

### A. Model mesh and bathymetry

The model bathymetry (shown in Figure 1) is defined in the vertical datum “Normaal Amsterdams Peil” (NAP).

To fulfil the requirement of the nautical shipping simulator at FHR, the mesh is locally refined in zones of interest (e.g. access channels to locks). The total number of computational nodes is 478,290 with 915,622 triangular elements.

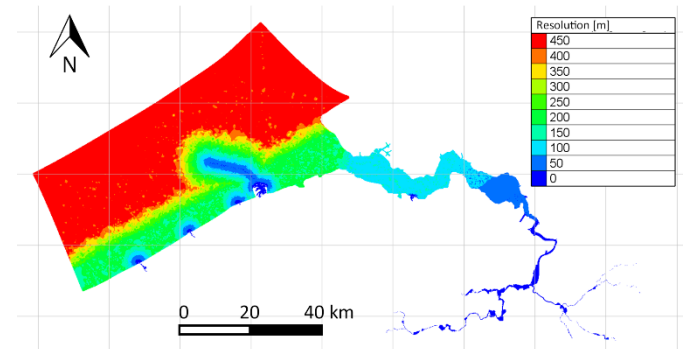


Figure 2 - Mesh resolution (edge length expressed in meters)

The SCALDIS model runs in 3D mode with 5 vertical planes at (generalised) sigma coordinates (bottom to top) 0, 0.12, 0.3, 0.6 and 1.0.

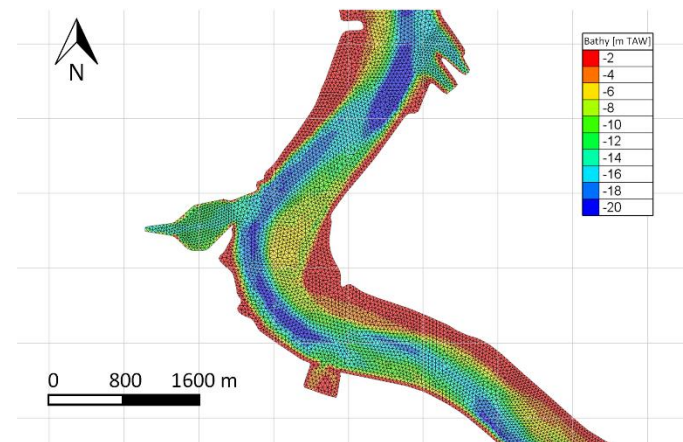


Figure 3 – Zoom of the grid, centered on the access channel to the Kallo lock



### B. Update cycle

Every 6 years, a new bathymetry becomes available that covers the Belgian part of the Scheldt estuary and its tributaries. Some zones are surveyed more frequently. The model update cycle follows this surveying cycle.

The SCALDIS 3D hydrodynamic model is maintained in an update cycle where every year, there is an *actualisation* of the model with any new bathymetric information that has become available in the preceding year. In an actualisation step, grid and model parametrisation (e.g. roughness) are not changed.

The model is subsequently verified against available measurements of that year, to keep track of the impact of the actualisation on the model skill.

Every 6 years the model is re-calibrated. The original model was calibrated against data of 2013 [3], so the re-calibration (currently ongoing) focuses on the year 2019. During re-calibration both the model grid and model parametrisation can be changed. After calibration, the model will also be validated against data from 2019 that were not used in calibration.

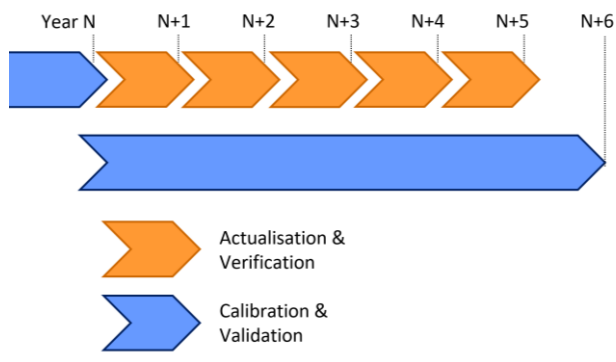


Figure 4 – The update cycle for the SCALDIS model

## III. VIMM TOOLBOX

VIMM stands for “Visualisation of Model and Measurements”, and is a toolbox developed at FHR in MATLAB for the purpose of assisting the modeller in the tasks of comparing models to measurements (e.g. during model calibration) and inter-model comparison (e.g. during scenario analysis).

### A. Why?

Comparing models to measurements, or models with each other is a non-trivial task that can require a lot of scripting to compare data in selected stations over a specified time interval. A modeller often faces multiple measurement data sources (each with their own data format), and/or different model output formats from different modelling suites.

Our aim when developing VIMM was to develop a generic codebase that can be deployed rapidly in any project, regardless of which data sources or which modelling suites are used. This improves efficiency, and ensures a high standard in code quality.

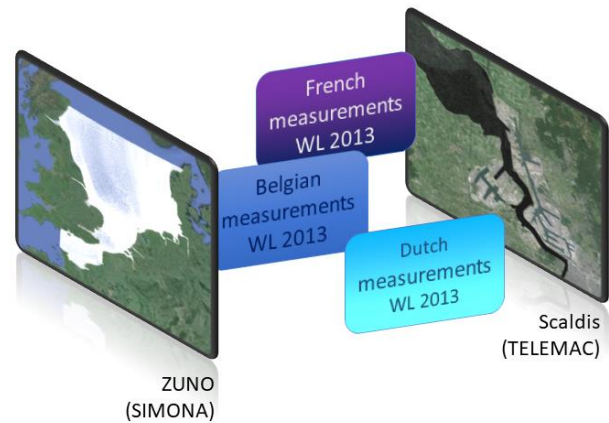


Figure 5 - Typical usecase where VIMM is useful: two models of different modelling suites (one structured, one unstructured) need to be compared against a dataset of water levels coming from different data sources

### B. VIMM as a knowledge platform

The typical use case for VIMM at FHR is model calibration and validation in a data rich environment [3] [4] [5]. The year-long use of the toolbox has de-facto standardised the model skill assessment of hydraulic models at FHR. It has helped in creating a common language to communicate on model skill, which in turn helps in the internal training of new modellers.

Because it is a shared codebase that is maintained in a central repository, any new developments are immediately available for all modelling teams. This way, knowledge on assessing model skill and calibration strategies can easily be captured and shared between researchers.

### C. Data source abstraction layer (DSAL)

A straightforward way to ensure that the code can handle different data sources (both file-based and based on webservices) is to design a data model to store measurement data. This introduces a data source abstraction layer (DSAL) in the typical workflow.

The DSAL is illustrated in Figure 6 for the case that the modeller uses water level (WL) data from different data sources. Below the DSAL in the schematised dataflow, VIMM becomes agnostic of the data source.

This requires that the VIMM data structure is self-describing (so containing both data and metadata) and feature-complete. Secondly, a set of scripts needs to be developed (typically one for every data source) to convert the data from any proprietary format to the VIMM data structure.

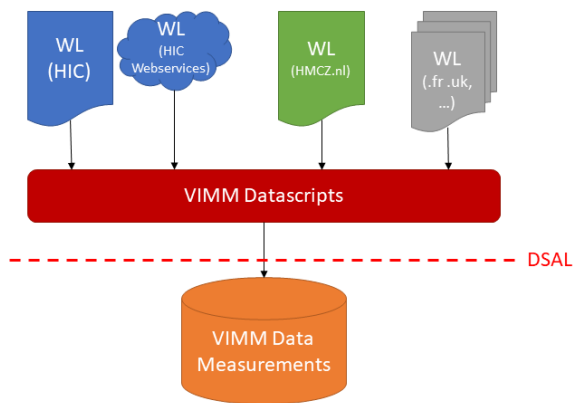


Figure 6 - The data source abstraction layer (DSAL) as the red dashed line in a VIMM workflow with different data sources of water level measurements

#### D. Model abstraction layer (MAL)

In a similar way, we can make sure that the code can easily handle different modelling software suites by creating a Model Abstraction Layer (MAL) and a self-describing data model to store model (meta)data, whether it is 1D, 2D or 3D, and for the last two cases, both for the structured and unstructured grid cases.

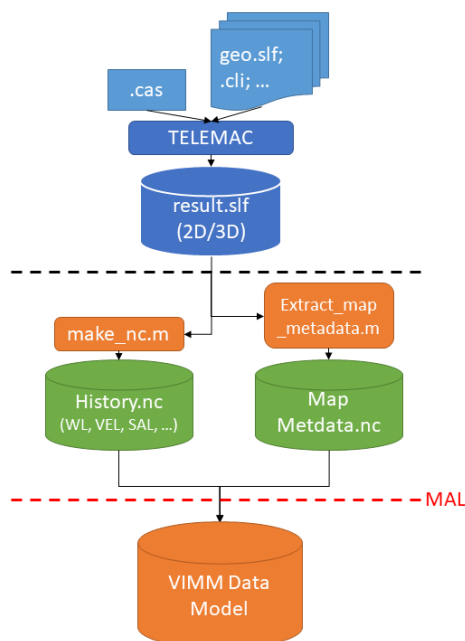


Figure 7 - The Model Abstraction Layer (MAL) as the red dashed line for a VIMM workflow involving TELEMAT results

The MAL is illustrated in Figure 7. Below this MAL, the code becomes agnostic of the modelling suite that was used.

Note a peculiarity in the case of post-processing TELEMAT results. Because the code (to the best of our knowledge) does not provide a standardised way to define output points in the model input to get history data (timeseries) in the model output, the user is left with two options. Either he/she implements a new subroutine to introduce output in history points in the

TELEMAT source code (e.g. by extending the HERMES module). This requires knowledge however by the modeller of both FORTRAN and of the code structure of TELEMAT, and may lead to possible risks in quality assurance, as errors can be made in this module. Therefore, at FHR we choose to follow the dataflow in Figure 7, in which the history output is generated in post-processing out of the map data that is the standard output in the 2D and 3D .slf output file. This is of course not the most efficient way in terms of processing steps and the size of the model output.

#### E. Modular design

Using a MAL and DSAL simplifies the task of extending the toolbox to include new measurement sources (or data formats) and/or software suites.

Currently Mike11, Delft3D, Delft-FM, Simona and TELEMAT are supported. To the best of our knowledge, there is no alternative available on the market that provides this kind of flexibility in terms of the modelling suites it can process.

The modular design also means that the VIMM processing suite (the most important components of which are shown in Figure 8) is easily extendable, since these functions are below the MAL and DSAL in the VIMM workflow, so they work on fixed data structures that are independent of the file formats of model output and measurements.

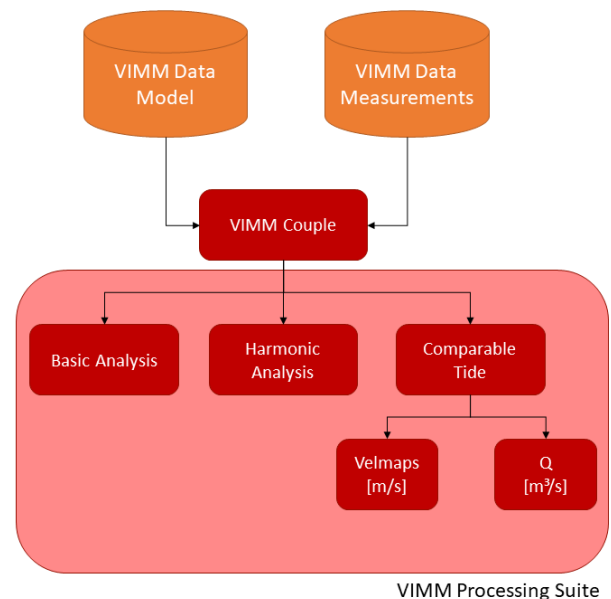


Figure 8 – Data flow in the VIMM processing suite

Two ideas of the VIMM processing suite are worked out below: Comparable Tide and Velmaps

#### IV. THE COMPARABLE TIDE (CT) METHOD

During model calibration of a hydraulic model, it is important to assess not only the model skill based on water levels (vertical tide), but also on the available velocity data (horizontal tide).

One useful data source for horizontal velocities is the so-called 13 hour measurement, in which a vessel sails the same

transect over an entire tidal cycle, while measuring the water velocity with a bottom-mounted ADCP (Acoustic Doppler Current Profiler) device.

Due to the cost of performing them, such measurements are rare and far between, both in space and in time. Suppose the modeller wants to calibrate a model for the year 2019 against a 13h ADCP velocity measurement performed in 2017. He/she has three options: (1) drop the measurement out of the calibration dataset, because the model period and measurement period do not overlap; (2) perform an additional model run of a period in 2017 so that the measured tide is a part of the modelled period; (3) search for a comparable tide in the modelled period in 2019 that closely matches the tidal conditions during the measurement in 2017.

It is clear that option (1) is sub-optimal, because we would be shrinking the calibration dataset. Option (2) is only marginally better. In the real-life usecase of the calibration of SCALDIS, we plan to use a set of 34 different ADCP campaigns distributed over the entire estuary in order to assess the model skill in reproducing velocities. If we would follow option (2), we could (in the worst case) be forced to model 34 different subperiods for every calibration step. This would significantly complicate the calibration task, as the required number of runs would quickly explode.

With the Comparable Tide (CT) algorithm, this usecase becomes much more manageable. Figure 9 illustrates the CT method.

#### A. The CT Algorithm

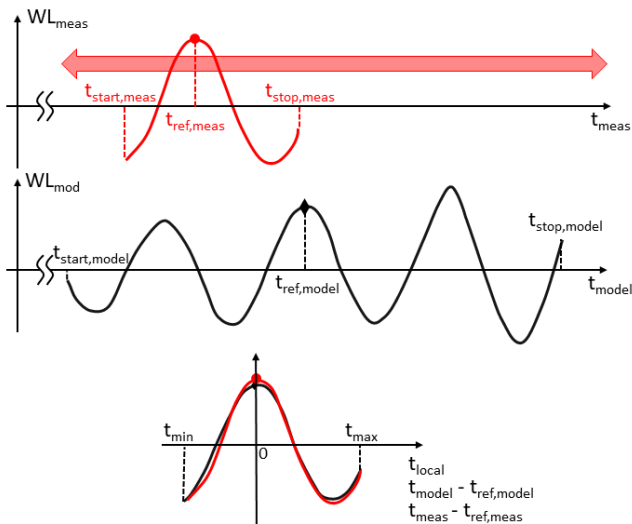


Figure 9 - The comparable tide method. Water level during the measurement campaign in red, modelled water level (at the same location) in black.

Imagine a measurement (e.g. a 13h ADCP campaign) that is executed in a timeframe  $[t_{start,meas} \ t_{stop,meas}]$ . The model run is executed in the timeframe  $[t_{start,model} \ t_{stop,model}]$ . Both periods do not necessarily overlap.

$WL_{meas}$  is the measured water level at a station nearby the measurement location, for the period of that measurement campaign. In the case where the CT method is applied on a 13h

ADCP measurement, this would be a water level station near the sailed transect.  $WL_{mod}$  is the modelled water level at the same station during the timeframe that the model results are available.

First one timestep in the measured time interval is designated as the reference time  $t_{ref,meas}$  for the measurement. In Figure 9, we pick the moment of high water inside the measured interval, but the method works for any reference time. The aim is to construct a local time axis, expressed in hours before and after this reference time.

The algorithm now searches for the  $t_{ref,model}$  that satisfies the following criteria: (1) it lies inside the modelled timeframe  $[t_{start,model} \ t_{stop,model}]$ ; (2) on the local time axis ( $t_{model} - t_{ref,model}$ ) the error between the modelled and measured water level is minimised.

In VIMM, the user is presented with two options to express this error: RMSE and the bias-corrected  $RMSE_0$ . They are calculated as follows:

$$RMSE = \sqrt{\frac{\sum_{t_{min}}^{t_{max}} (WL_{mod} - WL_{meas})^2}{N}} \quad (1)$$

$$RMSE_0 = \sqrt{\frac{\sum_{t_{min}}^{t_{max}} (WL_{mod} - WL_{meas} - \mu)^2}{N}} \quad (2)$$

$$\mu = \overline{WL_{mod} - WL_{meas}}$$

With  $[t_{min} \ t_{max}]$  the overlapping timeframe on the local time axis and  $\overline{WL_{mod} - WL_{meas}}$  the average error or bias between modelled and measured water level in the timeframe  $[t_{min} \ t_{max}]$ .

By choosing RMSE as the error quantification, the algorithm will pick the modelled period where the modelled water level in the vicinity of the measurement campaign is the closest to the water level that was measured during the campaign. The idea is that by matching the water levels, the modelled velocity expressed on a local time axis (e.g. the velocity 1 hour before high water) will match the measured velocity on that local time axis, even if the measurement timeframe  $[t_{start,meas} \ t_{stop,meas}]$  lies outside the modelled timeframe  $[t_{start,model} \ t_{stop,model}]$ .

By choosing  $RMSE_0$  as the error quantification, the reasoning is much the same, with the important difference that a (small) bias between modelled and measured water levels is not counted in the cost function that is minimised to find  $t_{ref,model}$ . What is thought here, is that it is primarily the tidal amplitude and the shape of the tidal curve in between the tidal extremes that determine the velocities. The mean tidal level has only a secondary influence on the velocities, e.g. by determining which part of the bathymetry is subject to wetting and drying. A small bias between measured and modelled tide could for instance be related to a difference in surge. The choice between RMSE and  $RMSE_0$  is ultimately up to the modeller.

Since local velocity is influenced by the bathymetry, the approximation that matching tidal conditions mean matching velocities only holds if the bathymetry in the model and the bathymetry during the measurement are not too different. In light of the morphological dynamics of the estuary, this means

that the measurement timeframe  $[t_{\text{start,meas}} t_{\text{stop,meas}}]$  should not be too far away from the modelled timeframe  $[t_{\text{start,model}} t_{\text{stop,model}}]$ . It is up to the modeller to decide which measurements he/she can still take into account in the model calibration. Another case where matching tidal conditions do not necessarily mean matching velocities would be when density currents are known to be important.

## V. THE VELMAPS MODULE

As shown in Figure 8, the output of the CT method (basically a list of  $t_{\text{ref,model}}$  for each model and for each measurement campaign) can be input for the VelMaps module. This module compares a modelled velocity field (map output, so representing a snapshot at one particular timestep in the model run) with a measured velocity transect. When using CT to determine  $t_{\text{ref,model}}$ , the timestamp of the measured transect and the modelled velocity field do not need to overlap.

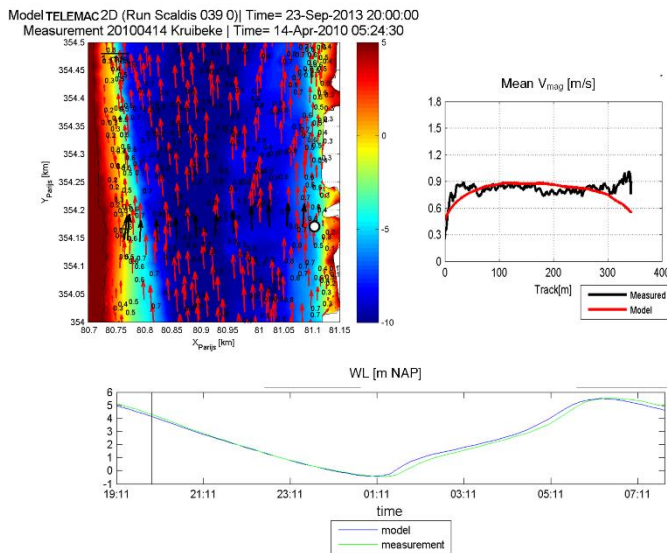


Figure 10 – Example output of the VelMaps module in VIMM

Figure 10 illustrates the different elements of the VelMaps module. The bottom panel illustrates the CT principle. Note in the figure title that we are comparing a model run of 2013 with a transect of an ADCP campaign measured in 2010. Modelled and measured velocities are compared on a local intratidal time-axis.

Once the modelled and measured velocities are superimposed, the modelled velocity field is interpolated on the measured transect. This allows the velocity magnitude to be compared in the top right panel. The following error statistics are subsequently calculated for each measured transect: bias of magnitude and direction, RMSE of magnitude and direction, and the Relative Mean Absolute Error (RMAE).

$$RMAE = \frac{\|\vec{v}_{mod} - \vec{v}_{meas}\|}{\|\vec{v}_{meas}\|} \quad (3)$$

With  $\|\cdot\|$  denoting the length of a vector and the overbar the average over the transect.  $\vec{v}_{mod}$  and  $\vec{v}_{meas}$  are depth

averaged velocity vectors. The result of equation 3 is one RMAE for every transect.

The error statistics (see also Table 3) are subsequently averaged over all transects to express the model skill in reproducing the flow distribution at that location.

If the measured transects are distributed over the estuary, this set of error statistics quantifies the model skill in reproducing the horizontal tide.

The RMAE can be classified in order to express model skill in a categorical way [6]:

TABLE 1 – ERROR CLASSIFICATION AND CATEGORISATION OF RESULTS FROM TIDAL FLOW MODELS, ACCORDING TO [6]

Model qualification		RMAE [-]
Excellent		<0.2
Good		0.2-0.4
Reasonable/fair		0.4-0.7
Poor		0.7-1.0
Bad		>1.0

Note that reference [6] actually uses an “adjusted RMAE”, where an estimate of the measurement error is subtracted from the error measure in the numerator of equation 3. In VIMM, this estimate of measurement error is set to zero by default. This means that the classification following Table 1 is actually more strict than the classification in the original reference [6].

Because  $\|\vec{v}_{meas}\|$  appears in the denominator of equation 3, the RMAE typically becomes larger during slack tide. We propose to also use the RMSE of velocity magnitude as a secondary error classification and categorisation [4].

TABLE 2 – PROPOSED ERROR CLASSIFICATION AND CATEGORISATION BASED ON THE RMSE OF VELOCITY MAGNITUDE FROM TIDAL FLOW MODELS

Model qualification		RMSE [m/s]
Good		<0.1
Reasonable/fair		0.1-0.2
Poor		0.2-0.3
Bad		>0.3

## VI. DIMENSIONLESS COST FUNCTION

When calibrating a model, it is important to start from the intended model use. While we would argue that it is always important to assess the model skill of a hydrodynamic model both for the vertical (water levels) and the horizontal tide (velocities, fluxes), the modeller still has to make a decision on the weight he/she is going to attribute to the different error statistics.

For each model run in a calibration process, the VIMM toolbox produces a broad range of different error statistics, both for the vertical and the horizontal tide. An overview of the different error statistics is given in Table 3.

Note that the different measurement data types that are listed for the vertical tide, are all derived from a regular timeseries, either by harmonic analysis, or by a local extrema analysis to



derive high water (HW) and low water (LW). On the local extrema, the error in timing and level are quantified separately. That may be important, as in some applications the correct prediction of the level of HW can be more important than getting the timing correct.

A dimensionless cost function expresses model skill in one objective factor which represents improvements (decrease) or deterioration (increase) of the model performance, when compared to a reference run. A value lower than 1 indicates an improvement [7] [8].

A dimensionless cost function can be easily derived from the statistical output of the VIMM toolbox.

$$C = \sum \frac{\max(\text{Factor}_i, \text{Threshold}_i)}{\max(\text{Factor}_{i,\text{ref}}, \text{Threshold}_i)} \times \text{Weight}_i \quad (4)$$

Each factor 'i' in the cost function is a different error statistic, with its own weight and threshold value. An expected observation error can be taken into account to assess the accuracy of the model reference in relation to the predefined modelling objective [9]. If an error statistic in the cost function drops below the threshold, the overall cost remains the same. This methodology helps to avoid giving too much weight to a very small improvement or deterioration of a parameter.

Table 3 – Overview of different error statistics that can be calculated by the VIMM toolbox.

	Measurement data type	Error statistic
Vertical Tide (water levels)	HW(LW)	RMSE of HW(LW), both of level and time
		Bias of HW(LW), both of level and time
		RMSE <sub>0</sub> of HW(LW), both of level and time
	Timeseries	Correlation coefficient
		Bias
		RMSE
		RMSE <sub>0</sub>
	Harmonic Analysis	For every component: amplitude and phase + uncertainty
		Vector difference
Horizontal Tide (velocities and fluxes)	Velocity at a fixed location	Velocity vectors: MAE and RMAE
		Magnitude: bias and RMSE
		Direction: bias and RMSE
	Fluxes	Bias
		RMSE
		Relative RMSE (to magnitude of measurement)
	Sailed ADCP	Magnitude: bias and RMSE
		Direction: bias and RMSE
		Velocity vectors: RMAE

## VII. DISCUSSION AND CONCLUSIONS

The VIMM toolbox helps the modeller to efficiently perform a quantitative skill assessment of a hydrodynamic model.

This kind of standardised method to evaluate model performance can be included in a more general modelling framework that considers performance criteria as part of an iterative modelling process (e.g. automatic calibration). The broad range of error statistics that is calculated automatically by the VIMM toolbox can easily be fed into a weighted,

dimensionless cost function that can serve as a guide during model calibration. The choice of which factors to include, with which weight and which threshold provides an objective and quantified way to communicate (and discuss) on a calibration strategy and should always be viewed in light of the intended model use.

The toolbox is coded in a generic way, so it can be easily set up for any model application, regardless of the modelling suite and the types of data sources that are used. This way the toolbox effectively becomes a knowledge platform that enables new insights to be shared more easily. The different forms of standard output of the toolbox (tables and figures) extend the vocabulary that modellers can use to communicate on model skill in a more objective way.

## References

- [1] J. Vanlede, S. Smolders, T. Maximova and M. Teles, "The unstructured SCALDIS model: a new 3D high resolution model for hydrodynamics and sediment transport in the tidal Scheldt," in *E-proceedings of the 36th IAHR World Congress*, The Hague, the Netherlands, 2015.
- [2] A. Van Braeckel, J. Speybroeck, J. Vanoverbeke, G. Van Ryckegem and E. Van den Bergh, "Habitatmapping Sea Scheldt subtidal - relation between benthic fauna and hydro- and morphodynamics (in Dutch)," INBO, Brussels - Belgium, 2018.
- [3] S. Smolders, T. Maximova, J. Vanlede, T. Verwaest and F. Mostaert, "Integraal Plan Bovenzeesche: Subreport 1 – SCALDIS: a 3D Hydrodynamic Model for the Scheldt Estuary. Version 5.0.," Flanders Hydraulics Research, Antwerp, Belgium., 2016.
- [4] K. Chu, J. Vanlede, B. Decrop, J. Verwilligen and F. Mostaert, "Update snelheidsvelden Zeeschelde en Sluistoegangen," Flanders Hydraulics Research, Antwerp, 2017.
- [5] K. Chu, J. Vanlede, B. Decrop and F. Mostaert, "Validation of North Sea models: Sub report 1 – Validation and," Flanders Hydraulics Research, Antwerp, 2020.
- [6] J. Sutherland, D. Walstra, T. Chesher, L. van Rijn and H. Southgate, "Evaluation of coastal area modelling systems at an estuary mouth," *Coast. Eng.*, vol. 51, no. 2, p. 119–142, 2004.
- [7] J. Vanlede, K. Delecluyse, B. Primo, B. Verheyen, G. Leyssen, Y. Plancke, T. Verwaest and F. Mostaert, "Verbetering randvoorwaardenmodel: Subreport 7 - Calibration of NEVLA 3D," Flanders Hydraulics Research, Antwerp, Belgium, 2015.
- [8] T. Maximova, S. Smolders and J. Vanlede, "Model calibration against different types of velocity data with a dimensionless cost function: application to the Scaldis model of the Scheldt estuary," in *Proceedings of the 22st TELEMAT-MASCARET User Conference, 15th-16th October 2015*, Daresbury Laboratory – UK, 2015.
- [9] R. Vos and P. ten Brummelhuis, "Integrated data-modelling approach for suspended sediment transport on a regional scale," *Coast. Eng.*, vol. 41, p. 177–200, 2000.

# Two-dimensional computations of Stokes drift and undertow at the near coast region

Qinghui Zhang<sup>1</sup>, Sebastian Escobar<sup>1</sup>, Erik Toorman<sup>1</sup>, Jaak Monbaliu<sup>1</sup>

<sup>1</sup>Department of Civil Engineering, KU Leuven

Leuven, Belgium

[Qinghui.zhang@kuleuven.be](mailto:Qinghui.zhang@kuleuven.be)

**Abstract**— Stokes drift is the net transport velocity experienced by water particles in the direction of wave propagation. In offshore regions, it plays a role in the fate and transport of pollutants (e.g. oil spills, plastics, POPs). When it comes to near-coastal regions, Stokes drift transports water mass towards the coastline, generating a return flow close to the bottom due to the no-flow boundary condition imposed by a beach [12]. This return flow, termed as ‘undertow’, plays an important role for the determination of wave-induced sediment transport and sandbar migration, shaping the ocean bottom close to the coast.

Under the Eulerian frame, the direct computation of Stokes drift and subsequent undertow is not possible due to their Lagrangian nature. Following the complete Lagrangian transport of individual water parcels, caused by the superimposed effect of waves and currents leads to a very huge, even impossible workload for multi-dimensional turbulent flow solvers. A mixed Eulerian-Lagrangian ‘GLM’ formalism, which splits the total motion into a mean part and an oscillatory part was proposed [1]. This framework averages on the Lagrangian feature of waves, and the final equations obtained are conveniently written under Eulerian coordinates.

In our work, we have introduced the depth-averaged GLM approach in TELEMAC-2D. The Stokes drift and the subsequent undertow were obtained from a coupled TELEMAC-2D-TOMAWAC calculation. It was shown that for a bottom with a constant slope, the wave energy breaking occurs further to the offshore than in the measurements. The undertow has also been underestimated.

The underlying reason could be attributed to the lack of a roller implementation in TOMAWAC, and the possible interference caused by the deactivation of the bottom friction laws in TELEMAC-2D for all laboratory cases listed in this study. The roller is responsible for partially transporting the wave energy during breaking and gradually releasing it during the surf zone wave propagation. The roller also brings water mass further to the coast, and leads to a larger return flow. This effect has been observed to be less important for a barred bottom and an irregular bathymetry, where the wave breaking occurs in several positions, and the effect of the roller is less significant. The influence of no bottom friction as well as the quadratic bottom friction should be investigated in further studies.

## I. INTRODUCTION

The interaction between ocean surface gravity waves caused by wind and slowly varying currents in near coastal

regions has drawn widespread attention. On one hand, the waves experience dramatic transformations in these regions and exert space- and time-dependent forces on the water body, generating water surface set-up, set-down and alongshore currents. On the other hand, the ambient currents and local water depth impact the propagation and breaking of the waves, exchanging energy with the mean currents. By means of intensive measurements and numerical computations on a rapidly eroding coast, the effects of important wave heights are emphasized in relation to the movements of sediments [12].

In practical applications, the computational cost is significant if the surface variations by short gravitational waves are resolved, a common practice is to use a spectral phase-averaged model for the wave energy propagation and transformation (third generation wind wave model). In the context of a depth-integrated hydrodynamic model, the waves influence the currents momentum distribution by adding an extra momentum flux (forcing) through the form of a divergence of radiation stress. For shoaling zones and wave breaking zones, this generates a set up and set down of the free surface. The formulation is well established in [7]. Waves influence also the mass transport of the water body through a high order phenomenon, Stokes drift. It is the net transport velocity experienced by water particles in the direction of wave propagation. In the near-coastal region, Stokes drift transports water mass towards the coastline, generating a undertow close to the bottom due to the non-flow boundary condition. In order to numerically capture the Stokes drift and undertow in nearshore models, a mixed Eulerian-Lagrangian ‘GLM’ formalism, which splits the total motion into a mean part and an oscillatory part was proposed [1]. This frame averages on the Lagrangian feature of waves, and final equations obtained are conveniently written under Eulerian coordinates.

The outline of the paper is as follows: the second section is devoted to the GLM formalism and the governing equations written in terms of the Lagrangian velocity in non-conservative forms; in the third section, the simulation of three experimental tests of wave set-up and set-down and return flow, including bathymetries composed of a constant slope, a barred bottom and an irregular topography are discussed; they are followed by the conclusion and future work.

## II. GLM FORMALISM, GOVERNING EQUATIONS

### A. Stokes drift and undertow

When surface gravity waves travel in water, the leading order of the particle movement caused by waves is periodic, forming from closed ellipses to circles depending on the water depth relative to wavelength. However, higher order mathematical calculations show that after one wave cycle, the particle experiences a net transport forward in the direction of wave propagation. It is a combined effect of particle spending more time in the forward-moving region and undergoing the forward motion at higher water height, where velocities are larger [5]. This higher-order phenomenon, termed as 'Stokes drift', is essential for certain coastal processes such as wave-induced sediment transport and subsequent coast erosion and bar migration close to near coast zone, where the zero flux beach condition imposes a return flow. Figure 1 demonstrates a typical vertical Stokes drift profile for a monochromatic wave. The resulting undertow due to the no-flow land condition is shown in figure 2.

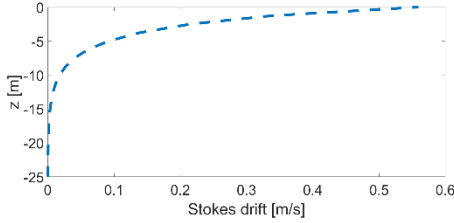


Figure 1 Stokes drift under monochromatic waves, the wave period is 5s and the wave amplitude is 1.5m. The mean water depth is 25m.

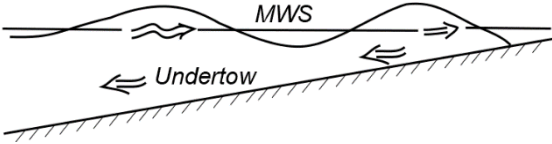


Figure 2 Stokes drift near the surface and undertow close to the bottom. Figure reproduced based on the figure in [4].

### B. Governing equations in GLM formalism

In light of considering the wave-induced Stokes drift and subsequent return flow, the shallow water equations in TELEMAC-2D are cast into a depth-averaged GLM formulation in terms of the Lagrangian velocity ( $u^L$  and  $v^L$ ). It is the sum of the averaged Eulerian velocity ( $u^E$  and  $v^E$ ) and the Stokes drift ( $\bar{u}^S$  and  $\bar{v}^S$ ). For a full three-dimensional description of the system, readers are referred to [8]. Aiming to be consistent with the TELEMAC system, we write the equation in non-conservative form:

$$\begin{aligned} \frac{\partial u^L}{\partial t} + g \frac{\partial \eta}{\partial x} &= f v^L + v_h \left( \frac{\partial^2 u^L}{\partial x^2} + \frac{\partial^2 u^L}{\partial y^2} \right) + \frac{\tau_{sx}}{\rho h} - \frac{\tau_{bx}}{\rho h} + \frac{F_x}{\rho h} \\ \frac{\partial v^L}{\partial t} + u^L \frac{\partial v^L}{\partial x} + v^L \frac{\partial v^L}{\partial y} + g \frac{\partial \eta}{\partial y} &= -f u^L + v_h \left( \frac{\partial^2 v^L}{\partial x^2} + \frac{\partial^2 v^L}{\partial y^2} \right) + \frac{\tau_{sy}}{\rho h} - \frac{\tau_{by}}{\rho h} + \frac{F_y}{\rho h} \end{aligned}$$

Where  $h$  is the water depth,  $\eta$  is the free surface level,  $f$  is the Coriolis coefficient,  $v_h$  is the horizontal viscosity,  $\tau_{sx}$  and  $\tau_{sy}$  are the wind shear stresses,  $F_x$ ,  $F_y$  are wave induced

forces  $\tau_{bx}^E$  and  $\tau_{by}^E$  are the bed shear stresses. Note that we consider that in reality, the depth-averaged Stokes drift is distributed close to the surface of the flow and thus the bottom shear stress is a function of only the quasi-Eulerian velocity, which in the vicinity of the coast is directed towards the offshore. In TELEMAC-2D, it is computed as follows:

$$\begin{aligned} \tau_{bx}^E &= -\frac{1}{2} \rho C_f u_E \sqrt{u_E^2 + v_E^2} \\ \tau_{by}^E &= -\frac{1}{2} \rho C_f v_E \sqrt{u_E^2 + v_E^2} \end{aligned}$$

where  $C_f$  is a dimensionless friction coefficient. The depth averaged Stokes drift is computed as:

$$(\bar{u}^S, \bar{v}^S) = \frac{\sigma_p \mathbf{k}_p H_s^2}{16 k_p h \tanh(k_p h)}$$

with  $\sigma_p$  and  $\mathbf{k}_p$  being the wave's intrinsic angular frequency and wave number of peak wave energy,  $H_s$  is the significant wave height and  $h$  is the water depth. The wave-driven force, thus the divergence of radiation stress:

$$\begin{aligned} F_x &= -\left( \frac{\partial S_{xx}}{\partial x} + \frac{\partial S_{xy}}{\partial y} \right) \\ F_y &= -\left( \frac{\partial S_{yx}}{\partial x} + \frac{\partial S_{yy}}{\partial y} \right) \end{aligned}$$

where the radiation stress components are given by:

$$\begin{aligned} S_{xx} &= \rho g \iint [n \cos^2 \theta + n - 0.5] E(f, \theta) df d\theta \\ S_{xy} &= \rho g \iint [n \sin \theta \cos \theta] E(f, \theta) df d\theta \\ S_{yy} &= \rho g \iint [n \sin^2 \theta + n - 0.5] E(f, \theta) df d\theta \end{aligned}$$

where  $n$  is the ratio between the wave's group velocity and the phase velocity.  $E(f, \theta)$  is the spectral density of the surface wave elevation.  $f$  is the wave frequency and  $\theta$  is the wave's propagation direction.

The two-way coupling of TELEMAC-2D and TOMAWAC is achieved in the following manner: TELEMAC-2D provides water depth and Lagrangian currents to TOMAWAC for the wave action conservation equation. Stokes drift and wave driven force are computed in TOMAWAC with wave parameters, and they are passed into TELEMAC-2D. The former provides extra mass transport together with the mean current, and the latter brings an added momentum flux into the force balance of currents. The effects of the coupling will be validated in the following theoretical tests, where the stationary wave shoaling and breaking exert space varying forces on currents, leading to a new equilibrium water level with set-up and set-down. Moreover, the undertow in these tests have been measured and compared to the numerical simulations.

## III. VALIDATION OF TELEMAC-2D-TOMAWAC IN THE GLM FORMALISM: WAVE SHOALING & BREAKING

The developed 2D averaged wave current interaction model has been validated with laboratory tests. The first test case consists of a laboratory test for which the bottom topography presents a constant slope. The test case has been presented in [11], with the undertow velocity measured by an Argon-Ion

Laser Doppler Velocimeter. The length of the test domain is 25m, and the width is 10m. At the lateral horizontal boundaries, a zero-gradient free surface boundary condition has been imposed. A fixed 0m free surface has been imposed at the offshore boundary, which leads to a water depth of 0.46 meters. The bathymetry has a constant slope of 1/35 therefore the bottom meets the surface level of 0m at 16.1m length (see figure 3).

A steady TMA spectrum is imposed at the offshore boundary, with a significant wave height of 0.0829m, and a peak period of 1.5s. The main direction of the waves is perpendicular to the coast, with a boundary directional spread of 1500, thus leading to a very narrow angular distribution function (see figure 4).

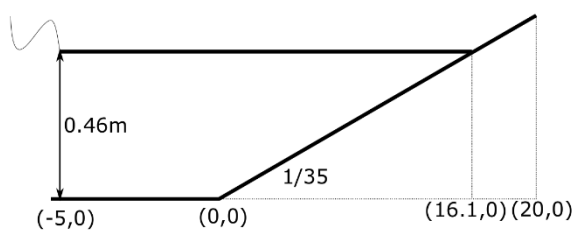


Figure 3 Bottom configuration for the test case of constant slope.

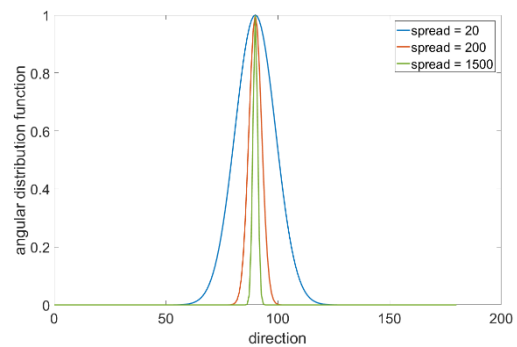


Figure 4 Angular distribution function for computing the boundary spectrum as a function of the directional spreading.

From a zero surface initial condition, the wave driving forces generate a velocity that transports water mass, and slowly brings the surface to an equilibrium state, balancing the radiation stress gradient in the cross-shore direction. The computed wave height, free surface (wave set-up, set-down) and undertow have been compared to the measurements (see figure 5). The wave height (wave energy) demonstrates a slight delay compared to the measurements. The free surface wave set-up has been well captured, except for the very shallow part. It could be related to the application of a numerical clipper in TELEMAC-2D to avoid negative water depth (for water depths less than 5cm). The undertow has been well captured at the deep part, but in the shallower zone it is underestimated. Both the undertow and delay of wave breaking could be caused by lack of a roller, which is a phenomenon that stores the wave energy and brings an extra mass of water to the coast. This is further testified by conducting a second test case, where the bottom is composed of a barred beach, leading to an extended wave breaking, which occurs in several positions.

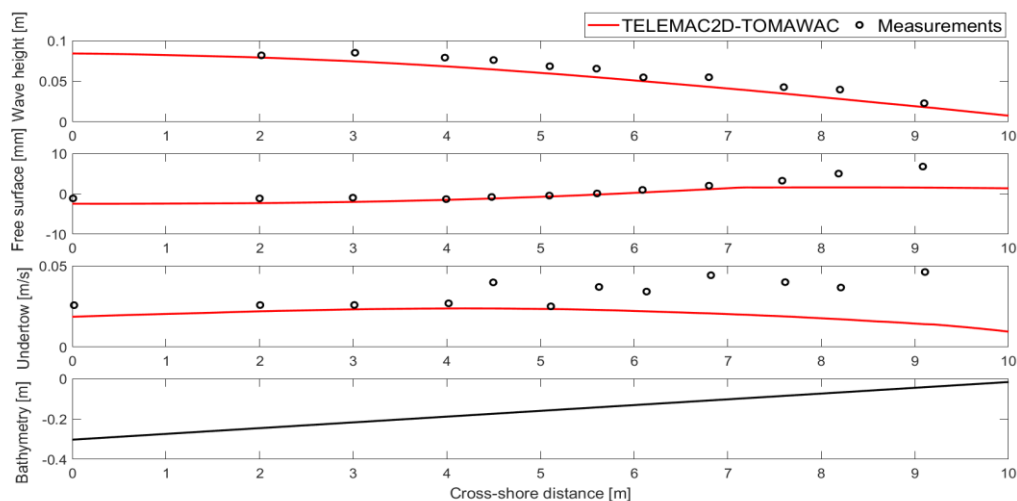


Figure 5 Simulate wave height, free surface and undertow have been compared to the measurements presented in [11].



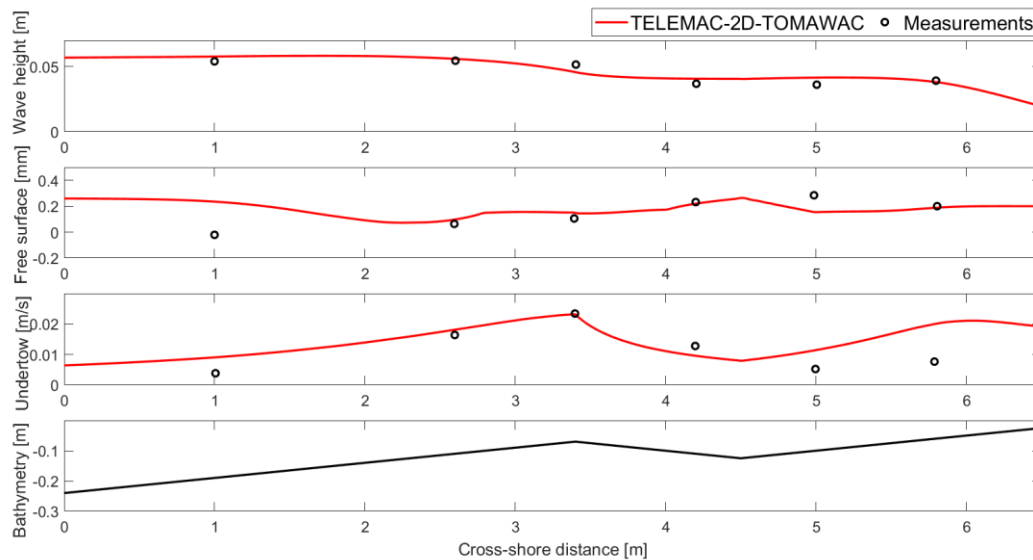


Figure 6 Simulate wave height, free surface and undertow have been compared to the measurements for the barred test case presented in [9].

The laboratory barred test case was presented in [9]. It is a one-dimensional case, with a length of 17m and a width of 2m. Similar to the previous case of the constant slope, at lateral boundaries a zero-gradient free-surface level was applied. The water depth at the offshore is 0.32m, where a Bretschneider-Mitsuyasu spectrum was imposed, with a rooted-mean-squared wave height of 0.0397m and a peak period of 0.945s. Other settings are identical to the previous case. The comparison between the computed quantities and the measurements is shown in figure 6. Compared to the case of a constant slope, the wave breaking occurs at two locations where the water depth decreases, with a slight wave shoaling in between. The wave height variation along the propagation is better captured, yielding also a satisfying free surface variation. The undertow variation and its magnitude are better simulated as well, with no systematic underestimation observed as for the previous test case.

The third case demonstrates to be a prototype of a large field campaign (DUCK 94 field experiment [6]). It has been presented in [10]. The model length is 110m long and 40m wide. The water depth at the left boundary is 4.6m, where a TMA spectrum with a wave height of 0.5 m and a peak period of 4s has been imposed. The irregular bottom profile has been obtained by approximating the bar geometry for the average profile observed of the DUCK94 campaign at a 1:3 scale. The undertow velocity measurements have been obtained with an Acoustic Doppler Velocimeter. The numerical simulation results have been compared to the measurements, and it is shown in figure 7.

The wave breaking has been well captured. In terms of the free surface, the set-down has been underestimated, which could be related to the imposed water depth boundary condition at the offshore. The overall undertow profile has been well reproduced as well, compared to the case of the constant slope.

#### IV. CONCLUSIONS AND FUTURE WORK

In this study, the Stokes drift and undertow computation have been implemented in the TELEMAC-2D-TOMAWAC system. Three validation test cases in laboratories have been demonstrated, yielding an overall satisfying cross-shore wave height, free surface set-up and set-down as well as the undertow, especially for the barred beach and a bathymetry composed of an irregular profile. For the test case of a constant slope, similar numerical settings produce a delayed wave breaking (to the offshore direction) compared to the measurements, as well as an underestimated undertow to an order of two. It could be related to the lacking of a roller, which stores partially the wave energy during breaking, and releases it gradually along with the wave propagation in the surf zone. The differences in model performances could also be attributed to the possible interference caused by the deactivation of the bottom friction laws in TELEMAC-2D for all laboratory cases listed in this study.

Another possibility is that to evaluate the Stokes drift for a spectrum, in our study, bulk parameters (such as the peak frequency wave number) have been used. It could also be evaluated for each component and then the total Stokes drift is the sum from the contribution of all components.

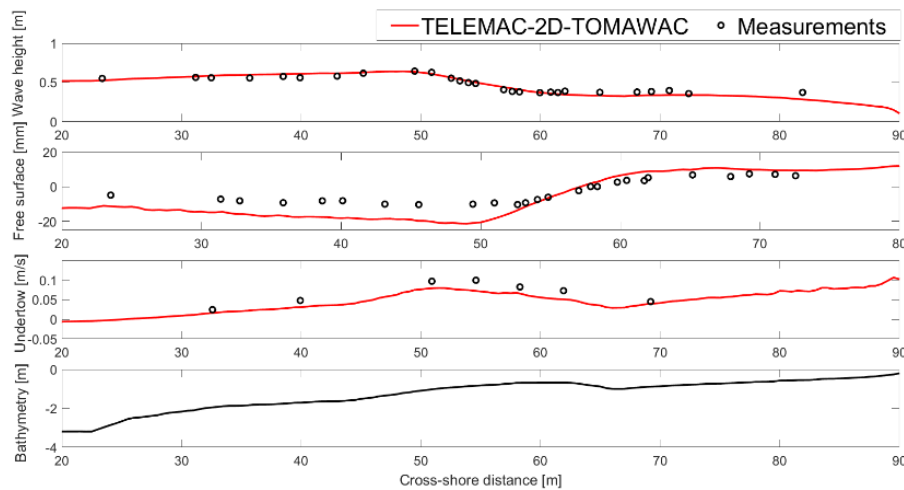


Figure 7 Simulate wave height, free surface and undertow have been compared to the measurements for the barred test case presented in [10].

#### ACKNOWLEDGEMENT

This work has been carried out in the framework of the CREST IWT-150028 project ([www.crestproject.be](http://www.crestproject.be))

#### REFERENCES

- [1] Andrews, D.G, McIntyre, M.E. (1978), An exact theory of nonlinear waves on a Lagrangian-mean flow, Vol. 89, part 4, pp. 609-646
- [2] Ardhuin, F, Rasle, N, Belibassakis, K. (2008), Explicit wave-averaged primitive equations using a Generalized Lagrangian mean, Vol. 20, Issue 1, pp. 35-60
- [3] Bühler, O. (2014), Waves and mean flows (2nd edition), Cambridge University Press.
- [4] Buhr Hansen, J, Svendsen I.A. (1984), A theoretical and experimental study of undertow, Proc. 19<sup>th</sup> Int. Conf. on Coastal Engineering, Houston: ASCE, pp 2246-2262.
- [5] Prandle, D., Hargreaves, J.C., McManus, J.P., Campbell, A.R., Duwe, K., Lane, A., Mahnke, P., Shimwell, S., Wolf, J. (2000), Tide, wave and suspended sediment modelling on an open coast – Holderness, Coastal Engineering, Vol.41, pp. 237-267.
- [6] Garcez Faria, A.F.G., Thornton, E.B., Lippmann, T.C., Stanton, T.P. (2000). Undertow over a barred beach, J. Geophys. Res., 105 (C7), 16999-1 7010
- [7] Longuet-Higgins, M., Stewart, R. (1962), Radiation stress and mass transport in gravity waves, with application to surf beats. J. Fluid Mech., Vol. 13, pp 481-504
- [8] Maria João Teles, Thierry Fouquet, Antonio Pires-Silva, Michel Benoit (2019), Computation of 3D coastal hydrodynamics through the vortex force formalism implemented by coupling TOMAWAC and TELEMAC-3D, Proceedings of the TELEMAC-User Conference 2019
- [9] Okayasu, A., Shibayama, T., Horikawa, K. (1998), Vertical variation of undertow in surf zone. In Proceedings, 21st international Conference on Coastal Engineering, ASCE, 1998.
- [10] Scott, C.P., Cox, D.T., Maddux, T. B., Long, J.W. (2005), Large-scale laboratory observations of turbulence on a fixed barred beach. Measurement Science and Technology 16, 1903–1912.
- [11] Sultan, N.J. (1995), Irregular wave kinematics in the surf zone, Ph.D thesis, Texas A&M University (1995).
- [12] Van den Bremer, T.S, Breivik, Ø (2018), Stokes drift, Philosophical Transactions. Series A, Mathematical, Physical, and Engineering Sciences, Vol. 376, pp. 2111.

**Appendix Subroutine for computing Stokes drift:**

```

SUBROUTINE UVSTOKES_2D
    & (UST, VST, FS,
    DEPTH, NPLAN, NF, NPOIN2, FREQ, DFREQ, TAILF, SCOSTE, SS
    INT)

    USE BIEF
    USE DECLARATIONS_TOMAWAC, ONLY: DEUPI
    USE INTERFACE_TOMAWAC

    IMPLICIT NONE

    INTEGER, INTENT (IN)          :: NPLAN, NF, NPOIN2
    DOUBLE PRECISION, INTENT (IN) :: TAILF,
    SCOSTE (NPLAN)
    DOUBLE PRECISION, INTENT (IN) ::
    FS (NPOIN2, NPLAN, NF)
    DOUBLE PRECISION, INTENT (IN) :: DEPTH (NPOIN2)
    DOUBLE PRECISION, INTENT (IN) ::
    FREQ (NF), DFREQ (NF)
    DOUBLE PRECISION, INTENT (IN) :: SSINTE (NPLAN)
    DOUBLE PRECISION, INTENT (OUT) :: UST (NPOIN2),
    VST (NPOIN2)

    DOUBLE PRECISION DTETAR, E (NPOIN2)
    DOUBLE PRECISION TAUX1 (NPOIN2), TAUX2 (NPOIN2)
    DOUBLE PRECISION TAUX3 (NPOIN2), TAUX4 (NPOIN2)
    DOUBLE PRECISION FP (NPOIN2)
    DOUBLE PRECISION SIGMA (NPOIN2)
    DOUBLE PRECISION XK (NPOIN2)
    DOUBLE PRECISION VARIAN (NPOIN2)
    DOUBLE PRECISION UV_STOKES (NPOIN2)
    DOUBLE PRECISION MEANDIR (NPOIN2)

    INTEGER IPP
    DOUBLE PRECISION GAMMA_BREAKING

    DTETAR=DEUPI/DBLE (NPLAN)
    GAMMA_BREAKING= 0.4D0

    DO IPP=1,NPOIN2
        UST (IPP) = 0.D0
        VST (IPP) = 0.D0
    ENDDO

    ! COMPUTE PEAK FREQUENCY FOR ALL THE NODES IN 2D
    MESH
    CALL FREPIC (FP, FS, FREQ, NF, NPLAN,
    NPOIN2, TAUX1, TAUX2)

    ! COMPUTE PEAK SIGMA AND K CORRESPONDING TO PEAK
    FREQUENCY
    DO IPP = 1, NPOIN2
        CALL WNSCOU (XK (IPP), FP (IPP), DEPTH (IPP))
    ENDDO

    ! COMPUTE TOTAL ENERGY/VARIANCE (UNIT: M2)
    CALL TOTNRJ
        & (VARIAN, FS, FREQ, DFREQ, TAILF,
        & NF, NPLAN, NPOIN2)

    ! COMPUTE TOTAL STOKES DRIFT
    DO IPP = 1, NPOIN2
        SIGMA (IPP) = DEUPI*FP (IPP)
        IF (DEPTH (IPP) .GT. 0.01D0) THEN
            UV_STOKES (IPP) =
            SIGMA (IPP)*VARIAN (IPP)/DEPTH (IPP) /
            TANH (XK (IPP)*DEPTH (IPP))
        ELSE
            UV_STOKES (IPP) = 0.D0
        ENDIF
    ENDDO

    ! COMPUTE MEAN DIRECTION
    CALL TETMOY (MEANDIR, FS, SCOSTE, SSINTE,
    &
    NPLAN, FREQ, DFREQ, NF, NPOIN2, TAILF, TAUX1,
    &
    TAUX2, TAUX3, TAUX4)

    DO IPP = 1, NPOIN2
        UST (IPP) = UV_STOKES (IPP)*SIN (MEANDIR (IPP))
        VST (IPP) = UV_STOKES (IPP)*COS (MEANDIR (IPP))
    ENDDO

    RETURN
END

```

International Marine and Dredging Consultants (IMDC)  
Van Immerseelstraat 66  
2018 Antwerp  
Belgium  
[tuc2020@imdc.be](mailto:tuc2020@imdc.be)  
<https://tuc2020.org/>

ISBN 9789464207194

